



Durham E-Theses

Towards Engineering and Understanding of Guest Host Interaction Between Dopants and Liquid Crystals in Liquid Crystal Displays

APPLEGARTH, LUCAS,M,S,G,A

How to cite:

APPLEGARTH, LUCAS,M,S,G,A (2010) *Towards Engineering and Understanding of Guest Host Interaction Between Dopants and Liquid Crystals in Liquid Crystal Displays*, Durham theses, Durham University. Available at Durham E-Theses Online: <http://etheses.dur.ac.uk/169/>

Use policy

The full-text may be used and/or reproduced, and given to third parties in any format or medium, without prior permission or charge, for personal research or study, educational, or not-for-profit purposes provided that:

- a full bibliographic reference is made to the original source
- a [link](#) is made to the metadata record in Durham E-Theses
- the full-text is not changed in any way

The full-text must not be sold in any format or medium without the formal permission of the copyright holders.

Please consult the [full Durham E-Theses policy](#) for further details.

Academic Support Office, Durham University, University Office, Old Elvet, Durham DH1 3HP
e-mail: e-theses.admin@dur.ac.uk Tel: +44 0191 334 6107
<http://etheses.dur.ac.uk>

Durham University

A Thesis Entitled

**Towards Engineering and Understanding of
Guest Host Interaction Between Dopants
and Liquid Crystals in Liquid Crystal
Displays**

Volume 1 & 2

Submitted By

By Lucas Michael Samuel George Alfred Applegarth MChem (Hons)

Department of Chemistry

University Science Laboratories

South Road, Durham

DH1 3LE

Submitted in partial fulfillment of the requirements for the degree of

Doctor of Philosophy, University of Durham

2010

This is dedicated to my hero, my father. A loving man to which I owe a lot to, and in the words of the great man himself.....

“How lucky am I?”

- Michael Applegarth

You may consider yourself lucky dad but I know I am lucky to have you. I couldn't have done this without you and I am only here due to your continued support and belief in me. Thank you and I love you.

MEMORANDUM

The work described in this thesis was carried out at Durham University between August 2005 and January 2009. This thesis is the work of the author, except where acknowledged by reference and has not been submitted for any other degree.

This work has been presented, in part, at:

- Chemistry Department Final Year Symposium, Durham University
May 2008

STATEMENT OF COPYRIGHT

No part of this thesis may be reproduced by any means, nor transmitted, nor translated into any machine language or hand written without the written permission of the author.

ACKNOWLEDGEMENTS

I would like to thank Dr. Andrew Beeby and Dr. Paul Low, my academic supervisors for their priceless help, guidance and support throughout my PhD and work. Without their help as a student, peer and friend this would not have been possible whilst reigning in my elaborate, articulate and flamboyant methods of communication.

Thanks also go to Dr. Lars Olof-Palssön and all at SONY MSL, Stuttgart, namely Tony Roberts, Pinar Kilickiran, Akira Masutani, Akio Yasuda, Gabriele Nelles, Nadine Hollfelder, and to SONY and the EPSRC for funding.

I thank all members, past and present, of the Beeby and Low research groups for the invaluable assistance, especially Ben Coombs for the earthquake tests and invaluable core muscle training.

I would like to thank the highly professional technical staff of the Durham University Chemistry Department for their help, without it this thesis would not have been possible. Namely Dr. Alan Kenwright, Dr. Jackie Mosely, Mr Ian McKeag, Mrs Catherine Heffermen, Dr. Mike Jones, Mrs Amber Thompson, Miss Hazel Sparkes, Mr Mike Probert, Dr. Andres Goeta, Mr Peter Coyne, Mr Malcolm Richardson, Neil Holmes, Judith Magee and Kelvin Appleby.

I would like to thank my family, especially my Parents, Katharine, Dan and Rebecca for their infinite support during my years at Durham University. For putting up with my stressed times and simplifying the necessities of my work. Without their continual guidance this thesis would have taken an eternity to write.

I would like to the John Dunwell, Seb Spain, Pippa Monks, John Coffey, Benjamin Coffey, Julian Farmer, Nick Hughes, William Tarran, Helen Watson, Emma Flynn, Richard Ward, Joe Lenthall, Jennifer Holden, Neil Brown, Mark Little, Jamie Little and all other friends for the good times I have had during my years at Durham.

Thank you all...

ABSTRACT

Liquid crystal displays are intricate devices which consist of many cells that are filled with liquid crystal hosts. The operation of the liquid crystal cell is to modulate the polarisation of light, by varying their birefringence, which in turn can be used to control the intensity of light and colour as a function of time. Many individual cells grouped together can be controlled to give specific intensity of light and colour, to build up images that are viewed on displays, i.e. pictures on TV's.

The properties of the liquid crystalline material used in a cell dictate the performance of the device which they are used. Commercially used liquid crystal material is typically a multi-component system that exhibits many physical properties such as birefringence, dielectric anisotropy, voltage holding ratio, visco-elastic, guest-host effect and the kinetic switching response time of the cell between the on state and off state. By manipulating the physical properties we can exert specific control over the properties of the cell of particular importance in display applications is the speed with which cells can be turned between the on and off state; these are known as the rise and decay response times respectively.

Introducing guest molecules into the liquid crystal host may alter the dielectric anisotropy which potentially increases the speed of the switching process, making the device faster. Guest molecules must be compatible with the dielectrically positive or negative liquid crystal host allowing good mixing of the components and alignment between the guest molecule and liquid crystal molecule. This compatibility is important as it allows both,

guest and host, to align with the applied electric field when turned on giving the on state of the cell and when turned off allowing both to re-align with the alignment layer in the cell bringing to the cell order of the medium back to the off state of the cell. The time taken for the cell to reach the on state and off state is an important part of this study.

Dopants have been designed with a head, tail and linker core moiety that are compatible with dielectrically positive and negative liquid crystals. Head groups will have polar substituents such as heteroarenes, fluorine and bromine, to exert control over the dielectric anisotropy. Alkoxy or alkyl tails were selected to increase solubility and size compatibility with the liquid crystal hosts. The linkers between the two arenes were selected as acetylene (linear, large Raman cross-section) and ether, methylene and propylene (to bring about a bend in the molecule).

The switching times for liquid crystal devices are studied using an electro-optic method developed in conjunction with SONY MSL (Stuttgart). These studies enable analysis of the transmission of light through the cell as it goes from the on/off state as a function of time and applied potential. By comparison with the currently used liquid crystal materials our work shows that the level of doping, the length of the tail and the nature of the linker do affect the switching time significantly. It is shown that a non-linear linker, which introduces a *'bite angle'* within the guest molecule brings about the best increase in response times.

Time-Resolved Raman spectroscopy studies of a liquid crystal cell during the turn on/off process were made. These demonstrate the capability of this technique to measure the

orientation of the molecules as a function of time as well allowing the independent motion of the guest and host molecules during the switching process. Raman spectroscopy gives a useful insight into the behaviour of the guest and host materials in an operating liquid crystal cell.

ABBREVIATIONS

+	Slight decrease in response time
++	Significant decrease in response time
-	Slight increase in response time
--	Significant increase in response time
2D	2 dimension
3D	3 dimension
AC	Alternating current
AM	Active matrix
Ar	Aryl
Bu	Butyl
CMC	Critical micelle concentration
CRT	Cathode ray tube
CTAB	Cetyltrimethylammonium bromide; cetyl = hexadecyl
CW	Continuous wave
d	cell thickness, the liquid crystal cell gap between the layers
DCM	Dichloromethane
DFT	Density functional theory
DME	1,2-dimethoxyethane
<i>E</i> ₁₀	The electric field at 10% of transmitted light
<i>E</i> ₉₀	The electric field at 90% of transmitted light
<i>E</i>	Applied electric field

EO	Electro-optic
Et	Ethyl
E_{th}	Electric field threshold
E_x	The applied electric field at the corresponding x% of transmitted light
GC-MS	Gas Chromatography Mass Spectroscopy
Het	Heteroarene
HR	Holding ratio
IPS	In-plane switching
ITO	Indium tin oxide
LC	Liquid crystal
-LC	Dielectrically negative liquid crystal
+LC	Dielectrically positive liquid crystal
LCD	Liquid crystal display
Me	Methyl
n	Director
NEt ₃	Triethylamine
NMR	Nuclear magnetic resonance
<i>p</i>	Para substituted
P ₂	Second Legendre polynomial
PI	Polyimide
Pd	Palladium
PPh ₃	Triphenylphosphine
S _m	Smectic phase, prefix m denotes the phase A-C, E-K

S	Order parameter
T_{NI}	Nematic-isotropic transition temperature (clearing temperature)
THF	Tetrahydrofuran
TFT	Thin film transistor
TMSA	Trimethylsilylacetylene
TN	Twisted nematic
TN-LCD	Twisted nematic liquid crystal display
TR	Time-Resolved
UV-Vis	Ultraviolet-Visible
V	Applied potential
V10	Voltage at 10% of transmitted light
V90	Voltage at 90% of transmitted light
VA	Vertically aligned
VA-LCD	Vertically aligned liquid crystal display
VHR	Voltage holding ratio
V_x	The applied potential at the corresponding x% of transmitted light
ν	Vibrational frequency (and mode)
α	Polarisability
α_x	Leslie viscosity parameters
ϵ_0	Dielectric permittivity of free space
ζ	Displacement co-ordinate
$\Delta\epsilon$	Dielectric anisotropy
K_x	Elastic constant

Δn	Birefringence
η	Shear viscosity
μ	Dipole moment
γ	Rotational viscosity

CONTENTS

THESIS VOLUME 1

1. Chapter 1: Introduction.....	1
1.1. A Brief History.....	2
1.2. The Fourth State of Matter.....	2
1.3. Liquid Crystals (LC).....	3
1.3.1. Classification of Liquid Crystals.....	3
1.3.1.1. Lyotropic Liquid Crystals.....	5
1.3.1.2. Thermotropic Liquid Crystals.....	6
1.3.1.2.1. Smectic Phase Liquid Crystal.....	7
1.3.1.2.2. Nematic Liquid Crystals.....	9
1.3.1.2.3. Other Thermotropic liquid crystal phases.....	9
1.4. Properties of Liquid Crystals.....	10
1.4.1. Basic Overview of Properties.....	10
1.4.1.1. Order Parameter (S).....	11
1.4.1.2. Dielectric Properties ($\Delta\epsilon$).....	13
1.4.1.2.1. Dielectric Anisotropy by Design.....	15
1.4.1.3. Birefringence (Δn).....	17
1.4.1.4. Viscosity (γ).....	18
1.4.1.5. Elastic Constants (K).....	23
1.4.1.6. Voltage Holding Ratio (VHR).....	26
1.4.1.7. Guest-Host Interactions.....	27

1.5. The Initial Understanding and Application of the Physical Phenomenon ...	29
1.6. Liquid Crystals Industrial Era Begins	30
1.6.1. Beginning of Commercial Liquid Crystal Technology.....	31
1.6.2. Brief Overview of the Critical Advances in Last 30 Years.....	32
1.7. Common Types of Present Day Liquid Crystal Display Technology.....	35
1.7.1. Twisted-Nematic Liquid Crystal Displays (TN-LCD)	35
1.7.2. Vertically Aligned Liquid Crystal Displays (VA-LCD).....	37
1.8. Aims and Objectives	38
1.9. References	39
2. Chapter 2: Synthesis of Guests for LC Hosts	49
2.1. Dopant Structure	50
2.2. Synthetic Strategy	53
2.3. Organic Reactions	53
2.3.1. Synthesis of Acetylenic Dopants.....	53
2.3.1.1. Sonogashira Cross Coupling Reaction.....	54
2.3.1.1.1. The Sonogashira Reaction Mechanism.....	55
2.3.1.1.2. Step 1: Catalytic Initiation	56
2.3.1.1.3. Step 2: Oxidative Addition.....	57
2.3.1.1.4. Step 3: Transmetallation	58
2.3.1.1.5. Step 4: Reductive Elimination	59
2.3.2. Higher Yielding Synthetic Route to Acetylenic Dopants	59
2.3.3. Synthesis of Acetylenic and Ether Dopants	62
2.3.4. Synthesis of ‘CR ₂ ’ Bridged Dopants.....	64

2.3.4.1. Synthesis of ‘CR ₂ ’ Methyl Unit Linker Dopants	64
2.3.5. Synthesis of Propylene Linker Dopants	65
2.4. References	66
3. Chapter 3: Electro-Optic Measurements and Analysis	70
3.1. Introduction	71
3.1.1. Introduction to Electro-optics.....	72
3.1.2. Switching in LC	74
3.2. Dopant Structure Reasons and Relations to EO.....	75
3.3. Preparation of LC Samples and LC Cells	77
3.3.1. Preparation of LC Samples	77
3.3.2. LC Cells and their Preparation	77
3.4. SONY EO Experimental Setup	81
3.4.1.SONY EO Experimental Rise Response Time Measurements	81
3.4.2. SONY EO Experimental Decay Response Time Measurements..	82
3.4.3. SONY EO Experimental VHR Measurements	83
3.5. EO Results and Discussion	83
3.5.1. EO Response Time Measurements for Acetylenic Linker Dopants	84
3.5.1.1. Acetylenic Linker Dopants in Dielectrically Negative LC Blends.....	85
3.5.1.1.1. Rise Time	85
3.5.1.1.2. Decay Time	87
3.5.1.1.3. Results Summary.....	89

3.5.1.2. Acetylnic Linker Dopants in Dielectrically Positive LC	
Blends.....	90
3.5.1.2.1. Rise Time	90
3.5.1.2.2. Decay Time	91
3.5.1.2.3. Results Summary.....	92
3.5.2. Electro-optic Response Time Measurements for Biphenyl Ether Linker	
Dopants	93
3.5.2.1. Biphenyl Ether Linker Dopants in Dielectrically Negative	
LC Blends.....	93
3.5.2.1.1. Rise Time	93
3.5.2.1.2. Decay Time	96
3.5.2.1.3 Results Summary.....	98
3.5.3. Electro-optic Response Time Measurements for ‘CR ₂ ’ Bridge Linker	
Dopants	99
3.5.3.1. ‘CR ₂ ’ Bridge Linker Dopants in Dielectrically Negative LC	
Blends.....	99
3.5.3.1.1. Rise Time	99
3.5.3.1.2. Decay Time	101
3.5.3.1.3 Results Summary.....	103
3.5.3.2. ‘CR ₂ ’ Bridge Linker Dopants in Dielectrically Positive LC	
Blends.....	104
3.5.3.2.1. Rise Time	104
3.5.3.2.2. Decay Time	106

3.5.3.2.3 Results Summary.....	107
3.6. Overall Conclusion.....	108
3.7. References	108
4. Chapter 4: Raman Measurements and Analysis.....	111
4.1. Introduction to Vibrational Spectroscopy	112
4.1.1. Electromagnetic Radiation	112
4.1.2. Polarisation of Light	115
4.2. Raman Spectroscopy Theory: Basics and Principles	118
4.2.1. Introduction to Raman Spectroscopy	118
4.2.2. Raman Scattering.....	119
4.2.3. Polarisability (α) and the Polarisability Ellipsoid	120
4.2.4. Vibrational Raman Spectra.....	125
4.2.4.1. Non-linear molecules: Vibrational Raman.....	125
4.2.4.2. Linear Molecules: Vibrational Raman	128
4.2.5. Rule of Mutual Exclusion	132
4.3. The Raman Instrument and Experimental Design	133
4.3.1. Raman Spectrometer: LabRAM HR 800	133
4.3.2. Confocal Raman Microscopy.....	135
4.3.3. Time-Resolved (TR) Raman Spectroscopy.....	137
4.3.4. Experiment Outline and Design	138
4.3.4.1. Design of the Improvised Oven and Dynamic Cell Holder.....	139
4.3.4.2 Electro-Optic (EO) Measurement Experiment	

Schematic	141
4.3.4.3 TR Raman Spectroscopy Experiment	
Schematic	143
4.4 Results and Discussion.....	144
4.4.1 Raman Spectra of Dopants and LC	144
4.4.2 Dielectrically Negative LC Raman Study and TR Raman	
Results	148
4.4.2.1 Preliminary Study and Understanding of the Behaviour and	
Internal Motion of a LC Cell Using Raman	
Spectroscopy	148
4.4.2.2 Time-Resolved Raman Studies	155
4.4.3 Dielectrically Positive LC Raman Study and TR Raman	
Results.....	167
4.4.3.1 Preliminary Study and Understanding of the Behaviour and	
Internal Motion of a LC Cell Using Raman	
Spectroscopy	167
4.4.3.2. Time-Resolved Raman Study of a 10 μm TN Cell with	
Merck LC BL037	173
4.5 Conclusion.....	181
4.6 References	181
5. Chapter 5: Experimental	184
5.1. Experimental Details	186

5.2. References	220
6. Chapter 6: Summary and Future Work	221
6.1. Project Summary	222
6.2. Future Work	223
 THEESIS VOLUME 2	
7. Chapter 7: Appendices.....	225
Appendix A: EO Data for Chapter 3	226
Appendix B: Raman Data for Chapter 4	285
Appendix C: Crystallographic Data and Tables for Chapter 5	323

FIGURES

THESIS VOLUME 1

1. Chapter 1: Introduction.....	1
Figure 1	4
Figure 2.	5
Figure 3.	8
Figure 4.	11
Figure 5	13
Figure 6.	16
Figure 7	19
Figure 8	21
Figure 9	26
Figure 10	30
Figure 11	32
Figure 12.	36
Figure 13.	38
2. Chapter 2: Synthesis of Guests for LC Hosts	49
Figure 1	51
Figure 2	52
Figure 3	60
Figure 4	64
3. Chapter 3: Electro-Optic Measurements and Analysis	70

Figure 1.	72
Figure 2	78
Figure 3	81
Figure 4.	86
Figure 5	88
4. Chapter 4: Raman Measurements and Analysis.....	111
Figure 1.	114
Figure 2	115
Figure 3	116
Figure 4	118
Figure 5	120
Figure 6.	123
Figure 7	127
Figure 8.	129
Figure 9	131
Figure 10.	134
Figure 11	136
Figure 12	137
Figure 13	140
Figure 14	141
Figure 15	142
Figure 16	143
Figure 17	145

Figure 18	145
Figure 19	147
Figure 20	147
Figure 21	149
Figure 22	150 – 151
Figure 23	153 – 154
Figure 24	156
Figure 25	157
Figure 26	159 – 160
Figure 27.	161 – 162
Figure 28	163
Figure 29	165
Figure 30	166
Figure 31	169
Figure 32	170
Figure 33	172 – 173
Figure 34.	175
Figure 35	176
Figure 36	177

THESIS VOLUME 2

7. Chapter 7: Appendices.....	225
Appendix A: EO Data for Chapter 3.....	226

Figure 1 – 31	227 - 284
Appendix B: Raman Data for Chapter 4	285
Figure 1 – 22	286 - 322
Appendix C: Crystallographic Data and Tables for Chapter 5	323
Figure 1.	324
Figure 2	335
Figure 3	347
Figure 4.	356
Figure 5	366

TABLES

2. Chapter 2: Synthesis of Guests for LC Hosts	49
Table 1.....	53
3. Chapter 3: Electro-Optic Measurements and Analysis.....	70
Table 1.....	86
Table 2.....	88
Table 3.....	90
Table 4.....	92
Table 5.....	94
Table 6.....	96
Table 7.....	97
Table 8.....	98
Table 9.....	100
Table 10.....	101
Table 11.....	102
Table 12.....	103
Table 13.....	104
Table 14.....	105
Table 15.....	106
Table 16.....	107
4. Chapter 4: Raman Measurements and Analysis.....	111
Table 1.....	130

7. Chapter 7: Appendices.....	323
Appendix C: Crystallographic Data and Tables for Chapter 5	324
Table 1.....	325
Table 2.....	326
Table 3.....	327
Table 4.....	331
Table 5.....	333
Table 6.....	335
Table 7.....	336
Table 8.....	338
Table 9.....	343
Table 10.....	345
Table 11.....	347
Table 12.....	348
Table 13.....	350
Table 14.....	353
Table 15.....	354
Table 16.....	356
Table 17.....	357
Table 18.....	359
Table 19.....	362
Table 20.....	364
Table 21.....	366

Table 22.....	367
Table 23.....	372
Table 24.....	380
Table 25.....	384
Table 26.....	386

EQUATIONS

1. Chapter 1: Introduction.....	1
Equation 1	13
Equation 2	14
Equation 3	18
Equation 4	19
Equation 5	21
Equation 6	22
Equation 7	24
Equation 8	27
Equation 9	27
3. Chapter 3: Electro-Optic Measurements and Analysis.....	70
Equation 1	80
Equation 2	82
4. Chapter 4: Raman Measurements and Analysis.....	111
Equation 1	116
Equation 2	117
Equation 3	121
Equation 4	121
Equation 5	123
Equation 6	124
Equation 7	124

SCHEMES

2. Chapter 2: Synthesis of Guests for LC Hosts	49
Scheme 1	54
Scheme 2	55
Scheme 3	56
Scheme 4	57
Scheme 5	58
Scheme 6	60
Scheme 7	61
Scheme 8	63
Scheme 9	65
Scheme 10	66

Chapter 1

Introduction

1. Introduction

1.1. A Brief History

In 1888 the Austrian botanist Friedrich Reinitzer was determining the melting points of cholesteryl benzoates. He observed an unusual melting characteristic, whereby the sample appeared to melt at 145 °C forming an opaque liquid. Further heating of the sample then caused a second transformation forming a transparent liquid at 178 °C. At the time it wasn't apparent that he had observed for the first time what is now recognised as the intermediate state between a crystalline solid and a liquid. Today this state is regarded as the liquid crystalline phase, also known as the *mesomorphic phase* (mesophase). [1, 2]

1.2. The Fourth State of Matter

Until 1890 there were only three known and accepted states of matter; solid, liquid and gas. However, when Lehmann also observed this intermediate phase he considered it novel enough to be addressed seriously. Using a hot stage microscope with polarised light, Lehman initially studied cholesteryl benzoate, and then related compounds that exhibited what was considered a double-melting point phenomenon. The observations led him to believe that the opaque materials had characteristics of both liquid and solid and he reported these findings in *Zeitschrift für Physikalische Chemie*. [3] Lehmann initially paraphrased the term “Flussige Krystalle” with regards to this phase, literally meaning “fluid crystal”. This translates to ‘*Liquid Crystal*’, which gives a better understanding of the dual nature of the phase which is fluid-like by nature but exhibits the anisotropic physical properties of

crystalline solids. Both scientists claimed the credit for the discovery of the new phase of matter, but Reinitzer is considered to be the first to observe the phenomenon.[2, 4, 5]

1.3. Liquid Crystals (LC)

Liquid crystals (LC) are now well established and remain the subject of fundamental research as well as being used in widespread applications and commercial use. The term *liquid crystal* signifies a state of aggregation and order of molecular material. This state self assembles to form the ordered soft state that is intermediate between a crystalline solid and amorphous liquid; thus it can flow like a liquid but it contains molecules that are aligned and orientated comparable to that of a crystalline lattice. They exhibit complex physical properties that will be demonstrated and discussed later in this introduction. Furthermore, it is these properties that have been exploited over recent years giving significant advances in display technology. The most important property is the ability to rotate the plane of polarisation of light, also known as birefringence. This property is used to facilitate the identification and classification of different types of LC, and forms the mainstay to many applications. It is possible to identify different types of LC phases when viewed under a microscope using polarized light as each phase has a different texture due to the abundance and appearance of domains. [2, 6-10]

1.3.1. Classification of Liquid Crystals

LC's can be divided into two main classes; lyotropic and thermotropic. There are over 35 different liquid crystalline phases known which can be observed for each class, for example both types of liquid crystals display a Smectic phase (the phases will be discussed later in

the thermotropic discussion due to the topic of this research programme being based on thermotropic liquid crystals). Transitions between any combination of thermotropic phases are prompted by changes in temperature, whilst lyotropic phases can also be caused by changes in concentration. Following the nomenclature proposed originally by Reinitzer [2, 11, 12], LC's are classified broadly into different types as shown in Figure 1 [2, 6-8, 12, 13]

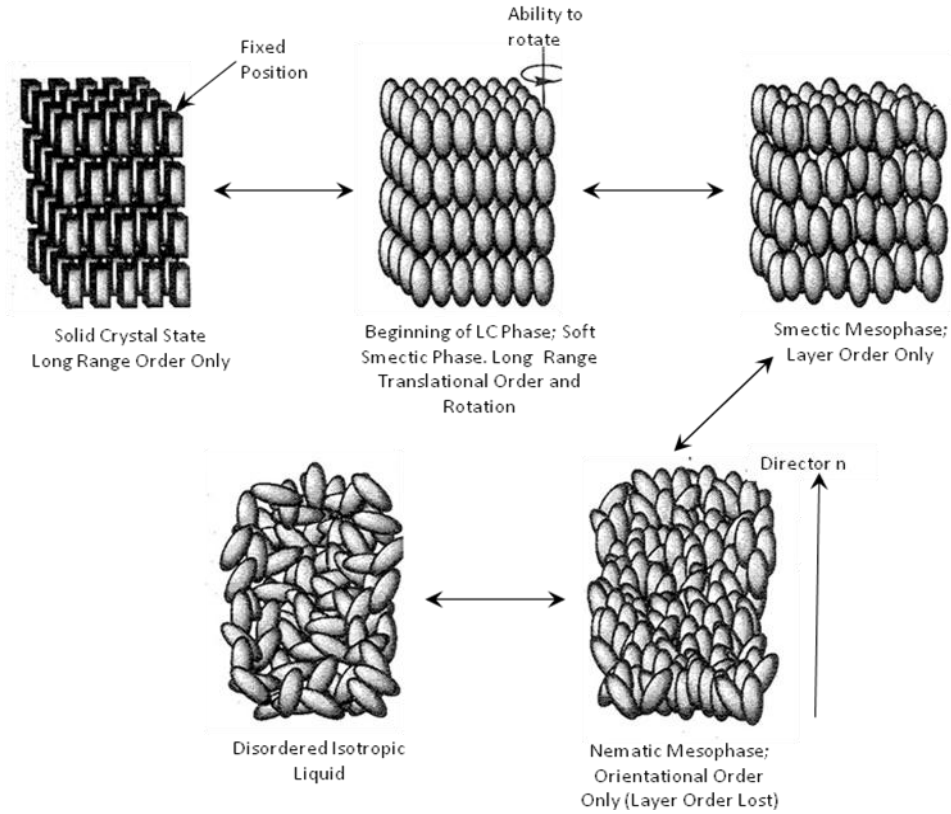


Figure 1. The phases of thermotropic mesophases upon heating. [12]

LC phases can be identified visually by analysis of the domain and its interaction with polarised light under a polarising microscope. Each will appear differently including the number of domains present. Domains are distinguished by order, whether it is positional order and/or orientational order. This in turn dictates the overall phase, giving it an order

alignment and director in the lattice of molecules. The order can be short or long range extending over distances from nm to μm . In the liquid crystal environment the term macroscopic refers to distances in μm , contrary to the much longer range order observed in crystalline materials, where the term may be used to refer to length scales in the order of mm or cm.

1.3.1.1. Lyotropic Liquid Crystals

Lyotropic LC's are also referred to as '*amphiphilic*' compounds; molecules that comprise of two distinctive components a "head" and a "tail". The head of the molecule is polar and attracted to water (*hydrophilic*), and whilst the tail is non-polar and attracted to hydrocarbons (*hydrophobic* or *lipophilic*). At moderate dilution these molecules can form structures known as micelles, whereby the *hydrophilic* or *lipophilic* components aggregate, presenting the like 'ends' to the solvent environment. For example, in aqueous solution, a surfactant molecule forms a core comprising of the hydrocarbon tail groups with a surface comprising of the polar head groups which interact favourably with the solvent, see Figure 2.

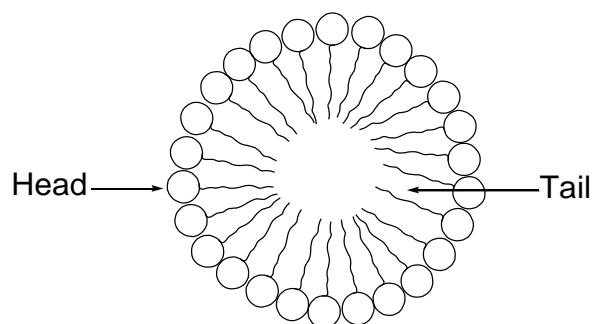


Figure 2. Schematic of a micelle assembly indicating the *hydrophobic* head and the *hydrophilic* tail.

The phases formed by lyotropic LC's are concentration dependant. Micelles will form at a specific minimum concentration, referred to as the critical micelle concentration, CMC. Below this minimum concentration the molecule is present as dissolved molecular entities. Increasing the concentration above the CMC increases the abundance of micelles where they have fairly well defined size and aggregation number until they reach another critical concentration where the high abundance of micelles result in a turbid solution; an emulsion. By increasing the concentration further another critical point is reached where LC phases form. During the early stages of the formation of the LC phase, micelles form a structure similar to a face-centered or body-centered cubic crystal lattice, where the micelles can be considered as a single point in a lattice like that of an atom or ion. On further increasing the LC concentration, the basic cubic lattice changes to form rod like structures and it is the composition and packing of these rods that lead to different lyotropic LC phases, such as 2D and 3D bilayers. The exact nature of the phases formed by lyotropic LC's are highly structure dependent and present complex phase diagrams. [14-21]

Lyotropic systems are ubiquitous and are common place in commercial products such as food [22, 23], cleaning processes [24, 25], surfactants [15], as well as finding applications in templating mesoporous materials. [26, 27] Most importantly they are seen in biological membranes. [28, 29]

1.3.1.2. Thermotropic Liquid Crystals

A substantial number of organic compounds can behave as thermotropic LC's, exhibiting smectic and nematic phases, where the anisotropic properties are dependent upon

temperature. At higher temperatures the compounds melt completely to form an isotropic liquid phase, this melting point is referred to as the clearing temperature. Below this limit they form structures with crystalline behaviour and may form a number of phases with defined transition temperatures. At a lower limiting temperature liquid ceases to exist and the material has an ordered structure characteristic of a crystalline solid. Molecules that behave as thermotropic LC's are typically rod-like in shape and characteristics but some are known to be disc-like. This rod-like shape, coupled with its anisotropic properties, i.e. optical and dielectric (see later), gives rise to electro-optic effects at relatively low driving voltages, and it is these properties that are exploited in current LC devices and displays.[6, 7, 30]

1.3.1.2.1. Smectic Phase Liquid Crystal

The Smectic LC phase is denoted with the abbreviation prefix "Sm". With regards to the different classes of mesophase, this type of phase has molecules arranged in layers with well defined periodicity. There are several types of the Sm phase, which are all characterised by their specific molecular arrangement within the layers. The different types of Sm phases are denoted with the suffix of a letter (A-C, E-K). Sm phases possess long-range orientational order giving them the layered structure. A key difference between Sm phases and other types of LC phases are their translational symmetry. The Sm phase maintains translational symmetry of a crystal as opposed to the comparable nematic phases which break the symmetrical state down in a minimum of one direction. Overall we can say that the Sm mesophase maintains 'translational' order in the long axis through and across the material but differs in the aggregated structure, as shown in Figure 3. The Sm layer

structure in the relationship between phase compositions was determined and established in 1923, by de Broglie and Friedel using X-ray diffraction. [2, 31] A number of classes of Sm phases can be chiral, which are referred to sometimes as ‘*Tilted Smectic*’ phases. These are recognised by the superindex “*”. These chiral Sm phases have reduced symmetry, and can display ferro- and antiferroelectric properties. These are important because they have enhanced speed and resolution when used in switching devices compared to those employing nematic LC’s.[32-34]

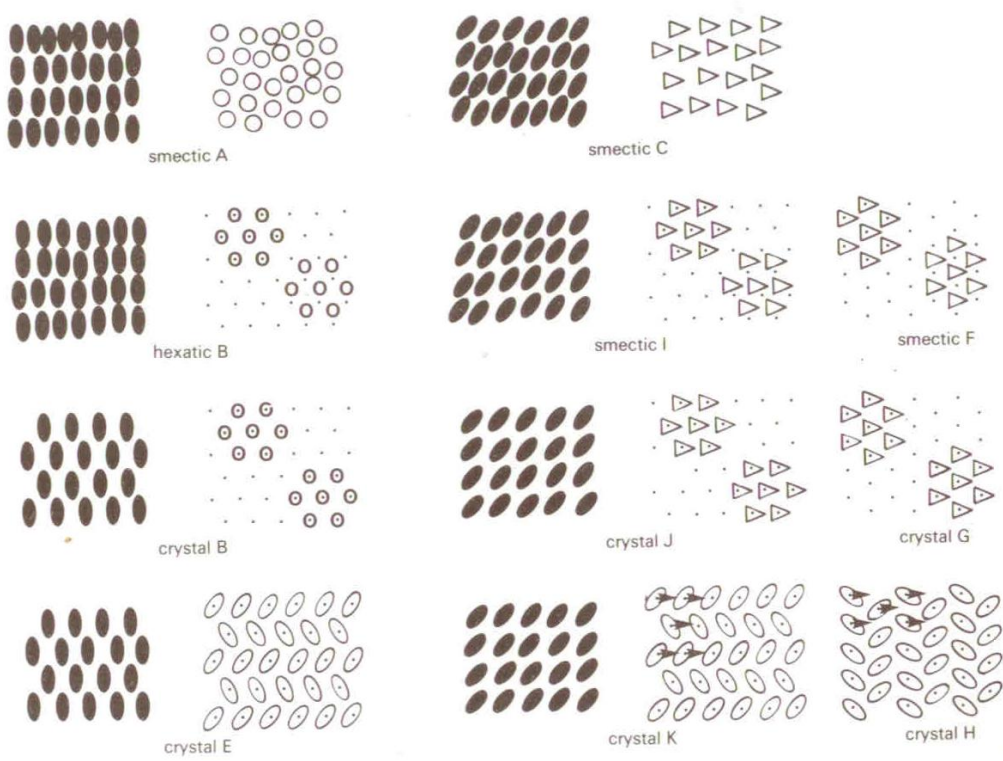


Figure 3. Side elevation and plan representations of the ordering of LC’s in each of the Sm mesophases. The tilt direction in the layers are represented by triangle points and arrows.

Reprinted from reference [34] © 1984 Leonard Hill publishing.

1.3.1.2.2. Nematic Liquid Crystals

As previously noted there are many types of LC's with a range of fluid or solid-like mesophases. Nematic LC's are currently used in commercial applications in display technology and as such remain the topic of intense research efforts. This phase exhibits a high degree of long range orientational order, but no long range translational order. The overall and preferred director within the LC phases usually varies between molecules themselves giving no fully correlated properties. However, when they align in such a fashion to make a homogenous sample, they exhibit a high birefringence, like the Sm phase (these properties will be discussed later within this chapter). [6, 12] The term '*nematic*', encompasses a number of subdivisions. These can be sub-divided into two categories, known as "*Positive*" and "*Negative*" nematic LC's referring to the relative orientations of the permanent electric dipole of the molecule and its molecular axis. This important difference gives rise to specific types of devices for applications in display technology.

1.3.1.2.3. Other Thermotropic liquid crystal phases

Over the years there have been significant advances made in the field of LC's and a greater understanding of how structure and LC phase may be controlled. Condensed matter physicists, display device scientists and engineers, physical chemists and synthetic chemists have demonstrated the use of LC's in a wide range of applications, including computers, e-papers, displays, commercial goods and optical communication technology. Each application requires specific properties and demands of the LC materials. Reviews and books of these are diverse and numerous. A main source for a very broad overview is the

“*Handbook of Liquid Crystals*” series by D. Demus *et al.* [9, 12, 18, 35] Some of the main aspects addressed are cholesteric LC’s, also known as chiral nematic, due to their chiral nature giving specific optical properties such as the reflection of specific polarised light,[36-39] polymeric LC’s; [40-43] oligomeric and dendrimeric systems have been suggested for holographic [44-47] and optical data storage, [48-51] discotic LC’s, which exhibit a novel columnar phase, have potential applications in electronics, especially as semi-conductors, [52-54] and metallomesogens with a range of potential applications, from luminescence to doping in polymers with advantageous optical properties. [55-59]

1.4. Properties of Liquid Crystals

1.4.1. Basic Overview of Properties

A complete understanding of the properties of LC’s is very complex, spanning chemistry, materials science and physics. What follows is a brief overview, touching principally upon the properties that concern the research described in the thesis, but does not dwell on the materials physics in detail.

The anisotropic nature of the LC’s governs their physical properties. Some of these properties, when combined with an applied magnetic or electric field, can give rise to a means of manipulating the orientation of the LC’s molecules, and hence the anisotropic behaviour and properties of the material. Changing the controlling electric or magnetic field brings about re-orientation of the molecular system, or director. This influencing effect by an applied field can allow a kinetic study of the movement and re-orientation within the LC

cell in response to a change in conditions. However, this response is not instantaneous and has associated rates at which the system changes in each direction, as shown in Figure 4. [60, 61] In the following section we will examine the main properties to provide a basic understanding of the anisotropic nature of LC's and considerations that have to be made when studying the behaviour of LC based display devices.

Material parameters we control to improve response time

$$\tau_{rise} = \frac{\gamma}{\Delta\epsilon(E^2 - E_0^2)} \approx \frac{\gamma}{\Delta\epsilon E^2}$$

$$\tau_{decay} = \frac{d^2 \gamma}{\pi^2 K} \quad E_0 = \frac{\pi}{d} \sqrt{K}$$

γ = Viscosity
 $\Delta\epsilon$ = Dielectric Anisotropy
 E = Applied electric field
 E_0 = Threshold electric field
 K = Elastic constants
 d = Cell thickness

Figure 4. The equations for calculating the response times of the LC with the anisotropic properties.[62]

1.4.1.1. Order Parameter (S)

The Order Parameter, S, is a measure of how ordered the LC medium is, and hence relates to the degree of anisotropy. An isotropic fluid will have an order parameter of 0, whilst a crystalline solid will have an order parameter of 1. S is calculated by taking the average of the directors for an LC medium across all of the domains and it is a useful measure of the degree of alignment of the direction and orientational order within the LC configuration. Increased order would indicate a more homogenous composition, giving a better and more

uniform behaviour of the components when external fields are applied to re-orientate the alignment. [63, 64]

The concept of orientational order present in LC's was initially addressed by Grandjean [65] and later by Born in 1916, [66] who proposed the first molecular field theory for the nematic LC phase. Their models treated the phase as a medium of an accumulated assembly of the same permanent electric dipoles. This demonstrated the phase transitions well enough, even with isotropic and anisotropic materials. Nevertheless, its flaw was that it was not applicable to polar compounds within LC's. This theory was later improved by Maier and Saupe which is known as the Maier-Saupe theory.[67-69] We understand that the characteristics of LC's are due to the underlying long range orientational order and it is this property that the Maier-Saupe theory utilises in relation to the nematic phase. The theory dispenses with the short-range forces and focuses on the long-range forces, which treat LC's as molecular fields contributing to the intermolecular potential. Although this is a qualitative evaluation, quantitative calculations can be made provided a known orientation director, n , and the order parameter, S , to account for the LC medium which comprises a mixture of molecules. [70] The order parameter can be calculated in various ways and by a number of techniques including Raman scattering, optical birefringence and diamagnetism. The most useful formulation to determine S is the calculation of an average of the second Legendre polynomial, denoted P_2 , which will specify the amount of order present, Equation 1. The parameter θ is the distribution function of the orientation or angle of the molecules with the known external director n , see Figure 5. [6-9, 71, 72]

$$S = \langle P_2(\cos \theta) \rangle = \left\langle \frac{3}{2} \cos^2 \theta - \frac{1}{2} \right\rangle$$

Equation 1. Order parameter S defined as an average of the second Legendre polynomial.

[9]

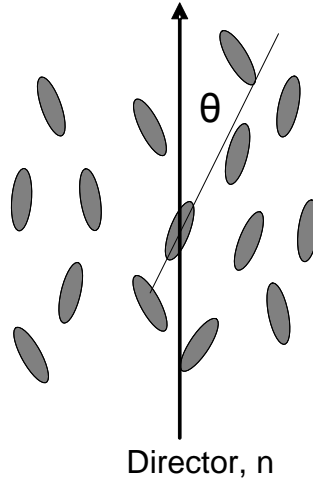


Figure 5. Representation of molecular order in a nematic LC identifying θ .

1.4.1.2. Dielectric Properties ($\Delta\epsilon$)

The dielectric anisotropy of a medium is a measure of the response of a charge free system interacting with an electric field, whilst the dielectric anisotropy describes how this value changes with respect to the axes of the molecule. It indicates the polarisability and dipole moment of the molecules, giving rise to an indication of how the molecule will align in an applied electric field. In LC devices, the most common method for controlling the realignment of the systems is the application of an electric field, of the order of 10^6V/m across the LC device and hence a change in the properties of the device. The dielectric parameter is a tensor quantity and both the magnitude and sign is important.

Dielectric anisotropy is defined as the difference between the dielectric constants (dielectric permittivity) parallel and perpendicular to the long axis of the rod-like molecule (director of the phase). These are known as the dielectric permittivities, denoted ϵ_{\parallel} and ϵ_{\perp} respectively. However, in 1961 W. Maier and G. Meier gave the first general interpretation of the dielectric anisotropy of LC's whilst deriving the generally adopted Maier-Meier theory of today (from the expansion of the isotropic fluid theory given by Onsager, [73]), see Equation 2. [74, 75]

$$\Delta\epsilon = \frac{NhF}{\epsilon_0} \left\{ \Delta\alpha - F \frac{\mu^2}{2k_B T} (1 - 3\cos^2 \beta) \right\} S$$

Equation 2. Maier-Meier equation defining $\Delta\epsilon$. [76]

where N is the number density, F and h are local field parameters; reaction field and cavity field factors respectively, which account for the dependence of the field interaction of the molecule with the surrounding environment and ϵ_0 is the dielectric permittivity of free space, μ is the dipole moment, α is the polarisability and β is the small angle the director makes with the defined axis.

The equation above has afforded an understanding and evaluation of the dielectric parameter, which has impacted upon the design of LC molecules. For its simplicity, there are a few assumptions that have been made. Firstly, molecules are considered to be spherical. The polarisability anisotropy, α , is composed of longitudinal and transverse components. Thus, when considering elongated rod-like molecules such as those used for nematic LC's, they have a greater contribution along the longitudinal axes than the

transverse axes. Secondly, it makes the assumption that the orientational axis is the long molecular axis. Finally, a molecule, of dipole moment, μ , will make a defined, yet typically small, angle with the molecular axis that is designated β . However, to simplify the understanding of the dielectric relationship β is assigned as a constant in all cases to be 54.7° . This reduces the contribution of the dipole to the dielectric parameter to zero (i.e. it is considered to be negligible). This leaves only the relationship of the difference between the two permittivity constants contributing to the parameter alone. [6-9, 71, 76-78] The dielectric anisotropy, $\Delta\epsilon$, are sub-divided into two categories; dielectrically *positive* (i.e. dielectric anisotropy is along the long molecular axis) and dielectrically *negative* (i.e. dielectric anisotropy is across the long molecular axis).

1.4.1.2.1. Dielectric Anisotropy by Design

The Maier-Meier theory is adequate for determining and explaining the dielectric parameters. This allows molecular modelling packages, such as GaussianTM [79], to predict potential liquid crystalline materials from the calculated dipole moments. However, from a “real world” (synthetic) approach this prediction is not plausible and a more accommodating method is required. Therefore, the method employed is linearly averaging the dielectric anisotropies of single components in the mixture by their weighted percentage. It averages the amount of influence components have on the system overall by so we gain an idea of whether the considered material will be dielectrically positive or *negative* ($\Delta\epsilon$). Substituents in the molecule will have stronger longitudinal or traverse dipoles competing with/or aiding each other to give an overall LC alignment. As for dopants, the considered dielectric average would then give an idea of whether it will

compete or aid the LC. A positive value indicates the overall dipole μ to be orientated parallel to the long molecular axis, and negative value indicates an overall dipole moment orientated perpendicular to the long molecular axis, see Figure 6.

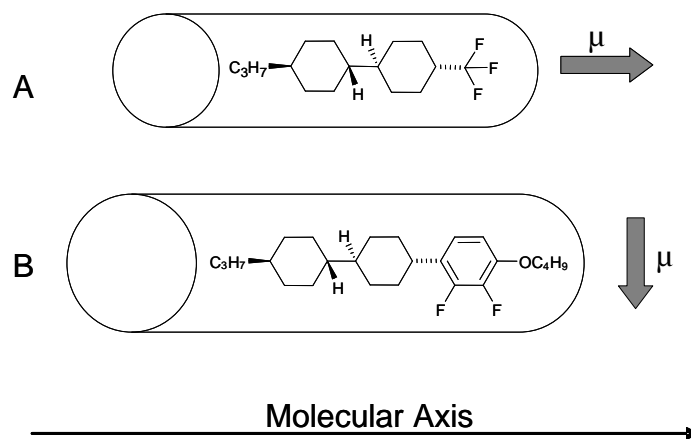


Figure 6. Commercially available LC materials from Merck that has a) *positive* and b) *negative* dielectric dipoles. [80]

Over the years the technology design of LC materials has advanced and today much focus has been given to the use of fluorinated core building blocks as these give relatively large negative $\Delta\epsilon$ values while maintaining the long rod-like character of the molecule. Although there are many commercially available dielectrically *positive* and *negative* materials, so far no simple product is suitable for all technological applications due to other properties being affected, such as viscosity. They are, however, used in today's most advanced Vertical Aligned (VA) display technology, used in TFT monitors. [81-84]

1.4.1.3. Birefringence (Δn)

Birefringence is unique and the most important property in LC technology. In LC's we can induce birefringence by relatively simple means and can be manipulated readily with a small electric or magnetic field compared to that of an isotropic liquid or crystalline solid. In an isotropic liquid a high field of the Kerr effect is needed to induce birefringence and in a crystalline solid the problem is that it is difficult to switch off the birefringence. To understand birefringence in a LC we must first understand the birefringence of a crystalline solid. Birefringence is the difference in refractive indices along different axes and gives rise to rotation of plane polarised light. It is best explained with respect to its relation of refractive index. When light enters a medium from a vacuum it will slow down, and the degree to which this occurs is called the index of refraction, n . When light travels between a different medium it can be reflected or refracted. Refraction results in the transmitted light being '*bent*', the light path changing direction. This alteration in the direction is effectively the basis of birefringence. Light can be treated as having two components; parallel polarised and perpendicular polarised light with respect to an arbitrary axis. Each of these will interact with the different refractive indices of the anisotropic assembly, denoted n_{\parallel} (also known as the ordinary component n_o) and n_{\perp} (also known as the extra-ordinary component n_e). The difference between the two indices is referred to as the birefringence Δn (optical anisotropy, see Equation 3a). Furthermore, this means that the birefringence is correlated to the LC's orientation and thus, any re-orientation in the LC gives rise to a change of the interaction of the polarisation of plane polarised light. Another simple way to quantify Δn is to simply take the square root of the dielectric constant (if you cannot measure the indices). Birefringence in LC's is related to a phase difference between the

ordinary and extra ordinary components. This phase difference is given by equation 3b, where d is the thickness of the medium, λ_0 is the wavelength in vacuum. By introducing this phase difference the polarisation of light will be rotated (see for instance half-wave plates). We can control this phase difference by the amount of re-orientation of an LC because in a non-magnetic anisotropic medium, which describes all LC's, the permittivity is different for electric fields in different directions; meaning that the index of refraction is orientation dependent. However, birefringence in an isotropic material is made by the application of a very high electric field and controlled through the Kerr effect (equation 3c). [8, 71, 85-87]

$$\Delta n = n_{\parallel} - n_{\perp} \quad (a)$$

$$\Delta\phi = \frac{2\pi}{\lambda_0} d(n_o - n_e) \quad (b)$$

$$n_o - n_e = \lambda KE^2 \quad (c)$$

Equation 3. Birefringence equation for (a) crystalline, (b) LC and (c) isotropic liquid materials.

1.4.1.4. Viscosity (γ)

Viscosity is the rate of dissipation of kinetic energy and is viewed as the sum of the rate at which the body is doing work (internal and surface stress tensors) on the volume of the medium. The viscosity of LC's is also known as *Hydrodynamics* and the theory was first developed in the 1960's by Leslie and Ericksen giving the *Leslie-Ericksen theory*, which is also referred to as the *Continuum Theory* based on earlier viscosity equations from Miesowicz, [88-90] Oseen [91] and Zöcher.[92] The theory is widely used over all

proposed quantitative descriptions of the mechanical behaviour (hydrodynamic effects) in the nematic LC phase. [93-95]

Miesowicz was the first to characterise physical viscous coefficients of the nematic LC phase. These are broken down into two areas; *Shear* and *Rotational* viscosity coefficients denoted $\eta_{1,2,3}$ and $\gamma_{1,2}$ respectively. Miesowicz's work shows that the LC can exist in three basic orientations of the director (n), relative to the x , y and z axis, and experiences a flow velocity, v , and also a flow gradient Δv . The orientation of the director, n , is given by the angles θ and Φ see Figure 7 and Equation 4.

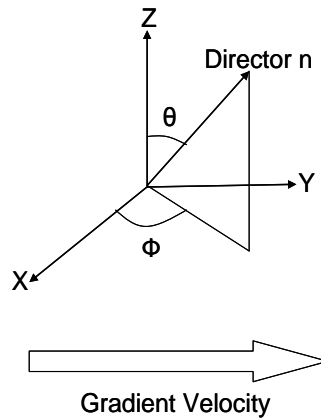


Figure 7. The given director orientation described with respect to the known gradient velocity of the LC that is parallel to the y axis. [9]

$$n = (\sin \theta \cos \phi, \sin \theta \sin \phi, \cos \theta)$$

Equation 4. Determining the spatial orientation of the dierector (x , y , z). [9]

If the LC is sheared between two planes, for example the plane of the x axis and z axis, there will be a gradient flow along the y axis. This will give rise to the following coefficients:

- η_1 : Director parallel to the flow velocity
- η_2 : Director parallel to the flow gradient
- η_3 : Director orthogonal to the flow velocity and gradient

The coefficients $\eta_{1,2,3}$ are depicted in, and are respective to Figure 8 (labelled (i), (ii) and (iii)) and the overall parameter for *shear* viscosity is given by Equation 5:

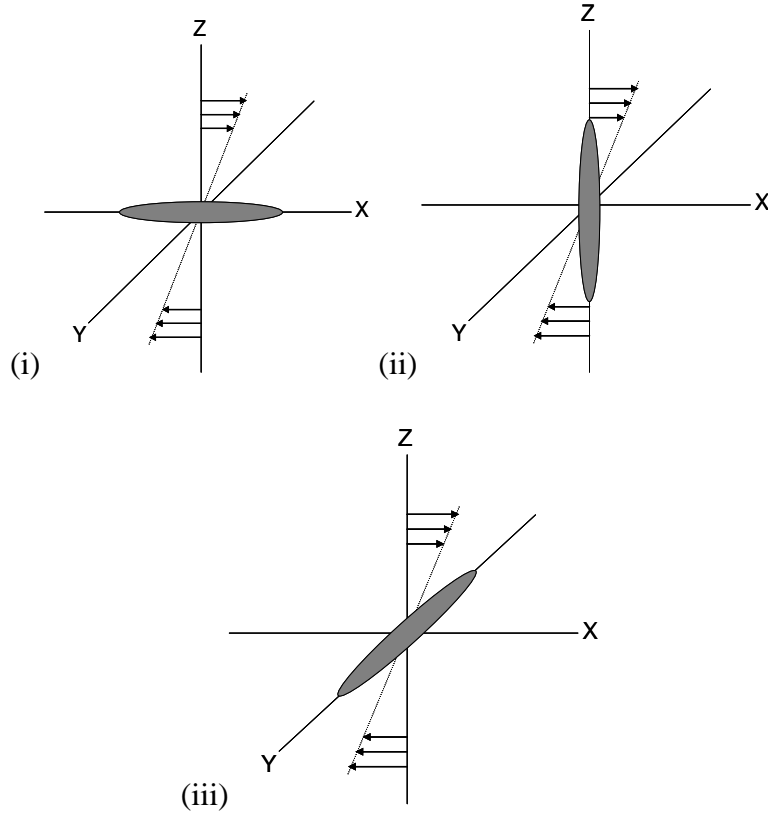


Figure 8. Shear flow coefficients η_x . (i) η_1 : Director parallel to the flow velocity (ii) η_2 : Director parallel to the flow gradient (iii) η_3 : Director orthogonal to the flow velocity and gradient [71]

$$\eta(\theta, \phi) = \eta_1 \cos^2 \theta + (\eta_2 + \eta_{12} \cos^2 \theta) \sin^2 \theta \cos^2 \phi + \eta_3 \sin^2 \theta \sin^2 \phi$$

Equation 5. Shear flow of viscosity parameter η_x . [71]

With LC's the situation is complicated by the fact that the molecules are not static and have flow properties. This has been mentioned earlier but it will be an influencing force on the director and thus encourages rotation. This now induces viscous torque and this is known as *Rotational* viscosity, $\gamma_{1,2}$. This new additional coefficient is further broken down to two components. Firstly, γ_1 is the characteristic torque associated with the induced rotation.

Secondly, γ_2 is the contribution to the torque of the flow. When discussions and values are expressed for *rotational* viscosity it is only referring to γ_1 .

The five independent coefficients are not easily determined from experimental procedures directly, but the most widely employed method, is the use of the *Leslie-Ericksen theory*. This uses the determined Leslie viscosity parameters α_x ($x = 1,2,3,4,5$), [93-95] in linear combination and simplifies the viscosity parameters, η and γ , to the following, see Equation 6:

$$\begin{aligned}\eta_1 &= \frac{1}{2}(\alpha_2 + 2\alpha_3 + \alpha_4 + \alpha_5) \\ \eta_2 &= \frac{1}{2}(-\alpha_2 + \alpha_4 + \alpha_5) \\ \eta_3 &= \frac{1}{2}\alpha_4 \\ \eta_{12} &= \frac{1}{2}\alpha_1 \\ \gamma_1 &= \alpha_3 - \alpha_2 \\ \gamma_2 &= \alpha_3 + \alpha_2\end{aligned}$$

Equation 6. The set of independent viscosity parameters using Leslie viscosity parameters [71]

This array of equations helps describe the viscosity parameter in an undemanding and accurate manner, thus it is widely accepted. In display applications, γ_1 , defines the time scale of the relaxation process of the director behaviour; the lower the value of γ_1 the faster the re-orientation and hence faster switching. In a display the LC cell is driven by an electrical signal controlled by a thin-film transistor (TFT) that is in turn controlled by a

series of signals; until a fresh signal is received the cell must sustain the charge and the orientation of the LC phase remains constant. [7-9, 71, 96, 97]

1.4.1.5. Elastic Constants (K)

Elastic constants are forces causing deformation in a LC medium and they are sometimes referred to as *Frank* elastic constants [98], denoted K_i ($i = 1,2,3$). They are the proportional constants between an acting force (in displays this is the applied electric field) and the deformation and distortion of the mediums director. These elastic properties are torsional and describe the mechanical stability; how “stiff” the LC medium is, which, to no surprise, is intermediate between liquids, that cannot support shear stress, and solids that can support compressional, torsional and shear stress.

Elastic constants are an extension to continuum theory. They are only pertinent to the elastic considerations of the medium and, therefore, assume that the orientational and positional order parameters are constant over the volume. Assuming the medium is non-varying we can consider the director as an alignment in space as a unit vector, n . The simplified view of LC's existing in space has three dimensions (3D). Therefore, when we consider the elasticity, the deviation by stress and strain forces from the equilibrium starting position in 3D can give many terms when taking into account of the x, y and z axes. However, theory indicates that the free energy, where the bulk free energy of the LC is associated to unit volume, limits the number of terms possible due to:

- No terms can give difference in energies due to positive and negative directors (n and $-n$, again assuming constant order).

- In non-chiral mediums there are no linear terms (rotation and inversion will bring about difference in energies).
- Surface effects are generally ignored as integration occurs over per unit volume and surface integral will change the volume term.

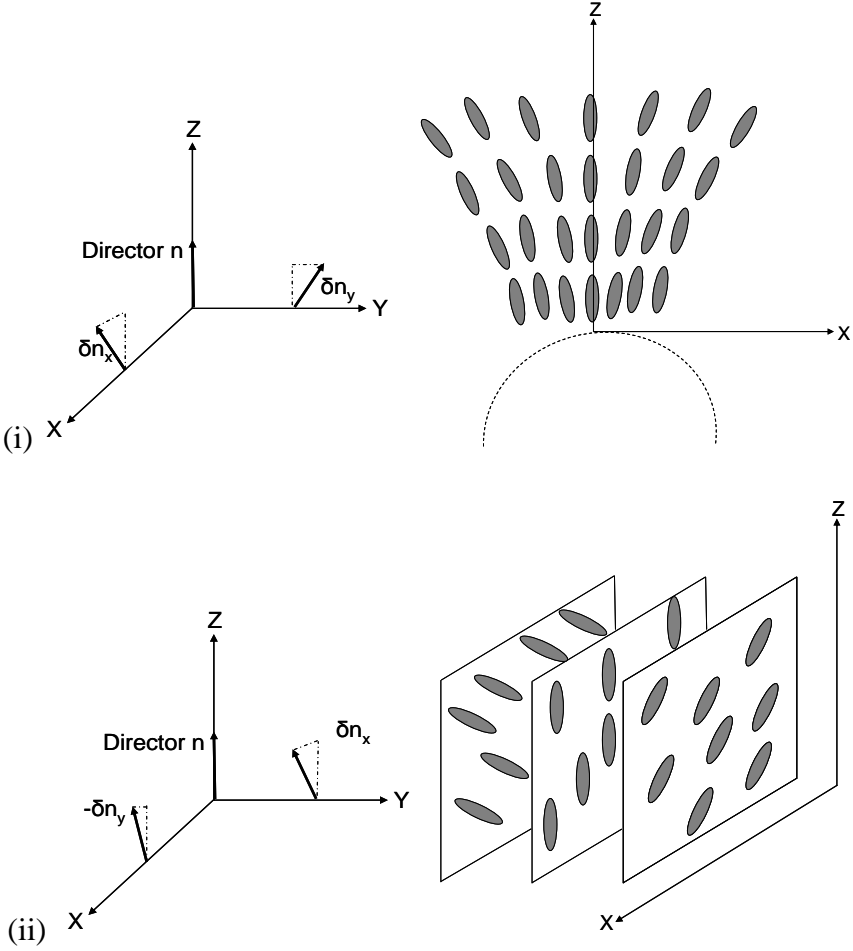
These criteria give rise to the three terms K_1 , K_2 and K_3 , for which there are long and complex derivations, that overall essentially give an equation expressing the free volume of the system, Equation 7. [6-8, 71]

$$F_V = \frac{1}{2} K_1 (\nabla \cdot n)^2 + \frac{1}{2} K_2 \{n \cdot (\nabla \times n)\}^2 + \frac{1}{2} K_3 \{n \times (\nabla \times n)\}^2$$

Equation 7. Equation of the elastic constants expressing the free volume of the medium for the allowance of deformation within the system [8]

To make better sense of this equation it is best to define the unit vector of the director, n , with regards to orientation whilst ignoring any physical contribution to the sign. This gives rise to a set of Cartesian co-ordinates (x, y and z with n at the origin) allowing for 3D positioning in space and arbitrary representation of the volume. If we assume n to be parallel to the z axis we can now propose three representations for when distortion occurs for n in the contributing terms associated to K_x from the equation 7, these are Splay, Twist and Bend (K_1 , K_2 and K_3 accordingly), Figure 9. [6-9, 71, 98] A method to measure the distortion in the LC due to an applied electric or magnetic field is known as the Freedericksz Transitions [92, 99, 100], which is the simplest method used to date. This method measures the change of re-orientation within a LC cell as a function of applied

magnetic field. Applying a magnetic field induces magnetic dipoles in the LC molecules. The molecules across the bulk of the LC sample tend only to align with the applied magnetic field at the threshold level. At this level the bulk has re-orientated except the molecules interacting with the alignment layer, where a greater energy thus larger magnetic field is required to reorient the molecules. The measure of the magnetic field required for bulk and total re-orientation gives rise to the determination of the elastic constants. [101]



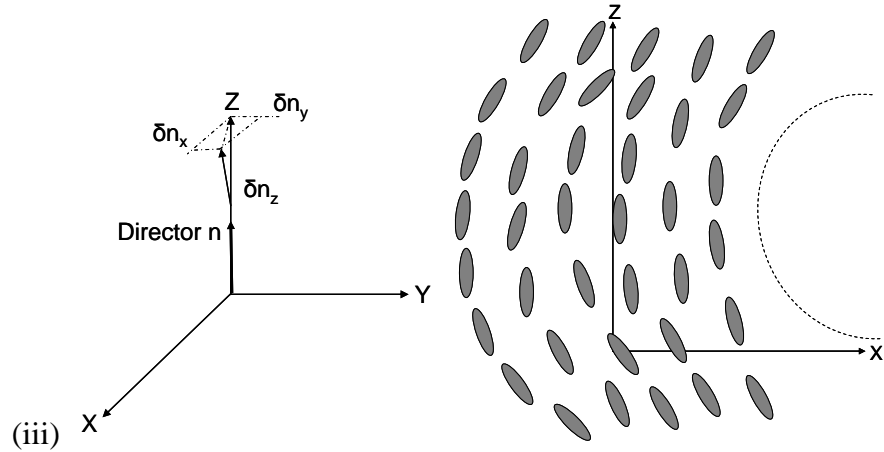


Figure 9. The representation of the elastic constants in Cartesian co-ordinates (3D) and 2D slice through a plane in the z and x axis showing a depiction of the elastic constants (i) Splay (ii) Twist and (iii) Bend.

1.4.1.6. Voltage Holding Ratio (VHR)

The VHR (also known as the holding ratio, HR) gives an indication of the period of time an electrical charge can be sustained across the LC cell. The materials placed within a LC cell must be absolutely free of ionic impurities which will bring about conduction through the sample. Hence it is critically important to have LC's that are analytically and spectroscopically pure with no free ions present. The HR can be expressed as a physical parameter as shown in Equation 8. The VHR defined by the fraction of the charge remaining across the cell after a period of time in an open circuit interval (time between pulse of the applied voltage) compared to the initial driving voltage. A high VHR means that the applied potential remains constant and hence gives a more stable image.

$$HR = \left[\left(1 - e^{-\frac{2T}{\tau}} \right) \left(\frac{\tau}{2T} \right) \right]^{\frac{1}{2}}$$

Equation 8. Expression for the Holding Ratio of a LC. This expression works for both magnetic and electric fields. It is VHR when dealing with electric fields. Where T is the frame time for the display pixel or cell and τ is the time constant for the cell. [61]

However, when understanding the parameter in terms of voltage alone it is easier to express the VHR as a percentage, Equation 9. In an operating video display, frame times are extremely small, in the order of tens to hundreds of ms, and many frame refreshes occur over a short period of time. [61, 102-105]

$$VHR = \frac{V_{END}}{V_{BEGINNING}} \times 100\%$$

Equation 9. VHR Expressed as a percentage of the beginning and ending voltage between pulse drives for the cell.

1.4.1.7. Guest-Host Interactions

The guest-host effect is when guest molecules (dopants) aid the operation of a specific property of the LC. It was initially studied by Heilmeyer and Zanoni in 1968 [106] with the use of dichroic dyes acting as the guest molecule and later in 1974 by White and Taylor [107] using pleochroic dyes.

The essence of this effect is that when an electric field is applied, in this case in a display device, the host molecules (LC) will align and orientate so that the director is parallel or

perpendicular to the field for a positive or negative dielectric anisotropy respectively. Guest molecules (dyes/dopants) will also orientate themselves in such a way that mimics the behaviour of the host. The effect is that the optical density measured perpendicular to the cell overall will increase or decrease depending on the direction of the transition dipole moments of the dyes with respect to the optical axis. The movement of the host and guest will be the same but the observed optical density will either increase or decrease relative to the amount of orientation of the host and guest. This in turn leads to a new electro-optic effect. The effect of controlling the property by guest inclusion in a system can be extended to other properties, such as dielectric anisotropy, by influencing the dielectric nature of a system. It can induce a stronger alignment and interaction between host and guest molecules with an applied external magnetic or electric field. Thus, there is a wide range of what is considered to be the guest-host effect [61] and much research into this effect for the demand of better LC device properties, such as contrast ratios (black and white are preferred for better luminescence) and brighter displays. [108-117]

The research presented in this thesis we will be investigating dopants that will primarily have no UV-Vis absorption and thus will not be acting as dyes. The dopants are intended to affect the host medium and interact with the LC in such a way that they will modify the speed of orientation when an external field is applied. They will be taking a guest role although not themselves interacting with the incident light.

1.5. Initial Understanding and Application of LC Physical Phenomenon

Structural observations and identification of LC's did not take place until 1911 by Manguin, [118, 119] when he discovered that they have a molecular twist within the medium itself due to the rotation of polarisation of transmitted light. This was later denoted "*twisted nematic*", which went on to set the basis for commercial LC devices. Manguin's research was initially composed of aligning a LC film by holding the material between two glass plates coated with *p*-azoxyanisole. The plates with the coated side had been rubbed in one direction with a piece of paper to obtain a uniform director with homogeneous alignment. One plate was twisted thorough 90°, resulting in the directors being orthogonal to each another. Using crossed light polarising crystals (crossed polarisers), it was observed that the plane of polarised light was rotated, following the twist in the nematic LC. This led to the hypothesis: "*the orientation of the liquid particles changes continually from the lower border of the orientation to the upper one; the structure is thus a helical one whose pitch is determined by the twisting of the two membranes against each other.*"[2, 4, 120] The nature of this LC device will be discussed in greater detail later.

In 1962 Williams studied physical phenomena of LC's by designing a cell that held the nematic LC in between the *p*-azoxyanisole coated plates, which in turn were sandwiched between transparent tin oxide electrodes coated on glass plates. The cell was placed on a hot stage microscope at 125 °C, and it was observed that a regular pattern of parallel '*stripes*' appeared when an electric field, approximately 1000 Vcm⁻¹, was applied across the cell under polarising conditions. These stripes were referred to as domains which were later referred to as *Williams Domains* (Figure 10). When the field was removed these apparent

domains disappeared to reform the original condition, i.e. no ‘*stripes*’ or domains. This electric field induced phenomenon became used as a basis for controlling the orientation of LC molecules and thus the basis to the control for display or light modulation devices. [2, 6, 121, 122]

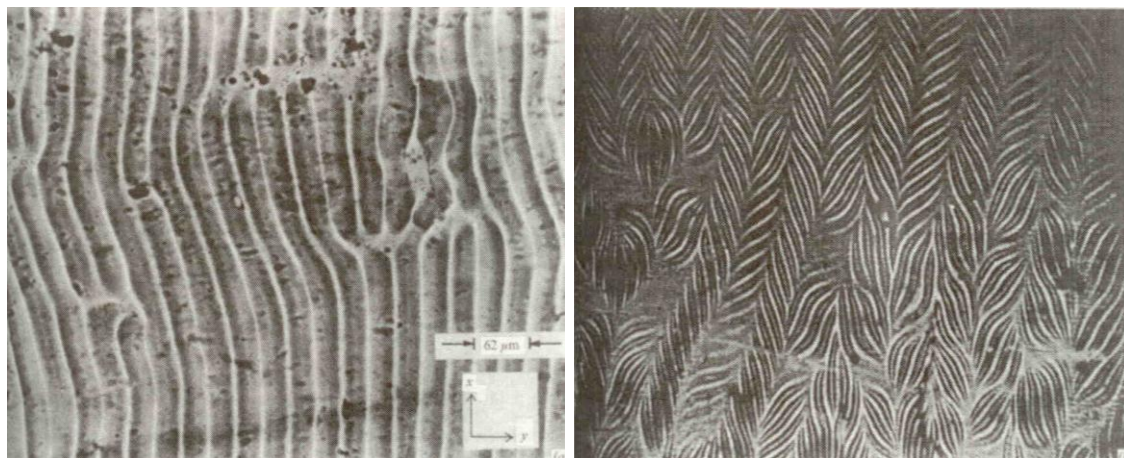


Figure 10. Electrohydrodynamic alignment patterns in nematic LC's. a) Williams domains of *p*-azooxanisole. b) Williams domains of MBBA. Reprinted from reference [6] with permission from [123] © 1971 Molecular Liquids and Liquid Crystals.

1.6. Liquid Crystals Industrial Era Begins

In 1964 Heilmeyer developed the incorporation and use of dichroic dyes in LC's to create what is known as the Guest-Host Effect. Heilmeyer and Zanoni designed the first device exhibiting this effect; the cell presented was in the form of a parallel plate capacitor with transparent electrodes and the LC material inserted between the plates. The nematic LC material used was deemed as the *host*, and the dopant dichroic dye was the *guest* which aligns alongside the LC host. A permanent dipole moment along the molecular axis of the LC molecule enables it to align in the cell along the direction of the applied field. This in

turn orientates the dye with its comparable dipole moment, allowing both to be perpendicular or parallel to the electric vector when an electric field was *on* or *off* respectively. Hence, the cell could switch by the applied potential, giving rise to the control of polarised light passing through the cell. This was of great interest as it demonstrated a way to electronically control the transmission of light and hence opened up display technologies based upon LC materials.

In 1968 liquid crystal displays (LCD's) were introduced to the technological world as a new display technology and were positive dielectric materials based on cyano-biphenyl derivatives. This led to rapid developments in the field which have culminated in the flat panel displays that we see today. [4]

1.6.1. Beginning of Commercial Liquid Crystal Technology

In 1972 Gray, Nash and Harrison developed liquid crystalline materials based upon 4'-alkyl (or alkoxy) 4-cyanobiphenyl systems. This class of material offer broad temperature ranges over which they exhibit LC phases and excellent electro-optical performance, i.e. faster response and better quality in the display device. The development of these new classes of LC materials revolutionised the industry and the development of new manufacturing techniques which led to high productivity at lower cost, allowing LC technology to be accessible to the general public in 1973, see Figure 11.



Figure 11. (a) The world's first commercially available LC product, a pocket calculator, developed by Tomio Wada, Tadashi Sasaki and their team at Sharp in 1973 reprinted from reference [124] © 2002 IEEE. (b) Seiko Watch Company introduces their first digital watch with a twisted nematic LC display to the commercial market reprinted from reference [124]

© 2002 IEEE.

The watch, as shown in Figure 11, was developed by the Seiko Watch Company and was named 06LC. It was the first product which adopted the twisted nematic mode. The low power consumption of the LCD meant that it would operate for at least two years. The watch was well received and became the first commercial success for LC's.[4, 124]

1.6.2. Brief Overview of The Critical Advances in LCD Technology in Last 30 Years

Within the past decade, LCD have very much become a part of our daily lives. By 1999 more than two billion LCDs were produced worldwide, half of which were used in small monochrome displays in wrist watches and calculators. Today the market is dominated by '*full-colour displays*' such as those used in computer displays, with ever-increasing high-

resolution graphics. Since 1979 the journal *Displays* has reported on display technology such as LCDs, with the first report from SRDL Developments Limited titled “*LCD Illumination*” in January 1980. It demonstrated that LCs can be externally controlled for illumination. [125] The most recent journal discusses the latest improvements on the deblurring filters for LCDs. [126] Over the past three decades we have seen how the industry has matured and how scientific advances have led to the first large text editor [127], to present day LCD touch screens [128].

The LCD market has expanded significantly with the most prominent example being the high information content displays seen in mobile phones, computer screens and televisions. Most of these displays are based on active matrix (AM) technology, [76, 129, 130] where the displays are made up of pixels forming a matrix. Each pixel is controlled by a thin film transistor (TFT's). TFT's are a semi conducting electronic component used to switch electrical signals or amplify them) integrated on the back of a glass panel. At the core of the LCD display is a 5-6 μm thick film of a proprietary blend of nematic liquid crystalline material.

The LC material used in such cells needs to be chemically, thermodynamically and photochemically stable for device longevity.

Gray and co-workers [131] discoveries and the realisation of the commercial importance of LCD's prompted further development for new classes of materials showing similar nematic phase behaviour at ambient temperature. In addition to these compounds, scientists utilised

the fact that mixtures of compounds exhibit melting point depression. They created mixtures of components in varying ratios enabled production of LCD's that could operate within broad working temperature ranges, above and below ambient room temperature. This allowed device operation to continue, over a range of climate zones, for example from Alaska to Australia.

Currently, although almost all LC technologies use nematic LC mixtures, there has not yet been a single component LC material that fulfils all of the desired specifications for even the simplest display.[81, 132-135]

The first twisted nematic LCDs (TN-LCDs) were simple, direct addressed, segment displays, such as those used in wrist watches which have relatively large areas of active material. As technology has evolved, attempts to increase the information content displays of cyano-biphenyl based TN-LCDs reach limitations. For example, increasing the resolution and information content, contrast ratio, response times and viewing angle, have all been difficult to improve upon, thus development and improvement of the TN-LCDs has been problematic. By increasing the components ratios used in a mixture the contrast was reduced. However, by 1984 new super-twisted nematic LCDs were developed allowing more components to be used and, thus higher multiplex ratios. This increased their potential and provided greater scope, but still did not solve all the problems, especially increasing information content. The solution was overcome with the development of the Active Matrix LCD's (AM-LCD) during the 1980's. By addressing the applied voltage to each individual pixel in the AM-LCD the optical transmission throughout the LCD could be controlled to a

greater degree and hence, better control for greater content display information. The first prototype was released in 1986 by SHARP with their 3” LCD screen. In 1989 the technology was brought to the market in notebook computer screens, demanding a significant financial investment in order for reliable mass production to take place.[12, 136-138]

1.7. Common Types of Present Day Liquid Crystal Display Technology

The principal of manipulating light inside a cell is applied to a few current display technologies; Twisted Nematic (TN), Vertically Aligned (VA) and In-plane Switching (IPS) mode. [60]

1.7.1. Twisted-Nematic Liquid Crystal Displays (TN-LCD)

The initial TN-LCD was first reported by Schadt and Helfrich when they exploited LC’s for applications such as watch displays. [139] For simplicity the configurations and the operation principle of a twisted-nematic (TN) cell are shown in Figure 12.

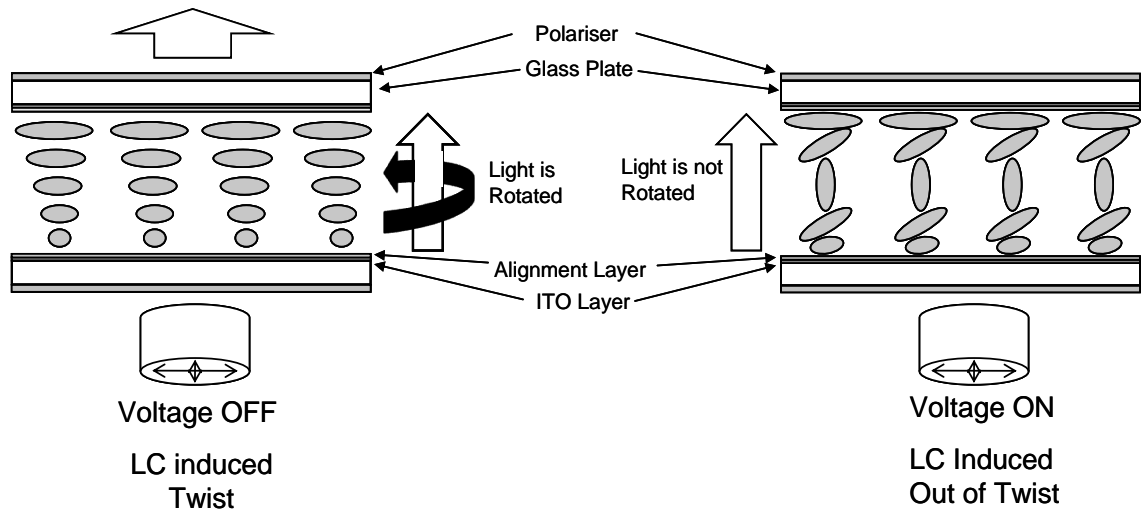


Figure 12. TN-LCD schematic

The cell consists of two transparent glass plates coated with a thin electrode layer of indium-tin oxide (ITO), followed by a polyimide alignment layer on the inner surfaces. The polyimide layer is rubbed in a unidirectional manner to allow the LC to align itself homogeneously parallel with the polyimide. This will give rise to the associated director, which can only be attained by a dielectrically positive LC (+LC). The parallel plates are held at 90° to each other, allowing a superimposed twist in alignment of the LC between the plates. Defects in the LC alignment can be avoided by doping it with a small amount of a cholesteric compound to reduce any reverse tilts and twists. Cholesteric LC's have similar energy requirements to nematic LC's with respect to twist and alignment, resulting in an overall reduction in possible defects. Polarisers are attached to the outer surfaces of each glass plate with their polarising axis parallel to the polyimide layer. This will convert non-polarised back-light to a polarised light when it enters the cell, and this will in turn allow the twist in the medium to rotate the plane of polarised light as it propagates through the

cell, allowing it to pass out through the opposite glass plate when the cell is off. When the cell is on the plane of polarisation of light is not affected and hence the cell appears dark.

The application of an electric field (above a critical threshold) orients the LC axis until a maximum strength is reached and the orientation has completely reduced the twist. Scaling the voltage between the minimum and the maximum limit will alter the twist between its lower and upper limits correspondingly; this is known as grey scaling. At a twist of 90° the light passes through the cell and appears white (off state). At a twist of 0° the light does not pass through and appears black (on state). The scaling controls the amount of light and, by combining the cell with a coloured filter, it is possible to obtain full colour display (a display only has three different coloured filters). By placing many cells or pixels closely together, an illuminated area would appear a certain colour as they amalgamate (our eyes cannot resolve individual cells). Consequently, when lots of these areas are close together we see the overlaid colour. This allows images to be compiled and built over larger scales, as in PC display screens. [6, 7, 12, 60]

1.7.2. Vertically Aligned Liquid Crystal Displays (VA-LCD)

The structural features of VA-LCDs are the same as that of the TN-LCD cell with the two main differences. The rubbed unidirectional polyimide layers are held in a parallel fashion (180°) rather than the previously preferred perpendicular alignment (90°). Secondly, the LC medium is dielectrically negative, which means the LC molecules align perpendicularly to the alignment layer. The configuration of the orientations between on and off is shown in Figure 13.

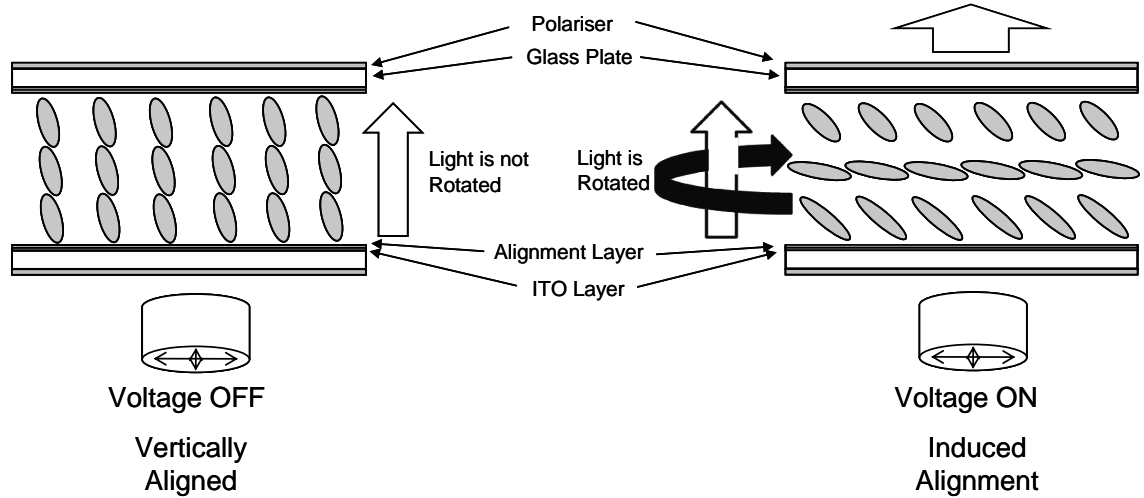


Figure 13. VA-LCD Schematic

The main mechanistic difference is that in the off state the cell appears black and hence opposite to that of the TN-LC cells. The application of an electric field induces a respective flip in orientation. When the alignment is all vertical (cell off) the polarisation of the transmitted light is unaffected and the cell appears black, whilst when the field is on the cell rotates the phase of polarisation and light passes through the cell and it appears white. The scaling controls the amount of light with colour filters working the same as in TN-LCDs. [6, 9, 60]

1.8 Aims and Objectives

The aims and objectives of this project are primarily to understand, at the macroscopic molecular level, the influence of dopants on commercial (and novel) LCD materials, in particular the switching speed. We will aim to make dopants that are soluble in the LC host and stable under device conditions (electrochemically, photochemically and

thermodynamically). Ideally we would like them to be of modular design to enable steric and electronic factors to be more readily distinguished, tuned and optimised.

Raman spectroscopy will be used to analyse these compounds structurally as well as a tool to monitor the guest-host interactions using their polarisability ellipsoid. LC molecules and dopants are highly anisotropic, thus Raman bands will show high degrees of polarisation. Raman polarisation studies provide information about the orientation of host and guest materials. The analysis will allow the study of their interactions. For example, do they ‘switch’ at the same rate as the host material? Time resolved measurements are proposed to determine the rates of host and guest re-orientation compared to data obtained by dichroism measurement studies.

1.9. References

1. F. Reinitzer, *Montash. Chem.*, 1888, **9**, 421.
2. T. J. Sluckin, D. A. Dunmar, and H. Stegemeyer, *Crystals That Flow: Classic Papers From The History of Liquid Crystals*. The Liquid Crystals Book Series; ed. G. W. Gray, J. W. Goodby, and A. Fukuda, 2004, Taylor & Fancis.
3. O. Lehmann, *Z. Phys. Chem.*, 1889, **4**, 462.
4. J. A. Castellano, *Liquid Gold: The Story of Liquid Crystal Displays and The Creation of an Industry*, ed. J. A. Castellano, 2005, World Scientific Publishing Co. Pte. Ltd.
5. B. Bahadur, *Mol. Cryst. Liq. Cryst.*, 1984, **109** (1), 1.
6. S. Chandrasekhar, *Liquid Crystals*, 2nd Rev. Ed., ed. M. M. Woolfson and J. M. Ziman. 1992, Cambridge University Press.

7. P. G. de-Gennes and J. Prost, *The Physics of Liquid Crystals*, 2nd ed., International Series of Monographs on Physics, 1995, Oxford University Press.
8. P. J. Collings and M. Hird, *Introduction to Liquid Crystals Chemistry and Physics*, The Liquid Crystals Book Series, ed. G. W. Gray, J. W. Goodby and A. Fukuda, 1997, Taylor & Francis.
9. D. Demus, *Hand Book of Liquid Crystals: Fundamentals*, 1st Ed., Handbook of Liquid Crystals Series, ed. D. Demu, J. W. Goodby, G. W. Gray, H. W. Spiess and V. Vill, Vol. 1, 1998, Wiley-VCH.
10. T. Kato, *Curr. Opin. Solid St. M.*, 2002, **6** (6), 513.
11. G. Friedel, *Ann. Phys.-Paris*, 1922, **18**, 273.
12. D. Demus, *Handbook of Liquid Crystals: Low Molecular Weight Liquid Crystals I*, 1st Ed., Handbook of Liquid Crystals Series, ed. D. Demu, J. W. Goodby, G. W. Gray, H. W. Spiess and V. Vill, Vol. 2A, 1998, Wiley-VCH.
13. I. Dierking, *Textures of Liquid Crystals*, Rev. Ed., 2003, Wiley-VCH.
14. C. Tschierske, *Chem, Soc. Rev.*, 2007, **36**, 1930.
15. M. J. Rosen, *Surfactants and Interfacial Phenomena*, 2nd Ed., 1989, John Wiley & Sons.
16. A. G. Petrov, *The Lyotropic State of Matter: Molecular Physics and Living Matter Physics*, 1999, Gordon and Breach Science Publishers.
17. V. Percec, C. M. Mitchell, W. D. Cho, S. Uchida, M. Glodde, G. Ungar, X. B. Zeng, Y. S. Liu, V. S. K. Balagurusamy and P. A. Heiney, *J. Am. Chem. Soc.*, 2004, **126** (19), 6078.

18. D. Demus, *Handbook of Liquid Crystals: High Molecular Mass Liquid Crystals*. 1st Ed. Handbook of Liquid Crystals Series, ed. D. Demu, J. W. Goodby, G. W. Gray, H. W. Spiess and V. Vill, Vol. 3, **1998**, Wiley-VCH.
19. D. Fazio, C. Mongin, B. Donnio, Y. Galerne, D. Guillon and D. W. Bruce, *J Mater. Chem.*, 2001, **11** (11), 2852.
20. S. Bandyopadhyay, M. L. Klein, G. J. Martyna, M. Tarek, *Mol. Phys.*, 1998. **95** (2), 377.
21. A. M. Figueiredo-Neto and S. R. A. Salinas, *The Physics of Lyotropic Lyquid Crystals: Phase Transitions and Structural Properties*, Monographs on the Physics and Chemistry of Materials, ed. R. J. Brook, A. Cheetham, A. Heuer, Sir P. Hirsch, T. J. Marks, D. G. Pettifor, M. Ruhle, J. Silcox, A. P. Sutton, M. V. Tirrell and V. Vitek, Vol. 62, 2005, Oxford University Press.
22. K. Larsson, *Curr. Opin. Colloid In.*, 2009, **14** (1), 16.
23. B. Ericsson, K. Larsson and K. Fontell, *Biochim. Biophys. Acta*, 1983, **729** (1), 23.
24. S. Paasch, F. Schambil, and M.J. Schwuger, *Langmuir*, 1989, **5** (6), 1344.
25. F. Schambil and M. J. Schwuger, *J. Am. Oil Chem. Soc.*, 1987, **64** (5), 662.
26. C. G. Goltner and M. Antonietti, *Adv. Mater.*, 1997, **9** (5), 431.
27. G. S. Attard, C. G. Goltner, J. M. Corker, S. Henke and R. H. Templer, *Angew. Chem. Int. Edit.*, 1997, **36** (12), 1315.
28. F. Livolant and A. Leforestier, *Mol. Cryst. Liq. Cryst.*, 1992, **215**, 47.
29. J. D. Bernal and I. Fankuchen, *Nature*, 1937, **139**, 923.
30. N. V. Madhusudana, *Curr. Sci. India.*, 2001, **80** (8), 1018.
31. M. D. Broglie and E. Friedel, *CR. Acad. Sci.*, 1923, **176**, 738.

32. J. P. F. Lagerwall and F. Giesselmann, *Chem. Phys.*, 2006, **7** (1), 20.
33. M. Baron, *Pure Appl. Chem.*, 2001, **73** (5), 845.
34. G. W. Gray and J. W. G. Goodby, *Smectic Liquid Crystals: Textures and Structures*, 1984, Leonard Hill.
35. D. Demus, *Handbook of Liquid Crystals: Low Molecular Weight Liquid Crystals I*, 1st Ed. Handbook of Liquid Crystals Series, ed. D. Demu, J. W. Goodby, G. W. Gray, H. W. Spiess and V. Vill, Vol. 2B, 1998, Wiley-VCH.
36. C. Oh and M. J. Escuti, *Liq. Cryst. Xii*, 2008, **7050**, 5019.
37. A. Bobrovsky and V. Shibaev, *J. Mater. Chem.*, 2009, **19** (3), 366.
38. S. S. Choi, S. M. Morris, W. T. S. Huck and H. J. Coles, *Soft Matter*, 2009, **5** (2), 354.
39. W. B. Li, M. J. Zhu, X. K. Ding, B. F. Li, W. Huang, H. Cao, Z. Yang, H. Yang, *J. Appl. Polym. Sci.*, 2009, **111** (3), 1449.
40. A. S. Matharu, S. Jeeva and P. S. Ramanujam, *Chem. Soc. Rev.*, 2007, **36**, 1868.
41. P. A. Henderson, A. G. Cook, and C. T. Imrie, *Liq. Cryst.*, 2004, **31** (11), 1427.
42. C. T. Imrie and P. A. Henderson, *Curr. Opin. Colloid In.*, 2002, **7** (5-6), 1359.
43. C. T. Imrie and P. A. Henderson, *Chem. Soc. Rev.*, 2007, **36**, 2096.
44. D. Gabor, *Nature*, 1948, **161** (4098), 777.
45. D. Gabor, *Nature*, 1965, **208** (5009), 422.
46. D. Gabor, *Science*, 1972, **177** (4046), 299.
47. H. Y. Tu, J. S. Chiang, J. W. Chou and C. J. Cheng, *Jpn. J. Appl. Phys.*, 2008, **47** (12), 8838.
48. B. Lohse, R. H. Berg, S. Hvilsted and P. S. Ramanujam, *Jpn. J. Appl. Phys. I*, 2006, **45** (1B), 488.

49. B. Lohse, R. H. Berg, S. Hvilsted and P. S. Ramanujam, *Chem. Mater.*, 2006, **18** (20), 4808.
50. B. Lohse, R. H. Berg, S. Hvilsted and P. S. Ramanujam, *Biopolymers*, 2005, **80** (4), 504.
51. B. Lohse, R. H. Berg, S. Hvilsted and P. S. Ramanujam, *Biopolymers*, 2005, **80** (4), 576.
52. S. Chandrasekhar, B. K. Sadashiva and K. A. Suresh, *Pramana*, 1977, **9** (5), 471.
53. S. Laschat, A. Baro, N. Steinke, F. Giesselmann, C. Hagele, G. Scalia, R. Judele, E. Kapatsina, S. Sauer, A. Schreivogel and M. Tosoni, *Angew. Chem. Int. Edit.*, 2007, **46** (26), 4832.
54. S. Sergeyev, W. Pisula and Y. H. Geerts, *Chem. Soc. Rev.*, 2007, **36**, 1902.
55. I. Aiello, A. Bellusci, A. Crispini, M. Ghedini, D. Pucci and T. Spataro, *Mol. Cryst. Liq. Cryst.*, 2008, **481**, 1.
56. H. Ayeb, F. Ciuchi, G. Lombardo and R. Barberi, *Mol. Cryst. Liq. Cryst.*, 2008, **481**, 73.
57. K. Binnemans, *J. Mater. Chem.*, 2009, **19** (4), 448.
58. C. V. Yelamaggad, I. S. Shashikala, V. P. Tamilenthir, D. S. S. Rao, G. G. Nair and S. K. Prasad, *J. Mater. Chem.*, 2008, **18** (18), 2096.
59. J. L. Serrano, *Metallomesogens: Synthesis, Properties and Applications*, 1996, Wiley VCH.
60. D. Pauluth and K. Tarumi, *J. Mater. Chem.*, 2004, **14** (8), 1219.
61. S. M. Kelly, *Flat Panel Displays: Advanced Organic Materials*, RSC Materials Monographs, ed. J. A. Connor, 2000, The Royal Society of Chemistry.
62. E. Jakeman and E. P. Raynes, *Phys. Lett. A*, 1972, **39**, 69.

63. C. M. Snively and J. L. Koenig, *J. Mol. Struct.*, 2000, **521**, 121.
64. Z. G. Zhu and T. M. Swager, *J. Am. Chem. Soc.*, 2002, **124** (33), 9670.
65. F. Grandjean, *B. Soc. Fr. Mineral. CR.*, 1916, **39**, 164.
66. M. Born, *Sitz. Phys. Math.*, 1916, **25**, 614.
67. W. Maier and A. Saupe, *Z. Naturforsch. Pt. A*, 1958, **13** (7), 564.
68. W. Maier and A. Saupe, *Z. Naturforsch. Pt. A*, 1959, **14** (10), 882.
69. W. Maier and A. Saupe, *Z. Naturforsch. Pt. A*, 1960, **15** (4), 287.
70. G. R. Luckhurst and C. Zannoni, *Nature*, 1977, **267** (5610), 412.
71. D. A. Dunmur, A. Fukuda and G. R. Luckhurst, *Physical Properties of Liquid Crystals: Nematics*, EMIS Data Reviews, 2001, INSPEC.
72. R. Seeliger, H. Haspeklo and F. Noack, *Mol. Phys.*, 1983, **49**, 1039.
73. L. Onsager, *J. Am. Chem. Soc.*, 1936, **58** (8), 1486.
74. W. Maier and G. Meier, *Z. Naturforsch. Pt. A*, 1961, **16** (3), 262.
75. W. Maier and G. Meier, *Z. Naturforsch. Pt. A*, 1961, **16** (5), 470.
76. P. Kirsch and M. Bremer, *Angew. Chem. In. Edit.*, 2000, **39** (23), 4217.
77. M. X. Gu, S. V. Shiyakovskii, and O. D. Lavrentovich, *Phys. Rev. Lett.*, 2008, **100**, 23.
78. M. X. Gu, Y. Yin, S. V. Shiyakovskii, and O. D. Lavrentovich, *Phys. Rev. E*, 2007, **76**, 6.
79. Gaussian 03, R.C., M. J. Frisch, G. W. Trucks, H. B. Schlegel, G. E. Scuseria, M. A. Robb, J. R. Cheeseman, J. A. Montgomery, Jr., T. Vreven, K. N. Kudin, J. C. Burant, J. M. Millam, S. S. Iyengar, J. Tomasi, V. Barone, B. Mennucci, M. Cossi, G. Scalmani, N. Rega, G. A. Petersson, H. Nakatsuji, M. Hada, M. Ehara, K. Toyota, R. Fukuda, J. Hasegawa, M. Ishida, T. Nakajima, Y. Honda, O. Kitao, H. Nakai, M. Klene, X. Li, J.

- E. Knox, H. P. Hratchian, J. B. Cross, V. Bakken, C. Adamo, J. Jaramillo, R. Gomperts, R. E. Stratmann, O. Yazyev, A. J. Austin, R. Cammi, C. Pomelli, J. W. Ochterski, P. Y. Ayala, K. Morokuma, G. A. Voth, P. Salvador, J. J. Dannenberg, V. G. Zakrzewski, S. Dapprich, A. D. Daniels, M. C. Strain, O. Farkas, D. K. Malick, A. D. Rabuck, K. Raghavachari, J. B. Foresman, J. V. Ortiz, Q. Cui, A. G. Baboul, S. Clifford, J. Cioslowski, B. B. Stefanov, G. Liu, A. Liashenko, P. Piskorz, I. Komaromi, R. L. Martin, D. J. Fox, T. Keith, M. A. Al-Laham, C. Y. Peng, A. Nanayakkara, M. Challacombe, P. M. W. Gill, B. Johnson, W. Chen, M. W. Wong, C. Gonzalez, and J. A. Pople, Gaussian, Inc., Wallingford CT, 2004.
80. M. Heckmeier, G. Lüssem, K. Tarumi and W. Becker, *Liquid Crystals for Active Matrix Displays in The Merck Group*, Merck, 2008.
81. P. Kirsch, V. Reiffenrath and M. Bremer, *Synlett.*, 1999, **4**, 389.
82. M. Klasen, M. Bremer and K. Tarumi, *Jpn. J. Appl. Phys. 2*, 2000, **39** (11B), 1180.
83. M. Bremer, M. Klasen-Memmer, D. Pauluth and K. Tarumi, *J. Soc. Inf. Display*, 2006, **14** (6), 517.
84. S. E. Lee, *P. Soc Photo-Opt. Ins.*, 2003, **5003**, 17.
85. S. Chandras and D. Krishnam, *Phys. Lett.*, 1966, **23** (7), 459.
86. S. Chandras, D. Krishnam and N. V. Madhusud, *Mol. Cryst. Liq. Cryst.*, 1969, **8**, 45.
87. B. van Tiggelen and H. Stark, *Rev. Mod. Phys.*, 2000, **72** (4), 1017.
88. M. Miesowicz, *Nature*, 1946, **158** (4001), 27.
89. M. Miesowicz, *Nature*, 1935, **17**, 261.
90. M. Miesowicz, *Bull. Int. Acad. Pol. Sci. Lett. Ser. A*, 1936, 228.
91. C. W. Oseen, *Trans. Faraday Soc.*, 1933, **29**, 833.

92. H. Zöcher, *Trans. Faraday Soc.*, 1933, **29**, 945.
93. J. L. Ericksen, *Arch. Ration. Mech. An.*, 1966, **23** (4), 266.
94. F. M. Leslie, *Q. J. Mech. Appl. Math.*, 1966, **19**, 357.
95. F. M. Leslie, *Arch. Ration. Mech. An.*, 1968, **28** (4), 265.
96. K. Tarumi, U. Finkenzeller and B. Schuler, *Jpn. J. Appl. Phys. 1*, 1992, **31** (9A), 2829.
97. V. Zwetkoff, *Acta. Physicochim. URS.*, 1939, **10**, 555.
98. F. C. Frank, *Discuss. Faraday Soc.*, 1958, **25**, 19.
99. V. Fréedericksz and V. Zolina, *Trans. Faraday Soc.* 1933, **29**, 919.
100. V. Freedericksz and V. Tsvetkov, *Phys. Z.*, 1934, **6**, 490.
101. T. Moses and B. Jensen, *Am. J. Phys.*, 1998, **66** (1), 49
102. P. S. Chen, C. C. Huang, Y. W. Liu and C. Y. Chao, *Appl. Phys. Lett.*, 2007, **90**, 21
103. S. Gauza, J. Li, S. T. Wu, A. Spadlo, R. Dabrowski, Y. N. Tzeng and K. L. Cheng, *Liq. Cryst.*, 2005, **32** (8), 1077.
104. T. Nakanishi, T. Takahashi, H. Mada and S. Saito, *Jpn. J. Appl. Phys. 1*, 2002, **41** (6A), 3752.
105. N. Sasaki, *Jpn. J. Appl. Phys. 1*, 1998, **37** (11), 6065.
106. G. H. Heilmeyer and L. A. Zanoni, *Appl. Phys. Lett.*, 1968, **13**, 91.
107. D. L. White and G.N. Taylor, *J. Appl. Phys.*, 1974, **45** (11), 4718.
108. D. Bauman, H. Moryson and E. Wolarz, *Acta Phys. Pol. A*, 1992, **81** (4-5), 559.
109. A. Ghanadzadeh, M. A. Shahzamanian, S. Shoarinejad, M. S. Zakerhamidi and M. Moghadam, *J. Mol. Liq.*, 2007, **136**, 22.
110. H. Iwanaga, K. Naito, K. Sunohara and M. Okajima, *B. Chem. Soc. Jpn.*, 1998, **71** (7), 1719.

111. A. Jafari, H. Tajalli and A. Ghanadzadeh, *Opt. Commun.*, 2006, **266** (1), 207.
112. L. O. Palsson, H. L. Vaughan, A. Smith, M. Szablewski, G. H. Cross, T. Roberts, A. Masutani, A. Yasuda, A. Beeby and D. Bloor, *J. Lumin.*, 2006, **117** (1), 113.
113. A. K. Srivastava, A. K. Misra, P. B. Chand, R. Manohar and J. P. Shukla, *Phys. Lett. A*, 2007, **371** (5-6), 490.
114. A. K. Srivastava, A. K. Misra, P. B. Chand, R. Manohar and J. P. Shukla, *Mol. Cryst. Liq. Cryst.*, 2008, **495**, 546.
115. A. K. Srivastava, A. K. Misra, R. Manohar and J. P. Shukla, *Phys. Lett. A*, 2008, **372** (41), 6254.
116. E. Wolarz, H. Moryson and D. Bauman, *Displays*, 1992, **13** (4), 171.
117. G. M. Zharkova, S. A. Streltsov and V. M. Khachatryan, *J. Struct. Chem.*, 1993, **34** (6), 930.
118. C. Mauguin, *B. Soc. Fr. Mineral. CR.*, 1911, **34**, 71.
119. C. Mauguin, *CR. Acad. Sci.*, 1911, **152**, 1680.
120. J. A. Castellano, *Mol. Cryst. Liq. Cryst.*, 1983, **94** (1-2), 33.
121. R. Williams, *J. Chem. Phys.*, 1963, **39** (2), 384.
122. R. Williams, *Nature*, 1963, **199**, 273.
123. Osray-Liquid-Crystal-Group, *Mol. Cryst. Liq. Cryst.*, 1971, **12**, 251.
124. H. Kawamoto, *IEEE. Power. Electron.*, **90** (4), 460.
125. S. D. Ltd, *Display*, 1980, **1** (4), 186.
126. J. Xia, Y. Shi and H. Yin, *Display*, 2009, **30** (1), 27.
127. Microscribe, *Displays*, 1985, **6** (3), 170.
128. E. U. Ltd., *Displays*, 1985, **6** (4), 229.

129. S. Kobayashi, H. Hori and Y. Tanaka, in *Handbook of Liquid Crystal Research*, ed. P. J. Collings and J. S. Patel. **1997**, Oxford University Press.
130. K. Nakao, *J. Jpn Liq. Cryst. Soc.*, 1999, **3**, 62.
131. G.W. Gray, K. J. Harrison and J. A. Nash, *Electron. Lett.*, 1973, **9** (6), 130.
132. R. Eidenschink, D. Erdmann, J. Krause and L. Pohl, *Angew. Chem.*, 1978, **90**, 133.
133. R. Eidenschink, D. Erdmann, J. Krause and L. Pohl, *Angew. Chem. Int. Edit.*, 1978, **17** (2), 133.
134. R. Eidenschink, G. Haas, M. Römer and B. S. Scheuble, *Angew. Chem. Int. Edit.*, 1984, **23** (2), 147.
135. R. Eidenschink, G. Haas, M. Römer and B. S. Scheuble, *Angew. Chem.*, 1984, **96**, 151.
136. B. J. Lechner, F. J. Marlowe, E. O. Nester and J. Tults, *IEEE. Power. Electron.*, 1971, **59** (11), 1566.
137. T. P. Brody, J. A. Asars and G. D. Dixon, *Trans. Electron Devices*, 1973, **20** (11), 995.
138. T. Geelhaar and D. Pauluth, *Nachr. Chem. Tech. Lab.*, 1997, **45** (1), 9.
139. M. Schadt and W. Helfrich, *Appl. Phys. Lett.*, 1971, **18** (4), 127.

Chapter 2

Synthesis of Guest Molecules for LC

Hosts

2. Synthesis of Guest Dopant Molecules for LC Hosts

2.1. Dopant Structure

Commercial materials used in LC devices are usually blends of many components, carefully composed to give a mixture that exhibits desirable properties including operating temperature range, switching times, voltage hold ratios, as well as the desired LC phases and optical properties. It is helpful, however, to consider these existing complex mixtures as a singular material, the host, into which a new component, the dopant, can be introduced to further modify or tune physical properties. For LC compositions for display applications, an ideal dopant will increase the switching rate of the LC host without causing any detrimental effect to other properties. The dopant may increase switching rate by increasing the free volume between host molecules and / or aligning the fast-switching dopant with the LC to “*drag*” the host in response to changes in the electric field. To aid studies of the mechanism of operation of the dopant, molecular substructures featuring a spectroscopic “*handle*” that will allow selective monitoring of the dopant will be an advantage. In the present case, Raman spectroscopy is a convenient tool, with time-resolved methods available to monitor motion of both the dopant and host. By following the time-response of individual components it may be possible to determine if the switching event of host and dopant take place in unison (the free volume model) or sequentially (the dragging mechanism).

To promote compatibility of the components, the dopant and LC host should feature common structural features. Given the rod-like nature of many common mesogens, a simple tail-linker-headgroup dopant structure was proposed for this study (Figure 1).

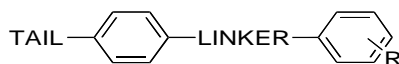


Figure 1. Dopant design based on many common mesogenic LC materials

The molecular structure of the dopant with distinct tail, linker and head group (R), allows considerable flexibility of both the molecular volume of the dopant, which will in turn control the free volume in the host/dopant mixture, and also the dipole moment of the dopant, which will allow the dielectric characteristics of the system to be systematically varied. The dopant should be capable of interchelating into the LC host, thereby reducing intermolecular interactions between the components of the LC host and also introduce a new dipolar component that will interact with the applied electric field as based on research within Sony from previous projects.

In this work, first generation dopants based on an acetylenic linker, which gives a rigid rod-like structure and an excellent Raman spectroscopic signature, were employed. The flexibility of alkyne coupling reactions permits a wide range of tail and head groups to be incorporated within the dopant structure. For these first generation dopants, tail moieties consisted of alkoxy or alkyl chains and the head groups were various halogenated arene rings, heteroarenes and bulky head groups. Following a serendipitous discovery, within the Sony research group, that doping LC phases with diphenyl ethers could increase switching speeds, second generation dopants were developed to expand the basic design to include not only a wide range of tail and head groups but also to introduce semi-rigid linkers, giving a variety of non-linear molecular motifs, defining a '*bite angle*' in the linker (Figure 2).

Geometry optimisations for a range of potential dopant structures (Gaussian03, DFT B3LYP 6-31g+) [1] were carried out as a function of the linker group.

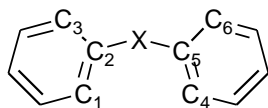


Figure 2

The results are shown in Table 1, which summarises the geometries of the two rings indicating the variation of the angle and how we can change it via different linking groups, with representations of molecules shown in appendix A (Figure A1 – A5). These second generation dopants can be considered as belonging to one of two sub-categories, distinguished by the nature of the linker. The carbonyl, dioxolane and methylene linkers form one class, as together they can be derived from acetalisation and reduction reactions from commercially available starting materials. The propylene linker forms a second class and can be synthesised using a relatively straight forward sequence of organic reactions, including aryl addition, lithiation, nucleophilic substitution and Friedel-Crafts arylation. The overall appeal of the series is, therefore, enhanced by the ability to manipulate the steric, geometric and electronic properties of the dopants through simple modifications to the tail, linker and head groups from commercially available starting materials.

X	Angle C ₂ -X-C ₅	Torsion Angle C ₂ -X-C ₅ -C ₆
-O-	109.47	81.46
-CH ₂ -	113.62	48.04
-CMe ₂ -	109.93	51.49
-CO-	120.87	31.56
Dioxolane (-C(OCH ₂ CH ₂ O)-)	113.02	55.41

Table 1.

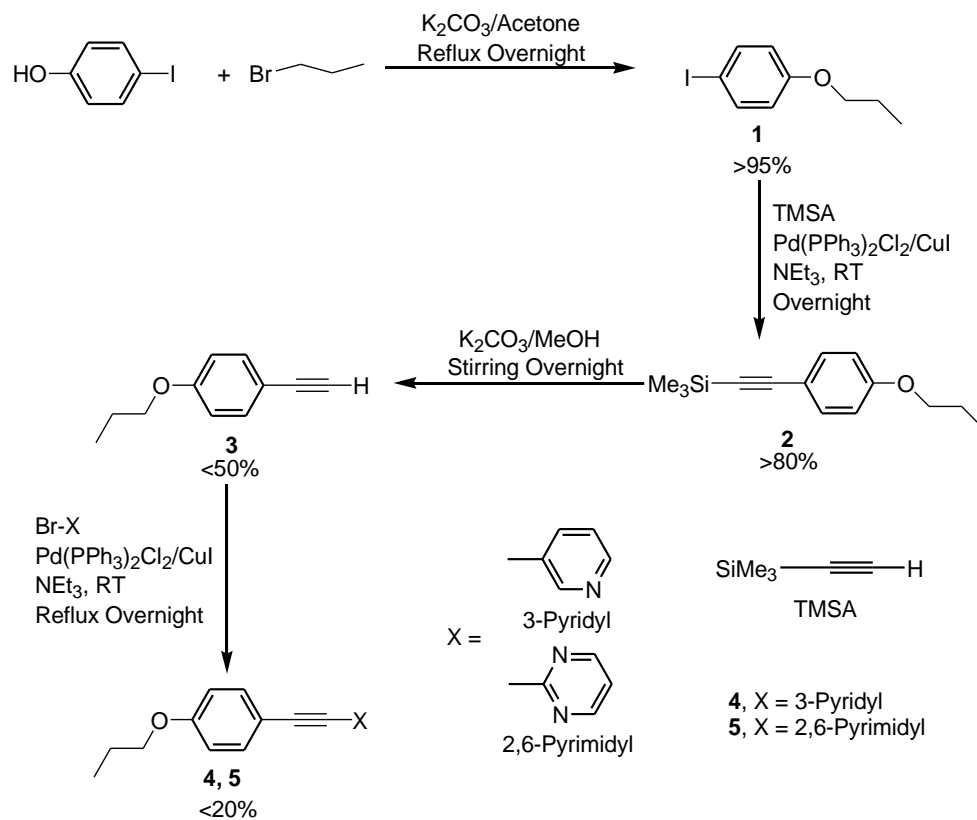
2.2. Synthetic Strategy

2.3. Organic Reactions

Elementary mechanistic detail of each of the key procedures used in the preparation of the dopants, such as the Williamson Reaction, Diels-Alder Reaction, Friedel-Crafts Reaction, Wolf-Kischner Reduction, formation of the dioxolane are identified and the Sonogashira reaction which will be discussed later.

2.3.1. Synthesis of Acetylenic Dopants

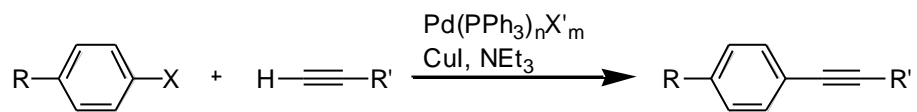
Our research started with synthesising iodo arylether **1** from 4-iodo phenol and bromopropane using the *Williamson Reaction* (Scheme 1), with retention of the aryl iodide allowing subsequent introduction of the acetylenic linker using the *Sonogashira Reaction* [2-11].



Scheme 1. Synthetic route for the acetylenic dopants.

2.3.1.1. Sonogashira Cross Coupling Reaction.

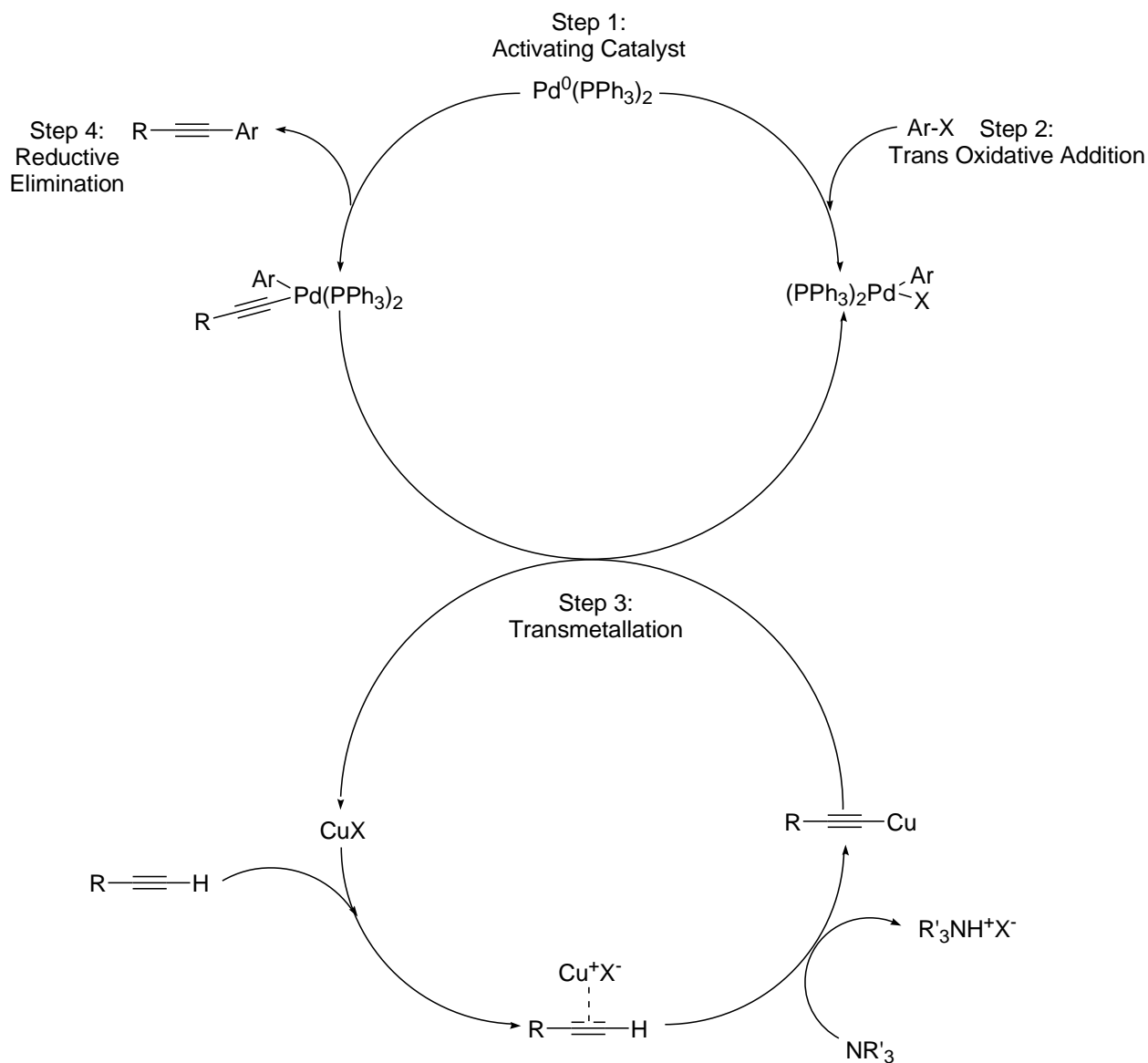
Within the general area of Palladium-catalysed cross coupling reactions, [12] useful reaction sequences are the Heck reaction [13-18] (coupling of aryl/vinyl halides to terminal alkenes), the Stille reaction [19-21] (coupling of aryl/vinyl halides to organo-tin compounds), the Suzuki-Miyaura reaction [22-24] (coupling of aryl/vinyl halides to organo-boron compounds) and the Sonogashira cross coupling reaction (coupling reactions of selective terminal acetylenes and aryl halides as shown in Scheme 2) [25, 26]



Scheme 2. The Sonogashira Reaction

2.3.1.1.1. The Sonogashira Reaction Mechanism [28]

The proposed Sonogashira catalytic cycle consists of the following steps: 1) Catalytic initiation, 2) Oxidative addition, 3) Transmetallation (*trans-cis* isomerisation) and 4) Reductive elimination, (Scheme 3).

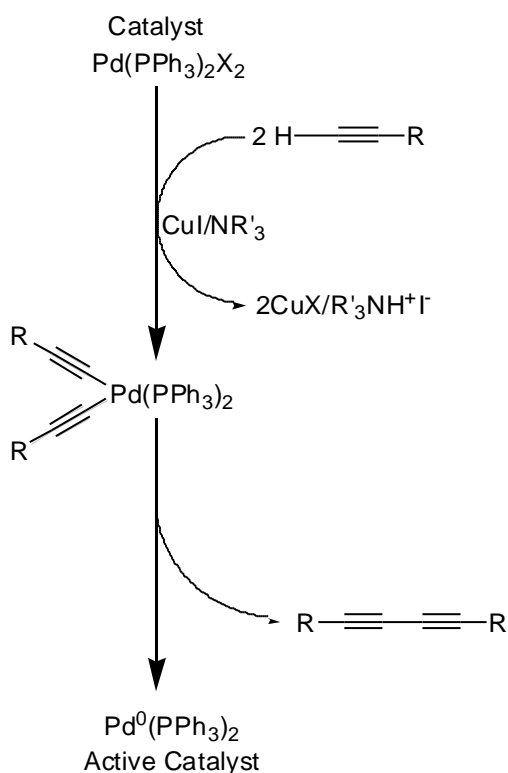


Scheme 3. The proposed catalytic cycle for the Sonogashira reaction.

2.3.1.1.2. Step 1: Catalytic Initiation

During the catalytic initiation the Palladium catalyst is converted to Pd^0 active state, which is extremely air sensitive (Scheme 4). The formation of the active species occurs *in situ* under an inert atmosphere from the precursor $\text{Pd}^{\text{II}}\text{Cl}_2(\text{PPh}_3)_2$. Initially the acetylene and copper reagents form the Cu-acetylide intermediate, which then couples to the Pd precursor

forming $(\text{PPh}_3)_2\text{Pd}(\text{C}\equiv\text{CR})_2$ species. This then reductively eliminates the diyne $\text{RC}\equiv\text{CC}\equiv\text{CR}$ and yielding the active species, “ $\text{Pd}^0(\text{PPh}_3)_2$ ”, although the precise formulation and coordination is not by any means well-defined in most reactions.

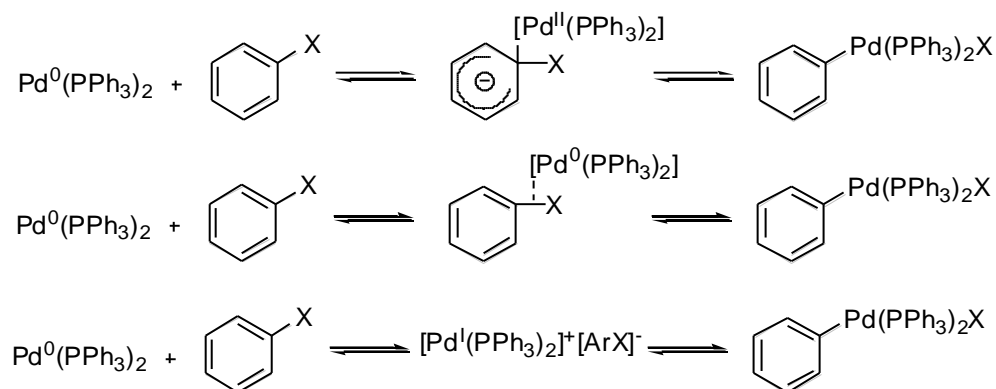


Scheme 4. Mechanism of the catalytic initiation.

2.3.1.1.3. Step 2: Oxidative Addition

The second step is an oxidative addition of the aryl halide. Phosphine ligands have electron donating properties along with steric bulk and both attributes aid the addition step. Early cross coupling reactions used $\text{Pd}(\text{PPh}_3)_4$ as it could readily dissociate in solution forming $\text{Pd}^0(\text{PPh}_3)_2$, which allows the oxidative addition of Ar-X to occur. There are three suggested pathways through which the oxidative addition step may proceed: (1) nucleophilic aromatic

substitution, (2) a 3 centred concerted addition and (3) a single electron transfer process (Scheme 5).



Scheme 5. The three possible separate pathways to the oxidative addition mechanisms: (1) nucleophilic aromatic substitution. (2) 3-centred concerted addition and (3) is the single electron transfer.

The oxidative addition step is rate limiting and a degree of control over the process can be exerted by either making the aryl halide more reactive or by increasing the nucleophilicity at the Pd catalyst centre. The aryl halide reactivity with Pd⁰ follows the simple trend Ar-I > Ar-Br >> Ar-Cl >> Ar-F. [27] The rates of reaction also increase when the electron-withdrawing group is present para to the halide and reflects the strength of the C-X bond. Indeed, the bond breaking between the halide and aryl moiety is suggested to be a major factor in determining the rate of reaction, and most rapid when the halide is iodine. [28-31]

2.3.1.1.4. Step 3: Transmetalation

Transmetalation is the exchange of the acetylide moiety from copper to palladium. Initial reaction of the terminal acetylene with Cu^(I) in the presence of the amine base affords a

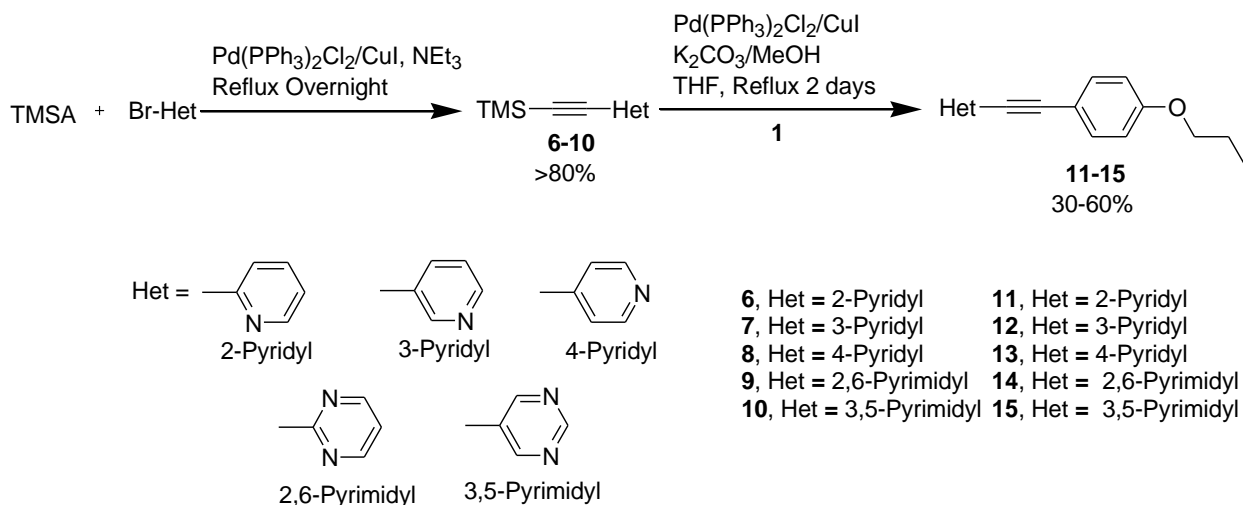
species approximating “Cu(C≡CR)”, although it is most likely that the copper centre is further coordinated by amine ligands. The differences in the transmetallation step usefully defines each metal-catalysed cross coupling reactions, for example, in the Sonogashira reaction it is the exchange of ligands between Cu- and Pd, while in the Stille and Suzuki-Miyaura reactions the Pd exchanges with an organo-tin and a boronate species, respectively.

2.3.1.1.5. Step 4: Reductive Elimination

This step regenerates the active Pd⁰(PPh₃)₂ catalyst and completes the catalytic cycle and generates the coupled product. Stille *et al.* showed that the reductive step proceeds through a *cis* geometry, which also retains the stereochemistry of the reactants. [19]

2.3.2. Higher Yielding Synthetic Route to Acetylenic Dopants

The terminal alkynes (**2**, **3**) in Scheme 1 decomposed over time giving low yields of the dopants **4** and **5** (Scheme 1). Therefore, the synthetic route was modified with the sequence reversed; the head group was initially cross-coupled with trimethylsilyl protected acetylene to afford the Me₃Si-capped alkynes **6-10**, to try and improve the yields. This method proved to be more robust offering a longer “shelf life” to the intermediates and a subsequent *in situ* de-protection and cross coupling with **1** in a “one-pot” approach (Scheme 6) leading to improved yields.



Scheme 6. Synthetic route to higher yielding acetylenic dopants.

The synthetic methodology outlined in Scheme 6 was also used in the preparation of a small derivative series of dopants (**16**, **17**, Figure 3) that kept the same head groups but varied the tail chain length. This enabled the “odd and even effect” of the number of hydrocarbon units in the tail to be assessed, [32, 33] whilst also qualitatively causing viscosity and molecular volume change of the guest-host effect inside the cell. However, these compounds proved to be prone to discolouration upon standing, possibly due to oxidation of the heterocycle.

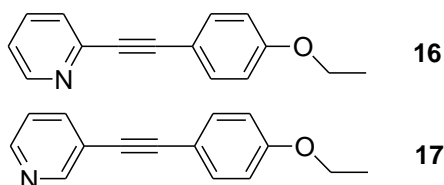
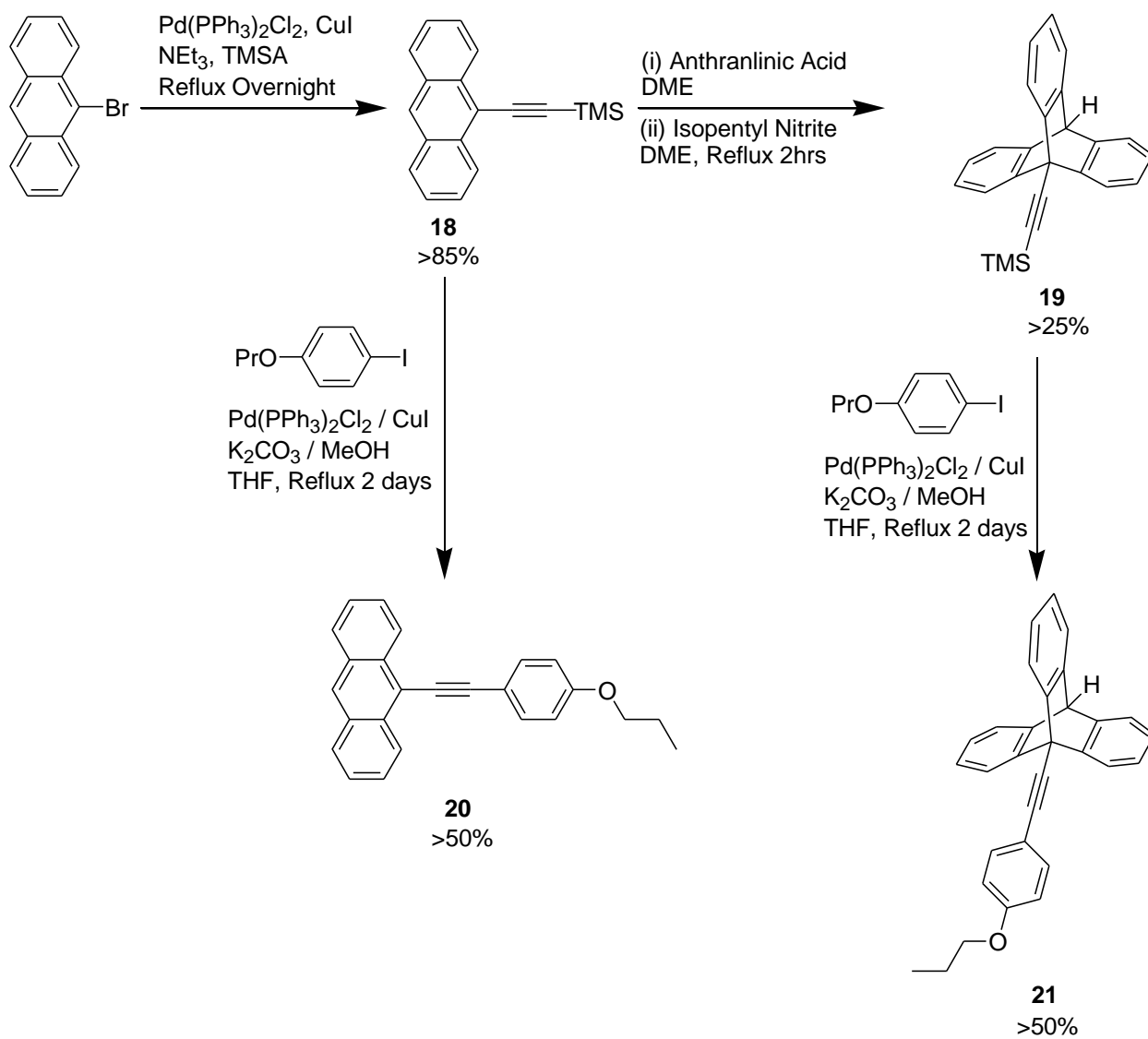


Figure 3. Dopants **16** and **17**.

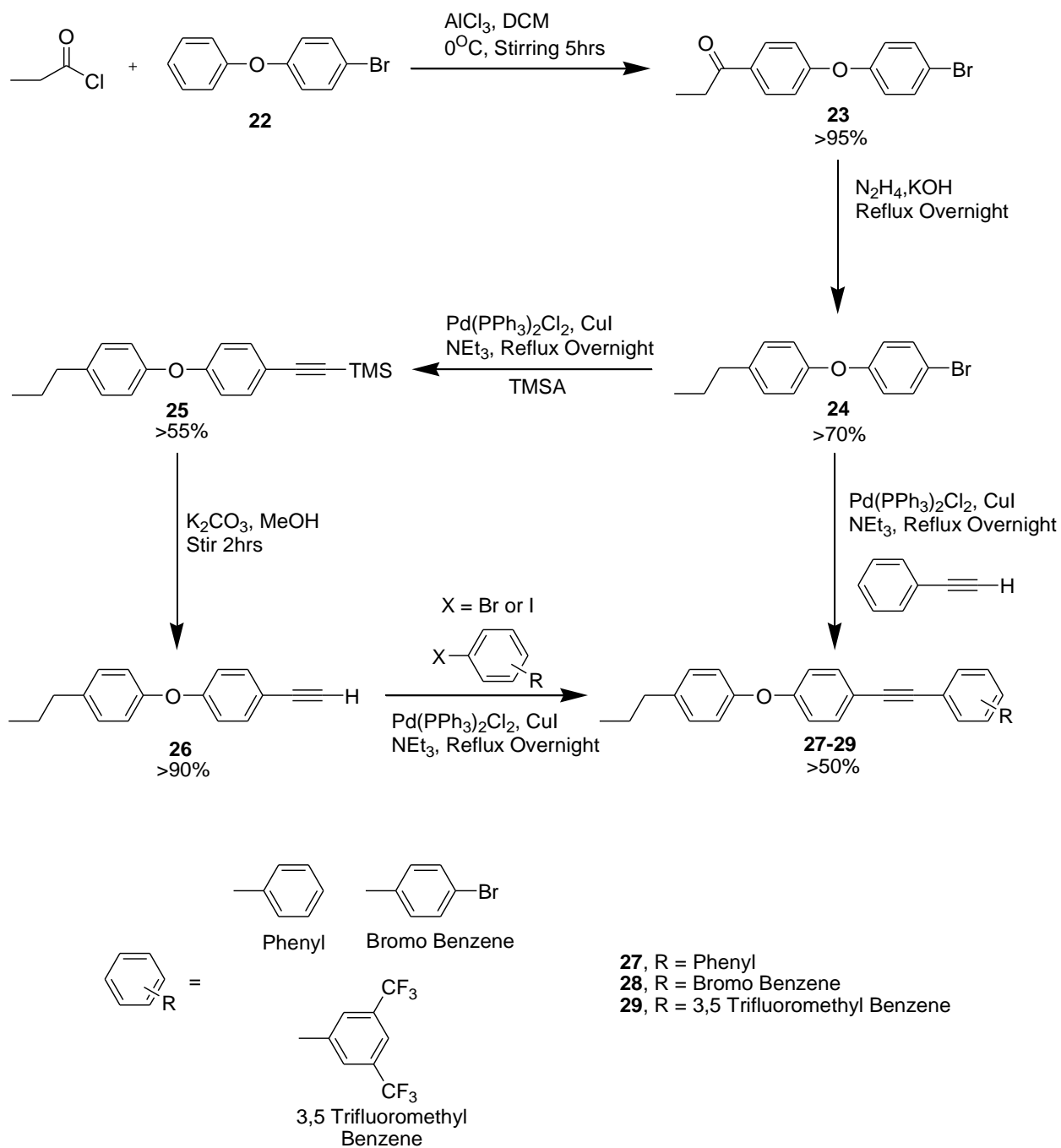
Swager *et al.* have demonstrated that the inclusion of the triptycene moiety into molecules increases the order parameter (along with such molecules like iptycenes). [34-36] The triptycene moiety which would also introduce more free volume, is synthesised by reaction of benzyne with an anthracene derivative (Scheme 7).



Scheme 7. Reaction scheme for acetylenic dopants with an anthracene (**20**) and tryptene (**21**) head groups

2.3.3. Synthesis of Acetylenic and Ether Dopants

Variation in the tail structure was also explored through the introduction of a biphenyl ether moiety into the general acetylenic linker dopant structure (Scheme 8).



Scheme 8. Synthetic reaction scheme of dopants containing both ether and acetylenic moieties.

The key intermediates **23** and **24** were also found to be useful dopants in their own right (Chapter 3), and a short series of derivatives based on this structure with different tail lengths (**30-31**, Figure 4) was also prepared in an entirely analogous manner.

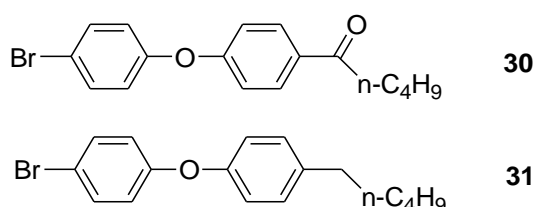
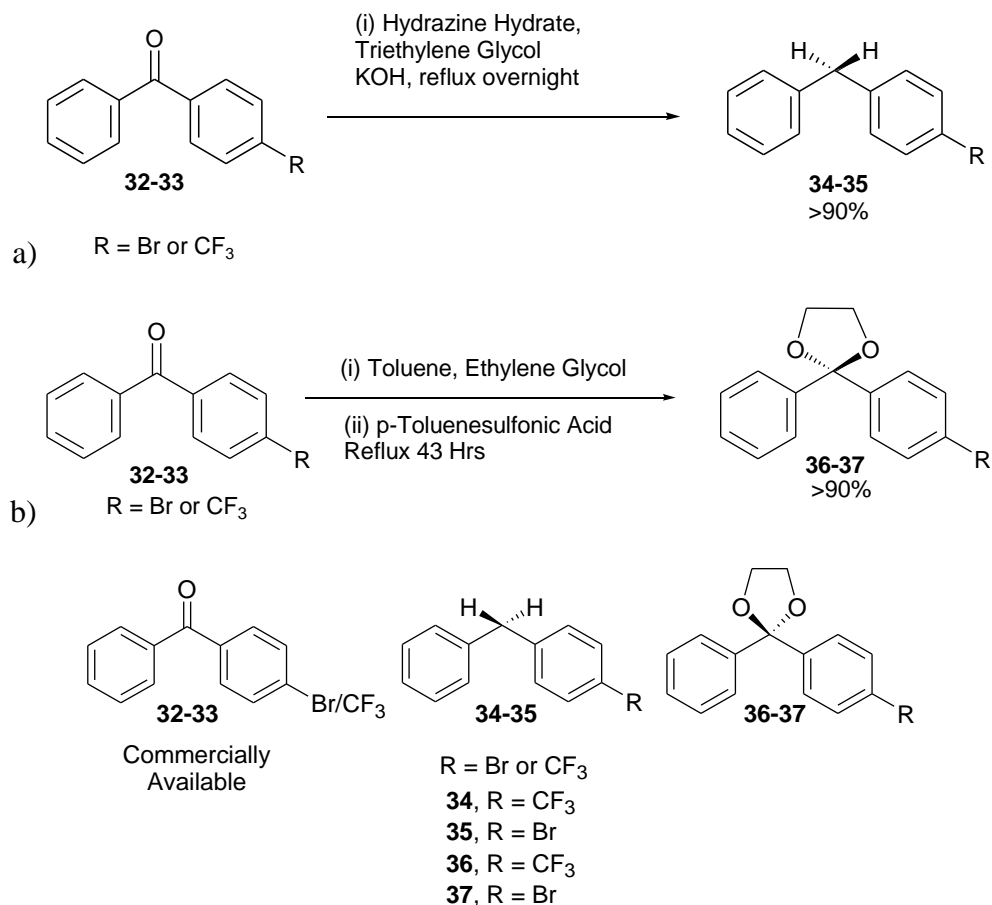


Figure 4. New dopants based on compounds **23** and **24** with longer tail lengths.

2.3.4. Synthesis of ‘CR₂’ Bridged Dopants

2.3.4.1. Synthesis of ‘CR₂’ – ‘Methylene’ Derivative Linker Dopants

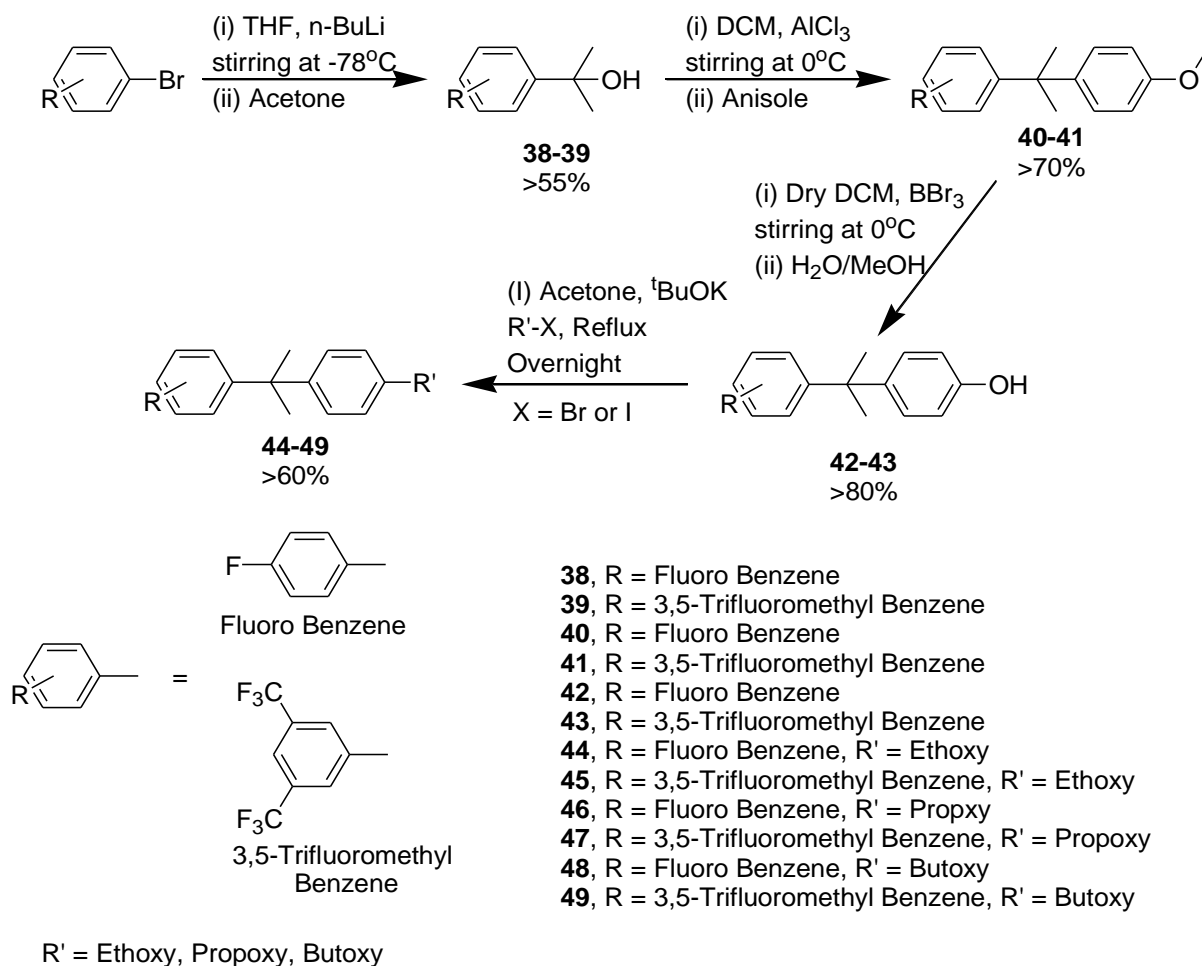
Commercially available starting materials (**32-33**) with a benzophenone sub-structure are a series of compounds that are comparable to Figure 3 where X = C=O with a bromine and trifluoromethyl substituent's. The design of these introduced differing dipole moments and compatibility to dielectrically negative LC's. The initial step was to synthesise the methylene linker (where X = CH₂) by reduction of a ketone (Scheme 9a), compounds **34-35**. Formation of the dioxolane was the next step in the series which was carried out by forming an acetal derivative with the carbonyl compound the commercial starting (Scheme 9b), giving compounds **36-37**.



Scheme 9. Synthetic reaction schemes to the Methylene linker and dioxolane compounds.

2.3.5. Synthesis of Propylene Linker Dopants

A 2, 2' propylene linker core was an appropriate structure target as this provides a smaller 'bite' angle between the two aryl rings than the ether and dioxolane moieties. With a number of commercial materials having a fluorine moiety alternated to bromo benzene derivative, a variety of potential dopants can, in principle, be synthesised. The molecules that were synthesised are shown and outlined in Scheme 10, with dopants **40-49** containing a range of head groups and also featuring tails of varying hydrocarbon chain lengths.



Scheme 10. Synthetic reaction scheme for the propylene linker dopants with varying head and tail groups.

2.4. References

1. Gaussian 03, R.C., M. J. Frisch, G. W. Trucks, H. B. Schlegel, G. E. Scuseria, M. A. Robb, J. R. Cheeseman, J. A. Montgomery, Jr., T. Vreven, K. N. Kudin, J. C. Burant, J. M. Millam, S. S. Iyengar, J. Tomasi, V. Barone, B. Mennucci, M. Cossi, G. Scalmani, N. Rega, G. A. Petersson, H. Nakatsuji, M. Hada, M. Ehara, K. Toyota, R. Fukuda, J. Hasegawa, M. Ishida, T. Nakajima, Y. Honda, O. Kitao, H. Nakai, M. Klene, X. Li, J. E. Knox, H. P. Hratchian, J. B. Cross, V. Bakken, C. Adamo, J. Jaramillo, R. Gomperts,

- R. E. Stratmann, O. Yazyev, A. J. Austin, R. Cammi, C. Pomelli, J. W. Ochterski, P. Y. Ayala, K. Morokuma, G. A. Voth, P. Salvador, J. J. Dannenberg, V. G. Zakrzewski, S. Dapprich, A. D. Daniels, M. C. Strain, O. Farkas, D. K. Malick, A. D. Rabuck, K. Raghavachari, J. B. Foresman, J. V. Ortiz, Q. Cui, A. G. Baboul, S. Clifford, J. Cioslowski, B. B. Stefanov, G. Liu, A. Liashenko, P. Piskorz, I. Komaromi, R. L. Martin, D. J. Fox, T. Keith, M. A. Al-Laham, C. Y. Peng, A. Nanayakkara, M. Challacombe, P. M. W. Gill, B. Johnson, W. Chen, M. W. Wong, C. Gonzalez, and J. A. Pople, Gaussian, Inc., Wallingford CT, 2004.
2. D. Toussaint, J. Suffert, and C. G. Wermuth, *Heterocycles*, 1994, **38** (6), 1273.
 3. P. J. Low, O. Koentjoro, P. Zuber, A. Beeby, K. Findlay, T. B. Marder, D. S. Yufit and J. A. K. Howard, *IEEE. Sys. Man. Cybern.*, 2002, 343.
 4. M. Lemhadri, H. Doucet and M. Santelli, *Tetrahedron*, 2005, **61** (41), 9839.
 5. M. Feuerstein, H. Doucet and M. Santelli, *Tetrahedron Lett.*, 2005, **46** (10), 1717.
 6. M. Feuerstein, H. Doucet and M. Santelli, *Tetrahedron Lett.*, 2004, **45** (8), 1603.
 7. M. Feuerstein, F. Berthoil, H. Doucet and M. Santelli, *Synthesis-Stuttgart*, 2004, **8**, 1281.
 8. T. L. Draper and T. R. Bailey, *J. Org. Chem.*, 1995, **60** (3), 748.
 9. S. H. Chanteau and J. M. Tour, *Tetrahedron Lett.*, 2001, **42** (17), 3057.
 10. C. J. Booth, D. A. Dunmur, J. W. Goodby, J. S. Kang and K. J. Toyne, *J. Mater. Chem.*, 1994, **4** (5), 747.
 11. W. M. Khairul, L. Porres, D. Albesa-Jove, M. S. Senn, M. Jones, D. P. Lydon, J. A. K. Howard, A. Beeby, T. B. Marder and P. J. Low, *J. Clust. Sci.*, 2006, **17** (1), 65.
 12. R. Rossi, A. Carpita and F. Bellin, *Org. Prep. Proced. Int.*, 1995, **27** (2), 127.

13. R. F. Heck and J. P. Nolley, *J. Org. Chem.*, 1972, **37** (14), 2320.
14. T. Mizoroki, K. Mori and A. Ozaki, *B. Chem. Soc. Jpn.*, 1971, **44** (2), 581.
15. K. Mori, T. Mizoroki, and A. Ozaki, *B. Chem. Soc. Jpn.*, 1973, **46** (5), 1505.
16. A. Schoenbe, I. Bartolet and R. F. Heck, *J. Org. Chem.*, 1974, **39** (23), 3318.
17. A. Schoenbe and R. F. Heck, *J. Org. Chem.*, 1974, **39** (23), 3327.
18. A. Schoenbe and R. F. Heck, *J. Am. Chem. Soc.*, 1974, **96** (25), 7761.
19. J. K. Stille and D. Milstein, *Abstr. Pap. Am. Chem. S.*, 1978, **176**, 168.
20. T. Masuda and J. K. Stille, *J. Am. Chem. Soc.*, 1978, **100** (1), 268.
21. D. Milstein and J. K. Stille, *J. Am. Chem. Soc.*, 1978, **100** (11), 3636.
22. N. Miyaura, K. Yamada and A. Suzuki, *Tetrahedron Lett.*, 1979, **36**, 3437.
23. N. Miyaura and A. Suzuki. *J. Chem. Soc. Chem. Comm.*, 1979, **19**, 866.
24. A. Suzuki and N. Miyaura, *Abstr. Pap. Am. Chem. S.*, 1979, **177**, 260.
25. R. Chinchilla and C. Najera, *Chem. Rev.*, 2007, **107** (3), 874.
26. K. Sonogashira, Y. Tohda and N. Hagihara, *Tetrahedron Lett.*, 1975, **50**, 4467.
27. M. Feuerstein, H. Doucet and M. Santelli, *J. Mol. Catal. A-Chem.*, 2006, **256** (1-2), 75
28. M. Biswas, P. Nguyen, T. B. Marder and L. R. Khundkar, *J. Phys. Chem. A*, 1997, **101**, (9), 1689.
29. H. A. Dieck and F. R. Heck, *J. Organomet. Chem.*, 1975, **93**, (2), 259.
30. I. J. S. Fairlamb, R. J. K. Taylor, J. L. Serrano and G. Sanchez, *New J. Chem.*, 2006, **30** (12), 1695.
31. P. Nguyen, S. Todd, D. Vandenbiggelaar, N. J. Taylor, T. B. Marder, F. Wittmann and R. H. Friend, *Synlett.*, 1994, **4**, 299.
32. D. Bauman, H. Moryson and J. Jadzyn, *Acta Phys. Pol. A*, 1994, **85** (3), 553.

33. S. F. Zheng, K. Q. Zhao, W. H. Yu, B. Q. Wang and P. Hu, *Acta Chim. Sinica*, 2009, **67** (8), 825
34. T. M. Long and T. M. Swager, *J. Mater. Chem.*, 2002, **12** (12), 3407.
35. Z. H. Chen and T. M. Swager, *Org. Lett.*, 2007, **9** (6), 997.
36. T. M. Swager, *Acc. Chem. Res.*, 2008, **41** (9), 1181.

Chapter 3

Electro-optic (EO) Measurements and Analysis

Chapter 3: Electro-Optic (EO) Measurements and Analysis

3.1. Introduction

Liquid crystal displays (LCD) offer many advantages over cathode ray tube (CRT) based displays, including physical size, cost of production and energy usage. However, improvements to LCD technology are still required, with on-going research on LC blends seeking to improve the kinetics of the LC switching process (to improve video refresh rates), increase the viewing angle, the voltage holding ratio (VHR) and extend contrast achievable. [1] As has been described in Chapter 1, composition of the LC blend can be manipulated to tune physical properties such as dielectric anisotropy ($\Delta\epsilon$), birefringence (Δn), viscosity (γ) and elastic constants (K) in order to improve the properties of the LCD. [1, 2] This project is primarily concerned with improvement in the kinetics and VHR of LCDs through the introduction of suitable additional components, referred to as “dopants”, to the LC blend. Since the first phase of the study is largely qualitative, i.e. does a particular dopant structure give reduced switching rates and improved VHR, the discussion will not be concerned in too much detail about the physics of LC properties. Figure 1 shows the relationship between the rise and decay times, and threshold voltage in terms of some of the physical properties of liquid crystals.

Material parameters we control to improve response time

$$\tau_{rise} = \frac{\gamma}{\Delta\epsilon(E^2 - E_0^2)} \approx \frac{\gamma}{\Delta\epsilon E^2}$$

$$\tau_{decay} = \frac{d^2 \gamma}{\pi^2 K} \quad E_0 = \frac{\pi}{d} \sqrt{K}$$

γ = Viscosity
 $\Delta\epsilon$ = Dielectric Anisotropy
 E = Applied electric field
 E_0 = Threshold electric field
 K = Elastic constants
 d = Cell thickness

Figure 1. The equations for calculating the response times of the liquid crystal with the anisotropic properties [3]

In the discussion that follows, the kinetic response times, VHR and associated properties were measured and calculated in collaboration with the team members at SONY's research facility in Stuttgart Germany from experimentally determined parameters. Results are reported graphically and illustrate what, if any, effect the dopants have on the response times of the LC host.*

3.1.1. Introduction to Electro-optics

The electro-optic effect is the change of the optical properties of medium in response to an applied electric field. The electro-optic effect is measured with optical wavelengths of the electromagnetic radiation spectrum in the order of 0.02 to 1000 μm , i.e. ultraviolet to the far-infrared region. Materials that display the electro-optic effect find application in areas as diverse as electro-optic sensors, optical signal processing, optical communications, computing, holography and displays.

* Many measurements were done by SONY but upon my visit I studied dopant compounds **22** and **23** with the starting material 4-bromo diphenyl ether.

The EO effect can be further divided into two sub categories; change in absorption coefficient and refractive index. LCDs exploit the change of the refractive index of the medium, which is related to birefringence using the EO effect.[^] The contributing coefficient that will arise when using crystalline substances with asymmetry (LCs) has been described as the linear EO effect, which is also known as the Pockel effect. The Pockel effect shows the relationship between the birefringence of the system and the optical properties, and is well-known in liquid crystals. [4, 5] Birefringence is generated in an optical medium by an applied external electric field. It has been noted that birefringence, and hence the optical properties of the medium, is proportional to the applied electric field. This is of no surprise as the increased electric field induces a proportional amount of re-orientation in the medium leading to an equivalent amount of light rotation (arising from the birefringence) and hence intensity, until the maximum driving force for the complete switch on for the cell is reached by the electric field. The EO effect orientates the molecules in such a way that aligns the dipole moment of the medium with the applied field. In other words, as the field is applied across the cell, i.e. z direction, then the birefringence occurs in the xy plane of the cell. The EO effect can therefore be used to define the specific orientation of the medium, which can then be switched between two positions as the applied field is on and off. [5-8]

3.1.2. Switching in LC

LCDs are presently based on the “*texture*” change which is the change in the observed Williams domains. The change in texture occurs when an external electric field is applied,

[^] Birefringence is the rotation and change of direction of polarisation of light. For example inside a LCD device (cell) it is the rotation of plan polarised light to allow or prevent the light passing through the device so that it is either illuminated or appears black.

and for useful display purposes the resulting texture must be homeotropic in nature (an overall same texture; no boundaries of more than one texture), which can only be achieved if the applied electric field surpasses the threshold voltage (minimum voltage required for change to occur). The optical properties of the LC are modified due to the applied electric field causing texture change which in turn causes the polarisation of the incident optical radiation to change when propagating through the cell. The texture can be observed through a polarised microscope giving a pattern of colours similar to that when a thin film of oil covers water.

To study the EO effect in a liquid crystal sample, the LC cell is placed between crossed polarisers such that the applied field will induce a re-orientation in the twist to either rotate or not to rotate the plane of polarisation of light passing through the cell. Rotation of the plane of polarisation of light is monitored via the analysing polariser and a photo-detector and, by measuring the intensity change over time, it is possible to calculate the response times of the cell. The induced perturbation will either induce a twist, causing the light to rotate and match up with a second polariser (vertically aligned or VA cell) or, if the perturbation reduces the twist, the light will not rotate taking it out of phase with the second polariser (twisted nematic or TN cell). When manipulating the director in order to bring about the texture change between the maximum (total change and EO switch of LC in the cell) and the minimum there is a specific range of the transmittance that is only considered when measuring the EO effect. The transmittance range is between 10% (E10) and 90% (E90) of the EO effect. The exclusion of the first and last 10% of the transmitted light is because it excludes the surface interactions and boundary forces such as the forces of

interaction between the alignment layer and the LC molecules that have to be overcome in the rise phase of the switch (0 – 10%) and the decay phase of the switch (100 – 90%). [6, 9, 10]

3.2. Dopant Structure Reasons and Relations to EO

The dopants **11-15** (Chapter 2) feature a linear rod-like molecular structure, comparable to that of nematic LC molecules. The inclusion of these species in the LC material potentially leads to an increase in molecular free volume for the LC host which has been attributed to potential increase in response times [11] whilst offering a wide range of polar head groups that induce different dipole moments from dopant to dopant. Thus dopants **16-17** introduce the odd and even effect, with the odd and even nomenclature referring to the number of hydrocarbon units in the tail. It has been reported that changing the odd / even number could alter the orientational ordering inside the cell and alter the broad temperature transition range of the nematic phase. [12-14] Also the tail chain length variation potentially alters the viscosity and molecular volume change of the guest-host effect inside the cell. Swager has demonstrated that triptycene based moieties increase the order parameter through a variation in free molecular volume. [11, 15-17] Dopants **20-21** allow triptycene-based dopants to be investigated, with the introduction of a bulky head group to manipulate the molecular ‘free’ volume permitting comparison with the polar head groups as moderating effects on the response times and the potential to lower VHRs (Chapter 1).

Preliminary studies by SONY had demonstrated that doping LC devices with diphenyl ether derivatives have a positive effect on response times. This positive result was attributed to the “*bite angle*” of the ether linker bringing about a disruption to the LC structure. The

introduction of the biphenyl ether moiety can be viewed as incorporating a phenyl ring into the alkoxy tails of the analogous non-acetylenic dopants **23-24**, thus making a systematic structural change in the dopant, and hence viscosity and molecular volume. Secondly, the biphenyl core is comparable to many commercially available positive liquid crystals and dopants of this type can therefore be used in TN-LCDs experiments. Finally, the bromine atom in **24** can be substituted to incorporate the acetylenic moiety and allowing the introduction of a head group, as well as being a Raman active probe. These head groups would be analogous to the proposed dopant design shown in Figure 2 giving potential for differing dipole moments and size that will be able to be tested in TN-LCDs and VA-LCDs. Dopants **25-31** were synthesised to further the study the effect of the bite angle.

Dopants **40-49** were synthesised to extend the study and concept of the effect of the bite angle in LC performance. By varying the linker group in size and rigidity, for example a carbonyl, methylene and propylene groups, we were able to synthesise a series of dopants that initially varied the bite angle, but by having a diphenyl moiety in relation to the linker we were able to vary the tails on some dopants.

3.3. Preparation of LC Samples and LC Cells

3.3.1. Preparation of LC Samples

LC samples containing any one of the dopants at 0, 1, 2, 4 or 6 % concentrations by weight with respect to the amount of the dielectrically positive or negative LC material (200 mg) used. The LC materials used were both commercially available blends (Merck) but due to

commercial sensitivity we were not privy to the information and thus was only treating the LC's as dielectrically positive or negative LC's. These doped samples were then heated to 60 °C for one hour to ensure complete mixing, and then placed under vacuum for another hour to degas the sample. For the Raman and EO studies undertaken in Durham, only 4 % dopant levels were used, with cells manufactured using the same protocol as carried out in SONY's laboratories to ensure consistency of results.

3.3.2. LC Cells and their Preparation

The TN and VA cells were obtained from E.H.C. Co. Ltd. The TN feature two alignment layers at 90° to each other, with the LC medium having an induced twist in the off and on state as shown in Figure 2a. The VA cells had parallel alignment layers rubbed at 180° with respect to each other causing the LC medium to be vertically aligned in the on and off state as shown in Figure 2b.

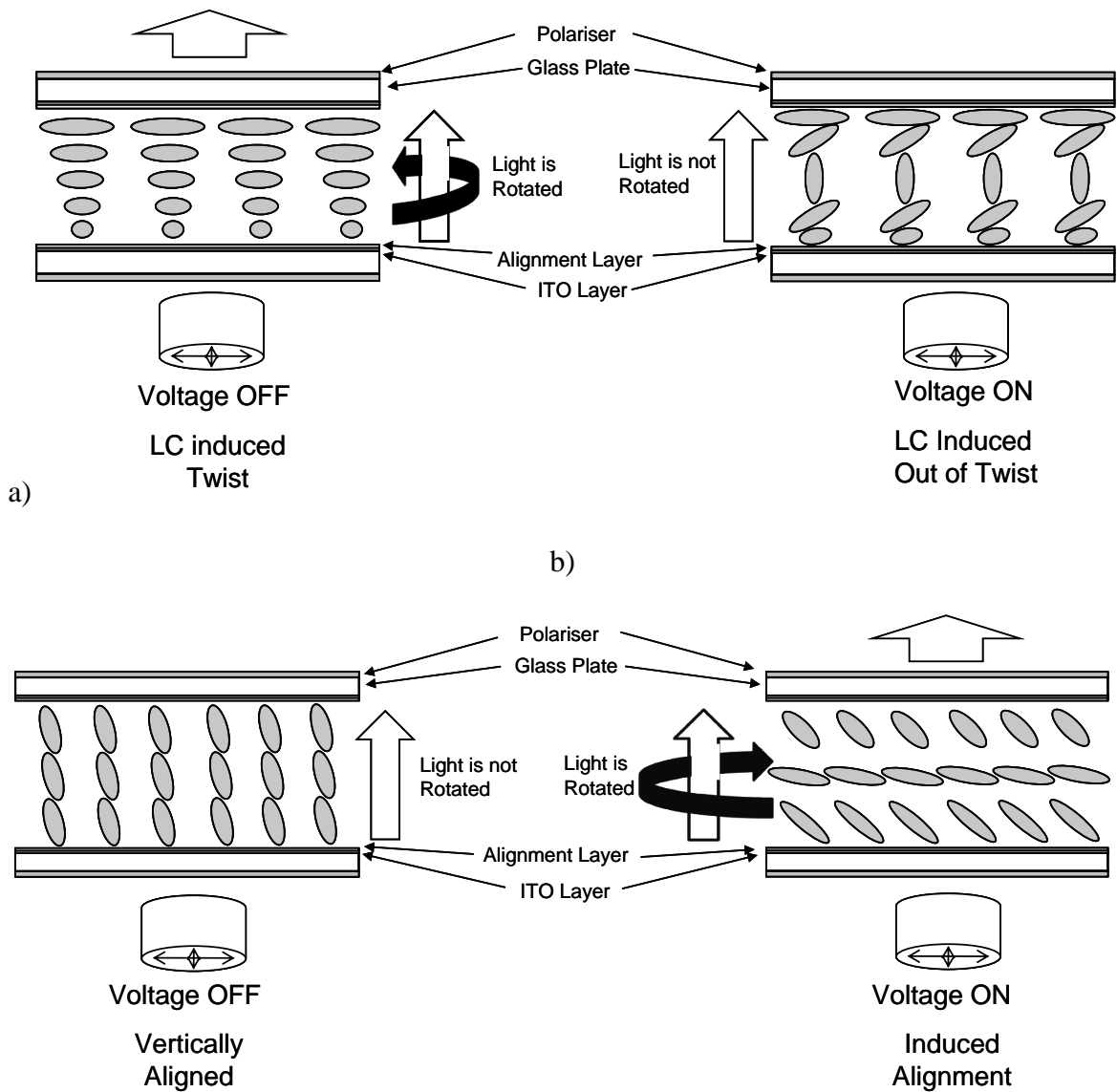


Figure 2. Representational schematics of (a) TN liquid crystal cell and (b) VA liquid crystal cell in display technology.

For EO measurements, cell thicknesses were 5 μm for VA cells and 10 μm for TN cells. The cells contain indium tin oxide (ITO) electrodes covering an active area of 10 x 10 mm. The alignment layer used in these cells was initially cetyltrimethylammonium bromide (CTAB). However, decomposition of the CTAB layer by moisture was found to lead to

poor alignment of the LC medium and, therefore, the manufacturer changed the alignment layer to a polyimide layer which resolved this issue. Prior to filling, cell quality was determined by examination of the interference fringes (number of dark and light reflected fringes) by surface reflectance of a monochromatic Opus Metrology sodium lamp light source. Too many fringes indicated a poor cell (lack of parallel cell windows) and were discarded.

Once a cell was selected it was placed on a hot plate, with a small part of the cell hanging over the edge, and heated to 60°C. Once heated to temperature droplets of the (doped) LC were placed at the very edge of the cell allowing it to fill via capillary action. The cells were then heated to 90°C in an oven and then annealed over a 2 hr period. The oven temperature was above the transition temperature (~90°C) for the phase change from nematic to isotropic (T_{NI}) giving a homogenous blend of LC and dopant when annealed. Once the cells had cooled they were sealed with UHU glue. At this point the cell gaps were measured because the gap can alter during the filling/annealing process. To measure the cell gaps, cells were scanned over the range of 500 – 400 nm and the data collated to show the interference patterns, characterised by a Varian Cary 500 Scan UV-Visible Spectrophotometer. The number of constructive maxima (x) and the refractive index (n) of the material were used to determine the cell gap by using Equation 1, where λ_1 and λ_2 are the minimum and maximum range of wavelength respectively. [18]

$$d = \frac{x\lambda_1\lambda_2}{10^3 n^2 (\lambda_2 - \lambda_1)}$$

Equation 1 [19]

Finally a wire with bare ends was glued (UHU) to the edge of each side of the cell allowing contact between electrode and the bare wire. The ends of the wire were painted to the electrode with silver paint to ensure electrical contact with the ITO layer and sticky tape was wrapped around the top part of the cell and over the painted wires, making sure the LC 10 x 10 mm area was not covered, to ensure that the wires were held in place and firmly in contact with the electrode.

When preparing any series of LC sample(s) for testing, all the cells used were from the same manufacturer's batch of cells and prepared at the same time. This precaution was taken to minimise batch-to-batch differences and to maintain qualitative significance of the results. Each cell was also prepared three times, as air bubbles, crystallisation, ionic impurities etc, introduced when preparing a cell causes unusable or unreliable results.

3.4. SONY EO Experimental Setup

The basic principles of the experiment is shown schematically in Figure 3.

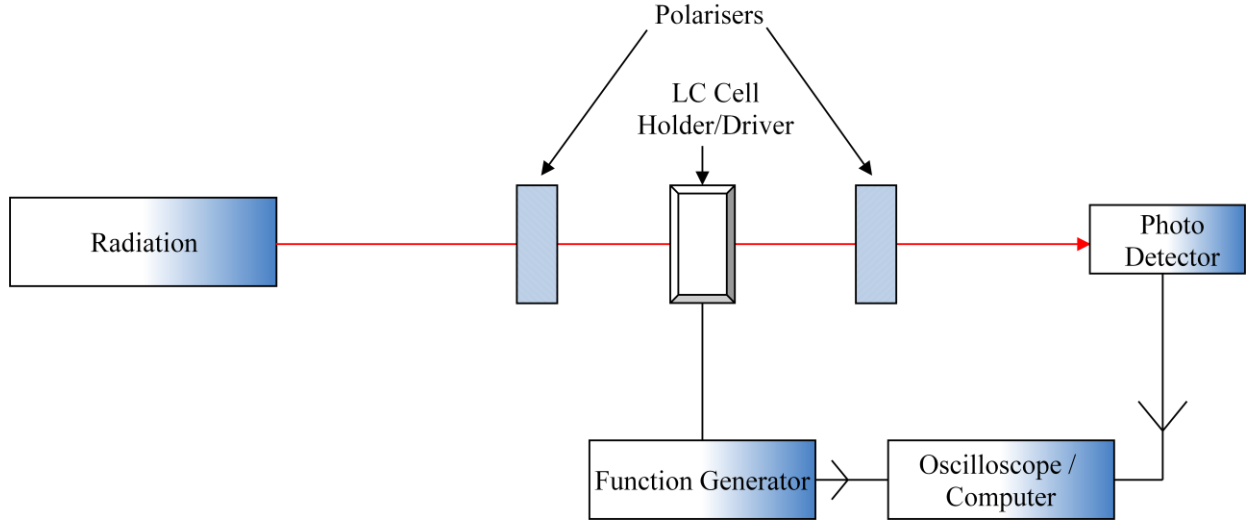


Figure 3. Schematic of the EO setup.

The LC cells were placed on a Linkam LTS 350 stage connected to a Linkam TMS 94 temperature controller preset to heat the cell to 35 °C. The cells were switched on and off using a PS-2403D power supply. The transmittance profiles of the switching were recorded using a Leica DMRX confocal polarising microscope driven by specific software written in-house by SONY. The polarisers used for TN cells were parallel-polarised and for VA they were cross-polarised, causing the switch to appear from white to black and black to white respectively to the corresponding cells when using a white light source.

3.4.1. SONY EO Experimental Rise Response Time Measurements

The specific program required data, e.g. cell gap, d , along with the recorded transmittance profiles to calculate the rise times at specific applied electric fields, E . The rise time is

calculated as the time taken for the transmitted light intensity to change from 10 % to 90 % of the maximum transmittance, which are denoted E_{10} and E_{90} respectively, and calculated by the ratio of the applied voltage and cell gap at the points of the transmittance as shown by Equation 2 where x is the percentage being evaluated, for example if x is 10 it means voltage at 10 % of the maximum voltage for the switch to occur.

$$\frac{Vx}{d}$$

Equation 2

The software repeats the measurement many times and calculates the average response time.

3.4.2. SONY EO Experimental Decay Response Time Measurements

The program will measure the transmittance of the cell between 90% and 10% of the maximum voltage of the transmitted light intensity, which are denoted V_{90} and V_{10} respectively of the decay as the applied electric field is switch off. These results are plotted graphically to represent the transmittance at maximum (90) and minimum (10) indicating the decay response time. The measurements are repeated many times to calculate the average response time by recording the points between V_{10} and V_{90} in increments of 10% of the maximum voltage.

3.4.3. SONY EO Experimental VHR Measurements

The VHR is defined as a percentage of the potential retained within the cell after the cell is switched off for a specified duration of time. The TFT allows the cell to stay charged up for a period of time after the applied electric field has been switched off until it is refreshed giving the cell better refresh rates. The more charge retained by the cell after the applied electric field has been switched off, the less work required for the desired switch and less time taken for the switch to occur. The desirable result is 100 % by the time the next applied signal is applied because this would require the minimum amount of work necessary for the switch. However, this is a difficult parameter to achieve due to VHR being related to resistivity and capacitance of the cell, and significantly reduces with the presence of ionic impurities. The VHR results were measured with a Toyo Corp. LCM-1 LC Material Characteristics Measurement System. Any cells that had a VHR under 95 % were discarded.

3.5. EO Results and Discussion

Discussion of the both types of dielectric blends (positive and negative) doped with molecules from the series of dopants synthesised will follow with the respective EO data of the rise and decay response times, VHR, $E_{10/90}$ and threshold voltage. The goal of this work was to find dopants that would decrease the rise and decay times, threshold voltage and $E_{10/90}$ while VHR is to be increased. Study of the response times will enable an overview of the effect of structure-property relationships in the grouped series of dopants on their relevant response times. All collated data is given in appendix A with the green arrow on the data used to indicate the desired effect on parameter being measured. For

example, the green arrow in response time graphs indicate the direction of the required deviation of the profile to indicate improved behaviour (faster switching) of the doped LC cells compared to that of undoped LC cells.

Due to batch-to-batch variations in cells from the manufacturer, any dopants re-tested in a new batch of cells could not be assumed to give results that were directly comparable with a previous measurement. After filling the cell, the cell gaps also vary, and so for comparative purposes a few samples of the same doped or undoped sample were made, with comparisons drawn from the closest match possible from the cell gaps. Given the batch-to-batch variations, the work must be considered as a qualitative study with generalisation of the results being used to promote or inspire further study or structure-property analysis.

3.5.1. EO Response Time Measurements for Acetylenic Linker Dopants

The acetylenic dopants **11-17** and **20-21** were inserted (doped) into both dielectrically negative LC (in VA cells) and positive LC (in TN cells). Only dopants **11-15** were studied in detail. Dopants **16-17** were found to have very poor VHR which could be attributed to the presence of ionic impurities; pyridine is particularly able to bind metal ions. Dopants **20-21** did not completely dissolve in the LC host, with crystallisation within the cell clearly evident.

3.5.1.1. Acetylnic Linker Dopants in Dielectrically Negative LC Blends

3.5.1.1.1. Rise Time

The data from dopants **11-17** tested in a negative dielectric LC blend in VA cells with a 5 μm cell gap and CTAB alignment layer are summarised in Table 1. The results of the EO rise data, threshold hold voltage and the E_{10} and E_{90} shown in Appendix A Figures 6a – e, 7 and 8 respectively. Figure 4 illustrates an example of the EO rise data of dopant **11** and shows that the rise time is slower (increased) compared to that of undoped –LC. The green arrow shows the desired movement required to decrease the rise time (primarily at low field strengths). All EO data for rise times will be quantified by a simple denotation of + and -, where + denotes a decrease in rise time, i.e. improved response time, and - denotes an increase in rise time, i.e. a worse response time. No change will be indicated by 0. The quantity of +'s or -'s will indicate the significance in the change of response time, a single +/- will indicate a slight change and ++/-- will indicate a significant change.

The threshold data (appendix A, Figure 7) show that there is a small increase in the minimum threshold applied electric field (volts per micron) required to begin switching the cell. The measurements of E_{10} and E_{90} demonstrate the reduction in the minimum electric field for 10 % and 90 % transmittance of the cell indicating an overall decrease in the driving voltage required for the cell (appendix A Figure 8).

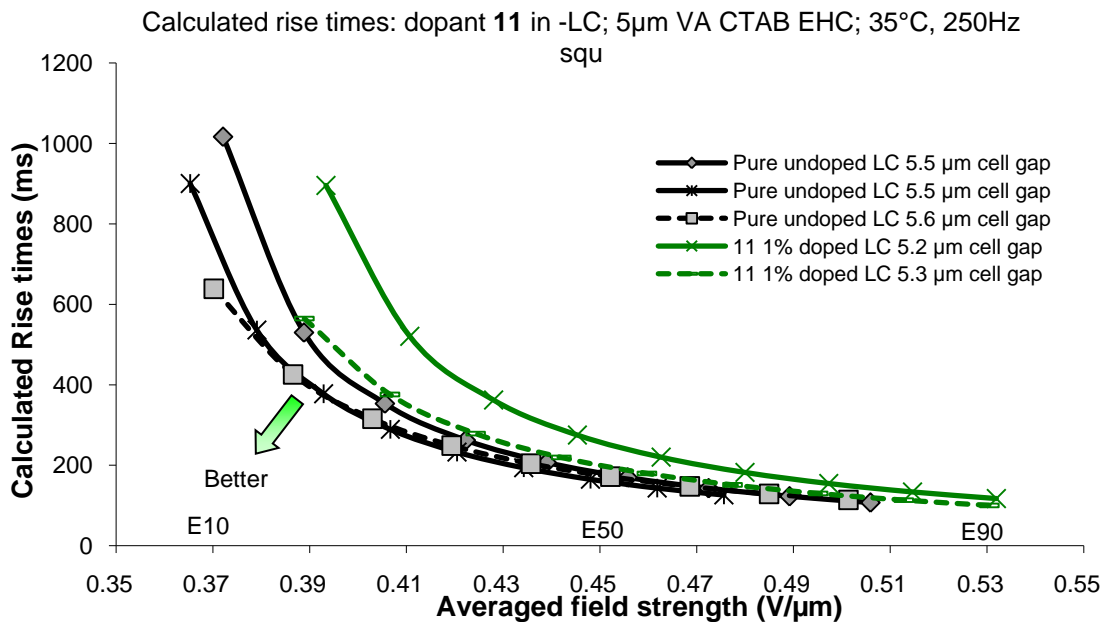


Figure 4. EO rise time data of dopant 11 in -LC host.

Dopant	Effect on Rise Time/ comparative to the pure LC cells measured	Dopant EO Rise Data (Appendix A)
11	- - rise time	Figure 6a
12	0 rise time	Figure 6b
13	- - rise time	Figure 6c
14	+ rise time	Figure 6d
15	- rise time	Figure 6e

Table 1. Comparison of effect on response rise times of the dopants **11-15** on dielectrically negative LC blends in VA – 5 μ m cells with CTAB alignment layer.

From examining the data in the dielectrically negative LC blend it is observed that dopant **14** is the only compound that shows an improvement in rise time; a positive result, decreasing the response rise time. However, this effect is positive but was not considered a significant enough change for further studies and thus no VHR studies were carried out on any of the materials of dopants **11-15**.

3.5.1.1.2. Decay Time

A collective comparison of all the dopants **11-15** tested in a dielectrically negative blend is shown in Table 2 from the EO decay data shown in appendix A Figures 9a – e. Figure 5 illustrates an example of the EO decay data of dopant **11** and shows that the decay time is slower (increased) compared to that of undoped –LC. The green arrow shows the desired movement required to decrease the decay time. All EO data for decay times will be quantified by a simple denotation of + and -, where + denotes a decrease in decay time, i.e. improved response time, and - denotes an increase in decay time, i.e. a worse response time. No change will be indicated by 0. The quantity of +'s or -'s will indicate the significance in the change of response time, a single +/- will indicate a slight change and ++/-- will indicate a significant change.

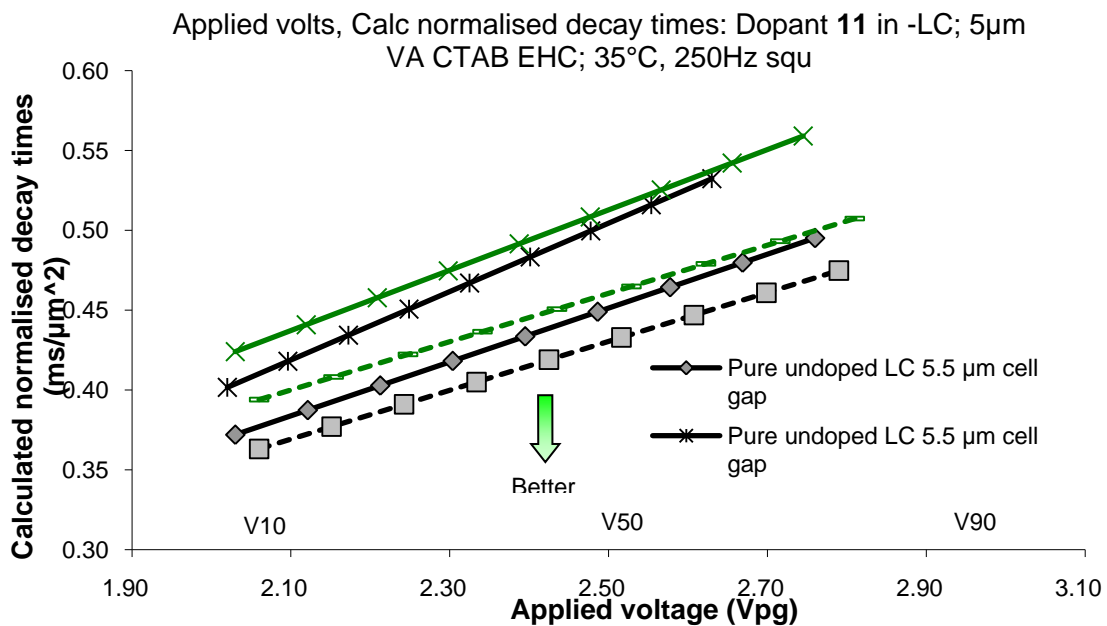


Figure 5. EO decay time data of dopant **11** in -LC host.

Dopant	Effect on Decay Time comparative to the pure LC cells measured	Dopant EO Decay Data (Appendix A)
11	- decay time	Figure 9a
12	0 decay time	Figure 9b
13	0 decay time	Figure 9c
14	0 decay time	Figure 9d
15	0 decay time	Figure 9e

Table 2. Comparison of effect on response decay times of the dopants **11-15** on dielectrically negative LC blends in VA – 5 μm cells with CTAB alignment layer.

From examination of the data in the dielectrically negative LC blend no beneficial effect on the decay time could be observed. The dopants were, therefore, considered ineffective and no VHR studies were carried out.

3.5.1.1.3. Results Summary

Comparing the structures to the results we can see that dopant **12** compared to **14** is the addition of the nitrogen; the pyrimidine moiety vs pyridine moiety, shows a slight increase in response times. The other dopants all had nitrogen atom(s) in a combination of 2, 4 and 6 positions on the heteroarene ring. This early observation would require further study of electron withdrawing groups in the 3 and 3,5 position of an arene ring to see if this relation is specific to response times. Though dopant **14** did improve the response rise time its decay time was not improved and, overall, both series of data for dopants **11-17** shows that none of these were particularly effective dopants for improving the response times of LC hosts for display devices.

No time was invested in EO measurements for dopants **12** and **13** due to the poor effect the previous related series of dopants (**11-15**) and poor VHR results[♥] as shown in appendix A Figure 10. Likewise for dopant **20** forming crystalline blends at room temperature inside the cell it was clear that the T_{NI} was poor, which means the clearing temperature for the LC blend when doped to become a liquid crystal was above room temperature and thus too high. Dopant **21** did not dissolve into the LC host.

[♥] There is no order too which experiment is carried out first. Usually EO is done, however, due to one instrument if there is a queue then other experiments are carried out first until the EO instrument is free unless poor results such as VHR occur.

3.5.1.2. Acetylnic Linker Dopants in Dielectrically Positive LC Blends

Dopants **11-15** were doped into a positive dielectric LC blend to be tested for both rise and decay response times. For the same reasons described above, dopants **16-17** and **20-21** were not tested here.

3.5.1.2.1. Rise Time

Table 3 shows the comparative data of the rise times for dopants **11-15** tested in a positive dielectric LC blend as shown in appendix A Figure 11a – e. These were carried out in a TN cell with a 10 μm cell gap and a polyimide (PI) alignment layer. The relevant threshold voltage and $E_{10/90}$ data are shown in appendix A Figures 12 – 13.

Dopant	Effect on Rise time comparative to the pure LC cells measured	Dopant EO Rise Data (Appendix A)
11	0 rise time	Figure 11a
12	0 rise time	Figure 11b
13	+ rise time	Figure 11c
14	0 rise time	Figure 11d
15	0 rise time	Figure 11e

Table 3. Comparison of effect on response rise times of the dopants **11-15** on dielectrically positive LC blends in TN – 10 μm cells with PI alignment layer.

The results showed that only dopant **9** had a slight beneficial effect on the rise times and the remainder effectively had no change. VHR studies were carried out on these doped +LC blends and the data is shown in appendix A Figure 14 indicating that with all of the dopants the VHR is decreased below 95% having various impacts giving a range from 35 – 95%. Dopant **15** VHR results show that it is within the acceptable limits ($VHR \geq 95\%$) but still a slight decrease comparatively to the undoped LC cell. Dopants **12** and **14** have had a large significant decrease (---) and dopants **11** and **13** have had the most significant decrease as $VHR < 50\%$. These VHR and rise time results have identified that the dopants are not ideal for decreasing the response rise times. This is believed to be attributed to the nature of the heteroarene head group. Pyridine and pyrimidine are particularly able to bind metals and thus potentially increasing ionic impurities. Also over time upon standing these dopants (**11-17**) discoloured thus indicating possible degradation.

3.5.1.2.2. Decay Time

Table 4 shows the comparative data of the rise times for dopants **11-15** tested in a positive dielectrical LC as shown in appendix A Figure 15a – e .

Dopant	Effect on Decay Time comparative to the pure LC cells measured	Dopant EO Decay Data (Appendix A)
7	- - decay time	Figure 15a
8	- - decay time	Figure 15b
9	- - decay time	Figure 15c
10	- - decay time	Figure 15d
11	- - decay time	Figure 15e

Table 4. . Comparison of effect on response decay times of the dopants **11-15** on dielectrically positive LC blends in TN – 10 μm cells with PI alignment layer.

The results showed that all dopants increased the decay times of the LC device which is contrary to the desired response. Thus we conclude that these dopants were not satisfactory for decreasing the response decay time of dielectrically positive LC devices.

3.5.1.2.3. Results Summary

Comparing the structures to the results we can see that acetylenic linker had very little beneficial effect on response times, making them unattractive as dopants in LC hosts for use in display devices.

3.5.2. Electro-optic Response Time Measurements for Biphenyl Ether Linker Dopants

Dopants **18-21** and **24-26** were tested using dielectrically negative LC material hosts.

3.5.2.1. Biphenyl Ether Linker Dopants in Dielectrically Negative LC Blends

3.5.2.1.1. Rise Time

Table 5 shows the data of the rise times for the dopants **22-24**, **27**, **28** and **30** in various doped percentages tested in a negative dielectric LC and the data is shown in appendix A figure 16a – r. Note dopant **22** is the commercially available starting material 4-bromo biphenyl ether. In some cases the same compound was studied more than once in different batches of cells. The data for two different batches were treated as two independent results with all of the data analysed to draw as much information as possible. Each series of samples belonging to a specific batch is identified by the suffix a, b, c, d or e.

Dopant (Batch)	%	Effect on rise time comparative to the pure LC cells measured	Dopant EO Rise Data (Appendix A)
22 (a)	4	++ rise time	Figure 16a
22 (d)	4	+ rise time	Figure 16b
23 (a)	4	++ rise time	Figure 16c
23 (b)	2	+ rise time	Figure 16d
23 (b)	4	++ rise time	Figure 16e
23 (c)	2	+ rise time	Figure 16f
23 (c)	4	++ rise time	Figure 16g
23 (c)	6	- rise time	Figure 16h
23 (d)	4	++ rise time	Figure 16i
24 (a)	4	++ rise time	Figure 16j
30 (d)	2	0 rise time	Figure 16k
30 (d)	4	+ rise time	Figure 16l
27 (e)	2	0 rise time	Figure 16m
27 (e)	4	0 rise time	Figure 16n
27 (e)	6	+ rise time	Figure 16o
28 (e)	2	-- rise time	Figure 16p
28 (e)	4	- rise time ^Ω	Figure 16q
28 (e)	6	-- rise time ^Ω	Figure 16r

Table 5. Comparative effect on response rise times of the dopants **22-24, 27, 28** and **30**

used in dielectrically negative LC blends.

^Ω In these samples the material was not completely dissolved but data was still obtainable but unreliable.

Consideration of the data from Table 5 shows that the dopants **23**, **24** and **30** have decreased the rise time. All of the data within each batch may be compared to each other from the compilation in Table 6 for a better understanding of each batch of cells. The commercially available 4-bromo biphenyl ether material (**22**) was found to give the largest improvement in the rise time in batch **a**. Comparing the result of varied dopant percentage of dopant **23** shows the optimal doping level for increasing the switching time is 4%. If we examine the data obtained for the -LC blend doped with **23** at 4 % in each batch the calculated rise times differ and thus not comparable to each other. This demonstrates that differing batches of cells are not the exact same. In addition this also demonstrates no two sets of results are strictly identical and not reproducible. Batch **d** from table 7 shows that comparing the data of dopants **23** and **30** which, is an increase by two carbon units in the tail length, increases the rise time. However, again this is still less of a change than observed for **22**. Finally batch **e**, which has the introduction of an acetylenic moiety with varying aryl head groups compared to dopant **24** has at best a slight decrease in rise time at 6% which is not as large as **24**. This suggests that the additional acetylene and aryl head group has no impact on the response time.

Dopant (Batch)	Comparative rise time of dopants in the batch compared to each other and pure LC cells measured (< indicates a better than scenario)	Dopant EO Rise Data (Appendix A)
a	Pure < 23 (4%) < 24 (4%) < 22 (4%)	Figure 17a
b	Pure < 23 (2%) < 23 (4%) at lower <i>E</i> values	Figure 17b
c	Pure < 23 (2%) \cong 23 (6%) < 23 (4%)	Figure 17c
d	Pure < 30 (2%) < 30 (4%) < 23 (4%) < 22 (4%)	Figure 17d
e	28 (6%) < 28 (2%) < Pure \cong 28 (4%) \cong 27 (4%) \cong 27 (2%) < 27 (6%) only at lower <i>E</i> values	Figure 17e

Table 6. Comparative rise time of dopants in the batches **a-e** identified in table 5 compared to each other and pure LC cells.

3.5.2.1.2. Decay Time

Table 7 contains the collated decay time data for the same dopants, **22-24**, **27**, **28** and **30**, however, the unreliable cells noted in Table 6 were omitted. The experimental results are shown in Appendix A figure 18a – 18p.

Dopant (Batch)	%	Effect on decay time comparative to the pure LC cells measured	Dopant EO Decay Data (Appendix A)
22 (a)	4	0 decay time	Figure 18a
22 (d)	4	+ decay time	Figure 18b
23 (a)	4	- - decay time	Figure 18c
23 (b)	2	0 decay time	Figure 18d
23 (b)	4	- - decay time	Figure 18e
23 (c)	2	+ decay time	Figure 18f
23 (c)	4	- - decay time	Figure 18g
23 (c)	6	- decay time	Figure 18h
23 (d)	4	- - decay time	Figure 18i
24 (a)	4	- decay time	Figure 18j
30 (d)	2	- decay time	Figure 18k
30 (d)	4	0 decay time	Figure 18l
27 (e)	2	0 decay time	Figure 18m
27 (e)	4	- - decay time	Figure 18n
27 (e)	6	- decay time	Figure 18o
28 (e)	2	+ decay time	Figure 18p

Table 7. Comparison of effect on response decay times of dopants **22-24, 27, 28** and **30** used in dielectrically negative LC blends.

Consideration of the consolidated data in Table 8 shows that **22** improves the response decay times more than the other synthesised dopants **23**, **24**, **27**, **28** and **30**. Nevertheless, there is positive evidence in the results suggesting that an ether linker core has potential for being a guest molecule in LC hosts for display devices. There is also evidence showing that differing levels of doping brings about varying response decay time.

Dopant (Batch)	Comparative decay time of dopants in the batch compared to each other and pure LC cells measured (< indicates a better than scenario)	Dopant EO Decay Data (Appendix A)
A	23 (4%) < 24 (4%) \cong Pure \cong 22 (4%)	Figure 19a
B	23 (4%) < 23 (2%) \cong Pure	Figure 19b
C	23 (6%) < 23 (4%) < Pure < 23 (2%)	Figure 19c
D	23 (4%) < 30 (2%) < 30 (4%) \cong Pure < 22 (4%)	Figure 19d
E	27 (4%) < 27 (6%) < 27 (2%) < Pure < 28 (2%)	Figure 19e

Table 8. Comparative decay time of dopants in the batches **a-e** identified in table 6 compared to each other and pure LC cells.

3.5.2.1.3 Results Summary

There is evidence showing that the incorporation of materials similar in structure to dopants **23**, **24** and **30** (4-bromo 4'-acyl/alkyl biphenyl ether) and, in particular, **22** (4-bromo biphenyl ether), into \pm LC hosts can improve the display characteristics of LC devices. With the limited data set presented here it is not possible to draw a conclusion regarding the

structure-activity relationships. When introducing an acetylenic moiety with various aryl head groups it was observed that the rise times for LC devices containing dopants **27** and **28** were no faster and for this reason dopant **29** was omitted from the testing. There is evidence showing that the level of dopant introduced to the LC host gives varying response times. It is observed that in some cases as we increase the level of doping the response times get faster and in other cases as we increase the level of doping we get slower response times. This shows that with each dopant there is an optimum level of doping whether it be 2, 4 or 6, or even more percentage level that will give a maximum influence on the response times. However, we must understand too high a level of doping will alter other properties, such as viscosity and operating/clearing temperature. In conclusion, the biphenyl ether linker has a positive effect on rise times, but not so significantly on decay times. This is particularly evident in **22**.

3.5.3. Electro-optic Response Time Measurements for ‘CR₂’ Bridge Linker Dopants

The dopants **32-37** and **40-49** all feature a methylene-based ‘CR₂’ linker . The results of these dopants will be discussed for both dielectrically negative and positive LC.

3.5.3.1. ‘CR₂’ Bridge Linker Dopants in Dielectrically Negative LC Blends

3.5.3.1.1. Rise Time

Table 9 shows the data of the rise times for dopants tested in dielectrically negative LC and at various dopant percentages are shown in appendix A Figure 20a – g. Again a series of batches of cells were used during the acquisition of the data.

Dopant (Batch)	%	Effect on Rise Time Field comparative to the pure LC cells measured	Dopant EO Rise Data (Appendix A)
32 (f)	2	0 rise time	Figure 20a
32 (f)	4	+ rise time	Figure 20b
34 (f)	2	0 rise time	Figure 20c
34 (f)	4	+ rise time	Figure 20d
44 (g)	4	+ rise time	Figure 20e
46 (g)	4	0 decay	Figure 20f
48 (g)	4	++ rise time	Figure 20g

Table 9. Comparison of effect on response rise times of the dopants **32**, **34**, **44**, **46** and **48** tested in a dielectrically negative LC blend in VA – 5 μm cells with PI alignment layer.

Table 10 shows a comparison of the response rise time data in each batch of cells. Cells made from batch **f** (samples of carbonyl and methylene linker) showed a slight decrease in the response rise time as the level of doping increases greater than 2 %. VHR studies from these cells showed that **32** (the commercially available 4-trifluoromethyl benzophenone) to has poor VHR, less than 20 %, and dopant **34** to be less than 80 % which, whilst better, is still not acceptable for a display devices (appendix A Figure 22). Both of these results, EO and VHR, combined together indicated that the dopants were not particularly effective, and thus the similarly structurally related dopants **35-37** were not tested. In batch **g** the dopant samples have a propylene core linker with varying chain lengths of the alkoxy tail, which

gives slight change in the bite angle of the dopant and slight alteration in molecular volume. Dopants **44**, **46** and **48** results were more positive as they all showed faster response rise times (decrease in response time) when the LC hosts were doped to 4 %. The VHR were good and within acceptable limits as all the dopants were approximately 95 % (± 1 %), see appendix A Figure 23. The VHR results alongside the EO results indicate that these were potentially useful dopants to investigate further. The results when compared to each other show that dopant **41** with the butyloxy tail was the most effective dopant, see table 10.

Dopant Batch	Comparative rise time of dopants in the batch compared to each other and pure LC cells measured (< indicates a better than scenario)	Dopant EO Rise Data (Appendix A)
F	27 (2%) \cong 32 (2%) \cong Pure < 32 (4%) \cong 34 (4%)	Figure 21a
G	Pure < 44 (4%) \cong 46 (4%) < 48 (4%)	Figure 21b

Table 10. Comparative rise time of dopants in the batches **f** and **g** identified in table 9 compared to each other and pure LC cells.

3.5.3.1.2. Decay Time

Table 11 shows the comparative data of the rise times dopants **32**, **34**, **44**, **46** and **48** (Appendix A Figure 24a – g).

Dopant (Batch)	%	Effect on Decay Time field comparative to the pure LC cells measured	Dopant EO Decay Data (Appendix A)
32 (f)	2	- - decay time	Figure 24a
32 (f)	4	0 decay time	Figure 24b
34 (f)	2	- - decay time	Figure 24c
34 (f)	4	- decay time	Figure 24d
44 (g)	4	- - decay time	Figure 24e
46 (g)	4	- - decay time	Figure 24f
48 (g)	4	- - decay time	Figure 24g

Table 11. Comparison of effect on response decay times of the dopants **32, 34, 44, 46** and **48** that were tested in dielectrically negative LC blends in VA – 5 μm cells with PI alignment layer.

None of the dopants **32, 34, 44, 46** and **48** tested show improvements upon the response decay time. Table 12 shows comparison of the data from the batches **f** and **g**. The commercially available 4-trifluoromethyl benzophenone (**32**) has a greater effect at each equivalent doping percentage than its derivative of the comparable methyl linker (CH_2) **34**. However, the VHR results from **32** and **34** were poor and thus dopants **35-37** were not tested further. Comparison of the ‘ CMe_2 ’ propylene linker, dopants **44, 46** and **48**, results shows a large increase in decay response time (a negative effect) across all of the comparable dopants tested. Though the corresponding rise times were good these results

were not good enough to invest time in the other structurally related dopants (**30-43**, **45**, **47** and **49**).

Dopant (Batch)	Comparative decay time of dopants in the batch compared to each other and pure LC cells measured (< indicates a better than scenario)	Dopant EO Decay Data (Appendix A)
F	34 (2%) < 32 (2%) < 34 (4%) < 32 (4%) \cong Pure	Figure 25a
G	44 (4%) < 46 (4%) \cong 48 (4%) < Pure	Figure 25b

Table 12. Comparative decay time of dopants in the batches **f** and **g** identified in table 11 compared to each other and pure LC cells.

3.5.3.1.3 Results Summary

Overall, our studies show that the benzophenone derived dopant **34** and the commercially available starting material (**32**) improve the rise times at a higher level of doping (4%) but has a negative effect on the decay time. This coupled with the VHR results which were poor, signifies keto or methylene linker structure types are poor dopants. Dopants with a propylene linker, CMe₂, **44**, **46** and **48**, all showed a decrease in the response rise times (a positive effect) with acceptable VHR. There is additional evidence indicating that increasing the alkoxy tail length decreases the response rise time. However, they significantly increase the decay response time that makes these dopants in conclusion unacceptable. Therefore, no further efforts were invested in the dopants containing the CMe₂ linker.

3.5.3.2. ‘CR₂’ Bridge Linker Dopants in Dielectrically Positive LC Blends

3.5.3.2.1. Rise Time

Table 13 shows the data of the rise times for the same dopants, **32**, **34**, **44**, **46** and **48**, tested in a dielectrically positive LC host with the inclusion of dopant **41** at various doped levels. The results are shown in appendix A Figure 26a – h. Again a series of batches of cells were used during the acquisition of the data.

Dopant (Batch)	%	Effect on Rise Time Field comparative to the pure LC cells measured	Dopant EO Rise Data (Appendix A)
32 (h)	2	- - rise time	Figure 26a
32 (h)	4	0 rise time	Figure 26b
34 (h)	2	- rise time	Figure 26c
34 (h)	4	+ rise time	Figure 26d
41 (h)	2	0 rise time	Figure 26e
44 (i)	4	- rise time	Figure 26f
46 (i)	4	++ rise time	Figure 26g
48 (i)	4	++ rise time	Figure 26h

Table 13. Comparison of effect on response rise times of the dopants **32**, **34**, **41**, **44**, **46** and **48** were tested in dielectrically positive LC blends in TN – 10 μ m cells with PI alignment layer.

Results from batch h, dopants **32** (commercially available starting material), **34** and **41** indicated that, at best, there was only a small decrease in the response rise times. The VHR results were (appendix A Figure 28) as they ranged from 92 – 99 %, except **34** at 4 % which was approximately 85 % (± 1 %) which was the only poor result. Table 14 shows the comparison of the data of the cells of each batch. The summarised observations shown in table 14 show that the cell doped with 4 % of **34** had the largest decrease on response times. However, **34** shows poor VHR which resulted in this most effective dopant being concluded to be an overall poor dopant. In batch i the dopants used had a propylene linker (CMe₂) with varying chain lengths of the alkoxy tail. The results for **46** and **48** decreased the response rise times. The dopants tested were then studied for VHR and it was observed that they were good as shown in appendix A Figure 29, all > 95 %. The results when compared as shown in table 14 indicate the propyloxy tail was the most effective dopant.

Dopant (Batch)	Comparative rise time of dopants in the batch compared to each other and pure LC cells measured (< indicates a better than scenario)	Dopant EO Rise Data (Appendix A)
H	32 (2%) < 34 (2%) < 32 (4%) ≅ Pure ≅ 41 (2%) < 34 (4%)	Figure 27a
I	44 (4%) < Pure < 48 (4%) < 46 (4%)	Figure 27b

Table 14. Comparative rise time of dopants in the batches **h** and **i** identified in table 13 compared to each other and pure LC cells.

3.5.3.2.2. Decay Time

Table 15 shows the data of the decay times for the same previous dopants tested and the results are shown in appendix A figure 30a – h.

Dopant (Batch)	%	Effect on Decay Time Field comparative to the pure LC cells measured	Dopant EO Data (Appendix A)
32 (h)	2	- decay time	Figure 30a
32 (h)	4	- decay time	Figure 30b
34 (h)	2	0 decay time	Figure 30c
34 (h)	4	- decay time	Figure 30d
41 (h)	2	- decay time	Figure 30e
44 (i)	4	- - decay time	Figure 30f
46 (i)	4	- - decay time	Figure 30g
48 (i)	4	- - decay time	Figure 30h

Table 15. Comparison of effect on response decay times of the dopants **32, 34, 41, 44, 46** and **48** were tested in dielectrically positive LC blends in TN – 10 μm cells with PI alignment layer.

The dopants, **32, 34, 41, 44, 46** and **48**, show no improvements upon the response decay time. Table 16 shows a comparison of the data from batch **h** and **i**. In both cases, the pure undoped LC cell out performs all levels of doped LC host with respect to all tested dopants.

Based on these results the dopants were considered poor overall as the effect on the decay times were too large and, therefore, the remaining dopants structurally related to these families were not studied.

Dopant (Batch)	Comparative decay time of dopants in the batch compared to each other and pure LC cells measured (< indicates a better than scenario)	Dopant EO Decay Data (Appendix A)
h	32 (4%) \cong 34 (4%) \cong 32 (2%) \cong 34 (2%) < 41 (2%) \cong Pure	Figure 31a
i	44 (4%) < 46 (4%) \cong 48 (4%) < Pure	Figure 31b

Table 16. Comparative rise time of dopants in the batches **h** and **i** identified in table 14 compared to each other and pure LC cells.

3.5.3.2.3 Results Summary

Overall, dopants with a methylene linker (**34**) or a dopant with a propylene linker (**46** and **48**) increase rise time the most. Though **34** was initially thought to be a good dopant, its VHR was poor and thus concluded in-effective as a dopant. The propylene linker dopants **46** and **48** had the largest increase on the response rise time and were within acceptable parameters for VHR. However, due to the large increase on the decay response time these dopants were deemed poor and no further time was invested investigating all structurally related dopants of the CR₂ bridged linker family.

3.6 Overall Conclusion

Electro-optical measurements of twisted nematic and vertically aligned LC devices with all various dopants have been made and the changes in turn on/off times observed. The acetylenic dopants have had the least effect on the turn on/off times of both dielectrically positive and negative LC hosts. The most promising results were compounds that incorporate a biphenyl ether linker core. However, a full structure-activity study would be required in order to more fully understand the relationship between host and guest, allowing various dopant designs to match both dielectrically and negative LC hosts. Based on the limited results presented here there is clear evidence that some of the dopants have a positive effect on the response times, i.e. reducing the turn on/off times as the level of doping increases. Replacing the ether linker moiety for an alternative functional group modify both the electronic properties of the dopant and the 'bite angle'. None of these compounds proved to be as good as the original ether at increasing the rate of switching of the LC devices.

Overall we have shown that low levels of molecular dopants possessing a slight angle in the linker core has a positive effect on the response times of LC devices. These results are preliminary and require in-depth research. Some consideration should also be given to the choices of head groups to allow more compatibility with the type of dielectric LC host.

3.7 References

1. P. Kilickiran, A. Masutani, N. Hollfelder, G. Nelles, A. Yasuda, A. Tadeusiak and G. Sandford, *Sid. Int. Symp. Dig. Tec.*, 2007, **38**, 999.

2. D. Pauluth and K. Tarumi, *J. Mater. Chem.*, 2004, **14** (8), 1219.
3. S. M. Kelly, *Flat Panel Displays: Advanced Organic Materials*. RSC Materials Monographs, ed. J. A. Connor, 2000, The Royal Society of Chemistry.
4. E. Jakeman and E.P. Raynes, *Phys. Lett. A*, 1972, **39**, 69.
5. S. T. Lagerwall, P. G. Rudquist and D. S. Hermann, *Liquid Crystals - Nonlinear Optical Effects in Liquid Crystals*, in *Encyclopedia of Optical Engineering*, Editor R. G. Driggers,. 2003, Marcel Dekker.
6. G. Forstmann, T. Herod, J. Wu, R. Duran and D. Johannsmann, *Mol. Cryst. Liq. Cryst.*, 2000, **350**, 29.
7. J. Wilson and J. F. B. Hawkes, *Optoelectronics: An Introduction*, 3rd Ed, ed. P. J. Dean. 1998, Prentice-Hall International Inc.
8. L. J. Pinson, *Electro-Optics*, 1985, John Wiley & Sons.
9. A. Rogers, *Essentials of Optoelectronics: with applications*, 1st Ed, Optical and Quantum Electronic Series, ed. G. Parry and R. Baets, 1997, Chapman & Hall.
10. C. Nuckolls, R. F. Shao, W. G. Jang, N. A. Clark, D. M. Walba and T. J. Katz, *Chem. Mater.*, 2002, **14** (2), 773.
11. A. L. Alexe-Ionescu, A. T. Ionescu, E. S. Barna, V. Barna and N. Scaramuzza, *Appl. Phys. Lett.*, 2004, **84** (1), 40.
12. T. M. Long and T. M. Swager, *J. Mater. Chem.*, 2002, **12** (12), 3407.
13. M. Mitra, *Phase Transitions*, 1992, **37** (2-3), 131.
14. C. D. Mukherjee, T. R. Bose, D. Ghosh, M. K. Roy and M. Saha, *Mol. Cryst. Liq. Cryst.*, 1986, **140** (2-4), 205.
15. C. Q. Shu and L. Lin, *Mol. Cryst. Liq. Cryst.*, 1984, **112** (3-4), 213.

16. Z. H. Chen and T. M. Swager, *Org. Lett.*, 2007, **9** (6), 997.
17. T. M. Swager, *Accounts Chem. Res.*, 2008, **41** (9), 1181.
18. Gaussian 03, R.C., M. J. Frisch, G. W. Trucks, H. B. Schlegel, G. E. Scuseria, M. A. Robb, J. R. Cheeseman, J. A. Montgomery, Jr., T. Vreven, K. N. Kudin, J. C. Burant, J. M. Millam, S. S. Iyengar, J. Tomasi, V. Barone, B. Mennucci, M. Cossi, G. Scalmani, N. Rega, G. A. Petersson, H. Nakatsuji, M. Hada, M. Ehara, K. Toyota, R. Fukuda, J. Hasegawa, M. Ishida, T. Nakajima, Y. Honda, O. Kitao, H. Nakai, M. Klene, X. Li, J. E. Knox, H. P. Hratchian, J. B. Cross, V. Bakken, C. Adamo, J. Jaramillo, R. Gomperts, R. E. Stratmann, O. Yazyev, A. J. Austin, R. Cammi, C. Pomelli, J. W. Ochterski, P. Y. Ayala, K. Morokuma, G. A. Voth, P. Salvador, J. J. Dannenberg, V. G. Zakrzewski, S. Dapprich, A. D. Daniels, M. C. Strain, O. Farkas, D. K. Malick, A. D. Rabuck, K. Raghavachari, J. B. Foresman, J. V. Ortiz, Q. Cui, A. G. Baboul, S. Clifford, J. Cioslowski, B. B. Stefanov, G. Liu, A. Liashenko, P. Piskorz, I. Komaromi, R. L. Martin, D. J. Fox, T. Keith, M. A. Al-Laham, C. Y. Peng, A. Nanayakkara, M. Challacombe, P. M. W. Gill, B. Johnson, W. Chen, M. W. Wong, C. Gonzalez, and J. A. Pople, Gaussian, Inc., Wallingford CT, 2004.
19. F. Bruyneel, H. De Smet, J. Vanfleteren and A. Van Calster, *Optical Engineering*, 2001, **40**, 259.
20. The equation used and given by SONY.

Chapter 4

Raman Measurements and Analysis

Chapter 4: Raman Measurements and Analysis

4.1. Introduction to Vibrational Spectroscopy

There are two main methods that are used to study the vibrational spectroscopy of molecules; infrared absorption and Raman spectroscopy. Both methods can be carried out on diatomic or polyatomic molecules, whereby the number of vibrational modes for a polyatomic molecule is given by $3N - 5$ and $3N - 6$ vibrations for linear or non-linear polyatomic molecules containing N atoms respectively. These techniques are used to gain information about chemical structure and configuration, providing characteristic information and quantitative analysis. Historically infrared absorption has been the most used technique due to its greater experimental simplicity, as opposed to Raman spectroscopy, where the high flux of visible excitation can lead to potential sample degradation and fluorescence. The underlying principle of Raman spectroscopy is the scattering of light by matter. [1-4]

4.1.1. Electromagnetic Radiation

It has been established over centuries of research that light is electromagnetic radiation, of which visible light is but a small fraction of the spectrum. Light is described as radiation with several tuneable properties; intensity and frequency, but most importantly in this context, polarisation. There has been much diverse research into the study of electromagnetic radiation that has caused two theoretical developments; firstly, classical electrodynamics demonstrating that light can be treated as a continuous form of flowing

energy by electromagnetic waves, and secondly, quantum electrodynamics describing the interaction of electromagnetic radiation as a specific quanta of energy (photon) and thus described as an “*elementary particle*”. However, modern day theory unites both theories forming what is known as wave-particle duality explaining the nature of light. This is such that light propagates through space (or medium) in a wave-like manner and yet displays particle-like behaviour during the absorption and emission processes.

To understand the wave-particle duality theory, we have to classically breakdown the nature of light into both wave and particle functions. The wave exists as a particle, so overall we can consider the wave to actually be a stream of continuous photons with a defined quantum of energy. This energy is a unit of charge and can be considered to be surrounded by an electric field. Therefore, the photons travelling under an acting velocity will be a moving electric charge which in turn induces a magnetic field. Furthermore, as a wave function we consider this magnetic field to be oscillating and thus generate an electric field. Consequently, a changing electric field induces a magnetic field; therein they go hand in hand. Thus the wave-particle duality considers light to be an oscillating electric and magnetic wave with particle like behaviour. This is a very basic summary to the foundation to Maxwell’s theory defining electromagnetic radiation due to the consequence of each field generating each other from the concept of light existing as both wave and particle.

Electromagnetic radiation is described as a *transverse wave* with an oscillating electric and magnetic field, both of which point perpendicular to each other along the propagating direction of the wave as shown in Figure 1. The light itself will have a property known as polarisation and this is conventionally denoted the plane at which the electric field exists, for example in Figure 1 the electric field is in the x axis, thus the plane of polarisation is in the XZ plane (the red wave). [5, 6]

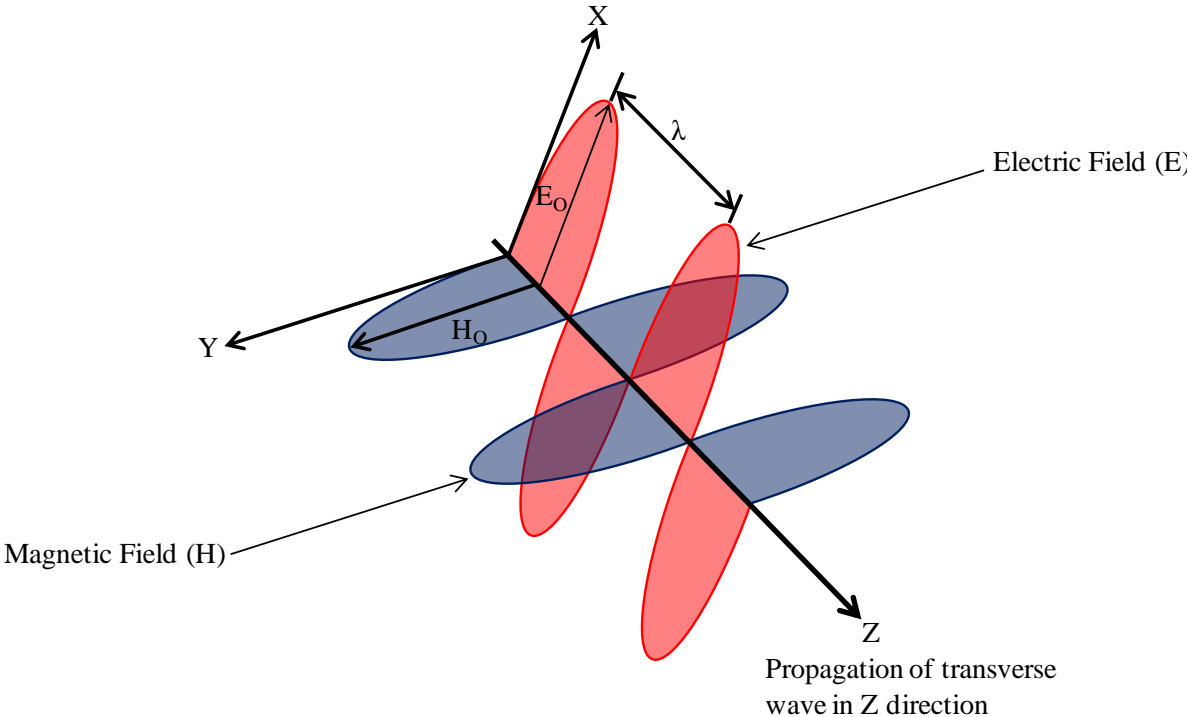


Figure 1. Diagram of the electric and magnetic components of electromagnetic radiation.

4.1.2. Polarisation of Light

White light consists of many quanta of light with each electric field randomly orientated with respect to an arbitrary axis, this is known to be unpolarised light, means that it contains all possible polarised orientations together as one, making it a non-specific propagating field (it is directional with “*disorder*”). However, when the light is specifically orientated so that the oscillating and propagating field is in one plane and one orientation (of one known initial angle), it is then said to be linearly polarised (or plane polarised) as shown in Figure 2. Polarisation is a descriptive way of demonstrating the oscillations of the wave perpendicular to the direction of travel in the considered electric field. The polarisation of light is a fundamental property of light in science and technology as it is exploited globally, for example, in optics and telecommunications for two global examples.

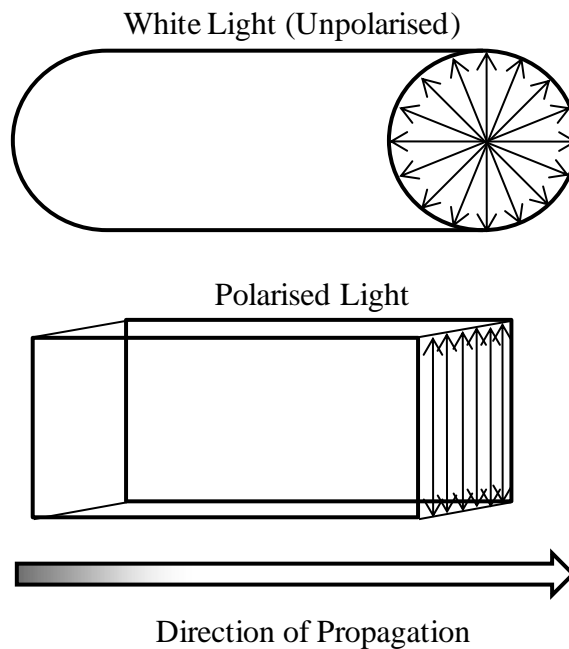


Figure 2. Diagram of unpolarised and polarised light.

When we are describing the polarisation of the wave we are conventionally describing what is known as the electric field vector, k , also known as the optical disturbance. To understand this better we firstly need to imagine that the electric field can be composed of two simple harmonic waves, one representing the x component and the other representing the y component, both of which are travelling in the z direction and orthogonal to each other. They can be expressed into two expressions as shown in Equation 1 and a visual depiction is shown in Figure 3. Where E is the electric field, t is time, x,y,z are dimensional points in space, i and j are the vectors, ϵ is the relative difference in the phase between each component and the defined phase of the component is $(kz - \omega t)$.

$$\mathbf{E}_x(z,t) = \hat{i}E_{0x} \cos(kz - \omega t) \quad (1a)$$

$$\mathbf{E}_y(z,t) = \hat{j}E_{0y} \cos(kz - \omega t + \epsilon) \quad (1b)$$

Equation 1

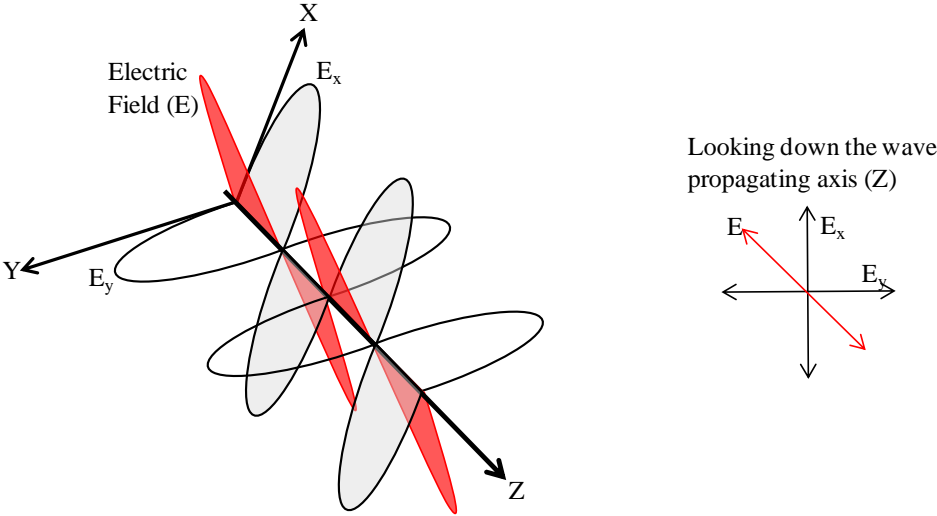


Figure 3. Representation of electric field components.

The addition of the positive factor ϵ means that each component will never reach the same value as a function of cosine, resulting in the expressions to be simplified as a product by accumulation of the two orthogonal optical disturbances, as shown in Equation 2. The accumulated product will be *in phase* when ϵ is 0 or a multiple of $\pm 2\pi$ (an even number of π), and be *out of phase* (180° difference) when ϵ is $\pm\pi$ (an odd number of π), resulting in plane polarised light.

$$\mathbf{E}(z,t) = \mathbf{E}_x(z,t) + \mathbf{E}_y(z,t)$$

Equation 2

When there is a different value for the phase, i.e. not 2π then the polarisation vector of the light appears to spiral as the wave propagates through space, and the light is said to be elliptically or circularly polarised.

To generate polarised light, we use an optical device known as a polariser; which allows a specific orientation of light to propagate through whilst blocking all other orientations. By definition the polariser will have a transmission axis and only the optical disturbance that has a parallel orientation will pass through and, thus, all non corresponding parallel waves will be blocked as shown in Figure 4. Though a polariser will essentially be based on the concept of manipulating light it will, however, come in differing configurations based on its

application on the type of manipulation of light intended; dichroism, scattering, reflection and birefringence.[4-6]

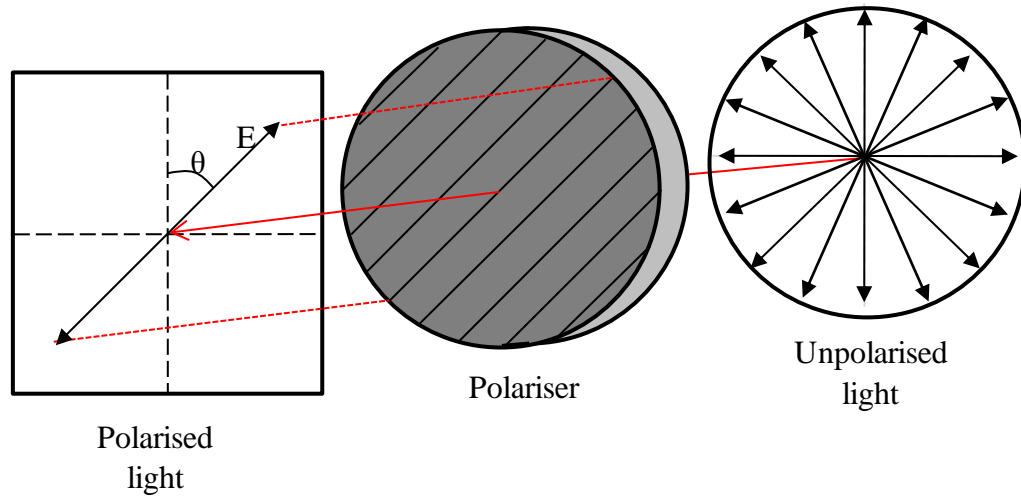


Figure 4. Diagram of a polariser and representation of its function.

4.2. Raman Spectroscopy Theory: Basics and Principles

4.2.1. Introduction to Raman Spectroscopy

When light is shone through matter it will scatter from the molecule in all directions. If the source of radiation is monochromatic then the major component of the scattered radiation will consist mostly of the incident monochromatic radiation, i.e. the light is scattered by an elastic process. This scattered radiation is known as Raleigh scattering, after Lord Raleigh who first characterised this process. However, in addition to this there is a small amount of

radiation with frequencies above and below the initial frequency being scattered at the same time, this inelastic scattering process is referred to as Raman Scattering. Raman scattering has been described in both prospects of classical theory and quantum theory; wave versus particles. The classical theory is based on waves of light, and it falters due to the deficiency of accounting for quantised vibrations and the quantum nature of light itself. Quantum theory is based on photons, particles, and can relate molecular properties to the Raman process. Qualitative and descriptive explanations of the process can be found in Banwell [4], Long [6] and Smith and Dent [7], whilst a more detailed description can be found in Koningstein [8] and Symanchi. [9, 10]

4.2.2. Raman Scattering

If we consider a radiation of frequency, ν , as a stream of photons then they will all have a discrete amount of energy, $E (h\nu)$. When these photons interact with matter they will scatter and deflect by collisions with the material, and these interaction can potentially transfer energy to or from the interacting photon via inelastic scattering. If the radiation gains energy then the scattered radiation has a higher frequency than the incident radiation and is referred to as Anti-Stokes scattering, whilst if the scattered radiation loses energy to the matter has a lower frequency than the incident radiation and is known to as Stokes scattering. During the instant of the light and molecule interacting with the energy of the system is illustrated by a ‘virtual state’. This state is conventionally illustrated on an energy level by a dotted line to represent its indeterminable energy and transient nature. All these scattering can be represented in Figure 5. [4, 6, 7]

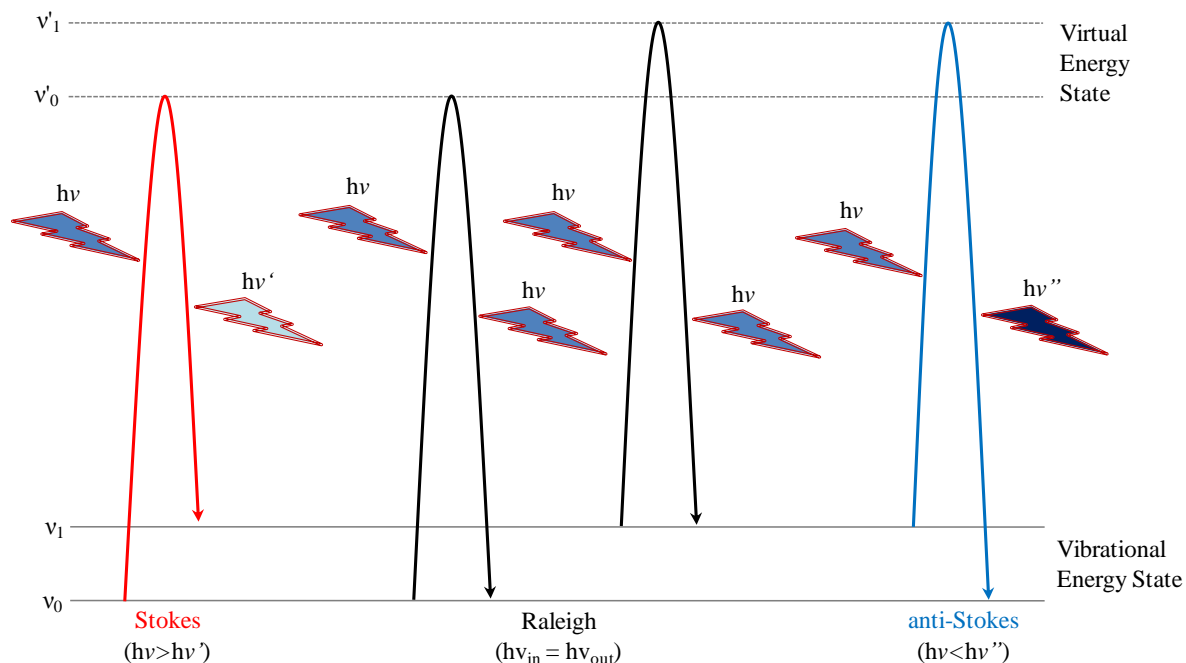


Figure 5. Energy level diagram of Raman (anti-Stokes and Stokes) and Rayleigh scattering.

4.2.3. Polarisability (α) and the Polarisability Ellipsoid

A fundamental and basic concept to Raman spectroscopy is molecular polarisability, α . A molecule in a static applied field, E , will gain an induced dipole moment due to the distortion of the electronic and nuclear charge that occurs across the molecule when it is placed in the field. The nuclei is positive and the electrons are negative, each will be drawn to the corresponding opposite charges of the electric field causing the positive and negative components inside the molecule to respectively increase in separation. It is this separation of charges that defines the induced dipole moment, μ . The degree to which the polarisation occurs depends upon how readily charge can move within a molecule and is clearly an

anisotropic process in most molecular systems. The dipole moment, applied field and polarisability can be expressed together in one expression, as shown in Equation 3.

$$\mu = \alpha E$$

Equation 3

When a molecule is subjected to in an oscillating electric field such as presented by electromagnetic radiation, where the electric field presents a time-dependent function $E(t)$ we gain Equation 4a. Thus, the induced dipole is now a time-dependent dipole function, $\mu(t)$, by the oscillating electric field (Equation 4b).

$$E = E_0 \sin 2\pi\nu t \quad (\text{a})$$

$$\mu = \alpha E_0 \sin 2\pi\nu t \quad (\text{b})$$

Equation 4

Molecular polarisability is anisotropic and is conventionally represented by a virtual polarisability ellipsoid. The ellipsoid is a three-dimensional virtual surface, whose distance

from the electrical centre of the molecule is proportional to $\frac{1}{\sqrt{\alpha_i}}$, where α_i is polarisability along the line joining the representative point i on the ellipsoid surface to the molecules electrical centre. This makes the shortest distance from centre to surface the greatest axis of polarisability and the maximum distance from centre to surface the least polarisable axis. The general way to think of it is “*small is big and big is small*” when talking about the ellipsoid axis and polarisability, i.e. a small ellipsoid axis means a large polarisability in that direction and vice versa. A more user friendly way to imagine the ellipsoid is to consider it as a measure of the ease of “*moving*” (interacting) with an electron. It is easier to move the electron along a molecular bond axis rather than perpendicular to it, making the distance to the surface from the electrical centre the shortest in reference to the long molecular bond axis, whilst perpendicular to the bond interaction, has the largest distance from the electrical centre to the surface of the ellipsoid.

A molecule vibrates and it is this change of the molecule displacement that will also cause the polarisability ellipsoid to change and thus the ellipsoid will invariably have its change and distortion which we need to consider. For example, if we consider a simple molecule with an identifiable molecule axis like that of carbon dioxide we can depict the polarisability ellipsoid and the change it will undergo in vibration between compression and stretching as shown in Figure 6.

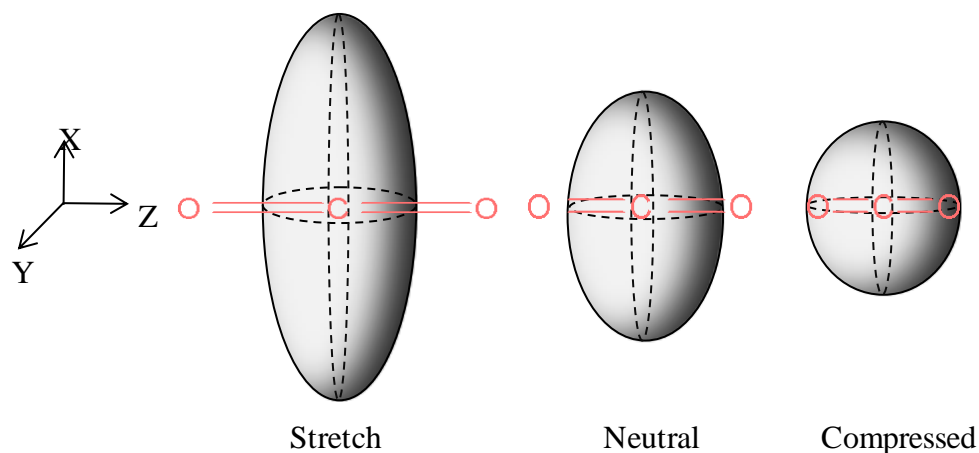


Figure 6. Carbon dioxide polarisability ellipsoid with respect to vibrational modes.

This change in polarisability occurs periodically with the frequency of the vibrational mode and at any given point from the neutral equilibrated position, α_0 . The polarisability is now changing at a rate, denoted β and thus the polarisability becomes a frequency dependent term as shown in Equation 5 (note that ν_{vib} is the frequency of the vibration and not ν of the denoted frequency of the electric field).

$$\alpha = \alpha_0 + \beta \sin 2\pi\nu_{\text{vib}}t$$

Equation 5

Now, when a vibrating molecule is placed in an oscillating field the instantaneous dipole moment term becomes a frequency dependent (equation 4b) and can now be expressed as Equation 6.

$$\mu = (\alpha_0 + \beta \sin 2\pi\nu_{vib} t) E_0 \sin 2\pi\nu t$$

Equation 6

Using equation 7a and expanding upon equation 6 we can show that the dipole moment when taking into account the internal motion (vibration) that the final dipole moment frequency dependent term to be Equation 7b. If there is no internal motion the rate, β , will be zero and the dipole will only oscillate with applied electric field frequency.

$$\sin A \sin B = \frac{1}{2} \{ \cos(A - B) - \cos(A + B) \} \quad (7a)$$

$$\mu = \alpha_0 E_0 \sin 2\pi\nu t + \frac{1}{2} \beta E_0 \{ \cos 2\pi(\nu - \nu_{vib}) t - \cos 2\pi(\nu + \nu_{vib}) t \} \quad (7b)$$

Equation 7

Equation 7b, the oscillating induced dipole μ , has components that contain two vibrational terms, $(\nu - \nu_{vib})$ and $(\nu + \nu_{vib})$, which correspond to the frequency of the Stokes and anti-Stokes terms and the first initial term of the expression is Raleigh scattering. [4, 6, 7]

4.2.4. Vibrational Raman Spectra

In order for Raman activity to be observed, the molecule vibration (or rotation) must bring about a change in the polarisability, whereby the polarisability has moved from the static state and thus $d\mu \neq 0$. If a molecule has limited or no symmetry then, it is fairly straightforward to deduce whether or not the molecule vibrations will be Raman active (or IR active), however, it is usually accurate to assume all modes to be Raman active. Conversely, if the molecule has symmetry then we would need to consider the symmetry of the three vibrational modes present, symmetric stretch, bending and anti-symmetric stretch (ν_1 , ν_2 , ν_3 respectively); to deduce whether or not they are Raman active and, hence, detected in the spectra.

4.2.4.1. Non-linear molecules: Vibrational Raman

If we consider a non-linear molecule such as water, during the symmetric stretch, the molecule as a whole will stretch and compress in unison to increase and decrease the shape and size. The stretch and compression will in its own right polarise the molecule as the held electrons will separate, moving to and fro, the nuclei will make it polarised by an increase and decrease in bond length. A bending motion will cause the shape of the polarisation ellipsoid to change the most. The bend will decrease and increase the angle to the most extreme displacement from the equilibrium point. As the molecule will be fluctuating between the two extreme positions from the equilibrium state the ellipsoid will continually be changing making the vibration Raman active. The asymmetric stretch is probably the

most difficult vibration to identify if it is Raman active due to the size and shape of the polarisability ellipsoid approximately remaining unchanged. However, what we need to understand is that the polarisability is a directional property and thus when this stretch occurs the major axis of the ellipsoid will alter; an induced tilt axis occurs, either increased or decreased and this in itself will cause a change in the position of the ellipsoid and thus making it Raman active. These vibrational modes are illustrated in Figure 7. [4, 7]

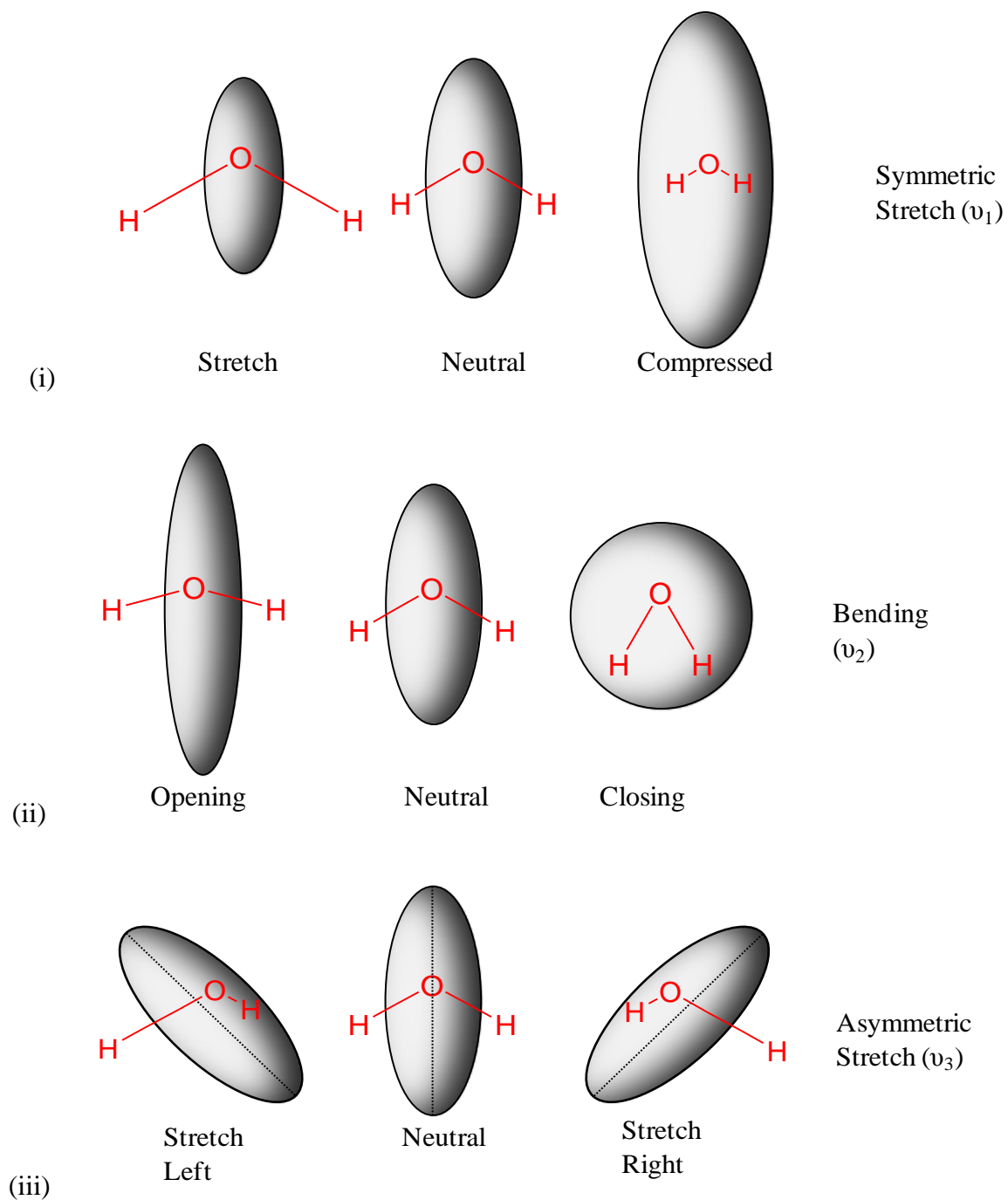


Figure 7. Polarisability ellipsoid displacement change with respect to vibrational modes of a water molecule.

4.2.4.2. Linear Molecules: Vibrational Raman

If we consider a linear molecule like that of carbon dioxide, as previously used in Figure 6, we can see that the stretching vibration mode will cause a change in polarisability comparable to that of a non-linear molecule. When visualising the other two modes, ν_2 and ν_3 , it can be potentially easy to presume that they too will be Raman active and cause a change in polarisation as shown in Figure 8. Noticeably there is little change in the latter two modes with regards to the polarisation ellipsoid, which is why confusingly it can be assumed that they are potentially Raman active. Understanding the displacement of a bond by using displacement coordinates, ζ , can explain Raman activity/inactivity. If we consider arbitrary values for the maximum and minimum displacement of bonds during any displacement from the neutral equilibrium state then we can assign an arbitrary values to the maximum and minimum displacement, $\pm\zeta$, relevant to each vibrational mode with respect to an increase or decrease in polarisation, α . Table 1 describes the vibrations with regards to the assigning of $\pm\zeta$ and they are characterised in Figure 8.

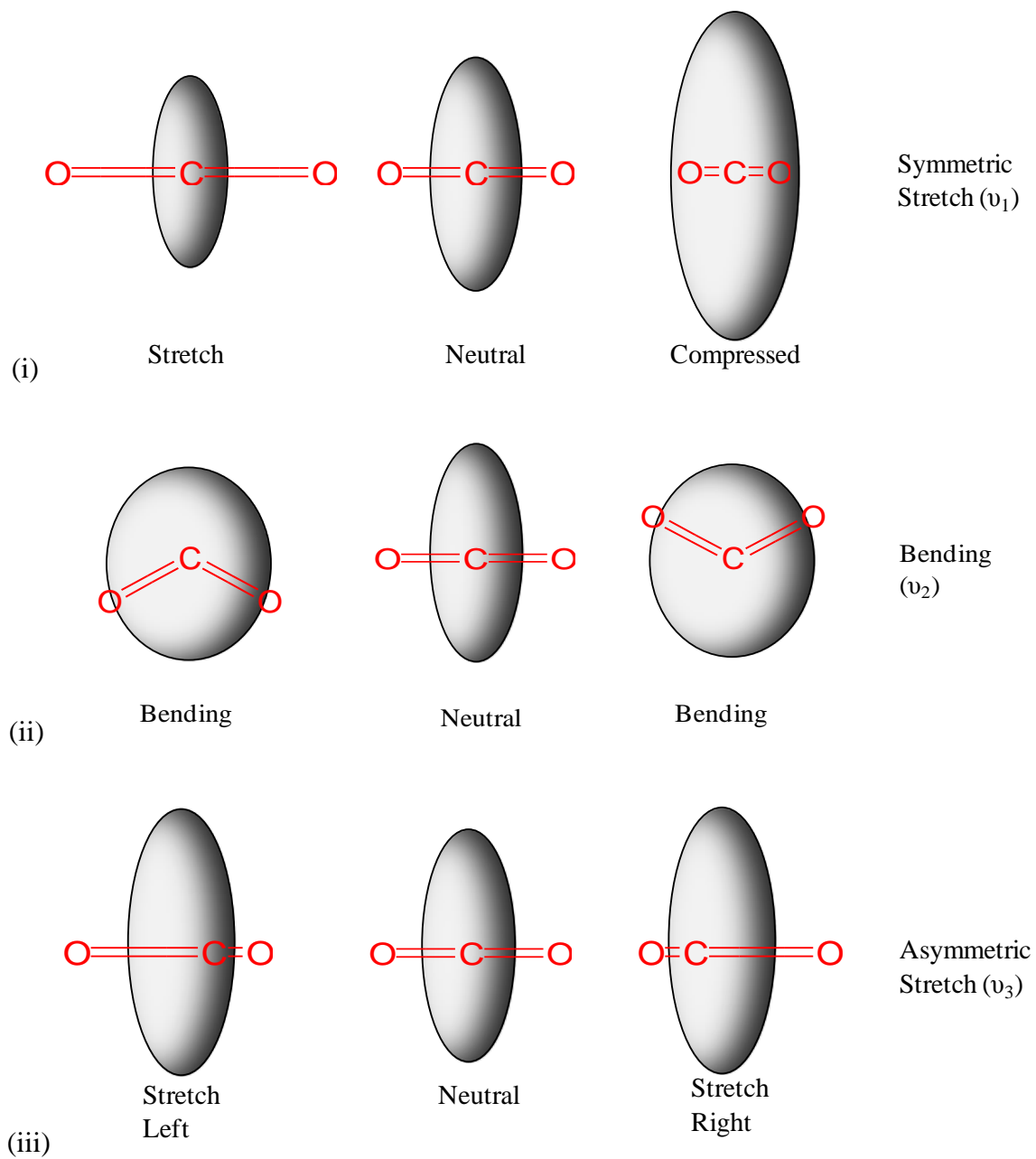


Figure 8. A carbon dioxide molecules polarisability ellipsoid displacement change with respect to vibrational modes.

Mode	Vibrational Mode State of Displacement	ξ	α
Symmetric Stretch ν_1	Equilibrium	$\xi = 0$	α_0
	Maximum stretch	$+\xi$	$\alpha > \alpha_0$
	Maximum Compression	$-\xi$	$\alpha < \alpha_0$
Bending ν_2	Equilibrium	$\xi = 0$	α_0
	Maximum bend	$+\xi$	$\alpha > \alpha_0$
	Equal and opposite maximum bend	$-\xi$	$\alpha > \alpha_0$
Asymmetric Stretch ν_3	Equilibrium	$\xi = 0$	α_0
	Maximum asymmetric stretch (left)	$+\xi$	$\alpha < \alpha_0$
	Equal and opposite maximum asymmetric stretch (right)	$-\xi$	$\alpha < \alpha_0$

1. Displacement co-ordinates for a carbon dioxide describing the polarisability

ellipsoid displacement during vibrational modes.

Graphically representing the assigned displacement coordinates as a function of the deviation in polarisability of the vibrational mode allows the concept of the gradient $\left(\frac{d\alpha}{d\xi}\right)$ to be identified to describe the rate of change at an equilibrium state. For displacement to occur one would expect $\frac{d\alpha}{d\xi} \neq 0$ at $\xi = 0$ and $\frac{d\alpha}{d\xi} = 0$ when there is no or little change in the displacement, therefore, suggesting the former indicating Raman activity whilst the latter having no Raman activity. Figure 9 shows the graphical representation of the various vibrational modes.

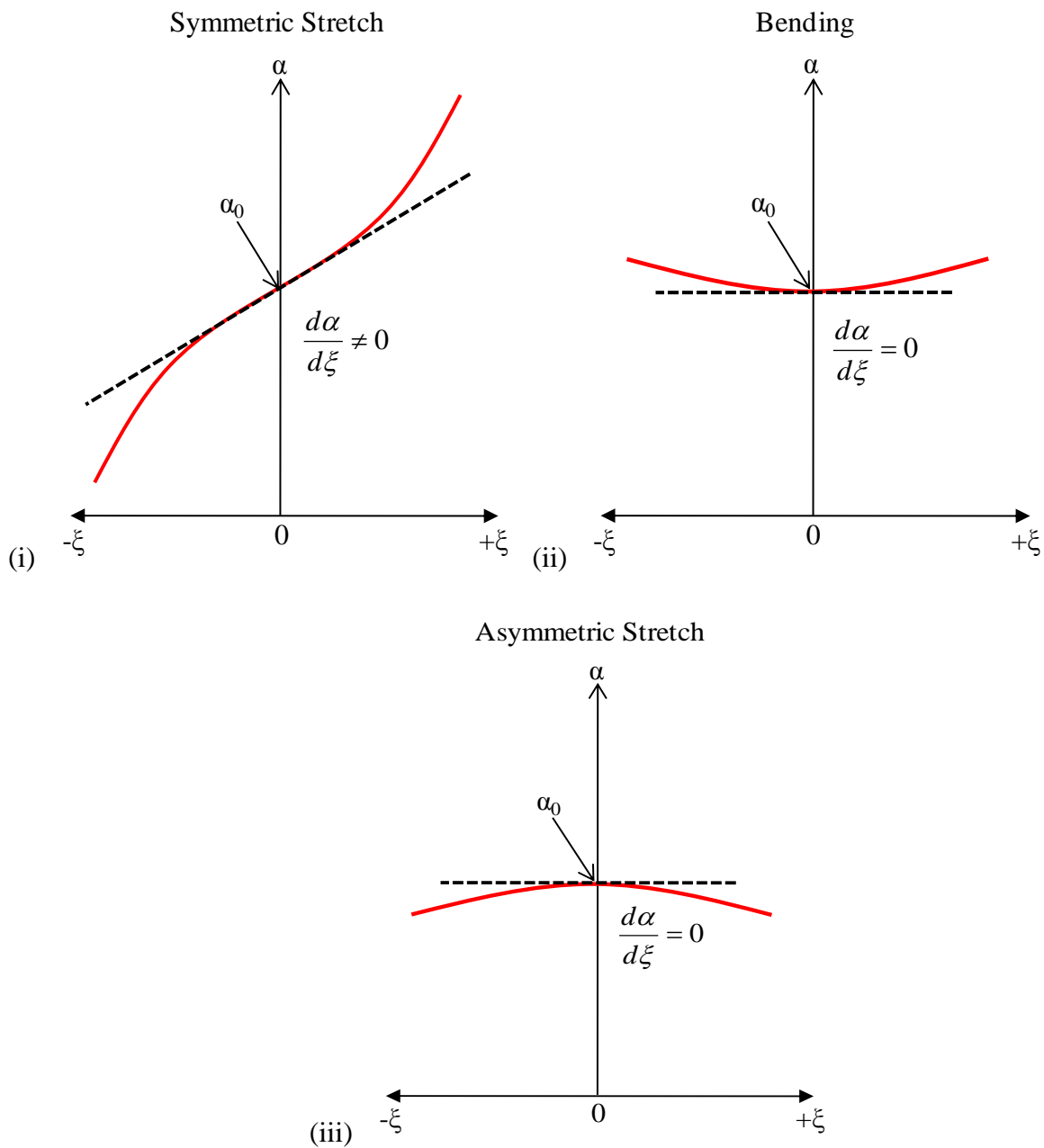


Figure 9. Graphical representation of the polarisability ellipsoid change in relation to displacement co-ordinates for the vibrational modes of carbon dioxide.

From the graphical representations we can determine that the symmetric stretch is the only mode that has displacement, the other two have very little and thus overall no displacement, which is why there is no Raman activity for these and would account to why there is little polarisation change in the ellipsoid. So overall we can assume that symmetric vibrations will give the most intense Raman bands due to their activity whilst the bends and asymmetric stretches will be the weakest if at all active. The displacement and gradients would differ for each molecule and as a consequence the amount of Raman activity would vary. However, the representation illustrates what is happening and how we can determine from observation qualitatively to whether or not a molecule could be Raman active. [4, 6, 7]

4.2.5. Rule of Mutual Exclusion

We can summarise the conclusion about Raman and infrared activities briefly but critically by a rule of mutual exclusion, which in summary indicates no vibration is simultaneously active in both Raman and infrared, if a molecule has a centre of inversion. In such a case Raman active modes will be infrared inactive and the infrared active modes will be Raman inactive. If the molecule has no centre of symmetry then some, not automatically all, modes may be Raman and infrared active.[4]

4.3. The Raman Instrument and Experimental Design

4.3.1. Raman Spectrometer: LabRAM HR 800

The LabRAM HR 800 is a high resolution Raman spectrometer instrument with an integrated confocal microscope for high spatial resolution imaging. The spectrograph has a focal length of 800 mm and has two interchangeable gratings (1800 and 600 grooves / mm) that provide different degrees of dispersion and spectral resolution. The bench top machine was initially setup for the built in 633 nm He:Ne and also had two externally mounted lasers; a 785 nm diode laser (NIR) and 532 Nd:Yag nm laser. The Raman spectrometer is shown in Figure 10.

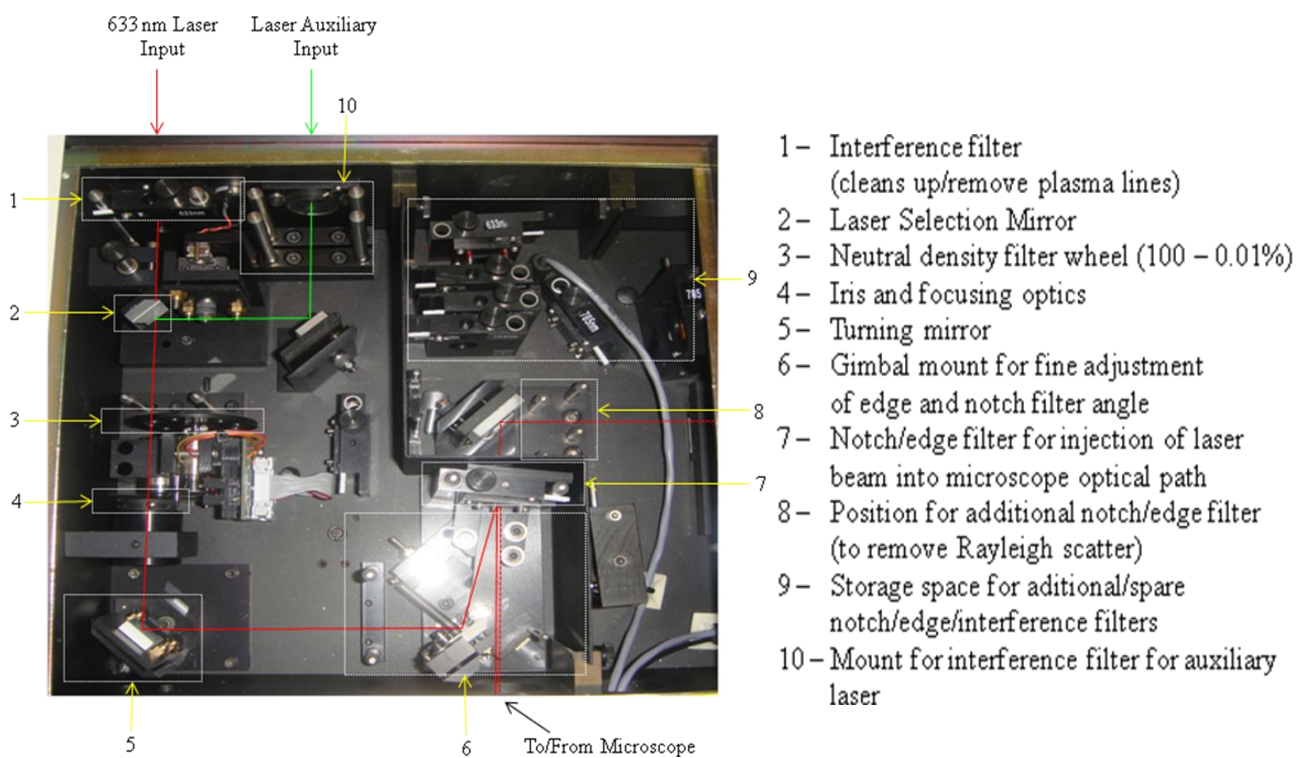
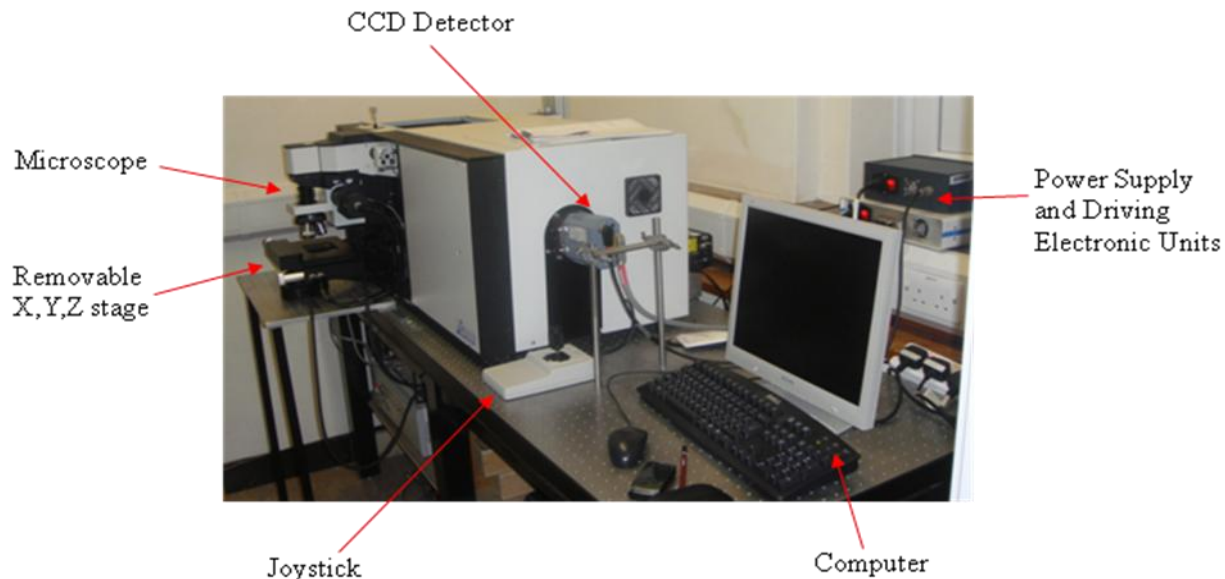


Figure 10. Picture of the Raman spectrometer and the internal path of the laser and components.

As the laser enters the optical bench there is an interference filter to remove any plasma lines from the laser before it travels through a density filter, controlled via the software of the computer enabling the selectivity of the laser power to be between 0.1 - 100 %. [The external lasers come through another location with additional mirrors bringing the beam onto the same optical path as the internal laser. There are locations for interchangeable interferential filters to be placed and removed in concurrence with the selected laser]. The laser is injected into the optical path of the microscope using a notch or edge filter mounted on a rotating table. The filter reflects the laser wavelength efficiently but allows wavelengths greater than that of the laser to pass through. Since this filter relies upon the interference filter technology it is highly sensitive to angle and its position can be pre-tuned using a spacer. The injected laser is passed down the microscope and focused onto the sample. The microscope is set up for back scatter and the notch filter will have a secondary purpose now of reflecting back the Raleigh scattering and allowing the selected frequency range of Raman scatter to pass into the spectrograph stage. The magnification between the confocal hole and the prepared sample is a factor of 1.4 relative to the objective lens (image = 1.4 * “objective lens”). This is due to the objectives having a length on 180 mm and the lens length forming the image having a focal length of 250 mm.

4.3.2. Confocal Raman Microscopy

A scanning confocal microscope allows sharper images to be obtained compared to those observed using a conventional microscope. This is achieved by the discrimination of most of the light that is not in the focal plane of the microscope, see Figure 11. This allows for

point-to-point identification and exclusion of all other out of focus light (images) reflected back at each point to the lens. In a confocal microscope the image is focused through a pin hole behind a lens through which only light originating from the well defined focal point will pass. Other points significantly larger than the pin hole do not provide significant intensity. The use of a pin hole reduces the detected intensity but contributions to the signal from areas other than the focal point are very small. Thus scanning the spot will allow for images to be built.

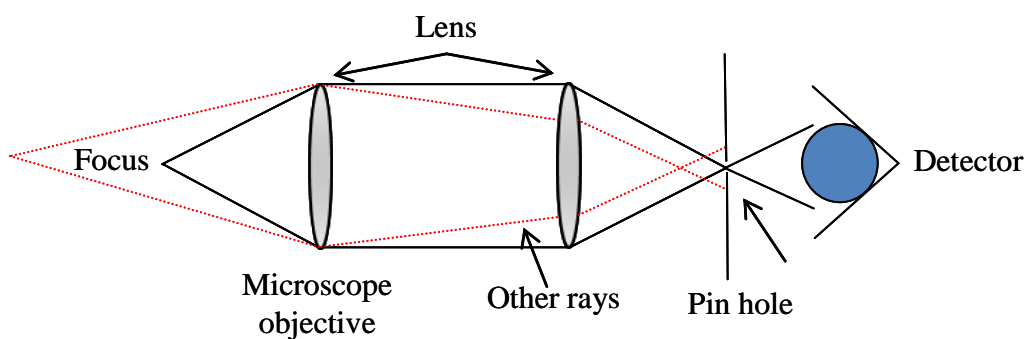


Figure 11. Representation of confocality and the discrimination of unwanted light.

Confocal Raman spectroscopy allows chemical analysis and potential mapping on a point by point basis. The additional capability of this technique is the examination of an interior point of a sample since the techniques defines a region of interest that is specifically defined by the x, y and z axis. An example of using the confocal technique is analysing inside a glass vial. The overall method uses the aperture to discriminate against Raman scatter that is out if the focal plane and incident beam as shown in Figure 12. [11, 12]

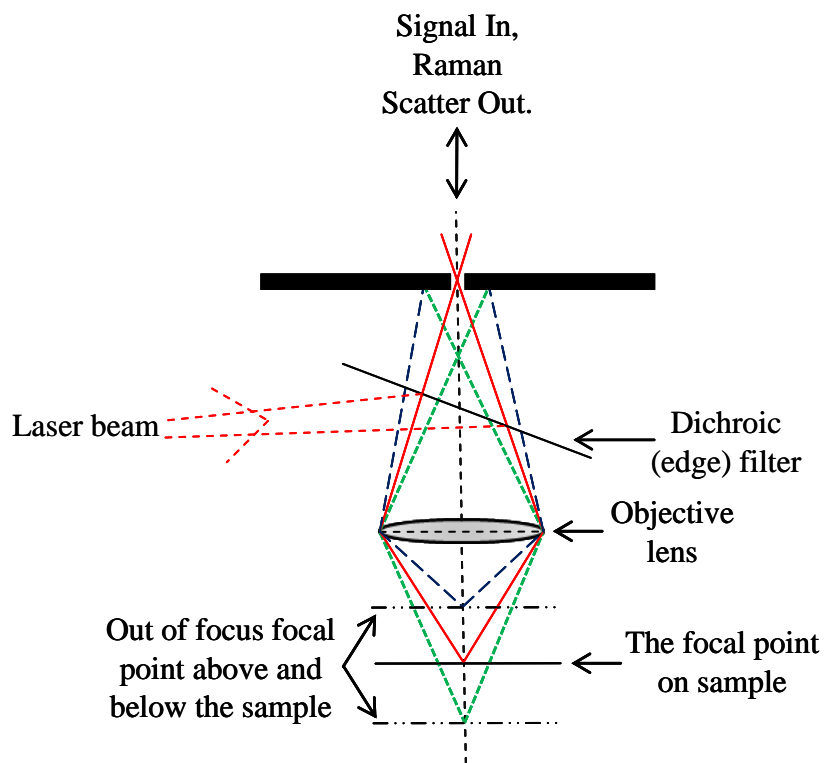


Figure 12. Representation of the confocal microscope with respect to the laser beam and Raman scattering.

4.3.3. Time-Resolved (TR) Raman Spectroscopy

TR spectroscopic experiments are methods to observe a response of a system following irradiation as a function of time. TR experiments have identified electronic and kinetic characterisation from time resolutions of milliseconds to picoseconds. Vibrational TR spectroscopy provides much richer information content due to a larger number of bonds observed in the spectra, and their dependence upon subtle chemical changes. The TR Raman technique generally uses a pulsed laser as a source of energy and a spectrograph

coupled to a photodiode array (or CCD camera). [13, 14] Commonly used techniques today use a pump-probe method giving the following possible techniques:

- TR Coherent Raman Spectroscopy [15]
- Picosecond [16] / Femtosecond [17] Time Resolution TR Raman Spectroscopy
- TR Resonance Raman Spectroscopy [18]

Publications by G. H. Atkinson [19-21] are technical sources for further information about TR Vibrational spectroscopy.

Our research is based on TR Stokes Raman spectroscopy; a transient spectroscopic method where a single wavelength excitation causes Raman scattering and the process measured as a function of time. The CW laser also acts as a primitive probe when chopped which allows for continual time slices and, thus, these being in continual repetitions of the same time slice allowing a profile being built.

4.3.4. Experiment Outline and Design

The outline of our experimental research is as follows:

- Identify the most suitable dopant for Raman study
 - The acetylene moiety is a good Raman scattering chromophore
- Record spectra of dopants and LC material, identifying non-coincident bands

- Record spectra of doped mixtures at low percentages
- Learn how to make LC devices
- Record Spectra of LC cells doped and undoped
- Record the EO properties of the LC cells
- Study the spectra of the LC cells as a function of orientation and potential
- Study the kinetic behaviour of the LC cell as a function of time

4.3.4.1. Design of The Improvised Oven and Dynamic Cell Holder

Preparation of the LC cells followed the procedure used in the SONY laboratories (refer back to chapter 3). However, the cells needed to be annealed and an improvised oven was made for this process by adapting a hotplate stirrer as shown in Figure 13. By fitting an aluminium base plate capable of holding and incorporating the temperature probe, the plate could be heated at a constant temperature. A circular groove, a few mm deep, allowed a Petri dish to sit over the cell creating a cavity which could be heated to anneal the LC devices. The size was chosen so as to allow multiple cells to be annealed under similar conditions.

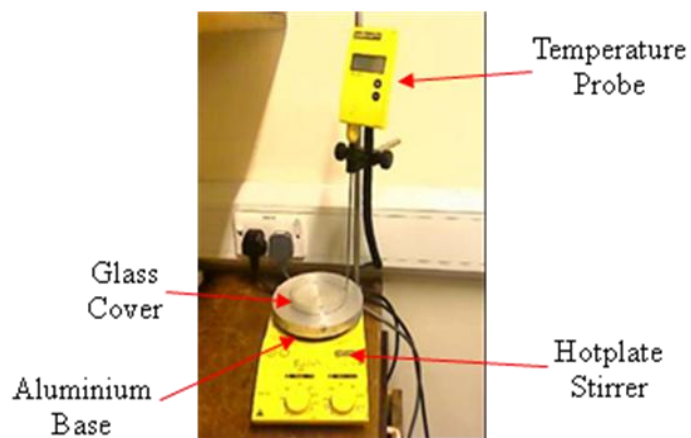


Figure 13. Picture of the adapted hotplate to make the improvised oven.

Holding the cells and providing good electrical contact whilst moving them in the light path of the spectrometer required the design of a new cell holder. The cell holder is shown in Figure 14a. We can see that the cell is robust and has a window, allowing the Raman microscope access to focus on, and into, the cell, as shown in Figure 14b. Electrical contact to the cell is made with the electrode via a slice of conducting rubber (Zebra strip) that conducts electricity in a 2-dimensional mode.

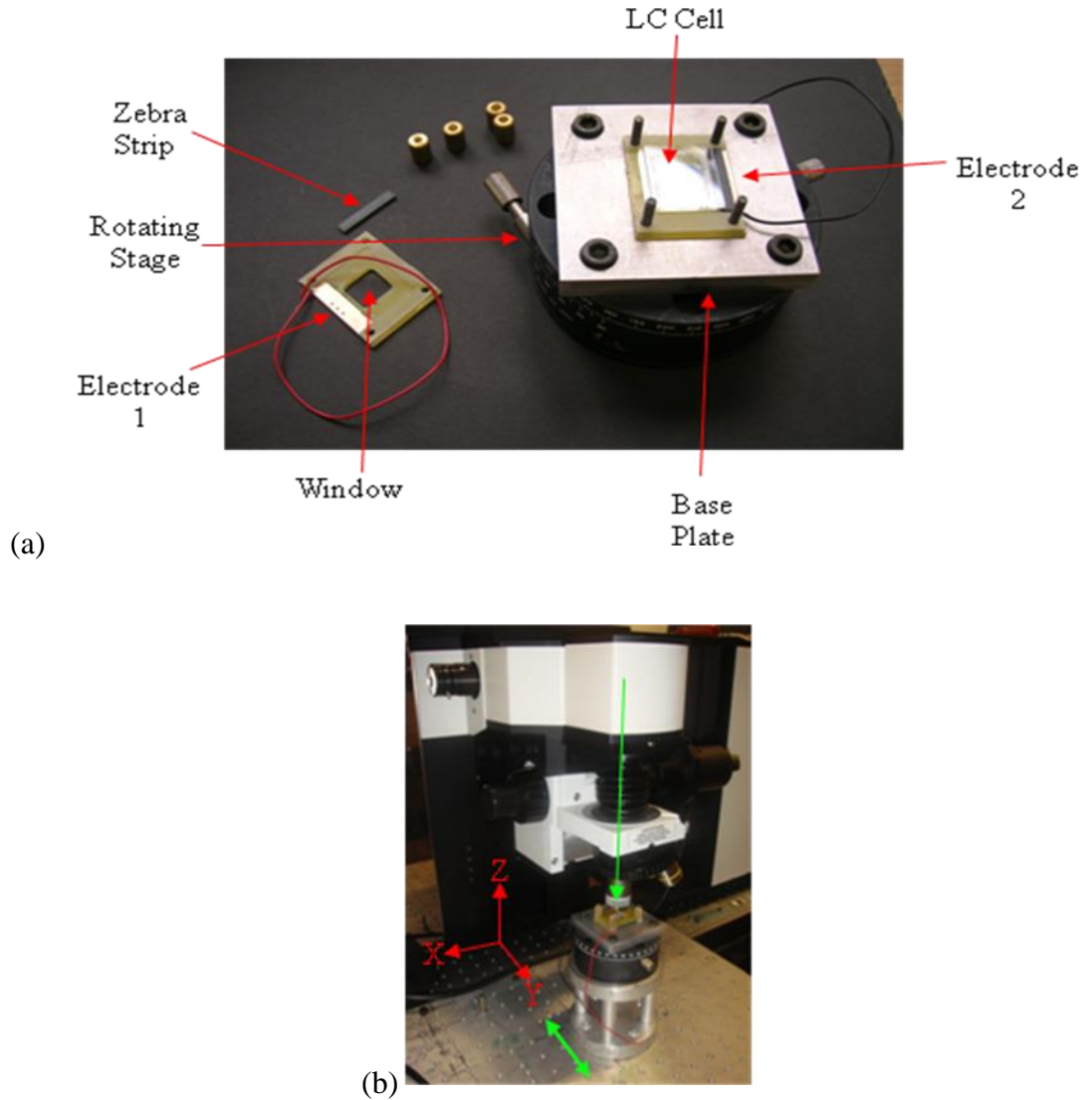


Figure 14. Picture of (a) the cell holder and (b) the cell holder mounted under the microscope.

4.3.4.2 Electro-Optic (EO) Measurement Experiments

EO measurements were carried out to determine the optical performance of the devices prior to Raman measurements. The switching of the cells brings about the rotation of the

plane of polarised light which is monitored by an analysing polariser and photo diode. As a cell is turned on, the plane of polarisation of light will start to rotate through the cell. The degree of rotation corresponds to re-alignment of the LC phase. By monitoring this rotation as a function of time we can study the turn-on and turn-off times of the cell. Figure 15 shows the schematic layout for this experiment.

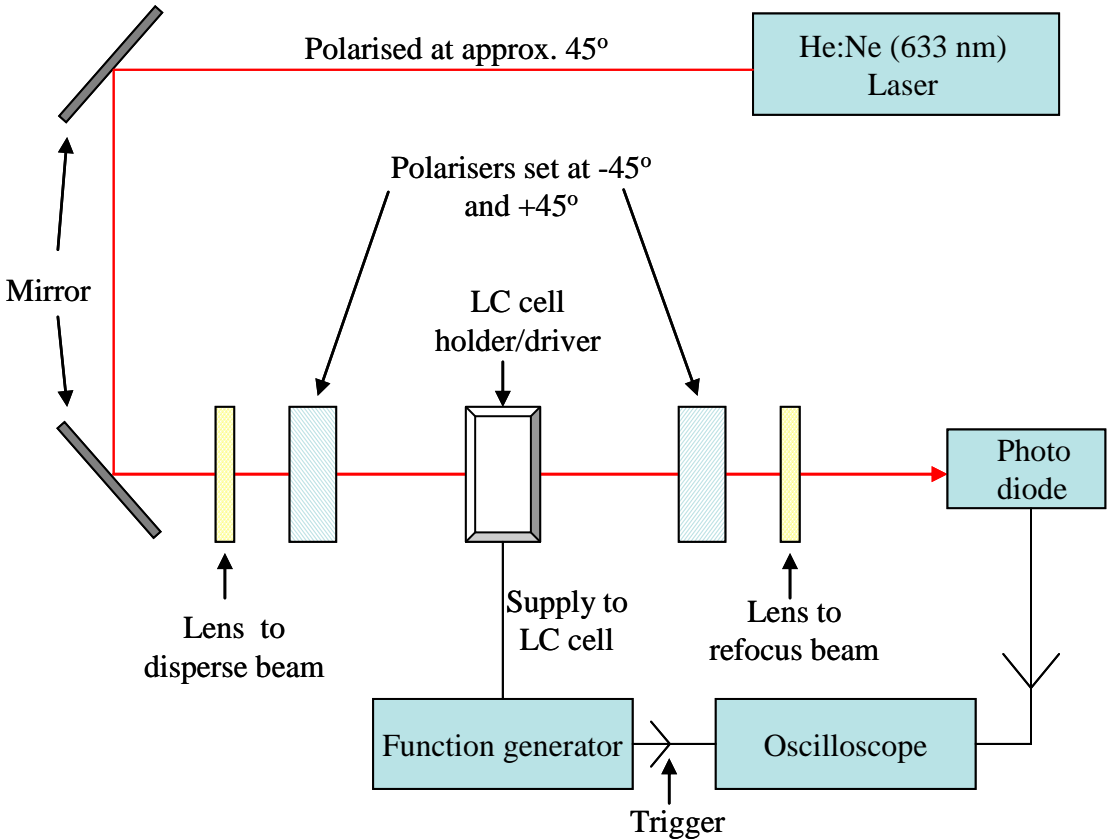


Figure 15. Schematic representation of the Electro-optic (EO) experiment.

4.3.4.3 TR Raman Spectroscopy Experiment Schematic

Figure 16 below shows the schematic outline of the experimental design of the TR Raman spectrometer and cell-holder used to measure the switching of the LC cells.

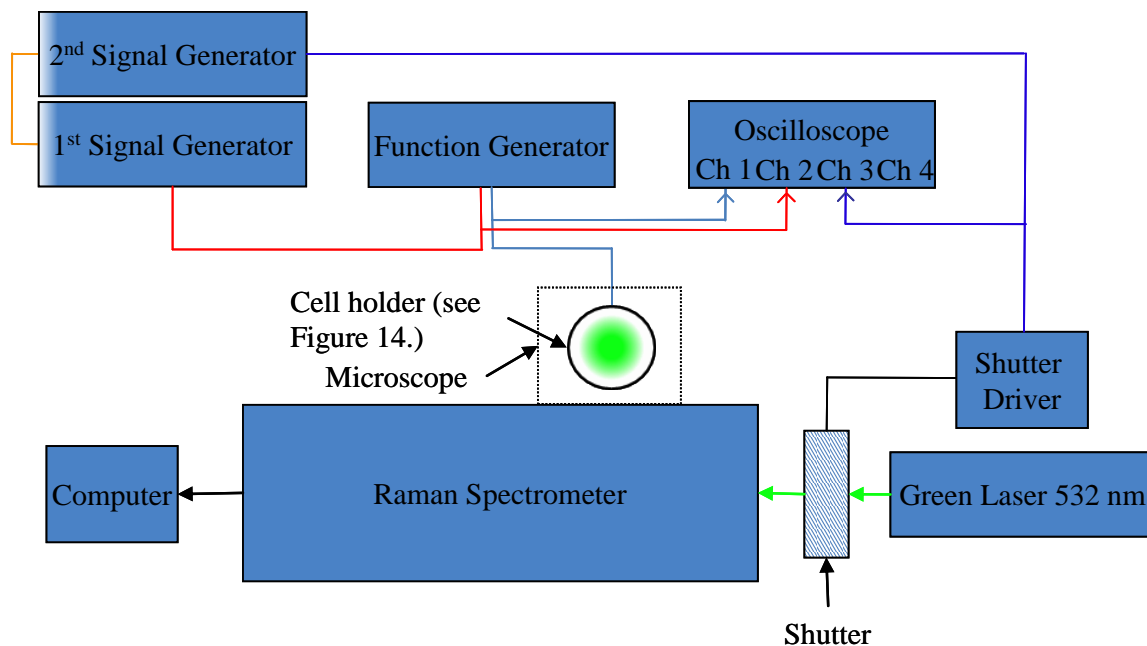


Figure 16. Schematic representation of the Time-Resolved (TR) Raman experiment.

The function generator produces the primary signal to drive the switch of the cell and act as a “*time keeper*” by keeping all other components in the setup to operate within the time of the generated signal. The first signal generator produces a pulse at the same time as the primary signal to switch on the second generator. The second signal generator in turn generates a delayed pulse to activate the shutter driver and thus in turn operates the shutter to gate the excitation laser specific to a time scale. The Raman microscope is an inherent steady state system and in order to obtain gated data we used the shutter to chop the excitation laser. Ideally we would use a pulsed laser but this was not available. However,

using a CW laser and shutter provided a pulsed light source giving us potential to operate the Raman spectrometer for a long period of time allowing many switching cycles to be accumulated to build a Raman profile of that specific part (slice of time) of the EO switch.

4.4 Results and Discussion

4.4.1 Raman Spectra of Dopants and LC

Initial experiments involved recording the Raman spectra of bulk samples of the acetylenic dopants **11-17**, **20**, **21** and **27-29**. The Raman signature that is common to these dopants is the alkyne stretch and aromatic ring stretch at approximately 2200 cm^{-1} and 1600 cm^{-1} respectively. The alkyne stretch is a particularly useful feature of the dopants due to it being an intense Raman signature as well as appearing in a region of the spectrum that is normally clear of other bands. A Raman spectrum of a dopant, **11**, is illustrated in Figure 17, along with that calculated by *ab initio* methods (Gaussian 03). The two spectra compare well, and the combination of theory and experiment allow the assignment of vibrational modes with a high level of confidence. Figure 18 shows the displacement within the vibrational mode of the acetylene with the initial image representing the ground state of the vibration. The Raman spectra of all acetylene dopants can be viewed in Appendix B Figure 1a – 11.

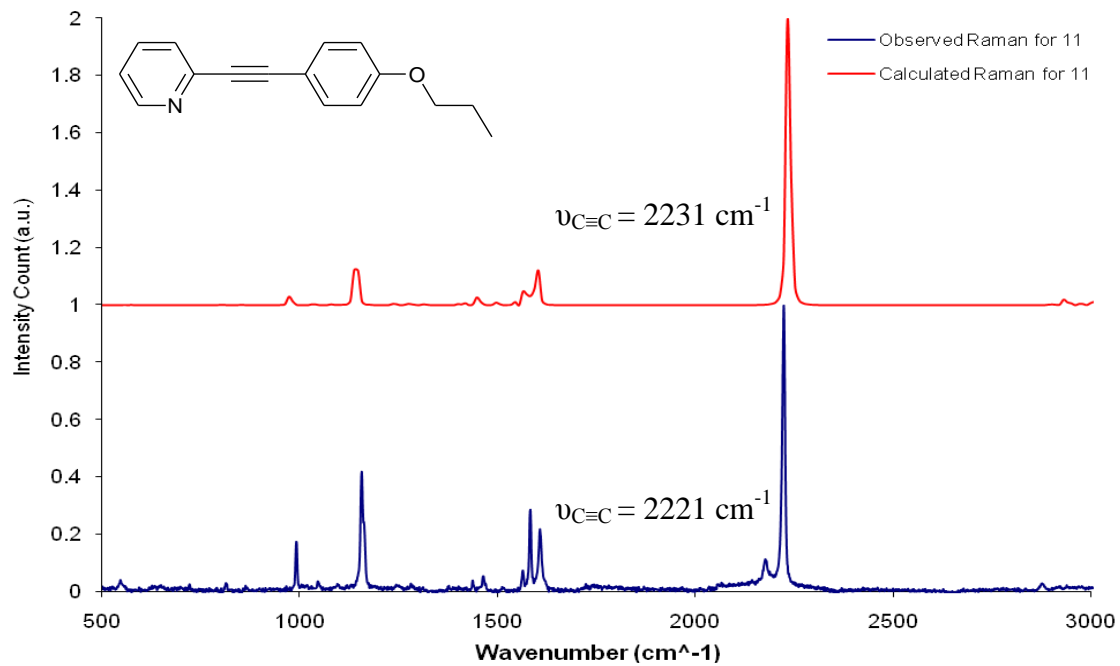


Figure 17. Normalized observed and calculated Raman Spectrum of **11**.

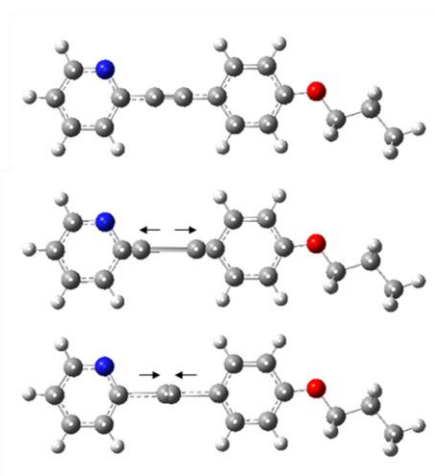


Figure 18. Snapshots of the displacement the acetylenic bond vibrating. The top image is the ground state of the bond.

The Raman spectra of the LC host materials were also recorded and are presented in Appendix B Figure 2a – b. A comparison between the dielectrically negative LC host (-LC) and dopant **11** are presented in Figure 19, showing two non-coincident Raman active bands that can be used for identification. The spectra are all normalised to the maximum signal in each spectrum for ease of comparative observation. The two independent identifiable characteristic signals between LC and dopant highlighted by the arrows. Figure 20 shows the spectra of a dielectrically positive cyanobiphenyl based LC host (+LC), BL037 (4-hexyl, 4'-cyano biphenyl), compared to a dopant. This shows that the acetylnic characteristic band in the dopant ($\sim 2200\text{ cm}^{-1}$) coincides with the cyano (CN) band of the host. Furthermore, the dopant aromatic ring stretch at $\sim 1600\text{ cm}^{-1}$ also coincides with the +LC host. This combination of overlapping bands is less suited to TR Raman measurements. Thus, the TR Raman measurements later focus upon the doped and undoped -LC devices and only undoped +LC devices.

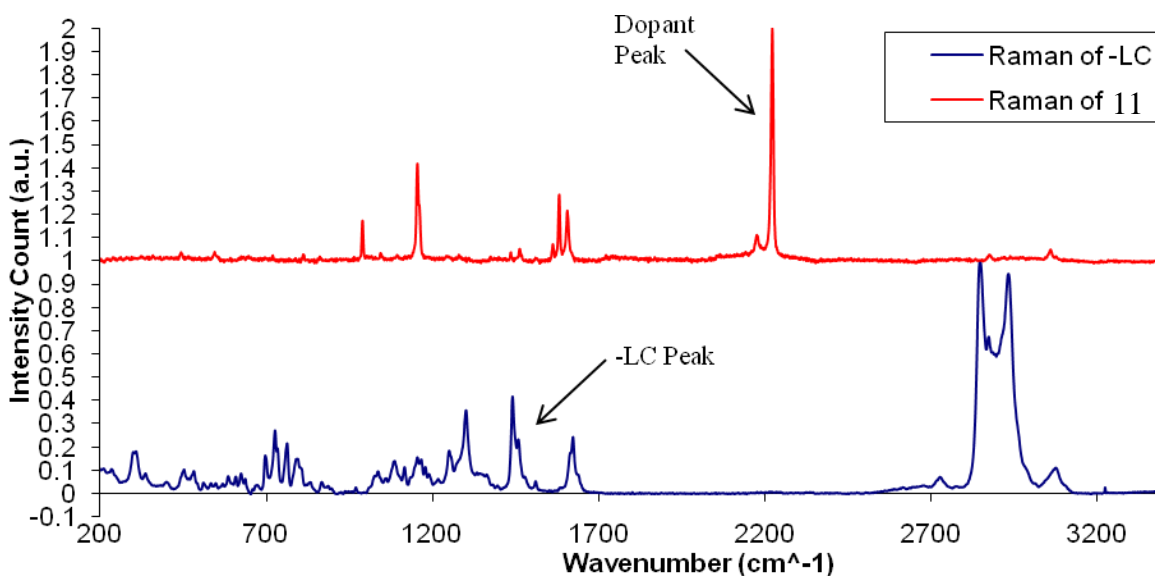


Figure 19. Overlaid Raman data of -LC material and dopant **11**

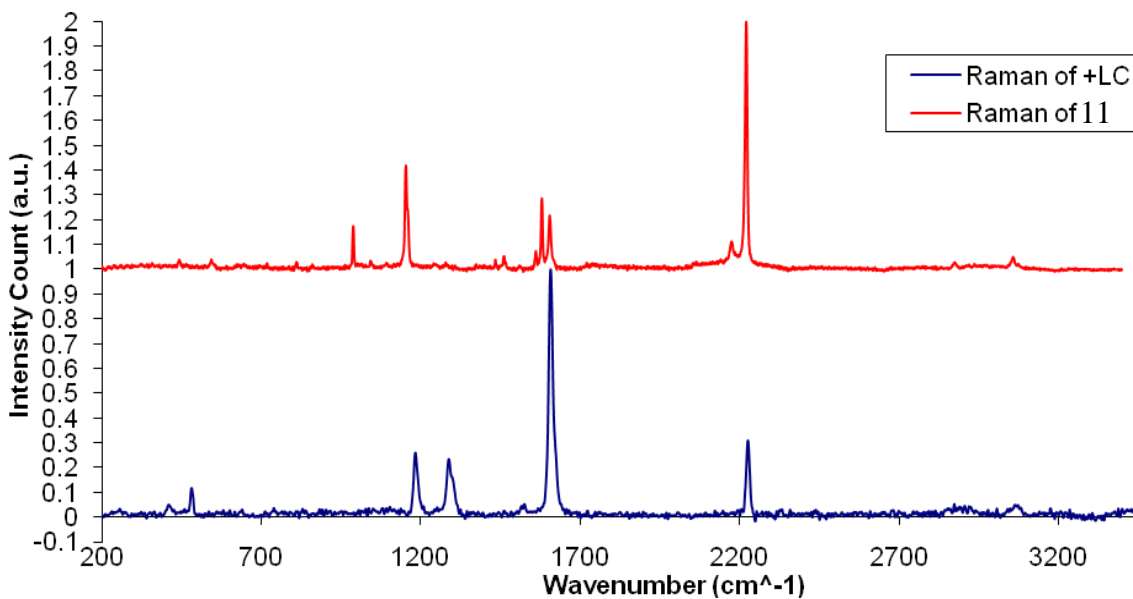


Figure 20. Overlaid Raman data of +LC material (BL037) and dopant **11**.

4.4.2 Dielectrically Negative LC Raman Study and TR Raman Results

The following results initially use a 20 μm VA cells for the preliminary Raman study of understanding the LC device and the internal mechanism of the EO switch of the LC phase respectively in orientation and applied potential. The Time-Resolved Raman studies that follow use a 5 μm VA cell as this is the smallest useable cell that is more suited to display devices.

4.4.2.1 Preliminary Study and Understanding of the Behaviour and Internal Motion of a LC Cell Using Raman Spectroscopy

The next step in the study involved the observation of the LC host and doped LC mixtures in LC cells which present some experimental challenges. The preliminary studies were carried out with a 20 micron VA cell allowing the determination of the spectra for a cell as a function of applied potential and orientation of the cell with reference to the plane of polarization of the Raman laser. Initially the cell was aligned and focused upon under the microscope. A VA cell has a rubbed director on the alignment layers which are orientated 180° to each other giving an 180° twist of the LC material through the cell when it is in the on state. The cell has to be switched on to determine the alignment of the cell as this gave the greatest Raman signal. The reference point was deemed when the cell was rotated until a maximum signal is observed. This information indicates LC orientation regarding the polarisability ellipsoid which was perpendicular to the laser orientation. Thus the molecular axis and director of the alignment layer was parallel to the plane of polarization of the laser.

The cell is then considered to be at an orientation of 0° with respect to the polarization of the laser.

Since the cell is usually operated with an electrical field of approximately $1\text{V}/\mu\text{m}$ initial experiments were carried out using a potential of 0V and 20V as the off and on state across the $20\ \mu\text{m}$ VA cell respectively. The spectra of a cell containing pure -LC show a band at $1600\ \text{cm}^{-1}$ and shown in Figure 21, which shows significant difference between the off and on state. This demonstrates that during the switching process re-orientation of the molecules and, hence, polarisability ellipsoid, with respect to the orientation of the laser brings about an enhancement of the Raman spectrum. This demonstrates the feasibility of using Raman spectroscopy as a tool to investigate the switching of LC devices.

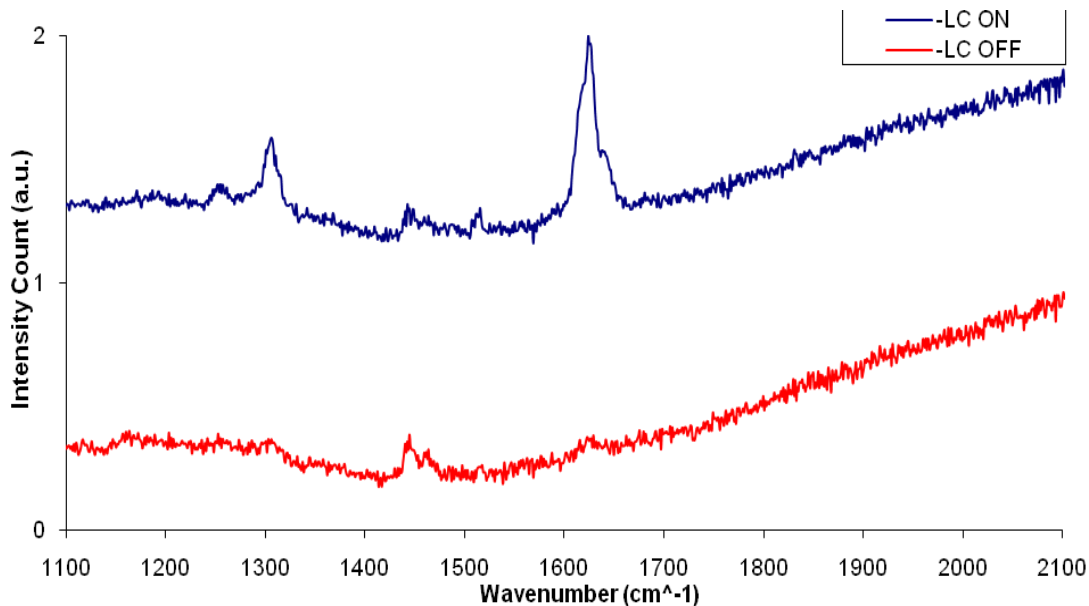


Figure 21 Raman Spectra of the pure -LC $20\ \mu\text{m}$ VA cell in the off and on state at 0° .

The work then went on to study the spectra as a function of applied potential and orientation with respect to the laser polarisation. Figure 22a)-c) shows the Raman spectra of the VA cells as a function of voltage and orientation in the on and off state for a pure -LC cell. We can see that below at approximately 6 V the signal is very weak and reaches a plateau at approximately 12 V. The signal intensity of the bands at $\sim 1450\text{ cm}^{-1}$ does not significantly change with orientation of applied electric field. However, the band at $\sim 1620\text{ cm}^{-1}$ and 1300 cm^{-1} are only observed when the potential is applied to the cell and reaches a maximum when the excitation beam is polarised parallel to the long axis of the LC cell.

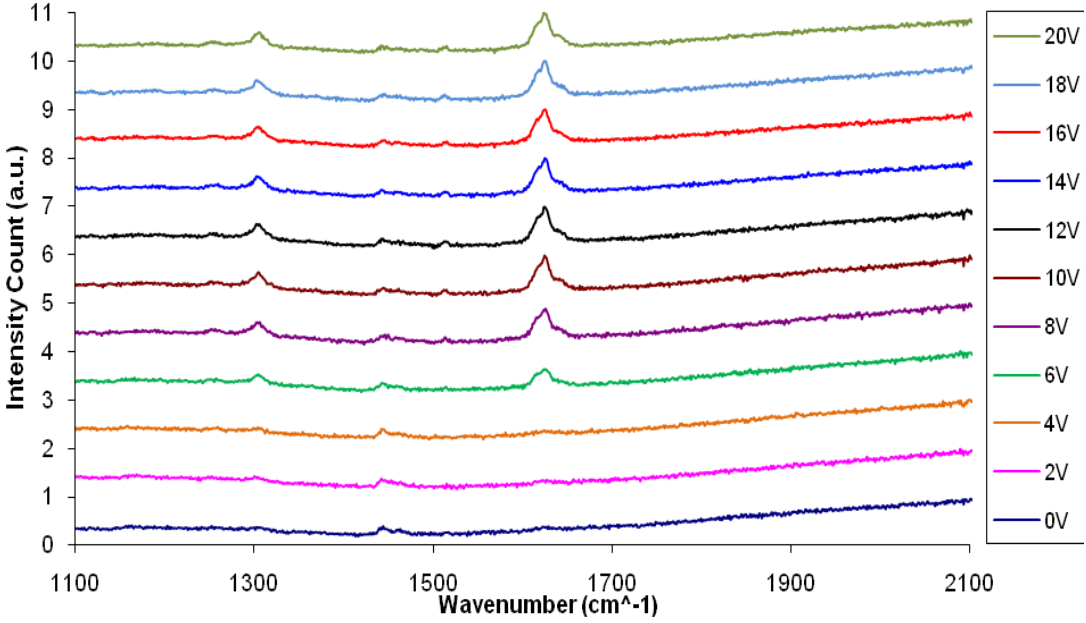


Figure 22a. Raman Spectra of pure undoped -LC 20 μm VA cell of varying the potential between 0V and 20V.

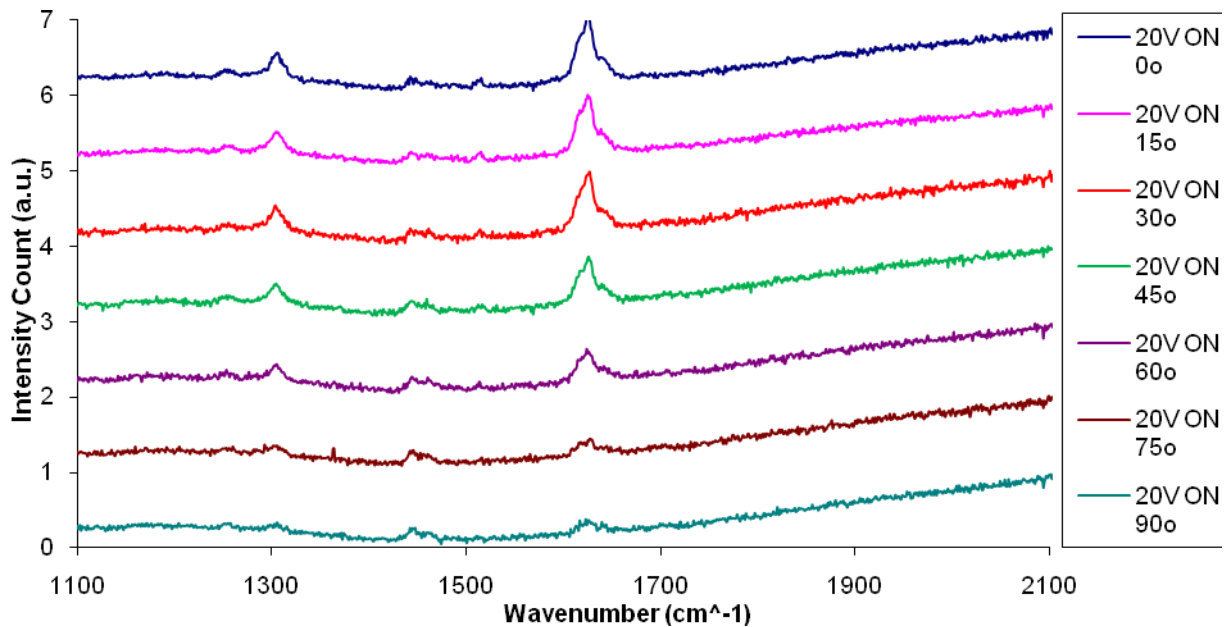


Figure 22b. Raman Spectra of pure undoped -LC 20 μm VA cell of the orientation between 0° and 90° in the on state.

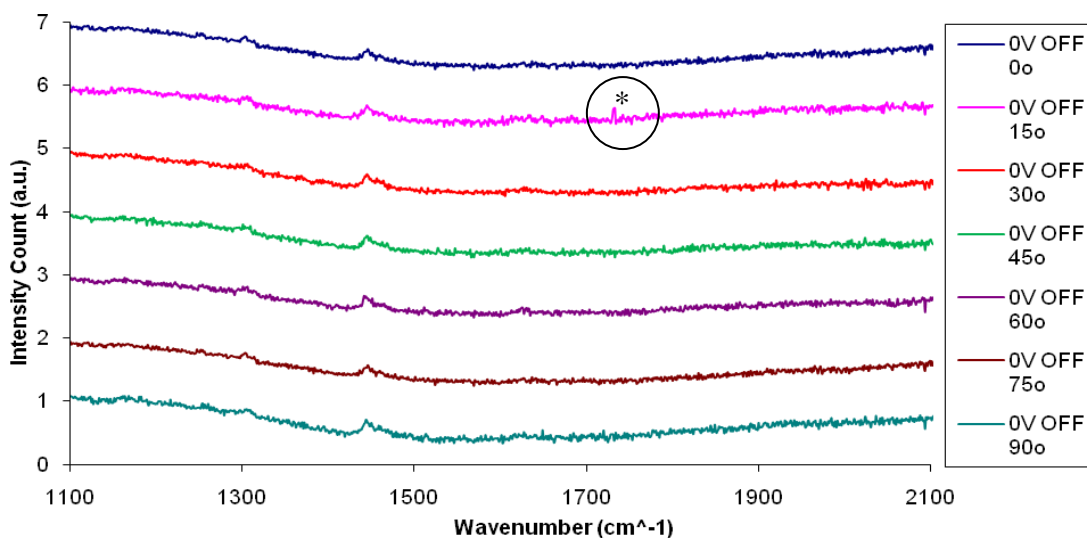
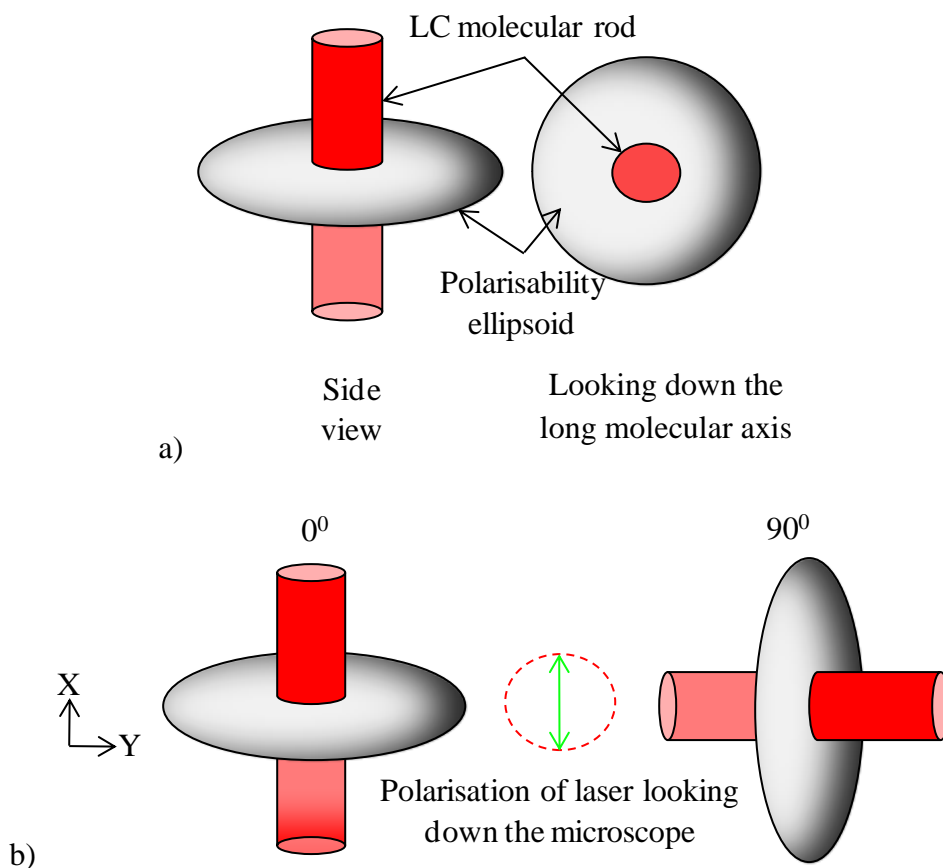


Figure 22c. Raman Spectra of pure undoped -LC 20 μm VA cell of the orientation between 0° and 90° in the off state.

NB. Highlighted bands denoted with a * indicates cosmic background radiation and appears randomly and thus not characteristic of the sample.

These sets of data imply that the polarisation ellipsoid changes in the xy plane, having defined the x,y,z point of interrogation, of the cell in the on state and when in the off state the same ellipsoid is independent of the cell orientation. The short axis of polarisability ellipsoid (maximum Raman signal) is aligned with the polarisation of the laser when the long axis of the cell is parallel to the plane of polarisation of the laser, determined as an orientation of 0° . Figure 23a shows a representation of the LC and its ellipsoid in the side view and when looking down the long axis of the rod-like molecule. In the on state the laser polarisation is aligned with the short axis of the polarisability ellipsoid and thus the long molecular axis along the long axis of the cell, perpendicular to the z axis. Rotating the cell through 90° in the same state brings the long ellipsoid axis (short molecular bond axis) into alignment with the laser and thus the Raman signal decreases. Figure 23b shows the LC and ellipsoid configuration when the cell is in the on state for the orientations of 0° and 90° as described. As the LC is a birefringent material the polarisation of the laser will be rotated throughout the cell following the path of the 180° twist. Therefore as the light penetrates the cell the orientation of the laser light and the molecules are the same as that for the initial molecule that we have considered at the first alignment layer. Thus, as the light arrives at the bottom layer it will be rotated 180° making the interaction constant throughout the cell. The Raman scatter from the LC material from the laser beam back into the microscope will also follow the same reorientation of rotation out of the cell.

When the cell is in the off state the laser is continually looking down the long axis of the molecule, as we know in the off state all molecules are vertically aligned and the cell has no birefringence. Therefore, we need only to consider one molecule as they will all be the same configuration. The interaction of the polarisation of the laser will always be bisecting the long molecular axis making it a continual interaction across the bond, which as noted before has the least polarisability (minimum Raman signal). Rotation of the sample through 90° in xy plane shows the Raman signal unchanging and thus indicates that the ellipsoid remains unchanged when rotated. Both orientations are depicted in Figure 23c, showing how a single component (representative of all molecules) is acting in the cell.



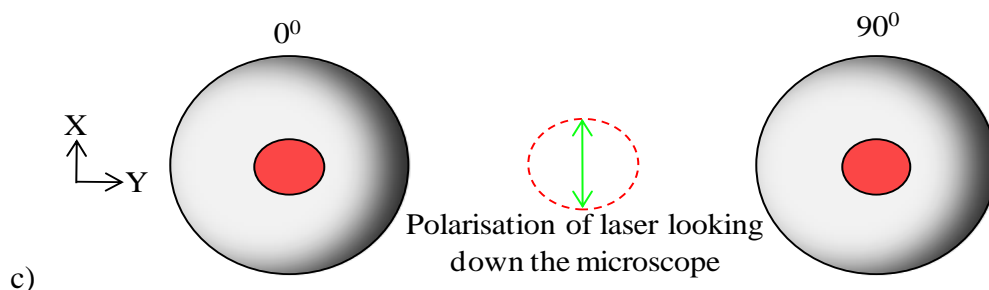


Figure 23. Representation when looking down the Z-axis (laser) of the LC material of (a) the side view and plan view of the LC alignment when the cell is (b) in the on state and (c) in the off state when rotated through 0° to 90° .

After the determination and rationalising the optical behaviour of the –LC cell by Raman spectroscopy we continued the study using the 20 micron VA cells and prepared doped cells with the Raman active dopants **11-17**, **20** and **27-29** at 4% by weight doping. The results of the optical behaviour with respect to varying the potential and orientation are shown in appendix B Figure 3a – d to Appendix B Figure 13a – d. These results showed similar behaviour to the undoped cell indicating early suggestions of alignment of the dopant and LC host are similar. Therefore, both compounds polarisation ellipsoids match up in the initial alignment and during the switch the dopants mimic the behaviour of the LC host from the on and off state as shown in Figure 23.

4.4.2.2 Time-Resolved Raman Studies of a 5 μm VA Cell of Both Doped and Undoped Dielectrically Negative LC Host

The research for the TR measurements began initially with preparing cells and determining the ideal cell gap to use. Experimentally it was found that fluorescence from the glass made using cells less than 5 μm difficult and hence TR measurements were carried with cell of a 5 μm path length. Initial experiments aimed to understand the EO properties of the cells and in particular, to obtain information regarding the switching time of the cells. Two cells containing undoped and doped LC samples were prepared for experimental consistency for the EO and TR Raman studies.

In the EO measurements an AC 0 – 20 V (1 kHz) potential was placed across the cell. The optical transmittance was recorded at intervals of every 0.5 V from 0 – 20 V in order to demonstrate that the cells optical behaviour was a function of the potential. Furthermore, it allowed the identification of the hysteresis of the EO switch being homogeneous. Figure 24 shows a typical trace for one of the prepared –LC doped cell with compound **14**, an example of the undoped -LC cell is shown in appendix B Figure 14. For each prepared cell the hysteresis was record and only if the traces were identical was the cell deemed homogenous and useable. Compound **14** was selected as the dopant that had shown the greatest effect on the switching in the measurements made by Sony (see appendix A), and has a Raman active chromophore present, making the compound an ideal dopant.

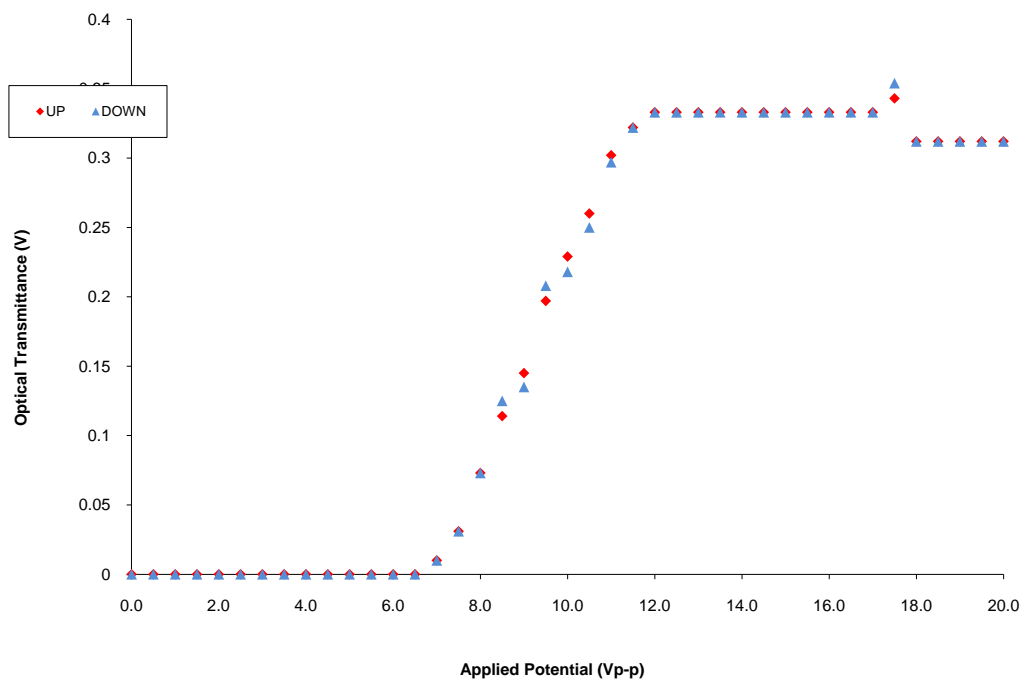


Figure 24. EO hysteresis measurements of the switch prepared -LC cell doped cell with compound **14**.

In order to identify the optimum time cycles for the TR experiments the cell was further investigated to fully characterise its switching behaviour and relaxation times. The cell was placed in the EO experiment and tests were carried out to determine the ideal voltage for a period of time for the switching between the off and on states. The first cell investigated was a -LC cell doped with 4% of compound **14**. The EO experiment started with varying the voltage from 8 to 15 V based on the initial observation that below 8V no optical activity could be detected and a plateau of optical activity was reached at 15V. A repetitive sequence composed with a 500 ms pulse and a 1500 ms delay between each pulse was applied to the cell and the transmitted light intensity was recorded as a function of time for each applied pulse. Once the ideal voltage was found from the observed profiles the effect

of changing the delay between the on and off periods was investigated as the results show that a 2 s period was sufficient. To determine a starting point we systematically studied a number of ms pulses with a minimum ms delay, i.e. at what point could we gain a stable off-on-off switch profile with the shortest pulse and delay possible. The EO data for variation in voltage and delay period can be seen in appendix B Figure 15a – b. The optimum conditions were found to be a 400 ms pulse of 1kHz, 12 V p-p, followed by 0V for 300 ms as illustrated in Figure 25. The optimal 12 V p-p is consistent with the optical transmittance data for the doped cell.

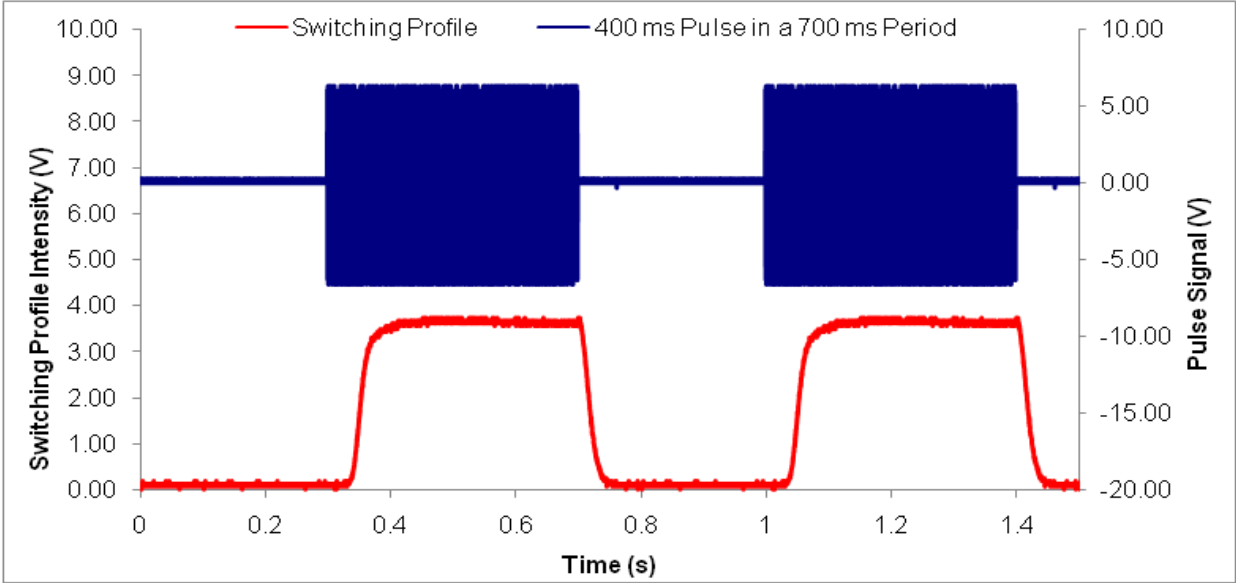
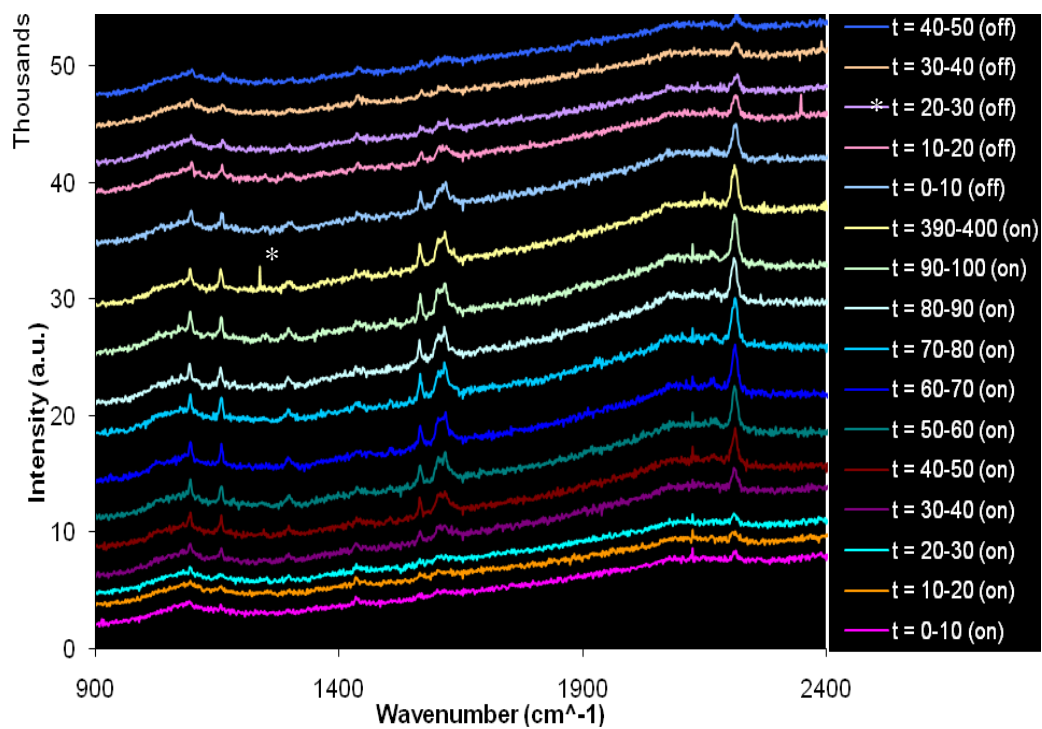


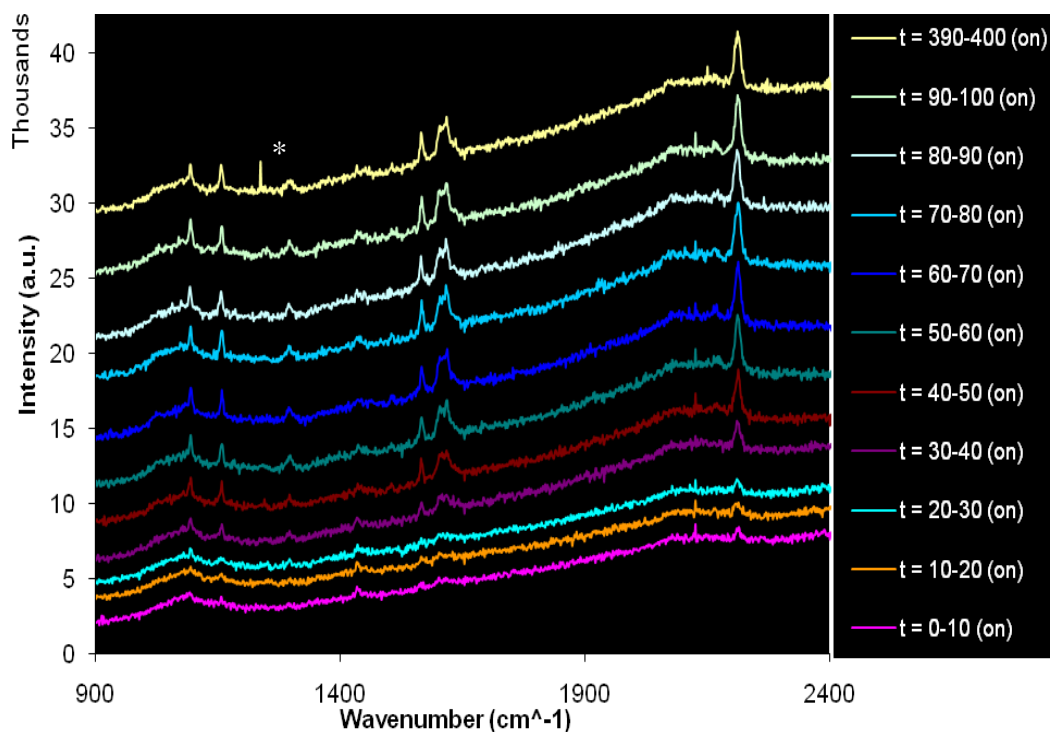
Figure 25. The EO signal and trace of the switch of the doped –LC with **14**.

The cell was placed in the cell holder and located in the Raman microscope aligned at 0°. The intensity of the observed Raman spectrum as a function of total exposure time and the

length of the shutter 'open' period was investigated in order to identify the optimum conditions for TR acquisition. The acquisition Raman signal for a 10 ms slice was found to be a total exposure (open aperture) for 150 s with 15 iterations and the 600 grating giving a spectral window of 1500 cm^{-1} . These experimental conditions showed both LC and dopant peak in the same spectrum with a good signal to noise ratio. This means the cell was switching for approximately 3,200 times whilst the Raman machine was setup up for summation of signals. The rise and decay of signal during the switch process was investigated by recording the Raman spectra of the 10 ms slices from the start of the signal ($t = 0$) to the top of the rise accordingly so to match the profile earlier observed by stopping the time gate. We then recording the last 10 ms of the signal and proceeding from there until the off state were obtained with the Raman signal ceasing to exist. These were collated and graphically represented in Figure 26. Note that in these graphs the data is not normalised since the signal intensity carries important information regarding the orientation/alignment.



a)



b)

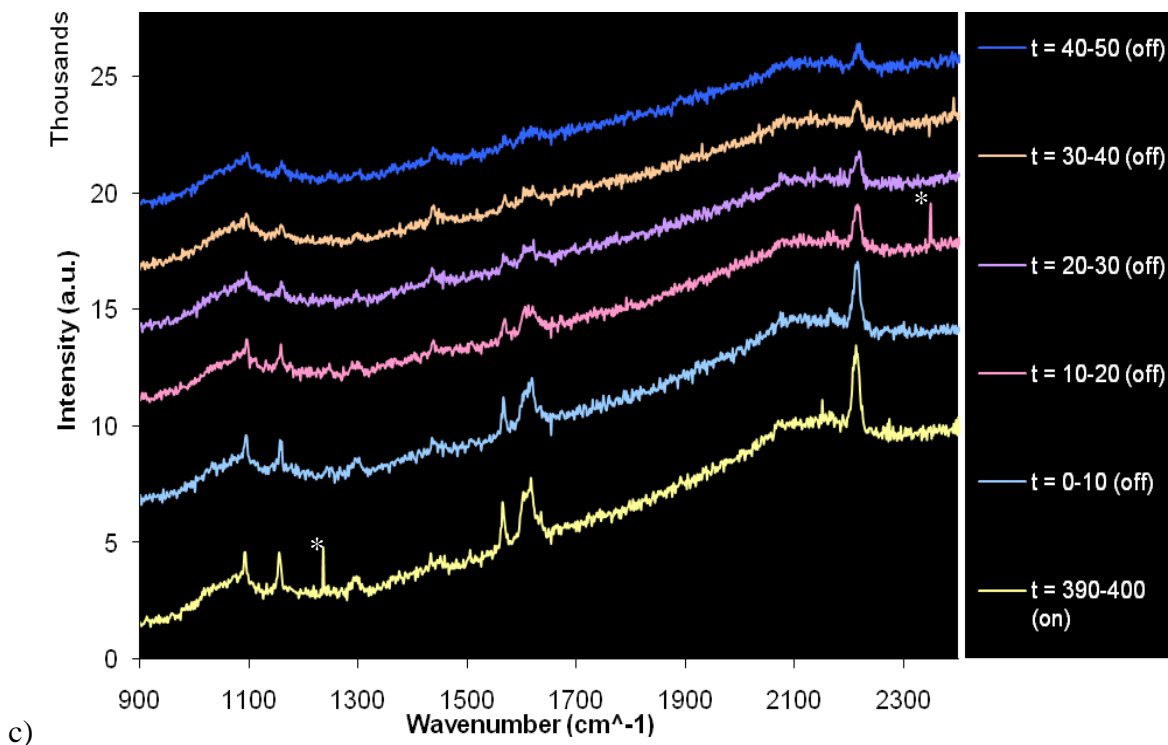
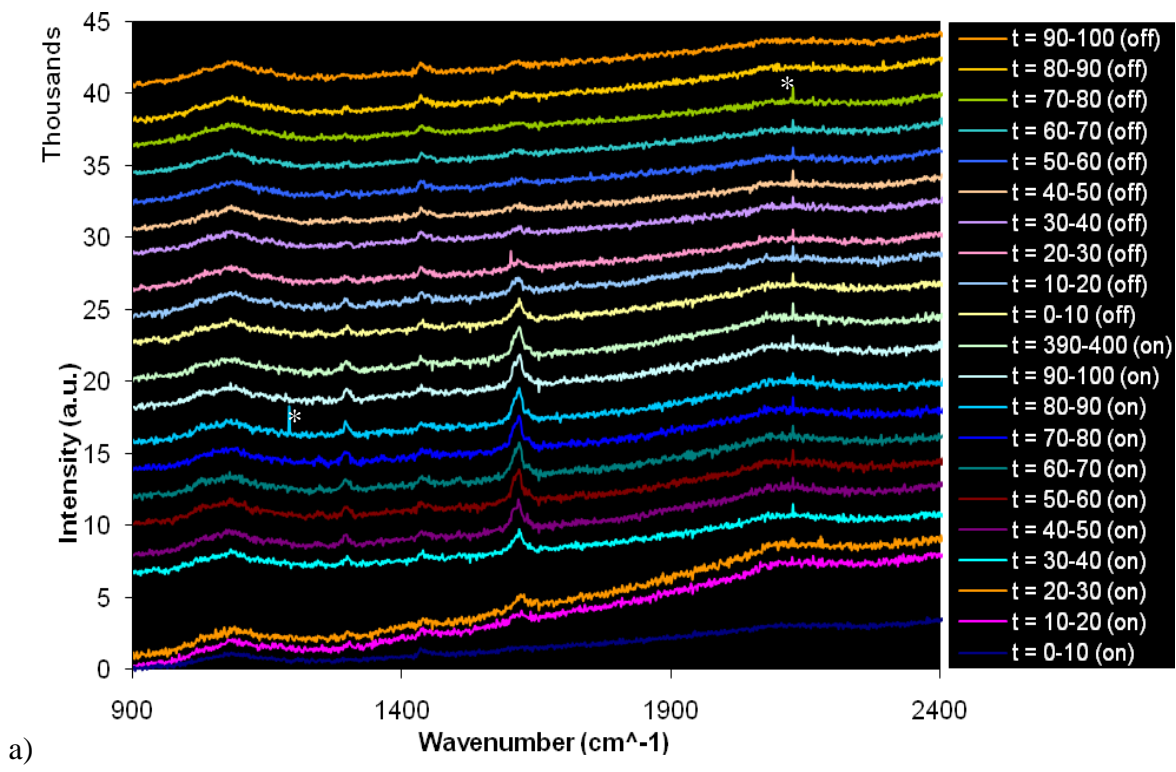


Figure 26. Time-Resolved Raman Spectroscopy Study: 5 μm VA Cell filled -LC Doped With 4% of Dopant Compound **14**, where (a) is the data for the whole experiment, (b) the rise and (c) the decay.

With the success of the doped -LC cell, we repeated the same study using an undoped cell. The optimal EO switch parameters were the same apart from the applied voltage as this is different in the EO profiling and hysteresis measurements. The EO study revealed that for an undoped -LC cell and discovered that the optimal voltage was 8 V p-p, which is shown in appendix B Figure 16. The TR Raman study of this undoped -LC cell used the same signal to drive the cell (400 ms pulse of 1kHz 8V p-p, 300 ms delay) and a 10 ms shutter period with a 15 x 150s acquisition as previously. The results are collated together and are

shown in Figure 27. All these experiments were carried out using two separate cells filled with the same LC mixture.



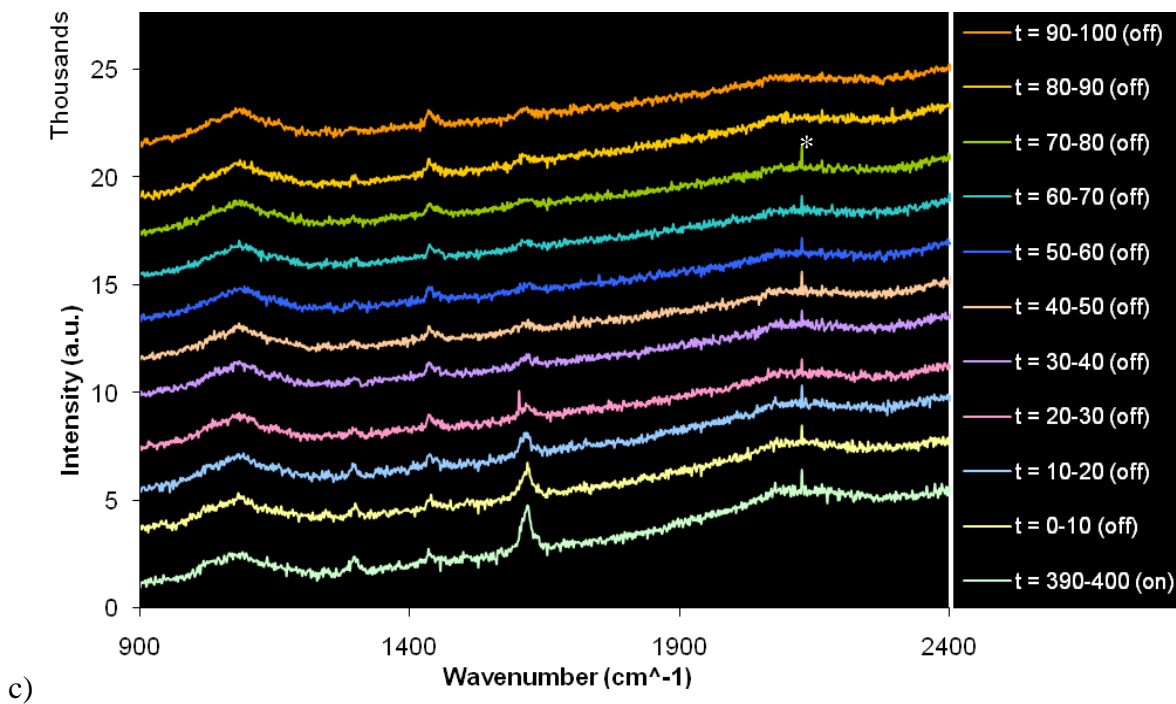
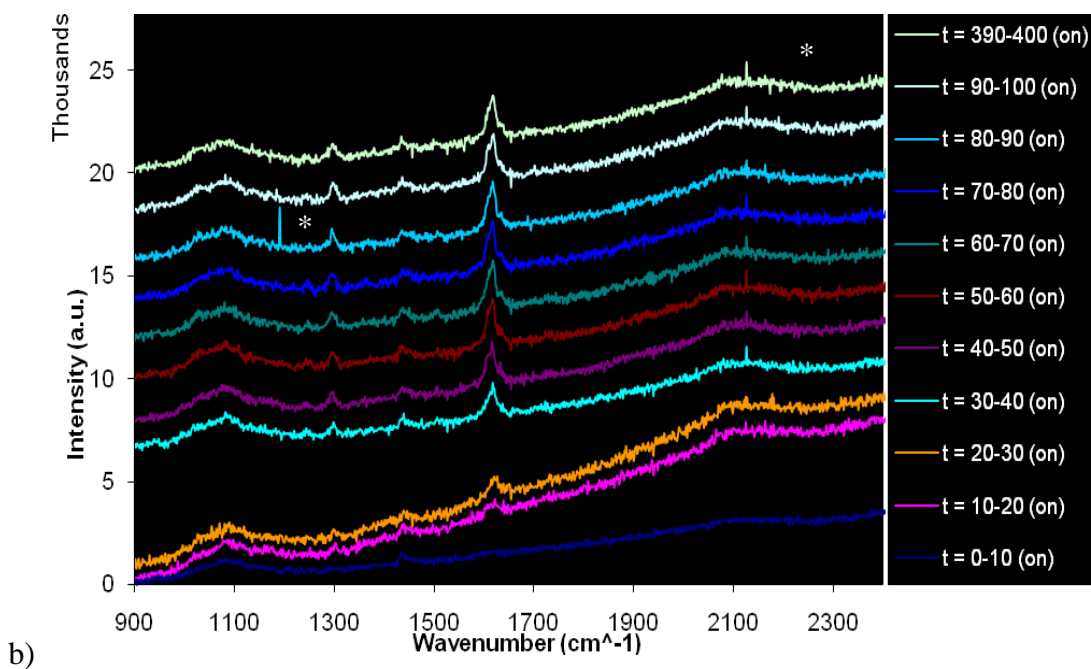


Figure 27. Time-Resolved Raman Spectroscopy Study: 5 μm VA Cell filled with undoped

-LC, where (a) is the data for the whole experiment, (b) the rise and (c) the decay.

The variation in signal intensity with time was determined by integrating selected peaks arising from the LC and dopant following baseline correction. The strongest LC (host) band was taken as $\nu = \sim 1600 \text{ cm}^{-1}$ and the dopant band of compound **14** was $\nu = \sim 2200 \text{ cm}^{-1}$, and these are plotted as a function of time, see Figure 28.

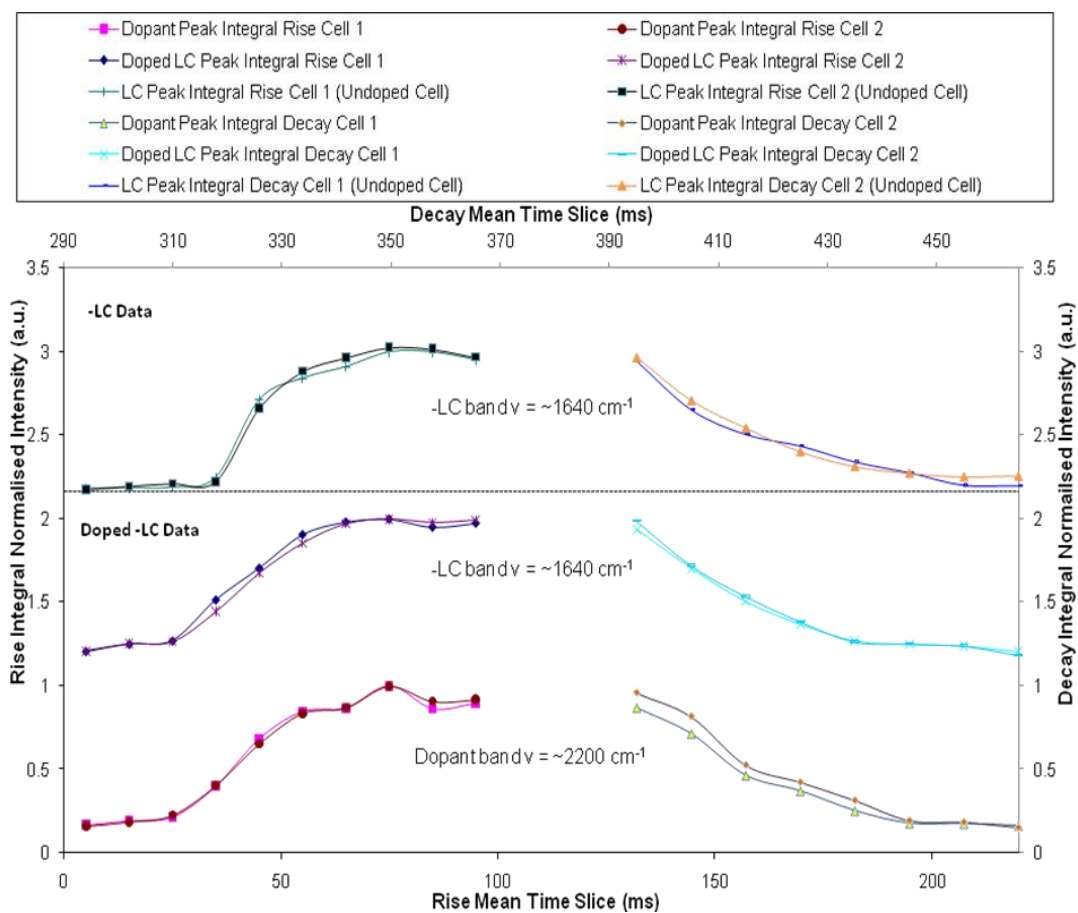


Figure 28. Integral intensity TR Raman data of both LC Host and compound **14** band at $\sim 1600 \text{ cm}^{-1}$ and $\sim 2200 \text{ cm}^{-1}$ respectively. Both rise and decay data are plotted for both doped and undoped cells for all cells investigated.

From these results it can be seen that in the doped cell the signal from both dopant and LC have similar time-intensity profiles. This suggests that both components move together in the applied field and no evidence was found for one component leading the other.

The Raman measurements reported here employ a CW laser, and in order to achieve time resolution the laser is ‘chopped’ using a mechanical shutter. Although the pulse division can be as short as 0.5 ms with the shutter employed here, this short division systematically reduces the average power of the laser, hence an optimum pulse division has to be found that gives good temporal resolution whilst offering reasonable signal strength. In this work it was found that a 10 ms division was needed. The EO measurements use a CW laser and a fast photodiode coupled to a digital oscilloscope. The response time of this system is $<1 \mu\text{s}$, much faster than that of the Raman experiment.

The shutter effectively provides a square wave optical pulse and, hence, the only temporal data acquired with this system is convoluted with this 10 ms square pulse. The effect of this is to reduce the effective time resolution of the experiment. Where times are reported in the results section these refer to the start of the optical (Raman) pulse. However, for the purpose of data analysis the *mean* time of the experiment period is used: thus a 10 ms pulse starting at $t = 0$ is plotted at 5 ms for comparison with the EO data.

The EO trace in Figure 29 shows that it is comparable to the Raman integral trace in Figure 28 as we see similar timescales for E10 and E90. The Raman results show there is a delay of 25 ms for any optical activity to occur and a maximum of activity at approximately at 75 ms. Therefore, within the 20 – 30 ms time slice orientation activity is occurring with it peaking at the 70 – 80 ms times slice so overall the rise time is approximately 40 – 60 ms

(difference between the extreme maximum and minimum). The considered E10 and E90 of the Raman data are highlighted in appendix B Figure 17a and 17b giving a projected rise time of 30 – 50 ms. The EO profile in Figure 29 shows indicates that the intensity begins to change approximately 30 ms after $t = 0$ and plateaus 70 ms later. Comparing the E10 and E90 show a rise time of 30 ms.

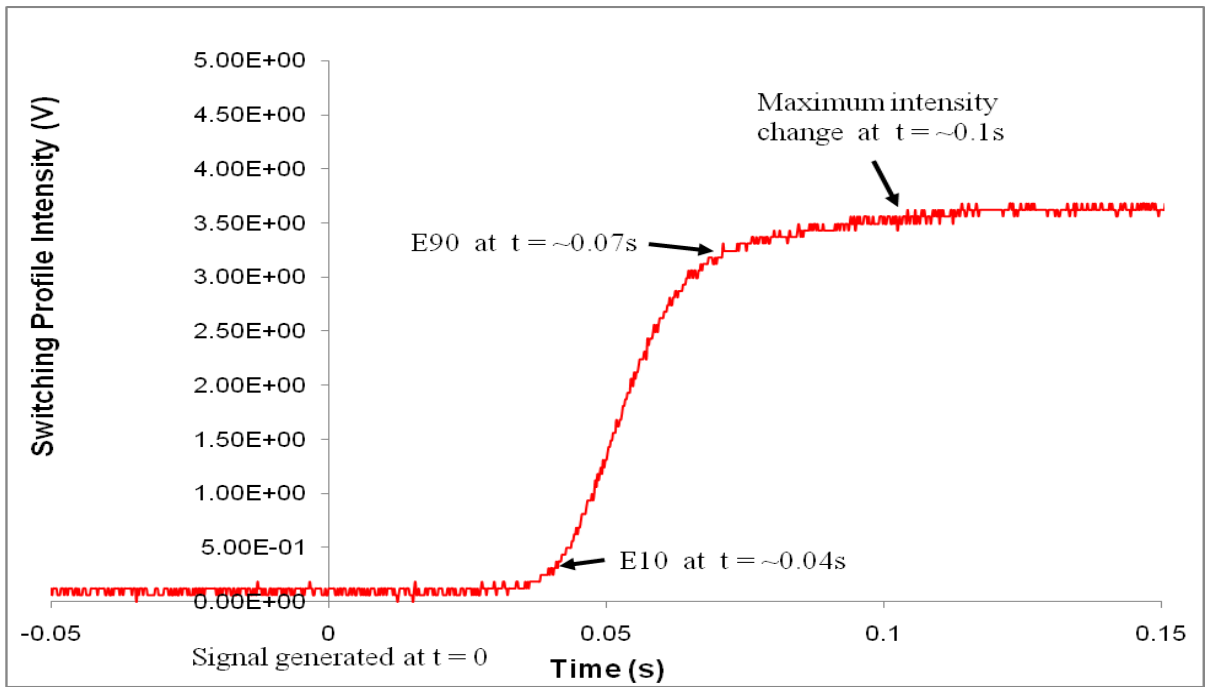


Figure 29. Enlarged EO rise trace of the doped -LC cell with 14.

The EO trace in Figure 30 shows that it is comparable to the Raman integral trace in Figure 27 as we see similar timescales for E10 and E90. The decay profiles observed in the TR Raman measurements of the doped cell indicate that both components re-orientate at similar rates, reaching equilibrium state approximately 45 ms after the electrical pulse is switched off. The decay time is thus 30 – 50 ms from the Raman integral plot. Examining the E10

and E90 of the Raman data of the intensities are highlighted in appendix B Figure 17a and 17b giving a theoretical decay time of 20 – 40 ms. The EO profile in Figure 29 shows at the end of the electrical pulse the decay time between E10 and E90 30 ms. This is comparable to that shown by the Raman data.

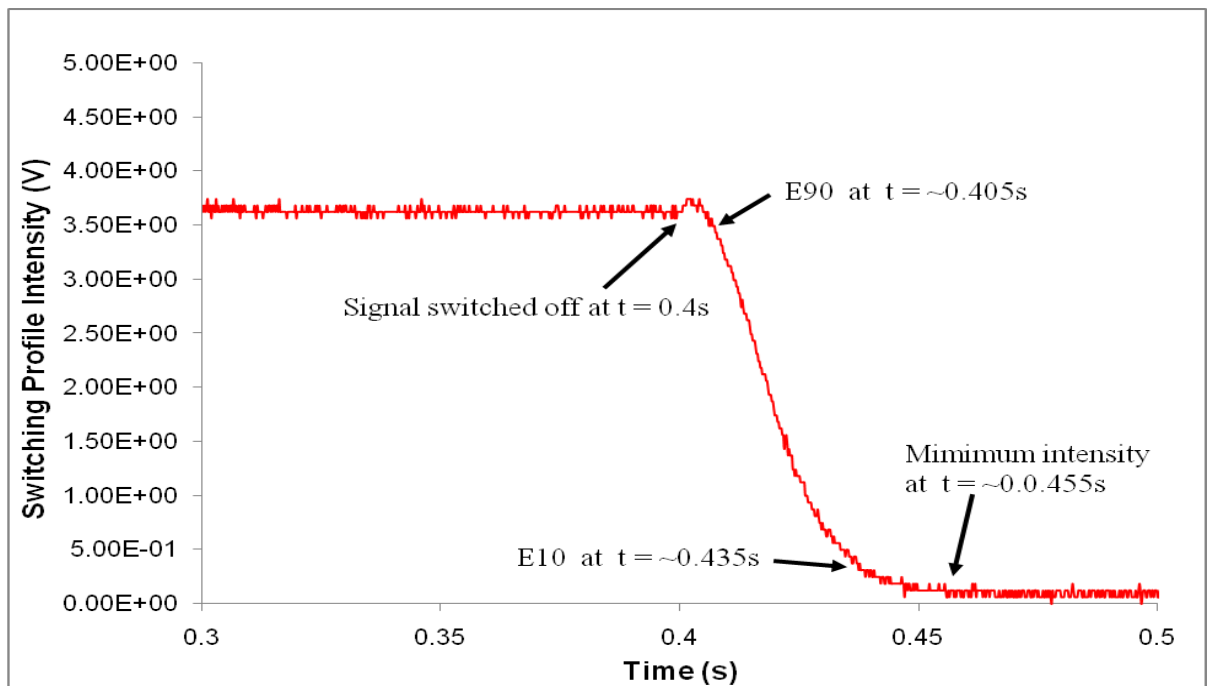


Figure 30. Enlarged EO decay trace of the doped -LC cell with 14

Using the same method of analysis with the undoped -LC cell data (Figure 27) shows a rise time of 50 - 70 ms. The E10 and E90 of the Raman data of the intensities are highlighted in appendix B Figure 17c giving a theoretical rise time of 20 – 40 ms. Analysing the EO

profile (Appendix B Figure 18a) like before and determining the difference in the E10 and E90 gives a rise time 55 ms.

The undoped -LC cell data (Figure 27) shows a decay time of 30 - 50 ms which is the same as the E10 and E90 of the Raman data of the intensities highlighted in appendix B Figure 17c. Analysing the EO profile (Appendix B Figure 18b) shows a 25 ms decay time.

In summary, TR Raman spectroscopy can be used to monitor orientation times of both dopant and LC components in an LC cell. The data recorded and analysed from Raman studies shows that it coincides and agrees with the EO data. The overall results indicate that the rise time has decreased (become quicker) for a doped LC device with compound **10** but the decay times are the same for both doped and undoped LC devices.

4.4.3 Dielectrically Positive LC Raman Study and TR Raman Results

4.4.3.1 Preliminary Study and Understanding of the Behaviour and Internal Motion of a LC Cell Using Raman Spectroscopy

Based on the successful Raman studies of the dielectrically negative LC host material in a VA cell the next step in the research was to use a dielectrically positive LC (+LC) mixture (BL037) based upon the cyanobiphenyl class of material. Earlier we established that our Raman active dopants used to modify the switching speeds of the cell would be no use in

+LC hosts due to overlap between dopant and host bands. As a result further TR studies were only carried out with cells containing the +LC host only.

A sample of the +LC was placed in a 10 μm path length TN cell. It was found that in the off state of the cell gave the strongest Raman signal, and when the field was applied the weakest Raman signal. With the cell in the off state the orientation was set to 0° . A TN cell has a rubbed director on each alignment layer that is orientated 90° to each other that induces a 90° twist of the LC material through the cell when in the off state. The orientation of the cell at this point has the long cell axis (director) perpendicular and thus to the short axis of the polarisability ellipsoid parallel to the electric field of the laser (plane of polarisation). This is considered at an orientation of 0° with respect to the polarization of the laser.

Switching the cell between the off and on state at 0V and 20V respectively gave rise to a significant change in the observed Raman signal as shown in Figure 31. This demonstrated that the applied field causes the orientation of the molecules and polarisability ellipsoids to change during the switch.

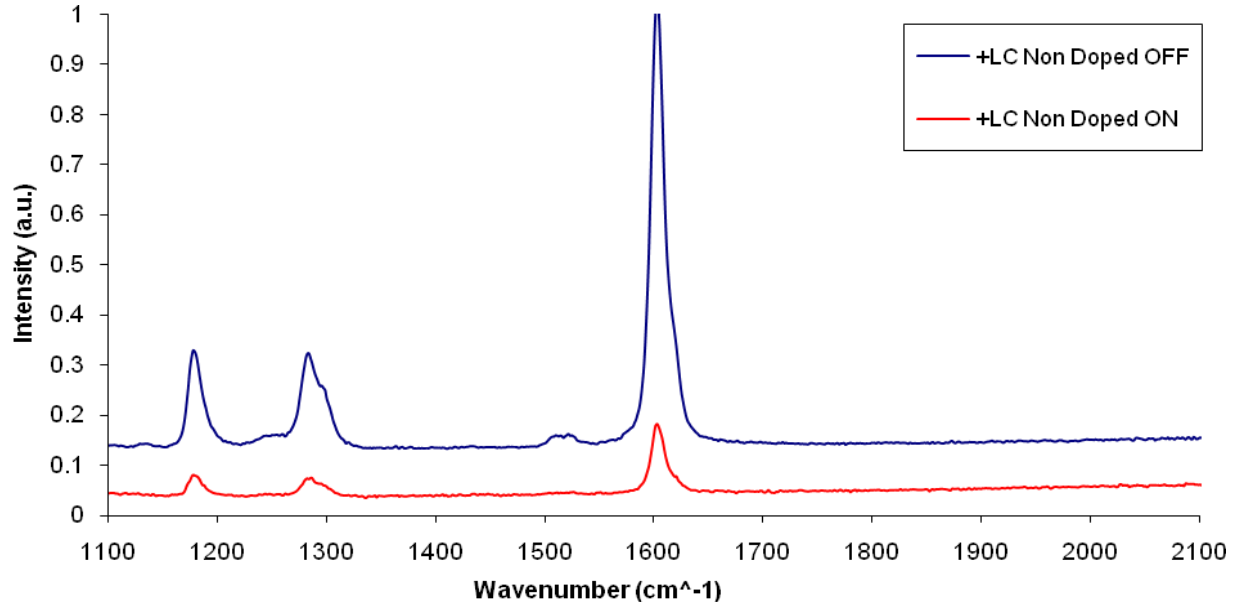


Figure 31. +LC (Merck BL037), 10 μm TN cell, 532nm Laser, 300 Micron hole, 100x obj Lens, 1s x 4 acquisitions.

From earlier research using -LC materials it was found that the optical transmittance observed with different applied voltages showed hysteresis, i.e. the transmittance of the cell is determined by the field under steady state conditions. The first study of the +LC devices was to investigate whether or not this is true for these cells. The cell was placed in the EO spectrometer and the polarisers were set at -45° and $+45^\circ$. Measurements were carried out whilst the applied AC signal (1kHz) was stepped from 0V to 20V p-p, showing that the optimum voltage of the switch occurs at 8 – 9V as seen in Figure 32.

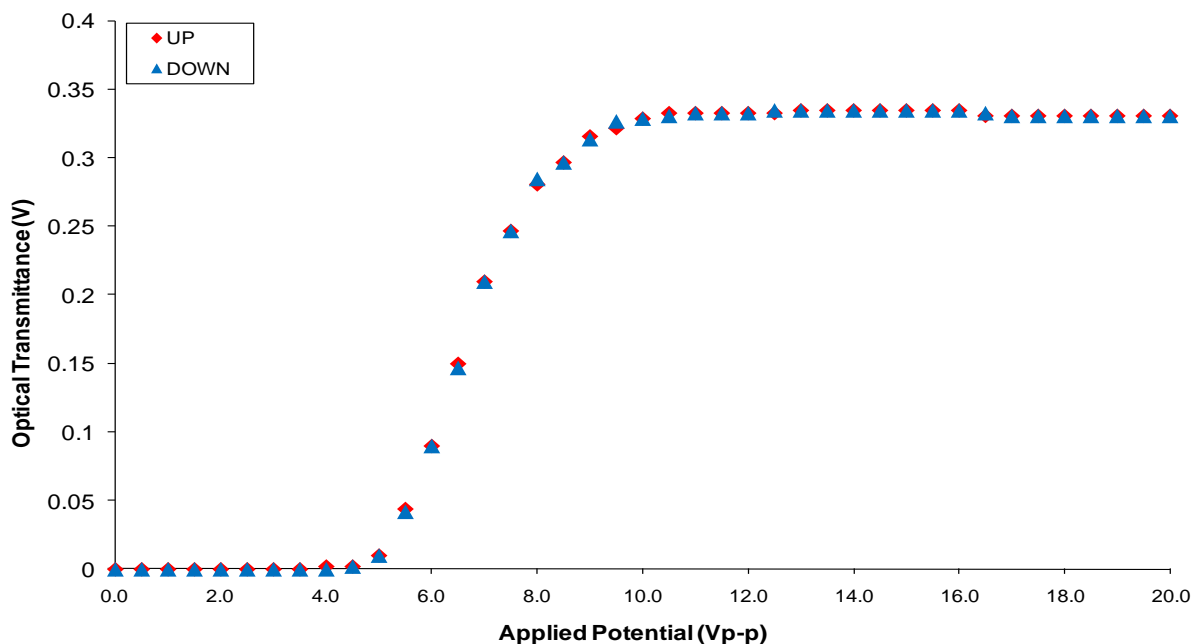
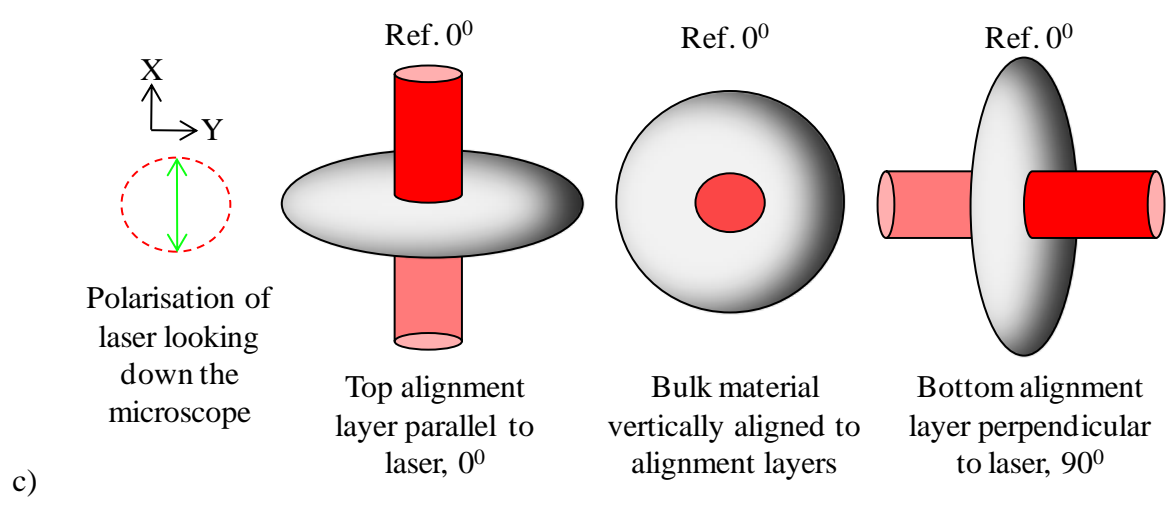
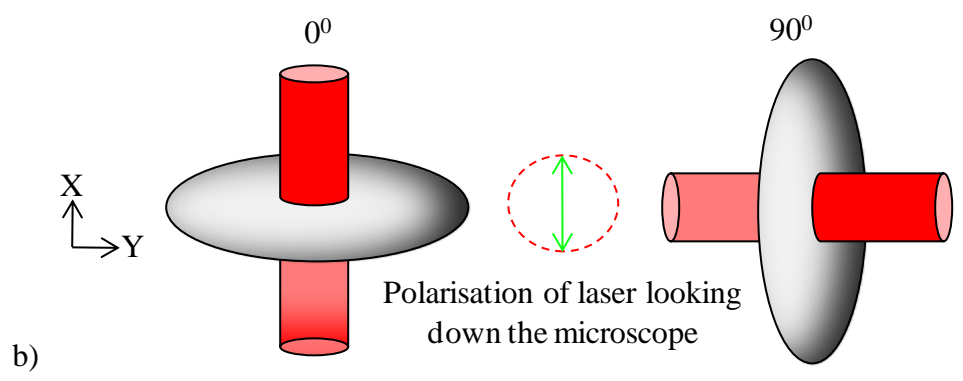
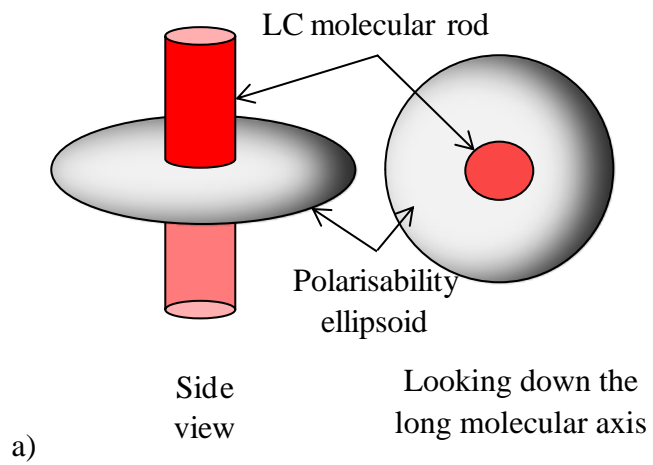


Figure 32. EO hysteresis measurements of the +LC (Merck BL037) cell.

Using an applied field of 8.5V the effect of rotating the cell in the x-y plane was investigated with the results shown in appendix B figure 19a-c. The data shows that in the off state, rotation of the sample with respect to the laser brings about modulation of the Raman signal, whilst in the on state the Raman signal is weak and not significantly affected by rotation. This indicates that in the off state the orientation of the cell influences the polarisability ellipsoid in the xy plane, whilst in the on state it remains unchanged. These observations can be rationalised using the same representations of looking down the molecular axis and polarisability ellipsoid as used to describe the -LC VA cell (Figure 33a). The first important point is that the data for the VA cell is reversed for the TN cell for the on and off states, although in the on state for a TN cell there is still some signal observed.

In the off state we previously identified the reference point 0° and at this point the short axis (long molecular bond axis) of the polarisation ellipsoid is aligned with the electric field of the laser (plane of polarisation). In the off state the 90° twist rotates the plane of polarisation of the laser as it propagates through the cell meaning the first considered interacting molecule can represent the whole LC sample. The rotation about 90° in the XY plane signifies that the interaction with the short polarisability axis is reduced and the long axis is increased as rationalised and illustrated in Figure 33b (data is shown in Appendix A Figure 19b).

In the on state the twist of the LC material is perturbed and re-orientated out of equilibrium to have no twist and thus the LC molecules are now perpendicular to the alignment layers. In this configuration there is no birefringence and, hence, the cell does not rotate the laser polarisation. However, the initial molecules next to the alignment layers will not totally re-orientate themselves altogether due to the surface interactive forces between the alignment layer and initial LC molecules. The discussed perturbation and re-orientation would account for a majority of the LC but still a small fraction of material that is aligned with the alignment layer would account for the weak Raman signal. Overall the laser interacts with 3 main LC orientations which are shown in Figure 33c and d. Furthermore the reason why the Raman signal is unchanging through a 90° rotation is that the opposition configurations at each alignment layer are equal and opposite so when rotation occurs one layer moves out of alignment with the plane of laser polarisation whilst the other moves into alignment.



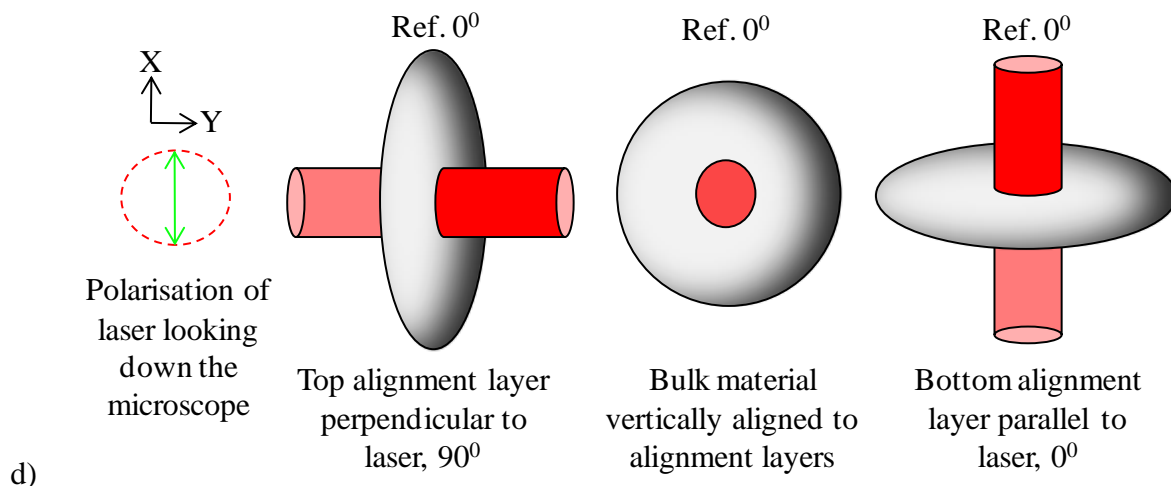


Figure 33. Representation of the LC material of (a) the side and plan view and LC alignment when the cell is (b) off and rotated through 90° . The interacting positional states of both (c) top alignment layer and (d) bottom alignment layer when the cell is on and rotated through 90° are shown.

4.4.3.2 Time-Resolved Raman Study of a $10\ \mu\text{m}$ TN Cell with Merck LC BL037

Two $10\ \mu\text{m}$ TN cells were filled with the +LC mixture (BL037) and characterised by monitoring the transmitted light intensity as a function of the applied field and were found to behave similarly. Prior to the TR Raman measurements the optimum on-off periods had to be found to optimise the data acquisition parameters. The EO experiment applied an 8V p-p AC signal (1kHz) to the cell and the on / off periods were adjusted to 800 / 1200 ms initially, however, the time-course of the signal was more complex than expected (Figure 34) with some oscillations of the signal during both the turn on and turn off periods. The second prepared cell transmittance data can be seen in appendix B figure 20. Results for

altering the voltage to 12 and 16 V are shown in appendix B Figure 21a – b. From all these graphs we can see that there is this similar oscillation occurring and by increasing the voltage we reduce the length of time for this phenomenon.

This complex oscillation is attributed to inhomogeneity within the cell during the switch process. As the LC is twisted from its initial state by the applied field (or lack of) domains of new alignment form, but these are metastable and reorient more slowly due to domain boundary forces. It is known that in general EO measurements are optimal when a field of $1\text{V} / \mu\text{m}$ is applied to the cell, therefore the cells having a potential of 12V would be just past the maximum of the optical transmittance as shown in the hysteresis curves but that the oscillation/settling period would be minimised. Applying a 12V p-p pulse to the cell gave the clearest rise with the shortest oscillation period and the time for decay to reach its first lowest level within 300 to 400 ms, which gave a reasonable effective duty cycle. The final pulse sequence selected on the basis of the EO measurements was a 12 V p-p signal with an 800 ms pulse over a 2s period. Although this is different from the preliminary work used to study the rotation of the cell and the LC in accordance to the Raman signal it must be realised that in the earliest measurements the settling time of the cell is of the order of seconds. Thus, both experiments can be considered independent and valid.

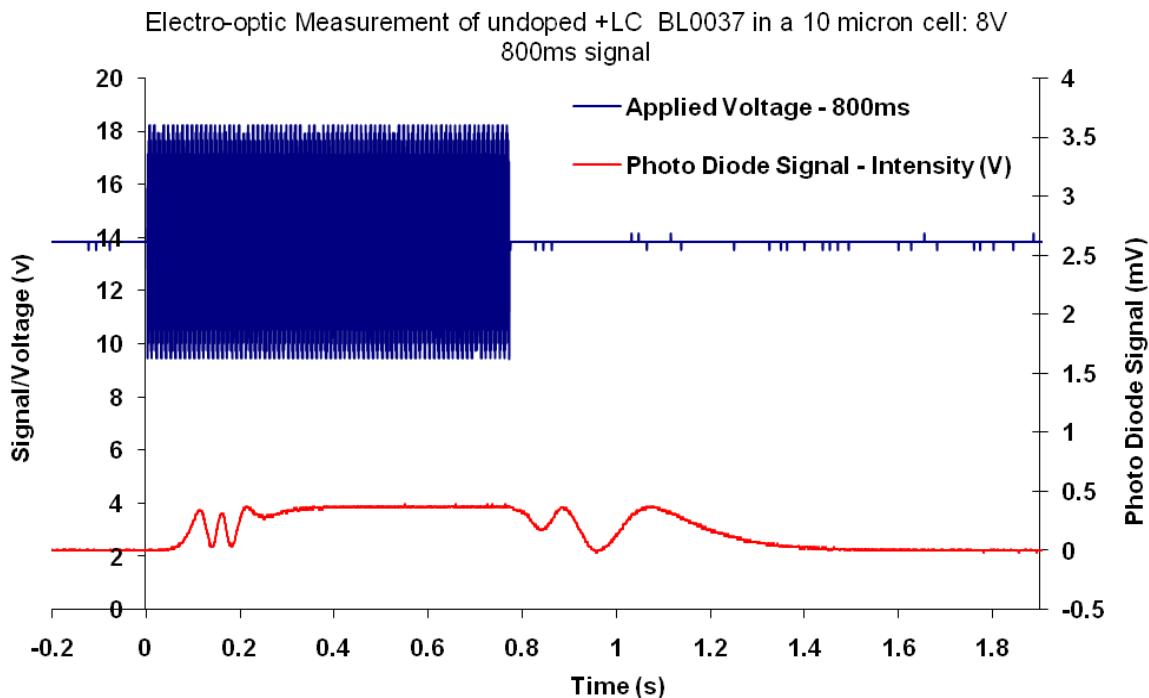


Figure 34. The EO profile of the rise and decay of a 10 μm TN cell with +LC Merck BL037 at 8V of a 800 ms generated pulse.

The TR Raman study was made by placing the cell in the spectrometer and investigating the sliced profile of the switch using 10 ms shutter periods stepped through the rise of the on state of the cell until the Raman signal appeared to have levelled at a considered decrease and for the decay the Raman signal had appeared to have levelled at a considered increased constant. The results of both the rise and decay phase of the cycle are shown in Figure 35.

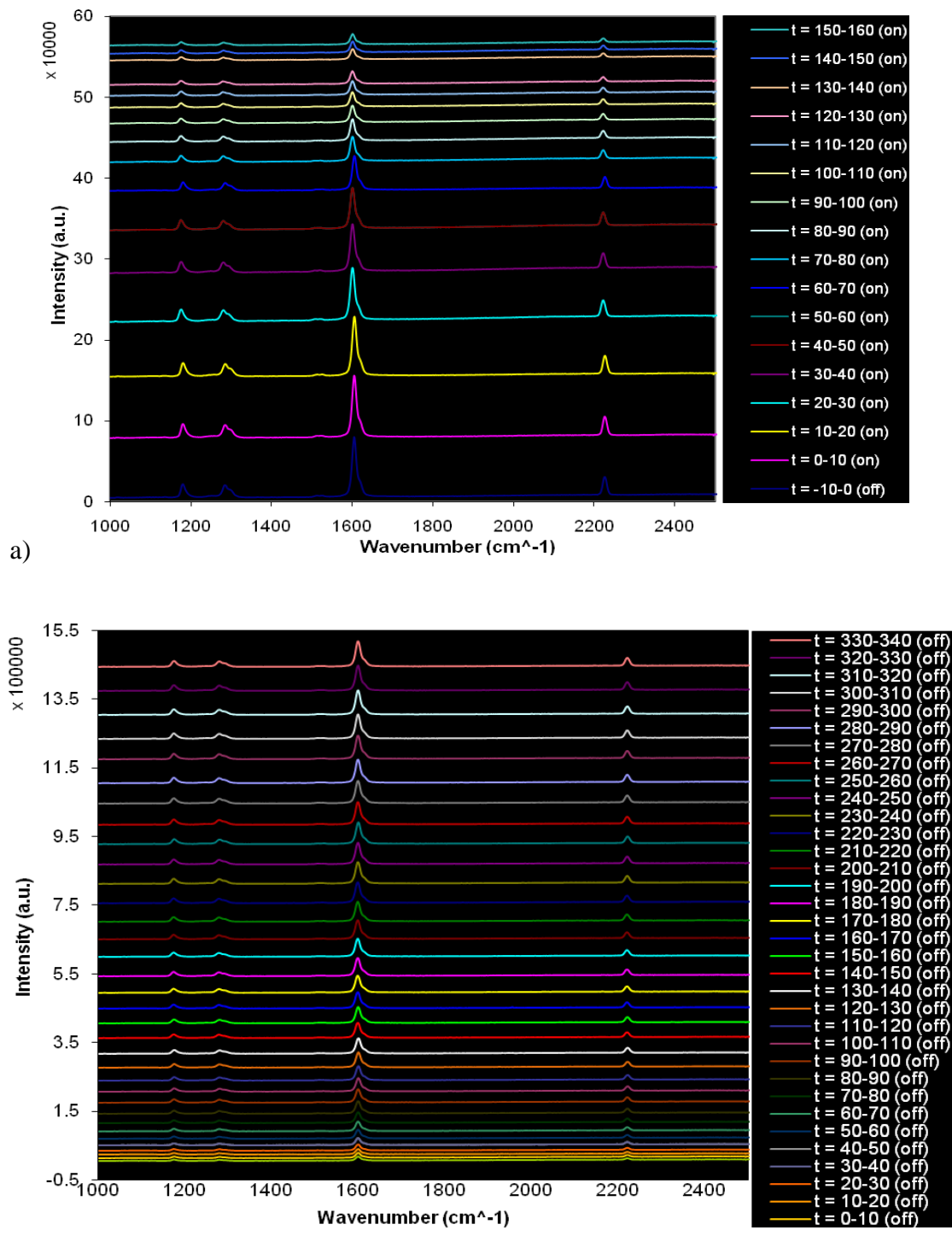


Figure 35. Time-Resolved Raman Spectroscopy Study: 10 μm TN Cell filled with +LC Merck BL037, where (a) is the rise time data and (b) is the decay time.

The integration (after baseline correction) of the data are compiled and normalised and shown in Figure 36. The graph represents a considered traditional concept of the rise and decay of the cell by taking the inverse of the Raman signal. There are two horizontal and vertical axes, one for the rise and another for the decay allowing the two analysed components to be fitted into one graph giving a better summary of the switching.

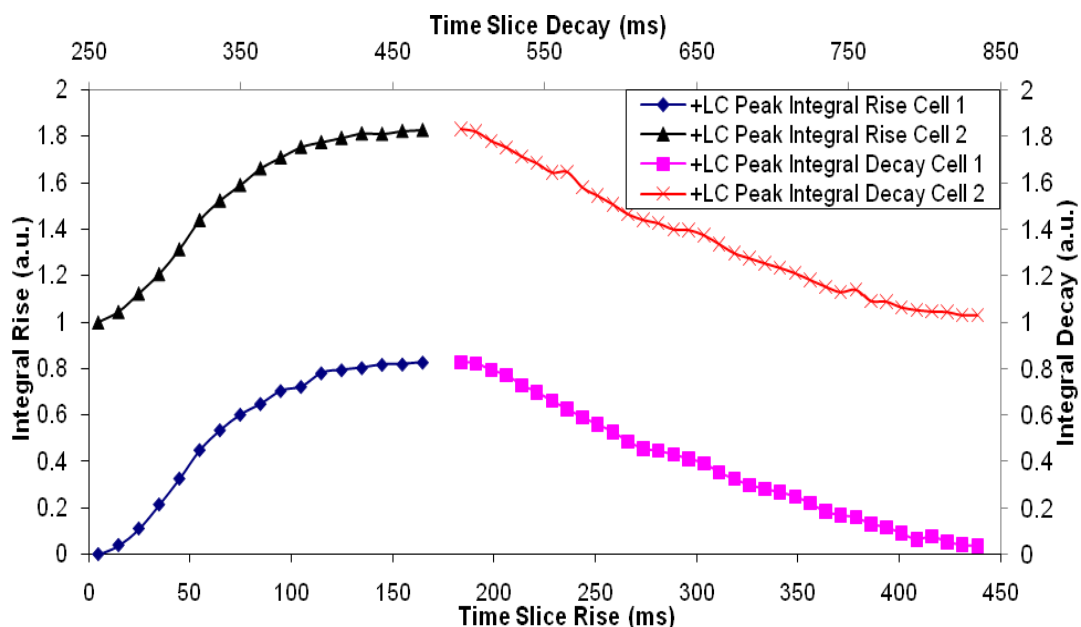


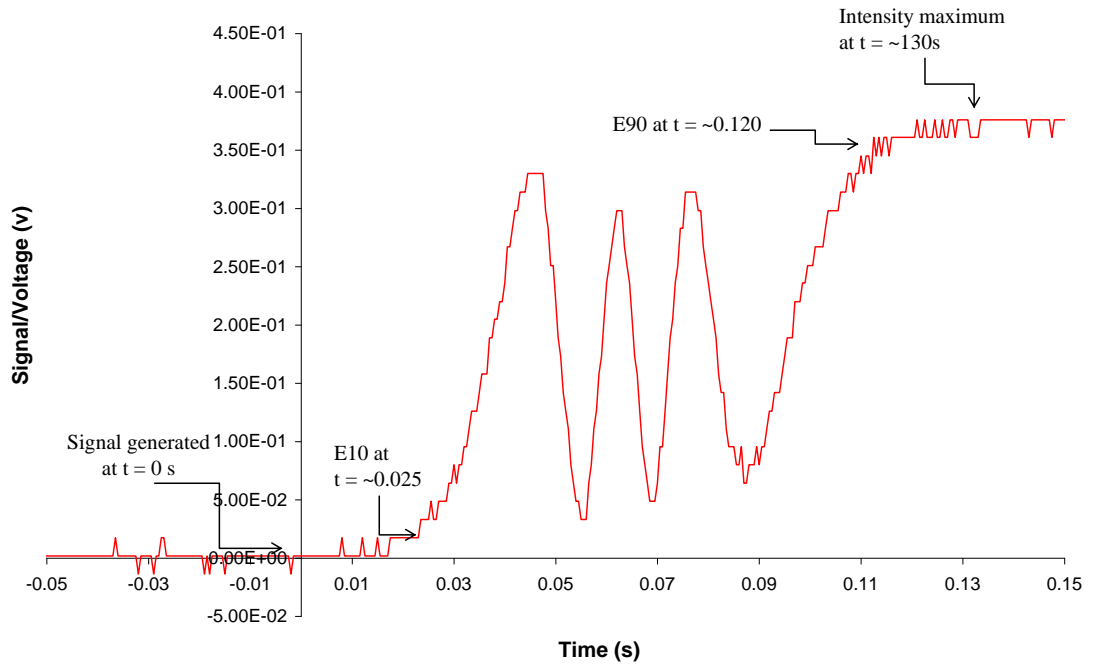
Figure 36. Integral intensity TR Raman data of the LC Host band at $\sim 1600 \text{ cm}^{-1}$.

The rise and decay profile show that the experiment is reproducible for the two cells used and that this oscillating phenomenon that was a concern in the beginning was not observed in the Raman studies most likely due to the convolution of the rapid oscillations with the

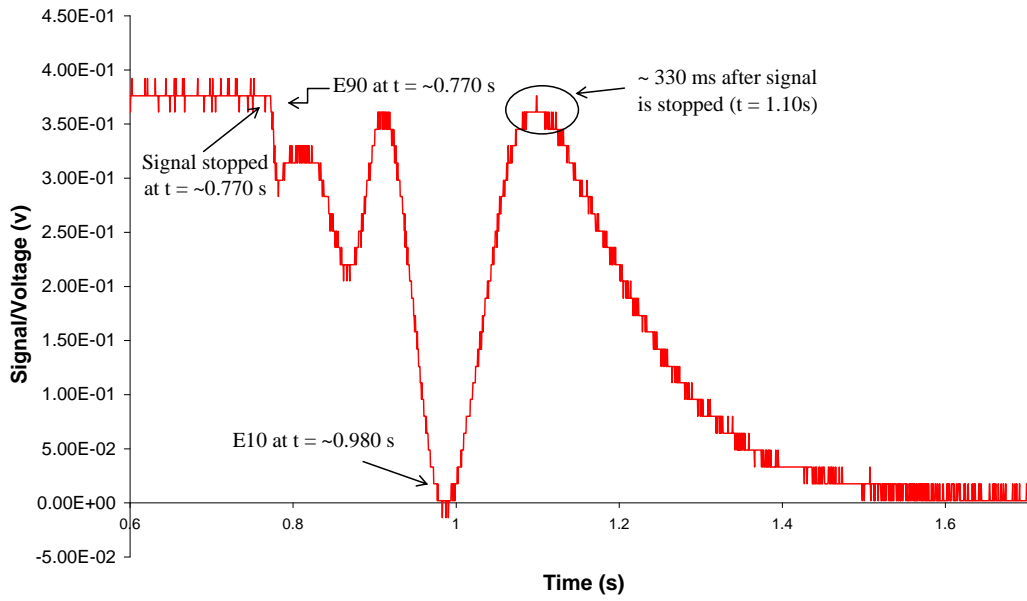
time frame (limitation) of the experiment. The rise time shows little delay in the switching, the mean time 15 shows that the signal has already changed at the time indicating it being in the 10 – 20 ms. This is approximately the same as the EO measurements; 10 ms after the pulse is applied the cell reaches what is considered E10. Furthermore, by analysing the EO data and looking only at the rise time we can see that it is approximately 100 ms between E10 and E90 and the total rise time between the minimum and maximum is approximately 100 ms, suggesting that the estimated rise time overall being 100 – 110 ms, see Figure 37a. The Raman intensity analysis, Figure 36, shows that the rise of the cells to be in approximate mean time slice of 115 ms to 125 ms when there is little to no change in the Raman signal, which indicates that the possible rise time would be between 90 – 120 ms (based on the 10 – 20 ms time slice being the time slice when activity occurs). The E10 and E90 of the Raman Intensity data (highlighted in appendix B Figure 22) shows the E90 is in the 115 ms mean time slice and E10 is in the 25 ms meant time slice giving a projected rise time of 90 – 100 ms.

So, overall, we gain similar data showing the experiments have been successful. The interesting point is that we did not see the oscillation as in EO and this is due the limitations of the experiment. The EO measurement acquires some 10, 000 data points over the switching period, which would have a higher time resolution than that of the Raman experiment which is limited to 10 ms gating period of the laser interacting with the sample. In the 10 ms window we are seeing an average of the switching to build an approximate profile indicating what is happening in that cell over time. This gives approximate rise times but most importantly a tracking effect and dynamic profile of the movement of the compounds and their respective Raman active bands.

Applying the same analysis to the EO measured decay we see that between the first point of E10 and E90 gives a decay time of ~210 ms (Figure 37b). The Raman integral intensity data shows that the E10 to E90 decay time to be 280- 300 ms. The difference between these two measurements are due the affect of the averaging of the LC motion (convolution) of the Raman experiment compared to the higher resolution of the EO experiment. However, comparing the Raman intensity data (appendix B Figure 22) the considered E10 to E90 decay time gives a projected decay time of 240 – 260 ms.



a)



b)

Figure 37. EO (a) rise and (b) decay data of the switch for Merck +LC BL037.

4.5 Conclusion

The results presented in this chapter show that the response times determined under identical conditions of field/pulse duration using Electro-optical studies and Raman spectroscopy give similar switching times. Significantly, in the case of the dielectrically negative LC in the VA cells doped with the acetylenic compound **14** we see from the Raman measurements that both the dopant and host signals change with similar time constants with no distinguishable time-lag between them. Thus, we conclude that both the dopant and LC reorient simultaneously when the electric field is applied and the cell switches.

The turn on/off times measured in these studies differ from those reported by Sony (chapter 3), attributed to the fact that EO measurements made at Sony Europe were made under different experimental conditions.

In summary, we have demonstrated that Raman spectroscopy can be used as a tool to uniquely identify components in LC hosts and study the switching times of individual components within LC cells. This is the first time Raman spectroscopy has been used in this way, however the results are only preliminary, and further research is needed to fully establish the potential of this science.

4.6 References

1. S. Duckett and B. Gilbert, *Foundations of Spectroscopy*, Oxford Chemistry Primers, ed. R. G. Compton, 2000, Oxford University Press.

2. J. M. Hollas, *Basic Atomic and Molecular Spectroscopy*, Tutorial Chemistry Texts, ed. E. W. Abel, A. G. Davies, D. Phillips and J. D. Woollins, 2002, Royal Society of Chemistry.
3. J. M. Brown, *Molecular Spectroscopy*, Oxford Chemistry Primers, ed. R. G. Compton. 1998, Oxford University Press.
4. C. N. Banwell, *Fundamentals of Molecular Spectroscopy*, 3rd Ed, 1983, McGraw-Hill Book Company.
5. E. Hecht, *OPTICS*, 2nd Ed, World Student Series, ed. B. Spatz, 1987, Addison-Wesley Publishing Company.
6. D. A. Long, *Raman Spectroscopy*, 1977, McGraw-Hill International Book Company.
7. E. Smith and G. Dent, *Modern Raman Spectroscopy: A Practical Approach*, 2005, John Wiley & Sons.
8. J. A. Koningstein, *Introduction to The Theory of The Raman Effect*, 1972, D. Reidel Company.
9. H. A. S. Ymanski, *Raman Spectroscopy: Theory and Practice*, Vol. 1, 1967, Plenum Press.
10. H. A. S. Ymanski, *Raman Spectroscopy: Theory and Practice*, Vol. 2. 1970, Plenum Press.
11. D. Semwogerere and E. R. Weeks, *Encyclopedia of Biomaterials and Biomedical Engineering*, ed. G. L. Bowlin and G. Wnek, Vol. 1 & 2, 2005, Taylor & Francis.
12. M. Minsky, *Scanning*, 1988, **10**, 128.
13. G. H. Atkinson, *Historical Perspective*, in *Time-Resolved Laser Raman Spectroscopy*, ed. D. Phillips and G. H. Atkinson, 1987, Harwood Academic Publishers.

14. R. E. Hester, *Raman Spectroscopic Studies of Transient Chemical Species*, in *Time-Resolved Laser Raman Spectroscopy*, ed. D. Phillips and G. H. Atkinson, 1987, Harwood Academic Publishers.
15. H. Hamaguchi and T. L. Gustafson, *Annu. Rev. Phys. Chem.*, 1994, **45**, 593.
16. M. Kubinyi, A. Grofcsik and W. J. Jones, *Ach-Models Chem.*, 1995, **132** (6), 915.
17. P. Kukura, D. W. McCamant and R. A. Mathies, *Annu. Rev. Phys. Chem.*, 2007, **58**, 461.
18. S. E. J. Bell, *Analyst*, 1996, **121** (11), 107.
19. G. H. Atkinson, *Time-Resolved Vibrational Spectroscopy*, 1983, Academic Press.
20. G. H. Atkinson, *Time-Resolved Raman Spectroscopy in Advances in Infrared and Raman Spectroscopy*, ed. R. J. N. Clark and R. E. Hester, 1982, Heyden.
21. G. H. Atkinson, *Time Resolved Raman Spectroscopy in Advances in Laser Spectroscopy*, ed. B. A. Garetz and J. R. Lombardi, Vol. 1, 1982, Heyden.

Chapter 5

Experimental

Chapter 5: Experimental

The solvents used in all coupling reactions were dried, distilled under a nitrogen atmosphere using the departmental SPS system. Before the reaction started the solvents and any the non-volatile reagent(s) were added and degassed via Freeze-Pump-Thaw method 3 times prior to adding the catalysts and any volatile reagent(s). All distillations were carried out using the Kugelröhr *in vacuo*.

Reagents and Materials

All starting materials were obtained commercially and used as received.

NMR Spectroscopy

All NMR obtained using one of the following instruments; Varian Mercury – 400, Bruker Avance – 400, Varian Inova – 500 and Varian VNMRS – 700, as stated in each compounds experimental details. All δ given are relative to the residual solvent peaks with coupling constants in Hz. All carbon spectra were recorded with broadband proton decoupling.

Gas Chromatography Mass Spectroscopy (GC-MS)

All GC-MS were recorded using an Agilent Technologies 5973 Inert Mass Selective Detector gas chromatography mass spectrometer.

Raman Spectroscopy

All Raman data was recorded using a HORIBA Jobin Yvon LabRAM HR 800. All spectra are referenced to Si band ($\nu = 520.07 \text{ cm}^{-1}$).

Elemental Analysis

Carbon, hydrogen and nitrogen elemental analyses were obtained using an Exeter Analytical CE – 440 analyser.

Accurate Mass Spectroscopy

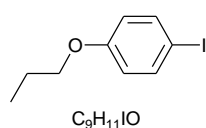
The data was recorded courtesy of two facilities; 1) Waters Corporation Ltd and 2) EPSRC National Mass Spectrometry Service Centre. The accurate mass recorded by Waters Corporation Ltd is denoted with “*”.

X-Ray Crystallography

Crystallographic data were collected on a Bruker SMART – CCD 6000 diffractometer (Mo K α , $\lambda = 0.71073 \text{ \AA}$, ω – scan, $0.3^\circ / \text{frame}$) at $T = 120 \text{ K}$ with and equipped Oxford Cryostream cooling device. Structures were resolved by direct method and refined by full matrix least squares on F^2 for all data using SHELXTL software. All non-hydrogen atoms were refined with anisotropic displacement parameters, H-atoms were located on the difference map and refined isotropically.

5.1. Experimental Details

(1) Synthesis of 1-bromo-4-propoxybenzene

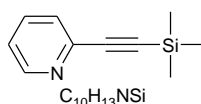


4-Iodophenol (10 g, 46 mmol) and potassium carbonate (17 g, 123 mmol) were added to 1-bromopropane (9.5 g, 77 mmol) in acetone

(120 mL) and refluxed under a nitrogen atmosphere overnight. The mixture was filtered, reduced by vacuum and extracted with dichloromethane (3 x 50 mL). The extract was

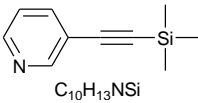
dried over magnesium sulphate and reduced by vacuum, yielding the crude product. This was distilled *in vacuo* to give the iodo propoxybenzene pure product as colourless oil (11.57 g, 96%). ^1H NMR (CDCl_3 , 500MHz) δ_{H} 7.56 (d, 2H, $J_{\text{HH}} = 9$, Ar-H), 6.67 (d, 2H, $J_{\text{HH}} = 9$, Ar-H), 3.88 (t, 2H, $J_{\text{HH}} = 6.5$, $-\text{CH}_2-$), 1.79 (m, 2H, $-\text{CH}_2-$), 1.02 (t, 3H, $J_{\text{HH}} = 7.5$, $-\text{CH}_3$). ^{13}C NMR (CDCl_3 , 125MHz, decouple H1 500 MHz) δ_{C} 10.72 (CH_3), 22.72 (CH_2), 69.84 (CH_2), 82.65 (C-I), 117.17 (CH-CO), 138.39 (CH-Cl), 159.25 (C-O). Found C; 41.46; H;4.31. Calcd for $\text{C}_9\text{H}_{11}\text{IO}$ C; 41.24; H4.23. GC-MS (EI) m/z 262.

(6) Synthesis of 2-(trimethylsilylethynyl)-pyridine

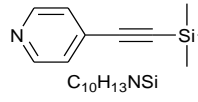


Trimethylsilylacetylene (3.2 g, 33 mmol, 3.02 mL), dichlorobis(triphenylphosphine) palladium (443 mg, 0.63 mmol), copper iodide (120 mg, 0.63 mmol) were added to a degassed solution of 2-bromopyridine (5 g, 31.6 mmol) in triethylamine (125 mL) and refluxed under a nitrogen atmosphere overnight. The mixture was reduced by vacuum and filtered through a silica pad with DCM and reduced to yield a crude oil. The crude product was extracted into DCM (3 x 50 mL) and dried over magnesium sulphate. The extract was reduced and distilled *in vacuo*, to give the pure product as a colourless solid (5.06 g, 92%). ^1H NMR (CDCl_3 , 500 MHz) δ_{H} 8.49 (d, 1H, $J_{\text{HH}} = 4.5$, Ar-H), 7.55 (td, 1H, $J_{\text{HH}} = 10, 1.5$, Ar-H), 7.37 (d, 1H, $J_{\text{HH}} = 8$, Ar-H), 7.142 (t, 1H, $J_{\text{HH}} = 6$, Ar-H), 0.20 (s, 9H, $-\text{Si}(\text{CH}_3)_3$). ^{13}C NMR (CDCl_3 , 125MHz, decouple H1 500 MHz) δ_{C} 0.10 ($(\text{CH}_3)_3\text{Si}-$), 94.86 ($\equiv\text{C}-\text{Si}(\text{CH}_3)_3$), 103.88 (Het-C \equiv), 123.23, 127.43, 136.27, 143.24 (N-C*-C \equiv), 150.13 ($-\text{CH}-\text{N}-$). Found C; 68.80; H; 7.39; N; 8.13. Calcd for $\text{C}_{10}\text{H}_{13}\text{NSi}$ C, 68.51; H, 7.47; N, 7.99. GC-MS (EI) m/z 175 (M $^+$), 160. Raman (633 nm) 2166 cm^{-1} ($-\text{C}\equiv\text{C}-$).

(7) Synthesis of 3-(trimethylsilylethynyl)-pyridine

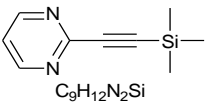
 Trimethylsilylacetylene (3.4 g, 34.7 mmol, 3.9 mL), dichlorobis(triphenylphosphine) palladium (443 mg, 0.63 mmol), copper iodide (120 mg, 0.63 mmol) were added to a degassed solution of 3-bromopyridine (5 g, 31.6 mmol) in triethylamine (125 mL) and refluxed under a nitrogen atmosphere overnight. The mixture was reduced by vacuum and filtered through a silica pad with DCM and reduced to yield a crude oil. The crude product was extracted into DCM (3 x 50 mL) and dried over magnesium sulphate. The extract was reduced and distilled *in vacuo*, to give the pure product as a colourless oil (4.1 g, 74%). ¹H NMR (CDCl₃, 500 MHz) δ_H 8.64 (s, 1H, Ar-H), 8.70 (d, 1H, J_{HH} = 4.5, Ar-H), 7.68 (d, 1H, J_{HH} = 8, Ar-H), 7.17 (dd, 1H, J_{HH} = 5, 7.5, Ar-H), 0.22 (s, 9H, -Si(CH₃)₃). ¹³C NMR (CDCl₃, 125 MHz, decouple H1 500 MHz) δ_C 0.03 ((CH₃)₃Si-), 98.42 (≡C-Si(CH₃)₃), 101.68 (≡C-Het), 120.49 (C-C≡), 123.08, 138.99, 148.93 (CH-C*H-N), 152.84 (N-C*-C-). Found C; 68.69; H; 7.40; N; 7.85. Calcd for C₁₀H₁₃NSi C, 68.51; H, 7.47; N, 7.99. GC-MS (EI) m/z 175. Raman (633 nm) 2164 cm⁻¹ (-C≡C-).

(8) Synthesis of 4-(trimethylsilylethynyl)-pyridine

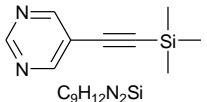
 Trimethylsilylacetylene (2.52 g, 31 mmol, 4.3 mL), dichlorobis(triphenylphosphine) palladium (365 mg, 0.521 mmol), copper iodide (100 mg, 0.521 mmol) was added to a degassed solution of 4-bromopyridine hydrochloride (5 g, 26 mmol) in triethylamine (125 mL) and refluxed under a nitrogen atmosphere overnight. The mixture was reduced by vacuum and filtered through a silica pad with DCM and reduced to yield a crude oil. The crude product was extracted into (DCM 3 x 50 mL) and dried over magnesium sulphate. The extract was reduced and distilled *in vacuo*, to give the pure product as a colourless oil.

(3.1 g, 68%). ^1H NMR (CDCl_3 , 500 MHz) δ_{H} 8.49 (d, 2H, $J_{\text{HH}} = 13.5$, Ar-H), 7.32 (d, 2H, $J_{\text{HH}} = 7.5$, Ar-H), 0.21 (s, 9H, $-\text{Si}(\text{CH}_3)_3$). ^{13}C NMR (CDCl_3 , 125MHz, decouple H1 500 MHz) δ_{C} 0.12 ($(\text{CH}_3)_3\text{Si}-$), 100.09 ($\equiv\text{C}-\text{Si}(\text{CH}_3)_3$), 102.17 ($\equiv\text{C}-\text{Het}$), 125.97 ($\text{C}^*-\text{C}\equiv$), 127.36 (CH-C), 149.87 (CH-N). Found C; 68.77; H; 7.6; N; 7.81. Calcd for $\text{C}_{10}\text{H}_{13}\text{NSi}$ C, 68.51; H, 7.47; N, 7.99. GC-MS (EI) m/z 175. Raman (633 nm) 2167 cm^{-1} ($-\text{C}\equiv\text{C}-$).

(9) Synthesis of 2-(trimethylsilylethynyl)-pyrimidine

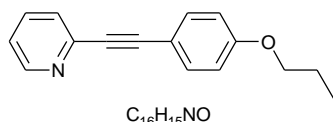

 Trimethylsilylacetylene (2.06 g, 21 mmol, 3 mL), dichlorobis(triphenylphosphine) palladium (265 mg, 0.38 mmol), copper iodide (72 mg, 0.38 mmol) were added to a degassed solution of 2-bromopyrimidine (3 g, 19 mmol) in Triethylamine (125 mL) and refluxed under a nitrogen atmosphere overnight. The mixture was reduced by vacuum and filtered through a silica pad with DCM and reduced to yield a crude oil. The crude product was extracted into (DCM 3 x 50 mL) and dried over magnesium sulphate. The extract was reduced and distilled *in vacuo*, to give the pure product as a colourless solid (2.54 g, 76%). ^1H NMR (CDCl_3 , 500 MHz) δ_{H} 8.70 (d, 2H, $J_{\text{HH}} = 5$, Ar-H), 7.23 (t, 1H, $J_{\text{HH}} = 5$, Ar-H), 0.28 (s, 9H, $-\text{Si}(\text{CH}_3)_3$). ^{13}C NMR (CDCl_3 , 125MHz, decouple H1 500 MHz) δ_{C} 0.26 ($(\text{CH}_3)_3\text{Si}-$), 94.73 ($\equiv\text{C}-\text{Si}(\text{CH}_3)_3$), 102.49 ($\equiv\text{C}-\text{C}$), 120.29, 152.80 (N-C-N), 157.48 (CH-N). Found C; 61.54; H; 7.11; N; 15.70. Calcd for $\text{C}_9\text{H}_{12}\text{N}_2\text{Si}$ C, 61.32; H, 6.86; N, 15.89. GC-MS (EI) m/z 176. Raman (633 nm) 2176 cm^{-1} ($-\text{C}\equiv\text{C}-$).

(10) Synthesis of 5-(trimethylsilylethynyl)-pyrimidine


 Trimethylsilylacetylene (3.5 g, 36 mmol, 5 mL), dichlorobis(triphenylphosphine) palladium (441 mg, 0.63 mmol),

copper iodide (120 mg, 0.63 mmol) were added to a degassed solution of 5-bromopyrimidine (5 g, 31 mmol) in triethylamine (125 mL) and refluxed under a nitrogen atmosphere overnight. The mixture was reduced by vacuum and filtered through a silica pad with DCM and reduced to yield a crude oil. The crude product was extracted into (DCM 3 x 50 mL) and dried over magnesium sulphate. The extract was reduced and distilled *in vacuo*, to give the pure product as a colourless solid (4.25 g, 77%). ¹H NMR (CDCl₃, 500 MHz) δ_H 9.03 (s, 2H, Ar-H), 8.69 (s, 1H, Ar-H), 0.19 (s, 9H, -Si(CH₃)₃). ¹³C NMR (CDCl₃, 125MHz, decouple H1 500 MHz) δ_C 0.19 ((CH₃)₃Si-), 97.87 (≡C-Si(CH₃)₃), 102.91 (≡C-Het), 119.89(-C-C≡), 156.93 (N-C-N), 159.20 (CH-N)s . Found C; 61.55; H; 6.97; N; 15.67. Calcd for C₉H₁₂N₂Si C, 61.32; H, 6.86; N, 15.89. GC-MS (EI) m/z 176. Raman (633 nm) 2164 cm⁻¹ (-C≡C-).

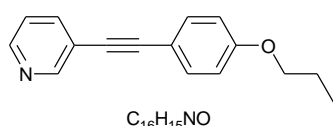
(11) Synthesis of 2-(4'-propoxyphenylethynyl)-pyridine



2-(Trimethylsilylethynyl)pyridine (3 g, 17 mmol), dichlorobis(triphenylphosphine) palladium (600 mg, 0.86 mmol), copper iodide (163 mg, 0.86 mmol) were added to a degassed solution of 1-iodo-4-propoxybenzene (4.45 g, 17 mmol) and potassium carbonate (11.73 g, 85 mmol) in MeOH (35 mL) / THF (65 mL) and a catalytic amount of triethylamine was then refluxed under a nitrogen atmosphere over 2 days. The mixture was reduced by vacuum and filtered through a silica pad with DCM / ethyl acetate and reduced to yield a solid. The solid product was extracted into DCM (3 x 50 mL) and dried over magnesium sulphate. The extract was reduced and the residue was purified by column chromatography in silica gel eluted with DCM-ethyl acetate 1:1, yielding a crude solid, (2.68 g, 66 %). The product was purified further by recrystallisation in hexane and distilled *in vacuo*, and give the pure product as a colourless solid (1.0 g, 39 %). ¹H

NMR (CDCl₃, 400 MHz) δ_{H} 8.60 (d, 1H, J = 4.9, Ar-H), 7.65 (td, 1H, J = 1.8, 7.7, Ar-H), 7.52 (d, 2H, J = 8.9, Ar-H), 7.49 (d, 1H, J = 7.9, Ar-H), 7.21 (ddd, 1H, J = 1.2, 4.8, 7.6, Ar-H), 6.87 (d, 1H, J = 8.7, Ar-H), 3.93 (t, 2H, J = 6.6, -CH₂-), 1.81 (m, 2H, -CH₂-), 1.03 (t, 3H, J = 7.4, -CH₃); ¹³C NMR (CDCl₃, 125MHz, decouple H1 400 MHz) δ_{C} 10.7 (-CH₃), 22.7 (-CH₂-), 69.8 (O-CH₂-), 87.7 (C-C \equiv), 89.9 (\equiv C-Het), 114.2, 114.8, 122.6, 127.1, 133.8, 136.3, 144.1 (N-C*-C \equiv), 150.2(-CH-N-), 160.0 (C-O); Found C; 80.80; H; 6.28; N; 5.86. Calcd for C₁₆H₁₅NO C, 80.98; H, 6.37; N, 5.90. GC-MS (EI) m/z 237. Raman (633 nm) 2221 cm⁻¹ (-C \equiv C-). Melting point 68.5°C.

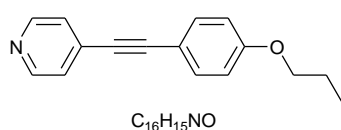
(12) Synthesis of 3-(4'-propoxyphenylethynyl)-pyridine



3-(Trimethylsilylethynyl)pyridine (1.2 g, 6.9 mmol), dichlorobis(triphenyl-phosphine) palladium (97 mg, 0.138 mmol), copper iodide (26 mg, 0.138 mmol) were added to a degassed solution of 1-iodo-4-propoxybenzene (1.81 g, 6.9 mmol) and potassium carbonate (4.76 g, 34.5 mmol) in MeOH (35 mL) / THF (65 mL) and a catalytic amount of triethylamine was then refluxed under a nitrogen atmosphere over 2 days. The mixture was reduced by vacuum and filtered through a silica pad with DCM / ethyl acetate and reduced to yield a solid. The solid product was extracted into DCM (3 x 50 mL) and dried over magnesium sulphate. The extract was reduced and the residue was purified by chromatography in silica gel eluted with DCM-ethyl acetate 1:1, yielding a crude solid, (1.21 g, 74%). The product was purified further by recrystallisation in hexane and distilled *in vacuo*, and give the pure product as a colourless solid (1.01 g, 61 %). ¹H NMR (CDCl₃, 400 MHz) δ_{H} 8.74 (s, 1H, Ar-H), 8.52 (d, 1H, J_{HH} = 4.9, Ar-H), 7.83 (dm, 1H, J_{HH} = 7.83, Ar-H), 7.47 (d, 2H, J_{HH} = 8.7, Ar-H), 7.28 (d, 1H, J_{HH} = 4.9, Ar-H), 6.88 (d, 2H, J_{HH} = 8.7, Ar-H), 3.95 (t, 2H, J_{HH} = 6.5, -CH₂-), 1.82 (m, 2H, -CH₂-),

1.05 (t, 3H, $J_{\text{HH}} = 7.4$, -CH₃); ¹³C NMR (CDCl₃, 125MHz, decouple H1 400 MHz) δ_{C} 10.7 (-CH₃), 22.7 (-CH₂-), 69.8 (O-CH₂-), 84.9 (-C-C \equiv), 93.1 (Het-C \equiv), 114.5, 114.8, 117.0, 123.2, 133.4, 138.4, 148.4 (-CH*-N-), 152.4 (N-CH*-), 159.9 (-C-O-); Found C; 80.92; H; 6.31; N; 5.93. Calcd for C₁₆H₁₅NO C, 80.98; H, 6.37; N, 5.90. GC-MS (EI) m/z 237. Raman (633 nm) 2218 cm⁻¹ (-C \equiv C-). Melting point 47.6°C.

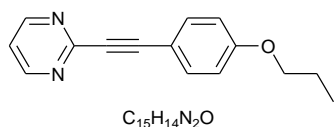
(13) Synthesis of 4-(4'-propoxyphenylethynyl)-pyridine



4-(Trimethylsilylethynyl)pyridine (2.5 g, 13 mmol), dichlorobis(triphenylphosphine) palladium (452 mg, 0.23 mmol), copper iodide (88 mg, 0.65 mmol) were added to 1-iodo-4-propoxybenzene (3.0 g, 13 mmol) and potassium carbonate (8.91 g, 65mmol) in MeOH (35 mL) / THF (65 mL) and a catalytic amount of triethylamine was then refluxed under a nitrogen atmosphere over 2 days. The mixture was reduced by vacuum and filtered through a silica pad with DCM / ethyl acetate and reduced to yield a solid. The solid product was extracted into DCM (3 x 50 mL) and dried over magnesium sulphate. The extract was reduced and the residue was purified by chromatography in silica gel eluted with DCM-ethyl acetate 1:1, yielding a crude solid, (1.88 g, 66%). The product was purified further by recrystallisation in hexane and distilled *in vacuo*, and give the pure product as a colourless solid (1.0 g, 35 %). ¹H NMR (CDCl₃, 400 MHz) δ_{H} 8.58 (d, 2H, $J_{\text{HH}} = 4.4$, Ar-H), 7.48 (d, 2H, $J_{\text{HH}} = 8.7$, Ar-H), 7.35 (d, 2H, $J_{\text{HH}} = 6.0$, Ar-H), 6.88 (d, 2H, $J_{\text{HH}} = 8.7$, Ar-H), 3.95 (t, 2H, $J_{\text{HH}} = 6.5$, -CH₂-), 1.83 (m, 2H, -CH₂-), 1.05 (t, 3H, $J_{\text{HH}} = 7.4$, -CH₃); ¹³C NMR (CDCl₃, 125MHz, decouple H1 400 MHz) δ_{C} 10.7 (-CH₃), 22.7 (-CH₂-), 69.8 (-CH₂-O), 85.8 (-C-C* \equiv), 94.7 (-Het-C \equiv), 114.0, 114.9, 125.6, 132.1 (-C*-C \equiv), 133.7, 149.9 (-N-C-), 160.2 (-C-O-); Found C; 81.27; H; 6.37; N; 5.82. Calcd for

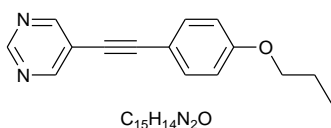
C₁₆H₁₅NO C, 80.98; H, 6.37; N, 5.90. GC-MS (EI) m/z 237. Raman (633 nm) 2223 cm⁻¹ (-C≡C-). Melting point 69.3°C.

(14) Synthesis of 2,6-(4'-propoxyphenylethynyl)-pyrimidine



2-(Trimethylsilylethynyl)pyrimidine (1.3 g, 7.4 mmol), dichlorobis(triphenyl phosphine) palladium (260 mg, 0.37 mmol), copper iodide (71 mg, 0.37 mmol) were added to a degassed solution of 1-iodo-4-propoxybenzene (1.95 g, 7.4 mmol) and potassium carbonate (5.11 g, 37 mmol) in MeOH (35 mL) / THF (65 mL) and a catalytic amount of triethylamine was then refluxed under a nitrogen atmosphere over 2 days. The mixture was reduced by vacuum and filtered through a silica pad with DCM / ethyl acetate and reduced to yield a solid. The solid product was extracted into DCM (3 x 50 mL) and dried over magnesium sulphate. The extract was reduced and the residue was purified by chromatography in silica gel eluted with DCM-ethyl acetate 1:1, yielding a crude solid, (543 mg (31%). The product was purified further by recrystallisation in hexane and distilled *in vacuo*, and give the pure product as a colourless solid (200 mg, 12 %) ¹H NMR (CDCl₃, 500 MHz) δ_H 8.75 (d, 2H, J_{HH} = 5.0, Ar-H), 7.62 (d, 2H, J_{HH} = 8.8, Ar-H), 7.23 (t, 1H, J_{HH} = 4.9, Ar-H), 6.95 (d, 2H, J_{HH} = 8.8, Ar-H), 3.96 (t, 2H, J_{HH} = 6.6, -CH₂-), 1.84 (m, 2H, -CH₂-), 1.06 (t, 3H, J = 7.4, -CH₃); ¹³C NMR (CDCl₃, 125MHz, decouple H1 500 MHz) δ_C 10.7 (-CH₃), 22.7 (-CH₂-), 69.8 (-CH₂-O-), 87.4 (-C-C≡), 89.1 (-Het-C≡), 113.2, 114.9, 119.6, 134.6, 153.9 (-N-C-N-), 157.5 (-C-C*-N-), 160.6 (-C-O-); Found C; 80.80; H; 6.28; N; 5.86. Calcd for C₁₆H₁₅N₂O C, 80.98; H, 6.37; N, 5.90. GC-MS (EI) m/z 238. Raman (633 nm) 2222 cm⁻¹ (-C≡C-). Melting point 97.6°C.

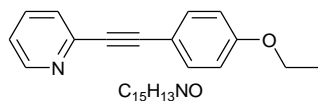
(15) Synthesis of 3,5-(4'-propoxyphenylethynyl)-pyrimidine



5-(Trimethylsilylethynyl)pyrimidine (3.0 g, 17 mmol), dichlorobis(triphenyl phosphine) palladium (596 mg, 0.85 mmol), copper iodide (162 mg, 0.85 mmol) were added to a degassed solution of 1-iodo-4-propoxybenzene (4.45 g, 17 mmol) and potassium carbonate (11.73 g, 85 mmol) in MeOH (35 mL) / THF (65 mL) and a catalytic amount of triethylamine was then refluxed under a nitrogen atmosphere over 2 days. The mixture was reduced by vacuum and filtered through a silica pad with DCM / ethyl acetate and reduced to yield a solid. The solid product was extracted into DCM (3 x 50 mL) and dried over magnesium sulphate. The extract was reduced and the residue was purified by chromatography in silica gel eluted with DCM-ethyl acetate 1:1, yielding a crude solid, (2.04 g, 61 %). The product was purified further by recrystallisation in hexane and distilled *in vacuo*, and give the pure product as a colourless solid (1.0 g, 50 %). The pure product was a colourless solid. 1H NMR ($CDCl_3$, 400 MHz) δ_H 9.11 (s, 1H, Ar-H), 8.82 (s, 2H, Ar-H), 7.47 (d, 2H, $J_{HH} = 8.7$, Ar-H), 6.89 (d, 2H, $J_{HH} = 8.7$, Ar-H), 3.95 (t, 2H, $J_{HH} = 6.5$, -CH₂-), 1.82 (m, 2H, -CH₂-), 1.04 (t, 3H, $J = 7.4$, -CH₃); ^{13}C NMR ($CDCl_3$, 125MHz, decouple H1 500MHz) δ_C 10.7 (-CH₃), 22.7 (-CH₂-), 69.8 (-CH₂-O-), 81.3 (-C-C \equiv), 96.9 (-Het-C \equiv), 113.7, 114.9, 120.6, 133.6, 156.6 (-N-C-N-), 158.6 (-C-O-), 160.3 (-N-C-); Found C; 80.80; H; 6.28; N; 5.86. Calcd for $C_{16}H_{15}N_2O$ C, 80.98; H, 6.37; N, 5.90. GC-MS (EI) m/z 238. Raman (633 nm) 2213 cm^{-1} (-C \equiv C-). Melting point 98.4°C. Crystal data for **15**: C15 H14 N2 O.74, M = 238.28, triclinic, space group P-1 (No. 2), a = 5.7450(5), b = 14.3643(11), c = 15.6327(13) Å, V = 1229.92(18) Å³, Z = 4, Dc = 1.287 Mg m⁻³, F₀₀₀ = 504, Mo K α radiation, $\lambda = 0.71073$ Å, T = 120 K, $2\theta_{max} = 55.0^\circ$, 11894 reflections collected, 5618 unique ($R_{int} = 0.0309$). Final *Goof* = 0.896, R1 = 0.0420, wR2 = 0.1020, R indices based on 3830 reflections with $I > 2.00\sigma$ (I)

(refinement on F^2), 327 parameters, 0 restraints. Lp and absorption corrections applied, $\mu = 0.082 \text{ mm}^{-1}$. For Figure and Table data see Appendix C.

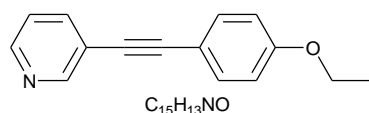
(16) Synthesis of 2-(4'-ethoxyphenylethynyl)-pyridine



2-(Trimethylsilylethynyl)pyridine (1.8 g, 10 mmol), dichlorobis(triphenylphosphine) palladium (350 mg, 0.5 mmol), copper iodide (95 g, 0.5 mmol) were added to a degassed solution of 4-iodophenetole (2.48 g, 10 mmol) and potassium carbonate (6.9 g, 50 mmol) in MeOH (35 mL) / THF (65 mL) and a catalytic amount of triethylamine was then refluxed under a nitrogen atmosphere over 2 days. The mixture was reduced by vacuum and filtered through a silica pad with DCM and reduced to yield a solid. The solid product was extracted into DCM (3 x 50 mL) and dried over magnesium sulphate giving a black oil that later solidified upon standing. The extract was reduced and the residue was purified by column chromatography in silica gel eluted with hexane-DCM, starting with pure hexane and increasing polarity by 5% every 100 mLs. The product came off at the eluting mix hexane-DCM 3:1, yielding a crude solid, (1.2 g, 54 %). The product was purified further by distillation *in vacuo* and recrystallisation in hexane giving a pure colourless solid (1.0 g, 45 %). ^1H NMR (CDCl_3 , 700 MHz) δ_{H} 8.57 (d, 1H, $J_{\text{HH}} = 4.8$, Ar-H), 7.62 (td, 1H, $J_{\text{HH}} = 1.7, 7.8$, Ar-H), 7.50 (d, 2H, $J_{\text{HH}} = 8.8$, Ar-H), 7.46 (d, 1H, $J_{\text{HH}} = 7.80$, Ar-H), 7.17 (ddd, 1H, $J_{\text{HH}} = 1.2, 4.9, 7.6$, Ar-H), 6.84 (d, 2H, $J_{\text{HH}} = 8.8$, Ar-H), 4.01 (q, 2H, $J_{\text{HH}} = 7.0$, $-\text{CH}_2-$), 1.39 (t, 3H, $J_{\text{HH}} = 7.0$, $-\text{CH}_3$); ^{13}C NMR (CDCl_3 , 176MHz, decouple H1 700 MHz) δ_{C} 14.9 ($-\text{CH}_3$), 63.7 ($-\text{C}-\text{O}-$), 87.8 ($-\text{C}-\text{C}\equiv$), 89.8 (Het- $\text{C}\equiv$), 114.3, 114.8, 122.6, 127.1, 133.8, 136.3, 144.0 ($-\text{N}-\text{C}-\text{C}\equiv$), 150.2 ($-\text{C}-\text{N}-$), 159.8 ($-\text{C}-\text{O}-$); Found C; 80.52; H; 5.81; N; 6.18. Calcd for $\text{C}_{15}\text{H}_{13}\text{NO}$; C; 80.72; H;

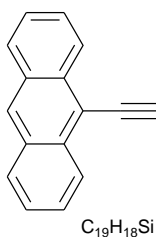
5.83; N; 6.28. GC-MS (EI) m/z 223. Raman (633 nm) 2223 cm⁻¹ (-C≡C-). Melting point 68.6°C.

(17) Synthesis of 3(4'-ethoxyphenylethynyl)-pyridine



3-(Trimethylsilylethynyl)pyridine (2 g, 11.4 mmol), dichlorobis(triphenylphosphine) palladium (401 mg, 0.57 mmol), copper iodide (109 mg, 0.57 mmol) were added to a degassed solution of 4-iodophenetole (2.83 g, 11.4 mmol) and potassium carbonate (7.89 g, 57 mmol) in MeOH (35 mL) / THF (65 mL) and a catalytic amount of triethylamine was then refluxed under a nitrogen atmosphere over 2 days. The mixture was reduced by vacuum and filtered through a silica pad with DCM and reduced to yield a black solid. The solid product was extracted into DCM (3 x 50 mL) and dried over magnesium sulphate. The extract was reduced and the residue was purified by column chromatography in silica gel eluted with hexane-DCM, starting with pure hexane and increasing polarity by 5% every 100 mLs. The product came off at the eluting mix hexane-DCM 3:1, yielding a crude solid, (1.9 g, 85 %). The product was purified further by distillation *in vacuo* and recrystallisation in hexane giving a pure colourless solid (1.24 g, 56 %). ¹H NMR (CDCl₃, 700 MHz) δ_H 8.72 (dd, 1H, J_{HH} = 0.9, 2.1, Ar-H), 8.50 (dd, 1H, J_{HH} = 1.7, 7.8, Ar-H), 7.76 (dt, 1H, J_{HH} = 1.9, 7.9, Ar-H), 7.45 (d, 2H, J_{HH} = 8.84, Ar-H), 7.24 (ddd, 1H, J_{HH} = 1.0, 4.8, 7.8, Ar-H), 6.86 (d, 2H, J_{HH} = 8.8, Ar-H), 4.03 (q, 2H, J_{HH} = 6.9, -CH₂-), 1.41 (t, 3H, J_{HH} = 7.0, -CH₃); ¹³C NMR (CDCl₃, 176MHz, decouple H1 700MHz) δ_C 14.9 (-CH₃), 63.8 (-CH₂-O-), 84.9 (-C-C≡), 93.1 (Het-C≡), 114.6, 114.8, 121.1, 123.2, 133.4, 138.4, 148.4 (-C*-N-C-), 152.3 (-N-C*-C-), 159.6 (-C-O-); Found C; 80.70; H; 5.81; N; 6.38. Calcd for C₁₅H₁₃NO; C; 80.72; H; 5.83; N; 6.28. GC-MS (EI) m/z 223. Raman (633 nm) 2218 cm⁻¹ (-C≡C-). Melting point 70.8°C.

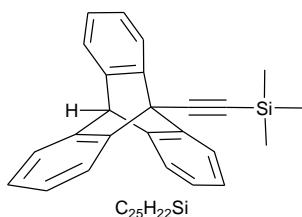
(18) Synthesis of 9-((Trimethylsilyl)ethynyl)-anthracene



Trimethylsilyl acetylene (3.82 g, 39 mmol, 5.5 mL), dichlorobis(triphenylphosphine) palladium (547 mg, 0.78 mmol), copper iodide (149 mg, 0.78 mmol) were added to a degassed solution of 9-bromoanthracene (5 g, 31.6 mmol) in triethylamine (150 mL) and refluxed under a nitrogen atmosphere overnight. The mixture was reduced by vacuum and filtered through a silica pad with DCM and reduced to yield a crude oil. The crude product was extracted into DCM (3 x 50 mL) and dried over magnesium sulphate. The extract was reduced and purified by column chromatography in silica gel eluted with hexane-DCM, starting with pure hexane and increasing polarity by 5% every 200 mLs. The product came off at the eluting mix hexane-DCM 1:1, yielding a deep orange-red solid (9.5 g, 89 %). 1H NMR ($CDCl_3$, 400 MHz) δ_H 8.51 (d, 2H, $J_{HH} = 8.7$, Ar-H), 8.42 (s, 1H, Ar-H), 8.1 (d, 2H, $J_{HH} = 8.51$, Ar-H), 7.58 (ddd, 2H, $J_{HH} = 1.3, 6.6, 8.5$, Ar-H), 0.43 (s, 9H, $-Si(CH_3)_3$); ^{13}C NMR ($CDCl_3$, 125MHz, decouple H1 400 MHz) δ_C 0.5 ($(CH_3)_3Si-$), 101.7 ($\equiv C-Si(CH_3)_3$), 106.4 (Anth-C \equiv), 117.3 ($-C^*-C\equiv$), 125.9, 126.9, 127.0, 128.1, 128.9, 131.3, 133.1; Found C; 82.79; H; 6.51. Calcd for $C_{19}H_{18}Si$; C; 83.15; H;6.61. GC-MS (EI) m/z 274. Raman (633 nm) 2149 cm^{-1} ($-C\equiv C-$). Crystal data for **18**: $C_{19}H_{18}Si$, $M = 274.42$, triclinic, space group P-1 (No. 2), $a = 10.1493(7)$, $b = 11.8886(9)$, $c = 14.1313(10)$ Å, $V = 1554.44(19)$ Å³, $Z = 4$, $D_c = 1.173$ Mg m⁻³, $F_{000} = 584$, Mo K α radiation, $\lambda = 0.71073$ Å, $T = 120$ K, $2\theta_{max} = 52.74^\circ$, 15220 reflections collected, 6328 unique ($R_{int} = 0.0559$). Final $Goof = 1.019$, $R1 = 0.0576$, $wR2 = 0.1262$, R indices based on 4172 reflections with $I > 2.00\sigma(I)$ (refinement on F^2), 367 parameters, 0 restraints. Lp and absorption corrections applied, $\mu = 0.139$ mm⁻¹.

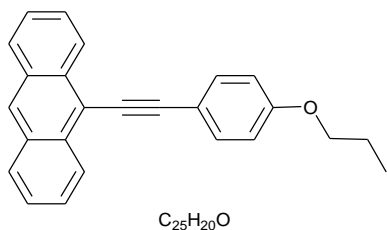
1. For Figure and Tables see Appendix C.

(19) Synthesis of 9-((trimethylsilyl)ethynyl)-triptycene



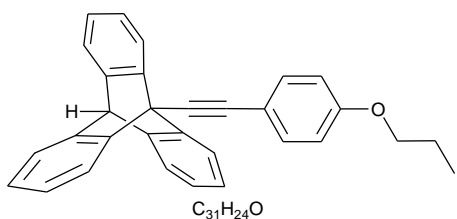
The preparation of this compound followed the method reported in reference [1]. A solution of 9-((trimethylsilyl)ethynyl) triptycene (1.1 g, 4 mmol) in 10 mL of 1,2-dimethoxyethane (DME) was brought to reflux in a 3-necked flask. The following respective solutions were each in their own dropping funnels: anthranilic acid (2.74 g, 20 mmol) in 10 mL of DME and isopentyl nitrite (3.51 g, 30 mmol) in 10 mL of DME were added drop-wise over 1.5 hrs. The mixture was further refluxed for another 2 hrs. After reflux the mixture was reduced by vacuum giving a dark brown tar and chromatographed on a silica gel dry loaded column eluting with hexane-DCM 1:1, yielding the product as a cream crude product. Recrystallisation from hexane gave white crystals (400mg, 29 %). 1H NMR ($CDCl_3$, 500 MHz) δ_H 7.74 (d, 3H, $J_{HH} = 7.4$, Ar-H), 7.40 (d, 3H, $J_{HH} = 7.4$, Ar-H), 7.09 (td, 3H, $J_{HH} = 1.4, 7.5$, Ar-H), 7.05 (td, 3H, $J_{HH} = 1.4, 7.5$, Ar-H), 5.43 (s, 1H, Ar-H), 0.49 (s, 9H, -Si(CH₃)₃); ^{13}C NMR ($CDCl_3$, 125MHz, Decouple H1 500 MHz) δ_C 0.65 ((CH₃)₃Si-), 53.5 (H-C-(Ar)₃), 54.0 ((Ar)₃-C-C \equiv), 97.9 (\equiv C-Si(CH₃)₃), 100.3 (Trypt-C \equiv), 122.7, 123.6, 125.4, 125.9, 144.4, 144.6; Found C; 85.53; H; 6.35. Calcd for C₂₅H₂₂Si; C; 85.66; H; 6.33. GC-MS (EI): m/z 350. Raman (633 nm) 2182 cm⁻¹ (-C \equiv C-). Crystal data for **19**: C₂₅ H₂₂ Si, M = 350.52, monoclinic, space group P2(1)/c (No. 14), a = 15.9236(9) b = 7.9583(4), c = 16.5790(9) Å, V = 1993.76(19) Å³, Z = 4, D_c = 1.168 Mg m⁻³, F₀₀₀ = 744, Mo K α radiation, $\lambda = 0.71073$ Å, T = 120 K, $2\theta_{max} = 54.98^\circ$, 16259 reflections collected, 4583 unique ($R_{int} = 0.0962$). Final *Goof* = 1.081, R1 = 0.0531, wR2 = 0.1025, R indices based on 3494 reflections with I > 2.00 σ (I) (refinement on F²), 323 parameters, 0 restraints. Lp and absorption corrections applied, $\mu = 0.123$ mm⁻¹. For Figure and Tables see Appendix C.

(20) Synthesis of 9-(4'-propoxyphenylethynyl)-anthracene



9-(Trimethylsilylethynyl) anthracene (2.5 g, 9.1 mmol), dichlorobis(triphenylphosphine) palladium (319 mg, 0.46 mmol), copper iodide (87 mg, 0.46 mmol) were added to a degassed solution of 1-iodo-4-propoxybenzene (2.39 g, 9.1 mmol) and potassium carbonate (6.3 g, 47 mmol) in MeOH (35 mL) / THF (65 mL) and a catalytic amount of triethylamine was then refluxed under a nitrogen atmosphere over 2 days. The mixture was reduced by vacuum and filtered through a silica pad with DCM and reduced to yield a brown-orange solid. The solid product was extracted into DCM (3 x 50 mL) and dried over magnesium sulphate. The extract was reduced and the residue was purified by column chromatography in silica gel eluted with hexane-DCM, starting with pure hexane and increasing polarity by 1% every 100 mLs. The product came off at the eluting mix hexane-DCM 23:2, yielding a crude solid, (2.33 g, 76 %). The product was purified further by distillation *in vacuo* and recrystallisation in ethanol giving a pure yellow solid (1.6 g, 52 %). 1H NMR ($CDCl_3$, 500 MHz) δ_H 8.67 (d, 2H, $J_{HH} = 8.9$, Ar-H), 8.43 (s, 1H, Ar-H), 8.03 (d, 2H, $J_{HH} = 8.59$, Ar-H), 7.72 (d, 2H, $J_{HH} = 8.8$, Ar-H), 7.60 (ddd, 2H, $J_{HH} = 1.2, 6.5, 8.5$ Ar-H), 7.53 (ddd, 2H, $J_{HH} = 1.2, 6.5, 8.5$, Ar-H), 6.99 (d, 2H, $J_{HH} = 8.8$, Ar-H), 4.01 (t, 2H, $J_{HH} = 6.6$, $-CH_2-$), 1.88 (Sextet, 2H, $J_{HH} = 7.0$, $-CH_2-$), 1.09 (t, 3H, $J_{HH} = 7.4$, $-CH_3$); ^{13}C NMR ($CDCl_3$, 125MHz, Decouple H1 500 MHz) δ_C 10.8 ($-CH_3$), 22.8 ($-CH_2-$), 69.9 ($-CH_2-O$), 85.2 (Ar- $C\equiv$), 101.2 (Anth- $C\equiv$), 115.0 ($-C^*-C\equiv$), 115.8, 118.0 (Anth C- $C\equiv$), 125.9, 126.7, 127.1, 127.5, 128.9, 131.5, 132.7, 133.4, 159.7 ($-C-O-$); Found C; 89.25; H; 5.92; Calcd for $C_{25}H_{20}O$; C; 89.25; H; 5.99. GC-MS (EI) m/z 336. Raman (633 nm) 2219 cm^{-1} ($-C\equiv C-$). Melting point $105.4^\circ C$.

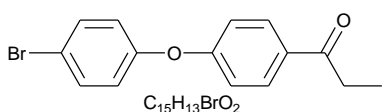
(21) Synthesis of 9-(4'-propoxyphenylethynyl)-tritycene



9-(Trimethylsilylethynyl) triptycene (0.8 g, 2.2 mmol), dichlorobis (triphenylphosphine) palladium (80 mg, 0.0114 mmol), copper iodide (22 mg, 0.0114 mmol) were added to a degassed solution of 1-iodo-4-propoxybenzene (0.6 g, 2.2 mmol) in and potassium carbonate (1.5 g, 11 mmol) MeOH (15 mL) / THF (30 mL) and a catalytic amount of triethylamine was then refluxed under a nitrogen atmosphere over 2 days. The mixture was reduced by vacuum and filtered through a silica pad with DCM and reduced to yield a brown-orange solid. The solid product was extracted into DCM (3 x 20 mL) and dried over magnesium sulphate. The extract was reduced and the residue was purified by column chromatography in silica gel eluted with hexane-DCM, starting with pure hexane and increasing polarity by 2% every 100 mLs. The product came off at the eluting mix hexane-DCM 4:1, yielding a crude solid, (2.33 g, 76 %). The product was purified further by recrystallisation hexane giving a pure colourless solid (1.6 g, 52 %). 1H NMR ($CDCl_3$, 500 MHz) δ_H 7.83 (dd, 3H, $J_{HH} = 1.7, 6.81$, Ar-H), 7.76 (d, 2H, $J_{HH} = 8.9$, Ar-H), 7.49 (dd, 3H, $J_{HH} = 1.7, 6.81$, Ar-H), 7.07 (m, 6H, Ar-H), 7.01 (d, 2H, $J_{HH} = 8.9$, Ar-H), 5.46 (s, 1H, Ar-H), 4.03 (t, 2H, $J_{HH} = 6.6$, $-CH_2-$), 1.89 (Sextet, 2H, $J_{HH} = 7.2$, $-CH_2-$), 8.67 (t, 3H, $J_{HH} = 7.5$, $-CH_3$); ^{13}C NMR ($CDCl_3$, 125MHz, decouple H1 500 MHz) δ_C 10.8 ($-CH_3$), 22.8 ($-CH_2-$), 53.5 ($(Ar)_3-C-C\equiv$), 53.8 (H-C-(Ar) $_3$), 69.9 ($-CH_2-O-$), 82.3 (Trypt=C \equiv), 92.9 (Ar-C \equiv), 114.9(Ar C-C \equiv), 122.8, 123.6, 125.4, 125.9, 128.8, 132.4, 133.8, 144.7, 159.8 ($-C-O-$); Found C; 89.81; H; 5.90. Calcd for $C_{31}H_{24}$; C; 90.26; H; 5.86. MS (ES^+) m/z $MH^+ = 413$ ($M = 412$). Raman (633 nm) 2238 cm^{-1} ($-C\equiv C-$). Melting point $54.5^\circ C$. Crystal data for **21**: $C_{31}H_{24}O$, $M = 412.50$, triclinic, space group P-1 (No. 2), $a = 9.0176(7)$, $b = 9.1859(7)$, $c = 13.7607(10)$ Å, $V = 1107.93(14)$ Å 3 , $Z = 2$, $D_c = 1.237\text{ Mg m}^{-3}$, $F_{000} =$

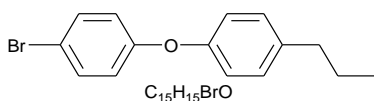
436, Mo K α radiation, $\lambda = 0.71073 \text{ \AA}$, $T = 120 \text{ K}$, $2\theta_{\max} = 50.04^\circ$, 7999 reflections collected, 3912 unique ($R_{\text{int}} = 0.0326$). Final $Goof = 1.043$, $R1 = 0.0626$, $wR2 = 0.1599$, R indices based on 2490 reflections with $I > 2.00\sigma(I)$ (refinement on F^2), 290 parameters, 0 restraints. Lp and absorption corrections applied, $\mu = 0.073 \text{ mm}^{-1}$. For Figure and Tables see Appendix C.

(23) Synthesis of 1-bromo 4'-propan-1-one diphenyl ether



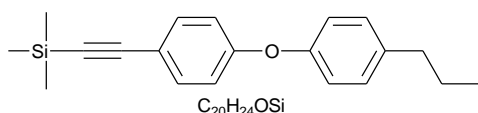
A solution of propanoyl chloride (9.25 g, 100 mmol, 8.7 mL) in 50 mL of dry DCM (in an inert atmospheric dropping funnel) was added drop-wise to a stirring solution of bromo diphenyl ether (24.9 g, 100 mmol, 17.51 mL) and aluminium chloride (13.3 g, 100 mmol) in 300 mL of dry DCM at 0°C . The mixture was continually stirred at 0°C for a further 5 hrs. The reaction was then poured over a mixture of 200 g of ice and 20 mL of concentrated hydrochloric acid and the organic layer was extracted and dried over magnesium sulphate. The extract was reduced and the residue was purified by recrystallisation from ethanol yielding a colourless solid (29.7 g, 97 %). $^1\text{H NMR}$ (CDCl_3 , 700 MHz) δ_{H} 7.94 (d, 2H, $J_{\text{HH}} = 8.7$, Ar-H), 7.47 (d, 2H, $J_{\text{HH}} = 8.7$), 6.98 (d, 2H, $J_{\text{HH}} = 8.7$, Ar-H), 6.93 (d, 2H, $J_{\text{HH}} = 8.7$, Ar-H), 2.94 (q, 2H, $J_{\text{HH}} = 7.4$, $-\text{CH}_2$), 1.20 (t, 3H, $J_{\text{HH}} = 7.4$, $-\text{CH}_3$); $^{13}\text{C NMR}$ (CDCl_3 , 176MHz, decouple H1 700 MHz) δ_{C} 8.5 ($-\text{CH}_3$), 31.8($-\text{CH}_2-$), 117.3(Br-C), 121.9, 130.5 (C-CO), 132.3, 133.2, 155.1 (C-O), 161.3 (O-C), 199.5 (C=O); Found C; 58.83; H; 4.17. Calcd for $C_{15}H_{13}N_1O_2Br$; C; 59.04; H; 4.29. GC-MS (EI) m/z 304. Raman (633 nm) 1675 cm^{-1} ($-\text{C}=\text{O}$ -). Melting point 61.8°C .

(24) Synthesis of 1-bromo 4'-propyl diphenyl ether



The preparation of this compound followed the method reported reference [2] using the Wolf-Kischner reduction. A mixture of 1-bromo 4'-propan-1-one diphenyl ether (20 g, 66 mmol), hydrazine monohydrate solution (9.9 g, 198 mmol) and potassium hydroxide pellets (KOH, 12.62 g, 230 mmol) in 300 mL of triethylene glycol was heated to reflux overnight. The reaction was cooled and poured over 200 mL HCl (2 M). The mixture was extracted with DCM (3 x 100 mL). The organic layers were combined and washed with sodium hydroxide solution (NaOH aq., 0.1 M, 150 mL). The extract was dried with magnesium sulphate and reduced to leave a crude oil. The oil was purified using column chromatography on silica gel eluting with hexane yielding a colourless oil (14.1 g, 73 %). 1H NMR ($CDCl_3$, 700 MHz) δ_H 7.42 (d, 2H, $J_{HH} = 9.0$, Ar-H), 7.17 (d, 2H, $J_{HH} = 8.4$, Ar-H), 6.94 (d, 2H, $J_{HH} = 8.4$, Ar-H), 6.88 (d, 2H, $J_{HH} = 9.0$, Ar-H), 2.60 (t, 2H, $J_{HH} = 7.6$, $-CH_2$), 1.66 (sextet, 2H, $J_{HH} = 7.6$) 0.99 (t, 3H, $J_{HH} = 7.4$, $-CH_3$); ^{13}C NMR ($CDCl_3$, 176MHz, Decouple H1 700 MHz) δ_C 14.1 ($-CH_3$), 24.9 ($-CH_2-$), 37.6 ($-CH_2-$ Ar), 115.4 (C-Br), 119.3, 120.3, 130.0 (C- CH_2), 132.8, 138.5, 154.7 (O-C), 157.3 (C-O); Found C; 61.77; H; 5.16. Calcd for $C_{15}H_{15}BrO$; C; 61.87; H; 5.19. GC-MS (EI) m/z 291.

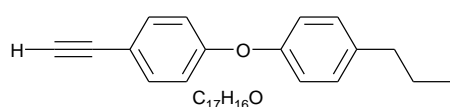
(25) Synthesis of 1-trimethylsilylethynyl 4'-propyl diphenyl ether



Trimethylsilyl acetylene (1.96 g, 20 mmol, 2.82 mL), dichlorobis(triphenylphosphine) palladium (301 mg, 0.43 mmol), copper iodide (82 mg, 0.43 mmol) were added to a degassed solution of 1-bromo 4'-propyl diphenyl ether (5 g, 17.2 mmol) in triethylamine (100 mL) and refluxed under a nitrogen atmosphere overnight. The mixture was reduced by

vacuum and filtered through a silica pad with DCM and reduced to yield a crude product. The crude product was extracted into DCM (3 x 50 mL) and dried over magnesium sulphate. The extract was reduced and purified with column chromatography on silica gel eluting with hexane to give the pure product as a colourless solid (3.2 g, 57 %). ^1H NMR (CDCl_3 , 700 MHz) δ_{H} 7.39 (d, 2H, $J_{\text{HH}} = 3.1$, Ar-H), 7.13 (d, 2H, $J_{\text{HH}} = 3.1$, Ar-H), 6.93 (t, 4H, $J_{\text{HH}} = 7.5$, Ar-H), 2.57 (t, 2H, $J_{\text{HH}} = 7.6$, $-\text{CH}_2$), 1.63 (sextet, 2H, $J_{\text{HH}} = 7.5$) 0.94 (t, 3H, $J_{\text{HH}} = 7.4$, $-\text{CH}_3$), 0.24 (s, 9H, $\text{Si}(\text{CH}_3)_3$); ^{13}C NMR (CDCl_3 , 176MHz, decouple H1 700 MHz) δ_{C} 0.23 ($(\text{CH}_3)_3\text{Si}-$), 14.0 ($-\text{CH}_3$), 24.8 ($-\text{CH}_2-$), 37.5 ($-\text{CH}_2\text{-Ar}$), 93.4 ($\equiv\text{C-Si}(\text{CH}_3)_3$), 105.0 (Ar C-C \equiv), 115.4, 117.5, 118.0, 119.3, 119.6, 130.0, 132.8, 138.6, 154.3 ($-\text{O-C Alkyl Ar}$), 158.4 (Alkyne Ar C-O-); Found C; 78.55; H; 7.42. Calcd. For $\text{C}_{18}\text{H}_{24}\text{Si}$; C; 77.87; H; 7.84. GC-MS (EI) m/z 308. Acc MS* (EI): (m/z) Calcd. For $\text{C}_{16}\text{H}_{15}\text{N}_2\text{O}$ 308.1596. Found 308.1597. Raman (633 nm) 2157 cm^{-1} ($-\text{C}\equiv\text{C}-$).

(26) Synthesis of 1-ethynyl 4'-propyl diphenyl ether



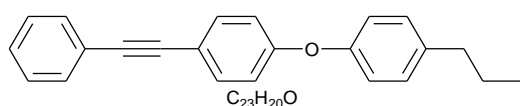
1-Trimethylsilyl ethynyl 4'-propyl diphenyl ether

(0.9 g, 2.92 mmol) was added to a solution of

tetrabutyl ammonium fluoride (TBAF, 1 mL) and methanol (50 mL) and stirred. After 2 hrs HCl acid (2 M, 10 mL) was added to neutralise the TBAF. The mixture was reduced and the product in the remaining aqueous solution was extract into DCM (3 x 20 mL) and dried over magnesium sulphate. The extract was reduced yielding a colourless product (0.65 g, 94 %). ^1H NMR (CDCl_3 , 700 MHz) δ_{H} 7.43 (d, 2H, $J_{\text{HH}} = 8.9$, Ar-H), 7.16 (d, 2H, $J_{\text{HH}} = 8.9$, Ar-H), 6.94 (d, 2H, $J_{\text{HH}} = 7.1$, Ar-H), 6.90 (d, 2H, $J_{\text{HH}} = 7.1$, Ar-H), 3.02 (s, 1H, Acetylene-H), 2.58 (t, 2H, $J_{\text{HH}} = 7.5$, $-\text{CH}_2$), 1.63 (sextet, 2H, $J_{\text{HH}} = 7.4$), 0.95 (t, 3H, $J_{\text{HH}} = 7.4$, $-\text{CH}_3$); ^{13}C NMR (CDCl_3 , 176MHz, decouple H1 700 MHz)

δ_C 14.0 (-CH₃), 24.9 (-CH₂-), 37.5 (-CH₂-Ar), 76.6 (H-C≡), 83.6 (Ar-C≡), 115.4 (Ar C-C≡), 116.4, 118.0, 119.2, 119.3, 119.8, 130.0, 130.1, 132.8, 138.7, 154.2 (-O-C Alkyl Ar), 158.8 (-O-C Alkyne Ar); Found C; 85.44; H; 6.48; Calcd for C₁₇H₁₆; C; 86.40; H; 6.82. GC-MS (EI) m/z 236.

(27) Synthesis of 1-phenylethynyl 4'-propyl diphenyl ether



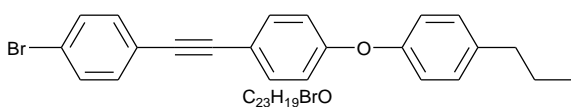
Phenyl acetylene (0.53 g, 5.17 mmol, 0.57 mL), dichlorobis(triphenylphosphine)

palladium (181 mg, 0.26 mmol), copper iodide (50 mg, 0.26 mmol) were added to a degassed solution of 1-Bromo 4'-propyl diphenyl ether (1.5 g, 5.17 mmol) in triethylamine (80 mL) and refluxed under a nitrogen atmosphere overnight. The mixture was reduced by vacuum and filtered through a silica pad with DCM and reduced to yield a crude product. The crude product was extracted into DCM (3 x 50 mL) and dried over magnesium sulphate. The extract was reduced and purified with column chromatography on silica gel and initially eluted with hexane working upto hexane:DCM 19:1 by 1% every 80 mL to give a crude product (1.21 g, 75 %). The product was further purified from hexane to yield the pure product as a colourless solid (0.7 g, 58 %). ¹H NMR (CDCl₃, 700 MHz) δ_H 7.51 (m, 2H, Ph-H), 7.47 (d, 2H, J_{HH} = 9.0, Ar-H), 7.33 (m, 3H, Ph-H), 7.16 (d, 2H, J_{HH} = 9.0, Ar-H), 6.94 (t, 4H, J_{HH} = 9.0, Ar-H), 2.58 (t, 2H, J_{HH} = 7.8, -CH₂), 1.64 (sextet, 2H, J_{HH} = 7.5), 0.95 (t, 3H, J_{HH} = 7.3, -CH₃); ¹³C NMR (CDCl₃, 176MHz, decouple H1 700 MHz) δ_C 14.0 (-CH₃), 24.9 (-CH₂-), 37.6 (-CH₂-Ar), 88.8 (Ar-C≡), 89.3 (-O-Ar-C≡), 117.6 (Ar C-C≡), 118.2, 119.7, 123.6, 128.3, 128.5, 130.0, 131.7, 133.4, 138.6, 154.4 (-O-C Alkyl Ar), 158.3 (-O-C (Ar Alkyne Ar)); Found C; 88.36; H; 6.41. Calcd for C₂₃H₂₀O; C; 88.43; H; 6.45. GC-MS

(EI) m/z 312. Acc MS (EI): (m/z) Calcd. For C₂₃H₂₀O: 312.1509. Found 312.1509.

Raman (633 nm) 2220 cm⁻¹ (-C≡C-). Melting point 112.8°C.

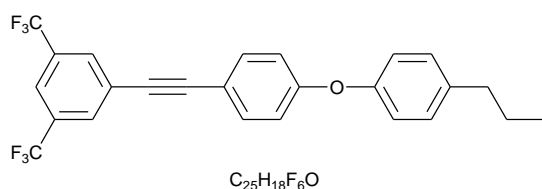
(28) Synthesis of 1-bromophenylethynyl 4'-propyl diphenyl ether



Dichloro bis(triphenylphosphine) palladium (217 mg, 0.31 mmol), copper

iodide (59 mg, 0.31 mmol) were added to a degassed solution of 1- ethynyl 4'-propyl diphenyl ether (2.93 g, 12.42 mmol), 4-iodo bromo benzene (3.52 g, 12.42 mmol) and triethylamine (3.8 g, 37.25 mmol, 5.2 mL) in 120 ml tetrahydrofuran (THF) then stirred at room temperature under a nitrogen atmosphere overnight. The mixture was reduced by vacuum and filtered through a silica pad with DCM and reduced to yield a crude product (3.8 g, 78 %). The product was recrystallised in hexane/DCM to yield a white solid (2.5 g, 52 %). ¹H NMR (CDCl₃, 700 MHz) δ_H 7.47 (d, 2H, J_{HH} = 4.5, Ar-H), 7.46 (d, 2H, J_{HH} = 4.5, Ar-H), 7.37 (d, 2H, J_{HH} = 8.4, Ar-H), 7.16 (d, 2H, J_{HH} = 8.4, Ar-H), 6.96 (d, 2H, J_{HH} = 8.6, Ar-H), 6.94 (d, 2H, J_{HH} = 8.6, Ar-H), 2.58 (t, 2H, J_{HH} = 7.5, -CH₂), 1.65 (sextet, 2H, J_{HH} = 7.5), 0.96 (t, 3H, J_{HH} = 7.4, -CH₃); ¹³C NMR (CDCl₃, 176MHz, decouple H1 700 MHz) δ_C 14.0 (-CH₃), 24.9 (-CH₂-), 37.6 (-CH₂-Ar), 87.8 (Br-Ar-C≡), 90.5 (-O-Ar-C≡), 117.2 (Ar C-C≡), 118.2, 119.5, 122.5, 122.6 (Br-C-), 130.0, 131.8, 133.1, 133.4, 138.7, 154.2 (-O-C Alkyl Ar), 158.7 (-O-C Alkyne Ar); Found C; 70.72; H; 4.91. Calcd for C₂₃H₁₉BrO; C; 70.60; H; 4.89. GC-MS (EI) m/z 391. Raman (633 nm) 2220 cm⁻¹ (-C≡C-). Melting point 138.3°C.

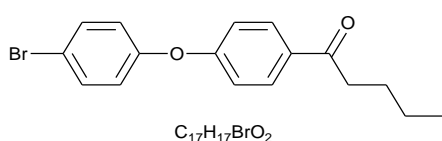
(29) Synthesis of 1-(3,5 trifluoromethyl)phenylethynyl 4'-propyl diphenyl ether



Dichloro bis(triphenylphosphine) palladium (149 mg, 0.21 mmol), copper iodide (40 mg,

0.21 mmol) were added to a degassed solution of 1- ethynyl 4'-propyl diphenyl ether (1 g, 4.24 mmol), 3,5-trifluoromethyl bromo benzene (1.24 g, 4.24 mmol, 0.73 mL) in 20 mL triethylamine and refluxed under a nitrogen atmosphere overnight. The mixture was reduced by vacuum and filtered through a silica pad with DCM and reduced to yield a crude product (1.2 g, 63 %). The product was purified further by column chromatography on silica gel initially eluting with hexane and working up to hexane:DCM 10:1 by 2% every 100 mL. The product was finally purified using preparative TLC on silica GF₂₅₄ in a hexane:DCM 10:1 solvent system, collecting the first fastest running UV active band to yield a cream/white solid (1.11 g, 58 %). ¹H NMR (CDCl₃, 700 MHz) δ_H 7.93 (s, 2H, Ar-H), 7.79 (s, 1H, Ar-H), 7.49 (d, 2H, J_{HH} = 8.5, Ar-H), 7.18 (d, 2H, J_{HH} = 8.5, Ar-H), 6.97 (d, 2H, J_{HH} = 6.8, Ar-H), 6.96 (d, 2H, J_{HH} = 6.8, Ar-H), 2.59 (t, 2H, J_{HH} = 7.6, -CH₂), 1.65 (sextet, 2H, J_{HH} = 7.6), 0.96 (t, 3H, J_{HH} = 7.2, -CH₃); ¹⁹F NMR (CDCl₃, 700 MHz) -63.16 (s, 6F, -CF₃); ¹³C NMR (CDCl₃, 176 MHz, decouple H1 700 MHz) δ_C 14.0 (-CH₃), 24.8 (-CH₂-), 37.6 (-CH₂-Ar), 85.9, 92.9, 116.0 (Ar C-C≡), 118.1, 120.0, 121.5 (septet, 1C, J_{CF} = 4.1), 123.2 (q, 1C, J_{CF} = 272.1), 126.1, 130.1, 131.5 (m), 132.1 (q, 2C, J_{CF} = 34.3), 133.7, 139.0, 153.9 (-O-C Alkyl Ar), 159.3 (-O-C Alkyne Ar). Found C; 66.70; H; 4.03. Calcd for C₂₅H₁₈F₆O; C; 66.96; H; 4.05. GC-MS (EI) m/z 448. Raman (633 nm) 2221 cm⁻¹ (-C≡C-). Melting point 170.0°C.

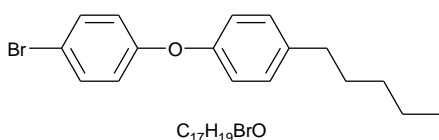
(30) Synthesis of 1-bromo 4'-penta-1-one diphenyl ether



A solution of valeroyl chloride (12 g, 100 mmol, 11.8 mL) in 50 mL of dry DCM (in an inert atmospheric dropping funnel) was added drop-wise to a stirring solution of bromo diphenyl ether (24.9 g, 100 mmol, 17.51 mL) and aluminium chloride (13.3 g, 100

mmol) in 300 mL of dry DCM at 0°C. The mixture was continually stirred at 0°C for a further 5 hrs. The reaction was then poured over a mixture of 200 g of ice and 20 mL of concentrated hydrochloric acid and the organic layer was extracted and dried over magnesium sulphate. The extract was reduced and the residue was purified by recrystallisation from hexane yielding a colourless solid (32.7 g, 98 %). ¹H NMR (CDCl₃, 700 MHz) δ_H 7.94 (d, 2H, J_{HH} = 8.4, Ar-H), 7.74 (d, 2H, J_{HH} = 9.1), 6.98 (d, 2H, J_{HH} = 8.4, Ar-H), 6.93 (d, 2H, J_{HH} = 9.1, Ar-H), 2.91 (t, 2H, J_{HH} = 7.4, -CH₂), 1.70 (quintet, 2H, J_{HH} = 7.4, -CH₂-), 1.39 (sextet, 2H, J_{HH} = 7.4, -CH₂-), 0.94 (t, 3H, J_{HH} = 7.4, -CH₃); ¹³C NMR (CDCl₃, 176MHz, decouple H1 700 MHz) δ_C 14.2 (CH₃), 22.7 (-CH₂-), 26.8 (-CH₂-), 38.4 (-CH₂-CO), 117.3 (C-Br), 117.8, 121.9, 130.6 (C-CO), 132.5, 133.2, 155.1 (C-O), 161.3 (O-C), 199.3 (C=O); Found C; 61.18; H; 5.09. Calcd for C₁₇H₁₇O₂Br; C; 61.28; H; 5.14. GC-MS (EI) m/z 332. Raman (633 nm) 1678 cm⁻¹ (-C=O-). Melting point 69.5°C

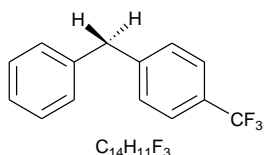
(31) Synthesis of 1-bromo 4'-pentyl diphenyl ether



The preparation of this compound followed the method reported in reference [2] using the Wolf-Kischner reduction. A mixture of 1-bromo 4'-penta-1-one diphenyl ether (15 g, 45 mmol), hydrazine monohydrate solution (6.7 g, 134 mmol) and potassium hydroxide pellets (8.7 g, 155 mmol) in 275 mL of triethylene glycol was heated to reflux overnight. The reaction was cooled and poured over 200 mL HCl (2 M). The mixture was extracted with DCM (3 x 100 mL). The organic layers were combined and washed with Sodium hydroxide solution (NaOH aq., 0.1 M, 150 mL). The extract was dried with magnesium sulphate and reduced to leave a crude oil. The oil was purified using column chromatography on silica gel eluting with hexane yielding a colourless oil (14.1

g, 73 %). ^1H NMR (CDCl_3 , 700 MHz) δ_{H} 7.42 (d, 2H, $J_{\text{HH}} = 8.4$, Ar-H), 7.17 (d, 2H, $J_{\text{HH}} = 9.1$), 6.94 (d, 2H, $J_{\text{HH}} = 8.4$, Ar-H), 6.88 (d, 2H, $J_{\text{HH}} = 9.1$, Ar-H), 2.61 (t, 2H, $J_{\text{HH}} = 7.7$, $-\text{CH}_2$), 1.64 (sextet, 2H, $J_{\text{HH}} = 7.7$, $-\text{CH}_2$), 1.37 (m, 4H, $-(\text{CH}_2)_2$), 0.94 (t, 3H, $J_{\text{HH}} = 6.9$, $-\text{CH}_3$); ^{13}C NMR (CDCl_3 , 176 MHz, decouple H1 700 MHz) δ_{C} 14.3 (CH_3), 22.8 (CH_2), 31.5 (CH_2), 31.7 (CH_2), 35.4 (CH_2), 115.4 (Br-C), 119.3, 120.2, 129.9, 132.8 (Ar C- CH_2), 138.8, 154.6 (Pentyl-Ar-C-O), 157.3 (Br-Ar-C-O); Found C; 63.77; H; 6.14. Calcd for $\text{C}_{17}\text{H}_{19}\text{BrO}$; C; 63.96; H; 6.00. GC-MS (EI) m/z 318.

(34) Synthesis of 4-trifluoromethyl diphenylmethane

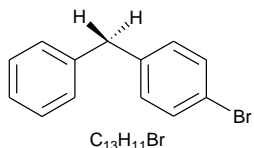


The preparation of this compound followed the method reported in reference [2] the Wolf-Kischner reduction. A mixture of 4-trifluoromethyl benzophenone (2 g, 8 mmol), hydrazine monohydrate solution (1.2 g, 24 mmol, 1.16 mL) and potassium hydroxide pellets (1.79 g, 32 mmol) in 50 mL of Triethylene glycol was heated to reflux overnight. The reaction was cooled and poured over 50 mL HCl (2 M). The mixture was extracted with DCM (3 x 30 mL). The organic layers were combined and washed with Sodium hydroxide solution (NaOH aq., 0.1 M, 150 mL). The extract was dried with magnesium sulphate and reduced to leave a crude oil (1.7 g, 90 %). The oil was purified using column chromatography on silica gel eluting with hexane yielding a colourless oil that solidified upon standing (1.42 g, 75 %). ^1H NMR (CDCl_3 , 500 MHz) δ_{H} 7.57 (d, 2H, $J_{\text{HH}} = 7.8$, Ar-H), 7.34 (m, 4H, Ph-H), 7.26 (m, 1H, Ph-H), 7.21 (dm, 2H, $J_{\text{HH/HF}} = 7.8$, Ar-H), 4.07 (s, 2H, $-\text{CH}_2$); ^{19}F NMR (CDCl_3 , 700 MHz) δ_{F} -62.39 (s, 3F, $-\text{CF}_3$); ^{13}C NMR (CDCl_3 , 100 MHz, decouple H1 400 MHz) δ_{C} 46.1 ($-\text{CH}_2$), 123.9 (q, $^1J_{\text{CF}} = 271.1$), 125.6 (q, $^3J_{\text{CF}} = 3.9$), 128.8, 130.3, 130.4, 133.4, 133.9 (q, $^2J_{\text{CF}} = 32.7$), 136.9 (Ar C*- CH_2), 140.9 (CF_3 -Ar C*- CH_2);

Found C; 70.67; H; 4.41. Calcd for C₁₄H₁₁F₃; C; 71.18; H; 4.69. GC-MS (EI) m/z 236.

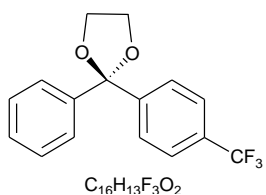
Melting point 49.7°C.

(35) Synthesis of 4-bromo diphenylmethane



The preparation of this compound followed the method reported in reference [2] using the Wolf-Kischner reduction. A mixture of 4-bromo benzophenone (2 g, 7.66 mmol), hydrazine monohydrate solution (1.15 g, 23 mmol, 1.12 mL) and potassium hydroxide pellets (1.72 g, 30.64 mmol) in 50 mL of Triethylene glycol was heated to reflux overnight. The reaction was cooled and poured over 50 mL HCl (2 M). The mixture was extracted with DCM (3 x 30 mL). The organic layers were combined and washed with Sodium hydroxide solution (NaOH aq., 0.1 M, 150 mL). The extract was dried with magnesium sulphate and reduced to leave a crude oil (1.78 g, 94 %). The oil was purified using column chromatography on silica gel eluting with hexane yielding a colourless oil (1.57 g, 83 %). ¹H NMR (CDCl₃, 500 MHz) δ_H 7.48 (d, 2H, J_{HH} = 8.6), 7.37 (m, 2H, Ph-H), 7.26 (m, 3H, Ph-H), 7.13 (d, 2H, J_{HH} = 8.6, Ar-H), 4.00 (s, 2H, -CH₂-); ¹³C NMR (CDCl₃, 100 MHz, decouple H1 400 MHz) δ_C 45.6 (-CH₂-), 121.1 (Br-C-), 126.7, 128.5, 129.7, 130.0, 133.2, 139.8 (Ar C-CH₂-), 140.1 (Br-Ar C*-CH₂-); GC-MS (EI) m/z 247. Acc MS (EI): (m/z) Calcd. For C₁₃H₁₁Br: 246.0039. Found 246.0042.

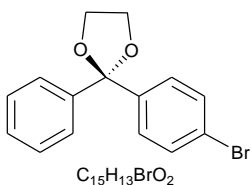
(36) Synthesis of 2-(4-(trifluoromethyl)phenyl)-2-phenyl-1,3-dioxolane



The preparation of this compound followed the method reported in reference [3]. 4-trifluoromethyl benzophenone (3 g, 12 mmol), ethylene glycol (11.4 g, 184 mmol, 10 mL), and a catalytic amount (10%) of p-toluenesulfonic acid (228 mg, 1.2 mmol) in toluene (100 mL) was

refluxed for 54 hrs. During the reflux the resulting water was collected and removed by azeotropic distillation (Dean-Stark apparatus). The reaction mixture was reduced and then washed with aqueous NaOH (0.1 M, 150 mL) and extracted into DCM (3 x 50 mL). The combined organic layers were dried with magnesium sulphate and reduced giving a crude solid (3.25 g, 92 %). The crude product was recrystallised in ethanol to yield a colourless solid (2.99 g, 85 %). ^1H NMR (CDCl_3 , 700 MHz) 7.88 (dm, 2H, $J_{\text{HH}} = 8.6$, Ar-H), 7.80 (dd, 2H, $J_{\text{HH}} = 8.3, 1.4$, Ph-H), 7.75 (dm, 2H, $J_{\text{HH}} = 8.6$, Ar-H), 7.50 (t, 2H, $J_{\text{HH}} = 7.8$, Ph-H), 7.34 (t, 1H, $J_{\text{HH}} = 7.4$, Ph-H), 4.06 (m, 4H, $-(\text{CH}_2)_2-$); ^{19}F NMR (CDCl_3 , 700 MHz) $\delta_{\text{F}} -62.39$ (s, 3F, $-\text{CF}_3$); ^{13}C NMR (CDCl_3 , 100 MHz, decouple H1 400 MHz) δ_{C} 62.7 ($-\text{CH}_2)_2-$, 124.1 (q, 1C, $J_{\text{CF}} = 272$), 125.6 (q, 2C, $J_{\text{CF}} = 3.5$), 127.5 ($-\text{O}-\text{C}-\text{O}-$), 129.0, 129.2, 132.1, 132.7 (q, 1C, $J_{\text{CF}} = 32.3$), 135.7, 139.7, 139.8 ;Found C; 65.68, H; 4.69. Calcd for $\text{C}_{16}\text{H}_{12}\text{F}_3\text{O}_2$; C; 65.30, H; 4.45. GC-MS (EI) m/z 293. Melting point 115.6°C .

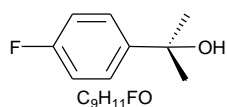
(37) Synthesis of 2-(4-(bromo)phenyl)-2-phenyl-1,3-dioxolane



The preparation of this compound followed the method reported in reference [3]. 4-bromo benzophenone (3 g, 11.5 mmol), ethylene glycol (11.4 g, 184 mmol, 10 mL), and a catalytic amount (10%) of p-toluenesulfonic acid (218 mg, 1.15 mmol) in toluene (100 mL) was refluxed for 54 hrs. During the reflux the resulting water was collected and removed by azeotropic distillation (Dean-Stark apparatus). The reaction mixture was reduced and then washed with aqueous NaOH (0.1 M, 150 mL) and extracted into DCM (3 x 50 mL). The combined organic layers were dried with magnesium sulphate and reduced giving a crude solid (3.45 g, 98 %). The crude product was recrystallised in ethanol to yield a colourless solid (3.3 g, 94 %). ^1H NMR (CDCl_3 , 400 MHz) δ_{H} 7.49 (m, 2H, Ph-H), 7.46

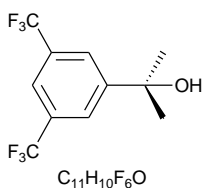
(d, 2H, $J_{\text{HH}} = 8.8$, Ar-H), 7.40 (d, 2H, $J_{\text{HH}} = 8.8$, Ar-H), 7.33 (m, 3H, Ph-H), 4.06 (s, 4H, $-(\text{CH}_2)_2-$); ^{13}C NMR (CDCl_3 , 100 MHz, decouple H1 400 MHz) δ_{C} 65.0 ($-(\text{CH}_2)_2-$), 109.1 (Br-C), 122.3 ($-\text{O}-\text{C}-\text{O}-$), 126.1, 128.1, 128.3, 131.3, 132.7, 136.4, 137.3; Found C; 59.20; H; 4.19. Calcd for $\text{C}_{15}\text{H}_{13}\text{BrO}_2$; C; 59.04; H; 4.29. GC-MS (EI) m/z 303. Melting point 37.1°C.

(38) Synthesis of 2-(4-fluorophenyl)-propan-2-ol



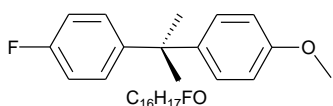
1-Bromo 4-fluorobenzene (5 g, 28.6 mmol, 3.14 mL) was stirred in dry THF (50 mL) at -78°C (dry ice / acetone bath) for 20 min. Then *n*-butyl lithium (2.5 M per 100 mL solution, 28.6 mmol, 11.43 mL) was added dropwise to the solution and stirred further for another 20 min at -78°C . The reaction was removed from the dry ice / acetone bath and dry acetone (4.98 g, 85.8 mmol, 5.7 mL) added. The reaction was stirred for another 20 min before quenching with water and reducing to an aqueous phase. The product was extracted into DCM (3 x 50 mL) and the combined organic layers were dried over magnesium sulphate and reduced. The crude product was further purified by distillation *in vacuo*, to give the pure product as a colourless oil (4.3 g, 98 %). ^1H NMR (CDCl_3 , 700 MHz) δ_{H} 7.42 (dd, 2H, $J_{\text{HF/HH}} = 5.4$, 9.0, Ar-H), 6.98 (t, 2H, $J_{\text{HF/HH}} = 9.0$, Ar-H), 1.54 (s, 6H, $-\text{CH}_3$); ^{19}F NMR (CDCl_3 , 700 MHz) δ_{F} -116.26 (tt, 1F, $J_{\text{HF}} = 5.4$, 8.4, Ar-F); ^{13}C NMR (CDCl_3 , 176 MHz, decouple H1 700 MHz) δ_{C} 32.0 (CH_3-), 72.4 ($-\text{C}(\text{CH}_3)-\text{OH}$), 115.1 (d, 1C, $J_{\text{CF}} = 21.1$), 126.4 (d, 1C, $J_{\text{CF}} = 7.6$), 145.1 (d, 1C, $J_{\text{CF}} = 3.5$), 161.7 (d, 1C, $J_{\text{CF}} = 244.6$); Found C; 69.20; H; 7.71. Calcd for $\text{C}_9\text{H}_{11}\text{FO}$; C; 70.11; H; 7.19. GC-MS (EI) m/z 138. Acc MS (EI): (m/z) Calcd. For 154.0794 Found 154.0796

(39) Synthesis of 2-(Bis 3,5-trifluoromethyl)phenyl propan-2-ol



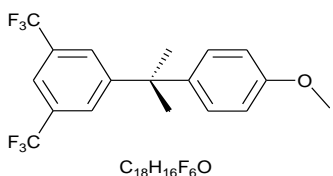
5-Bromo bis 1,3-(trifluoromethyl)benzene (8.5 g, 29 mmol, 5 mL) was stirred in dry THF (70 mL) at -78°C (dry ice / acetone bath) for 20 min. Then n-butyl lithium (2.5 M per 100 mL solution, 29 mmol, 11.6 mL) was added drop-wise to the solution and stirred further for another 20 min at -78°C. The reaction was removed from the dry ice / acetone bath and dry acetone (5.05 g, 87 mmol, 5.8 mL) added. The reaction was stirred for another 20 min before quenching with water and reducing to an aqueous phase. The product was extracted into DCM (3 x 50 mL) and the combined organic layers were dried over magnesium sulphate and reduced. The crude product was further purified by distillation *in vacuo*, to give the pure product as a colourless oil that solidified upon standing. (4.5 g, 57 %). ¹H NMR (CDCl₃, 500 MHz) δ_H 7.98 (s, 2H, Ar-H), 7.79 (s, 1H, Ar-H), 1.65 (s, 6H, -CH₃); ¹⁹F NMR (CDCl₃, 700 MHz) δ_F -62.87 (t, 6F, J_{HF} = 2.5, -CF₃); ¹³C NMR (CDCl₃, 125 MHz, decouple H1 500 MHz) δ_C 32.0 (CH₃-), 72.6 (-C(CH₃)-OH), 121.0 (septet, 1C, J_{CF} = 15), 123.7 (q, 1C, J_{CF} = 272), 125.2 (m), 131.7 (q, 1C, J_{CF} = 131), 151.9; Found C; 47.92; H; 3.68; Calcd for C₁₁H₁₀F₆O; C; 48.54; H; 3.68. GC-MS (EI) m/z 272. Crystal data for **39**: C₁₁ H₁₀ F₆ O, M = 272.19, monoclinic, space group C 2/c (No. 15), a = 23.6068(4), b = 23.5051(4), c = 18.5135(4) Å, V = 9339.1(3) Å³, Z = 32, D_c = 1.549 Mg m⁻³, F₀₀₀ = 4416, Mo Kα radiation, λ = 0.71073 Å, T = 120 K, 2θ_{max} = 52.74°, 40576 reflections collected, 9546 unique (R_{int} = 0.0559). Final *Goof* = 1.039, R1 = 0.0552, wR2 = 0.1349, R indices based on 7653 reflections with I > 2.00σ (I) (refinement on F²), 751 parameters, 639 restraints. Lp and absorption corrections applied, μ = 0.162 mm⁻¹. For Figure and Tables see Appendix C.

(40) Synthesis of 2-(4-fluorophenyl)-2'-(4-methoxyphenyl)-propane



2-(4-Fluorophenyl)-Propan-2-ol (5 g, 32 mmol) in 150 mL of DCM was stirred for 20 min at 0°C. Then add Anisole (3.5 g 32 mmol, 3.53 mL) and Aluminium chloride (8.54 g, 64 mmol) to the solution turning it deep orange/red and stir for 5 hrs at 0°C. Pour the reaction over 100 g ice in HCl (2 M, 20 mL) in a separating funnel and shake until colourless. Extract the organic layer and dry over magnesium sulphate and then reduce to give a crude product (7 g, 89.6 %). Further purification was carried out with column chromatography on silica eluting with hexane / DCM 10:1 giving colourless oil (6.8 g, 87 %). ¹H NMR (CDCl₃, 700 MHz) δ_H 7.19 (dd, 2H, J_{HF/HH} = 5.5, 8.9, Ar-H), 7.14 (d, 2H, J_{HH} = 9.2, Ar-H), 6.95 (t, 2H, J_{HF/HH} = 8.4), 6.83 (d, 2H, J_{HH} = 9.2, Ar-H), 3.80 (s, 3H, -OCH₃), 1.54 (s, 6H, -CH₃); ¹⁹F NMR (CDCl₃, 700 MHz) δ_F -118.21 (tt, 1F, J_{HF} = 5.9, 10.5); ¹³C NMR (CDCl₃, 176 MHz, decouple 1H 700 MHz) δ_C 31.3 (CH₃-), 42.2 (-C(CH₃)₂-), 55.4 (-O-CH₃), 113.6, 114.8 (d, 1C, J_{CF} = 21.1), 127.9, 128.4 (d, 1C, J_{CF} = 7.6), 142.8, 146.9 (d, 1C, J_{CF} = 2.6), 153.6 (Ar C-O), 161.2 (d, 1C, J_{CF} = 243.9); GC-MS (EI) m/z 244. Acc MS (EI): (m/z) Calcd. For C₁₆H₁₇OF: 244.1258 Found 224.1258

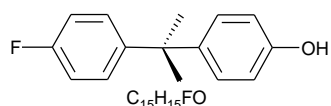
(41) Synthesis of 2-((Bis 3,5-trifluoromethyl)phenyl)-2'-(4-Methoxyphenyl)-Propane



2-((Bis 3,5-trifluoromethyl)phenyl)-propan-2-ol (3.3 g, 12.15 mmol) in 100 mL of DCM was stirred for 20 min at 0°C. Then add anisole (1.31 g, 12.15 mmol, 1.32 mL) and aluminium chloride (3.24 g, 24.3 mmol) to the solution turning it deep orange/red and stir for 5 hrs at 0°C. Pour the reaction over 100 g ice in HCl (2 M, 20 mL) in a separating funnel and shake until colourless. Extract the organic layer and dry over

magnesium sulphate and then reduce to give a crude product (4.2 g, 95.5 %). Further purification was carried out with column chromatography on silica eluting with Hexane / DCM 10:1 giving a colourless oil (3.1 g, 71 %). ^1H NMR (CDCl_3 , 700 MHz) δ_{H} 7.73 (s, 1H, Ar-H), 7.69 (s, 2H, Ar-H), 7.14 (d, 2H, $J_{\text{HH}} = 9.0$, Ar-H), 6.88 (d, 2H, $J_{\text{HH}} = 9.0$, Ar-H), 3.84 (s, 3H, $-\text{CH}_3$), 1.65 (s, 6H, $-\text{CH}_3$); ^{19}F NMR (CDCl_3 , 700 MHz) δ_{F} -62.75 (s, 6F, $-\text{CF}_3$); ^{13}C NMR (CDCl_3 , 125 MHz, decouple H1 500 MHz) δ_{C} 34.3 (CH_3 -), 43.0 ($-\text{C}(\text{CH}_3)_2$ -), 55.5 ($-\text{O}-\text{CH}_3$), 114.0, 120.1 (septet, 1C, $J_{\text{CF}} = 3.8$), 123.8 (q, 1C, $J_{\text{CF}} = 272$), 127.2 (m), 127.9, 131.5 (q, 1C, $J_{\text{CF}} = 32.0$), 140.9, 154.0, 158.2 (Ar C-O); GC-MS (EI) m/z 362. Acc MS (EI): (m/z) Calcd. For $\text{C}_{18}\text{H}_{16}\text{F}_6\text{O}$: 362.1100. Found 362.1103.

(42) Synthesis of 2-(4-fluorophenyl)-2'-(4-hydroxyphenyl)-propane

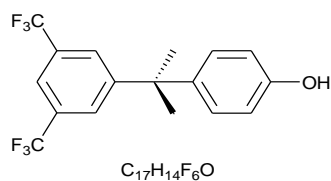


The preparation of this compound was achieved using the method reported in *J. Am. Chem. Soc.*, 2006, **128** (7), 10388.

2-(4-Fluorophenyl)-2-(4-methoxyphenyl)-propane (500 mg, 2 mmol) in dry DCM (30 mL) in an inert atmosphere was placed in an ice bath and stirred for 20 min. Tribromoborane (100 mg, 0.4 mmol, 0.04 mL) in dry DCM (2 mL) was added dropwise from an inert dropping funnel slowly. Once all the tribromoborane solution was added the reaction mixture was stirred for a further 5 min. Bring the reaction up to room temperature and leave to stir for a further 48 hrs. Add a 20 mL of H_2O / MeOH 40:1 solution to quench the reaction. Wash the mixture with DCM (3 X 20 mL) in a separating funnel and combine the organic layers and dry them over magnesium sulphate. Reduce and purify with column chromatography eluting with DCM to yield a brown oil (375 mg, 82 %). ^1H NMR (CDCl_3 , 700 MHz) δ_{H} 7.17 (dd, 2H, $J_{\text{HF/HH}} = 5.4$, 8.8, Ar-H), 7.08 (d, 2H, $J_{\text{HH}} = 8.4$, Ar-H), 6.94 (t, 2H, $J_{\text{HF/HH}} = 8.4$), 6.74 (d, 2H, $J_{\text{HH}} = 8.4$, Ar-H), 4.91 (s, 1H, $-\text{OH}$), 1.64 (s, 6H, $-\text{CH}_3$); ^{19}F NMR (CDCl_3 , 700 MHz) δ_{F} -

118.21 (tt, 1F, $J_{\text{HF}} = 5.9, 9.8$); ^{13}C NMR (CDCl_3 , 176 MHz, decouple H1 700 MHz) δ_{C} 31.3 (CH_3 -), 42.2 ($-\text{C}(\text{CH}_3)_2-$), 114.8 (d, 1C, $J_{\text{CF}} = 20.4$), 128.2, 128.4 (d, 1C, $J_{\text{CF}} = 8.1$), 143.1, 146.8 (d, 1C, $J_{\text{CF}} = 2.6$), 153.6 (C-OH), 161.1 (d, 1C, $J_{\text{CF}} = 244.1$); GC-MS (EI) m/z 230. Acc MS (EI): (m/z) Calcd. For $\text{C}_{15}\text{H}_{15}\text{OF}$: 230.1101 Found 230.1100.

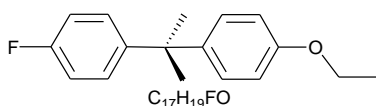
(43) Synthesis of 2-((bis 3,5-trifluoromethyl)phenyl)-2'-(4-hydroxyphenyl)-propane



The preparation of this compound was achieved using the method reported in *J. Am. Chem. Soc.*, 2006, **128** (7), 10388. 2-((Bis 3,5-trifluoromethyl)phenyl)-2-(4-

methoxyphenyl)-propane (2.4 g, 6.63 mmol) in dry DCM (50 mL) in an inert atmosphere was placed in an ice bath and stirred for 20 min. Tribromoborane (333 mg, 1.33 mmol, 0.13 mL) in dry DCM (5 mL) was added drop-wise from an inert dropping funnel slowly. Once all the tribromoborane solution was added the reaction mixture was stirred for a further 5 min. Bring the reaction up to room temperature and leave to stir for a further 48 hrs. Add a 30 mL of H_2O / MeOH 40:1 solution to quench the reaction. Wash the mixture with DCM (3 X 30 mL) in a separating funnel and combine the organic layers and dry them over magnesium sulphate. Reduce and purify with column chromatography eluting with DCM to yield a brown oil (1.85 g, 80 %). ^1H NMR (CDCl_3 , 700 MHz) δ_{H} 7.73 (s, 1H, Ar-H), 7.69 (s, 2H, Ar-H), 7.09 (d, 2H, $J_{\text{HH}} = 8.7$, Ar-H), 6.81 (d, 2H, $J_{\text{HH}} = 8.7$, Ar-H), 1.73 (s, 6H, $-\text{CH}_3$); ^{19}F NMR (CDCl_3 , 700 MHz) δ_{F} -62.75 (s, 6F, $-\text{CF}_3$); ^{13}C NMR (CDCl_3 , 125 MHz, Decouple 1H 500 MHz) δ_{C} 31.0 (CH_3 -), 43.0 ($-\text{C}(\text{CH}_3)_2-$), 120.1 (septet, 1C, $J_{\text{CF}} = 3.9$), 123.5 (q, 1C, $J_{\text{CF}} = 271.9$), 127.2 (m), 128.2, 131.5 (q, 1C, $J_{\text{CF}} = 31.7$) 141.1, 153.9, 154.1 ($-\text{C}-\text{OH}$); GC-MS (EI) m/z 348. Acc MS (EI): (m/z) Calcd. For $\text{C}_{17}\text{H}_{14}\text{F}_6\text{O}$: 348.0943. Found 348.0944.

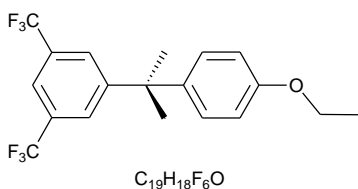
(44) Synthesis of 2-(4-fluorophenyl)-2'-(4-ethoxyphenyl)-propane



2-(4-Fluorophenyl)-2-(4-hydroxyphenyl)-propane (0.5 g, 2.05mmol), iodoethane (0.384 g, 2.46 mmol, 0.25 mL)

and potassium tert-butoxide (0.689 mg, 6.15 mmol) were added to dry acetone (50 mL) and refluxed over night under an inert atmosphere. Reduce the solution and extract the product in DCM (3 x 50 mL) and combine the organic layers. Dry over magnesium sulphate and reduce giving crude orange/yellow oil (0.45 g, 81 %). Purified further with column chromatography eluting with DCM yielding a colourless oil (0.4 g, 76 %). ^1H NMR (CDCl_3 , 700 MHz) δ_{H} 7.18 (dd, 2H, $J_{\text{HF/HH}} = 5.5, 8.9$, Ar-H), 7.12 (d, 2H, $J_{\text{HH}} = 9.1$, Ar-H), 6.94 (t, 2H, $J_{\text{HF/HH}} = 8.8$), 6.81 (d, 2H, $J_{\text{HH}} = 9.1$, Ar-H), 4.01 (q, 2H, $J_{\text{HH}} = 7.1$, $-\text{CH}_2-$), 1.65 (s, 6H, $-\text{CH}_3$), 1.41 (t, 3H, $J_{\text{HH}} = 7.1$, $-\text{CH}_3$); ^{19}F NMR (CDCl_3 , 700 MHz) δ_{F} -118.27 (tt, 1F, $J_{\text{HF}} = 4.8, 9.1$); ^{13}C NMR (CDCl_3 , 176 MHz, decouple 1H 700 MHz) δ_{C} 15.1 (CH_3-), 31.3 (CH_3-), 42.1 ($\text{CH}_3\text{-C}^*\text{-CH}_3$), 63.6 ($-\text{CH}_2\text{-O-}$), 114.1, 114.8 (d, 1C, $J_{\text{CF}} = 21.1$), 127.9, 128.5 (d, 1C, $J_{\text{CF}} = 7.6$), 142.7, 146.9 (d, 1C, $J_{\text{CF}} = 3.3$), 157.1 (Ar C-O), 161.1 (d, 1C, $J_{\text{CF}} = 243.9$); GC-MS (EI) m/z 258. Acc MS (EI): (m/z) Calcd. For $\text{C}_{17}\text{H}_{19}\text{FO}$: 258.1414. Found 258.1414

(45) Synthesis of 2-((Bis 3,5-trifluoromethyl)phenyl)-2'-(4-ethoxyphenyl)-propane

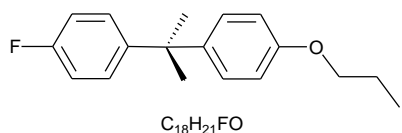


2-((Bis 3,5-trifluoromethyl) phenyl)-2-(4-hydroxyphenyl)-propane (0.5 g, 1.44 mmol), iodoethane (0.268 g, 1.72 mmol, 0.14 mL) and potassium tert-butoxide (0.484 mg,

4.32 mmol) were added to dry acetone (50 mL) and refluxed over night under an inert atmosphere. Reduce the solution and extract the product in DCM (3 x 50 mL) and combine the organic layers. Dry over magnesium sulphate and reduce giving crude orange/yellow oil (0.5 g, 92 %). Purified further with column chromatography eluting

with DCM yielding a colourless oil (0.35 g, 65 %). ^1H NMR (CDCl_3 , 700 MHz) δ_{H} 7.70 (s, 1H, Ar-H), 7.67 (s, 2H, Ar-H), 7.10 (d, 2H, $J_{\text{HH}} = 8.9$, Ar-H), 6.84 (d, 2H, $J_{\text{HH}} = 8.9$, Ar-H), 3.92 (q, 2H, $J_{\text{HH}} = 6.7$, $-\text{CH}_2-$), 1.71 (s, 6H, $-\text{CH}_3$), 1.05 (t, 3H, $J_{\text{HH}} = 7.4$, $-\text{CH}_3$); ^{19}F NMR (CDCl_3 , 700 MHz) δ_{F} -62.73 (s, 6F, $-\text{CF}_3$); ^{13}C NMR (CDCl_3 , 125 MHz, decouple H1 500 MHz) δ_{C} 22.9 (CH_3-), 31.0 (CH_3-), 43.0 ($\text{CH}_3-\text{C}^*-\text{CH}_3$), 69.9 ($-\text{CH}_2-\text{O}-$), 114.5, 120.0 (septet, 1C, $J_{\text{CF}} = 3.9$), 123.7 (q, 1C, $J_{\text{CF}} = 273.4$), 127.2 (m), 127.8, 131.4 (q, 1C, $J_{\text{CF}} = 33.1$), 140.6, 154.0, 157.8 (Ar C-O); GC-MS (EI) m/z 375. Acc MS (EI): (m/z) Calcd. For $\text{C}_{29}\text{H}_{18}\text{F}_6\text{O}$: 376.1262 Found 376.1266

(46) Synthesis of 2-(4-fluorophenyl)-2'-(4-propoxyphenyl)-propane

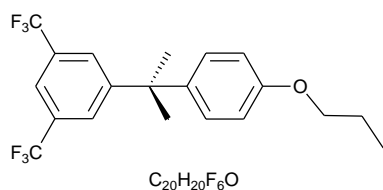


2-(4-Fluorophenyl)-2-(4-hydroxyphenyl)-propane (0.5 g, 2.05 mmol), bromopropane (0.384 g, 2.46 mmol,

0.25 mL) and potassium tert-butoxide (0.689 mg, 6.15 mmol) were added to dry acetone (50 mL) and refluxed over night under an inert atmosphere. Reduce the solution and extract the product in DCM (3 x 50 mL) and combine the organic layers. Dry over magnesium sulphate and reduce giving crude orange/yellow oil (0.557 g, 95 %). Purified further with column chromatography eluting with DCM yielding a colourless oil (0.385 g, 66 %). ^1H NMR (CDCl_3 , 700 MHz) δ_{H} 7.19 (dd, 2H, $J_{\text{HF/HH}} = 5.4, 9.0$, Ar-H), 7.12 (d, 2H, $J_{\text{HH}} = 8.8$, Ar-H), 6.94 (t, 2H, $J_{\text{HF/HH}} = 8.8$), 6.82 (d, 2H, $J_{\text{HH}} = 8.8$, Ar-H), 3.90 (t, 2H, $J_{\text{HH}} = 6.7$, $-\text{CH}_2-$), 1.80 (sextet, 2H, $J_{\text{HH}} = 7.3$, $-\text{CH}_2-$), 1.65 (s, 6H, $-\text{CH}_3$), 1.04 (t, 3H, $J_{\text{HH}} = 7.1$, $-\text{CH}_3$); ^{19}F NMR (CDCl_3 , 700 MHz) δ_{F} -118.27 (tt, 1F, $J_{\text{HF}} = 5.2, 9.1$); ^{13}C NMR (CDCl_3 , 176 MHz, decouple 1H 700 MHz) δ_{C} 10.8 (CH_3-), 22.9 ($-\text{CH}_2-$), 31.3 (CH_3-), 42.1 ($\text{CH}_3-\text{C}^*-\text{CH}_3$), 69.7 ($-\text{CH}_2-\text{O}-$), 114.1, 114.3 (d, 1C, $J_{\text{CF}} = 20.4$), 127.9, 128.5 (d, 1C, $J_{\text{CF}} = 8.3$), 142.6, 147.0 (d, 1C, $J_{\text{CF}} = 2.8$), 157.3 (Ar C-O),

161.1 (d, 1C, $J_{CF} = 243.9$); GC-MS (EI) m/z 272. Acc MS (EI): (m/z) Calcd. For $C_{18}H_{21}OF$: 272.1571. Found 272.1570.

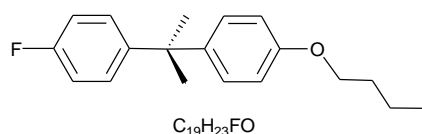
(47) Synthesis of 2-((bis 3,5-trifluoromethyl)phenyl)-2'-(4-propoxyphenyl)-propane



2-((Bis 3,5-trifluoromethyl)phenyl)-2-(4-hydroxyphenyl)-propane (0.5 g, 1.44 mmol), bromopropane (0.212 g, 1.72 mmol, 0.16 mL) and

potassium tert-butoxide (0.484 mg, 4.32 mmol) were added to dry acetone (50 mL) and refluxed over night under an inert atmosphere. Reduce the solution and extract the product in DCM (3 x 50 mL) and combine the organic layers. Dry over magnesium sulphate and reduce giving a crude orange/yellow oil (0.55 g, 98 %). Purified further with column chromatography eluting with DCM yielding a colourless oil (0.335 g, 60 %). 1H NMR ($CDCl_3$, 700 MHz) δ_H 7.69 (s, 1H, Ar-H), 7.66 (s, 2H, Ar-H), 7.08 (d, 2H, $J_{HH} = 8.7$, Ar-H), 6.83 (d, 2H, $J_{HH} = 8.7$, Ar-H), 3.91 (t, 2H, $J_{HH} = 6.7$, $-CH_2-$), 1.80 (sextet, 2H, $J_{HH} = 6.9$, $-CH_2-$), 1.70 (s, 6H, $-CH_3$), 1.03 (t, 3H, $J_{HH} = 7.4$, $-CH_3$); ^{19}F NMR ($CDCl_3$, 700 MHz) δ_F -62.74 (s, 6F, $-CF_3$); ^{13}C NMR ($CDCl_3$, 176 MHz, decouple H1 700 MHz) δ_C 10.7 (CH_3-), 22.8 ($-CH_2-$), 30.9 (CH_3-), 43.0 ($CH_3-C^*-CH_3$), 69.9 ($-CH_2-O-$), 114.5, 120.0 (septet, 1C, $J_{CF} = 3.8$), 123.8 (q, 1C, $J_{CF} = 273.4$), 127.1 (m), 127.8, 131.4 (q, 1C, $J_{CF} = 32.2$), 140.6, 154.0, 157.8 (Ar C-O-); GC-MS (EI) m/z 390. Acc MS (EI): (m/z) Calcd. For $C_{20}H_{20}F_6O$: 390.1418 Found 390.1421

(48) Synthesis of 2-(4-fluorophenyl)-2'-(4-butoxyphenyl)-propane

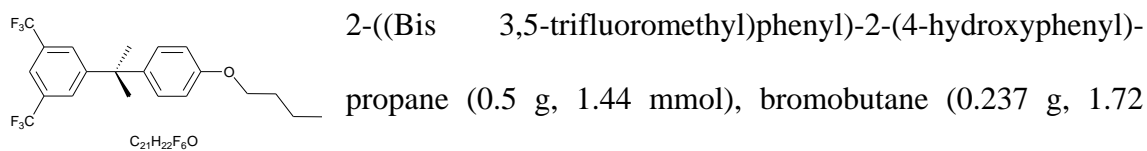


2-(4-Fluorophenyl)-2-(4-hydroxyphenyl)-propane (0.8 g, 3.48 mmol), bromobutane (0.572 g, 4.18

mmol, 0.45 mL) and potassium tert-butoxide (1.17 mg, 10.44 mmol) were added to dry

acetone (50 mL) and refluxed over night under an inert atmosphere. Reduce the solution and extract the product in DCM (3 x 50 mL) and combine the organic layers. Dry over magnesium sulphate and reduce giving crude orange/yellow oil (0.846 g, 85 %). Purified further with column chromatography eluting with DCM yielding a colourless oil (0.701 g, 70 %). ¹H NMR (CDCl₃, 700 MHz) 7.18 (dd, 2H, J_{HF/HH} = 5.2, 8.6, Ar-H), 7.12 (d, 2H, J_{HH} = 8.8, Ar-H), 6.94 (t, 2H, J_{HF/HH} = 8.6), 6.81 (d, 2H, J_{HH} = 8.8, Ar-H), 3.94 (t, 2H, J_{HH} = 6.5, -CH₂-), 1.76 (quintet, 2H, J_{HH} = 6.5, -CH₂-), 1.65 (s, 6H, -CH₃), 1.49 (sextet, 2H, J_{HH} = 6.5, -CH₂-), 0.98 (t, 3H, J_{HH} = 6.5, -CH₃); ¹⁹F NMR (CDCl₃, 700 MHz) -118.28 (tt, 1F, J_{HF} = 5.4, 9.1); ¹³C NMR (CDCl₃, 176 MHz, decouple H1 700 MHz) 14.1 (CH₃-), 19.5 (-CH₂-), 31.3 (CH₃-), 31.6 (-CH₂-), 42.1 (CH₃-C*-CH₃), 67.8 (-CH₂-O-), 114.1, 114.8 (d, 1C, J_{CF} = 20.4), 127.9, 128.5 (d, 1C, J_{CF} = 8.3), 142.6, 147.0 (d, 1C, J_{CF} = 2.8), 157.3 (Ar C-O-), 161.1 (d, 1C, J_{CF} = 243.9); GC-MS (EI) m/z 286. Acc MS (EI): (m/z) Calcd. For C₁₉H₂₃O₂F: 286.1727. Found 286.1731

(49) Synthesis of 2-((bis 3,5-trifluoromethyl)phenyl)-2'-(4-butoxyphenyl)-propane



acetone (50 mL) and refluxed over night under an inert atmosphere. Reduce the solution and extract the product in DCM (3 x 50 mL) and combine the organic layers. Dry over magnesium sulphate and reduce giving crude orange/yellow oil (0.524 g, 90 %). Purified further with column chromatography eluting with DCM yielding a colourless oil (0.406 g, 70 %). ¹H NMR (CDCl₃, 700 MHz) 7.74 (s, 1H, Ar-H), 7.71 (s, 2H, Ar-H), 7.13 (d, 2H, J_{HH} = 8.9, Ar-H), 6.88 (d, 2H, J_{HH} = 8.9, Ar-H), 3.99 (t, 2H, J_{HH} = 6.4, -CH₂-), 1.81 (quintet, 2H, J_{HH} = 7.0, -CH₂-), 1.75 (s, 6H, -CH₃), 1.54 (sextet, 2H, J_{HH} =

7.6, -CH₂-), 1.02 (t, 3H, J_{HH} = 7.5, -CH₃); ¹⁹F NMR (CDCl₃, 700 MHz) -62.76 (s, 6F, -CF₃); ¹³C NMR (CDCl₃, 125 MHz, decouple H1 500 MHz) 14.1 (CH₃-), 19.5 (-CH₂-), 31.0 (CH₃-), 31.6 (-CH₂-), 43.0 (CH₃-C*-CH₃), 67.9 (-CH₂-O-), 114.5, 120.0 (septet, 1C, J_{CF} = 3.6), 123.8 (q, 1C, J_{CF} = 273.3), 127.2 (m), 127.9, 131.4 (q, 1C, J_{CF} = 32.8), 140.6, 154.0, 157.8 (Ar C-O-); GC-MS (EI) m/z 404. Acc MS (EI): (m/z) Calcd. For C₂₁H₂₂F₆O: 404.1575 Found 404.1572

5.2. References

1. S. Toyota, T. Yamamori, M. Asakura and M. Oki, *Bull. Chem. Soc. Jpn.*, 2000, **73** (1), 210.
2. B. Becker, A. Bohnen, M. Ehrenfreund, W. Wohlfarth, Y. Sakata, W. Huber, K. Muellen, *J. Am. Chem. Soc.*, 1991, **113** (4), 1121.
3. H. Masuhara, Y. Maeda, H. Nakajo, N. Mataga, K. Tomita, H. Tatemitsu, Y. Sakata, S. Misumi, *J. Am. Chem. Soc.*, 1981, **103** (3), 634

Chapter 6

Summary and Future Work

6.1 Project Summary

- A series of novel dopants, designed to act as guests dopants for incorporation into LC hosts with a view to increasing the rate of switching on/off of LC devices, have been synthesised to electronic grade purity. The guest molecules have been categorised based upon the linker groups used to join two aromatic rings and various head and tail moieties.
- Electro-optical measurements have been performed on devices using the standard conditions developed by Sony Europe to determine the effects on dopants on the switching times of the host LC in devices. These results have indicated that the novel series of compounds in which the two aromatic rings are linked by a non-linear group that imports a '*bite angle*' between them have shown more promise than the rigid linear acetylenic moiety. The most favoured dopant is that with ether linking the two rings. However the results are only preliminary and suggest that the areas in which research should be focused for a more in-depth analysis of what design features are favoured for dopants of LC hosts. These further experiments should also examine the role of the head and tail groups have on the response times, especially the length and type of alkyl/alkoxy tail.
- Preliminary Raman spectroscopic studies have indicated that it is possible to uniquely identify the host and guest compounds by their spectroscopic signatures. Time-resolved studies have allowed the identification and the ability to study the rates of alignments of individual materials within the cell during the switching of

the LC devices. Thus, this approach uniquely provides kinetic switching data of the motion of guest and host during the turn on and off of the LC cell. It has also provided the ability to determine information about the mechanistic details of the switching process, in particular that both the guest and host species move/reorientate simultaneously.

6.2 Future Work

- This project has shown guest (dopant) molecules for LC devices can be designed. The next step into the molecular design of guest molecules would be to focus upon the '*bite angle*' of the linker group, extending the range of examples available beyond the alkyl and ether groups. The design of the molecules acting as guests in LC hosts would need further consideration to the type of alkyl/alkoxy tail. It is suggested that short chains are used for tails as it is with these we had most success, with the propyl tail being optimal. Whilst the head group would be bromo/fluorinated arenes which is ideal for dielectrically negative LCs (the most predominant host used today in LCDs) and also had shown positive results in the EO measurements and the switching times.
- The Raman experiment was a success as it enabled the independent observation of the mechanistic profiles of the guest and host during the switching of the LC device. However, the major limitation of the experiment was the relatively low time resolution of our equipment. Because we only had a continuous wave laser setup equipped with a millisecond mechanical shutter acting as the time resolution was very limited. This meant the whole experiment had poor temporal resolution and

required long data acquisition periods. In the future this could be significantly improved by using a pulsed laser system (e.g. Q-switched Nd:YAG laser) which would provide better time resolution ($<10\text{ns}$) and shorter data acquisition times due to the higher intensity of laser. This would not be without some challenges; due in part to the passing of an intense laser through the optics of a confocal microscope setup could damage the optics and/or the LC device. The ability of this type of equipment will increase resolution of the kinetic switch of the LC cell and give rise to greater detail of the mechanistic switch and the readiness to use small cell gap in LC cells.

Chapter 7

Appendices

Appendix A

EO Data for Chapter 3

APPENDIX A

Figure 1 – Gaussian calculations representing an O linker viewing it from front and side view and looking down the O – Ph bond respectively.

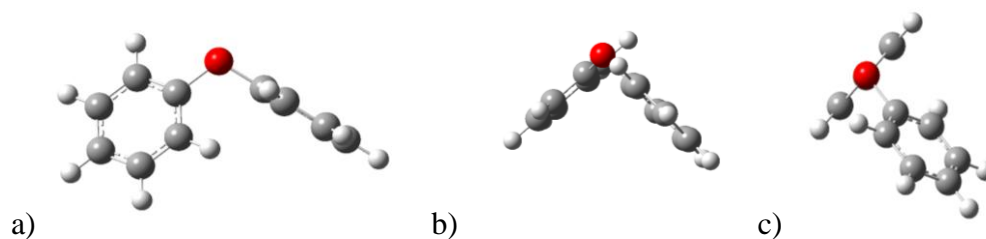


Figure 2 – Gaussian calculations representing a CH₂ linker viewing it from front and side view and looking down the CH₂ – Ph bond respectively.

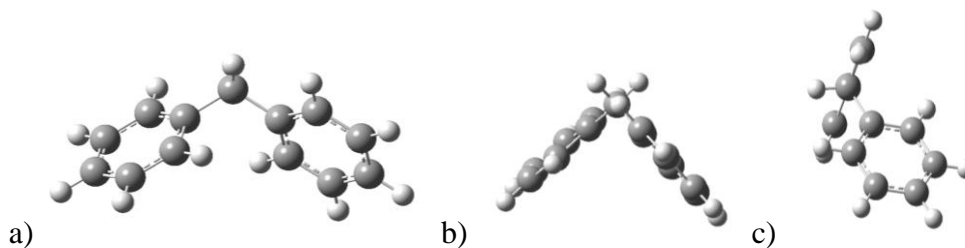


Figure 3 – Gaussian calculations representing a CMe₂ linker viewing it from front and side view and looking down the CMe₂ – Ph bond respectively.

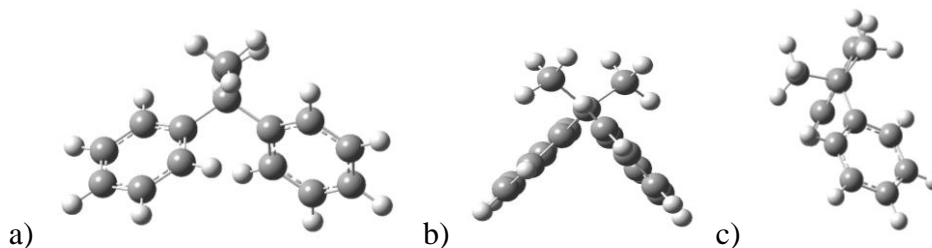


Figure 4 – Gaussian calculations representing a CO linker viewing it from front and side view and looking down the CO – Ph bond respectively.

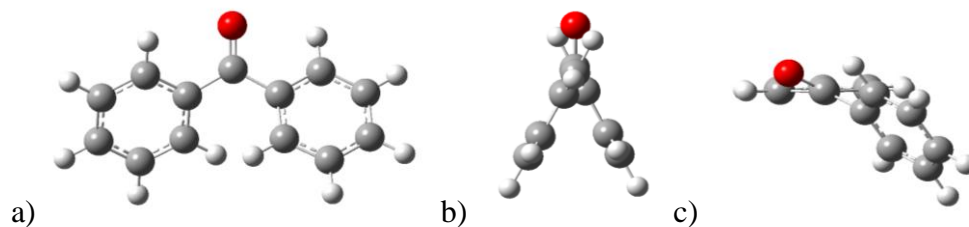


Figure 5 – Gaussian calculations representing a Dioxolane linker viewing it from front and side view and looking down the Dioxolane – Ph bond respectively.

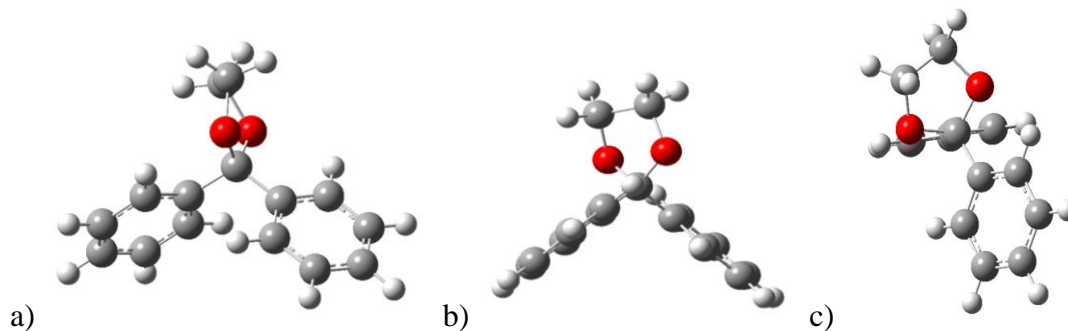


Figure 6a – Calculated rise time for 1% of dopant **11** in –LC host

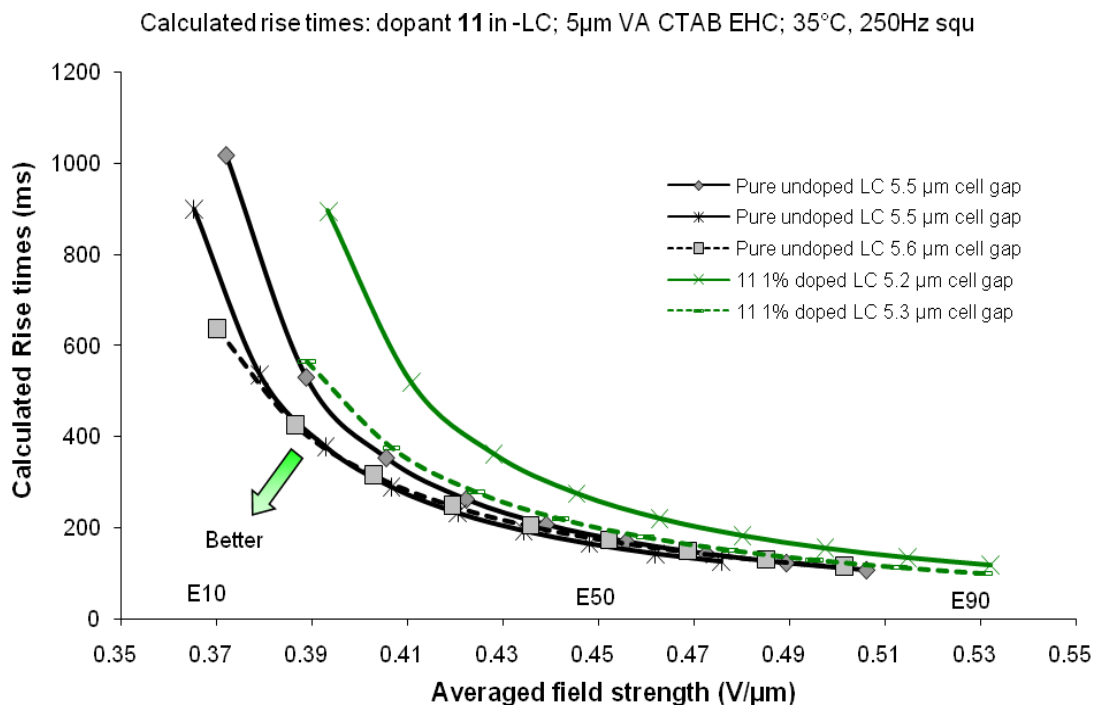


Figure 6b – Calculated rise time for 1% of dopant **12** in –LC host

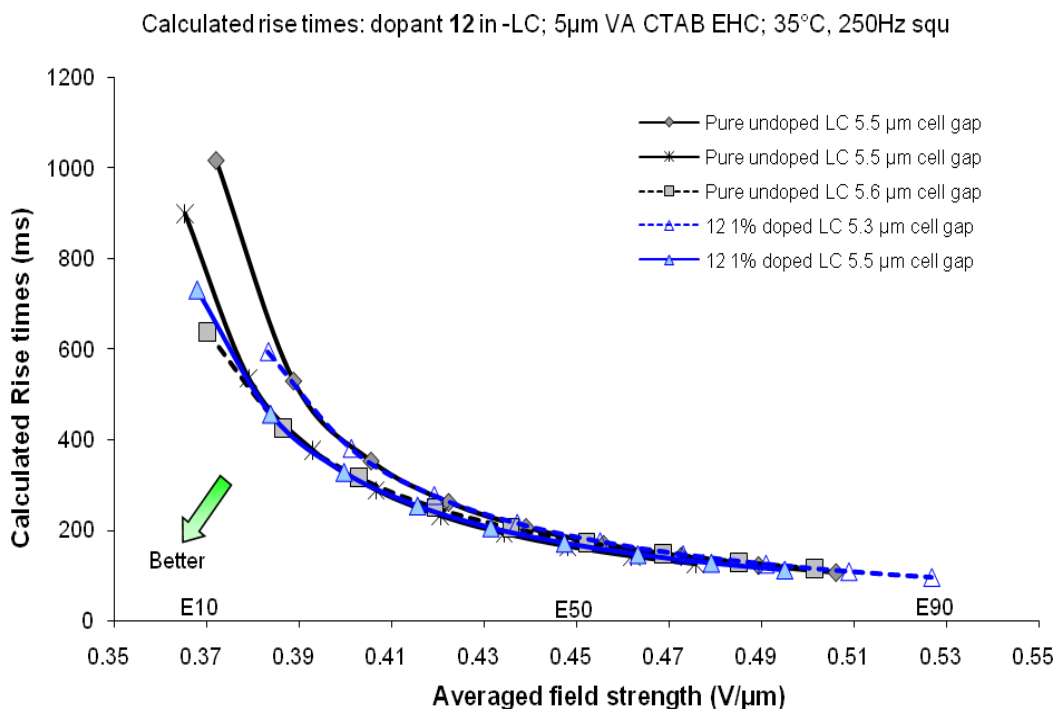


Figure 6c – Calculated rise time for 1% of dopant **13** in –LC host

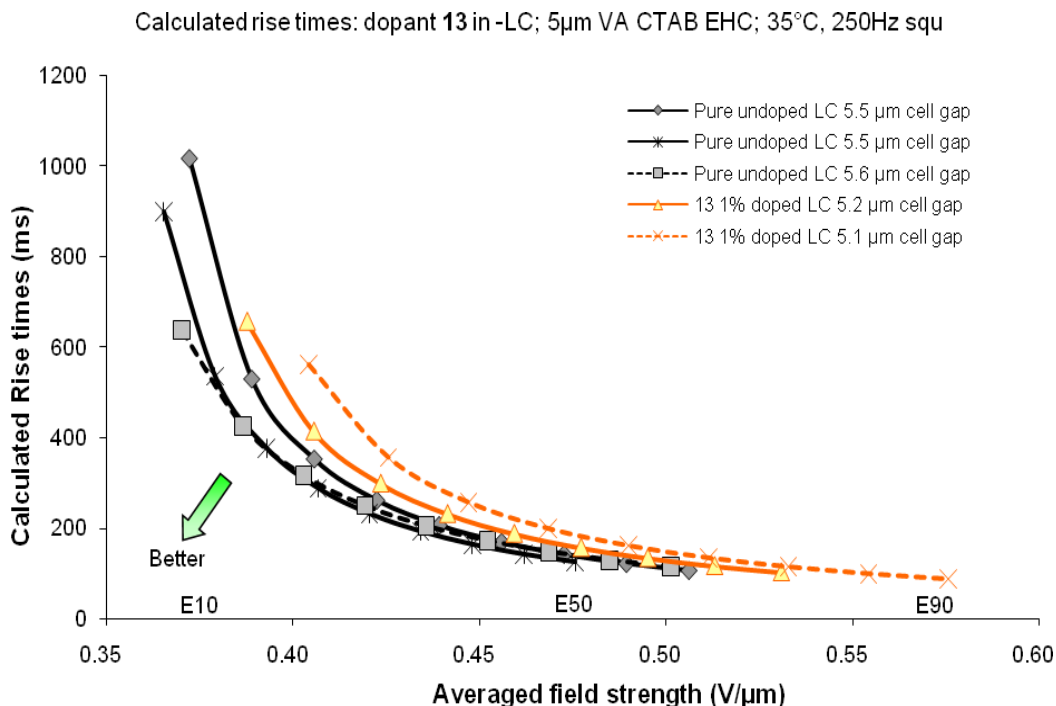


Figure 6d – Calculated rise time for 1% of dopant **14** in –LC host

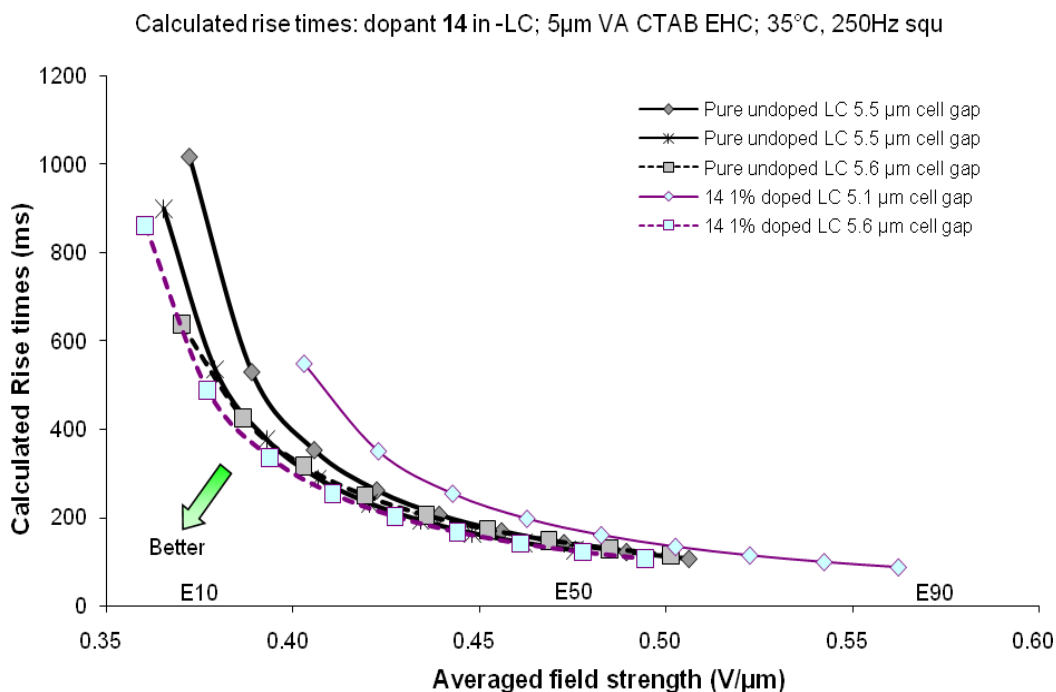


Figure 6e – Calculated rise time for 1% of dopant **15** in –LC host

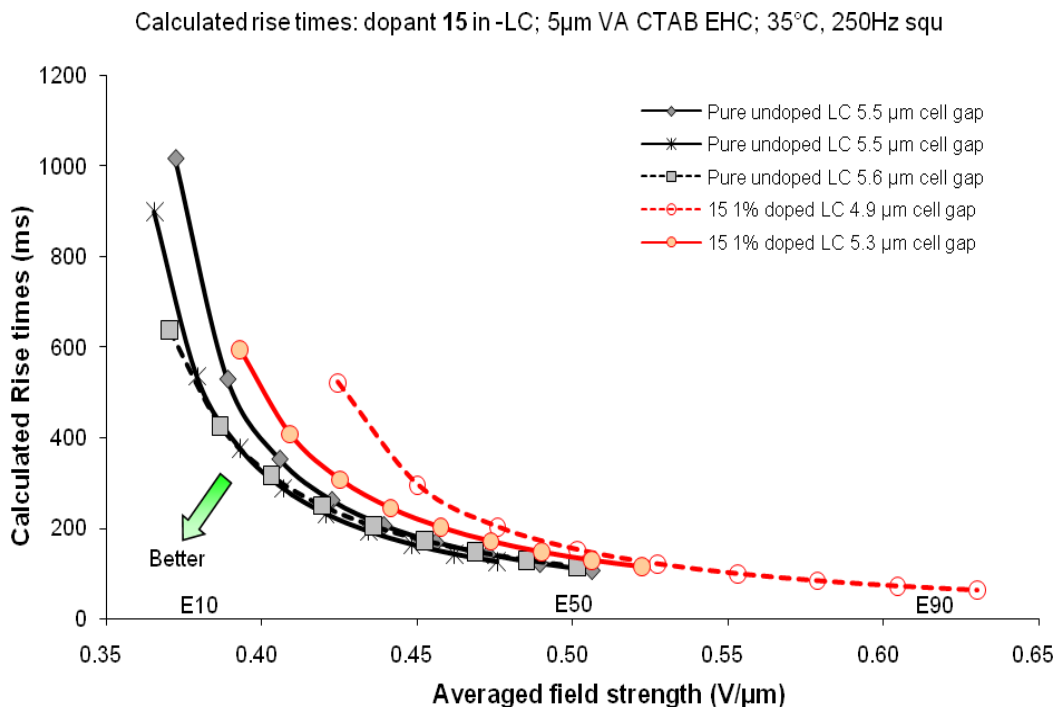


Figure 7 – Threshold electric field data for dopants **11-15** in –LC host

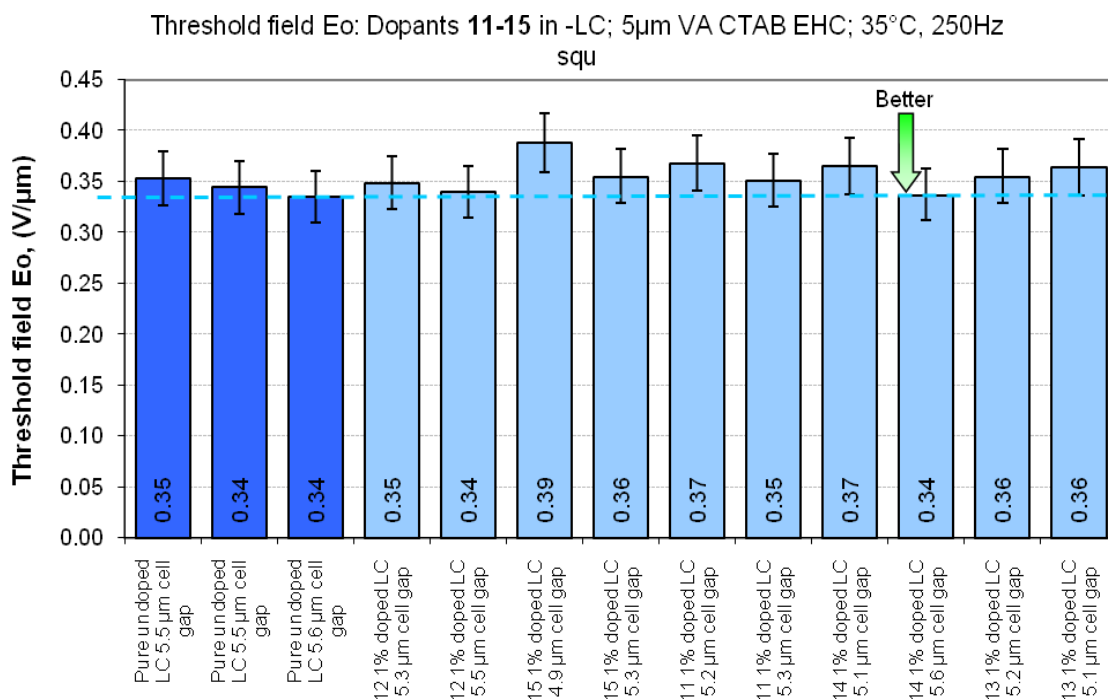


Figure 8 – E10 & E90 data for dopants **11-15** in –LC host

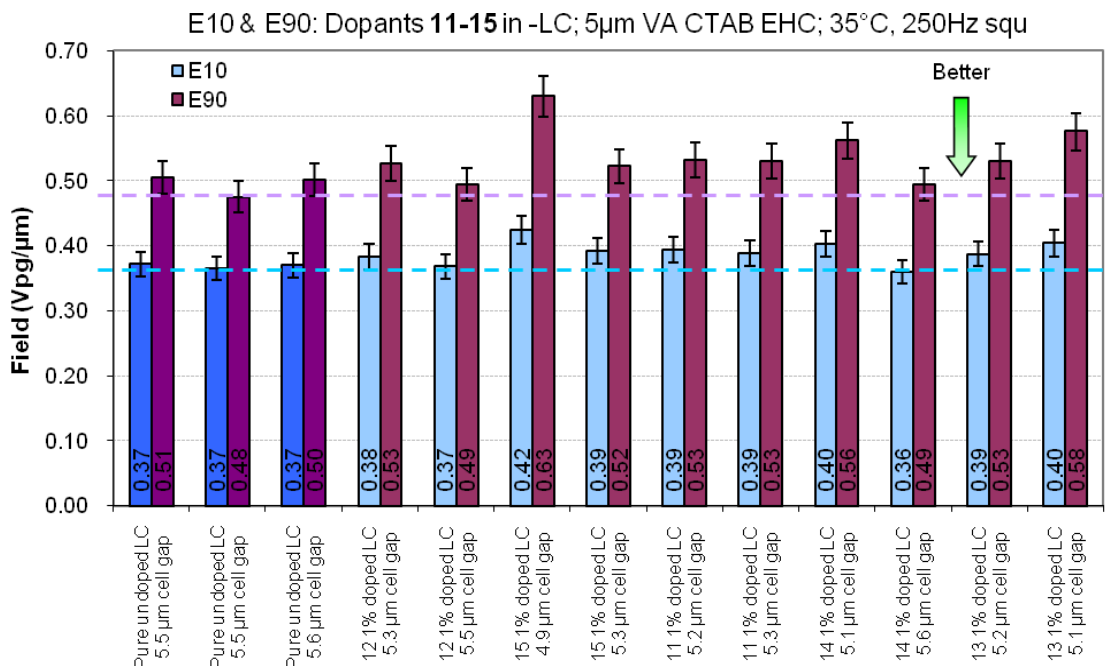


Figure 9a – Calculated decay time for 1% of dopant **11** in –LC host

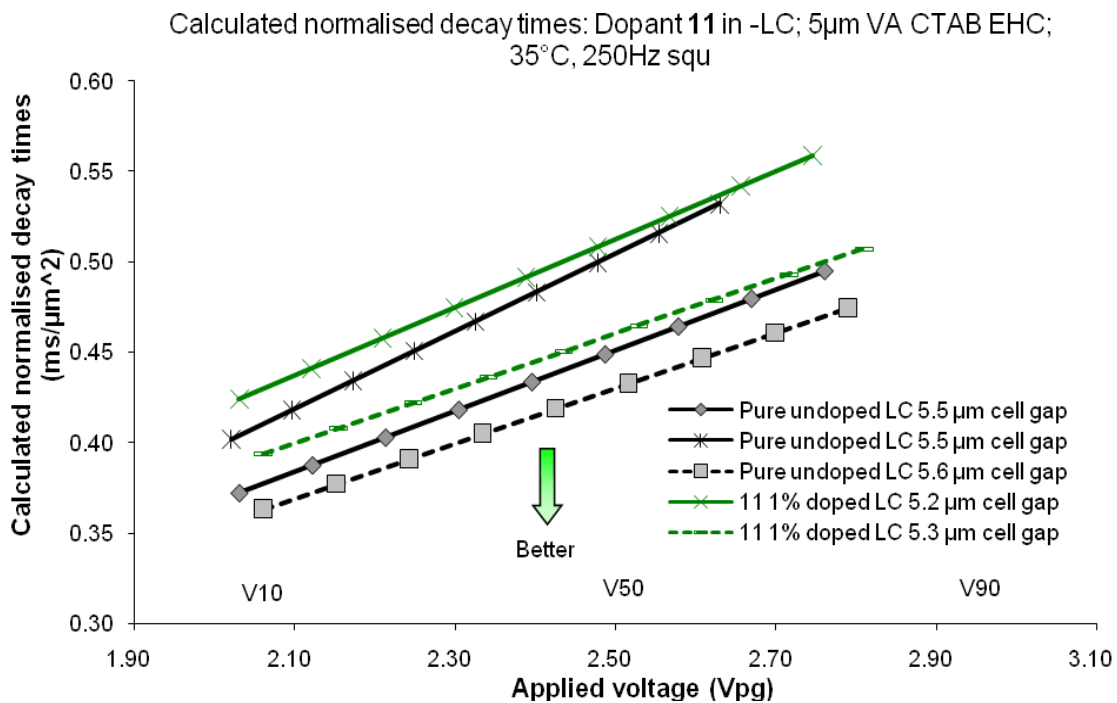


Figure 9b - Calculated decay time for 1% of dopant **12** in -LC host

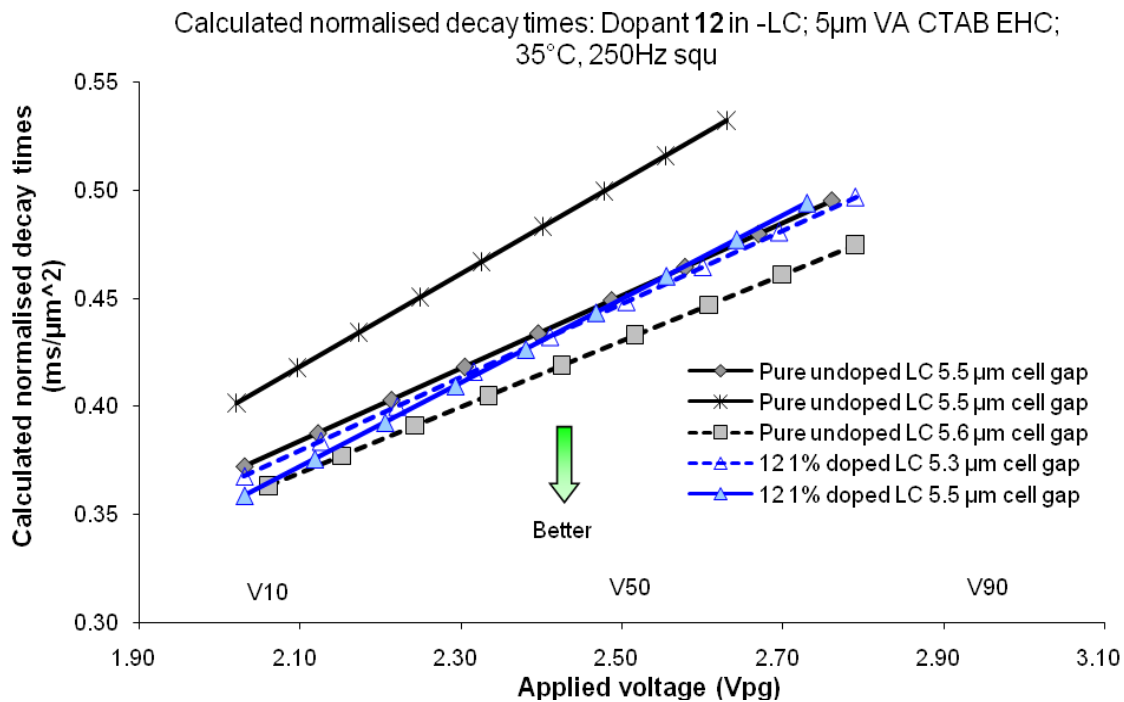


Figure 9c - Calculated decay time for 1% of dopant **13** in -LC host

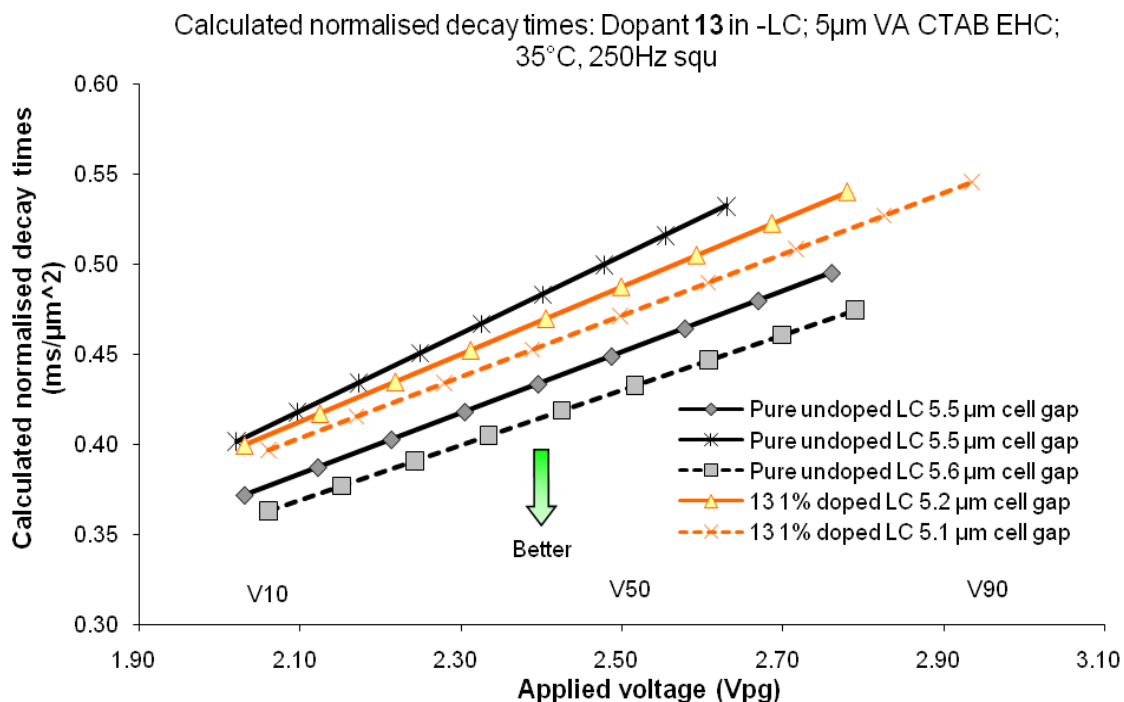


Figure 9d - Calculated decay time for 1% of dopant **14** in -LC host

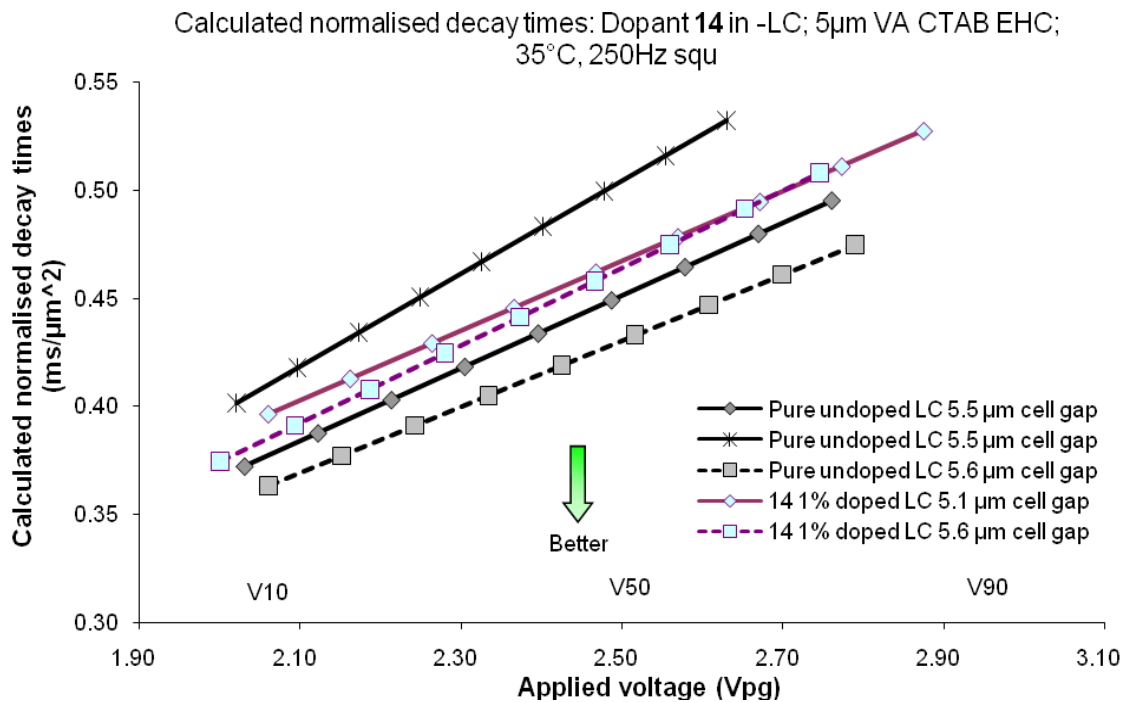


Figure 9e - Calculated decay time for 1% of dopant **15** in -LC host

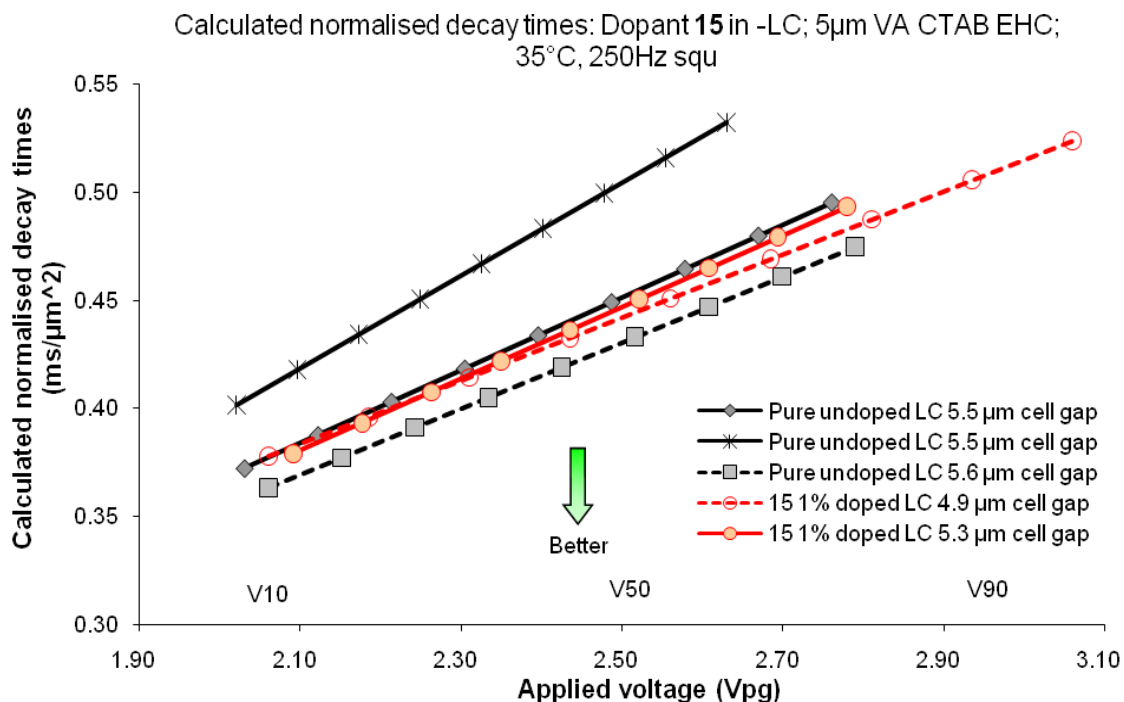


Figure 10 – VHR data for dopants **16** -**17** in -LC host

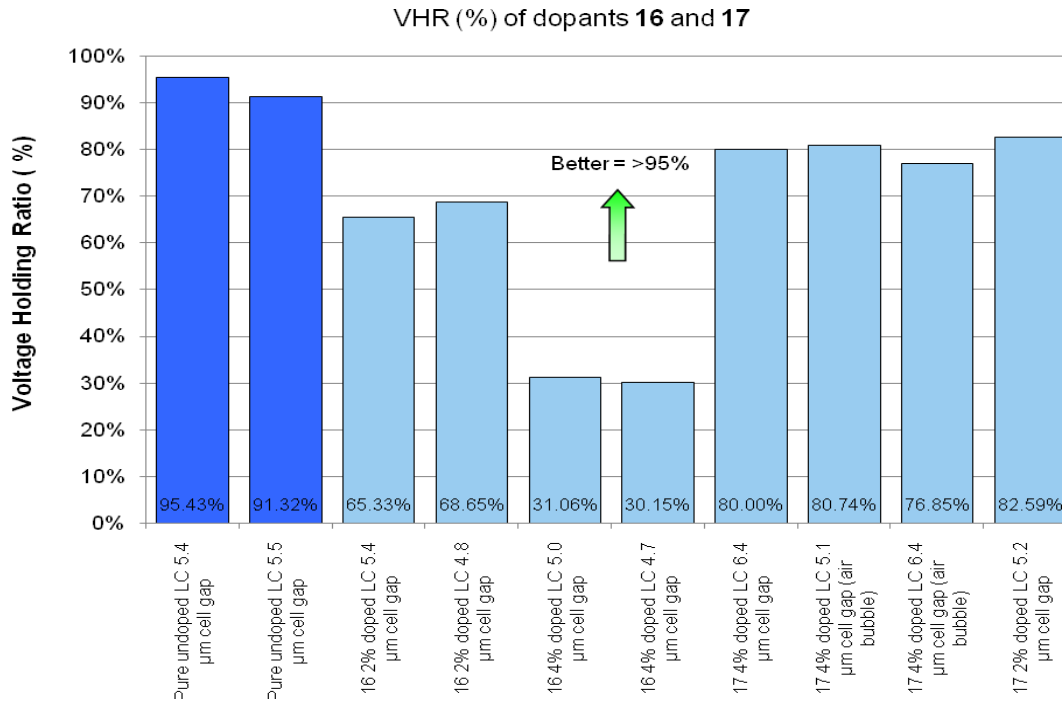


Figure 11a - Calculated rise time for 1% of dopant **11** in +LC host

Calculated rise times: dopant **11** in +LC; 10μm TN PI EHC; 35°C, 250Hz squ

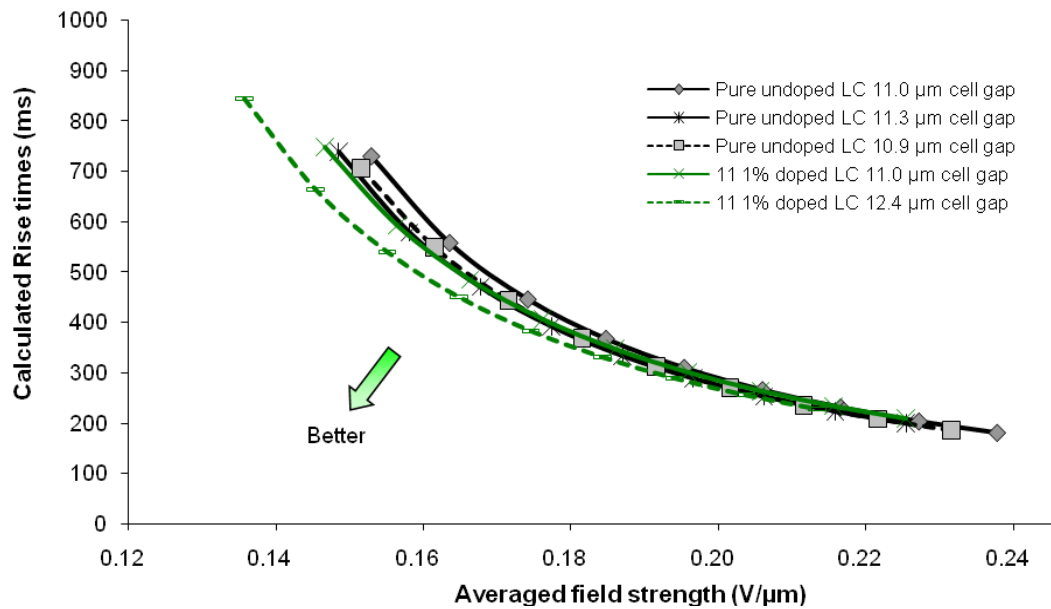


Figure 11b - Calculated rise time for 1% of dopant **12** in +LC host

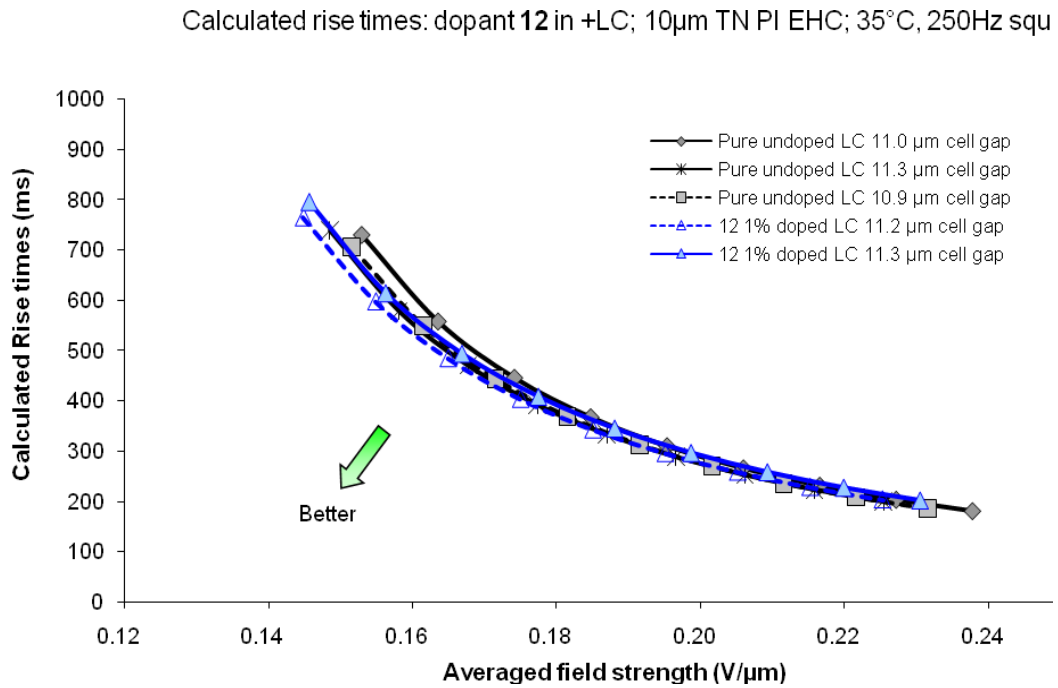


Figure 11c - Calculated rise time for 1% of dopant **13** in +LC host

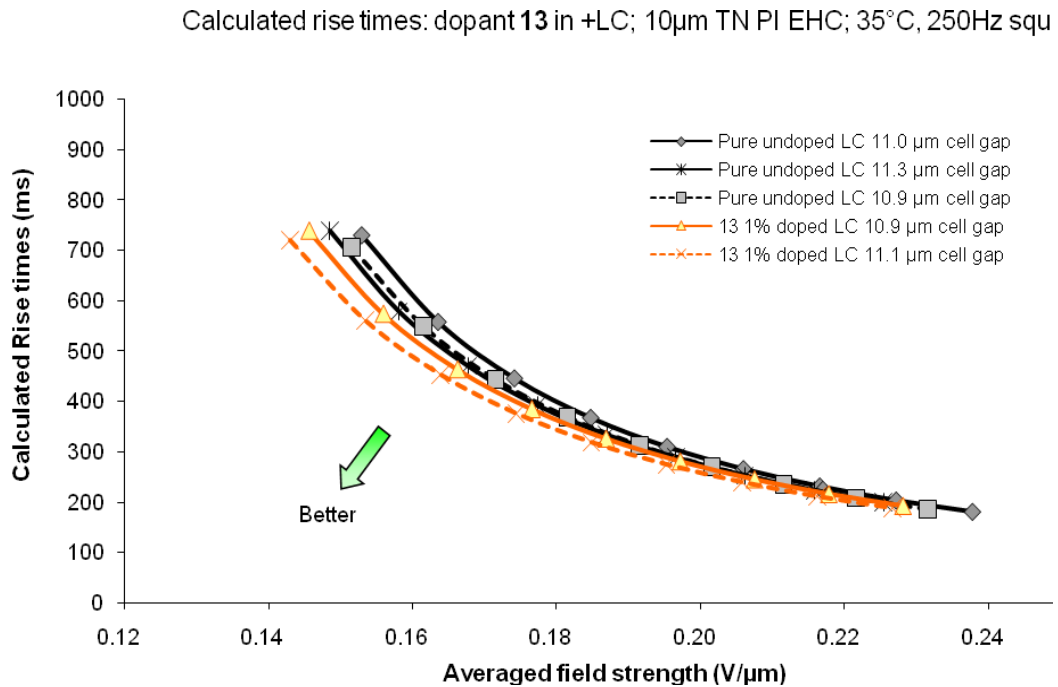


Figure 11d - Calculated rise time for 1% of dopant **14** in +LC host

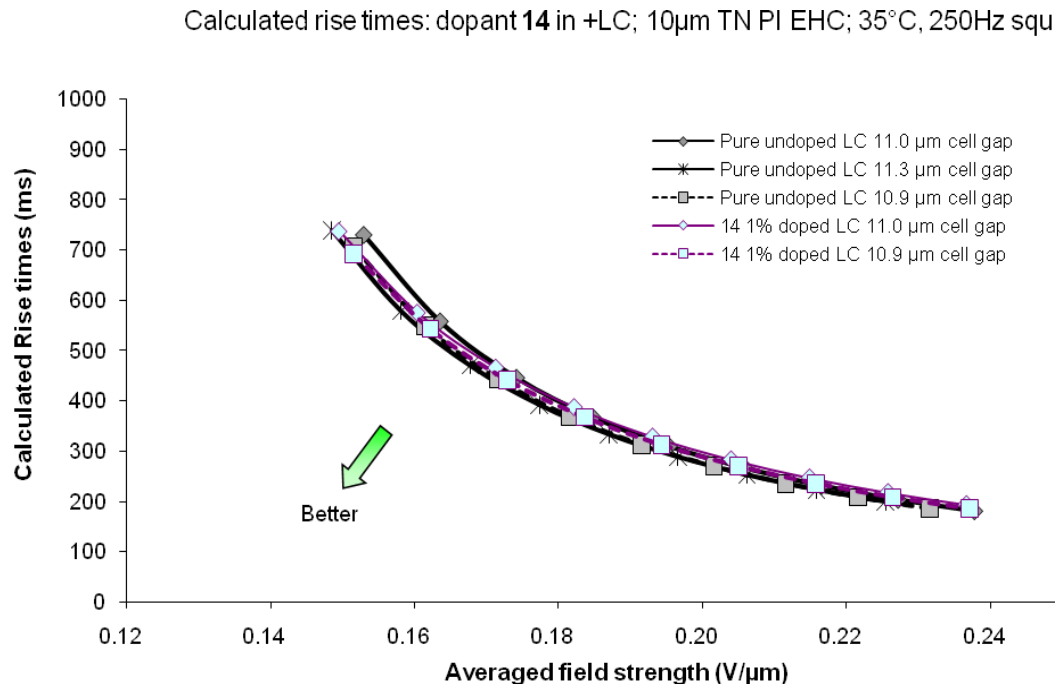


Figure 11e - Calculated decay time for 1% of dopant **15** in +LC host

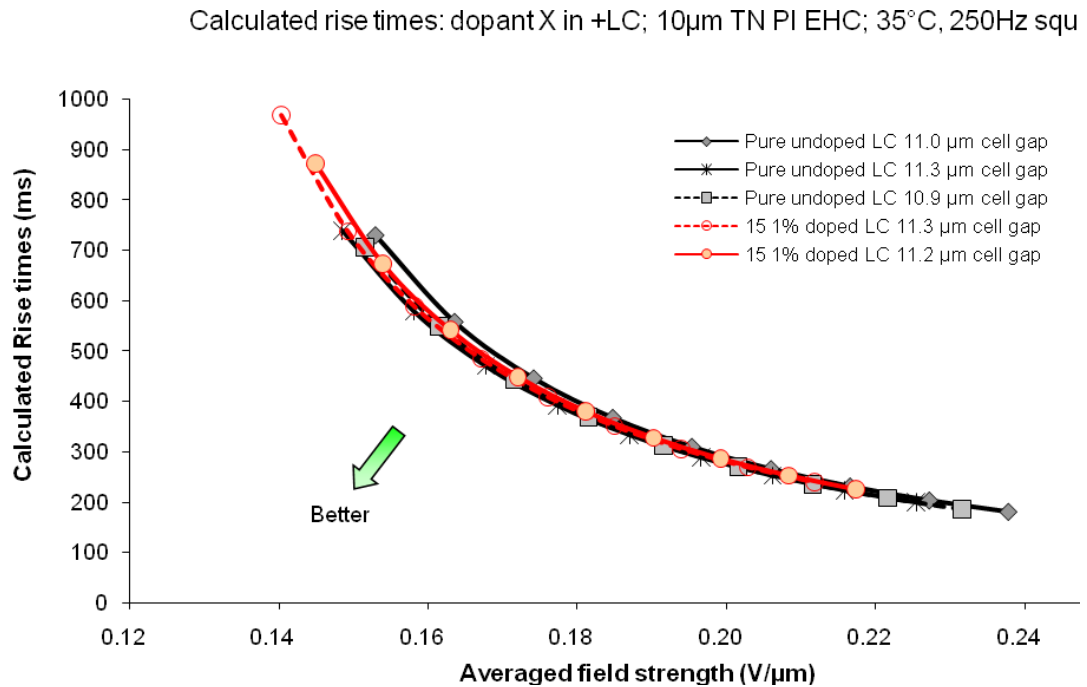


Figure 12 -- Threshold electric field data for dopants **11-15** in +LC host

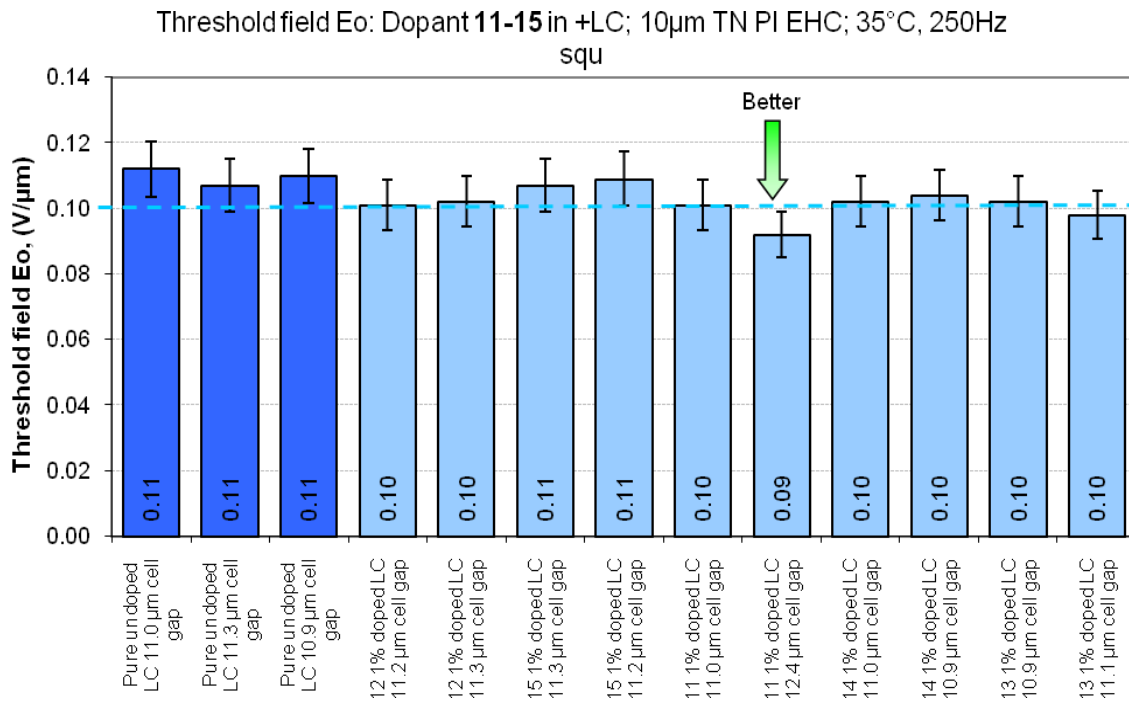


Figure 13 - E_{10} & E_{90} data for dopants **11-15** in +LC host

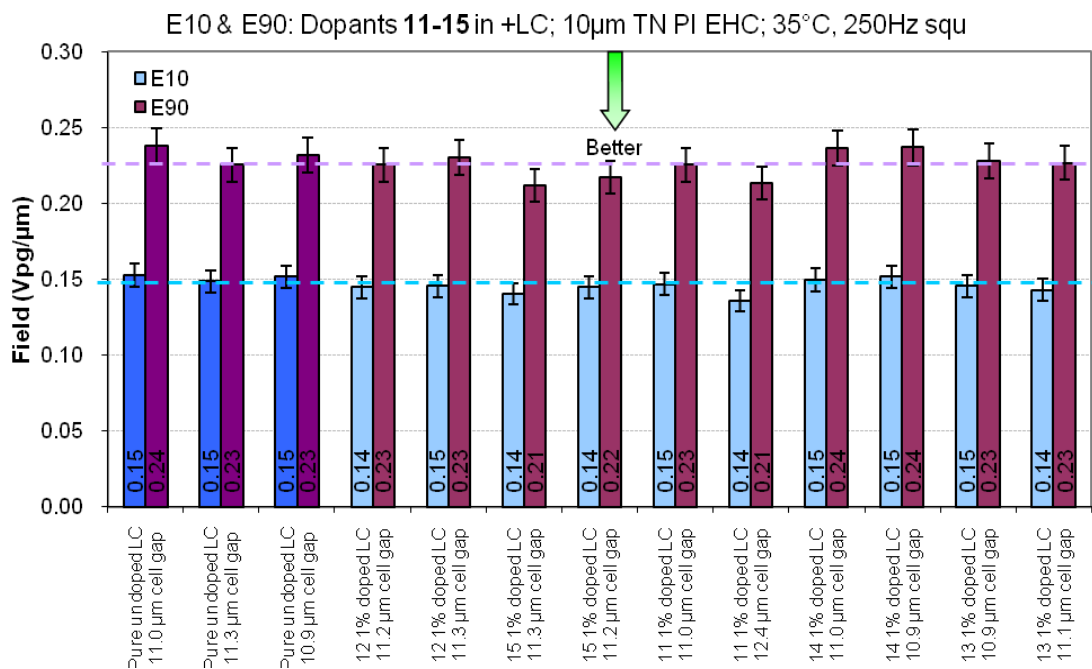


Figure 14 - VHR data dopants **11-15** in +LC host

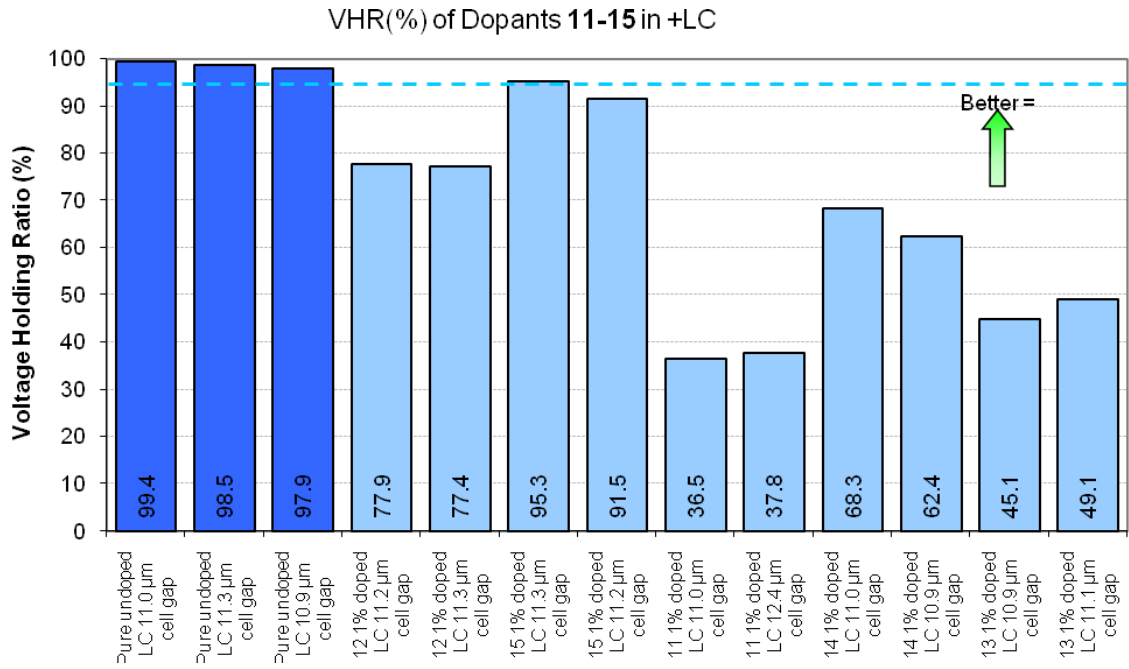


Figure 15a - Calculated decay time for 1% of dopant **11** in +LC host

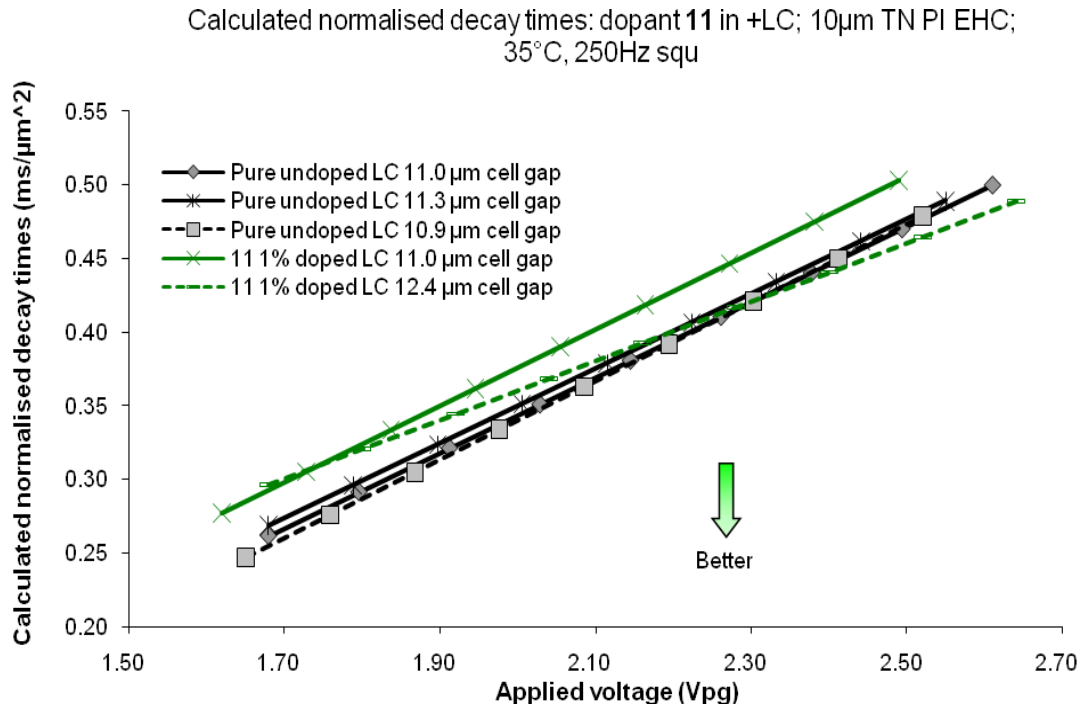


Figure 15b - Calculated decay time for 1% of dopant **12** in +LC host

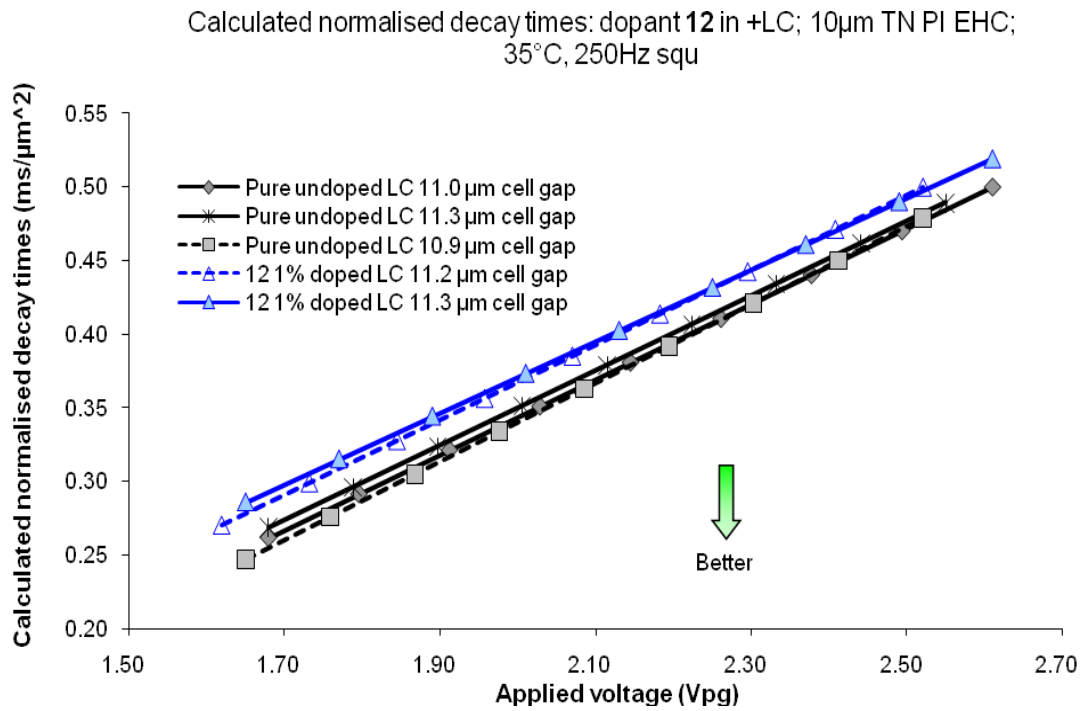


Figure 15c - Calculated decay time for 1% of dopant **13** in +LC host

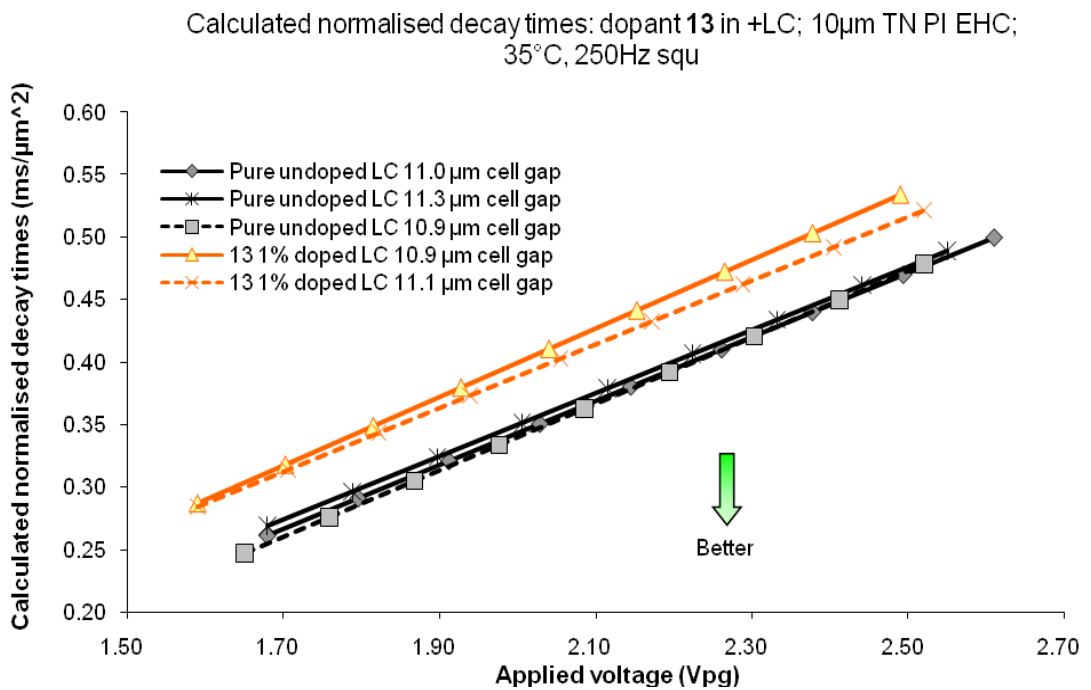


Figure 15d - Calculated decay time for 1% of dopant **14** in +LC host

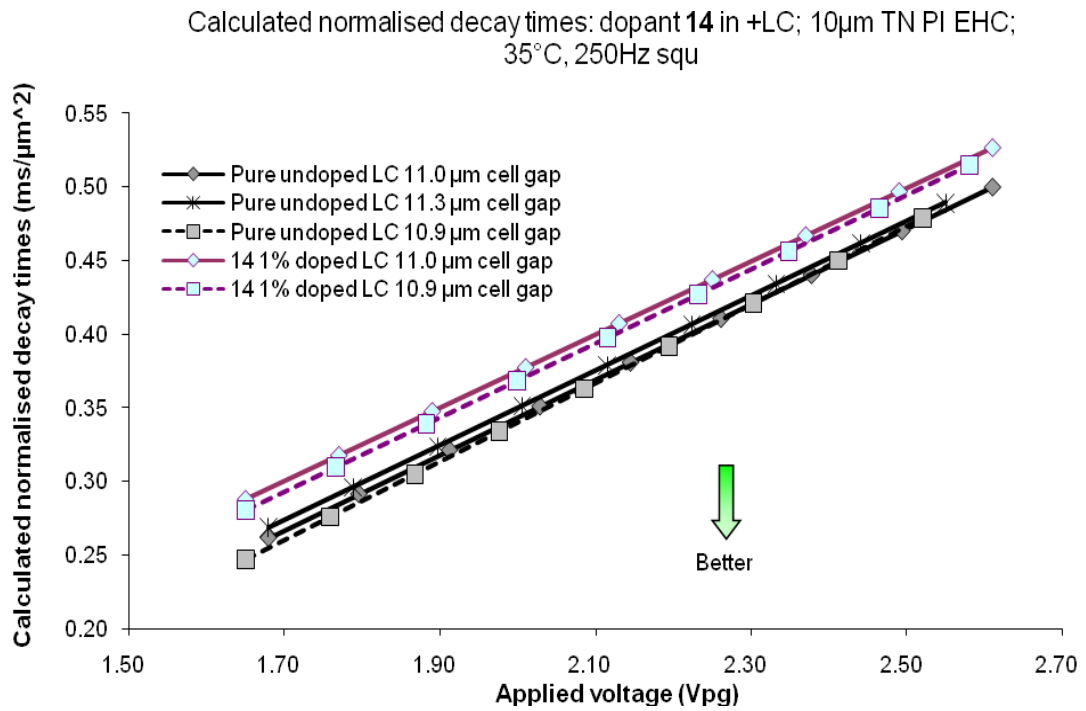


Figure 15e - Calculated decay time for 1% of dopant **15** in +LC host

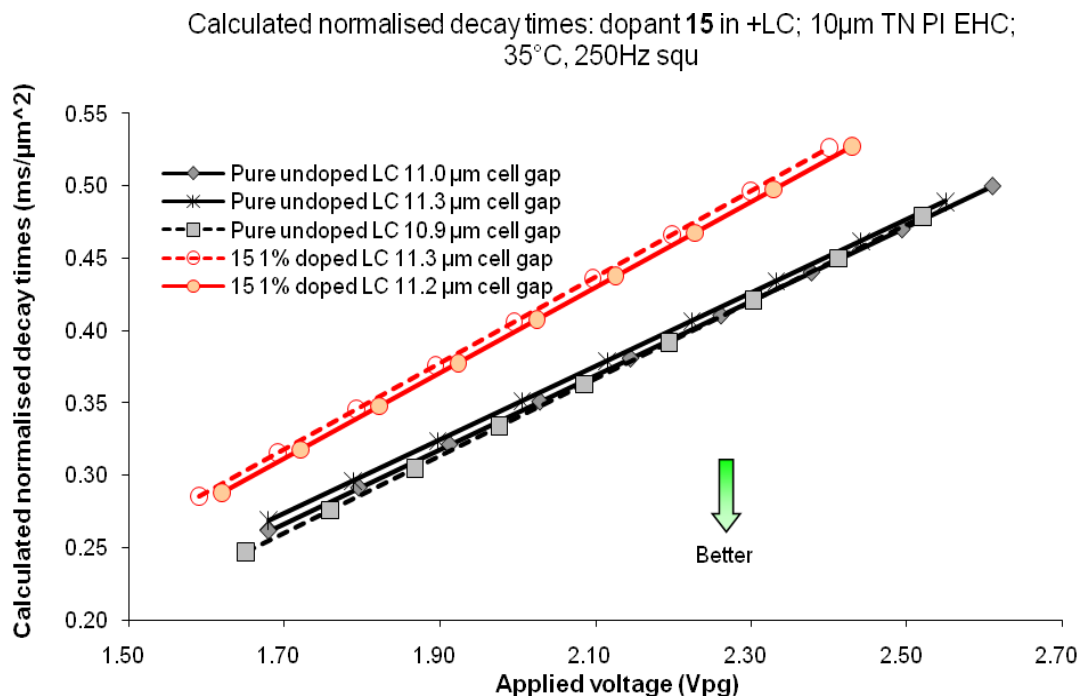


Figure 16a – Calculated rise times for 4% of dopant **22** in –LC Host, batch A

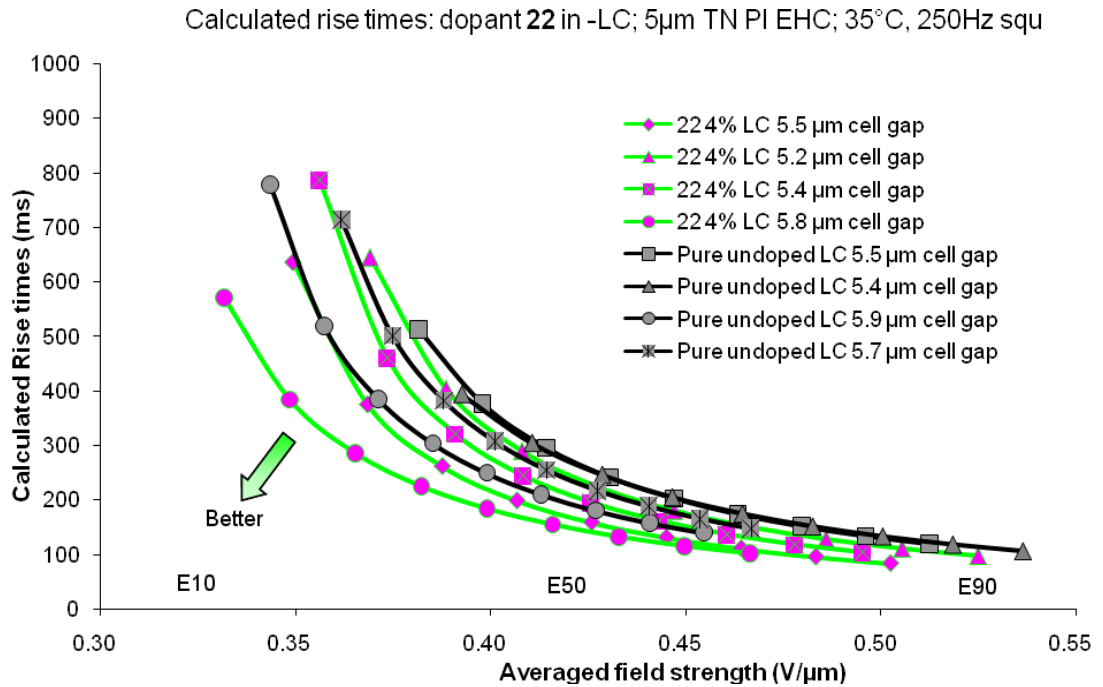


Figure 16b – Calculated rise times for 4% of dopant **22** in –LC Host, batch D

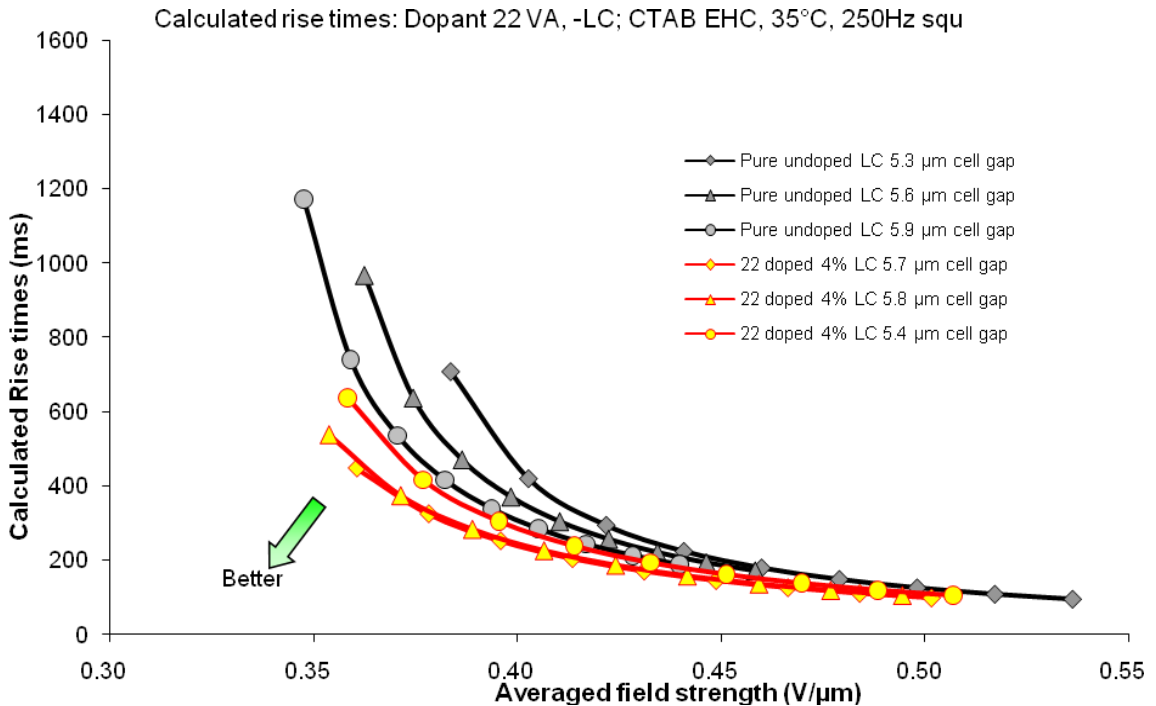


Figure 16c - Calculated rise times for 4% of dopant **23** in -LC Host, batch A

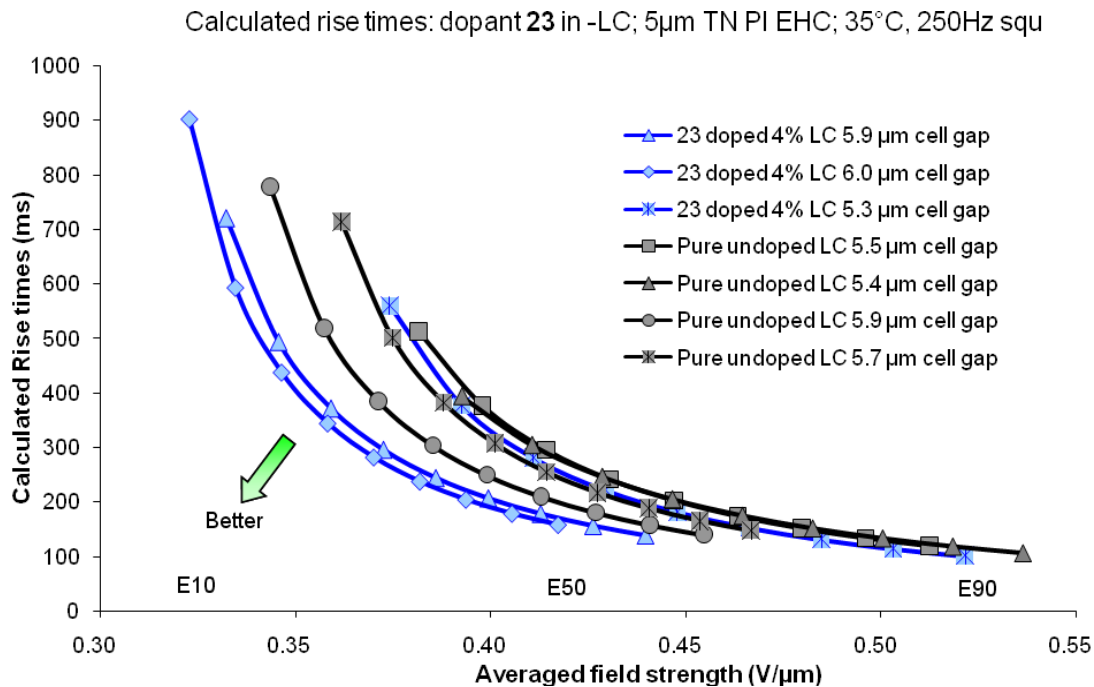


Figure 16d – Calculated rise times for 2% of dopant **23** in -LC Host, batch B

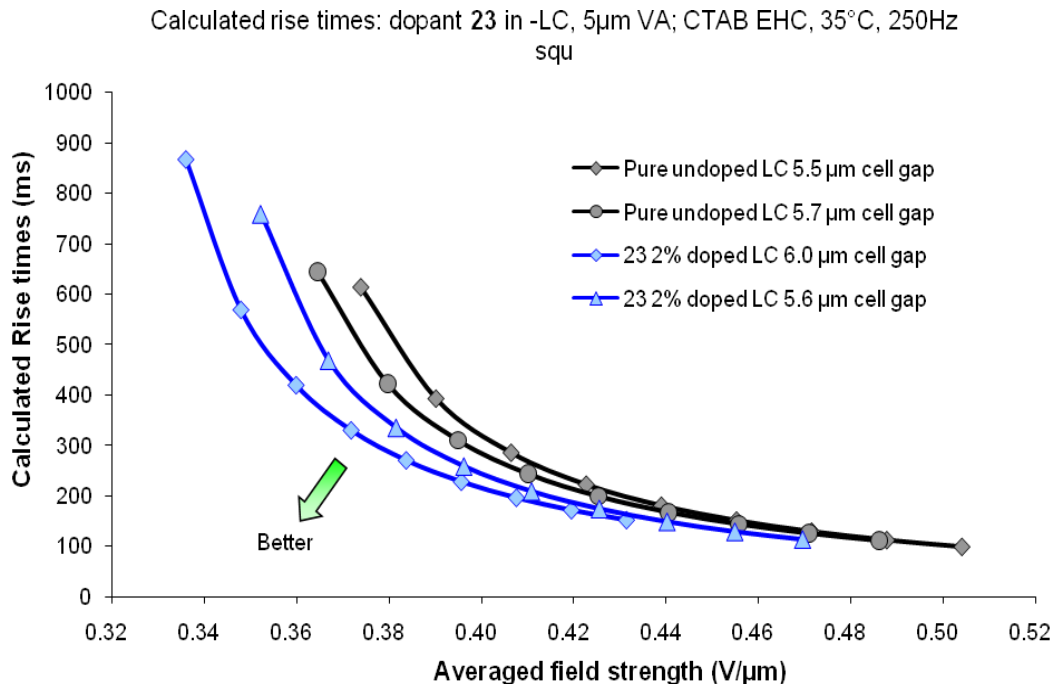


Figure 16e - Calculated rise times for 4% of dopant **23** in -LC Host, batch B

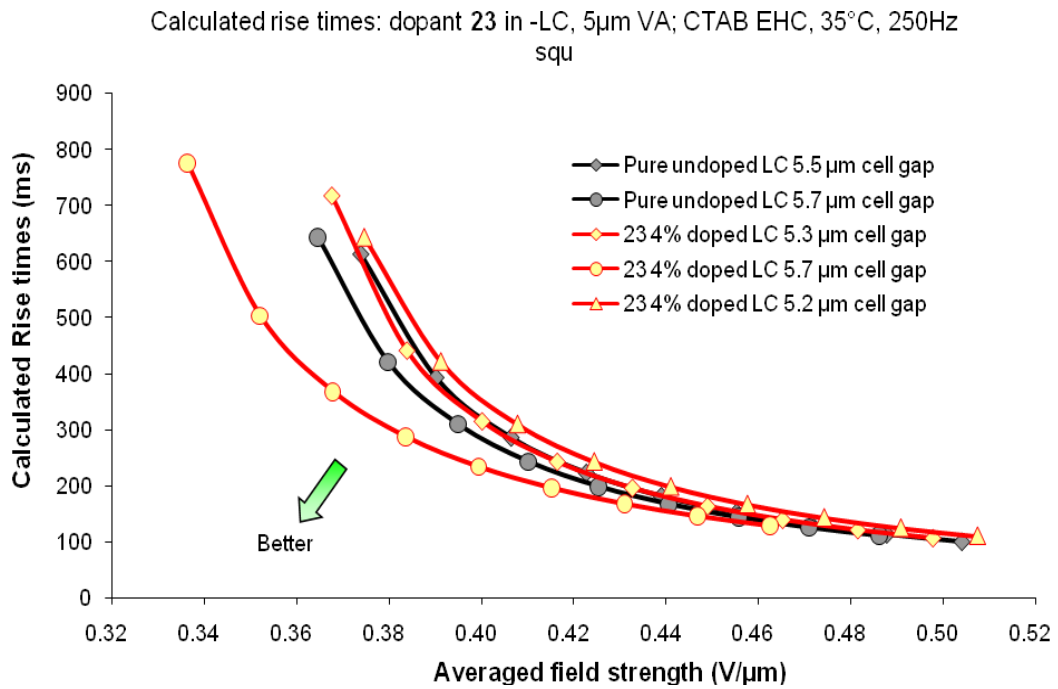


Figure 16f – Calculated rise times for 2% of dopant **23** in -LC Host, batch C

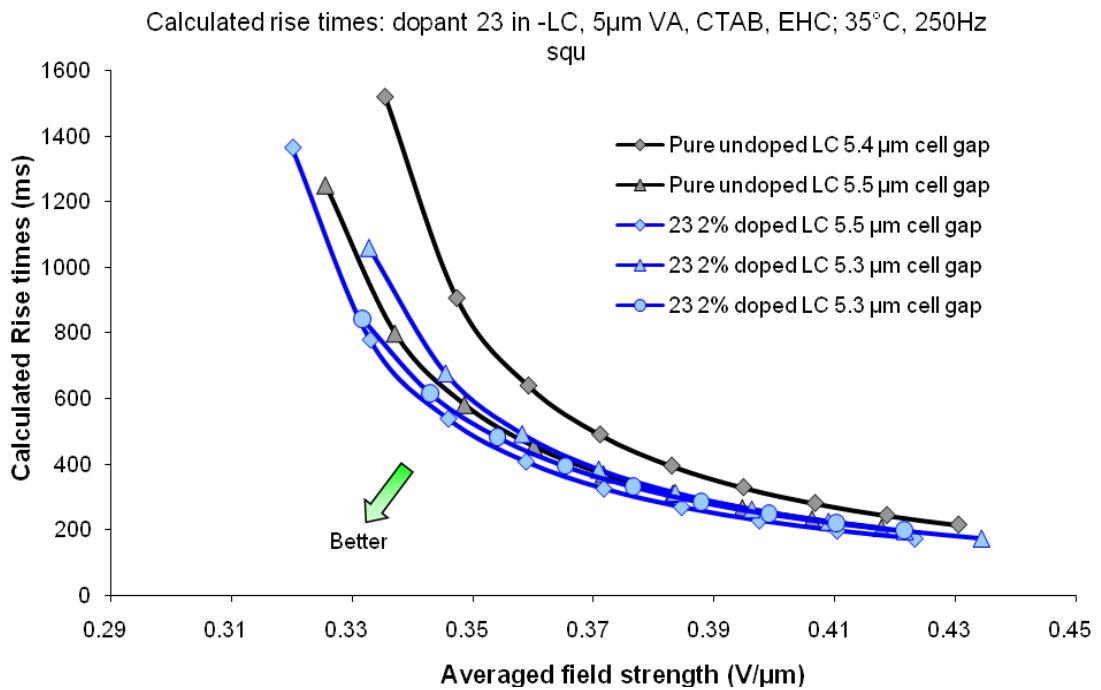


Figure 16g - Calculated rise times for 4% of dopant **23** in –LC Host, batch C

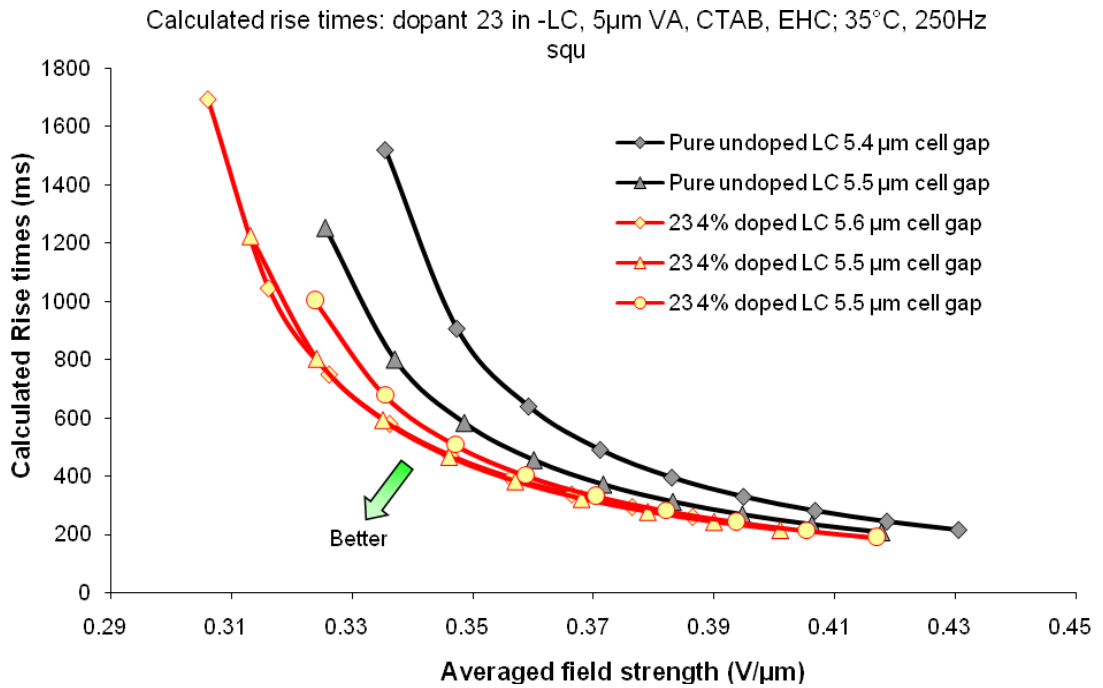


Figure 16h - Calculated rise times for 6% of dopant **23** in –LC Host, batch C

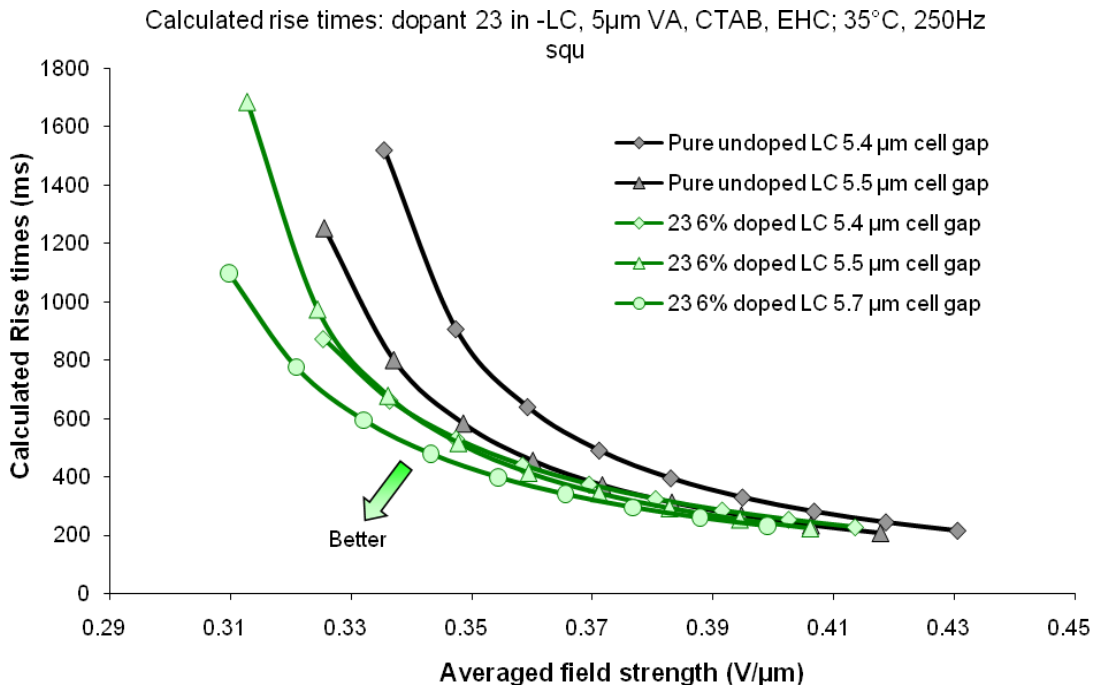


Figure 16i – Calculated rise times for 4% of dopant **23** in –LC Host, batch D

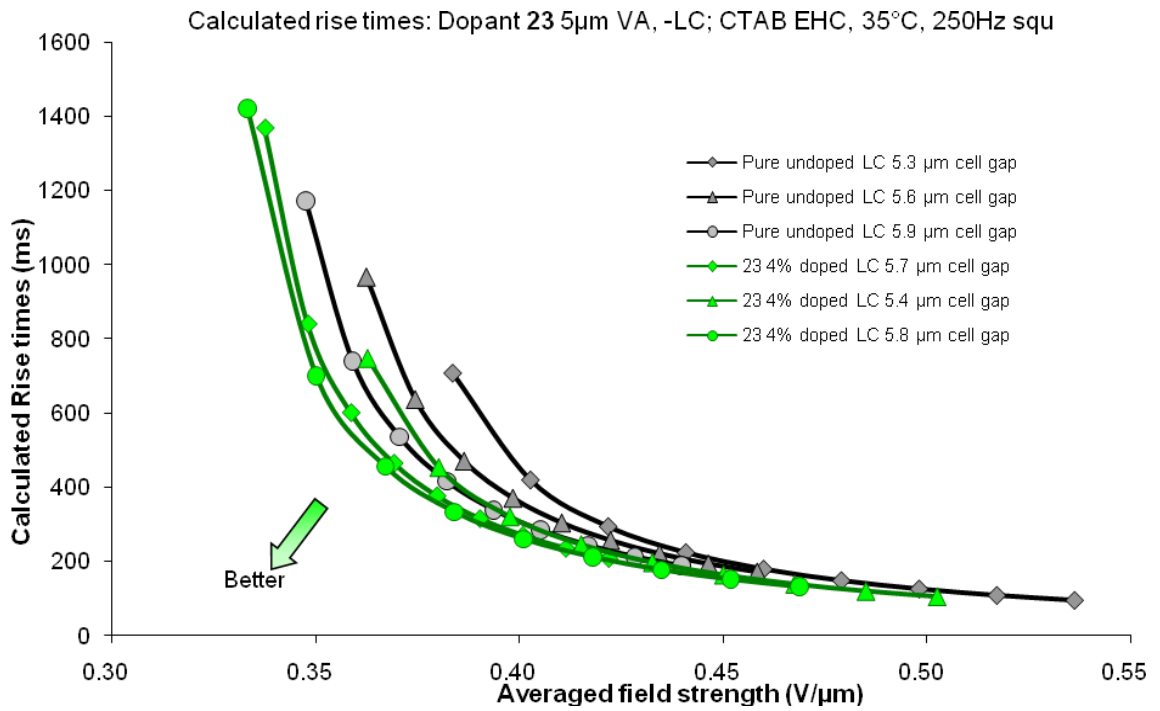


Figure 16j – Calculated rise times for 4% of dopant **24** in –LC host, batch A

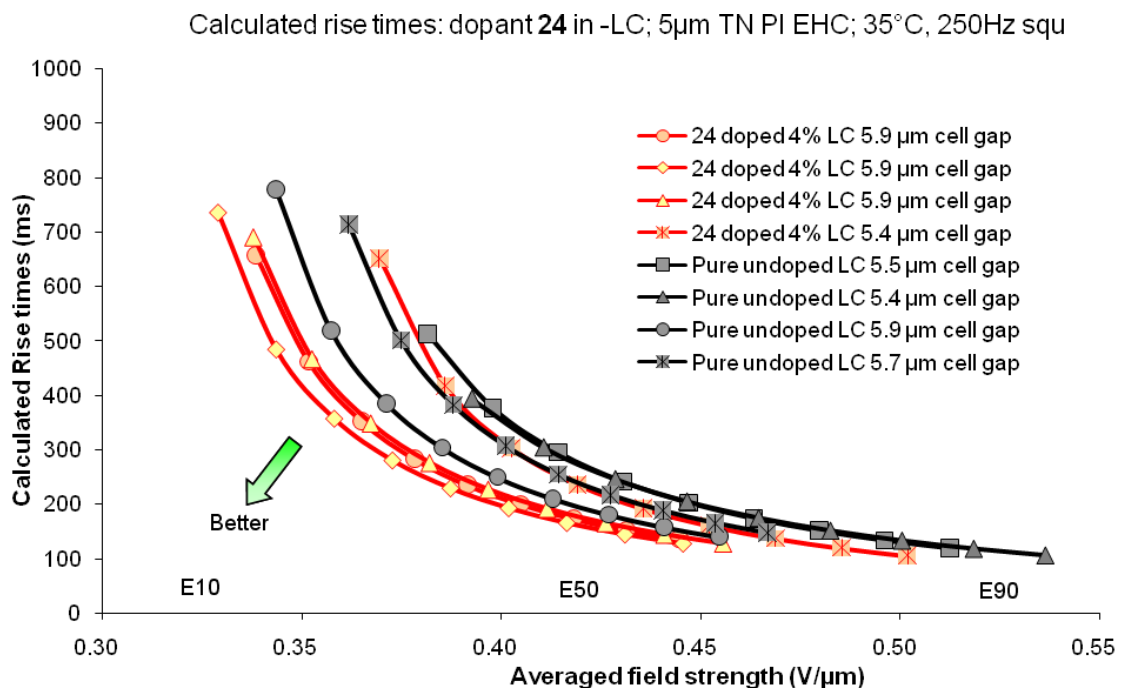


Figure 16k – Calculated rise times for 2% of dopant **30** in –LC Host, batch D

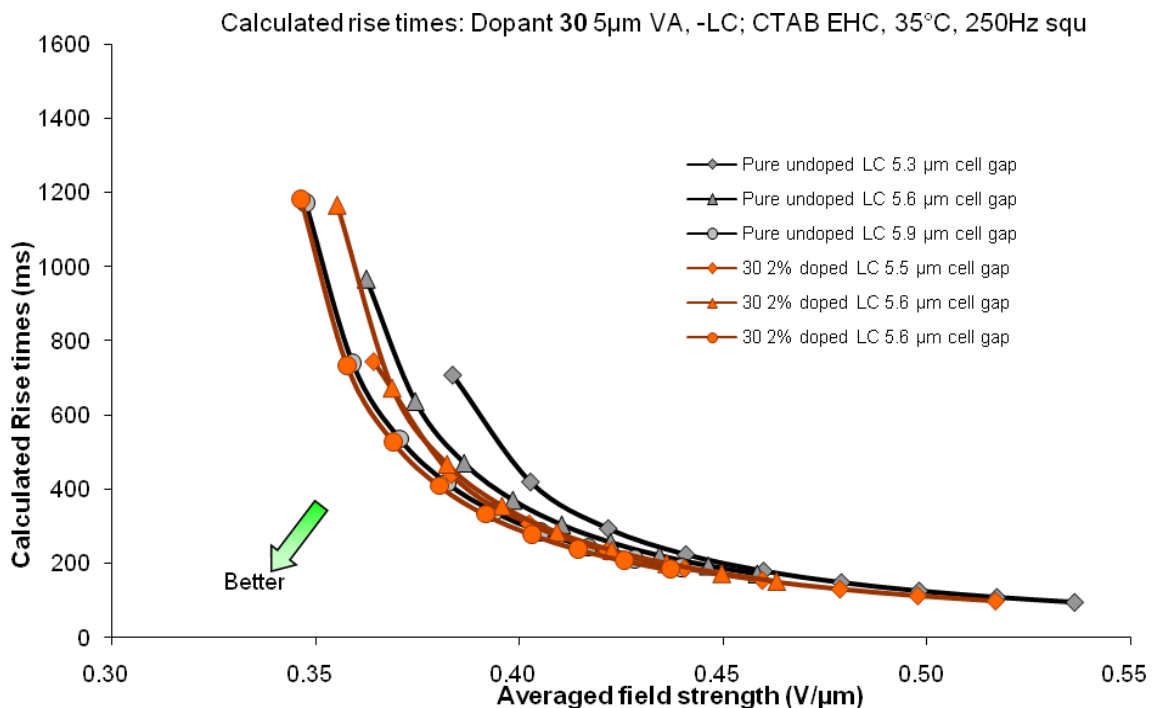


Figure 16l – Calculated rise times for 4% of dopant **30** in –LC Host, batch D

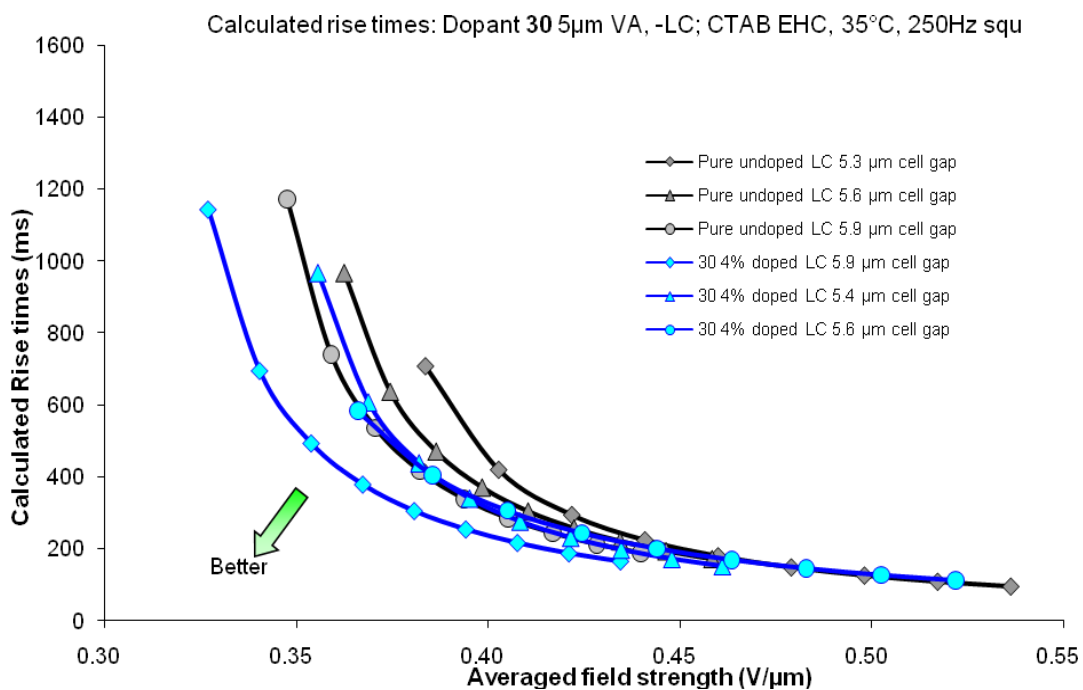


Figure 16m – Calculated rise times for 2% of dopant **27** in –LC Host, batch E

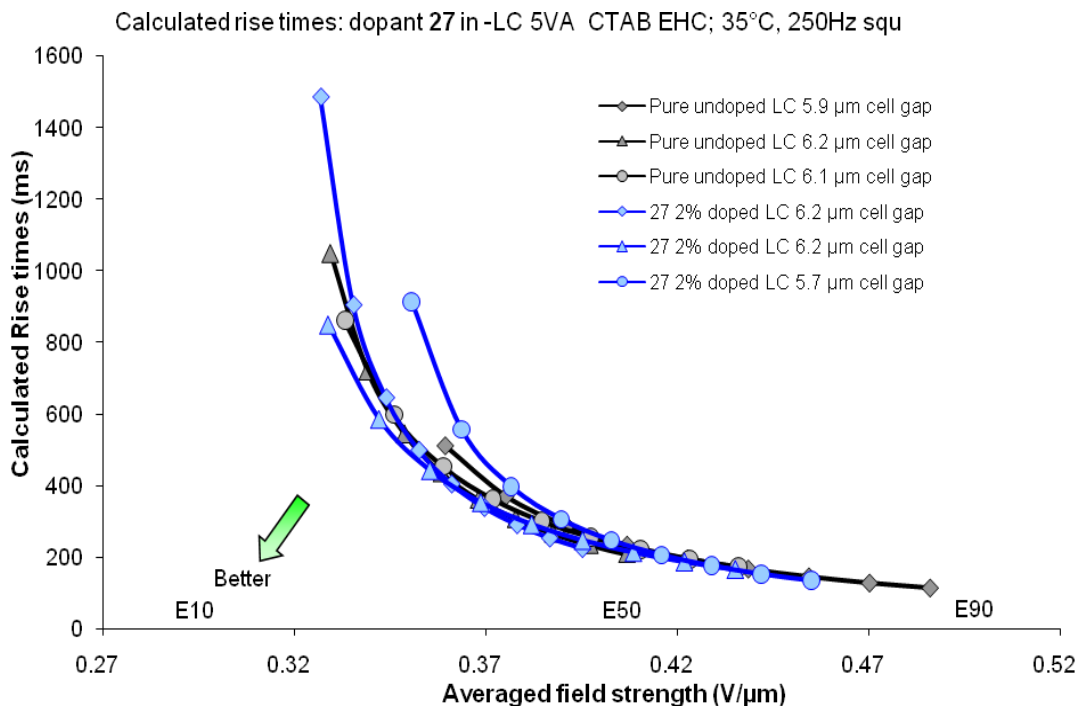


Figure 16n – Calculated rise times for 4% of dopant **27** in –LC Host, batch E

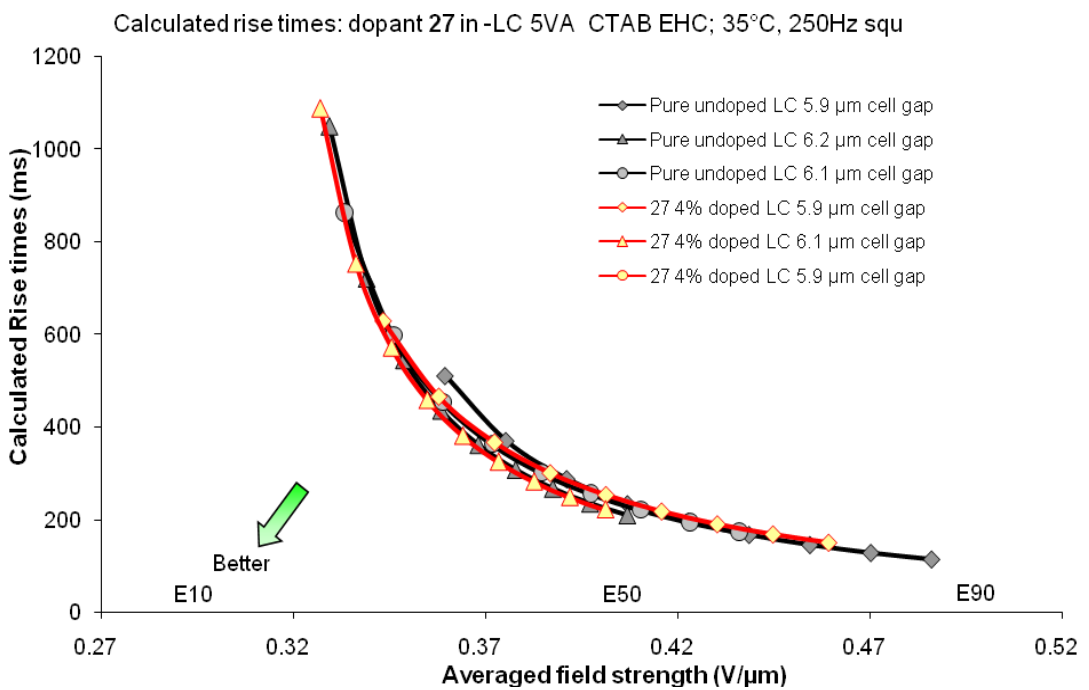


Figure 16o – Calculated rise times for 6% of dopant **27** in –LC Host, batch E

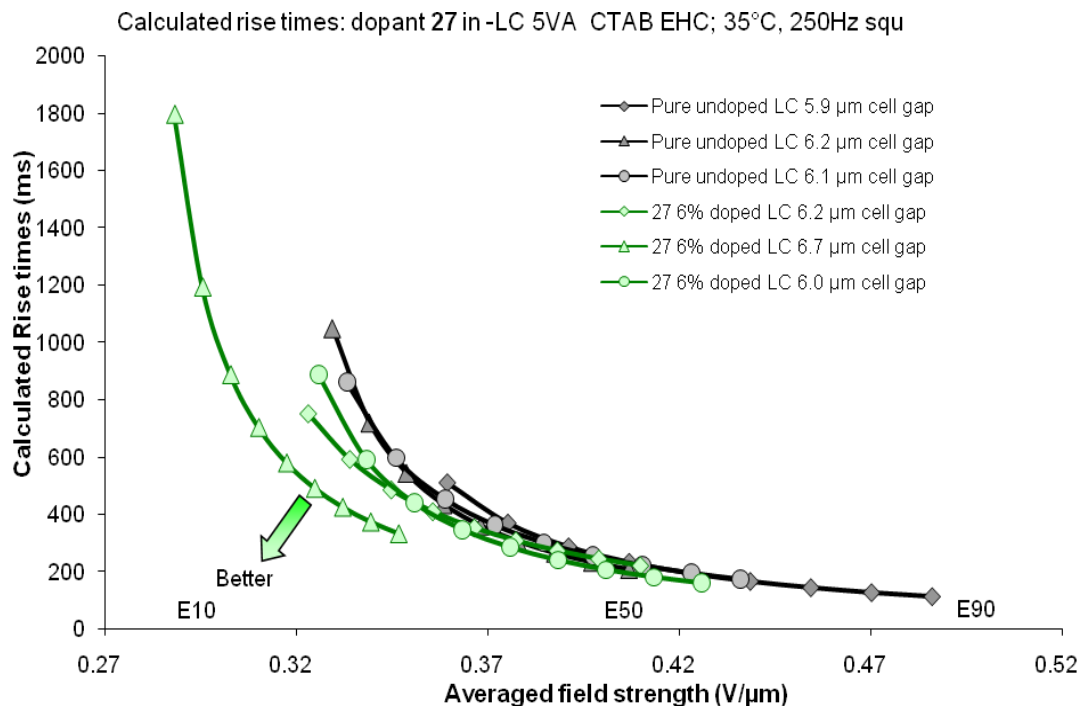


Figure 16p – Calculated rise times for 2% of dopant **28** in –LC Host, batch E

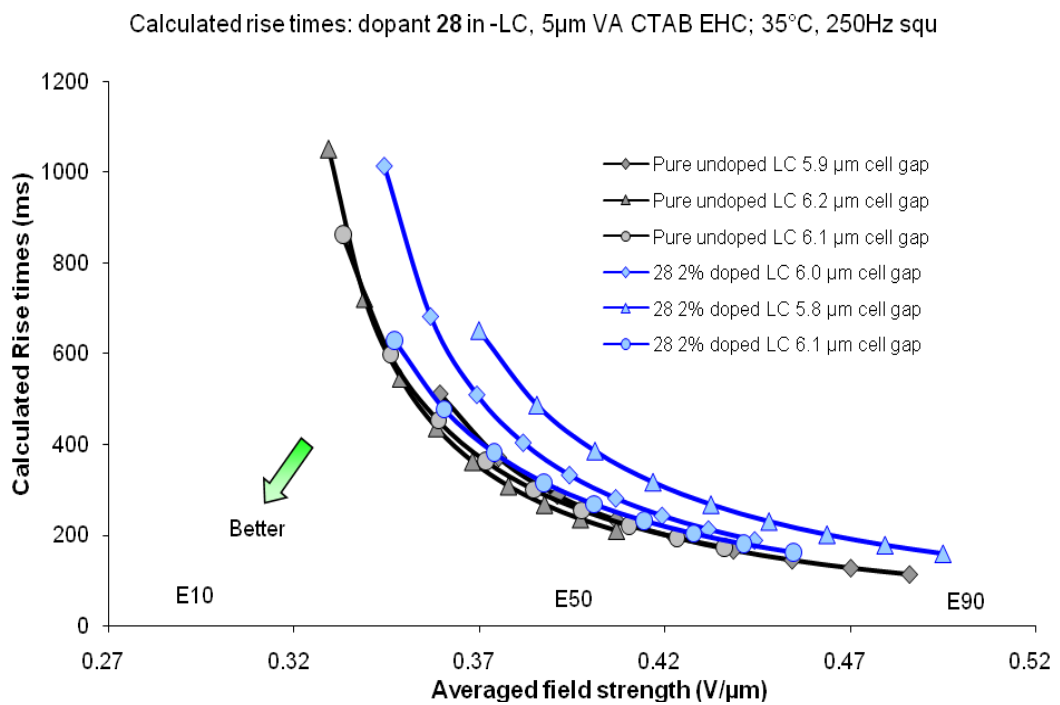


Figure 16q – Calculated rise times for 4% of dopant **28** in –LC Host, batch E

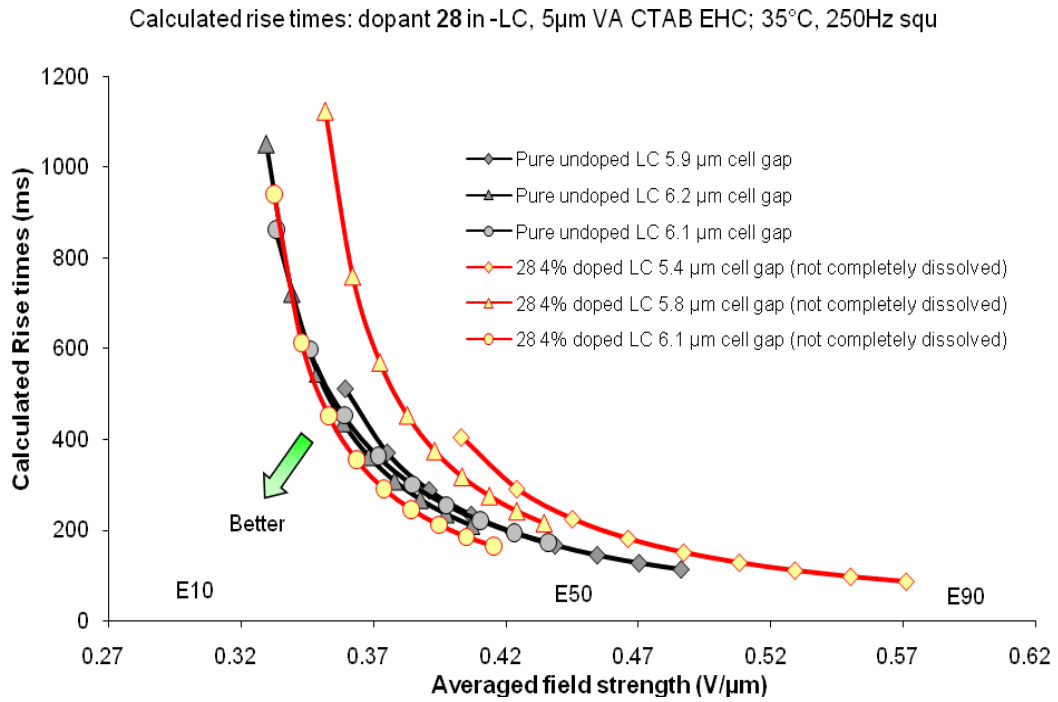


Figure 16r – Calculated rise times for 6% of dopant **28** in –LC Host, batch E

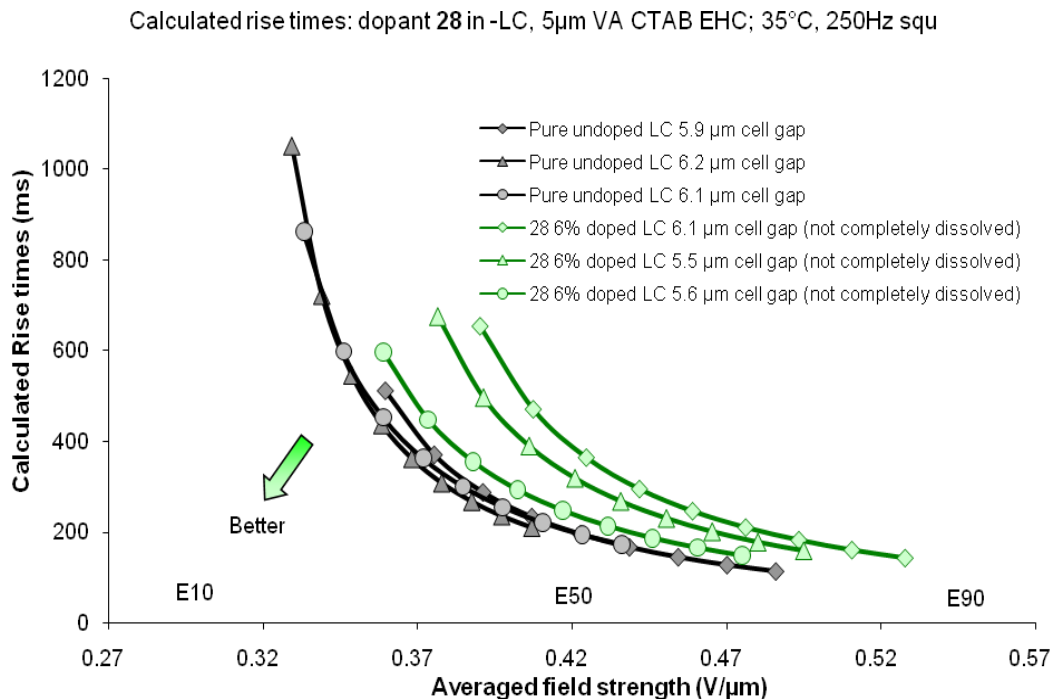


Figure 17a – Calculated rise times for comparable cell gaps of batch A samples

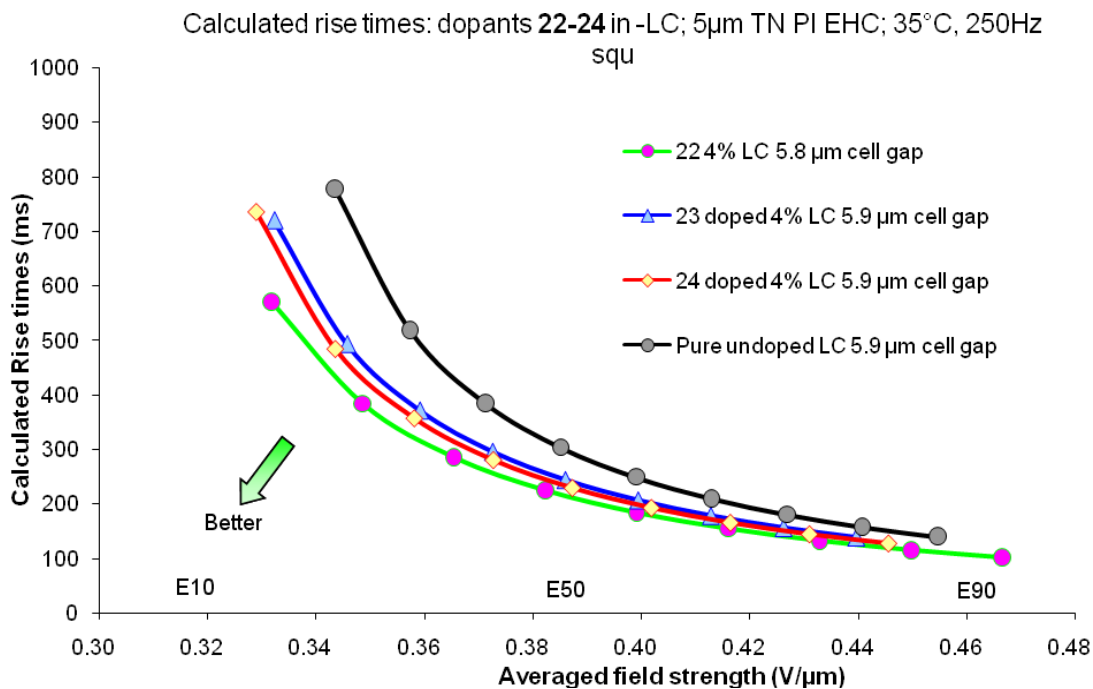


Figure 17b – Calculated rise times for comparable cell gaps of batch B samples

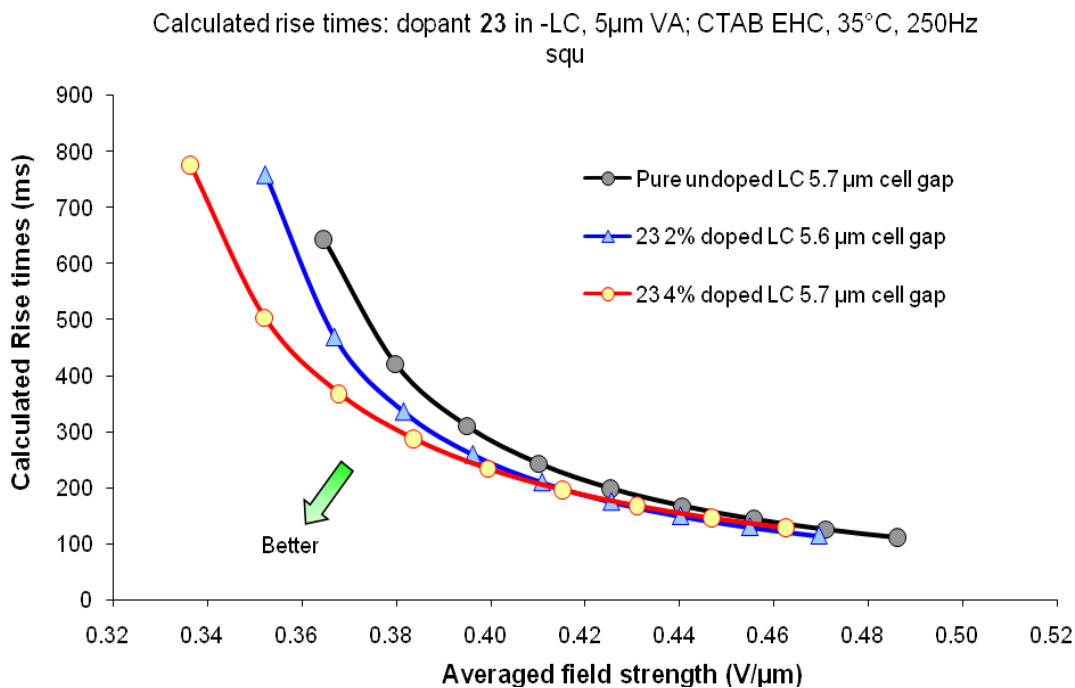


Figure 17c – Calculated rise times for comparable cell gaps of batch C samples

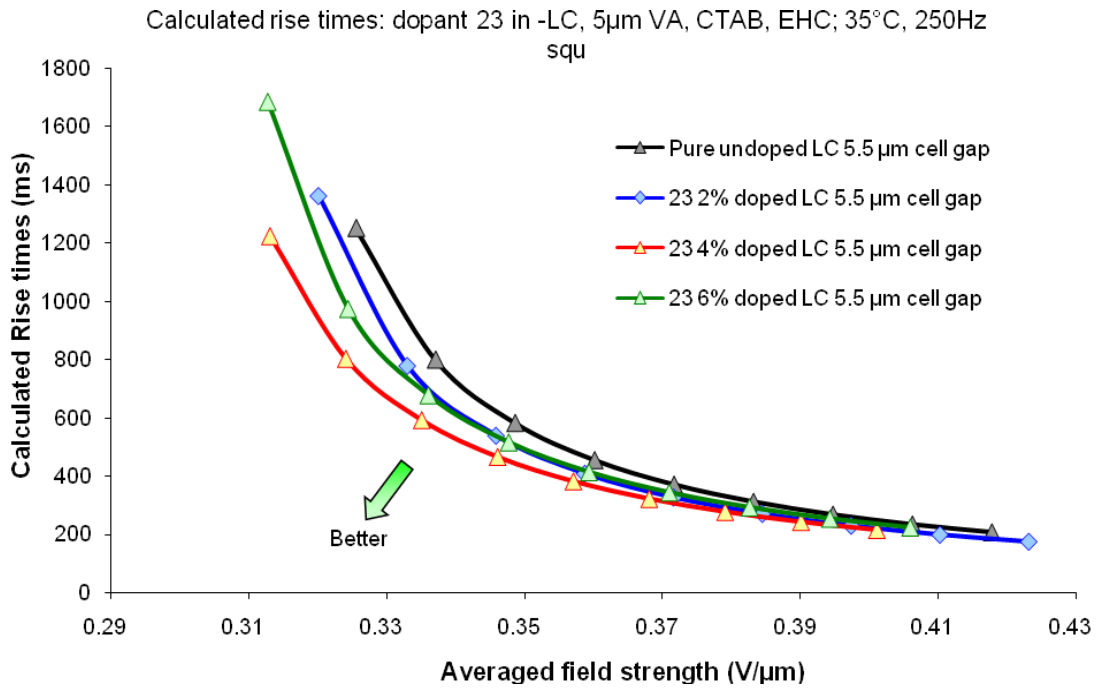


Figure 17d – Calculated rise times for comparable cell gaps of batch D samples

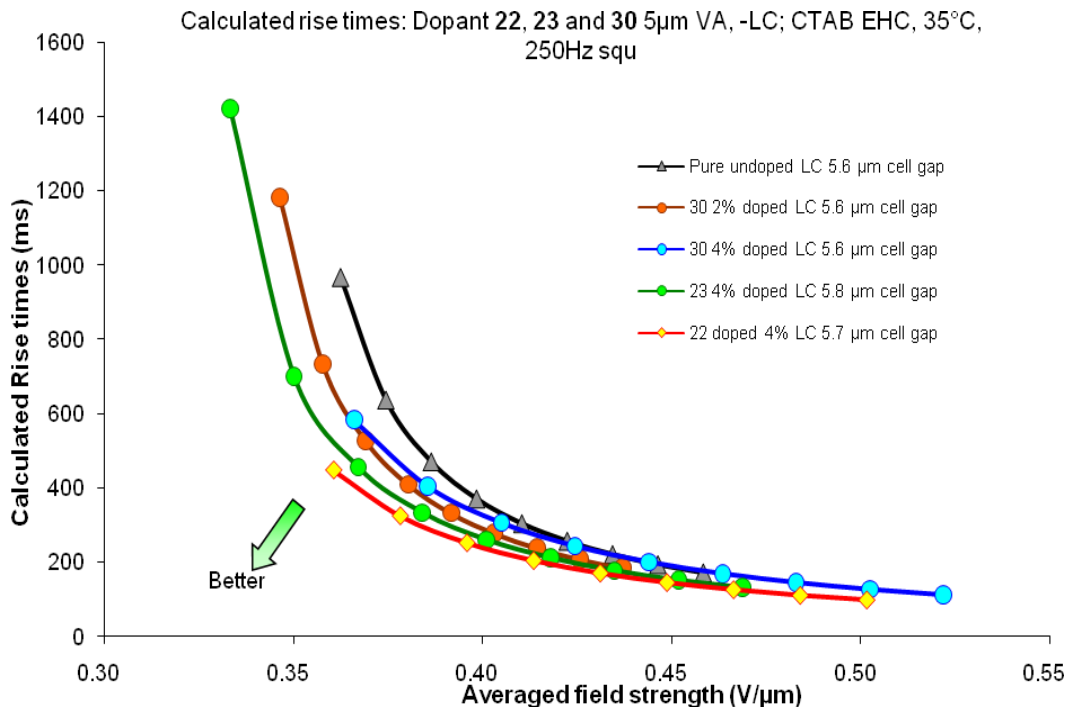


Figure 17e – Calculated rise times for comparable cell gaps of batch E samples

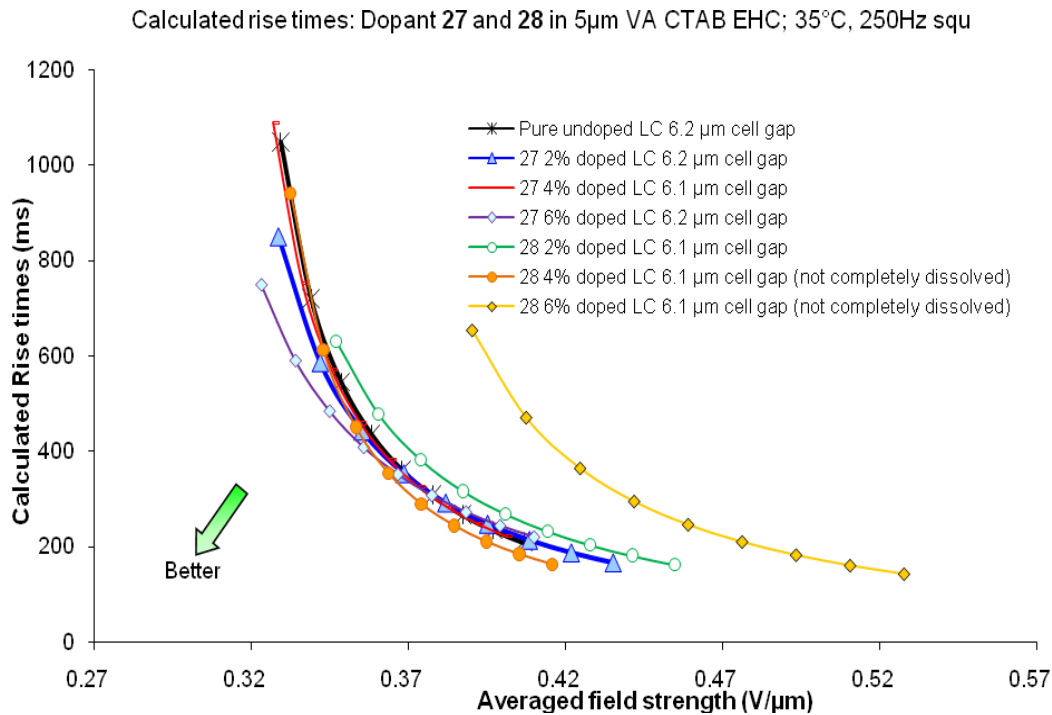


Figure 18a – Calculated decay times for 4% of dopant 22 in -LC Host, batch A

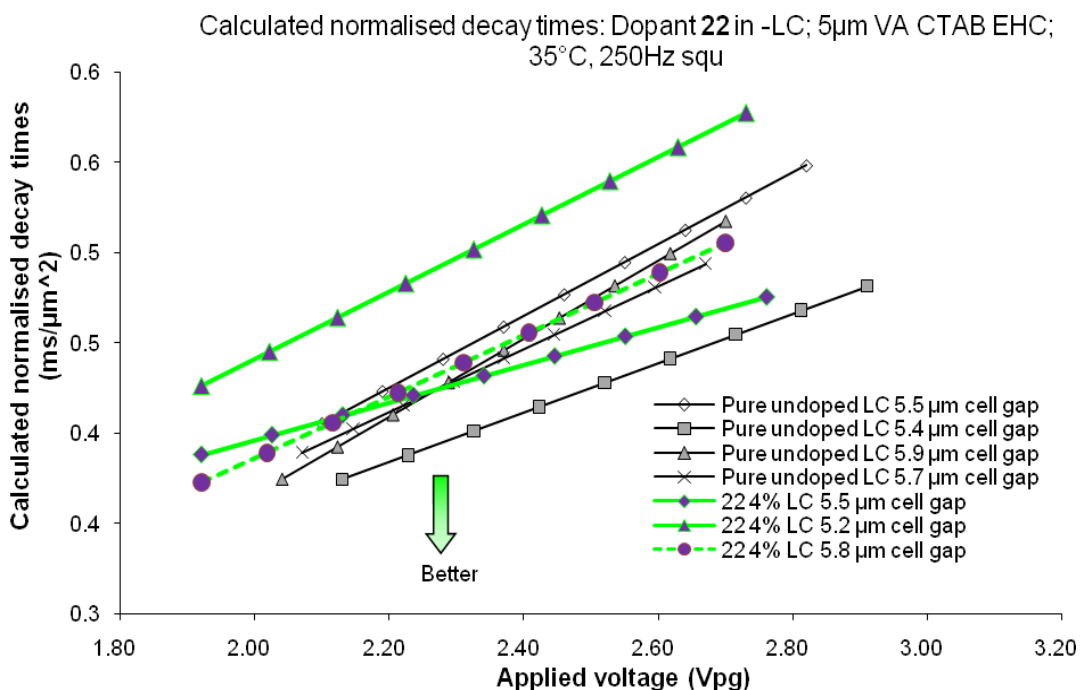


Figure 18b – Calculated decay times for 4% of dopant **22** in –LC Host, batch D

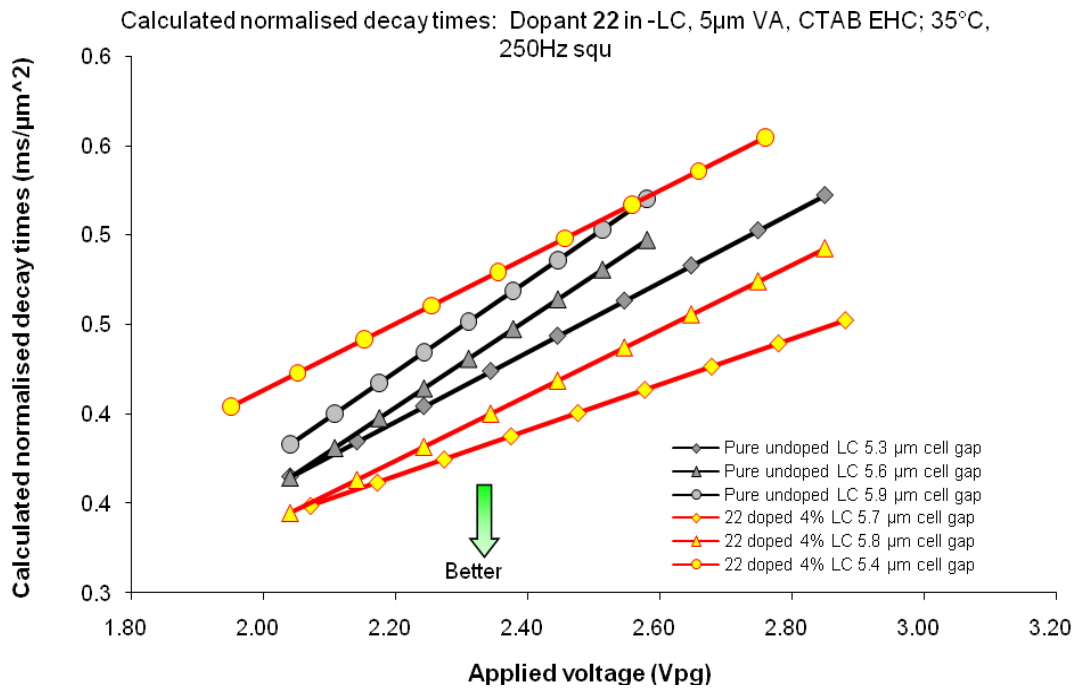


Figure 18c – Calculated decay times for 4% of dopant **23** in –LC Host, batch A

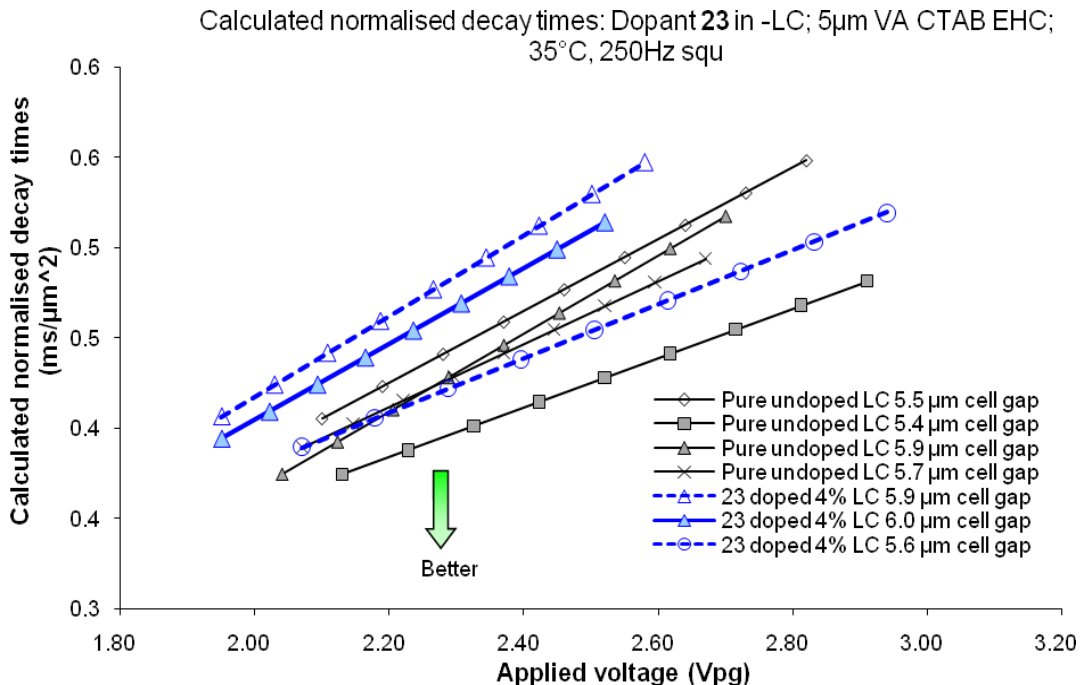


Figure 18d – Calculated decay times for 2% of dopant **23** in –LC Host, batch B

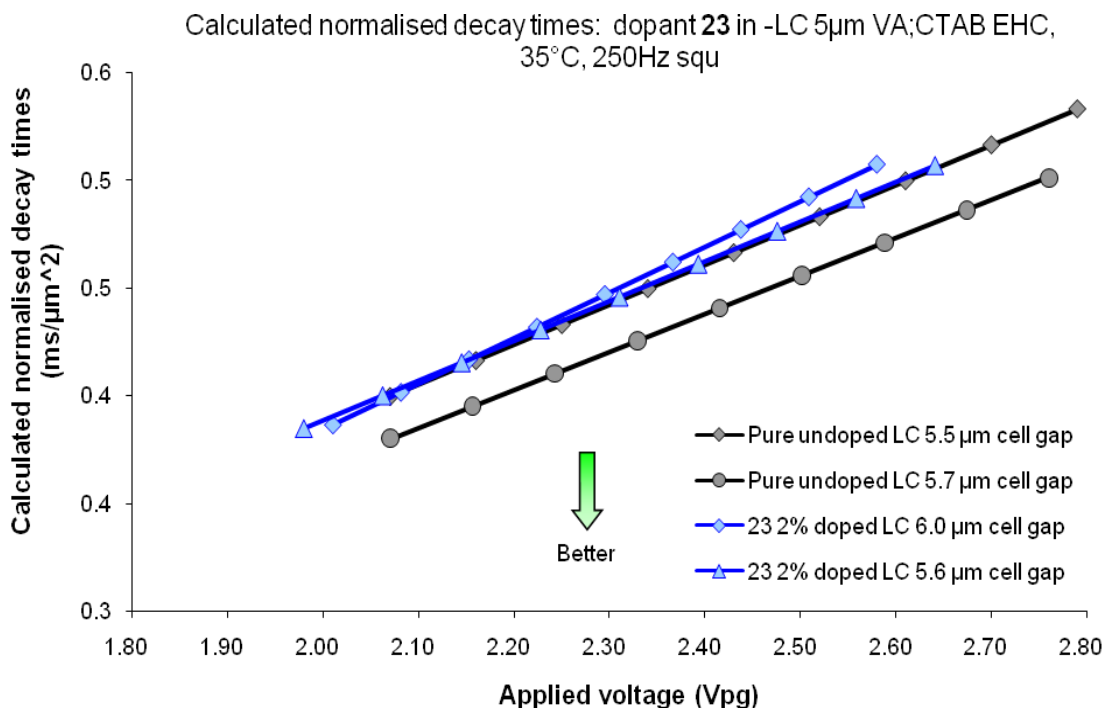


Figure 18e – Calculated decay times for 4% of dopant **23** in –LC Host, batch B

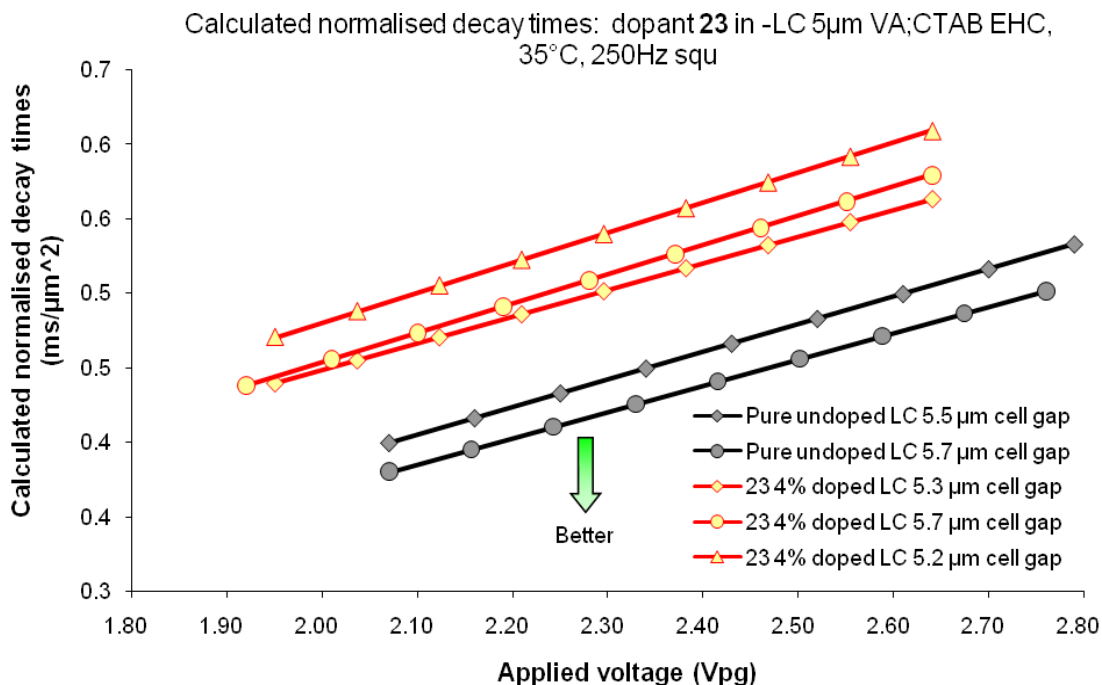


Figure 18f – Calculated decay times for 2% of dopant **23** in –LC Host, batch C

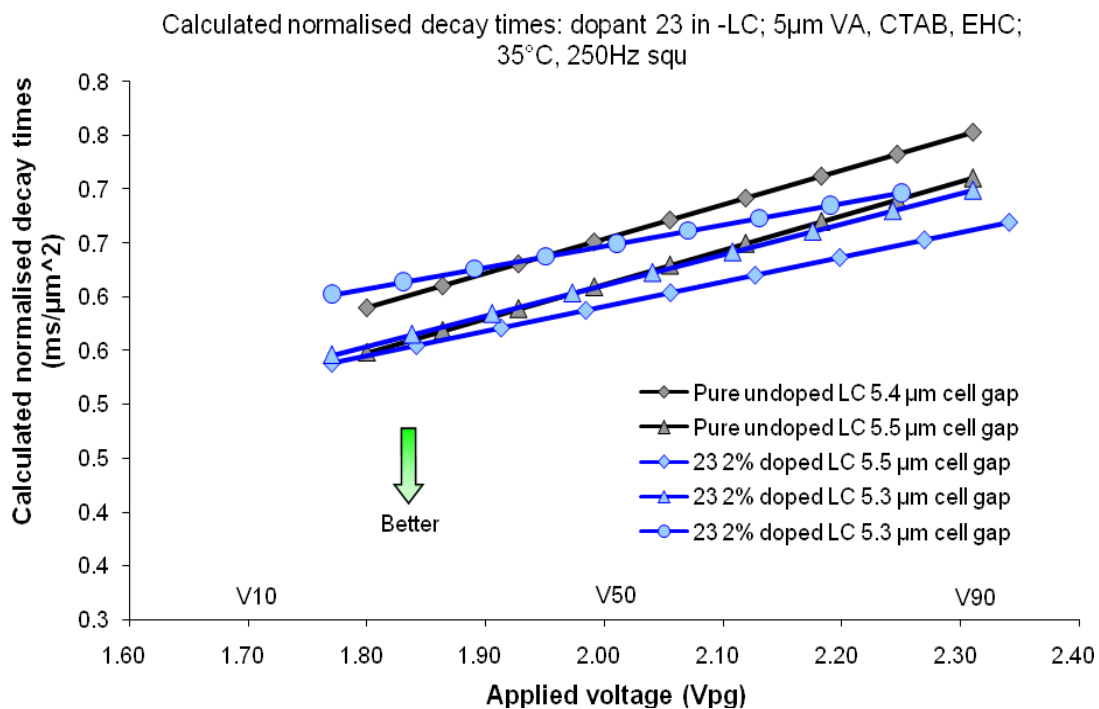


Figure 18g – Calculated decay times for 4% of dopant **23** in –LC Host, batch C

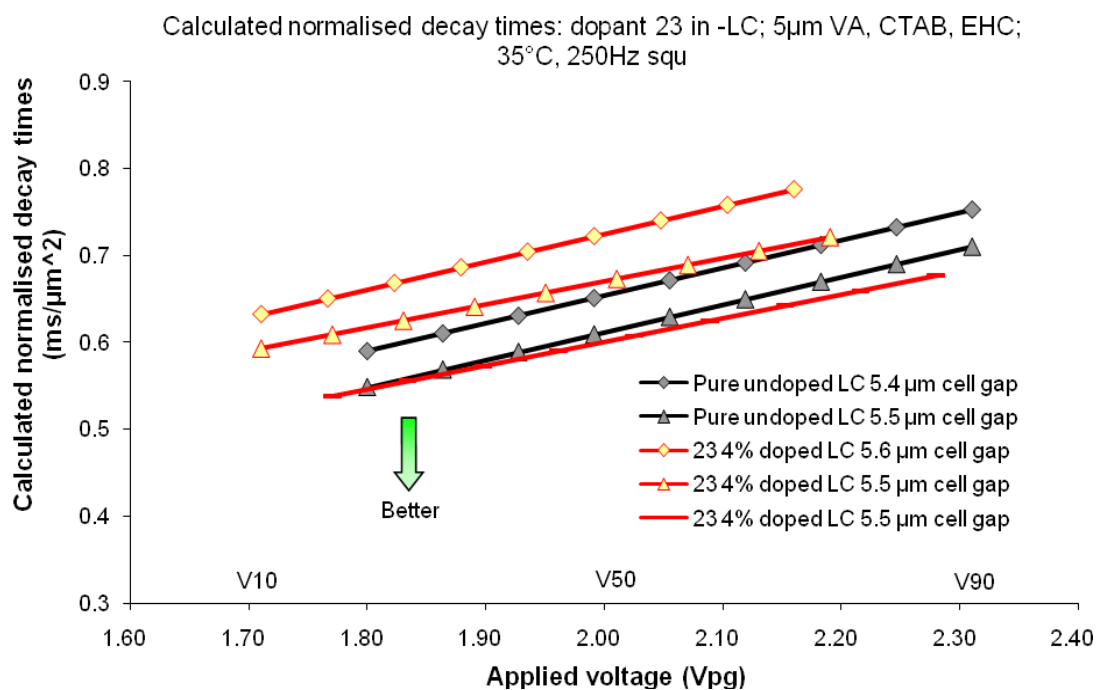


Figure 18h – Calculated decay times for 6% of dopant **23** in –LC Host, batch C

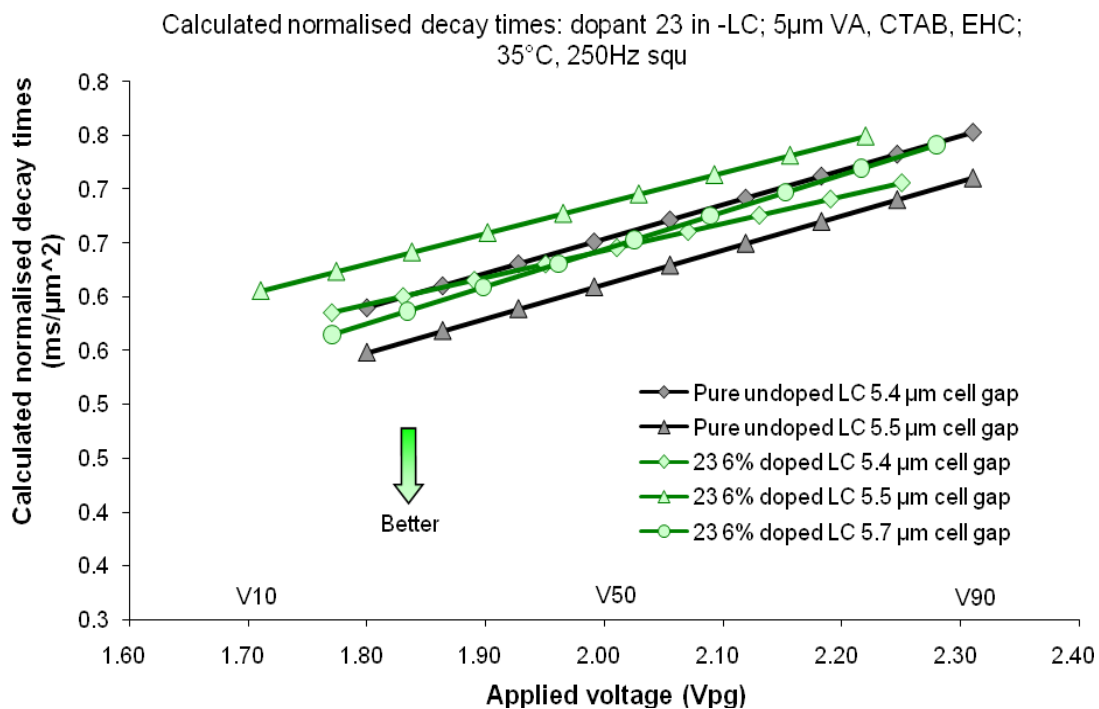


Figure 18i – Calculated decay times for 4% of dopant **23** in –LC Host, batch D

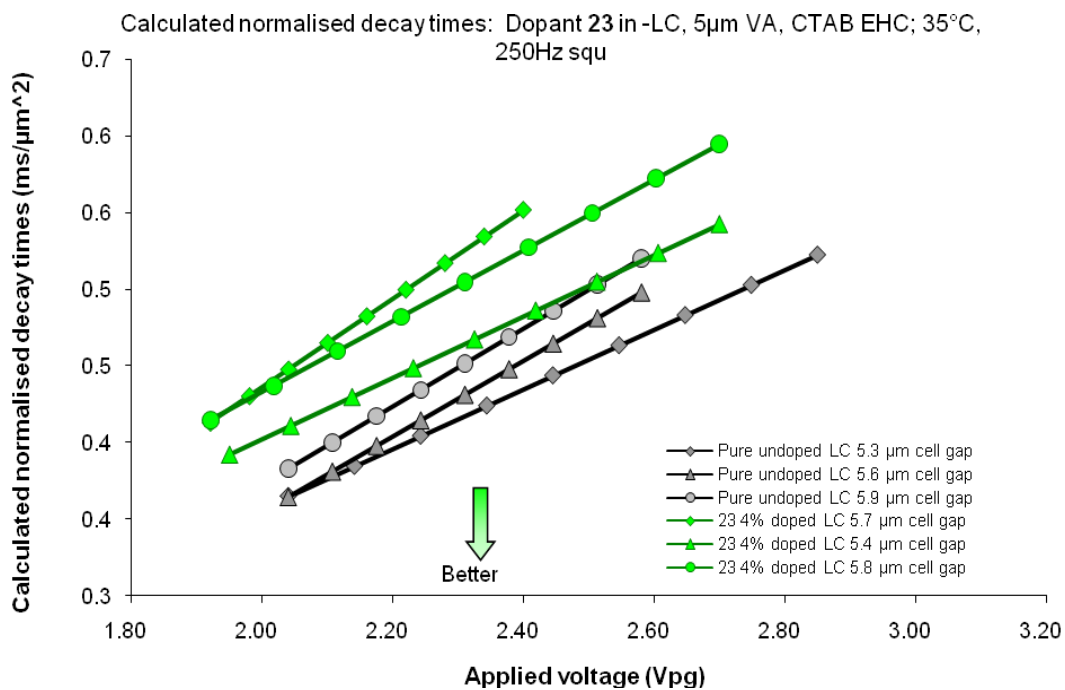


Figure 18j – Calculated decay times for 4% of dopant **24** in –LC Host, batch A

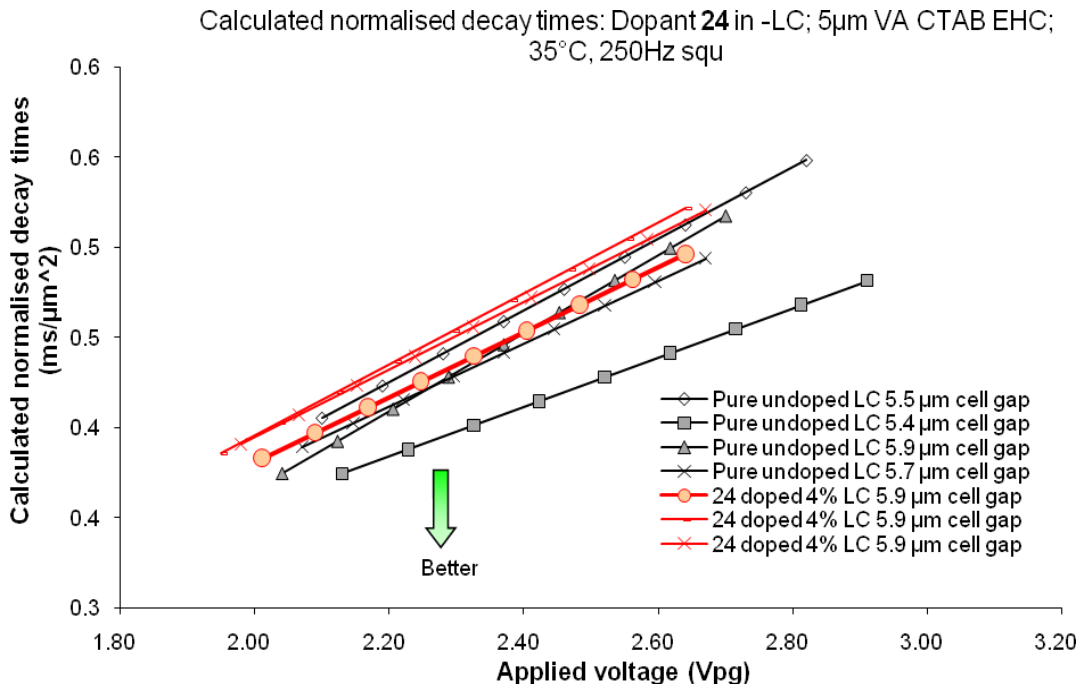


Figure 18k – Calculated decay times for 2% of dopant **30** in –LC Host, batch D

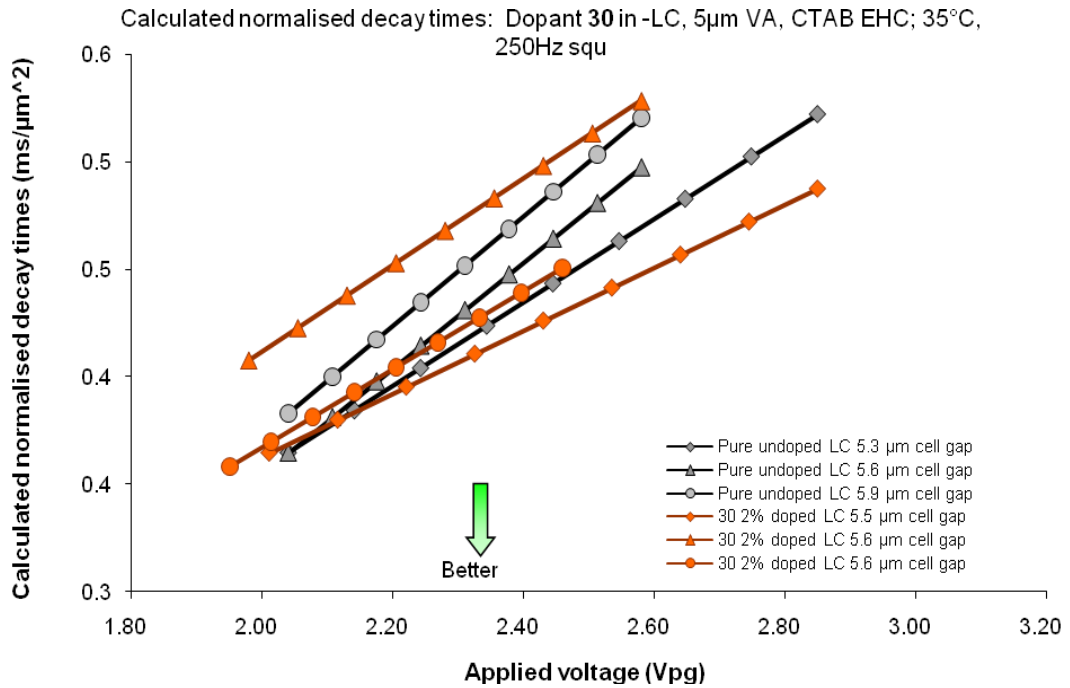


Figure 18l – Calculated decay times for 4% of dopant **30** in –LC Host, batch D

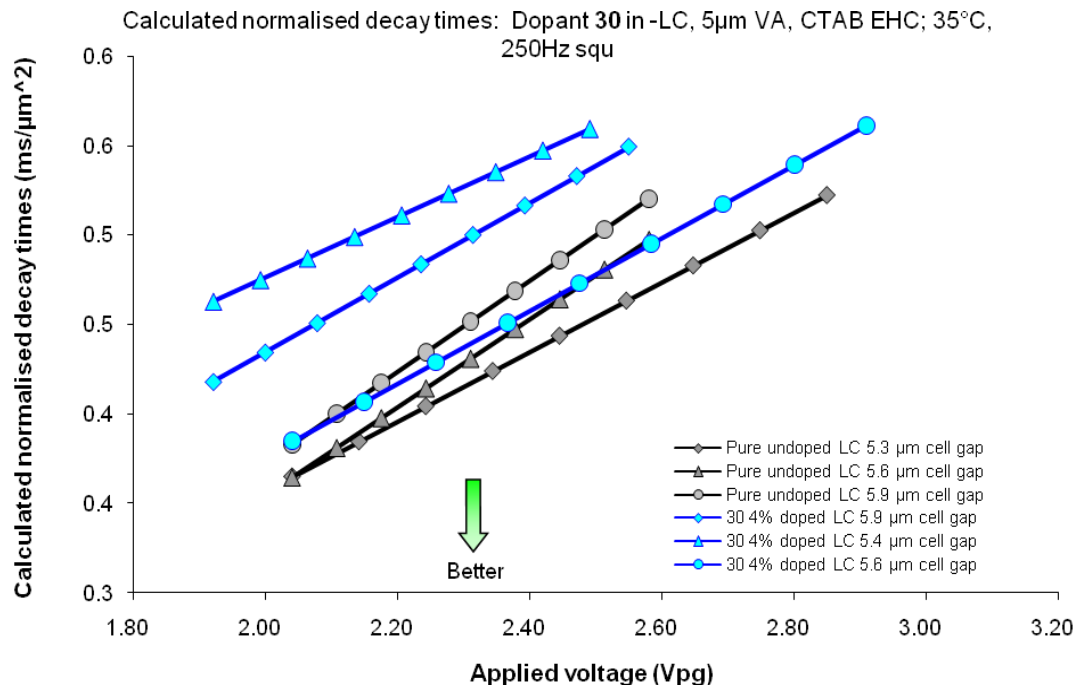


Figure 18m – Calculated decay times for 2% of dopant **27** in –LC Host, batch E

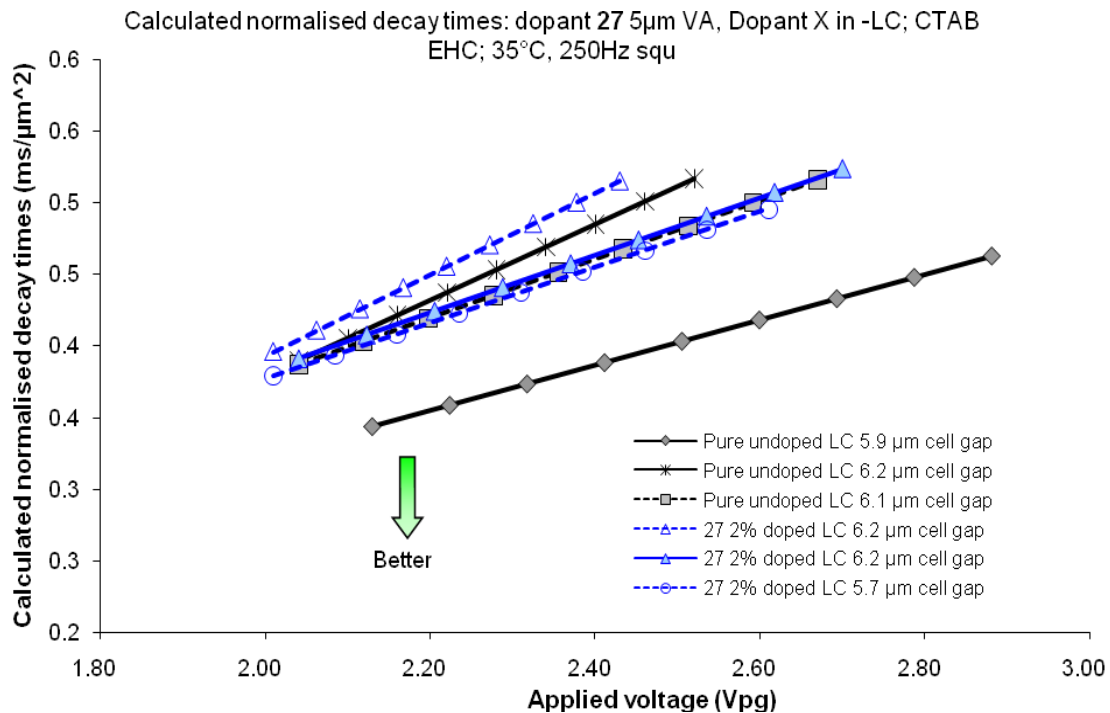


Figure 18n – Calculated decay times for 4% of dopant 27 in –LC Host, batch E

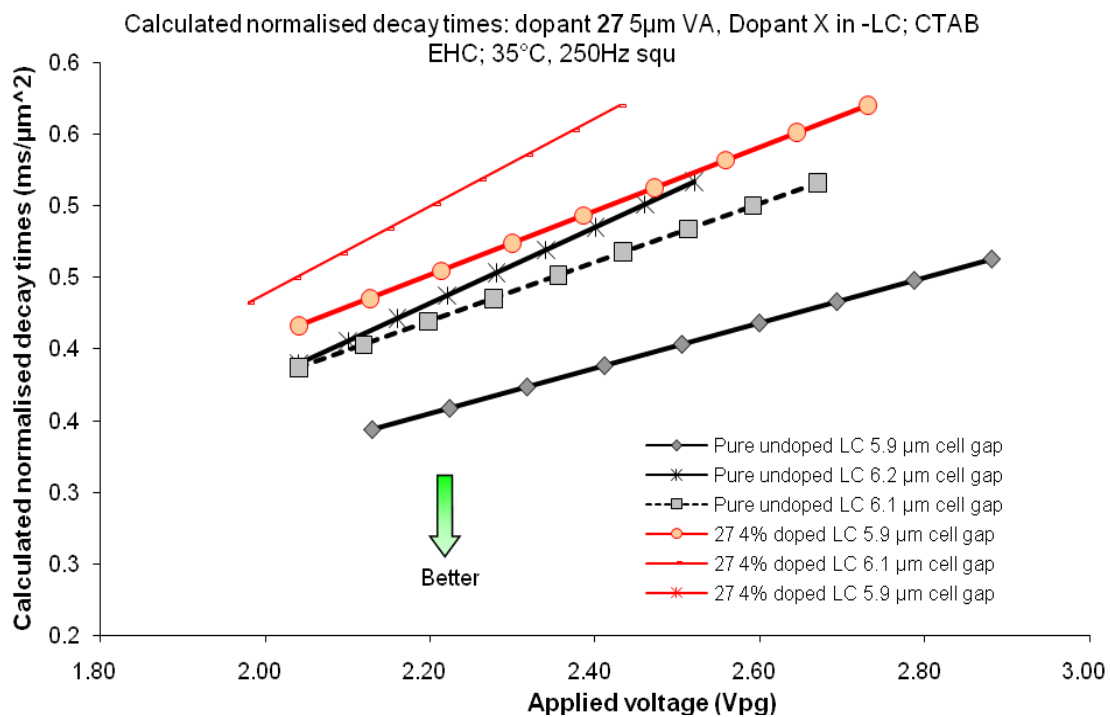


Figure 18o – Calculated decay times for 6% of dopant 27 in –LC Host, batch E

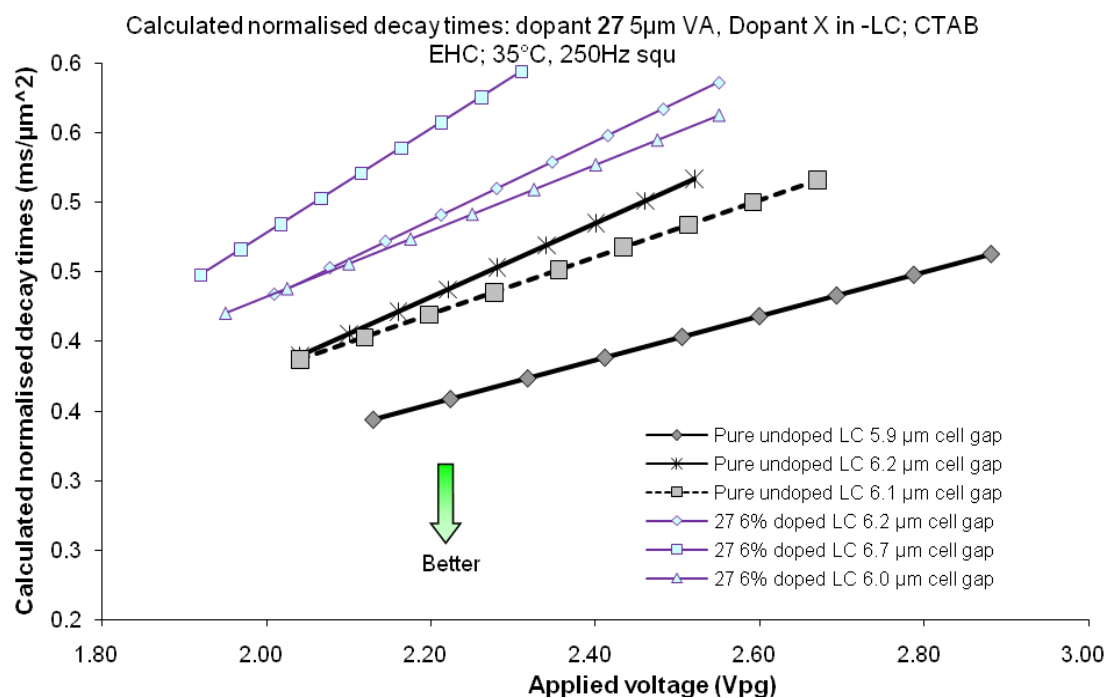


Figure 18p – Calculated decay times for 2% of dopant **28** in –LC Host, batch E

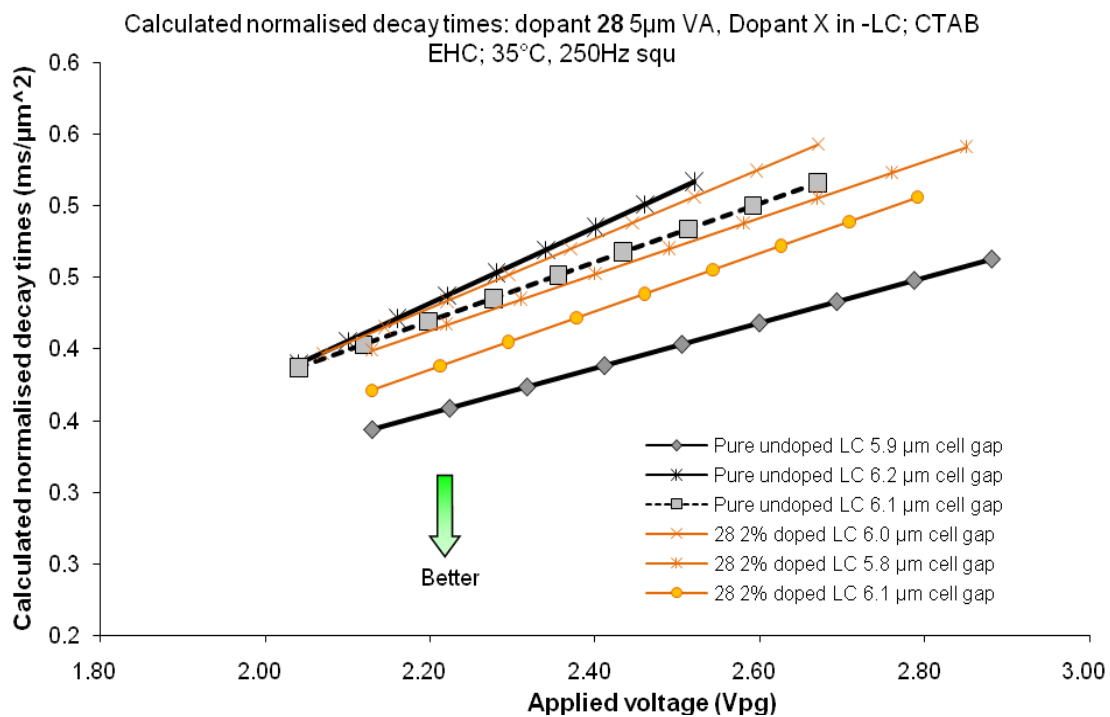


Figure 19a – Calculated decay times for comparable cell gaps of batch A samples

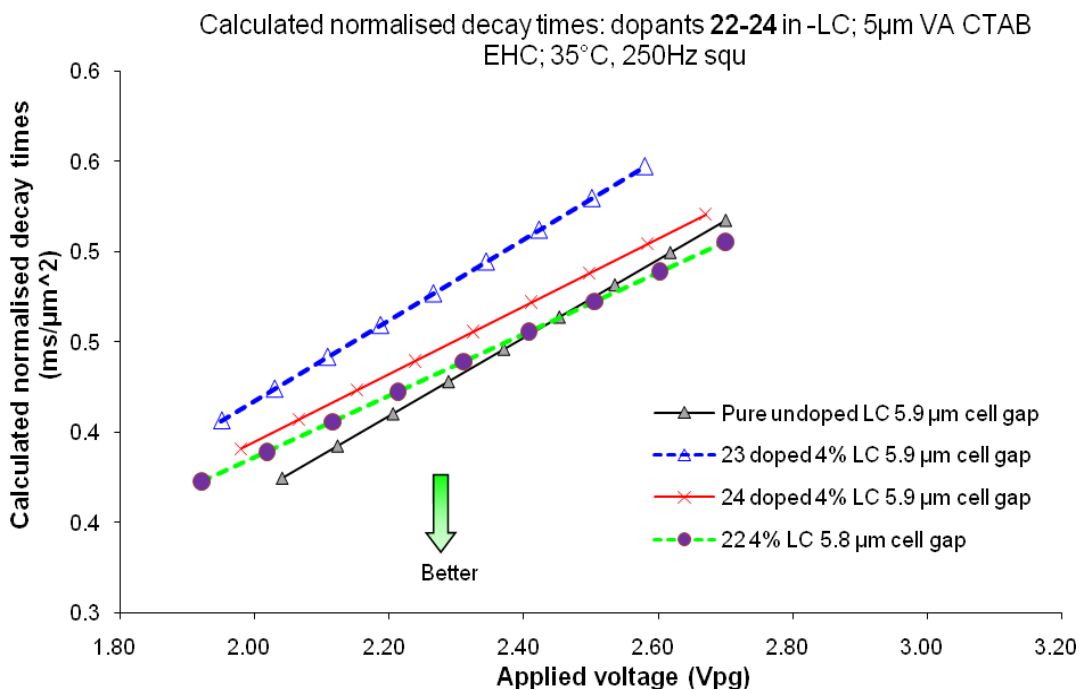


Figure 19d – Calculated decay times for comparable cell gaps of batch D samples

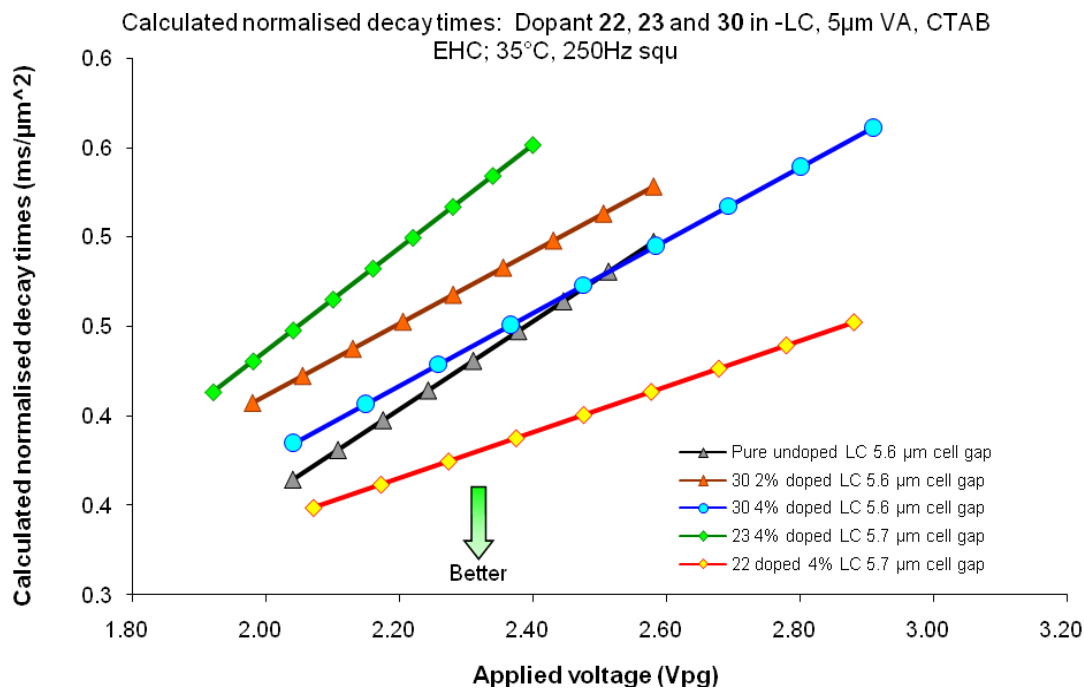


Figure 19e – Calculated decay times for comparable cell gaps of batch E sample

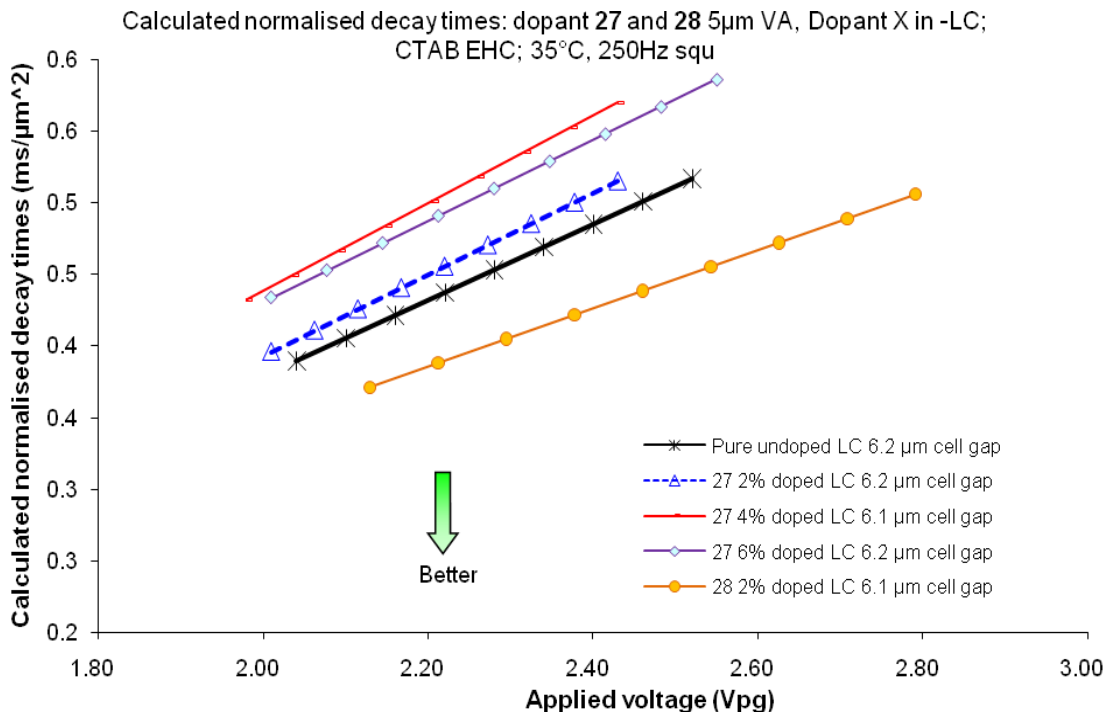


Figure 20a – Calculated rise times for 2% of dopant **32**, Batch F

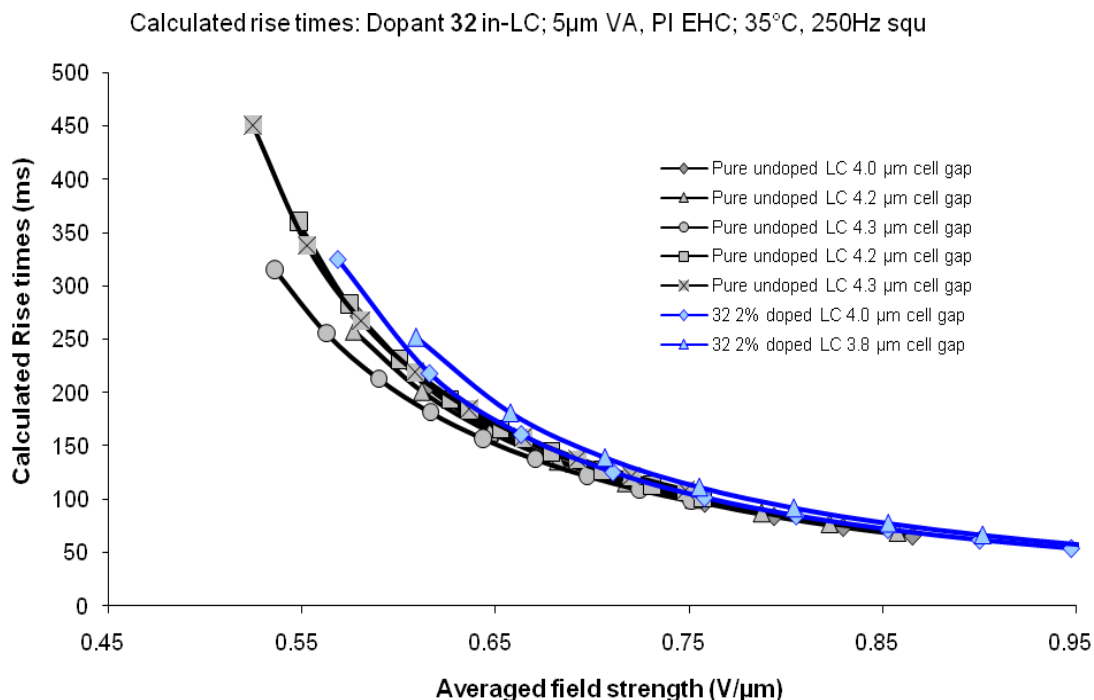


Figure 20b – Calculated rise times for 4% of dopant **32**, Batch F

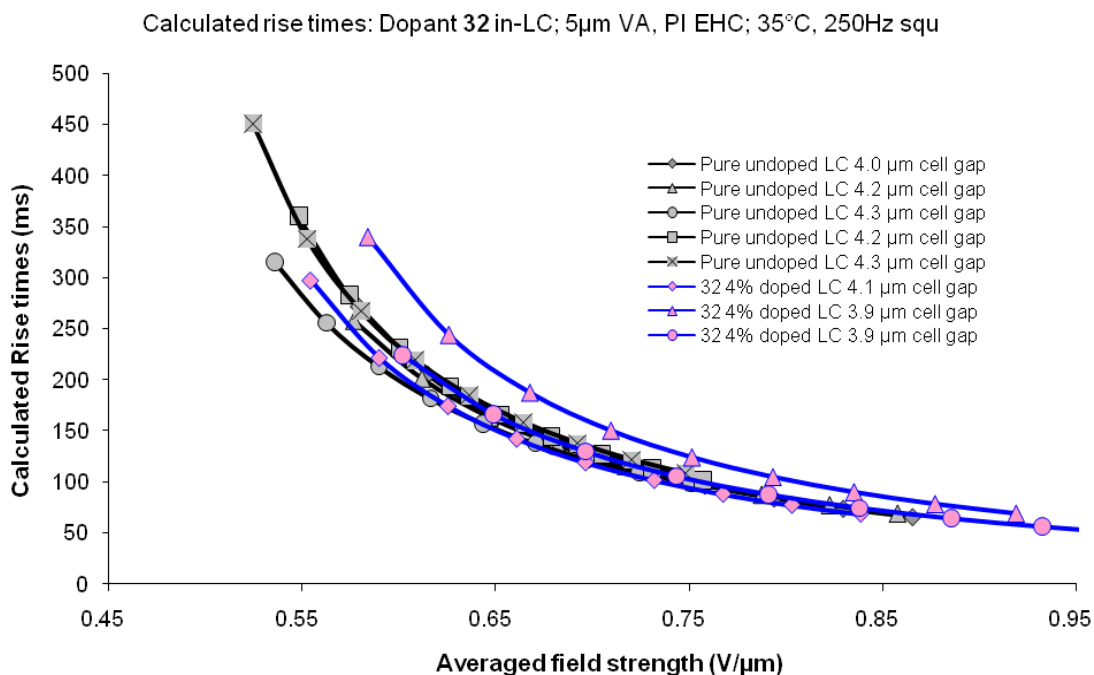


Figure 20c – Calculated rise times for 2% of dopant **34**, Batch F

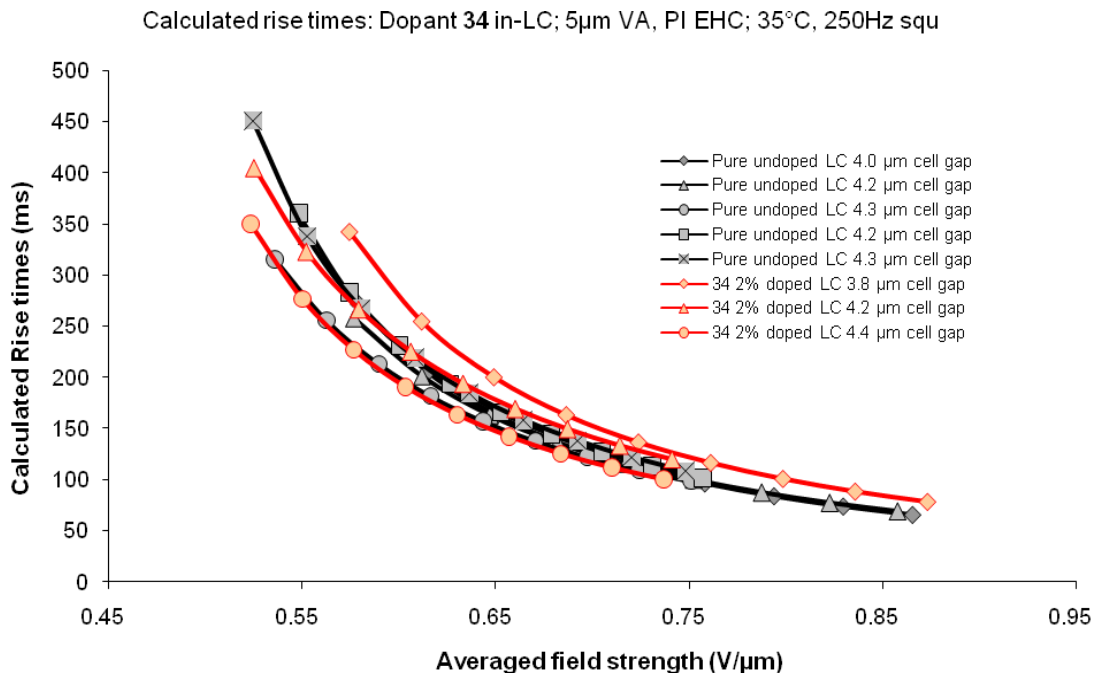


Figure 20d – Calculated rise times for 4% of dopant **34**, Batch F

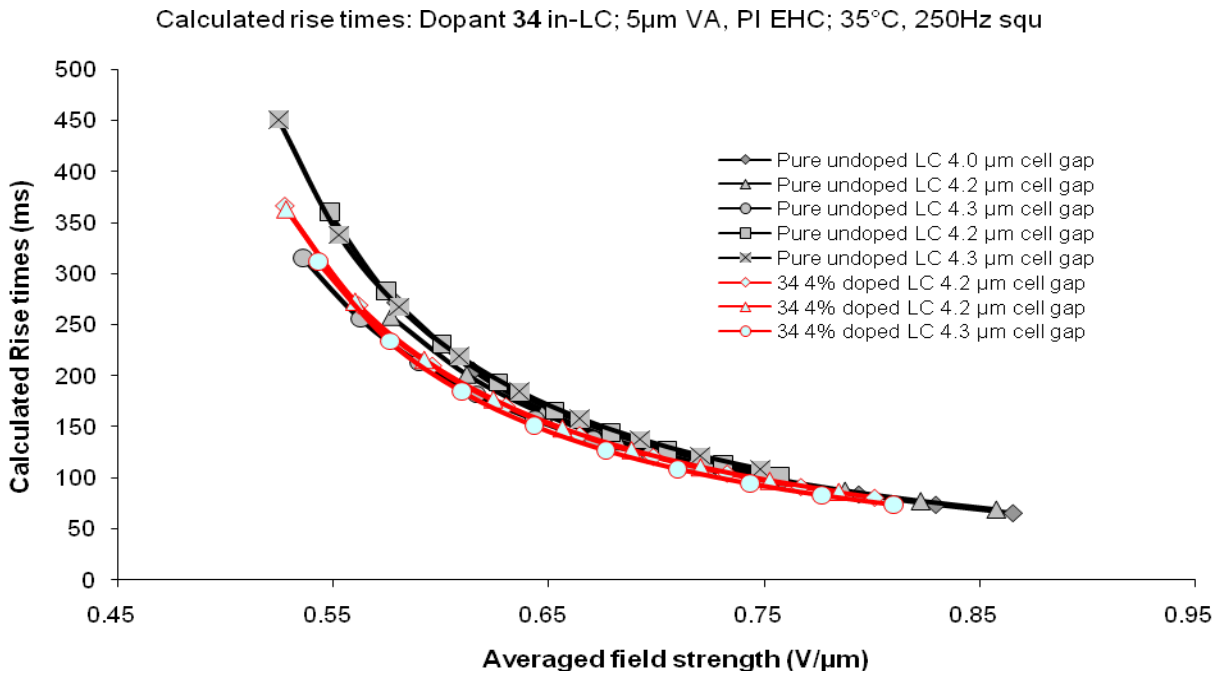


Figure 20e – Calculated rise times for 4% of dopant **44**, Batch G

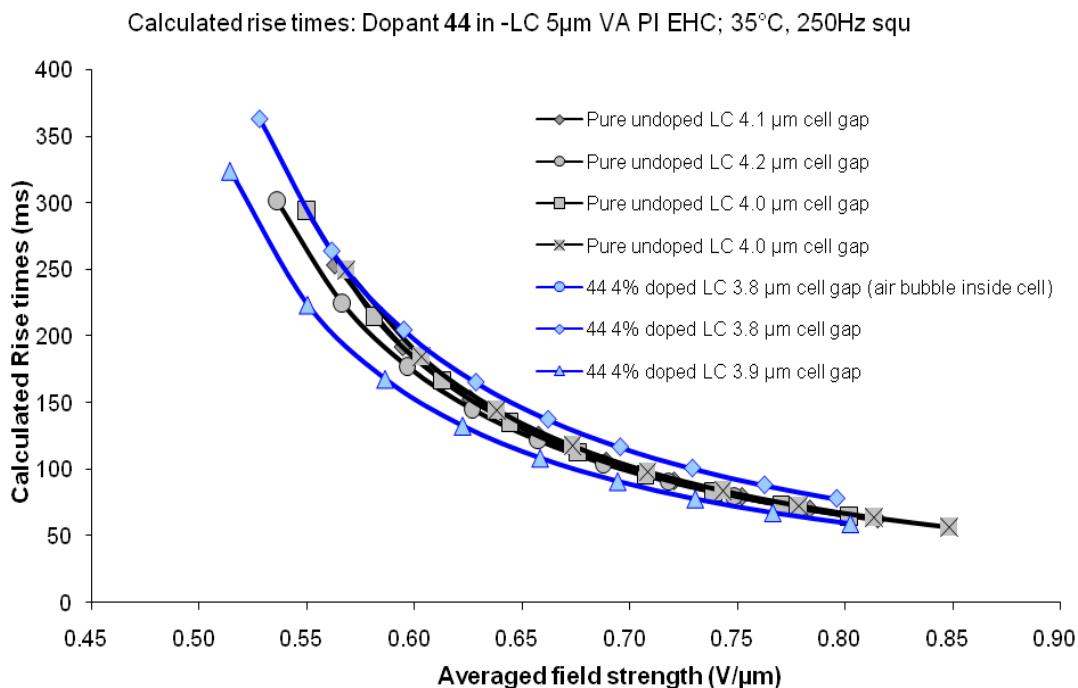


Figure 20f – Calculated rise times for 4% of dopant **46**, Batch G

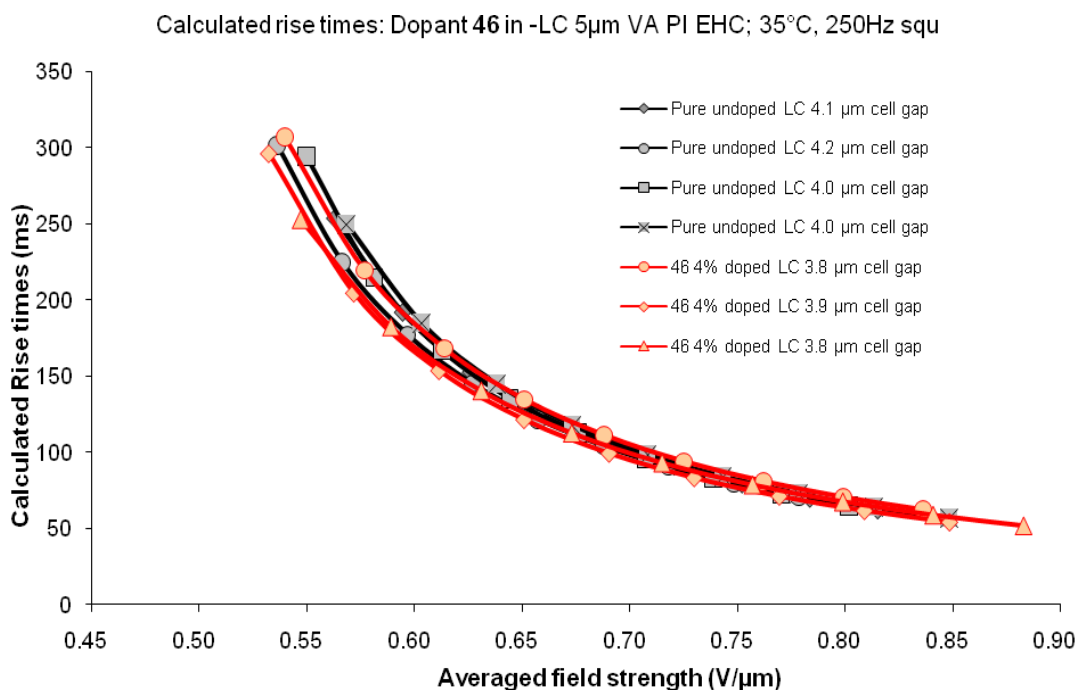


Figure 20g – Calculated rise times for 4% of dopant 48, Batch G

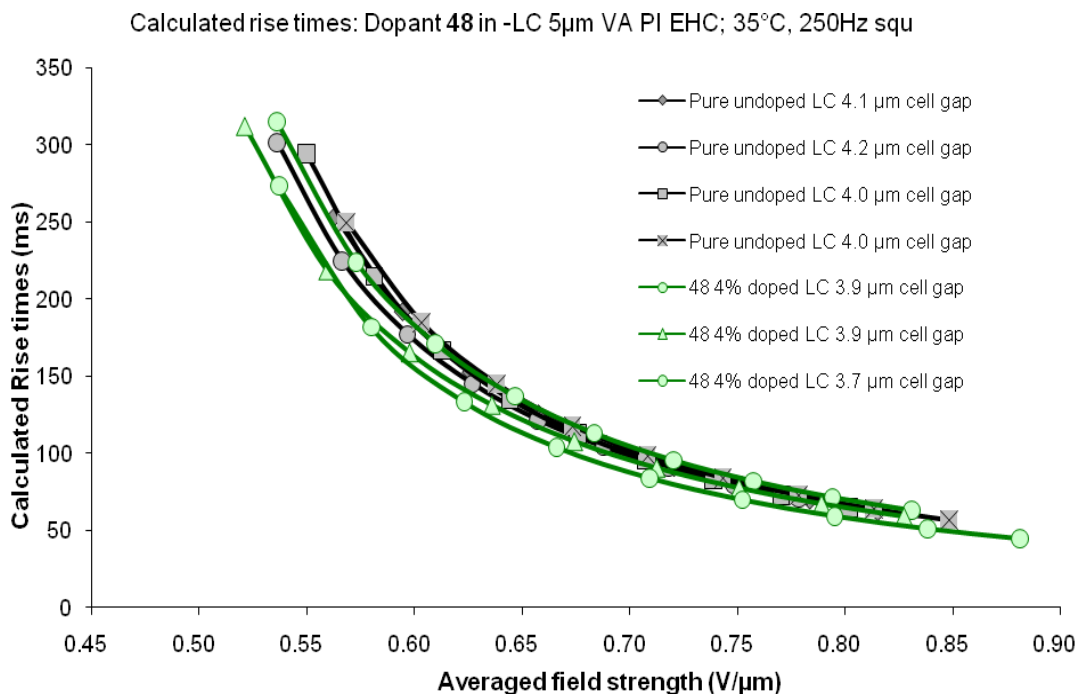


Figure 21a – Calculated rise times for comparable cell gaps of batch F samples

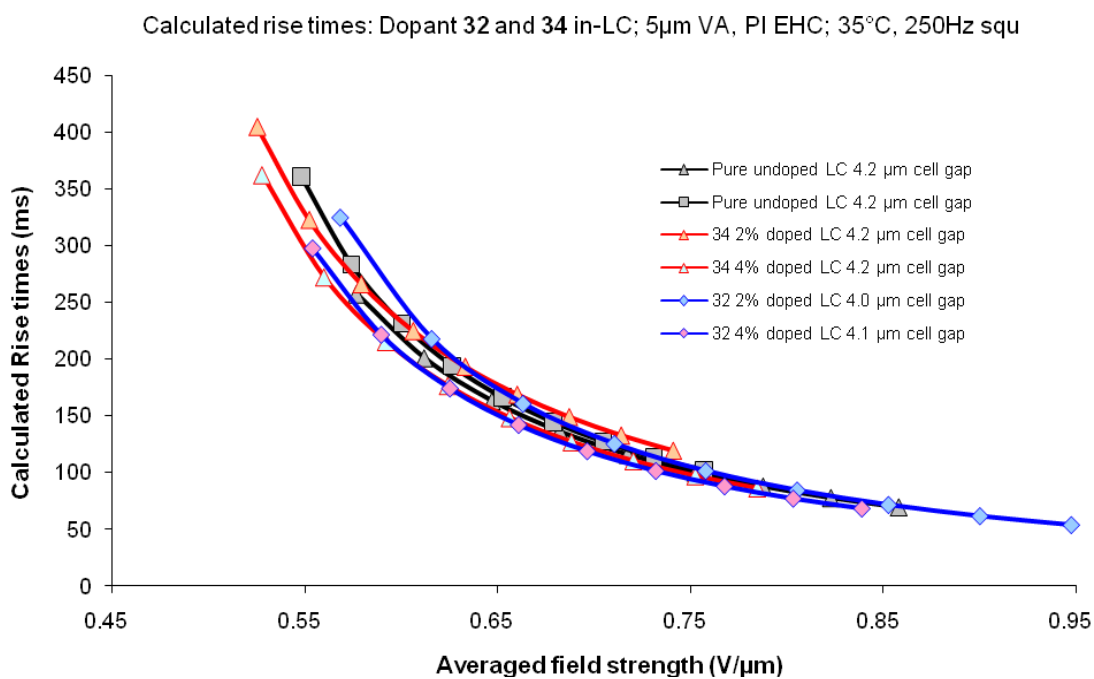


Figure 21b – Calculated rise times for comparable cell gaps of batch G samples

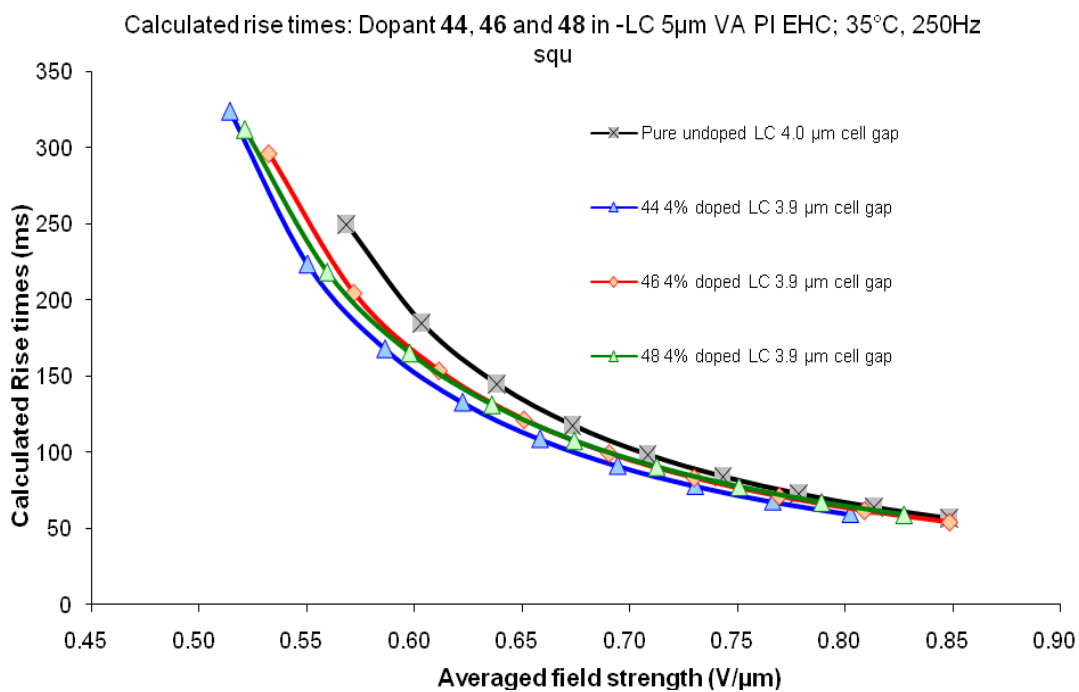


Figure 22 – VHR data of dopant 32 and 34 in -LC host

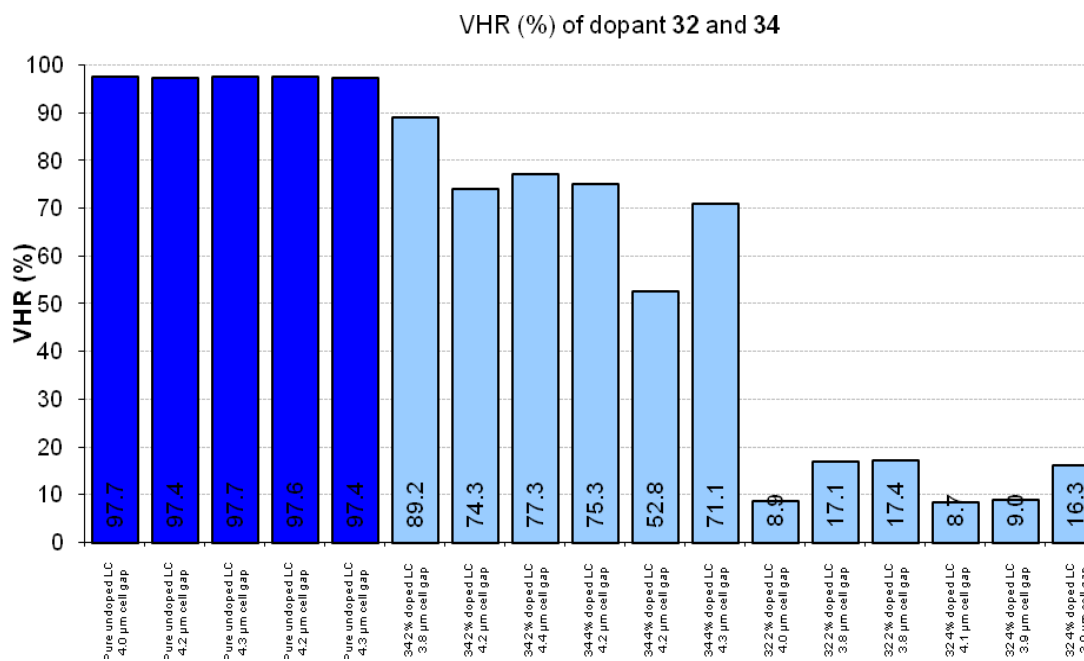


Figure 23 – VHR data of dopants **44**, **46** and **48** in -LC host

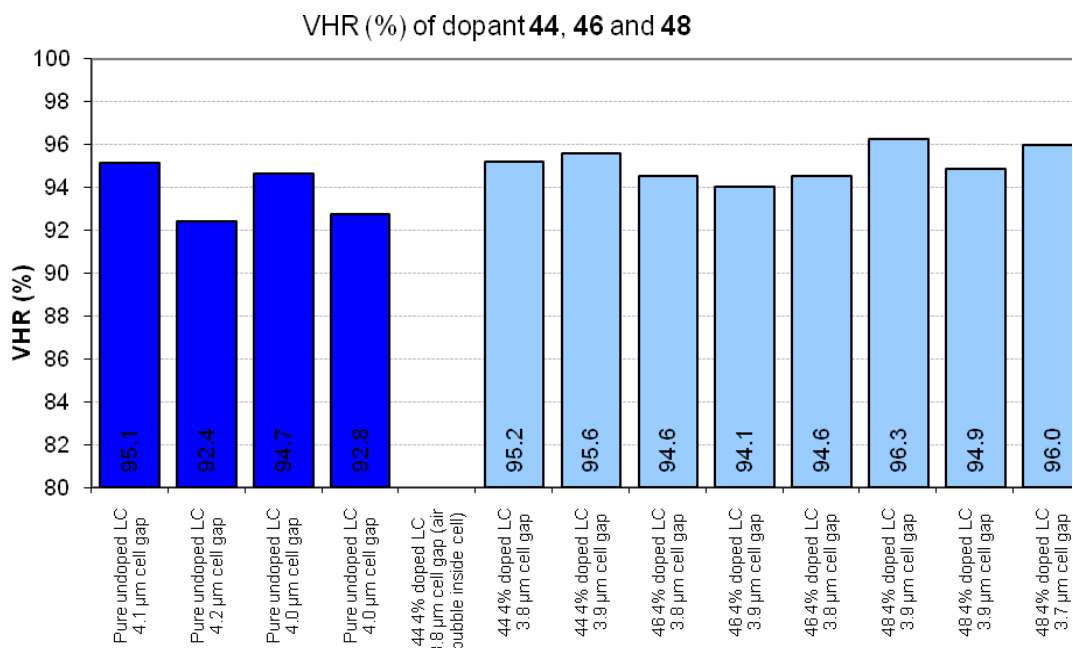


Figure 24a – Calculated decay times for 2% of dopant **32**, Batch F

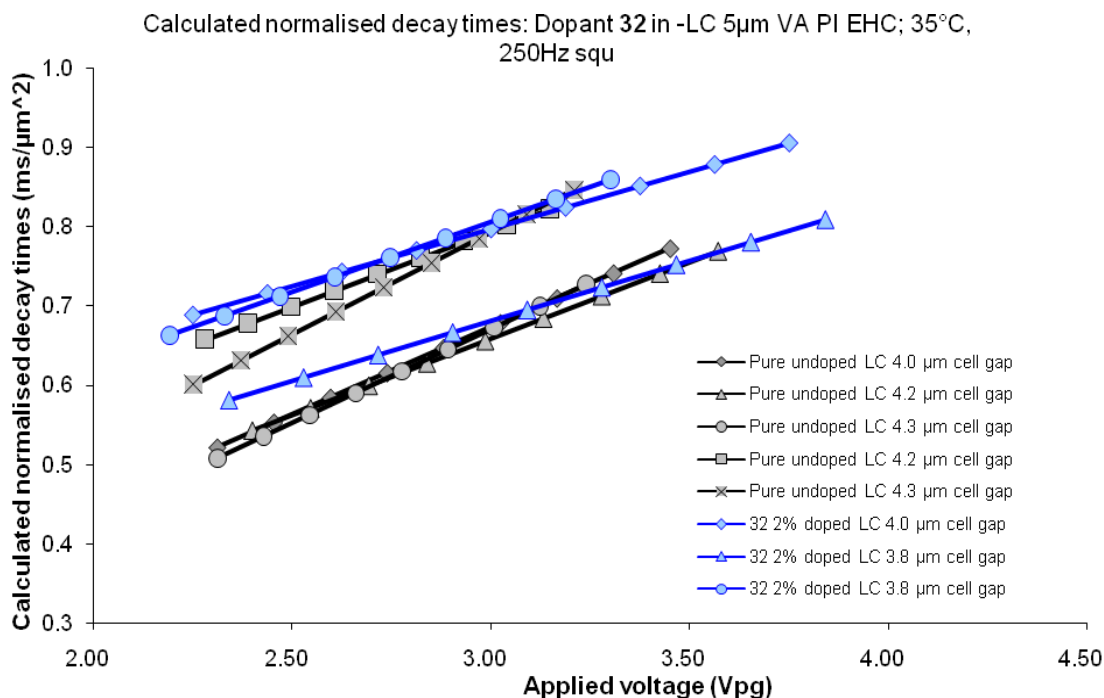


Figure 24b – Calculated decay times for 4% of dopant **32**, Batch F

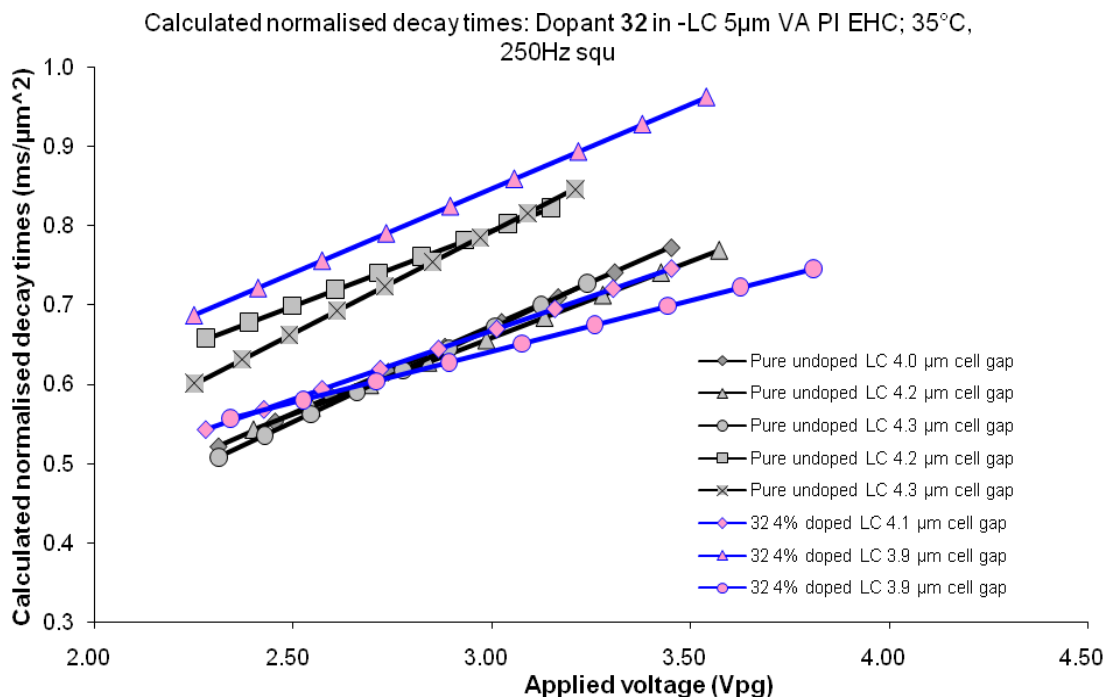


Figure 24c – Calculated decay times for 2% of dopant **34**, Batch F

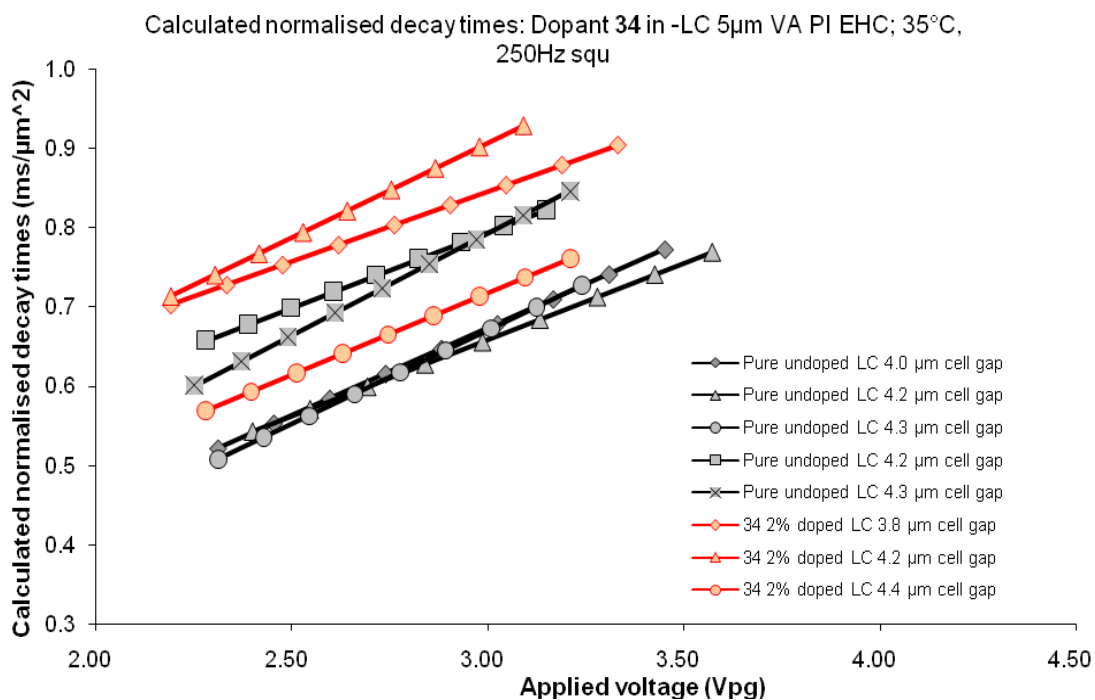


Figure 24d – Calculated decay times for 4% of dopant **34**, Batch F

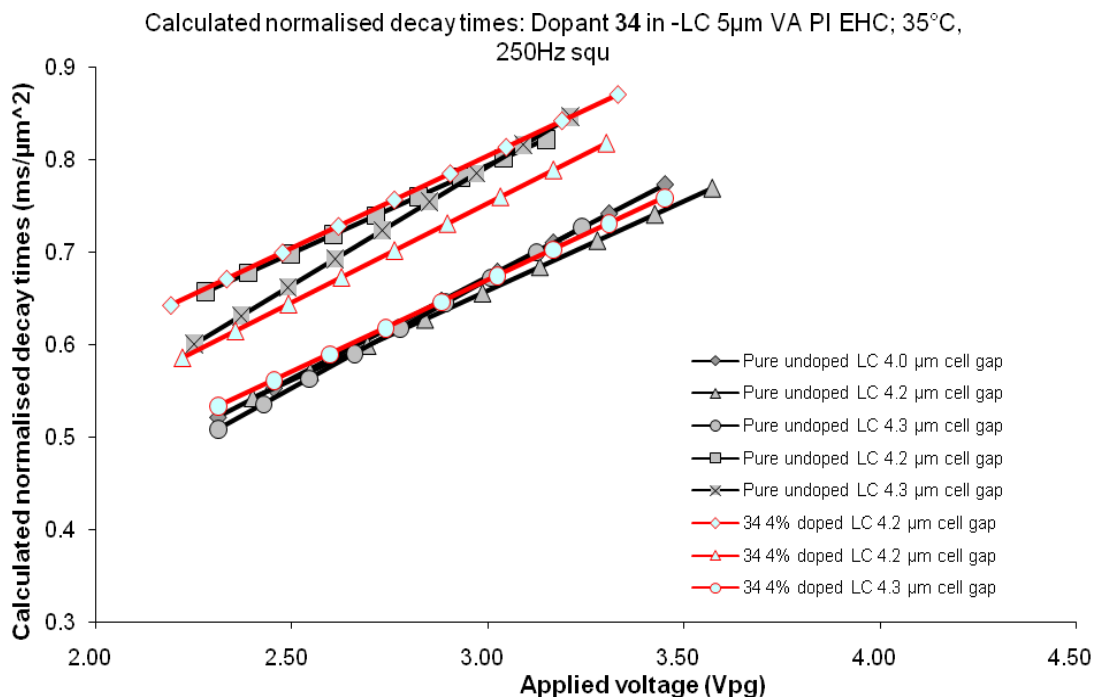


Figure 24e – Calculated decay times for 4% of dopant **44**, Batch G

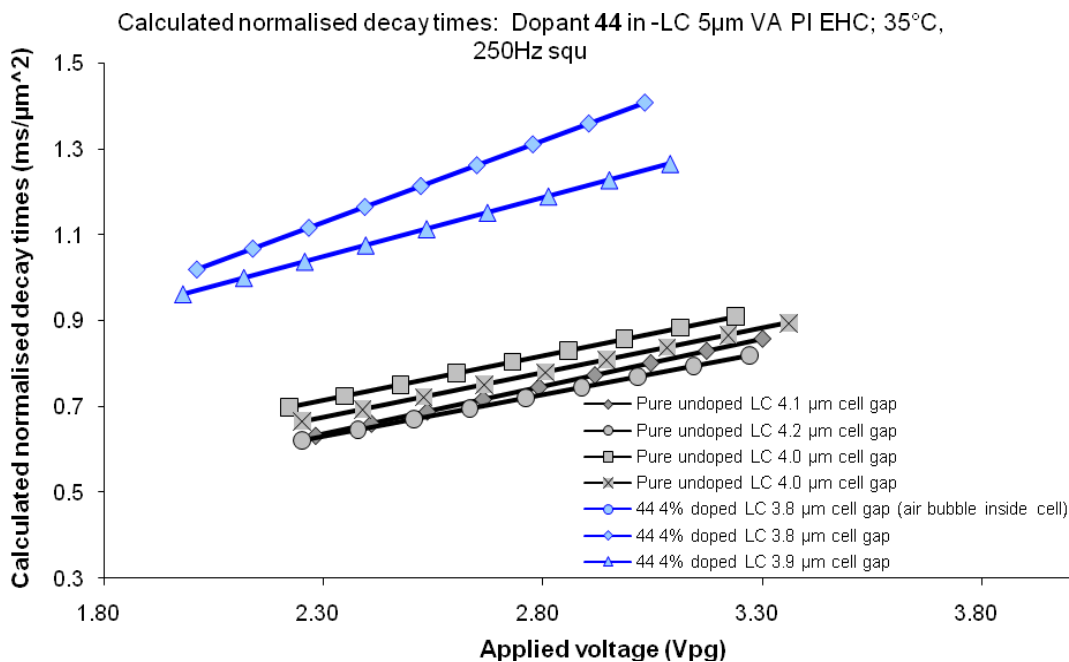


Figure 24f – Calculated decay times for 4% of dopant **46**, Batch G

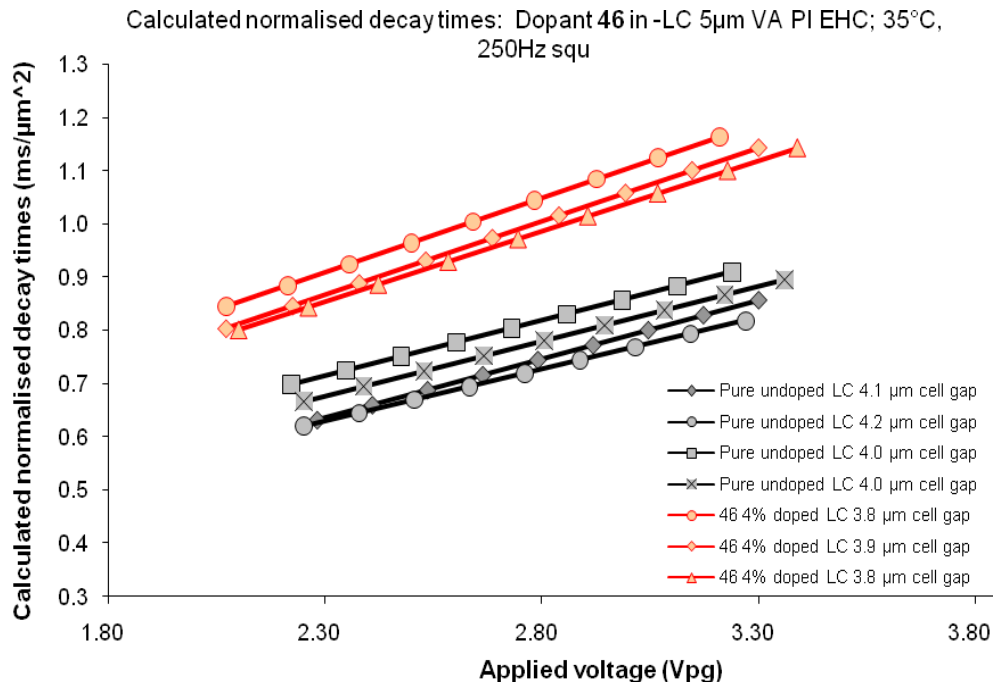


Figure 24g – Calculated decay times for 4% of dopant **48**, Batch G

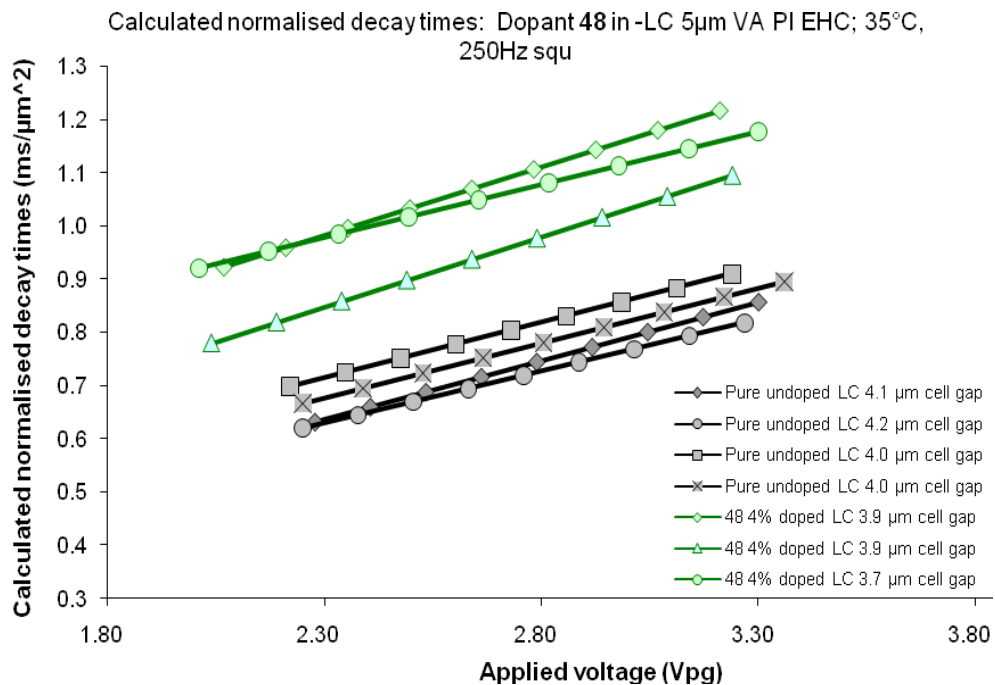


Figure 25a – Calculated decay times for comparable cell gaps of batch F samples

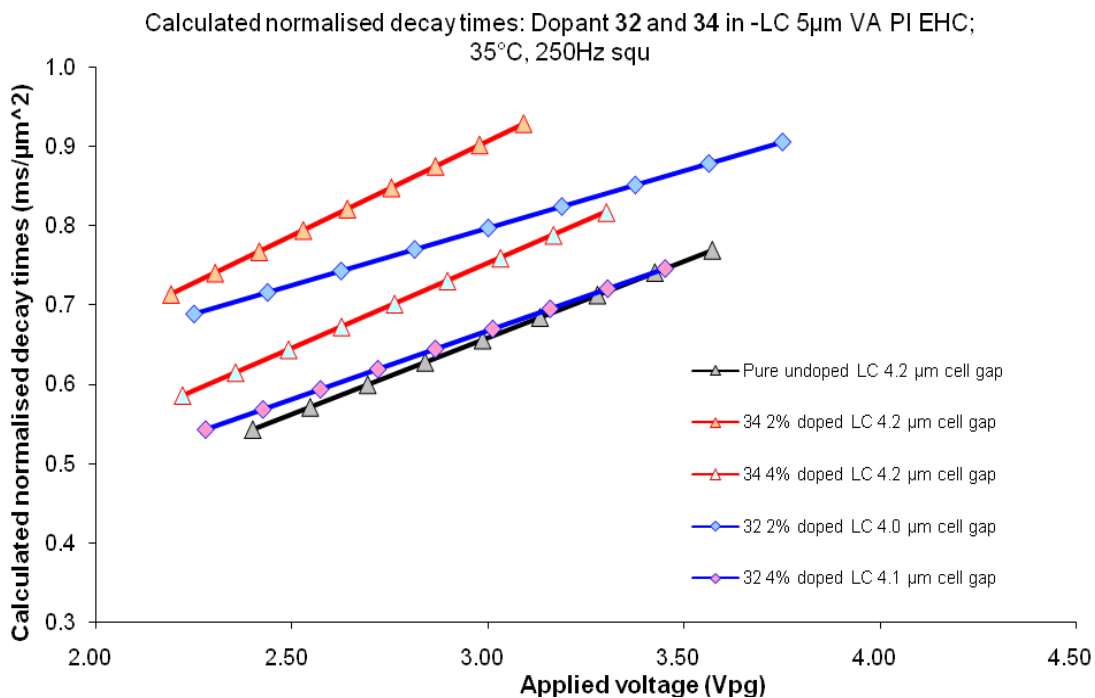


Figure 25b – Calculated decay times for comparable cell gaps of batch G samples

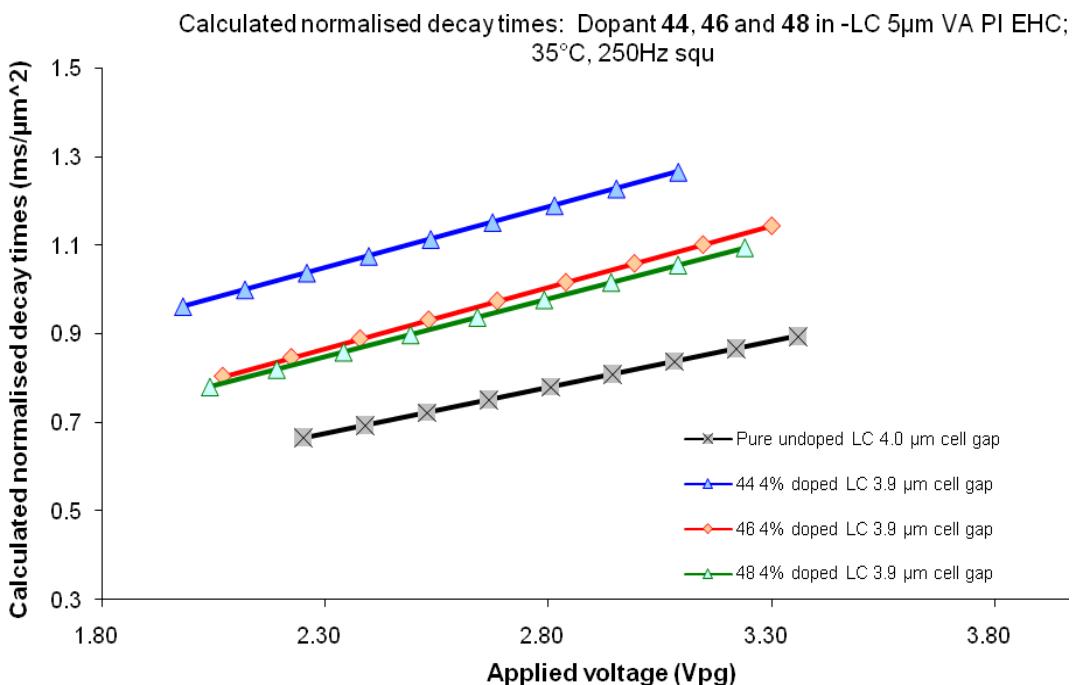


Figure 26a – Calculated rise times for 2% of dopant **32**, Batch H

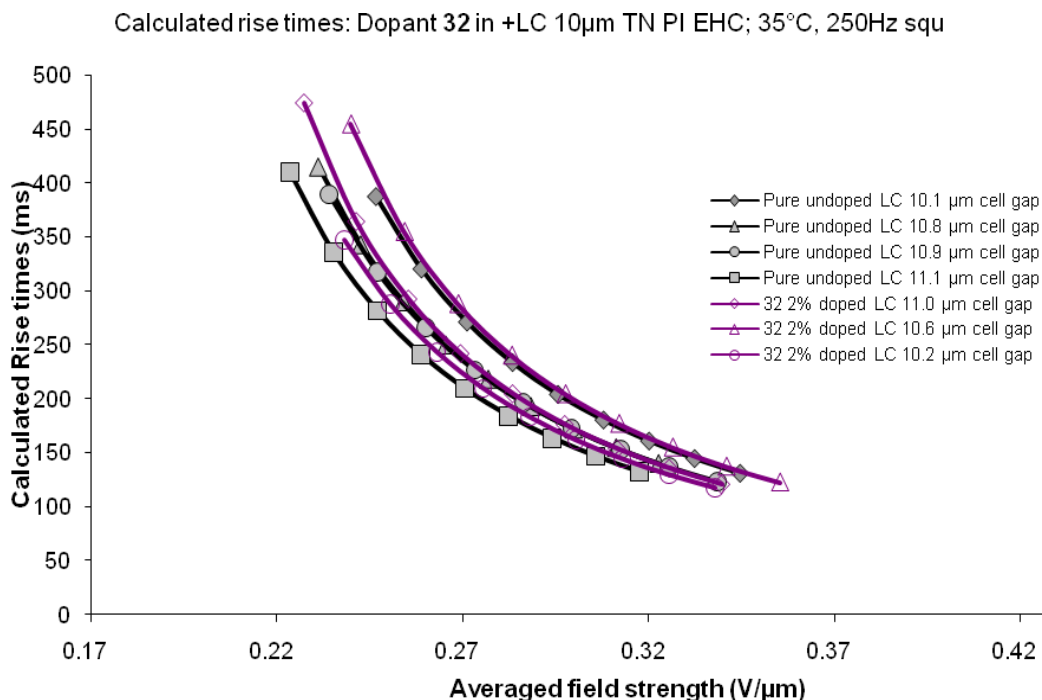


Figure 26b – Calculated rise times for 4% of dopant **32**, Batch H

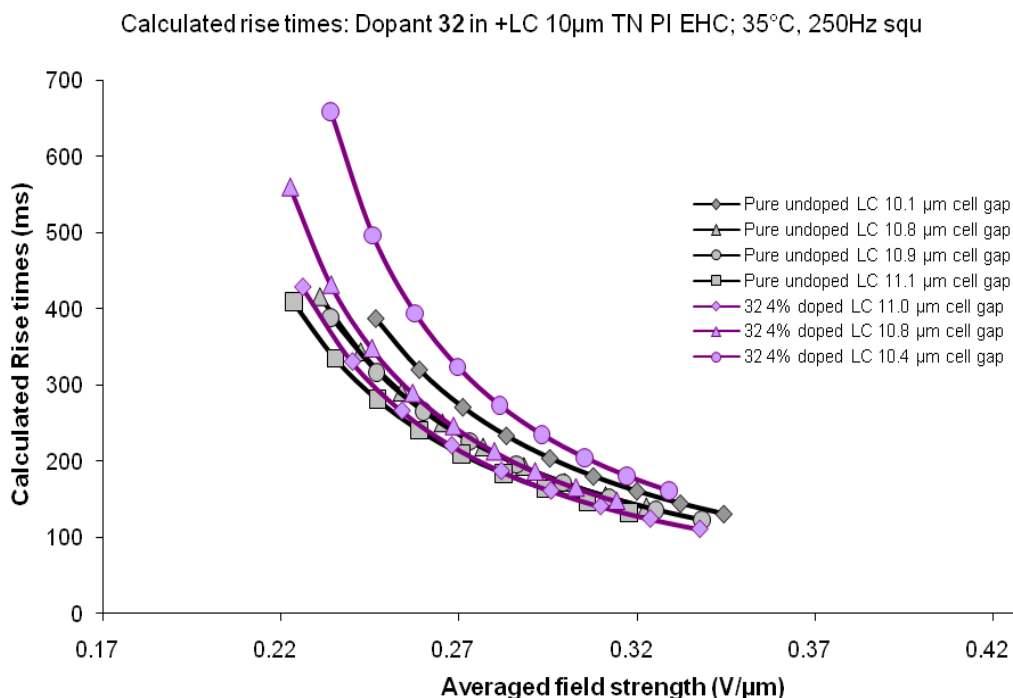


Figure 26c – Calculated rise times for 2% of dopant **34**, Batch H

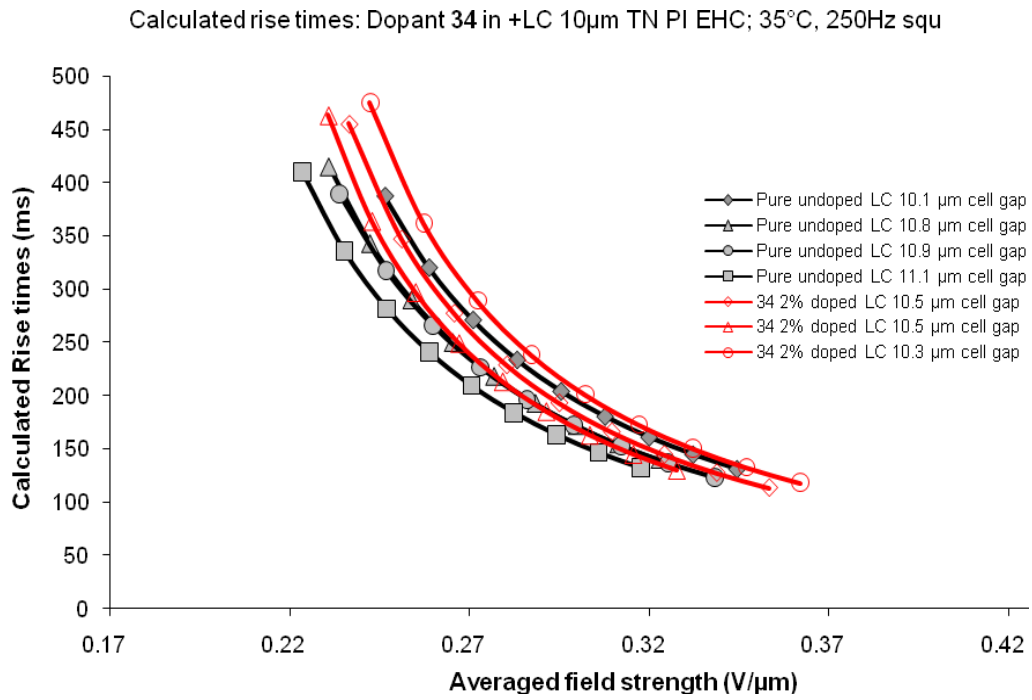


Figure 26d – Calculated rise times for 4% of dopant **34**, Batch H

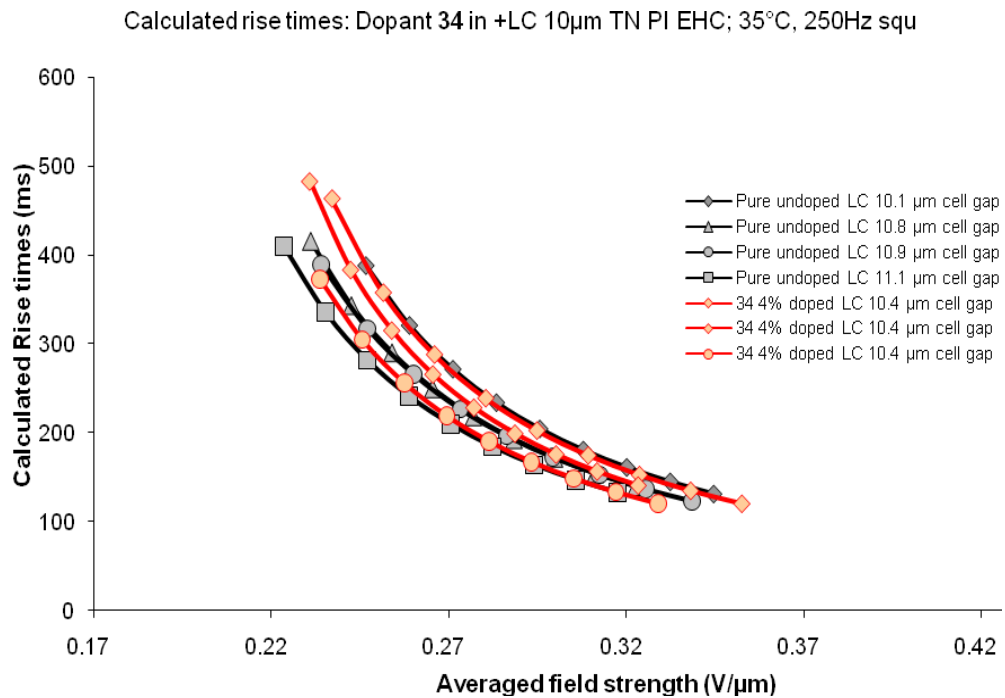


Figure 26e – Calculated rise times for 4% of dopant **41**, Batch H

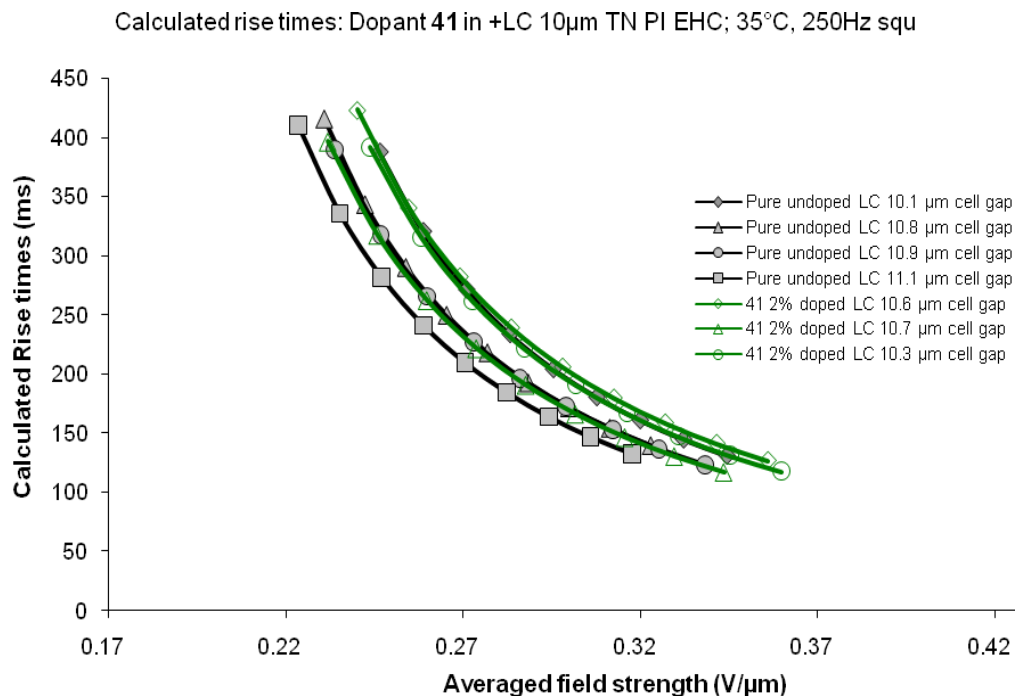


Figure 26f – Calculated rise times for 4% of dopant **44**, Batch I

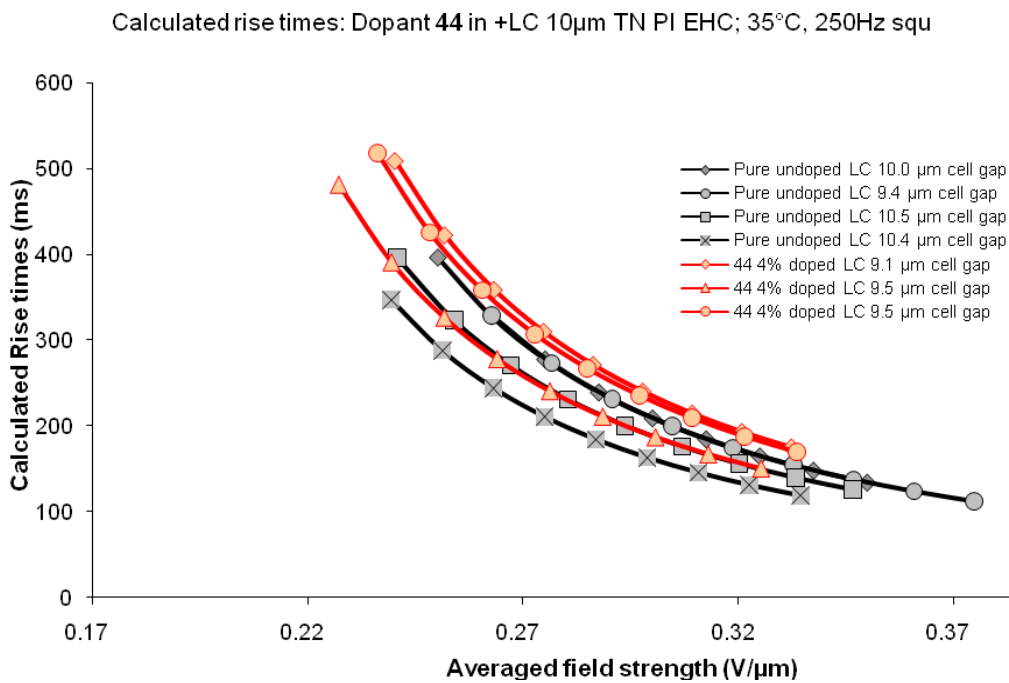


Figure 26g – Calculated rise times for 4% of dopant **46**, Batch I

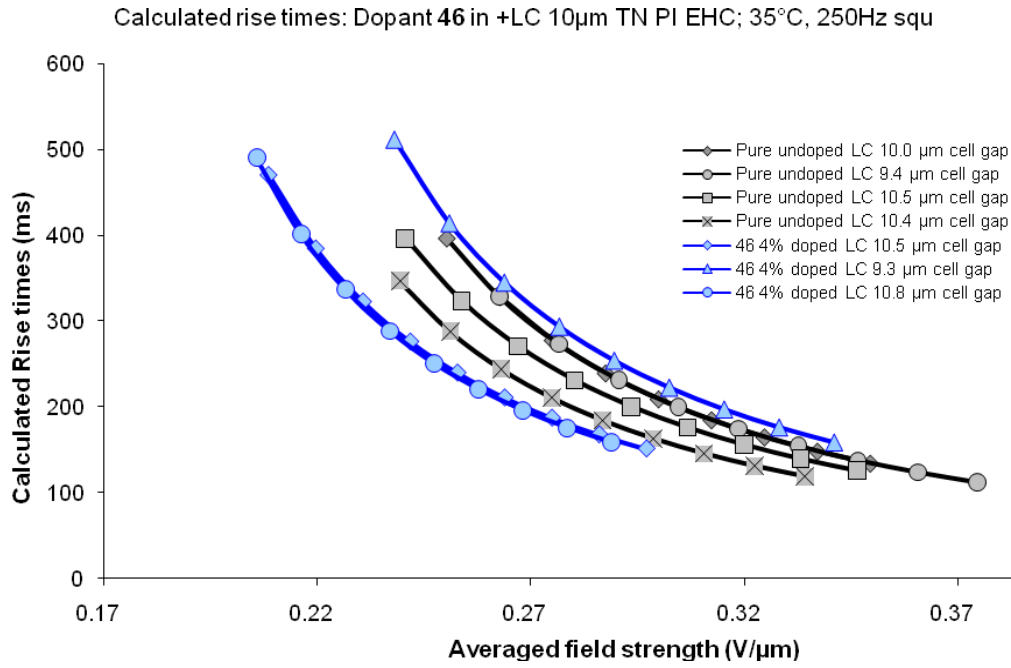


Figure 26h – Calculated rise times for 4% of dopant **48**, Batch I

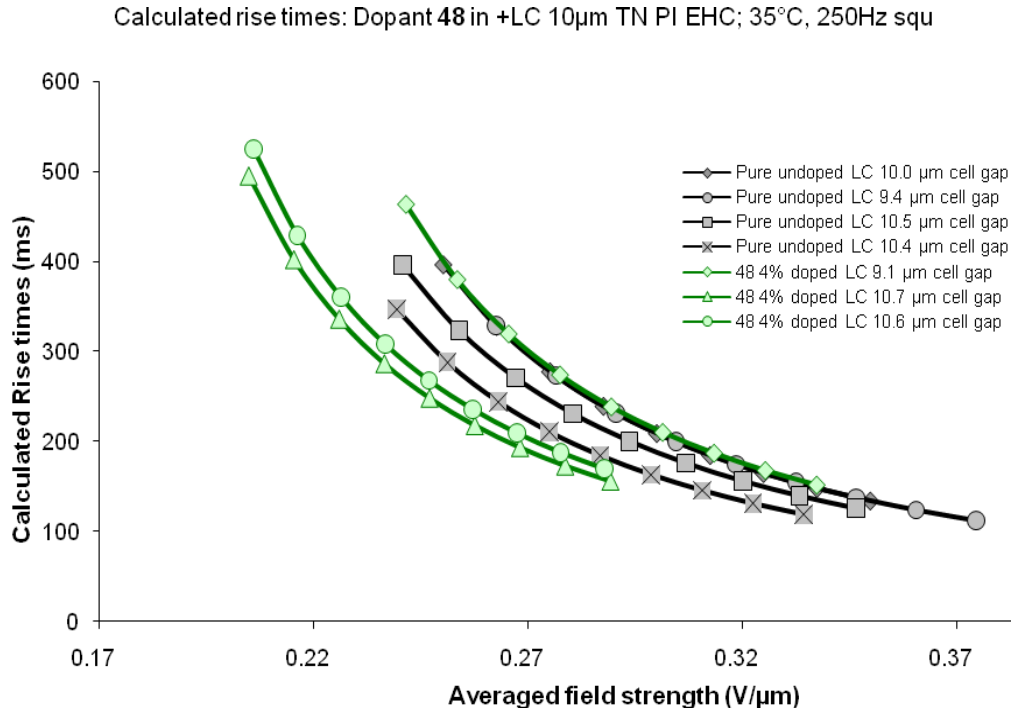


Figure 27a – Calculated rise times for comparable cell gaps of batch H samples

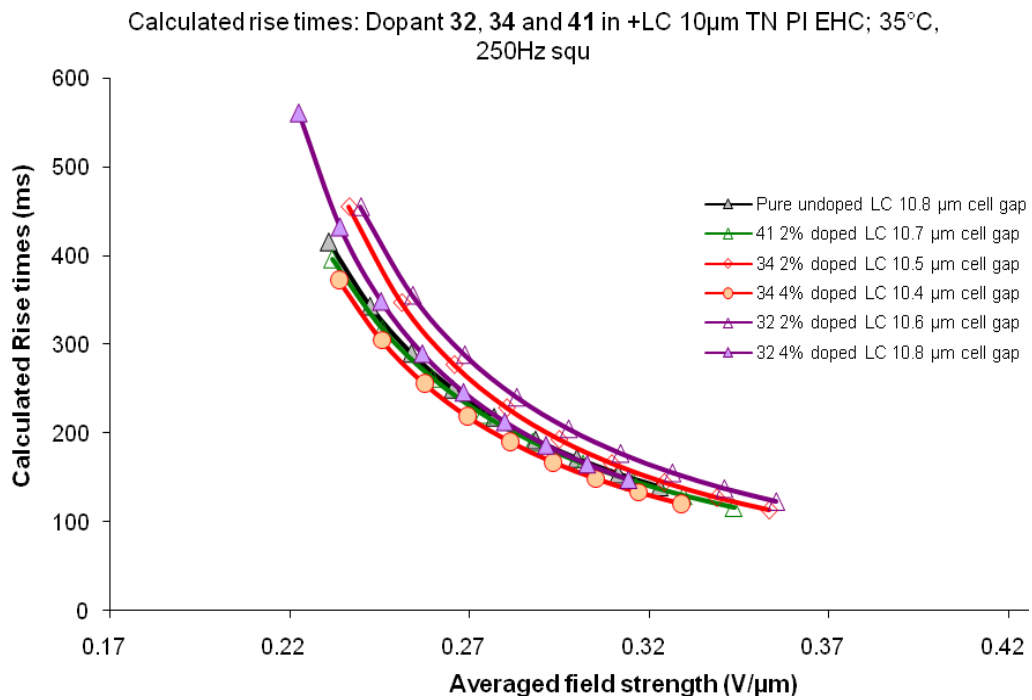


Figure 27b – Calculated rise times for comparable cell gaps of batch I samples

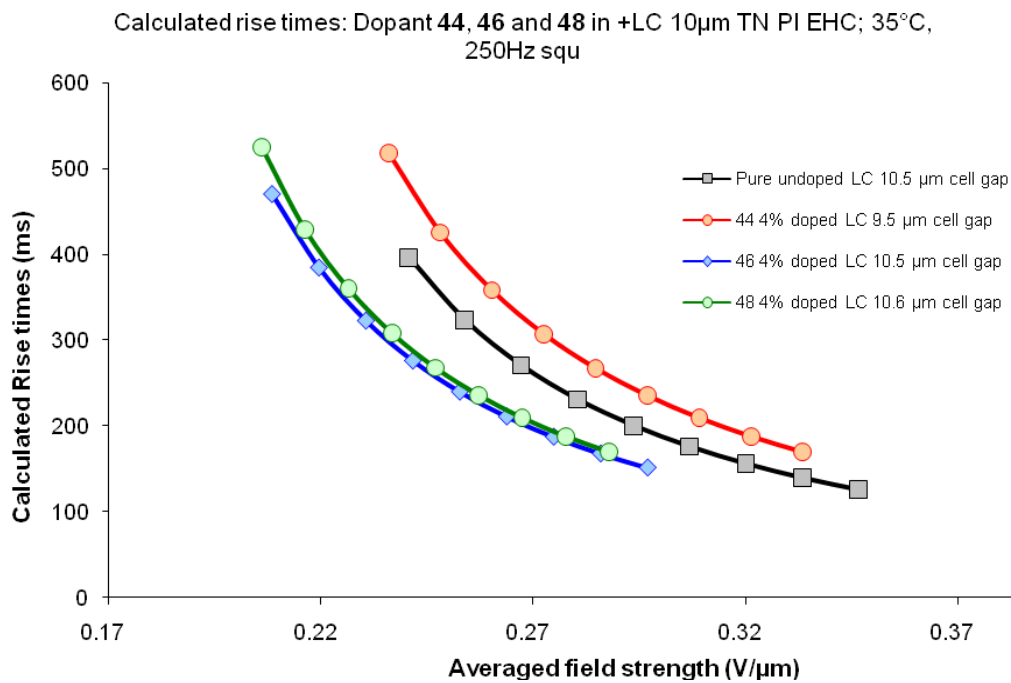


Figure 28 – VHR data of dopant **32**, **34** and **41** in +LC host

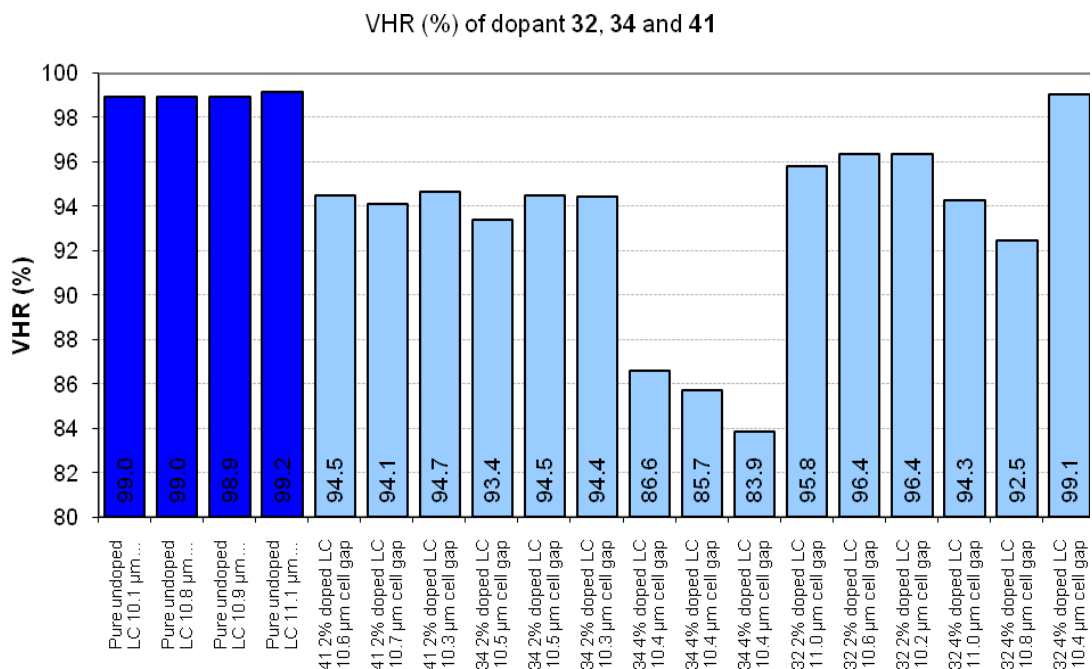


Figure 29 – VHR data of dopants **44**, **46** and **48** in +LC host

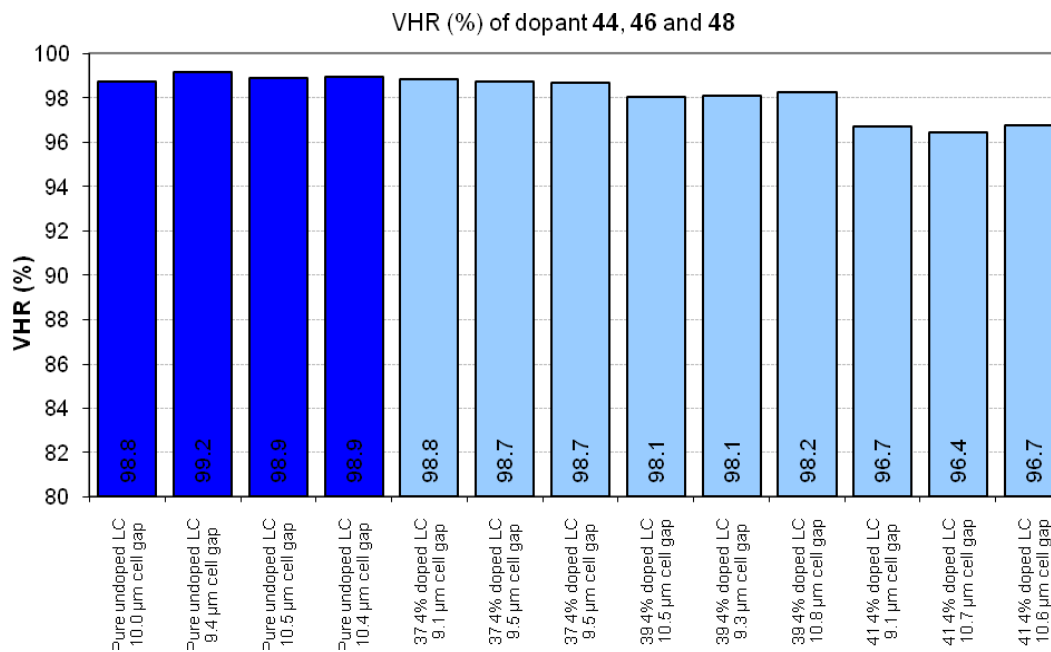


Figure 30a – Calculated decay times for 2% of dopant **32**, Batch H

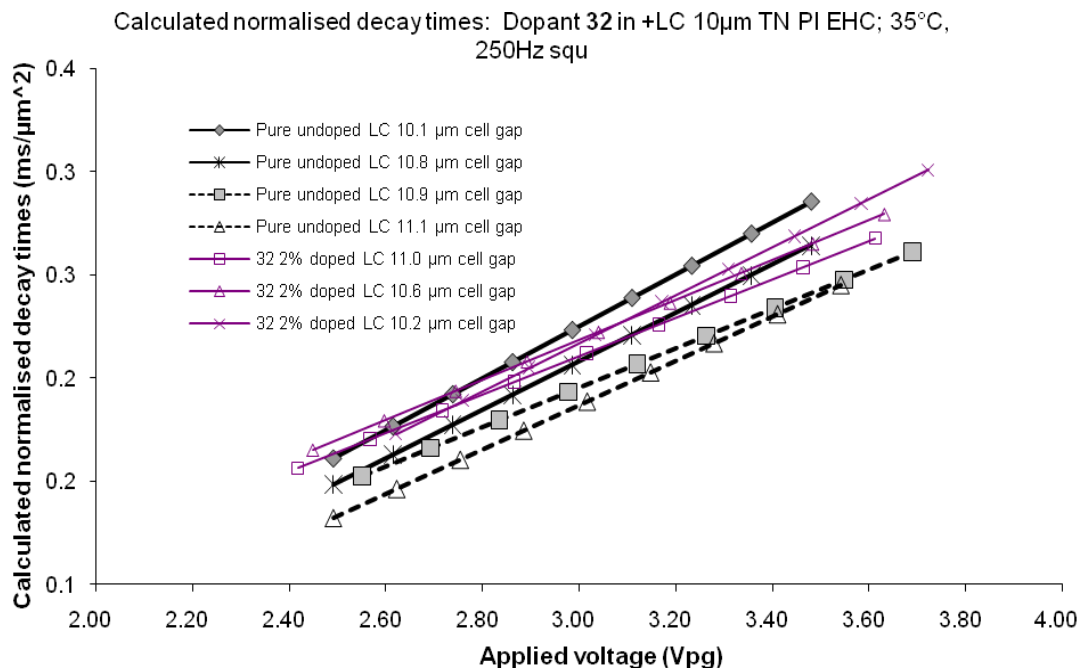


Figure 30b – Calculated decay times for 4% of dopant **32**, Batch H

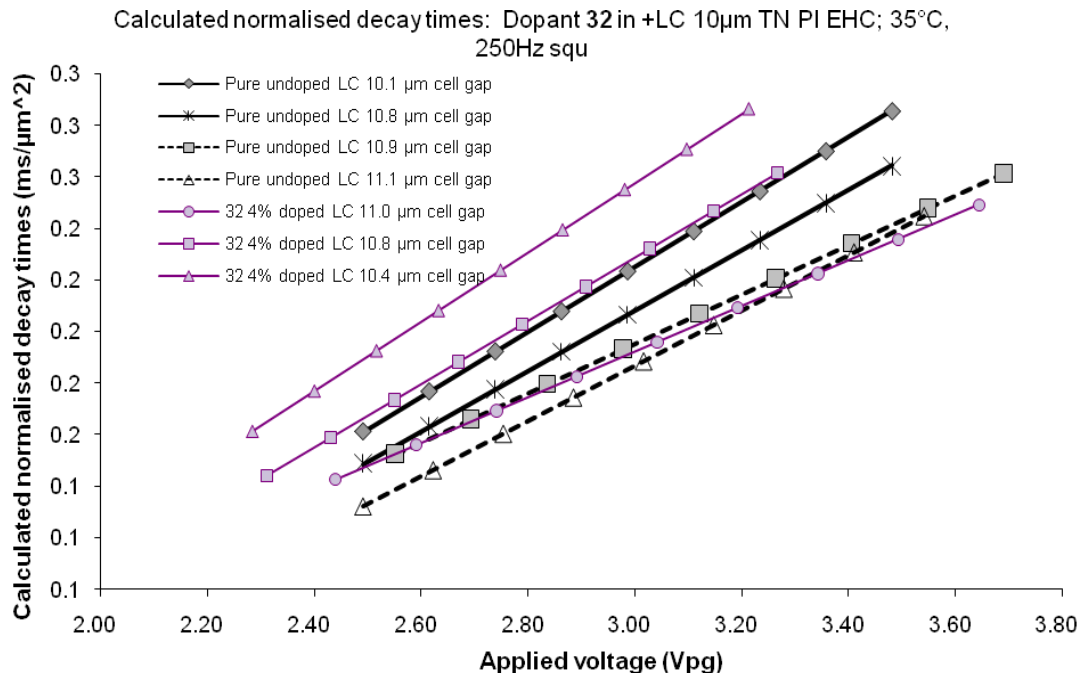


Figure 30c – Calculated decay times for 2% of dopant **34**, Batch H

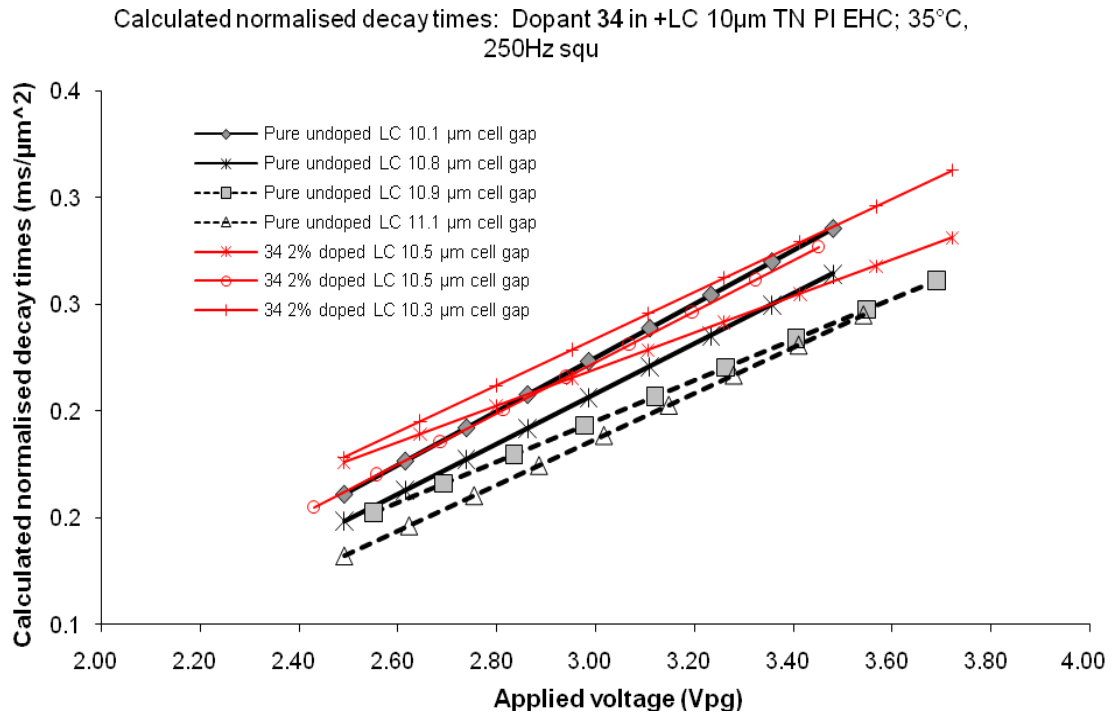


Figure 30d – Calculated decay times for 4% of dopant **34**, Batch H

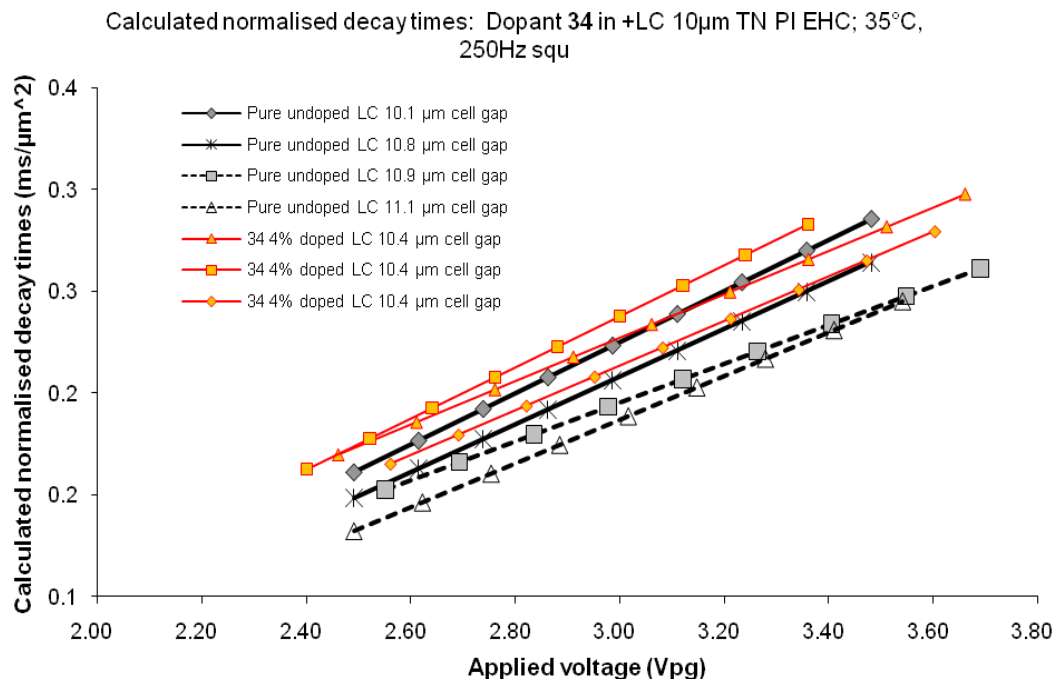


Figure 30e – Calculated decay times for 2% of dopant **41**, Batch H

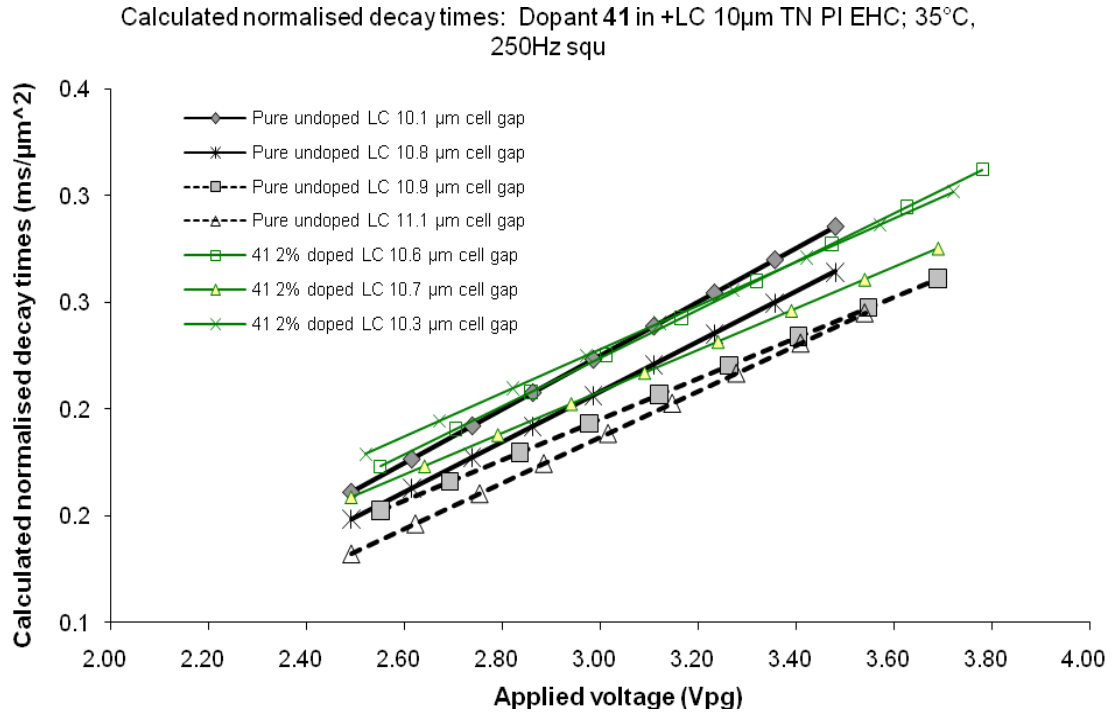


Figure 30f – Calculated decay times for 4% of dopant **44**, Batch I

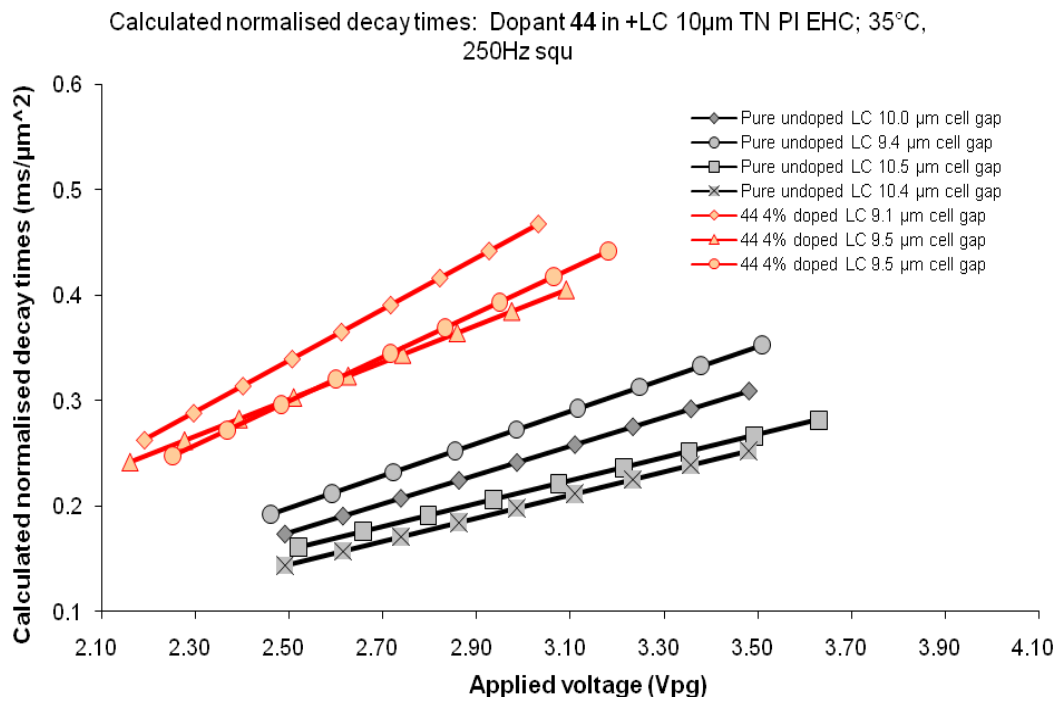


Figure 30g – Calculated decay times for 4% of dopant **46**, Batch I

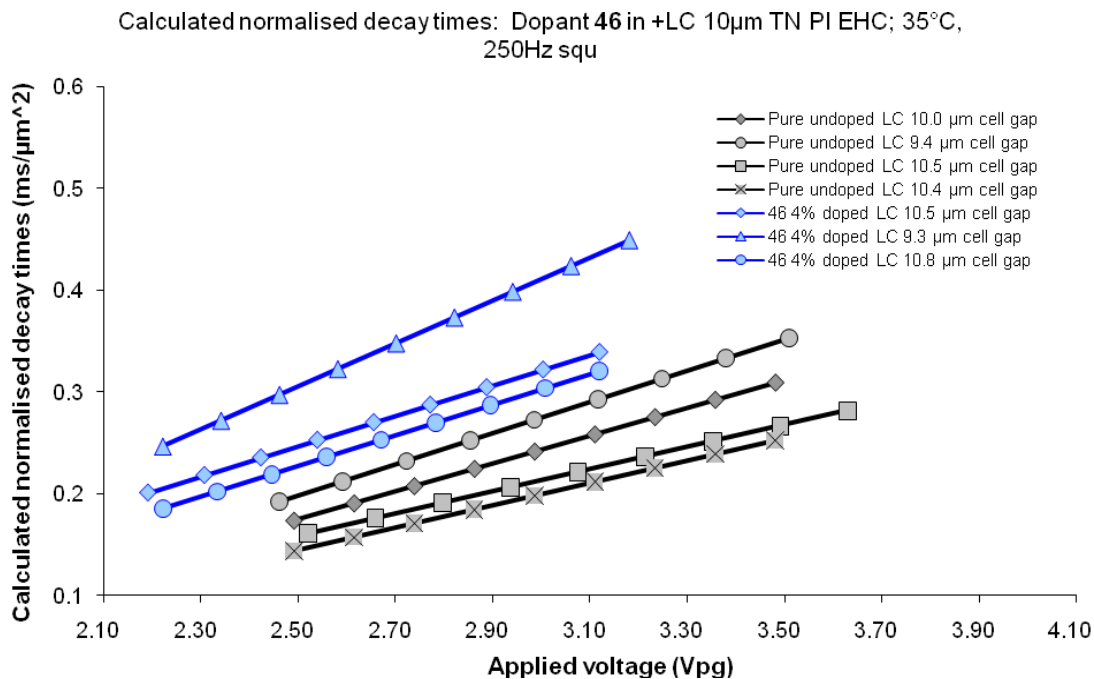


Figure 30h – Calculated decay times for 4% of dopant **48**, Batch I

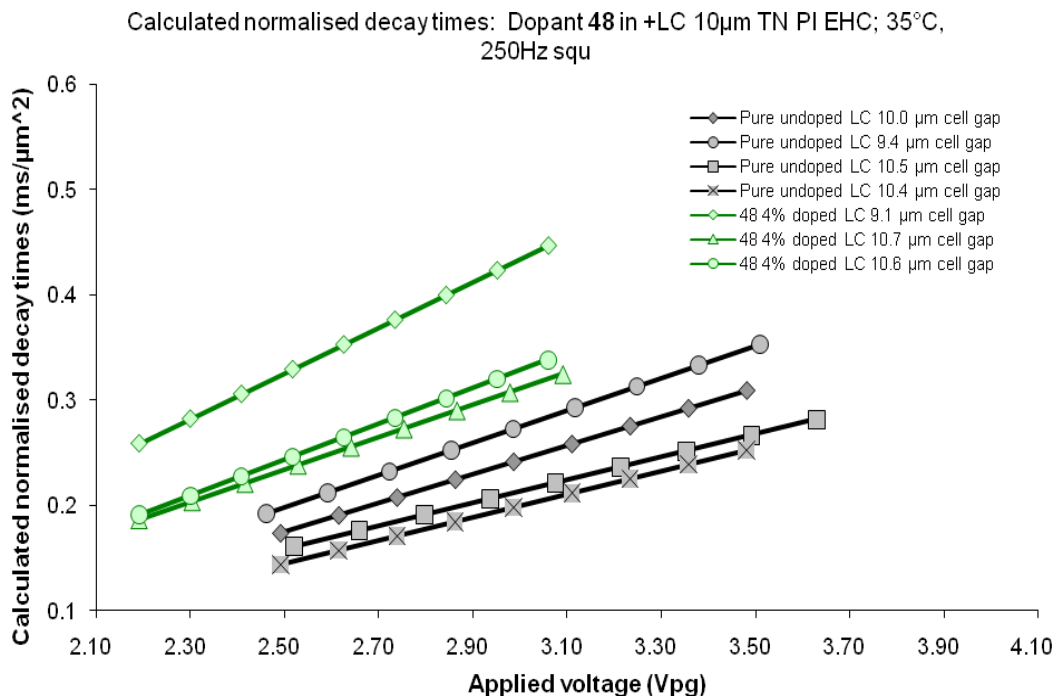


Figure 31a – Calculated decay times for comparable cell gaps of batch H samples

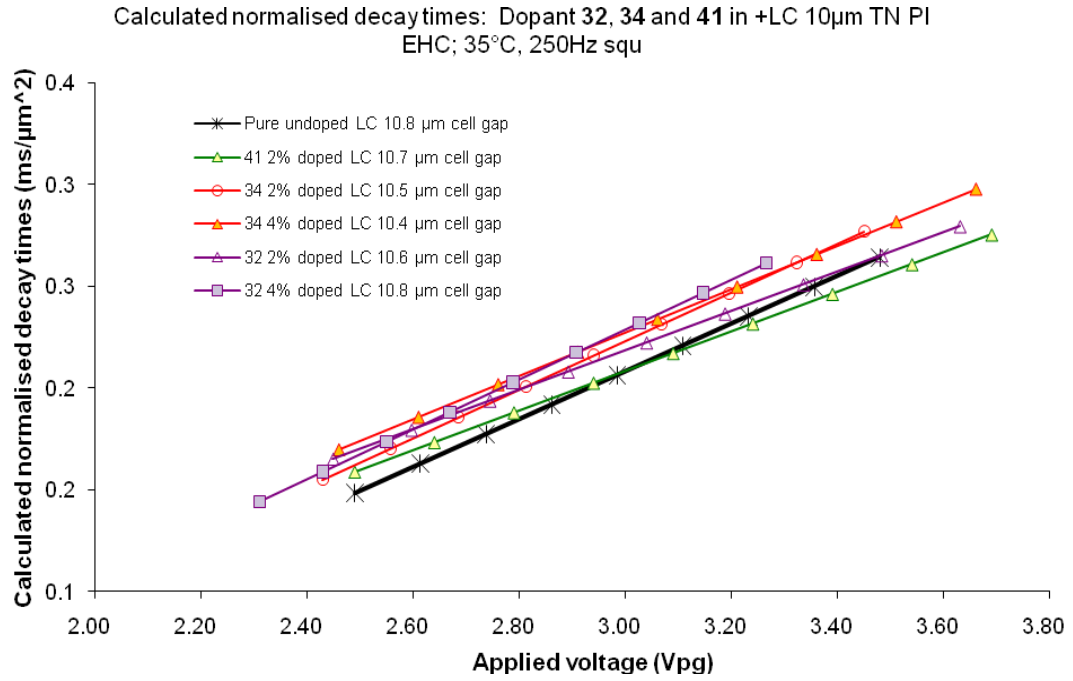
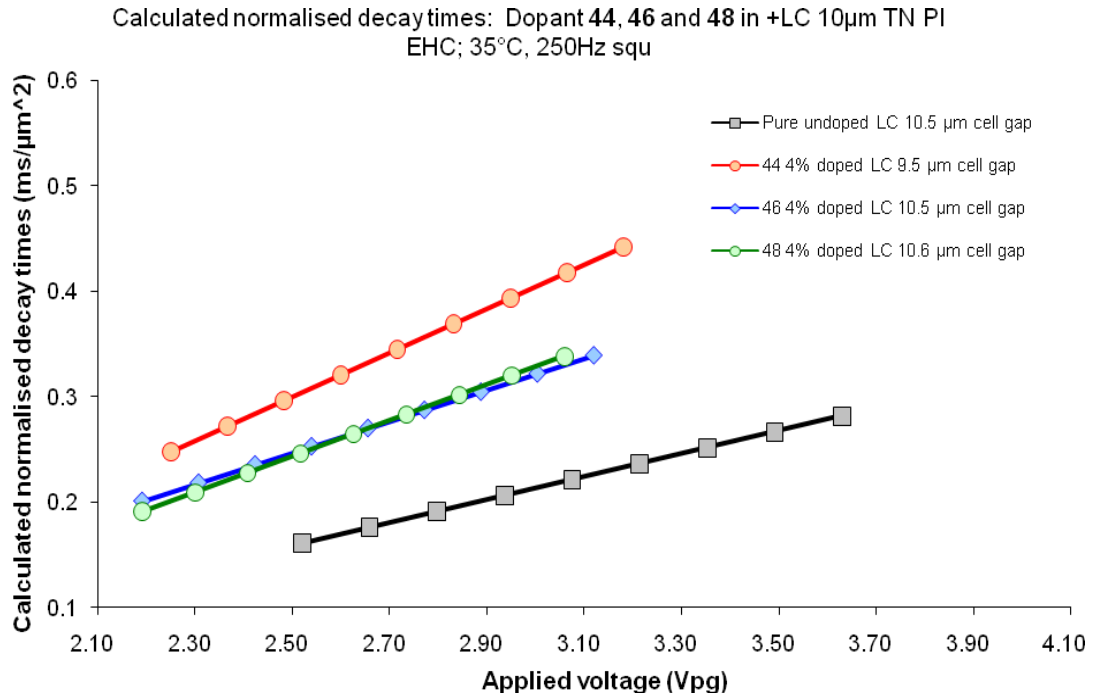


Figure 31b – Calculated decay times for comparable cell gaps of batch I samples



Appendix B

Raman Data for Chapter 4

APENDIX B: Raman Data

Figure 1a – Dopant **11** Raman data Normalized: 633nm laser 100%, x50 lens, 300 μm hole

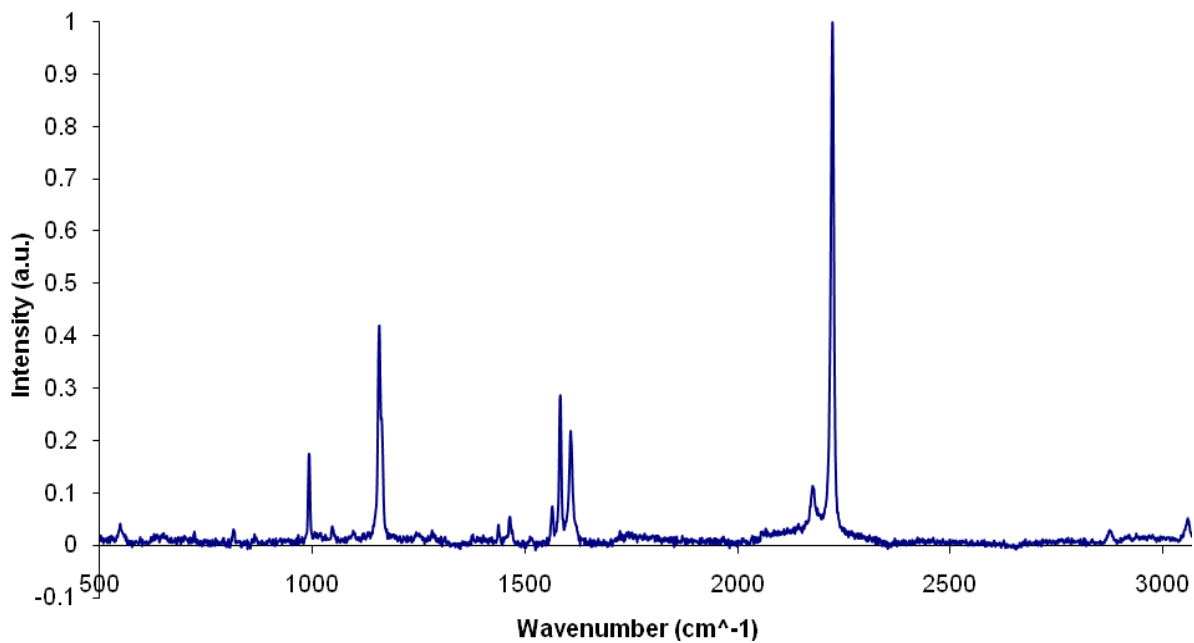


Figure 1b – Dopant **12** Raman data Normalized: 63 nm laser 100%, x50 lens, 300 μm hole

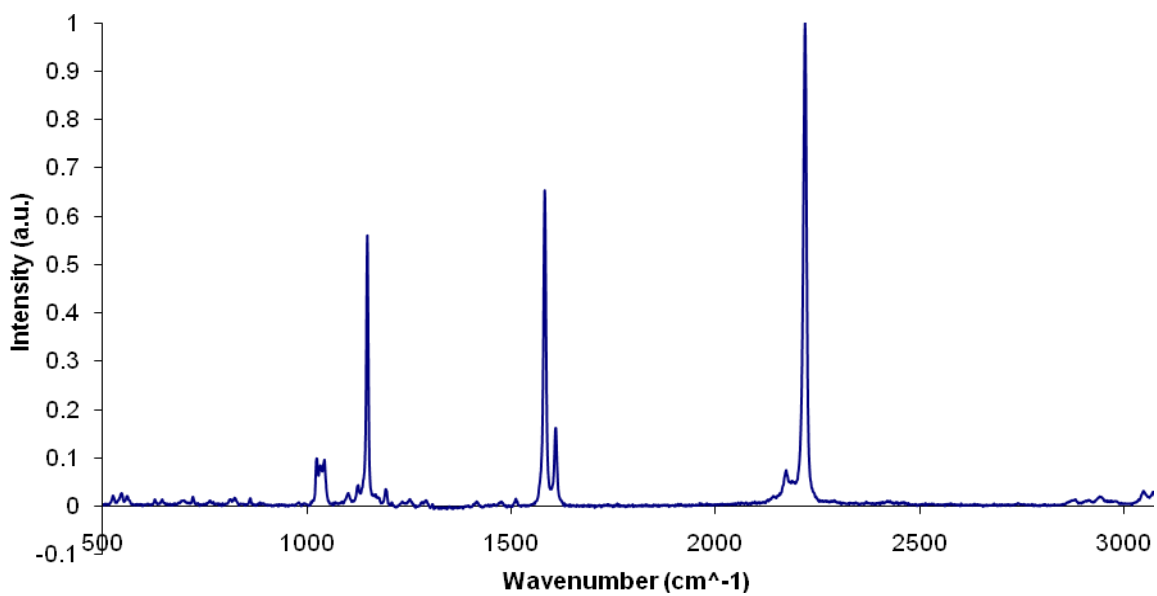


Figure 1c – Dopant **13** Raman data Normalized: 63 nm laser 100%, x50 lens, 300 μm hole

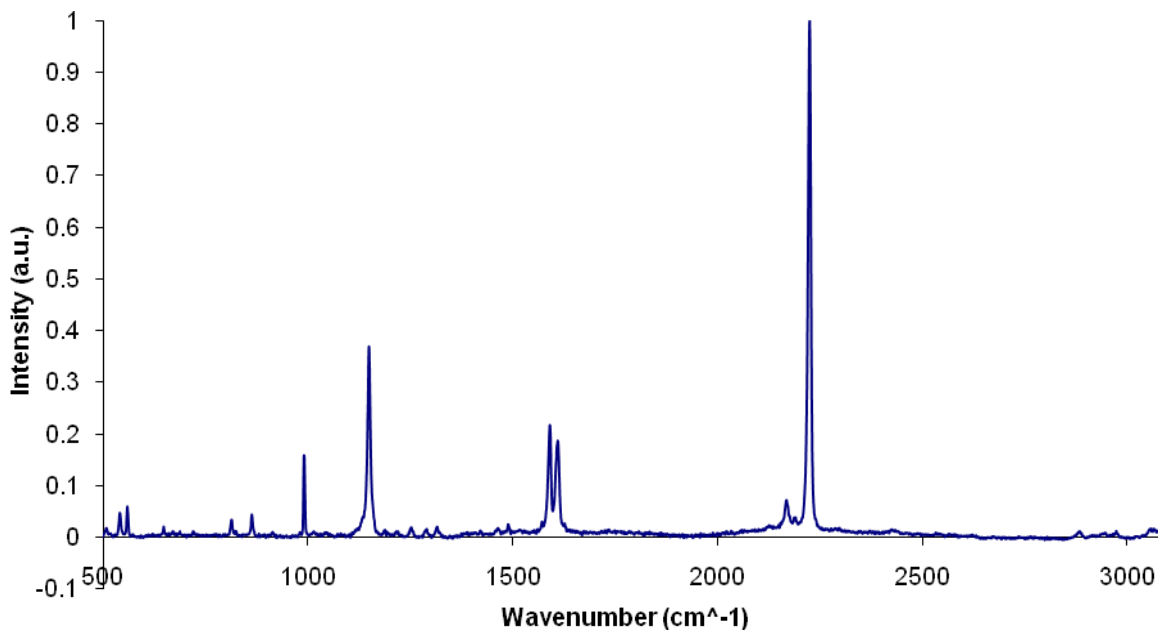


Figure 1d – Dopant **14** Raman data Normalized: 633nm laser 100%, x50 lens, 300 μm hole

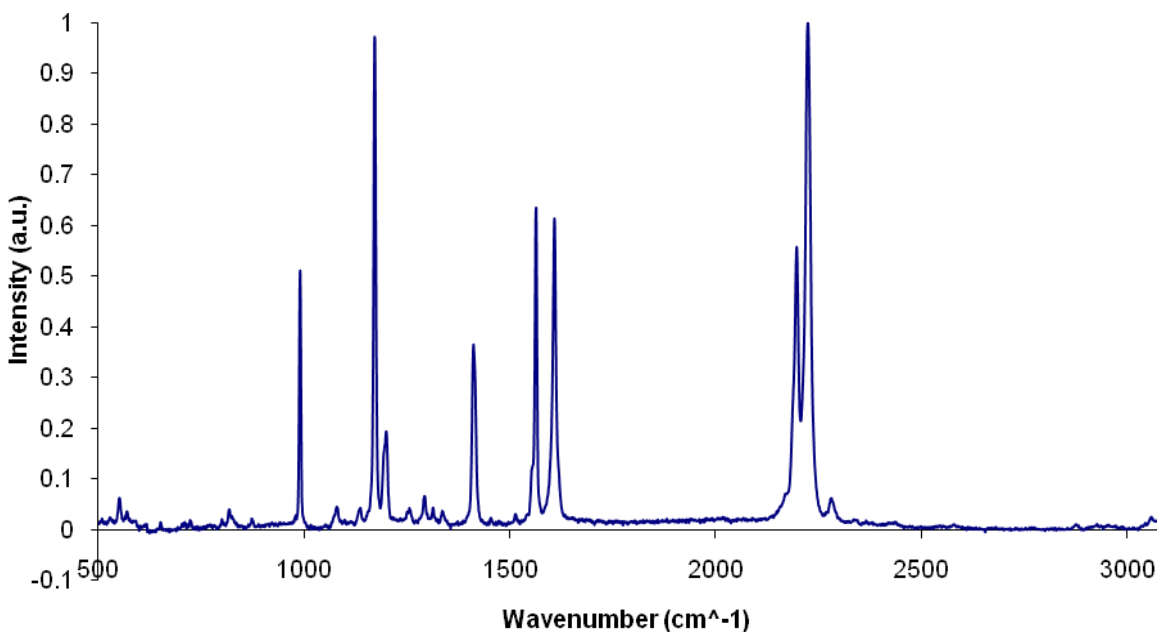


Figure 1e – Dopant **15** Raman data Normalized: 633nm laser 100%, x50 lens, 300 μm hole

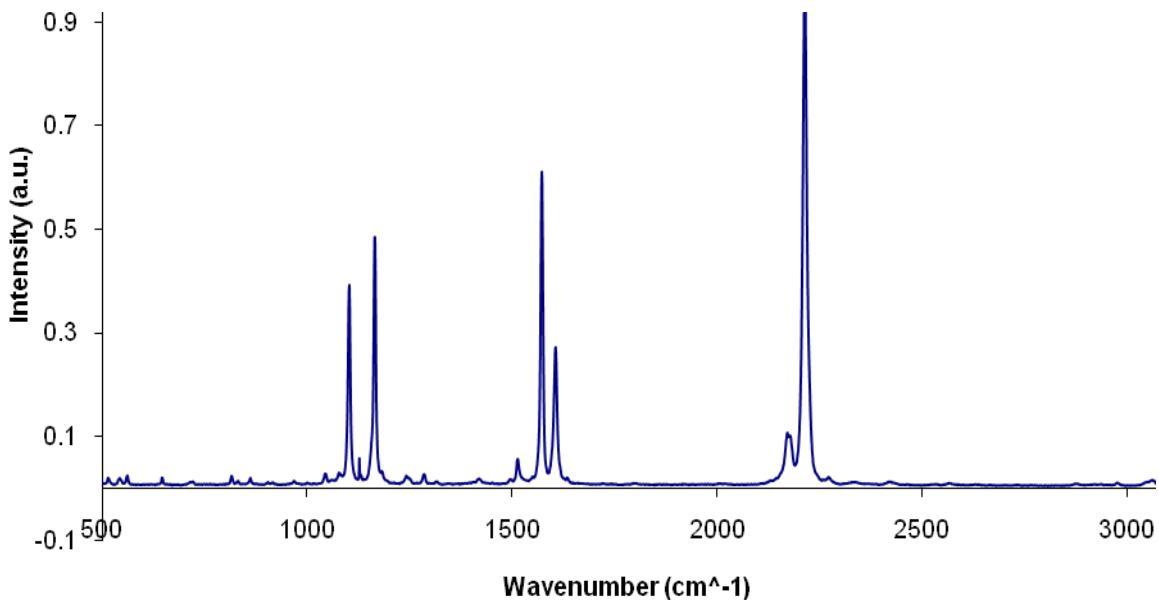


Figure 1f – Dopant **16** Raman data Normalized: 633 nm laser 100%, x50 lens, 300 μm hole

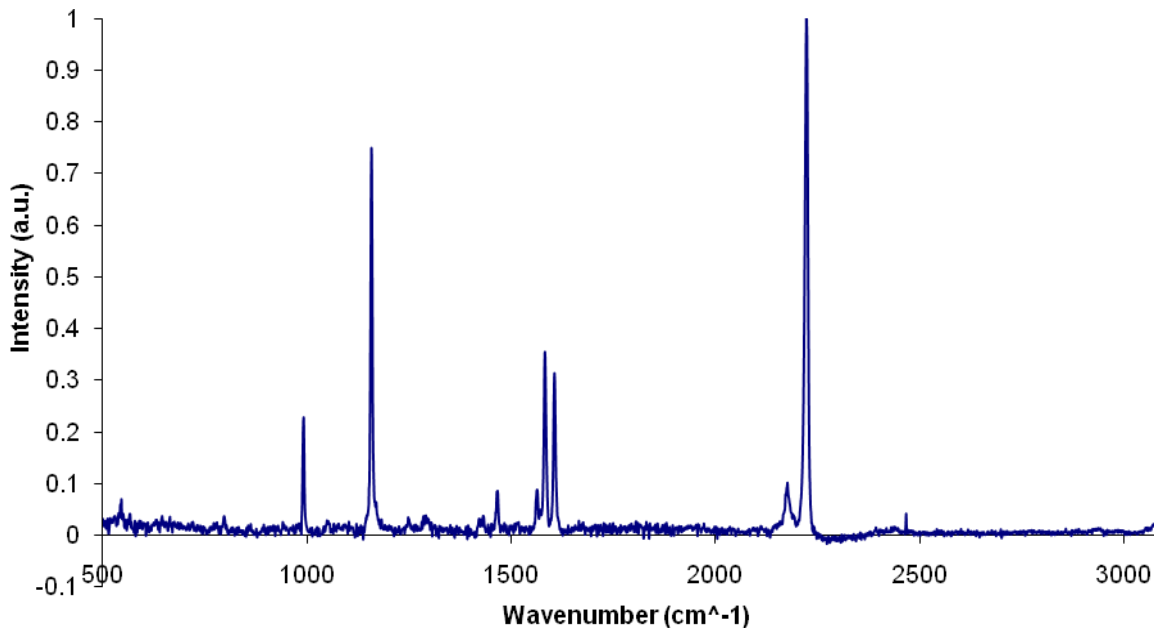


Figure 1g – Dopant **17** Raman data Normalized: 633nm laser 100%, x50 lens, 300 μm hole

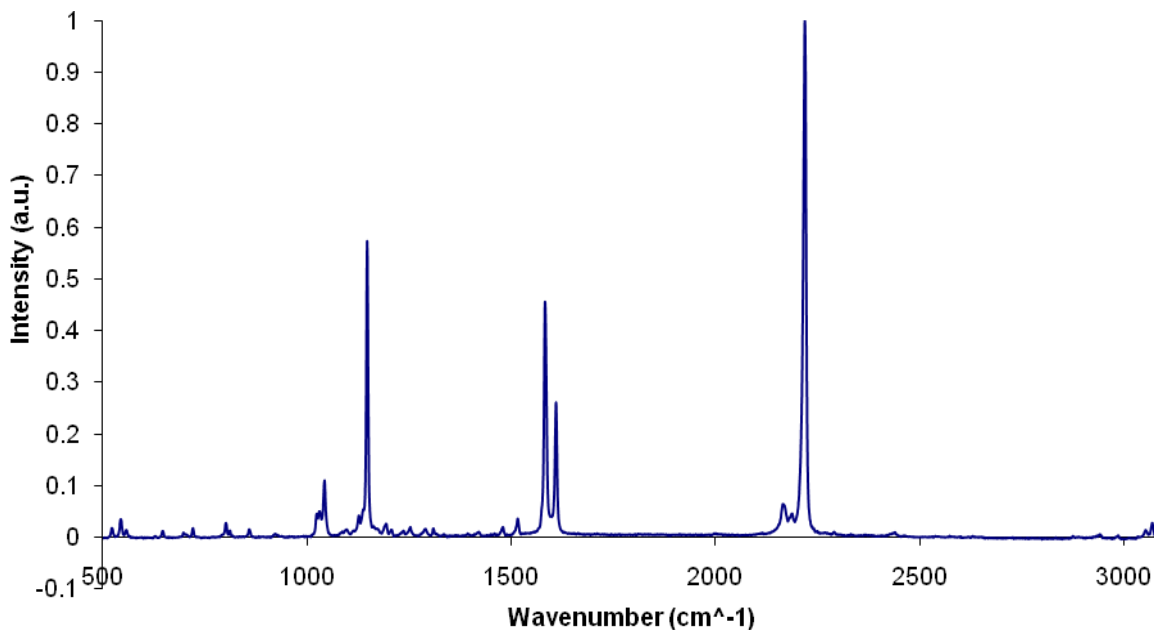


Figure 1h – Dopant **20** Raman data Normalized: 633nm laser 100%, x50 lens, 300 μm hole

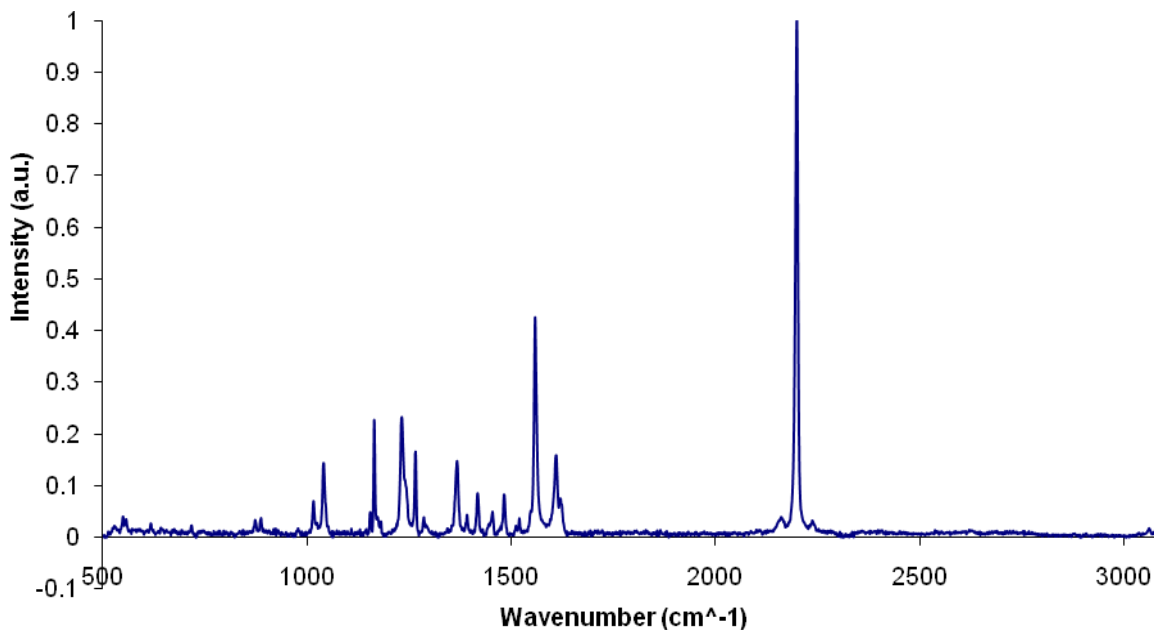


Figure 1i – Dopant **21** Raman data Normalized: 633 nm laser 100%, x50 lens, 300 μm hole

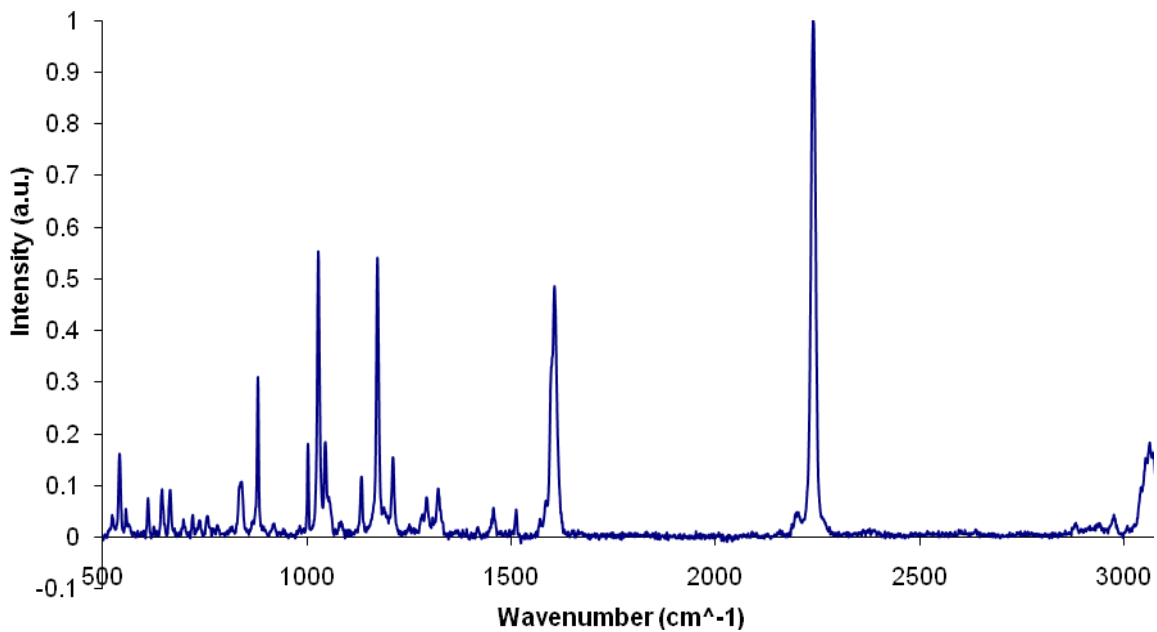


Figure 1j – Dopant **27** Raman data Normalized: 633 nm laser 100%, x50 lens, 300 μm hole

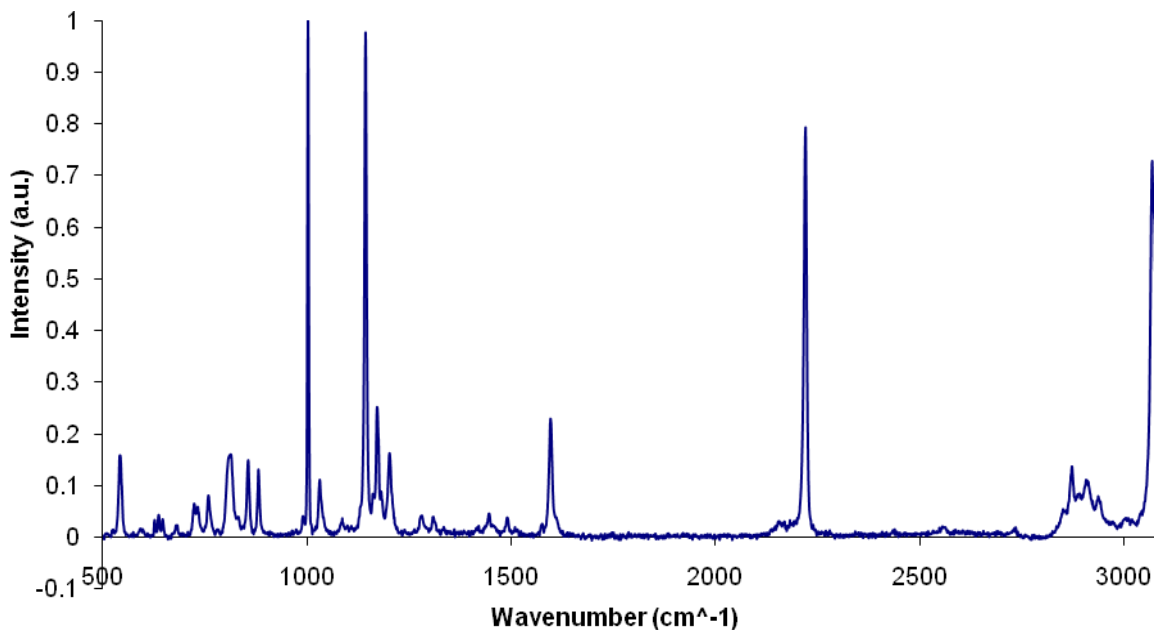


Figure 1k – Dopant **28** Raman data Normalized: 633nm laser 100%, x50 lens, 300 μm hole

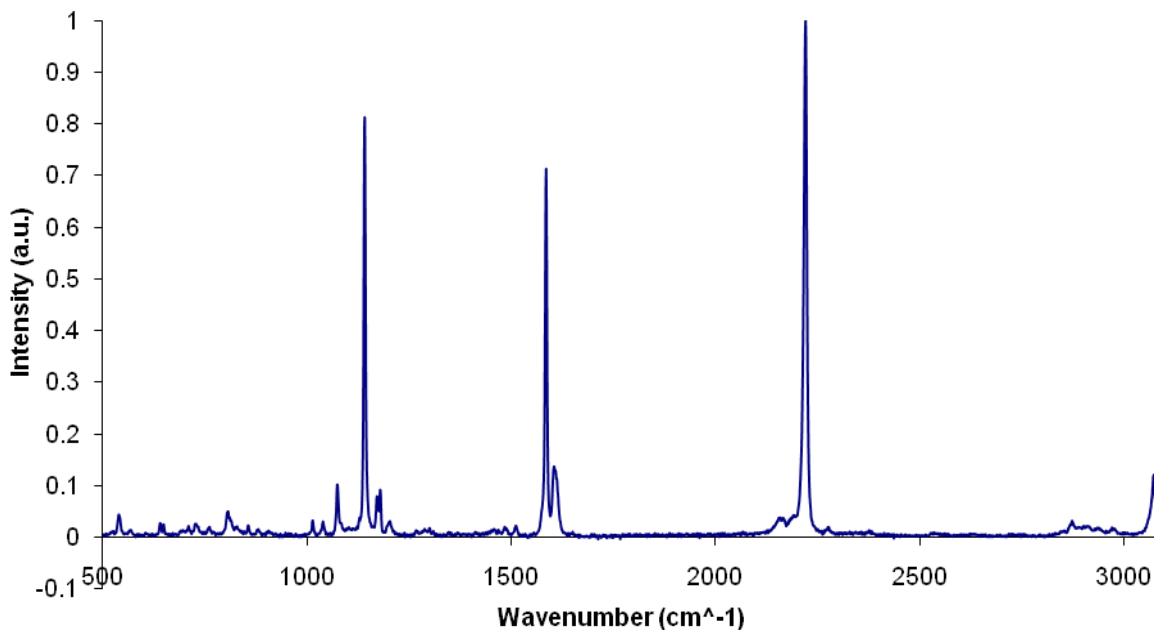


Figure 1l – Dopant **29** Raman data Normalized: 633 nm laser 100%, x50 lens, 300 μm hole

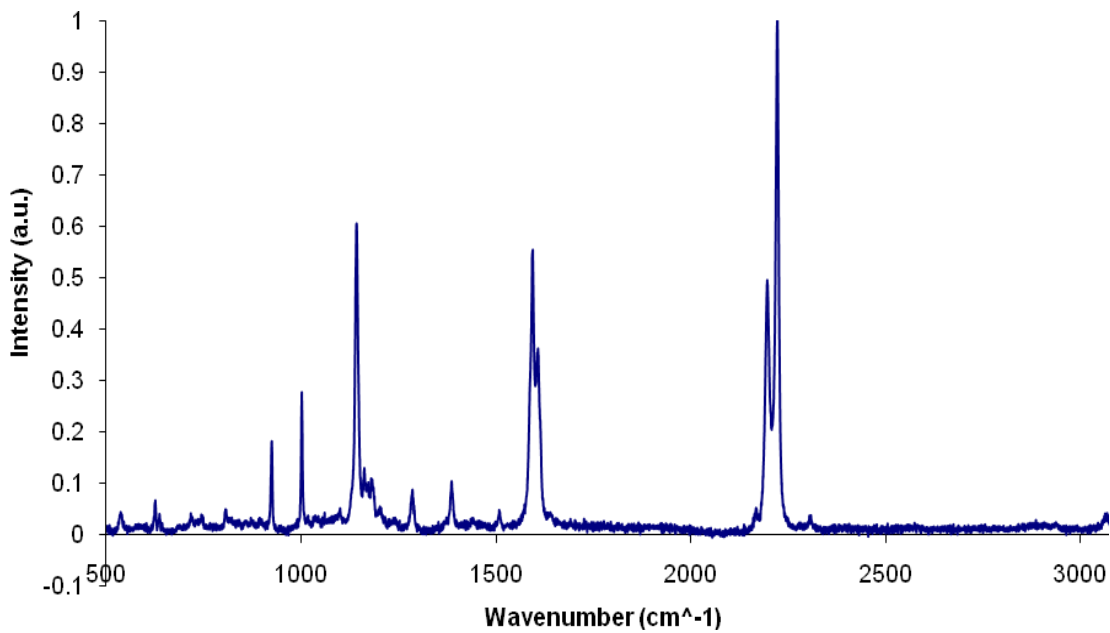


Figure 2a – Raman Spectrum of -LC material: 633 nm laser 100%, x50 lens, 300 μm hole

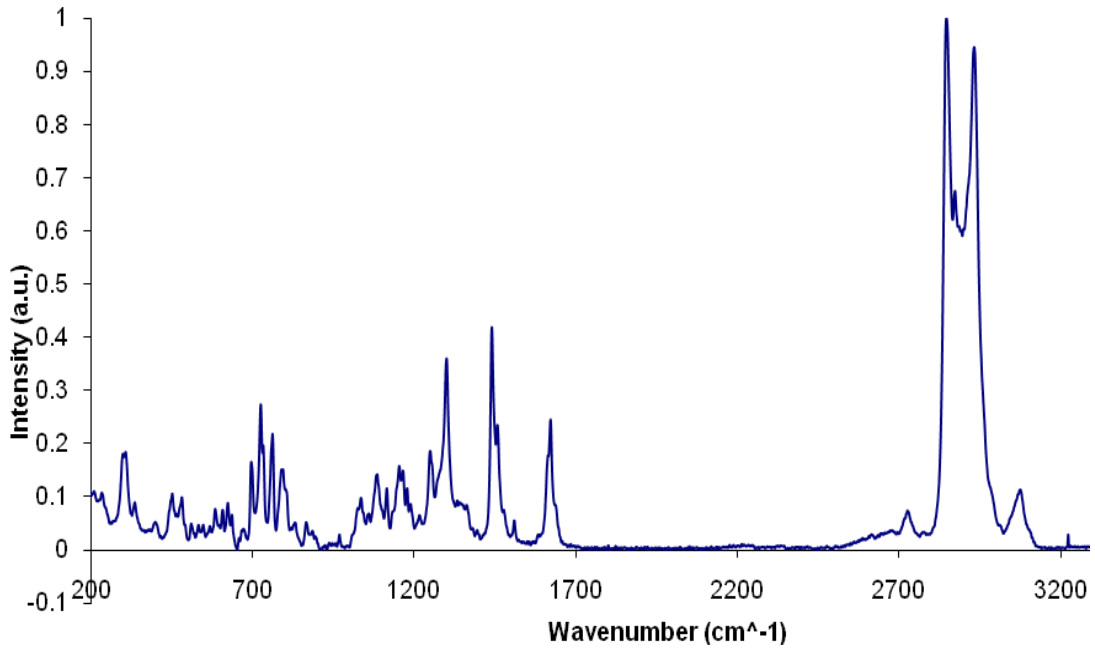


Figure 2b – Raman Spectrum of +LC material: 633 nm laser 100%, x50 lens, 300 μm hole

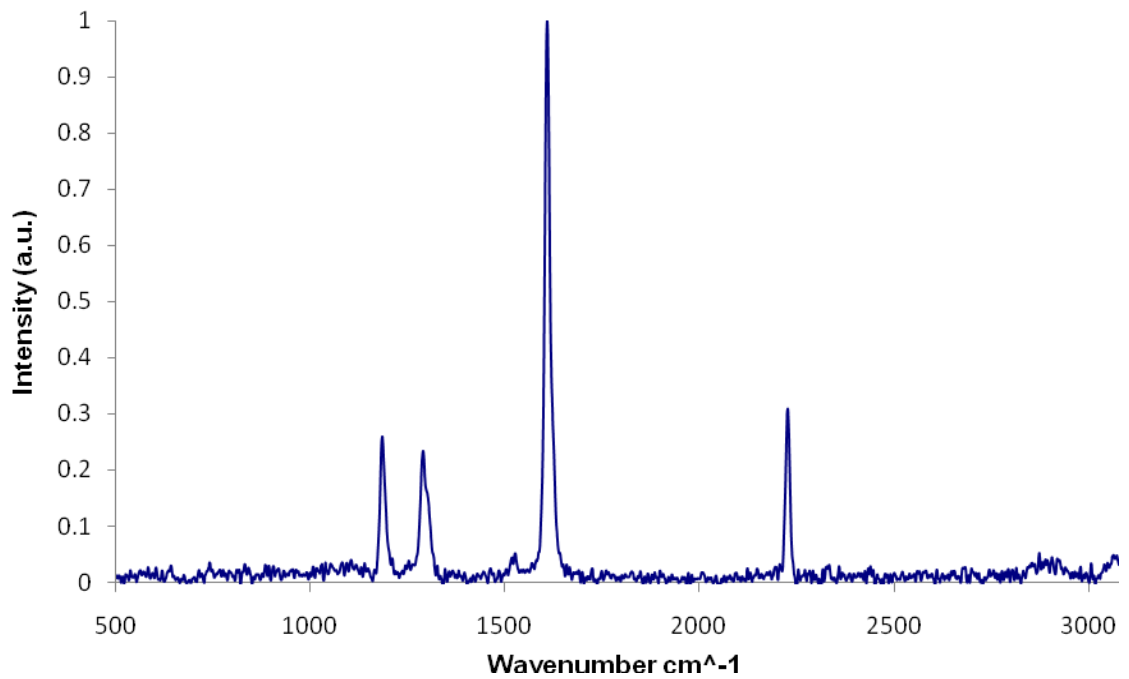


Figure 3a – Raman data of a droplet of 4% doped LC with dopant **11**

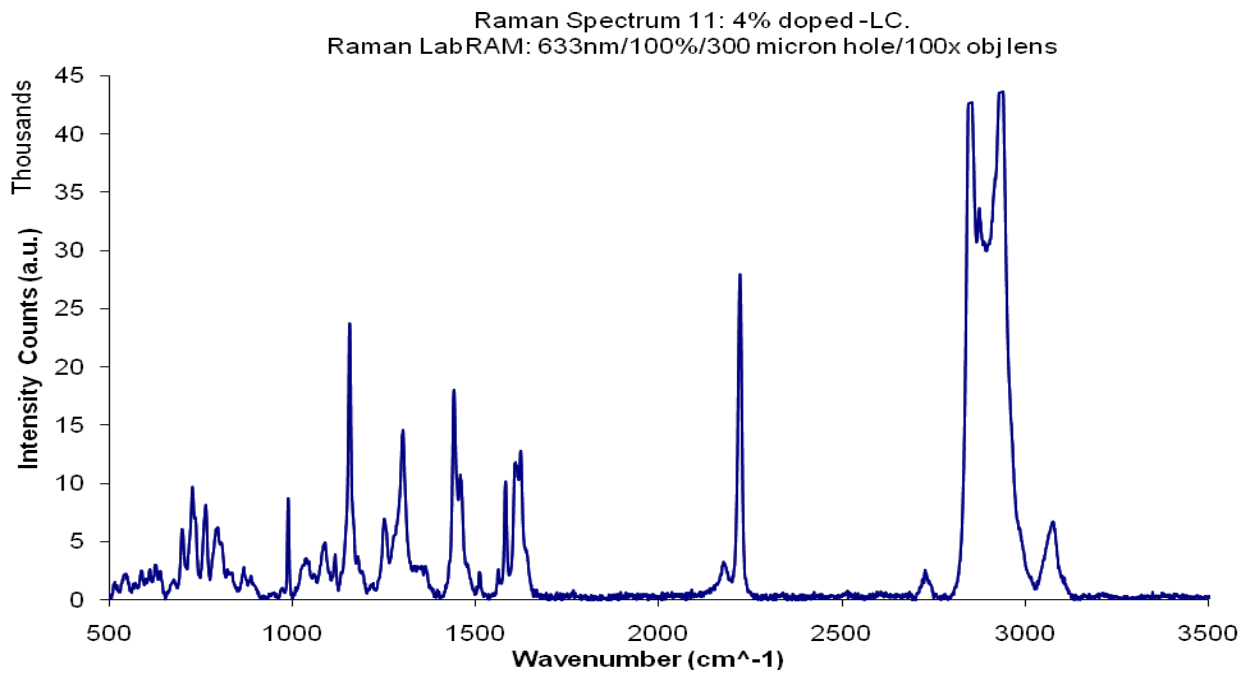


Figure 3b – Raman data of dopant **11** when the cell is switched on and off.

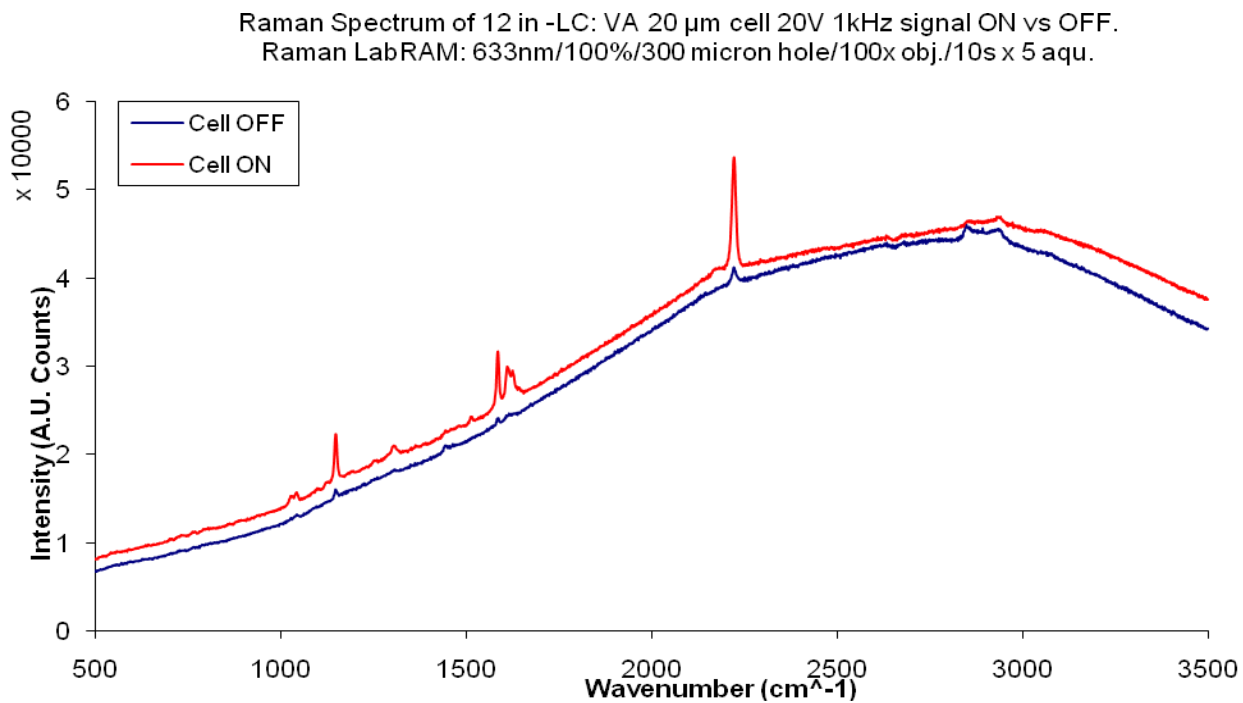


Figure 3c – Raman data of dopant **11** orientated when the cell is switched on.

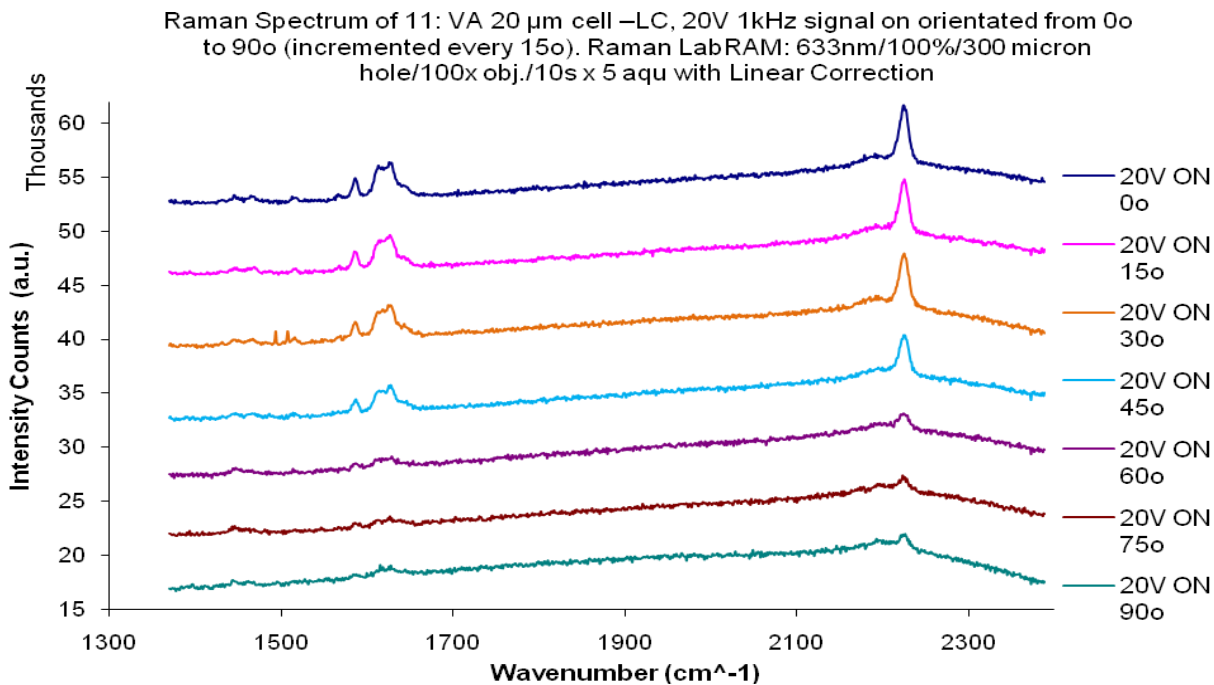


Figure 3d – Raman data of dopant **11** orientated when the cell is switched off.

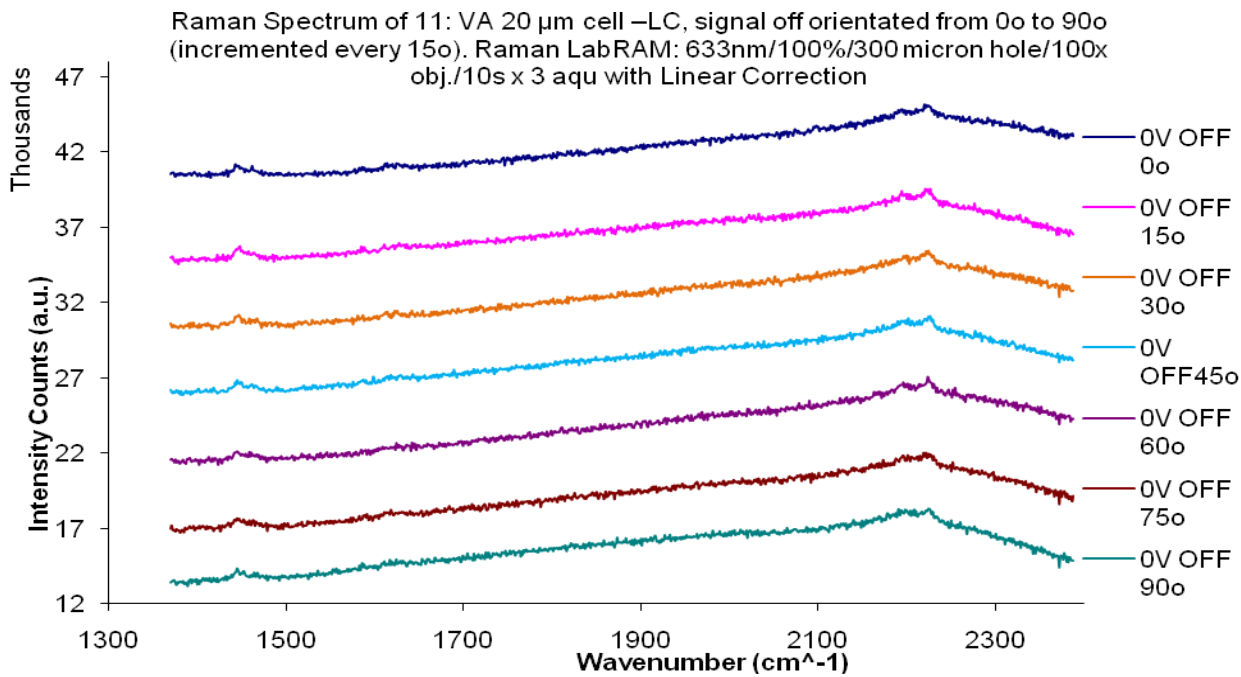


Figure 4a – Raman data of a droplet of 4% doped LC with dopant **12**

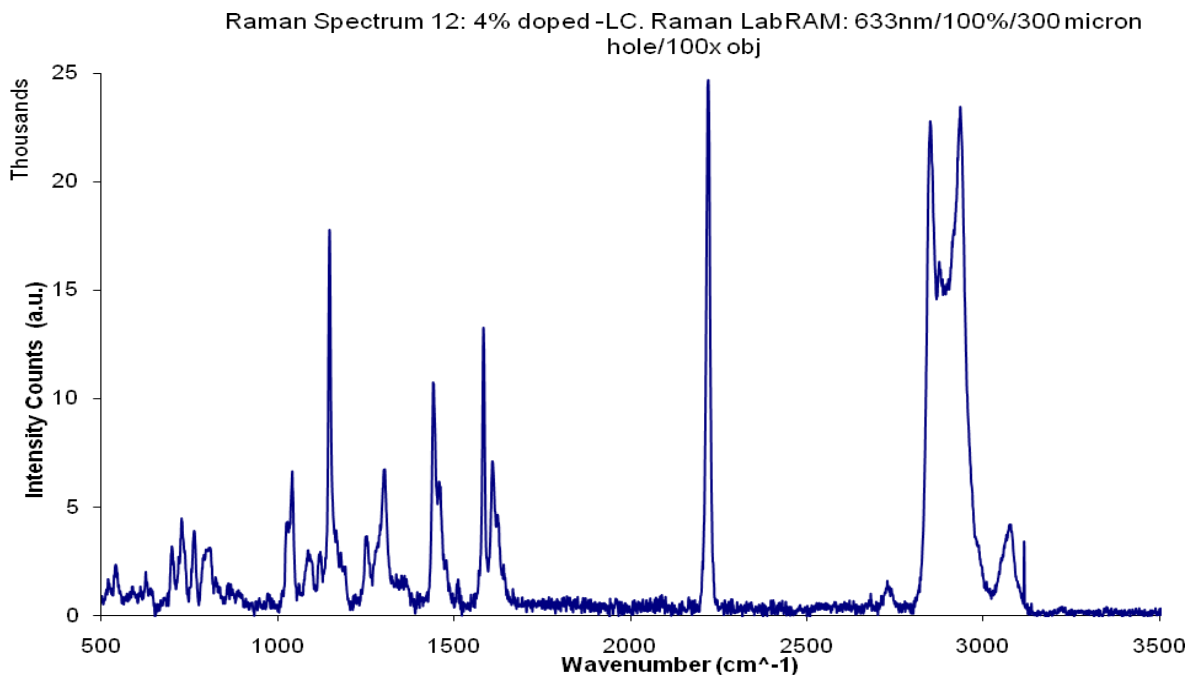


Figure 4b – Raman data of dopant **12** when the cell is switched on and off.

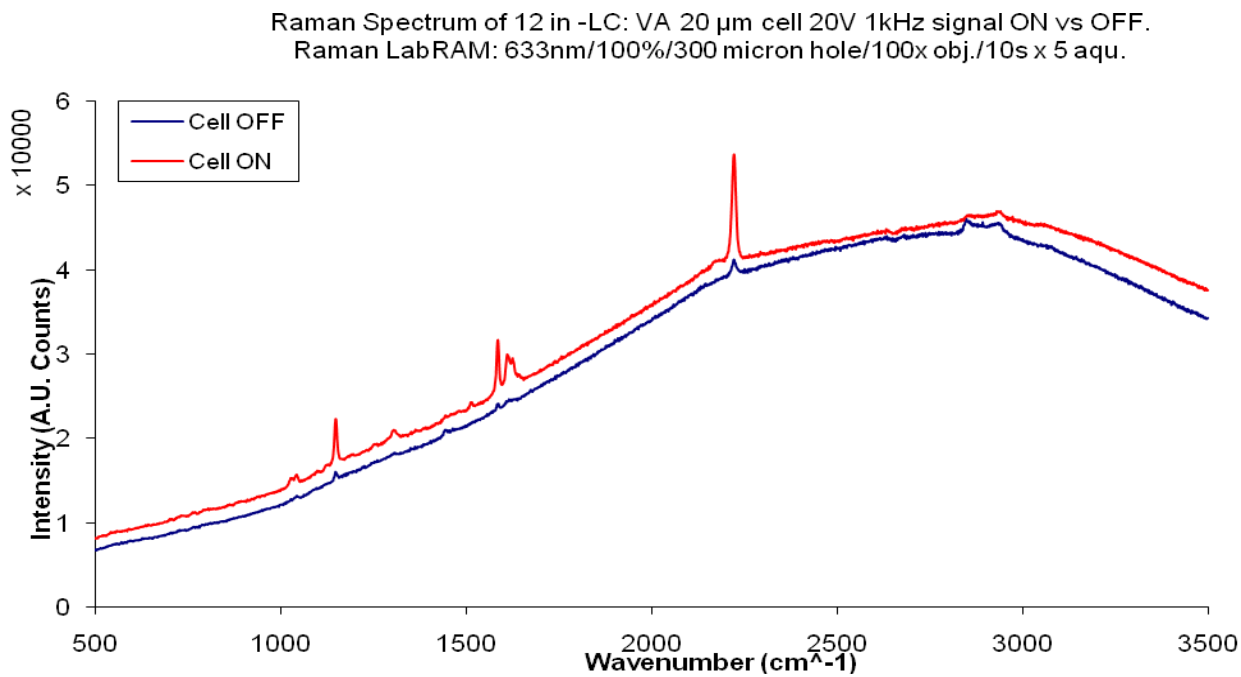


Figure 4c – Raman data of dopant **12** orientated when the cell is switched on.

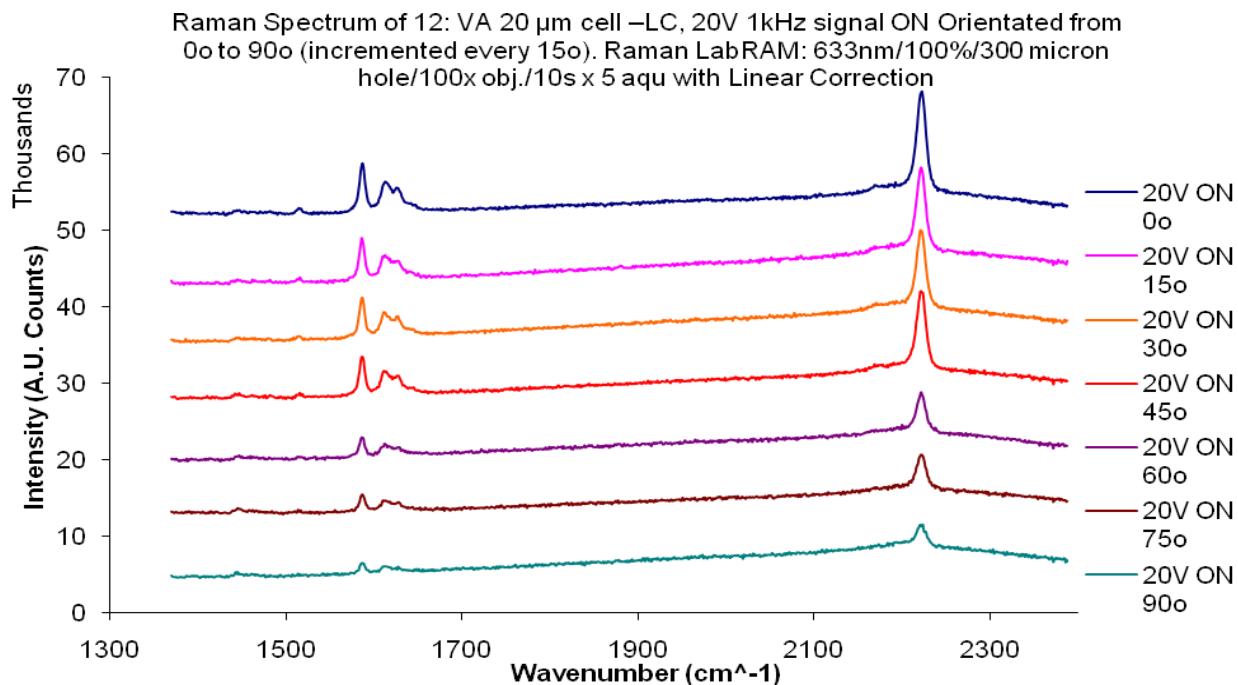


Figure 4d – Raman data of dopant **12** orientated when the cell is switched off.

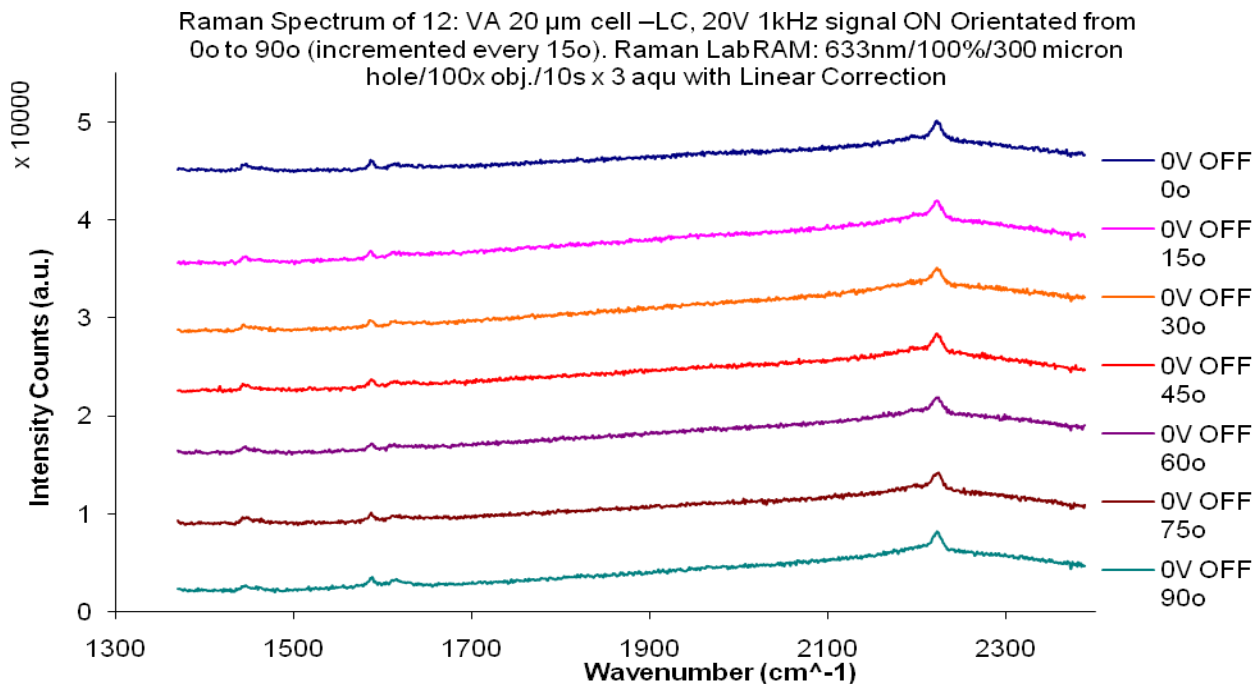


Figure 5a – Raman data of a droplet of 4% doped LC with dopant **13**

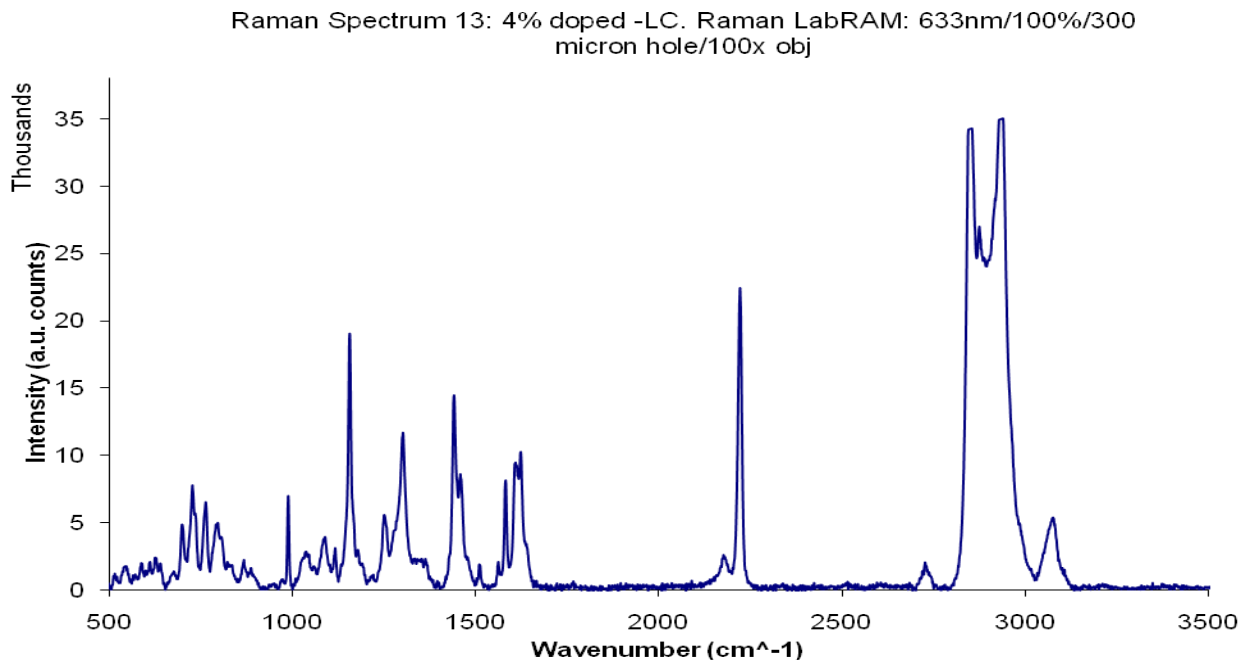


Figure 5b – Raman data of dopant **13** when the cell is switched on and off.

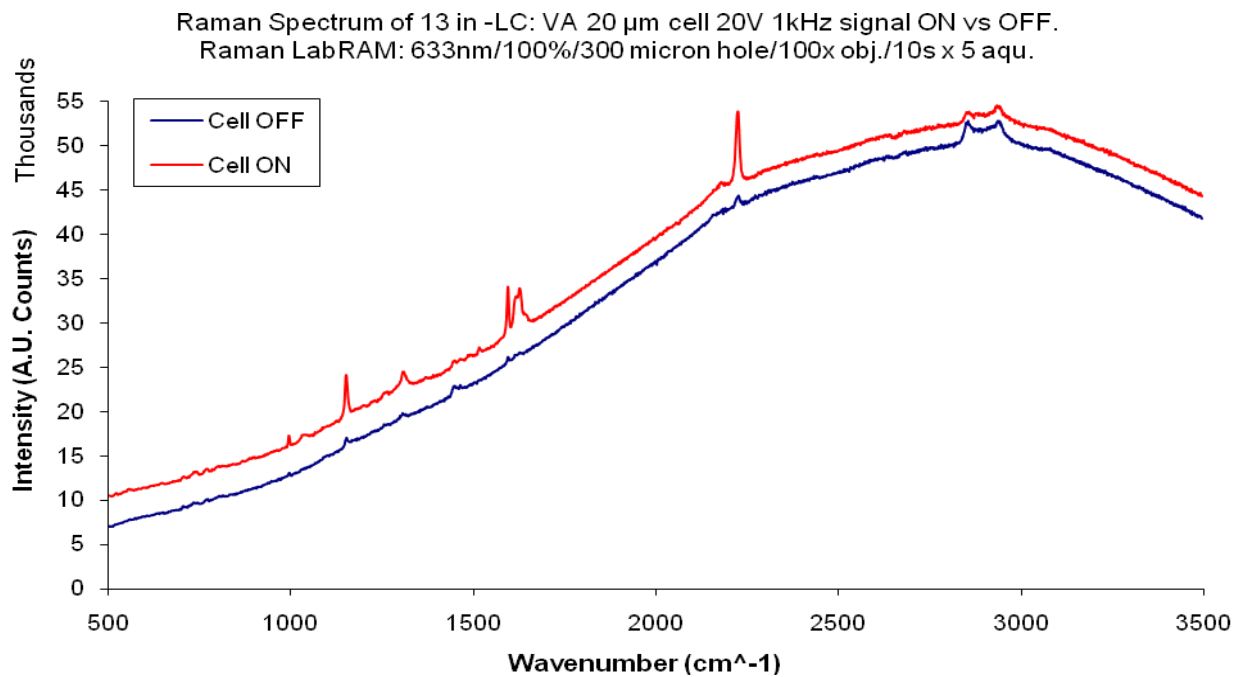


Figure 5c – Raman data of dopant **13** orientated when the cell is switched on.

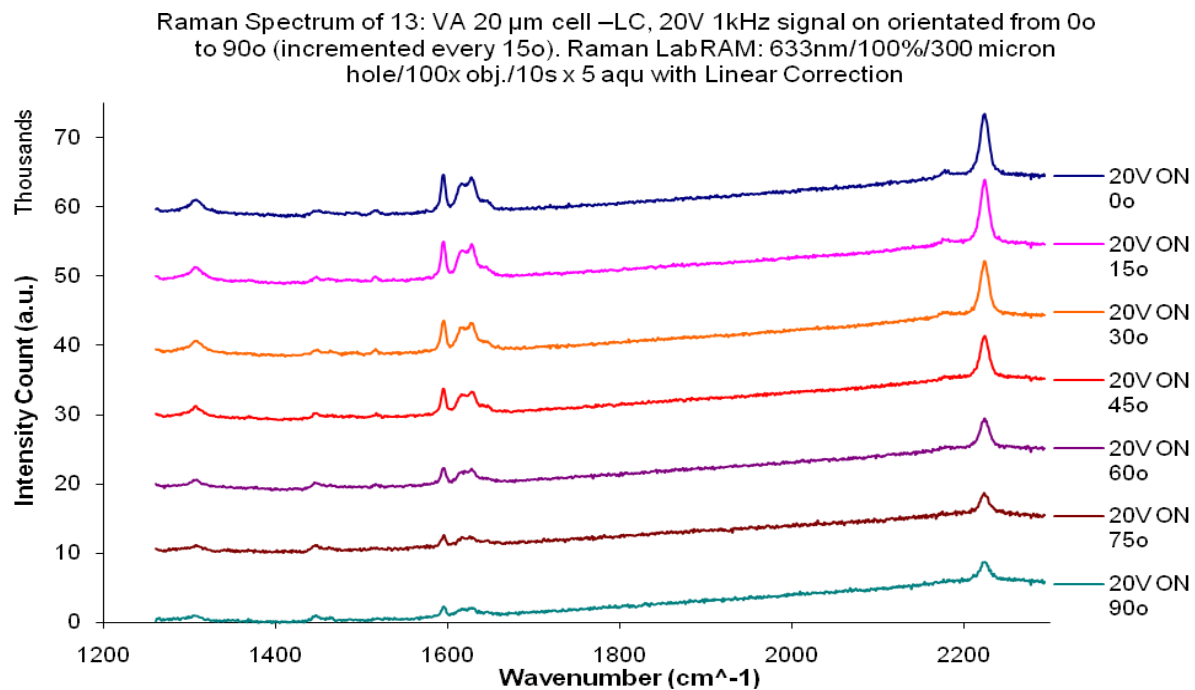


Figure 5d – Raman data of dopant **13** orientated when the cell is switched off.

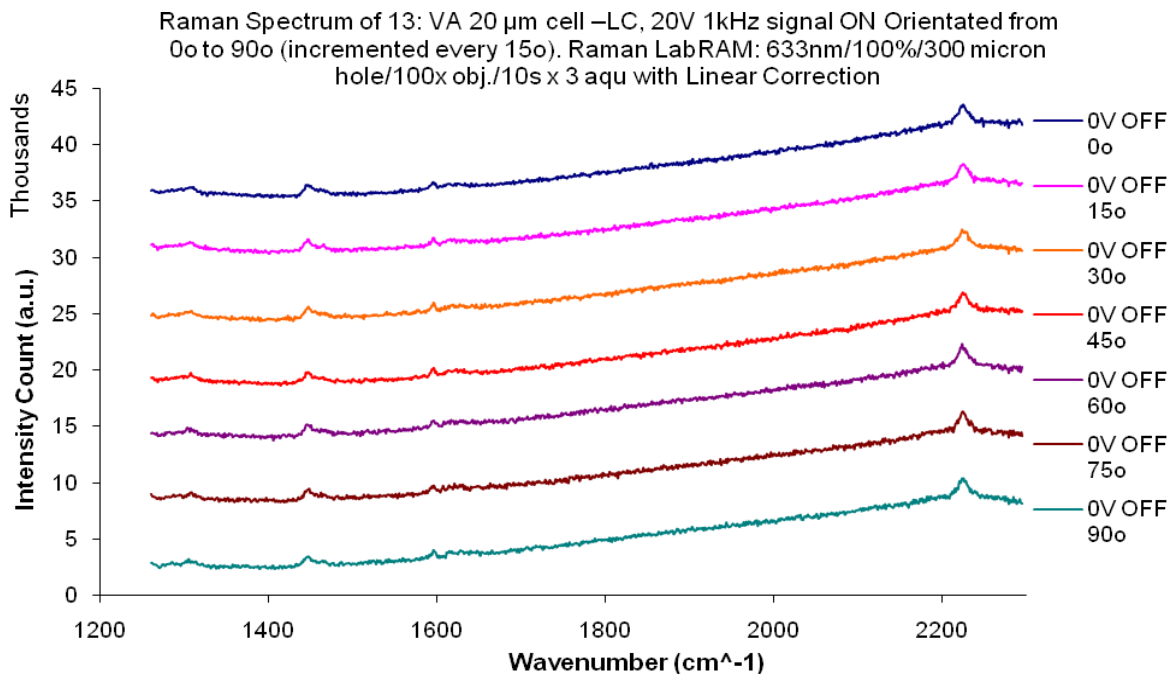


Figure 6a – Raman data of a droplet of 4% doped LC with dopant **14**

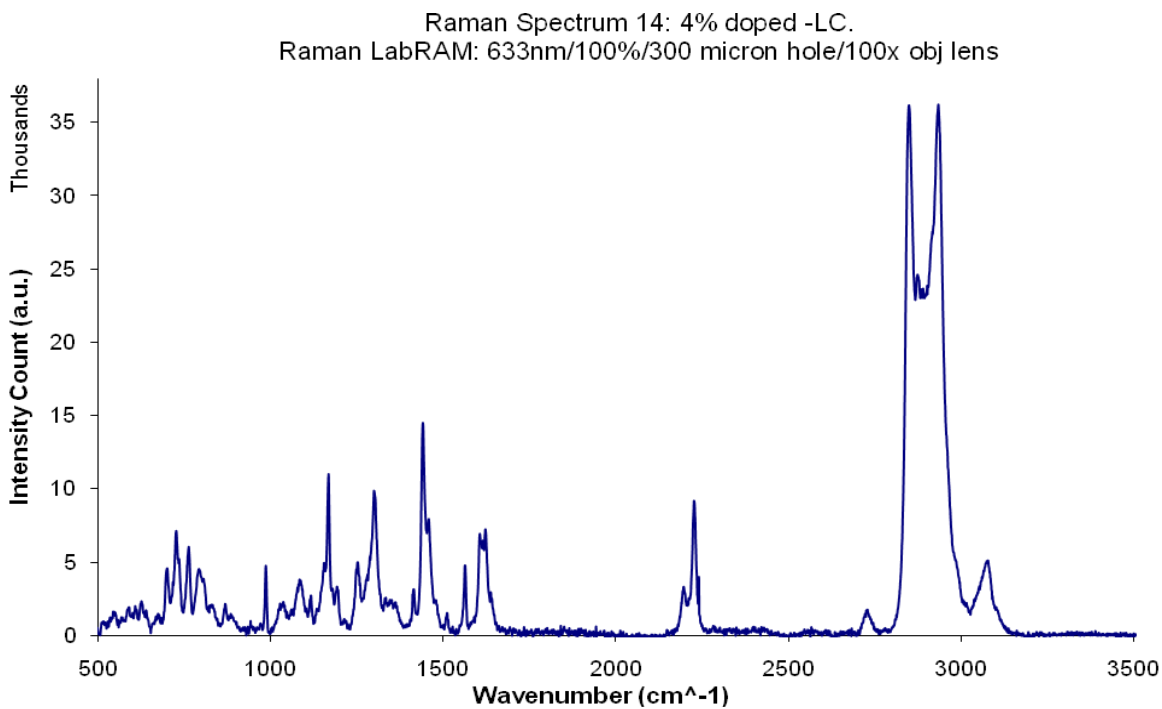


Figure 6b – Raman data of dopant **14** when the cell is switched on and off.

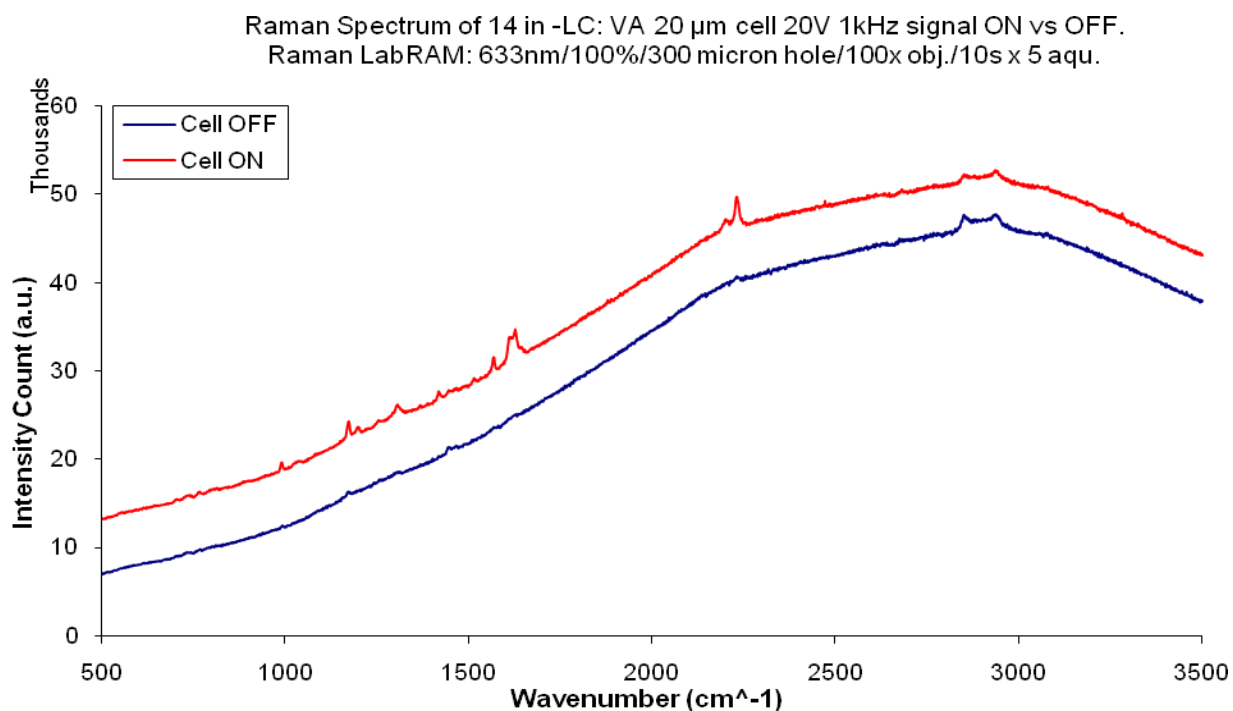


Figure 6c – Raman data of dopant **14** orientated when the cell is switched on.

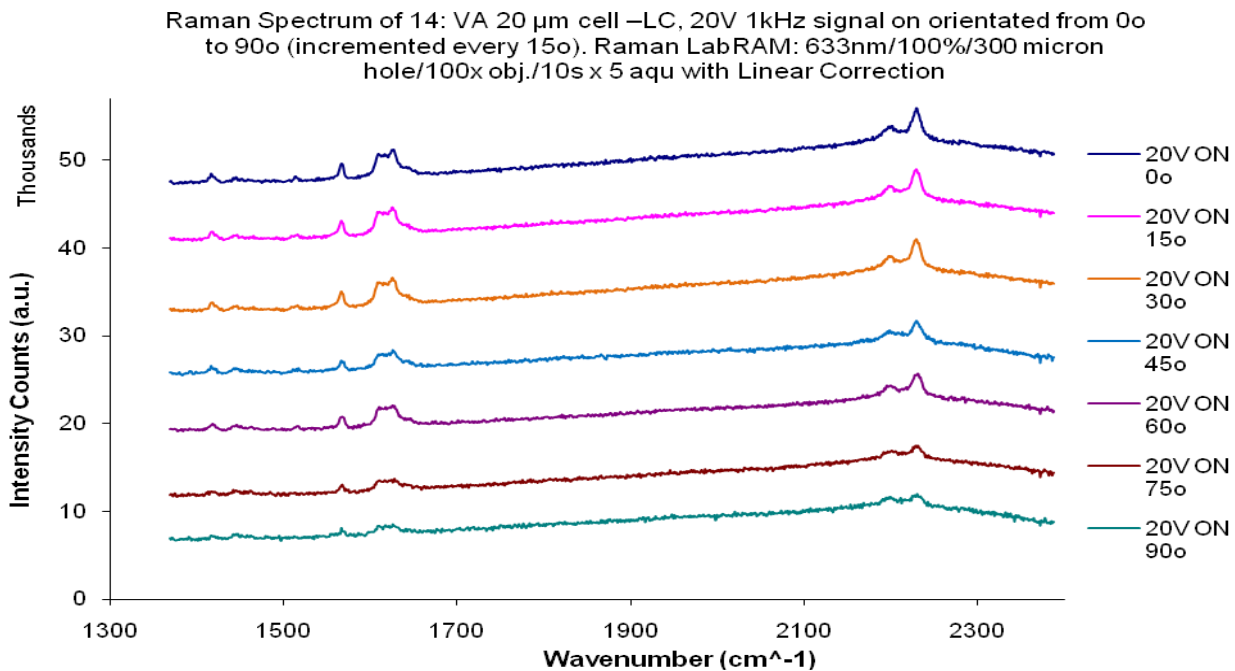


Figure 6d – Raman data of dopant **14** orientated when the cell is switched off.

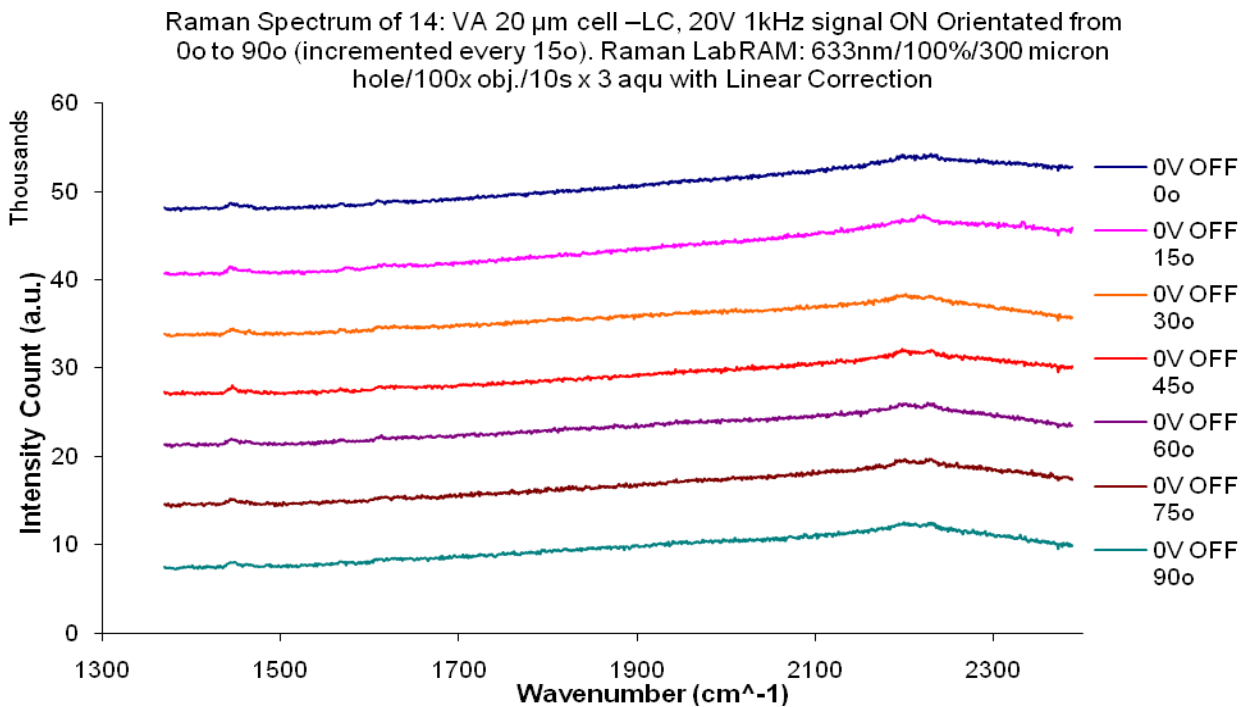


Figure 7a – Raman data of a droplet of 4% doped LC with dopant **15**

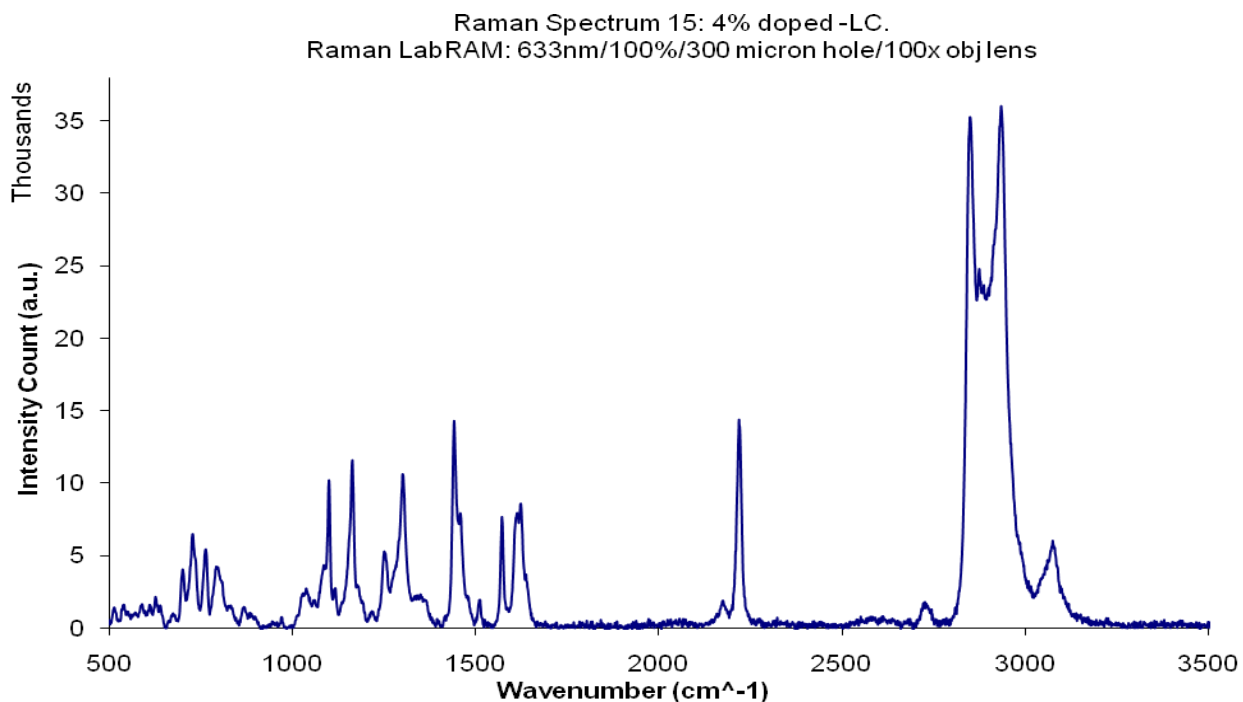


Figure 7b – Raman data of dopant **15** when the cell is switched on and off.

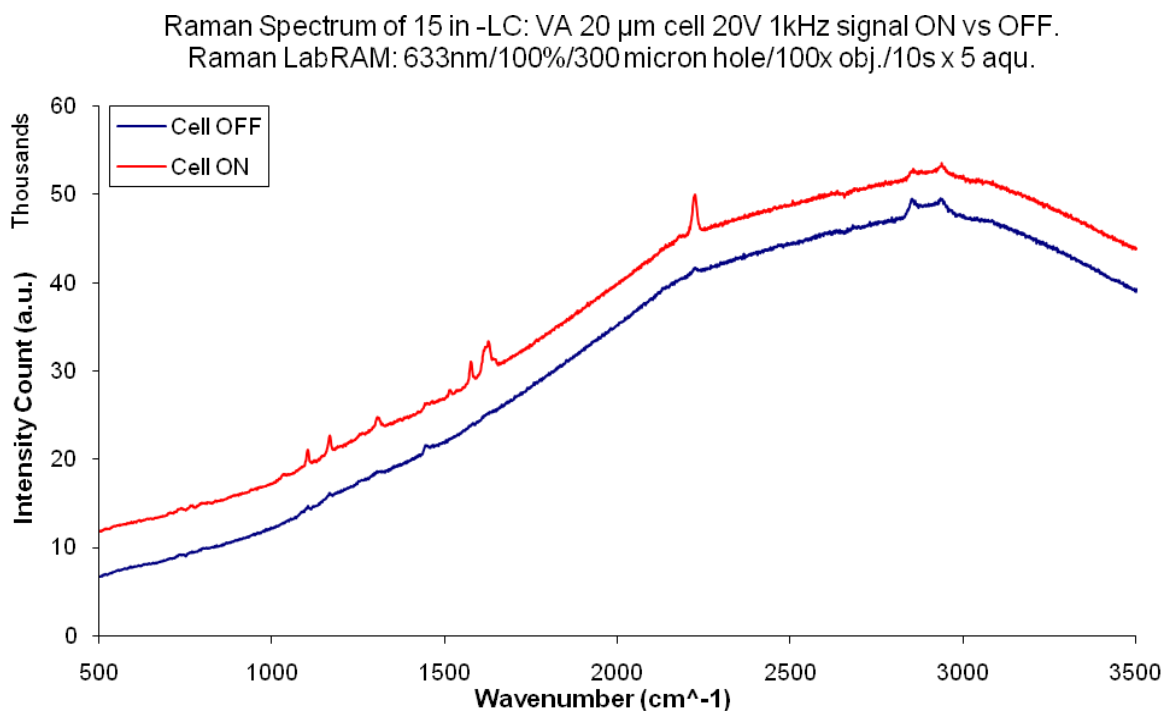


Figure 7c – Raman data of dopant **15** orientated when the cell is switched on.

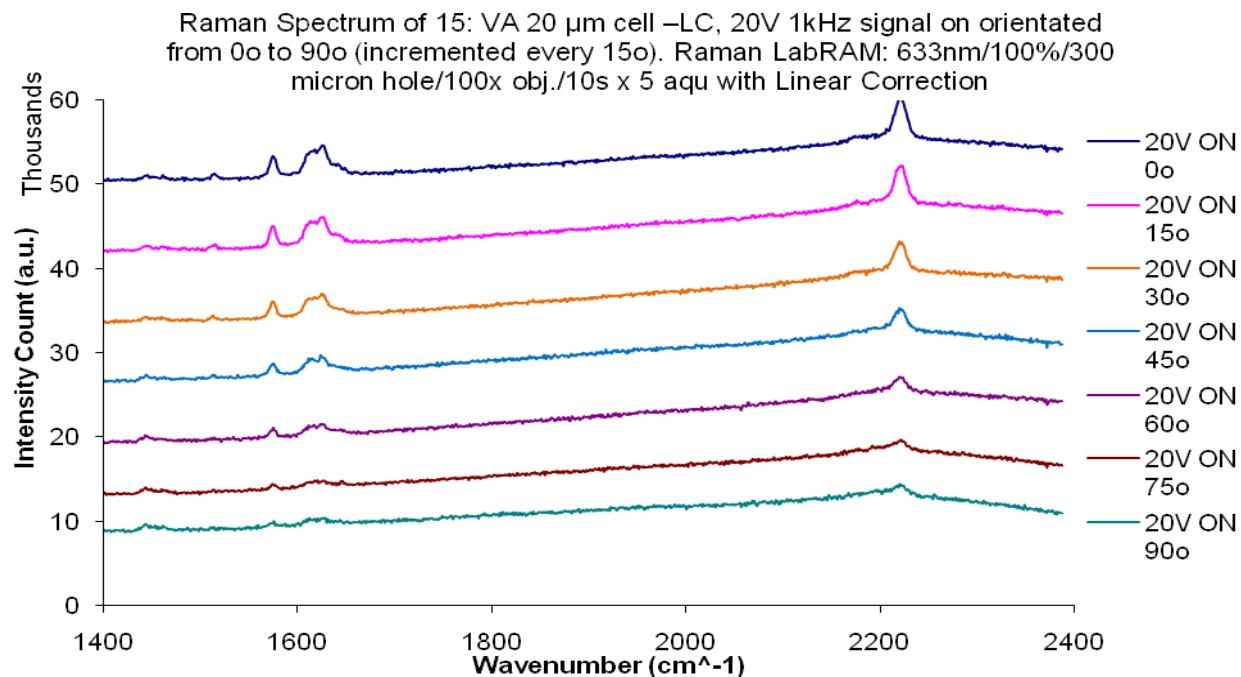


Figure 7d – Raman data of dopant **15** orientated when the cell is switched off.

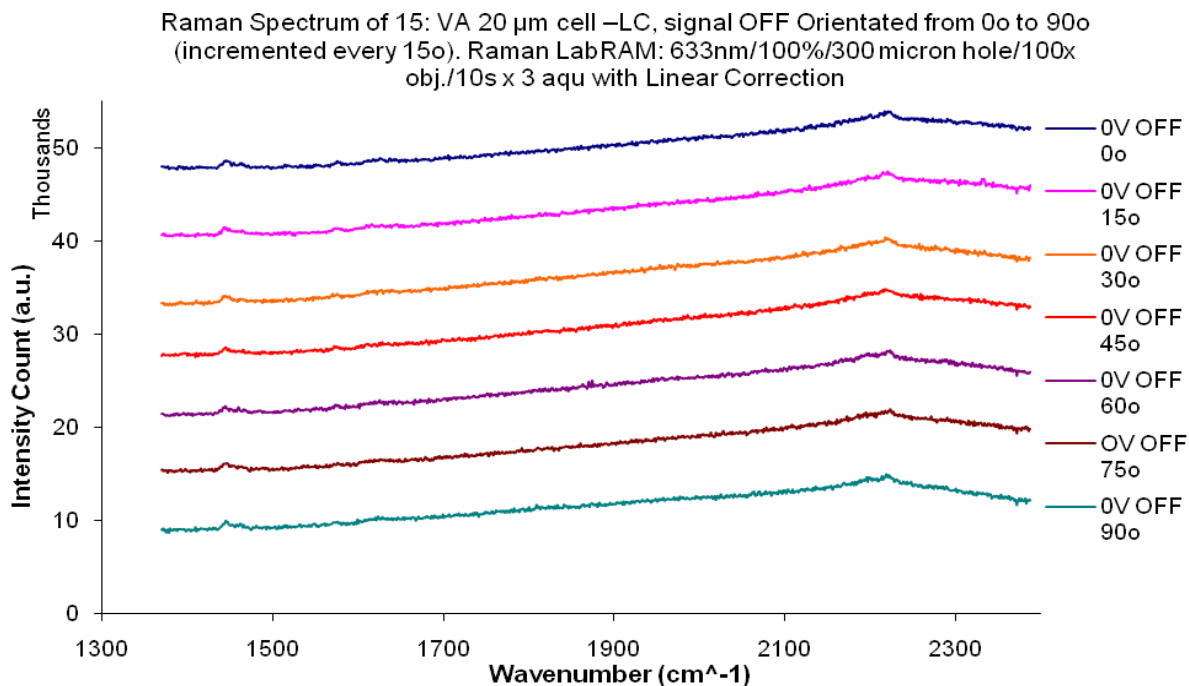


Figure 8a – Raman data of a droplet of 4% doped LC with dopant **16**

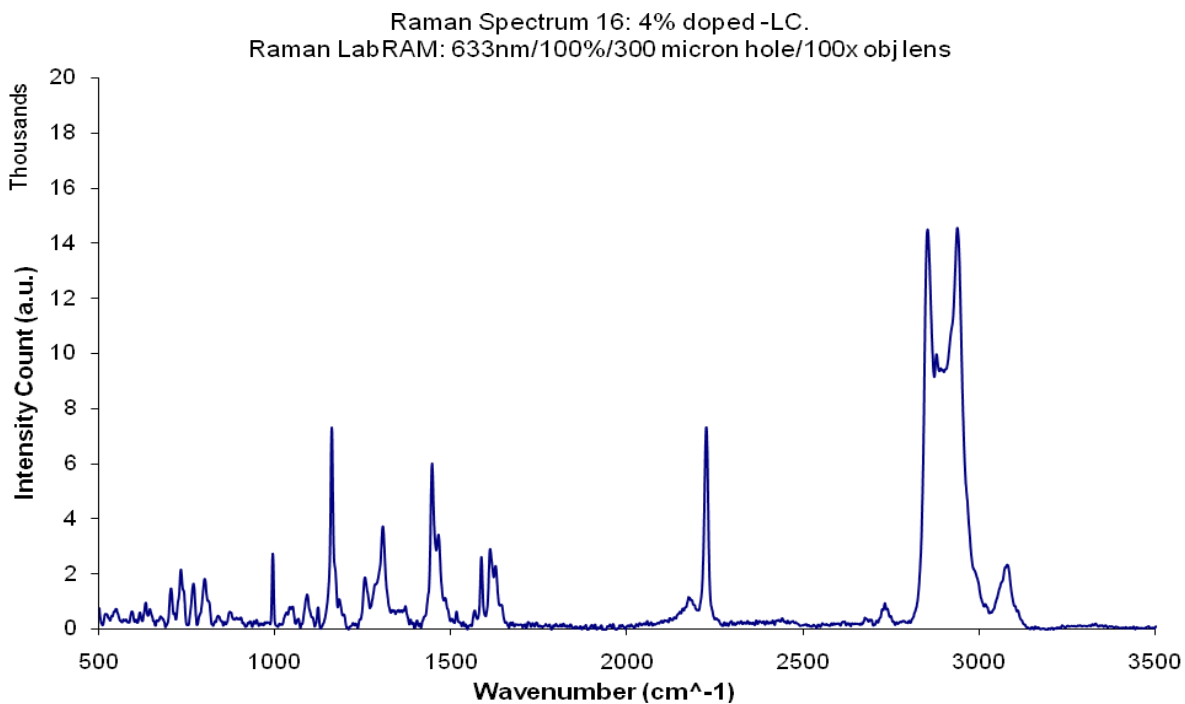


Figure 8b – Raman data of dopant **16** when the cell is switched on and off.

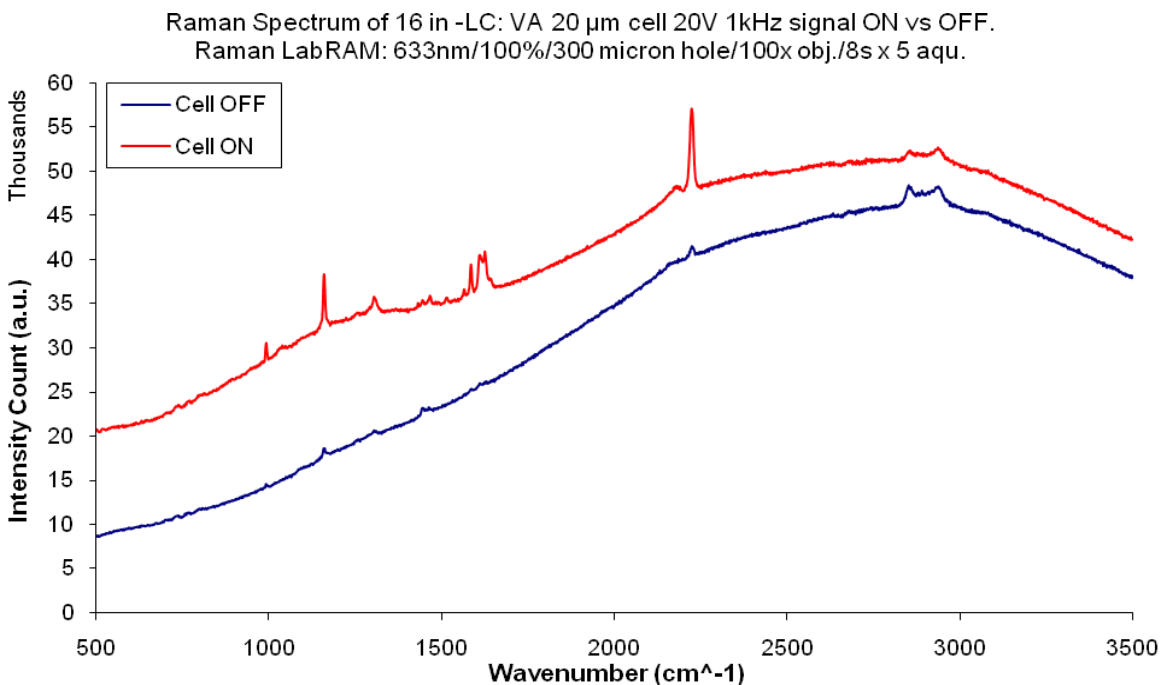


Figure 8c – Raman data of dopant **16** orientated when the cell is switched on.

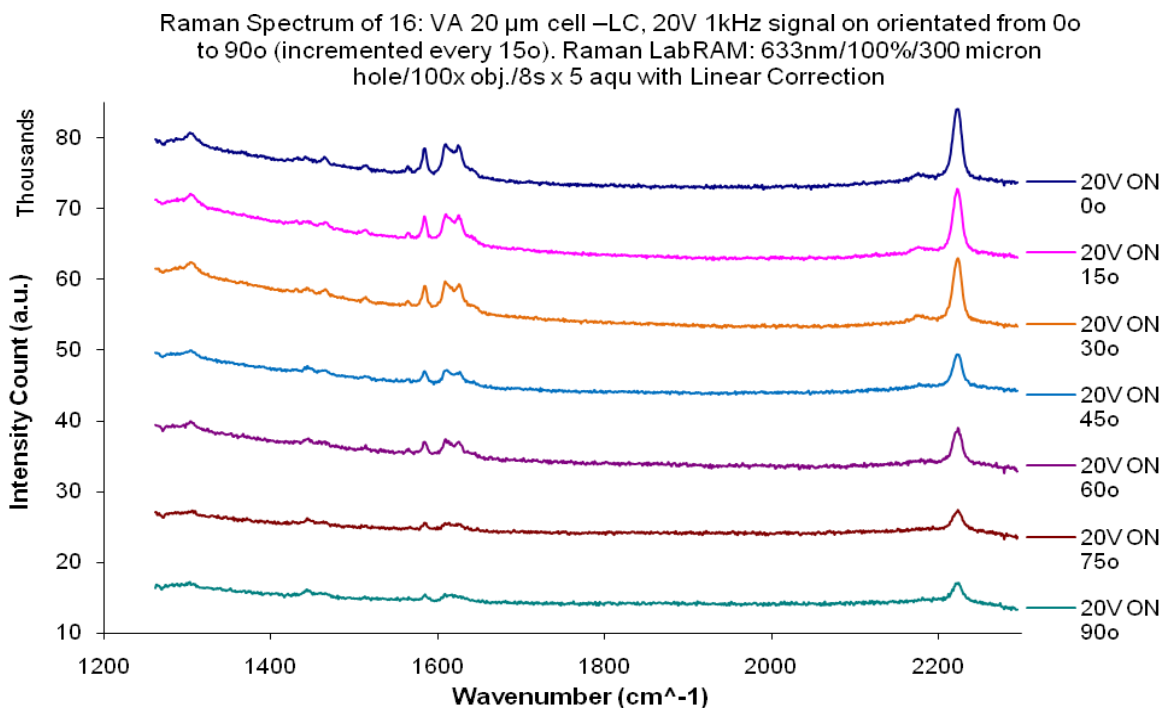


Figure 8d – Raman data of dopant **16** orientated when the cell is switched off.

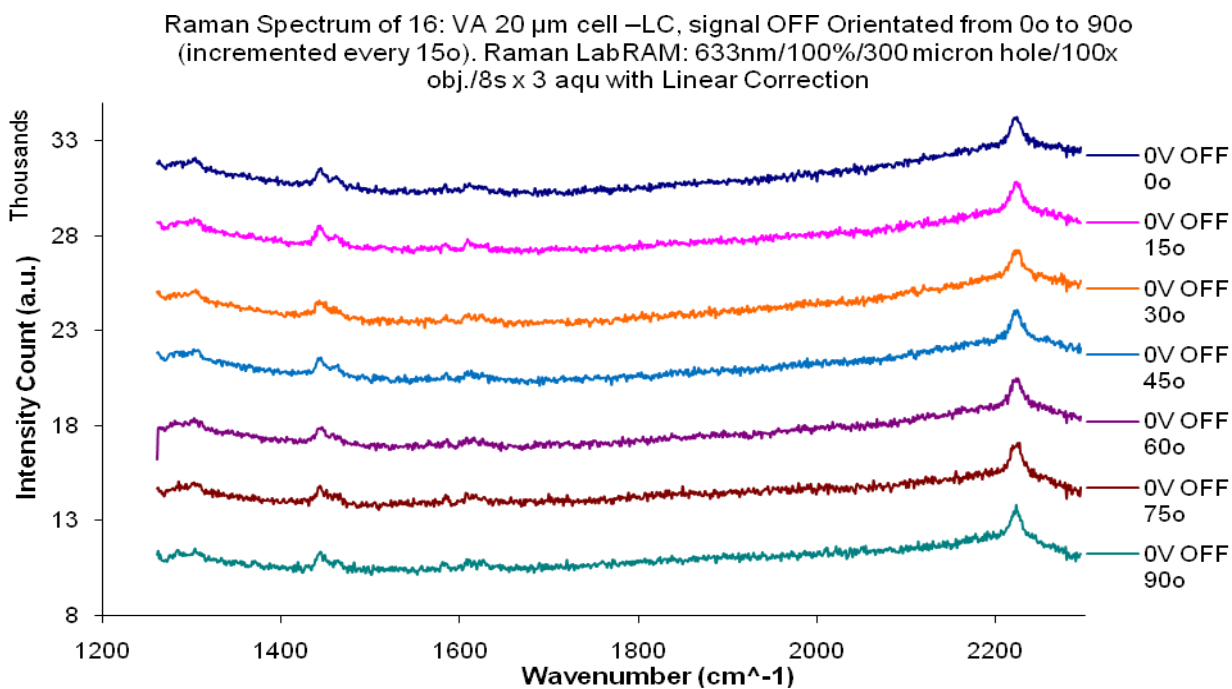


Figure 9a – Raman data of a droplet of 4% doped LC with dopant **17**

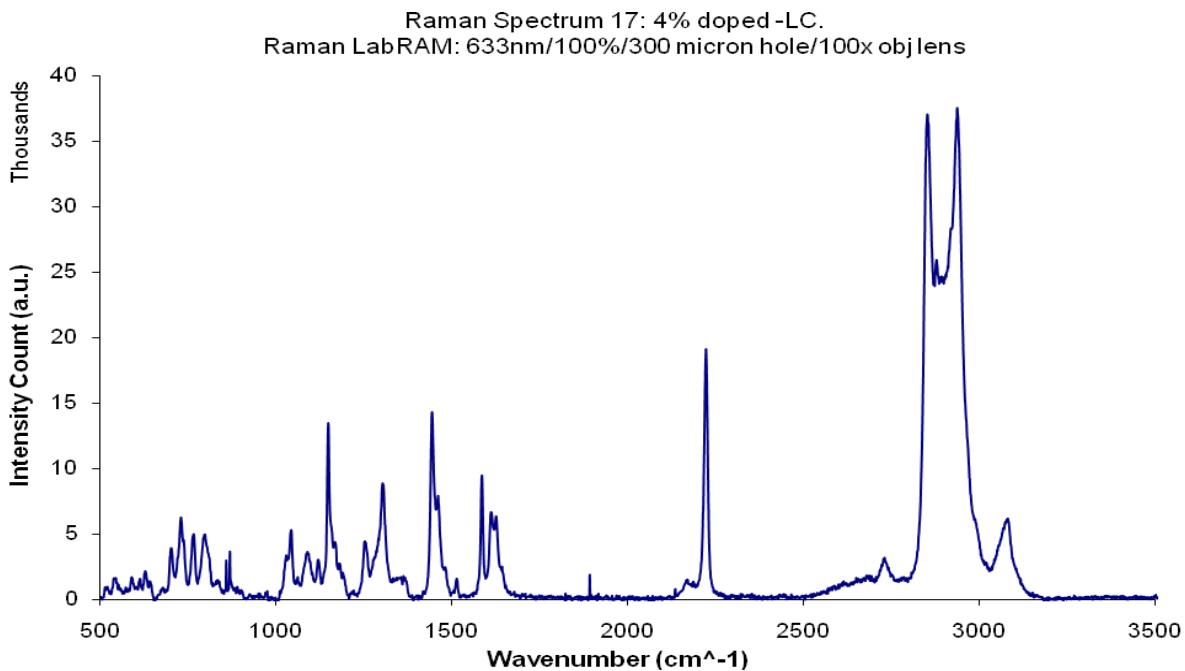


Figure 9b – Raman data of dopant **17** when the cell is switched on and off.

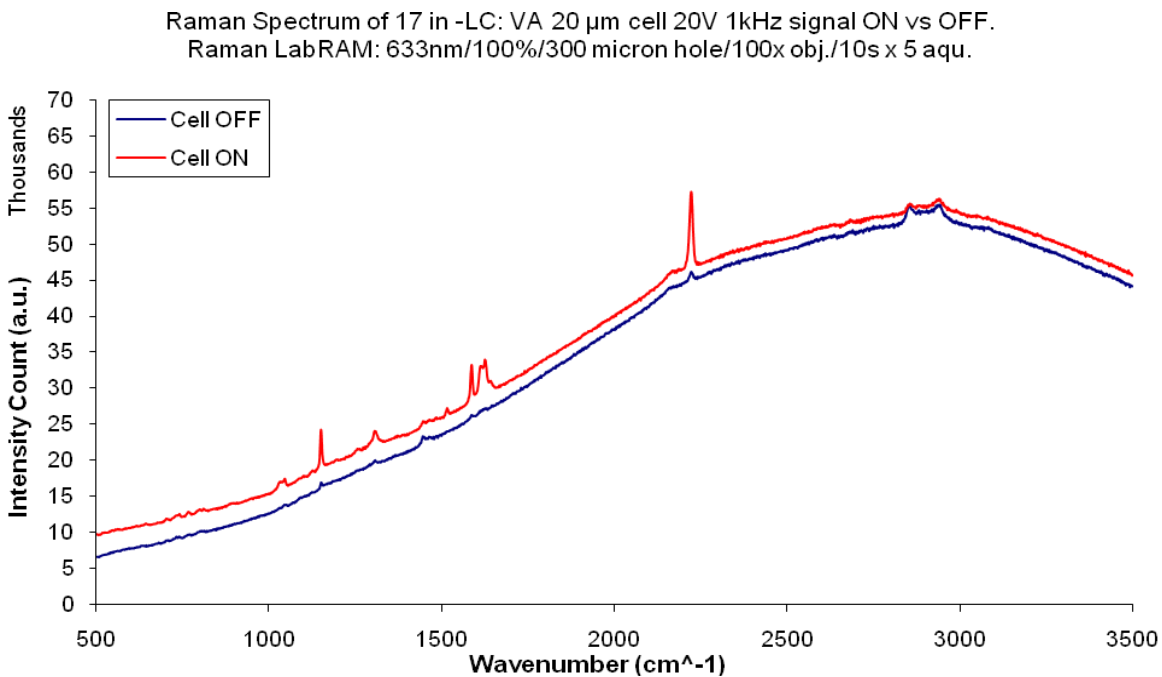


Figure 9c – Raman data of dopant **17** orientated when the cell is switched on.

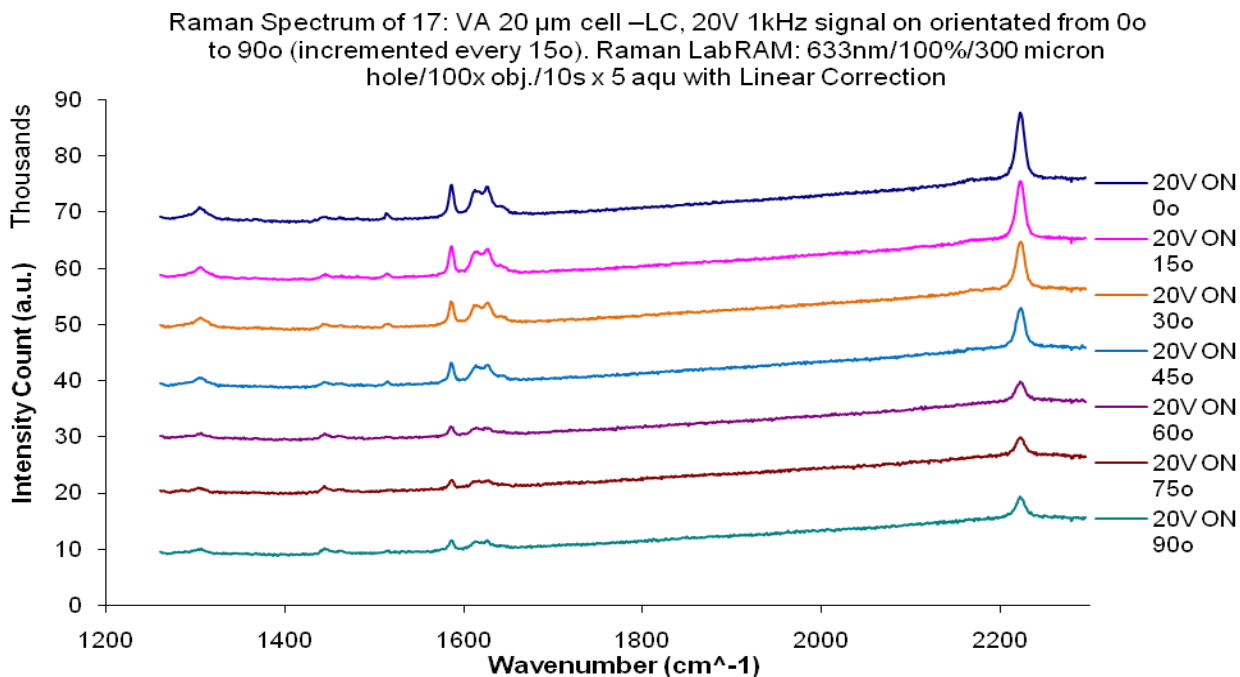


Figure 9d – Raman data of dopant **17** orientated when the cell is switched off.

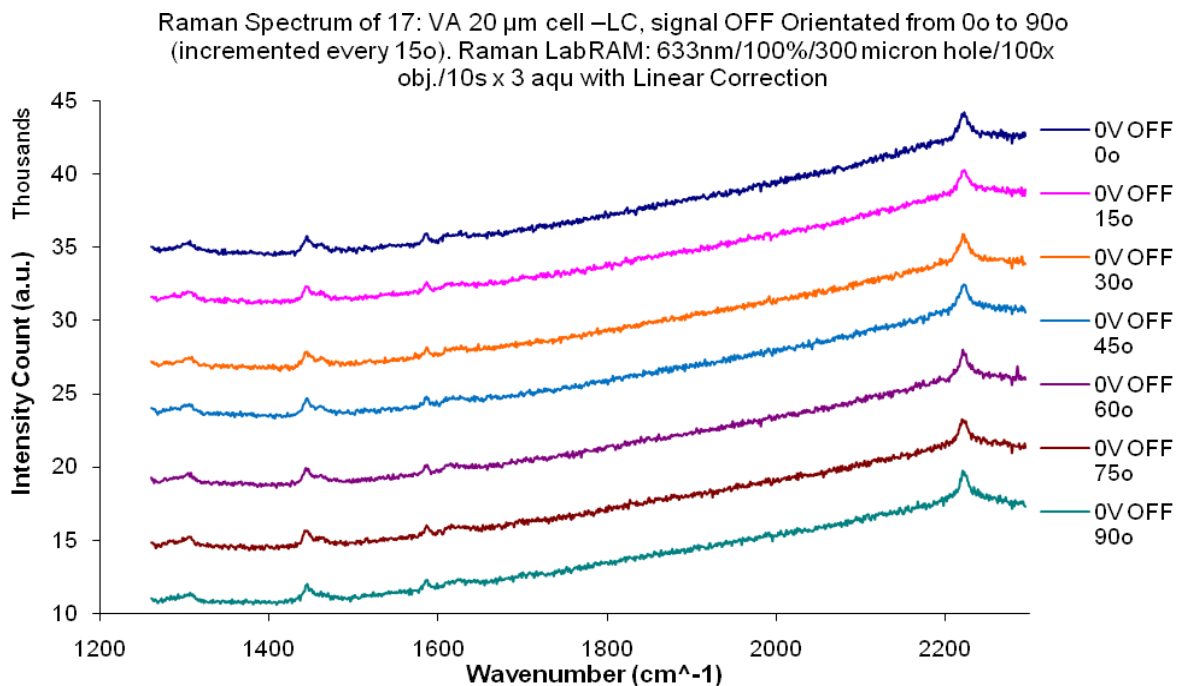


Figure 10a – Raman data of a droplet of 4% doped LC with dopant **20**

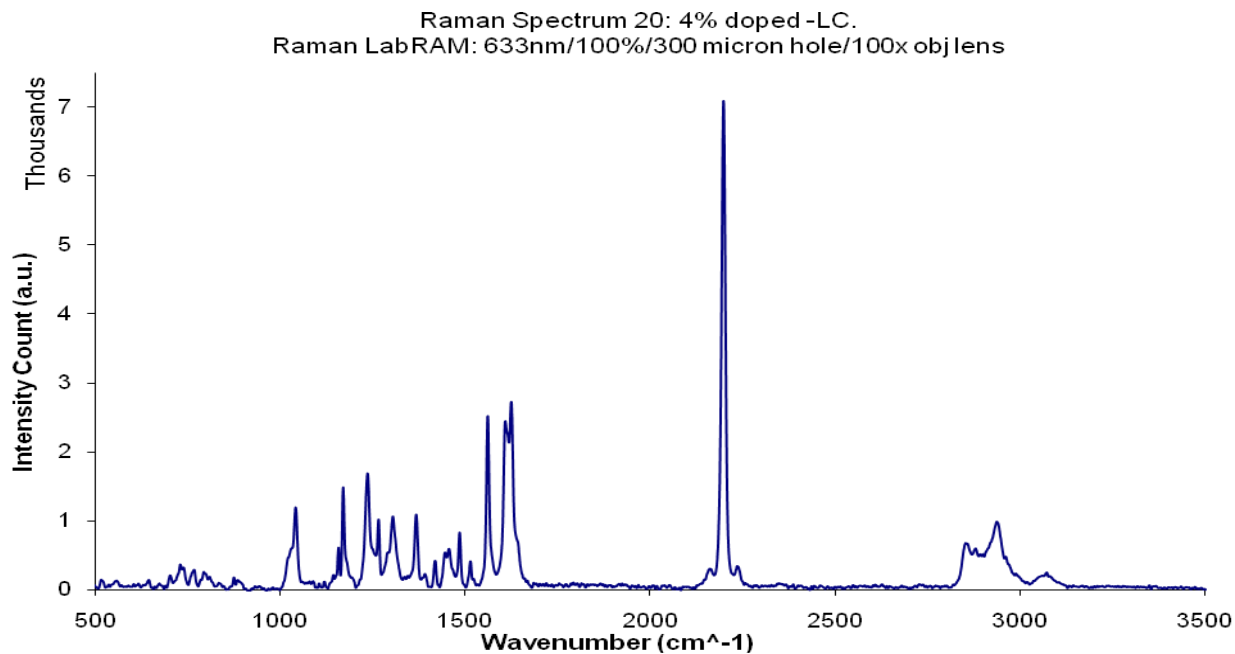


Figure 10b – Raman data of dopant **20** when the cell is switched on and off.

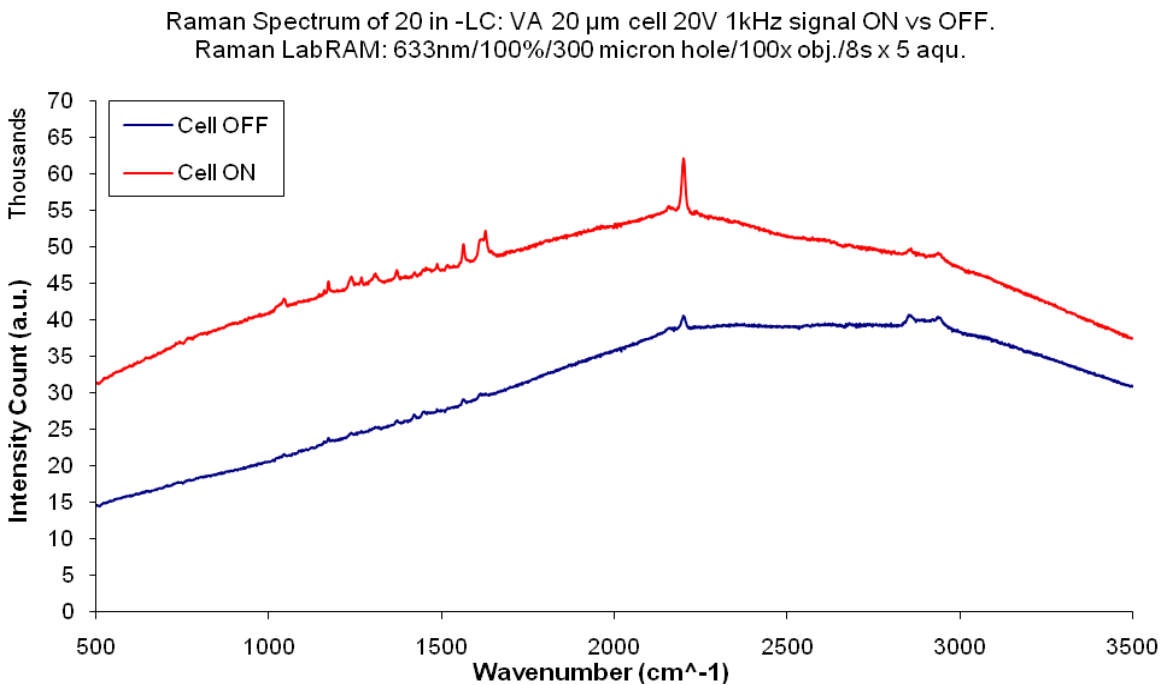


Figure 10c – Raman data of dopant **20** orientated when the cell is switched on.

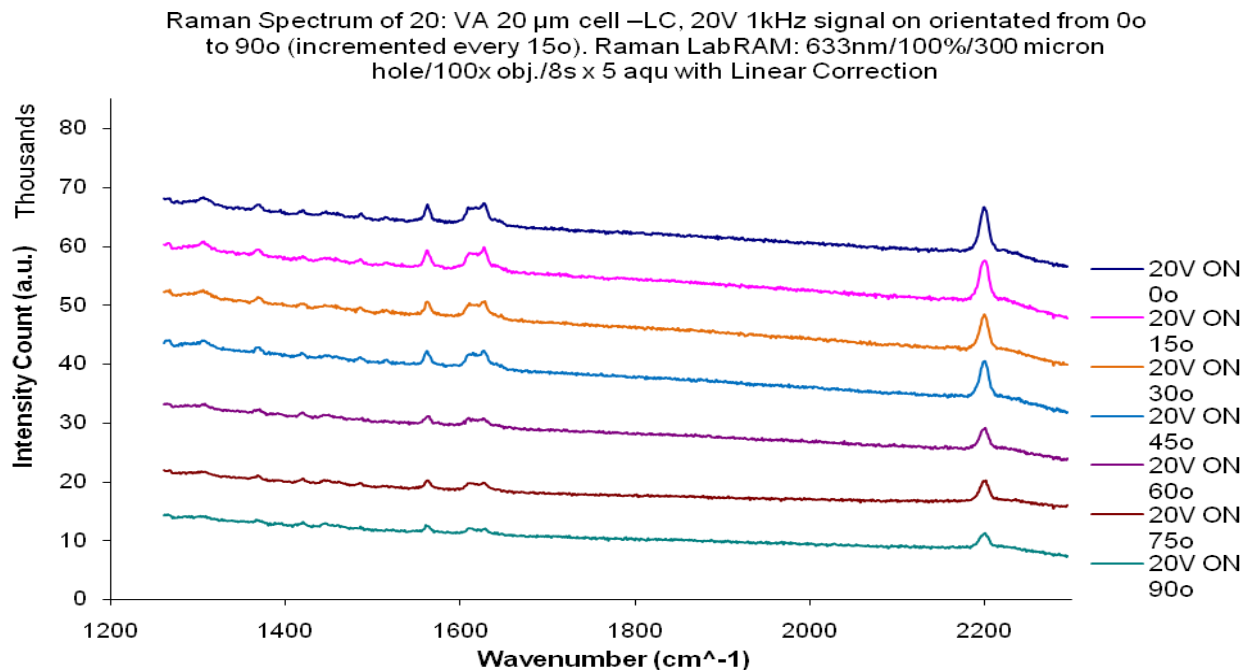


Figure 10d – Raman data of dopant **20** orientated when the cell is switched off.

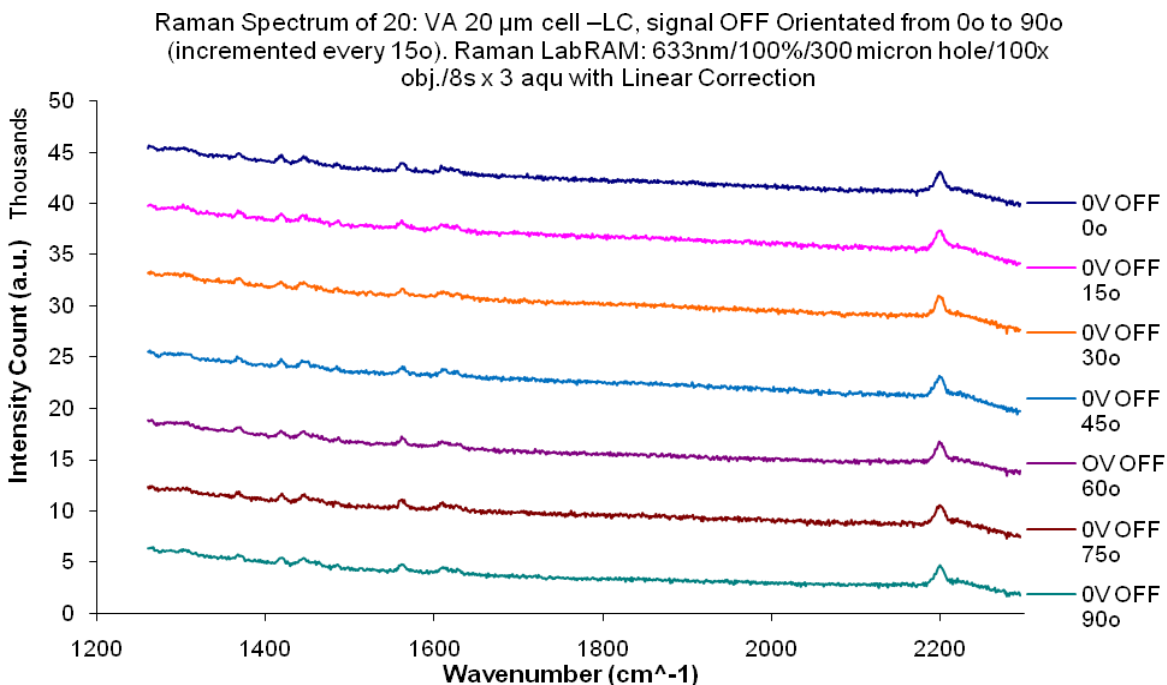


Figure 11a – Raman data of a droplet of 4% doped LC with dopant **27**

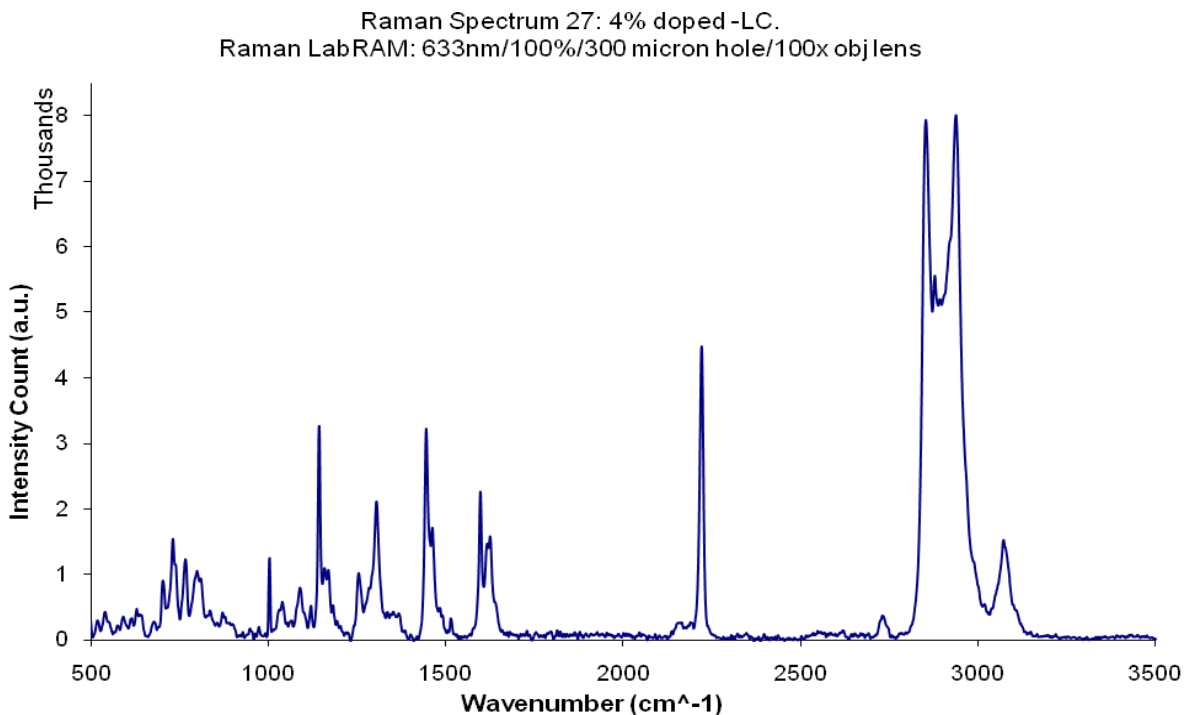


Figure 11b – Raman data of dopant **27** when the cell is switched on and off.

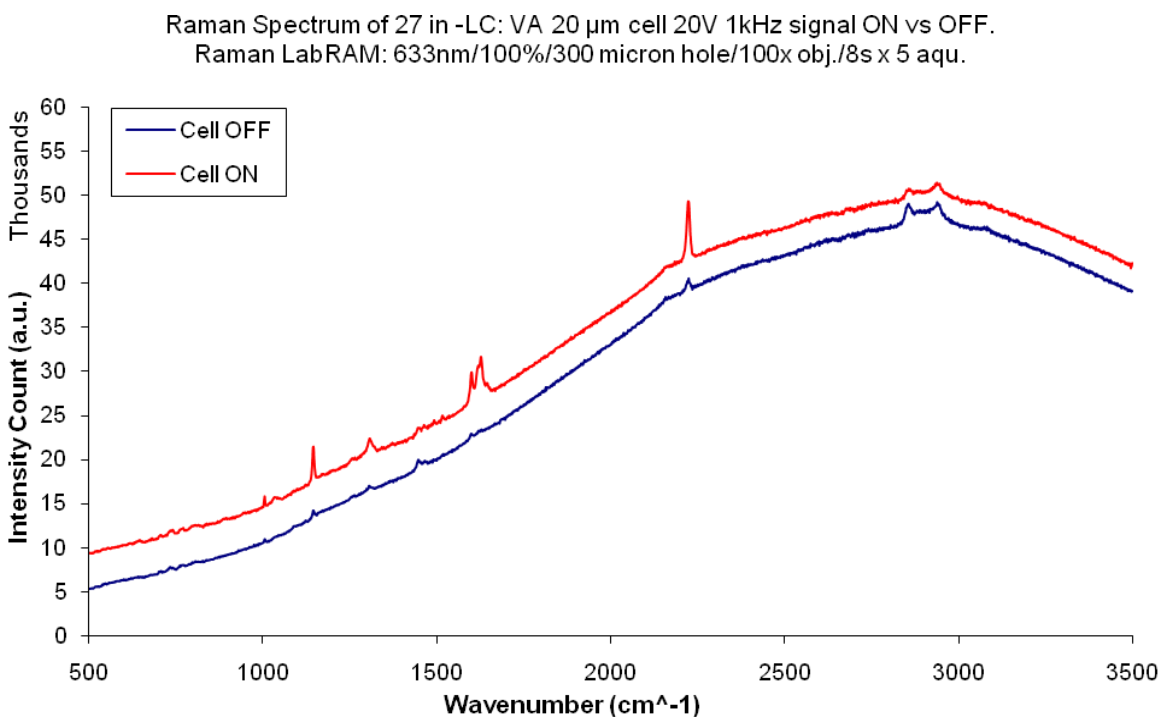


Figure 11c – Raman data of dopant **27** orientated when the cell is switched on.

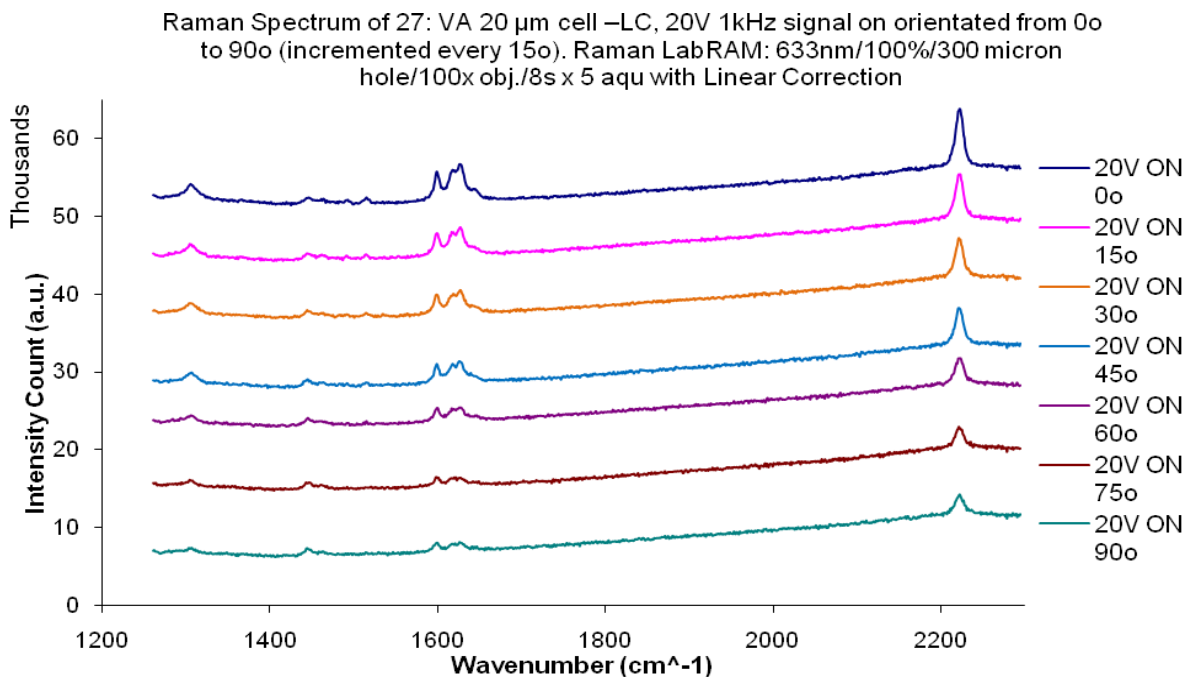


Figure 11d – Raman data of dopant **27** orientated when the cell is switched off.

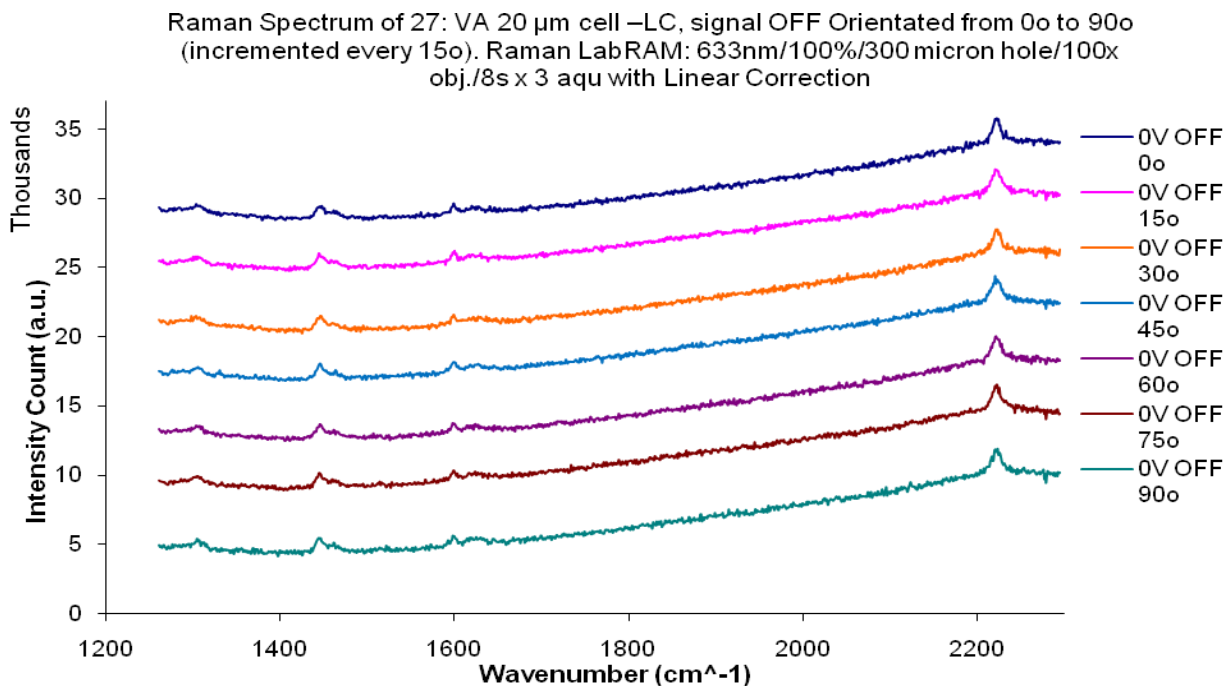


Figure 12a – Raman data of a droplet of 4% doped LC with dopant **28**

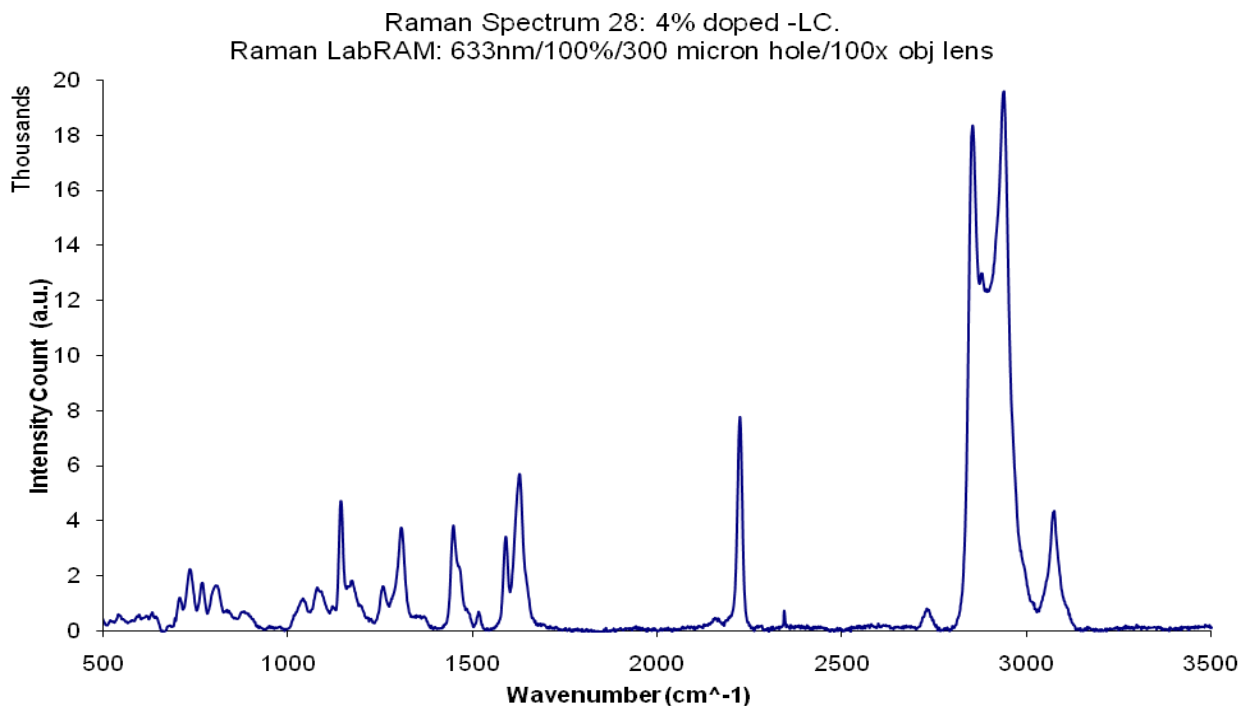


Figure 12b – Raman data of dopant **28** when the cell is switched on and off.

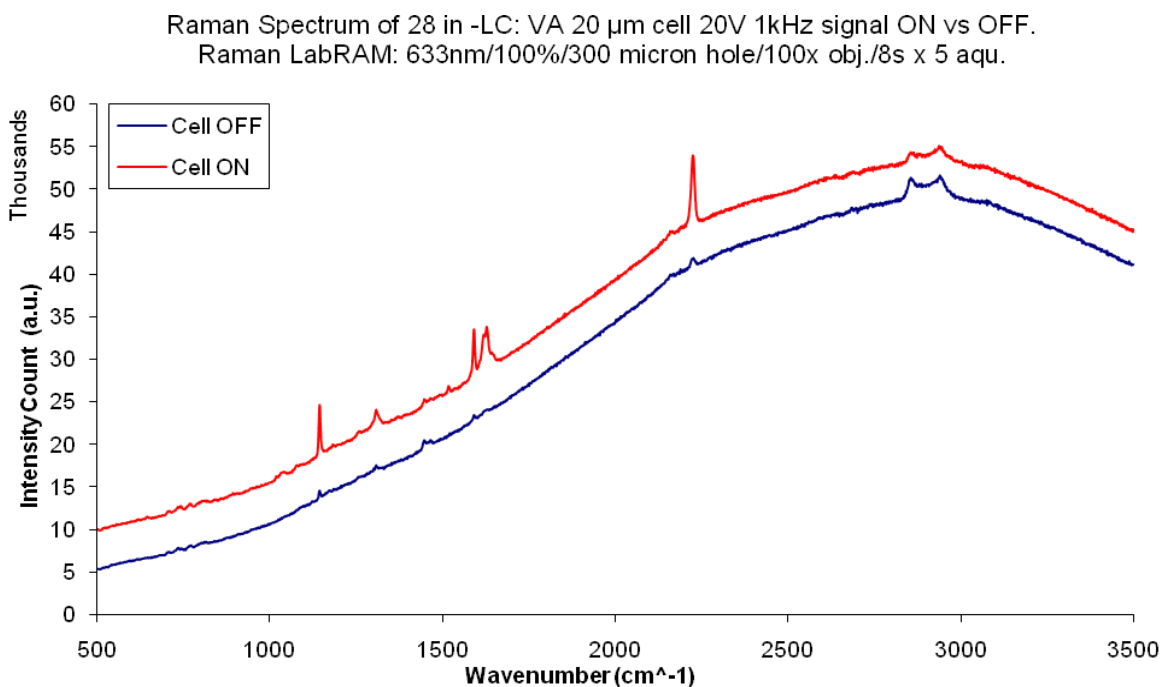


Figure 12c – Raman data of dopant **28** orientated when the cell is switched on.

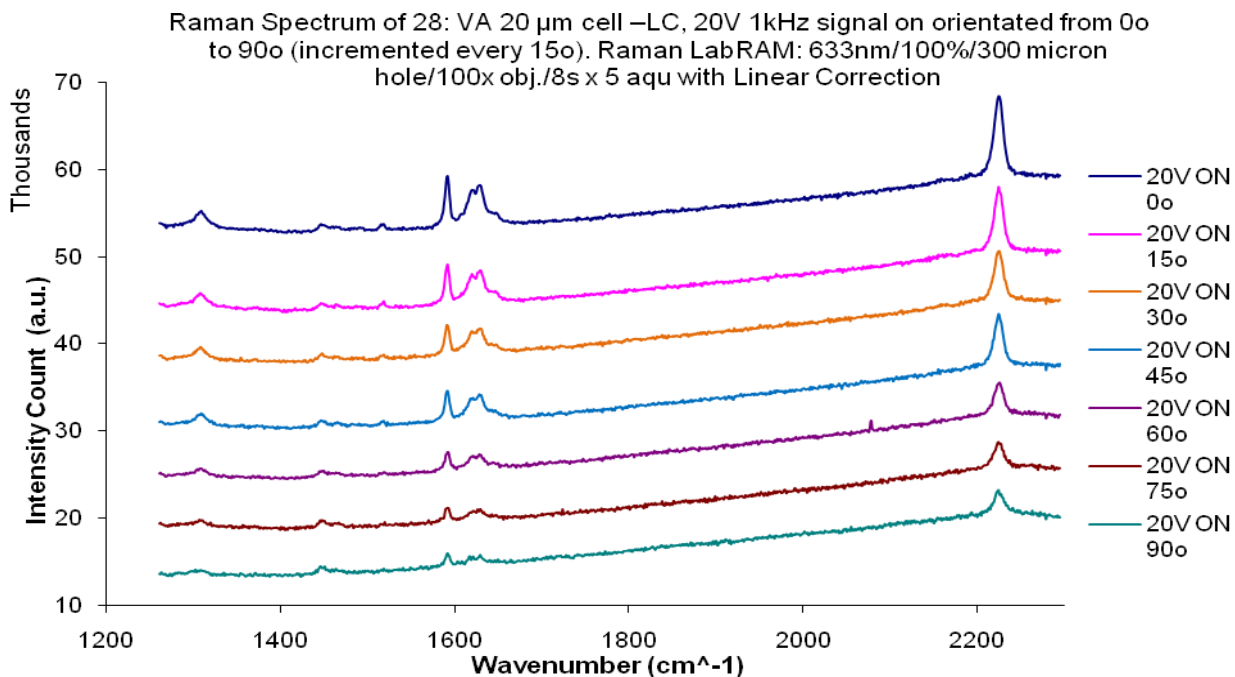


Figure 12d – Raman data of dopant **28** orientated when the cell is switched off.

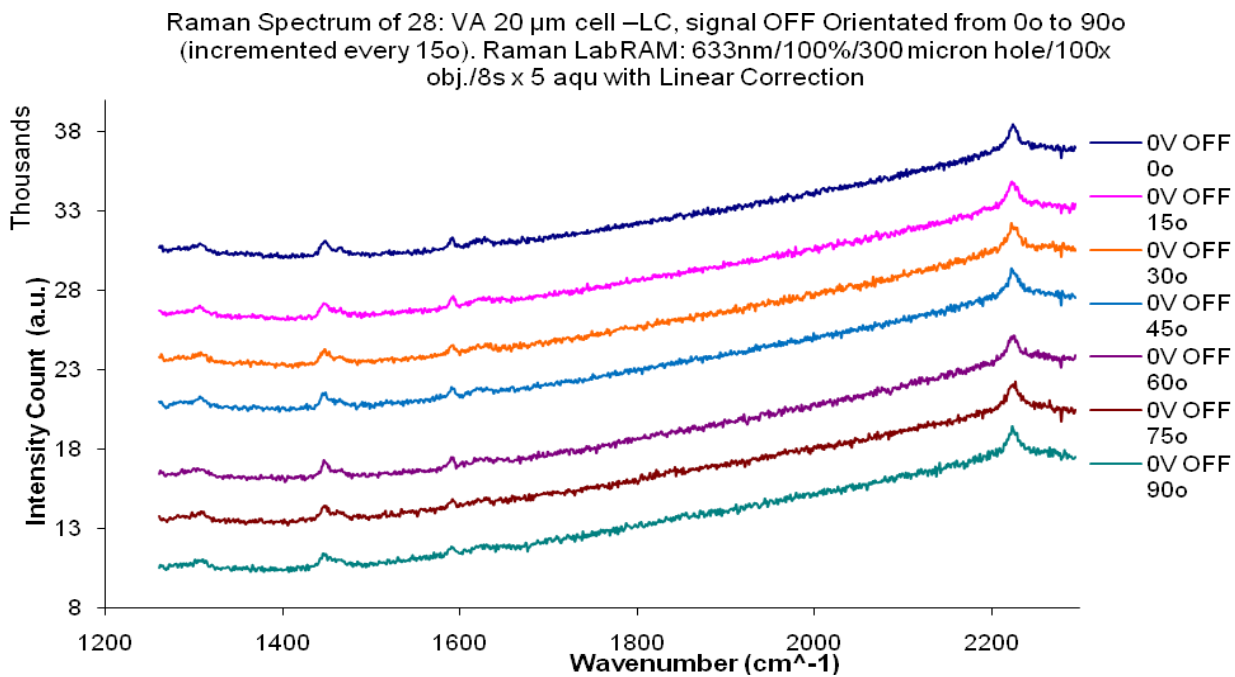


Figure 13a – Raman data of a droplet of 4% doped LC with dopant **29**

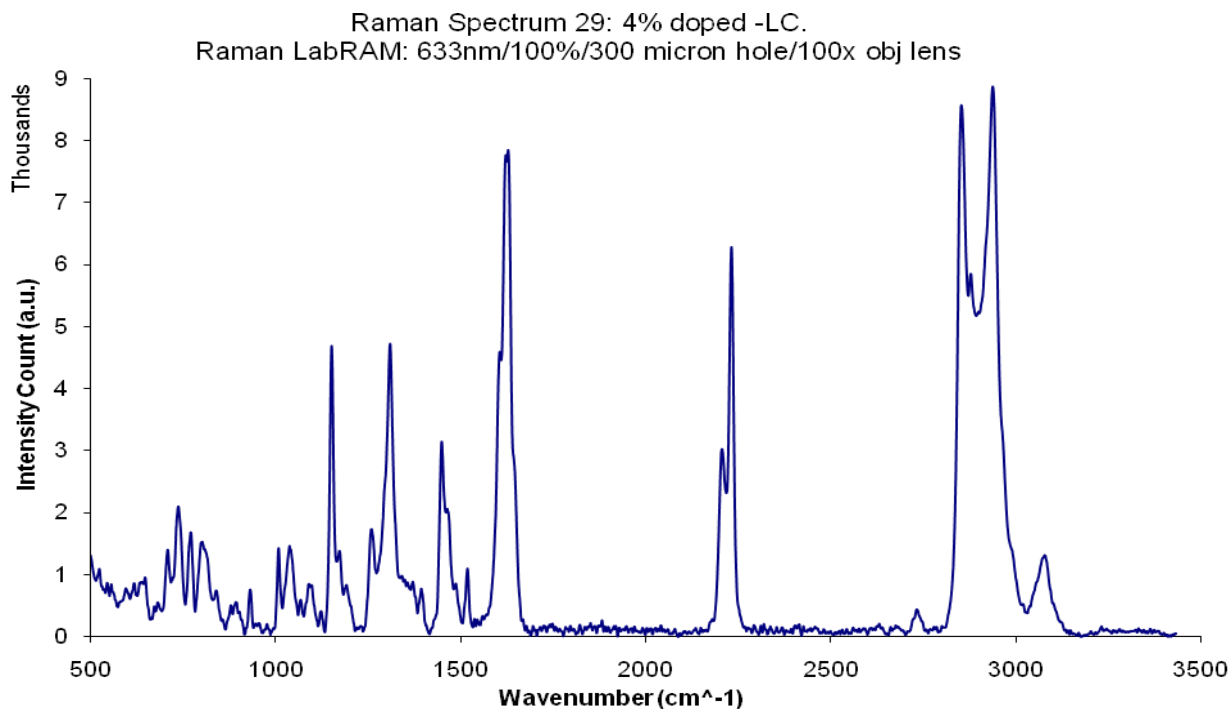


Figure 13b – Raman data of dopant **29** when the cell is switched on and off.

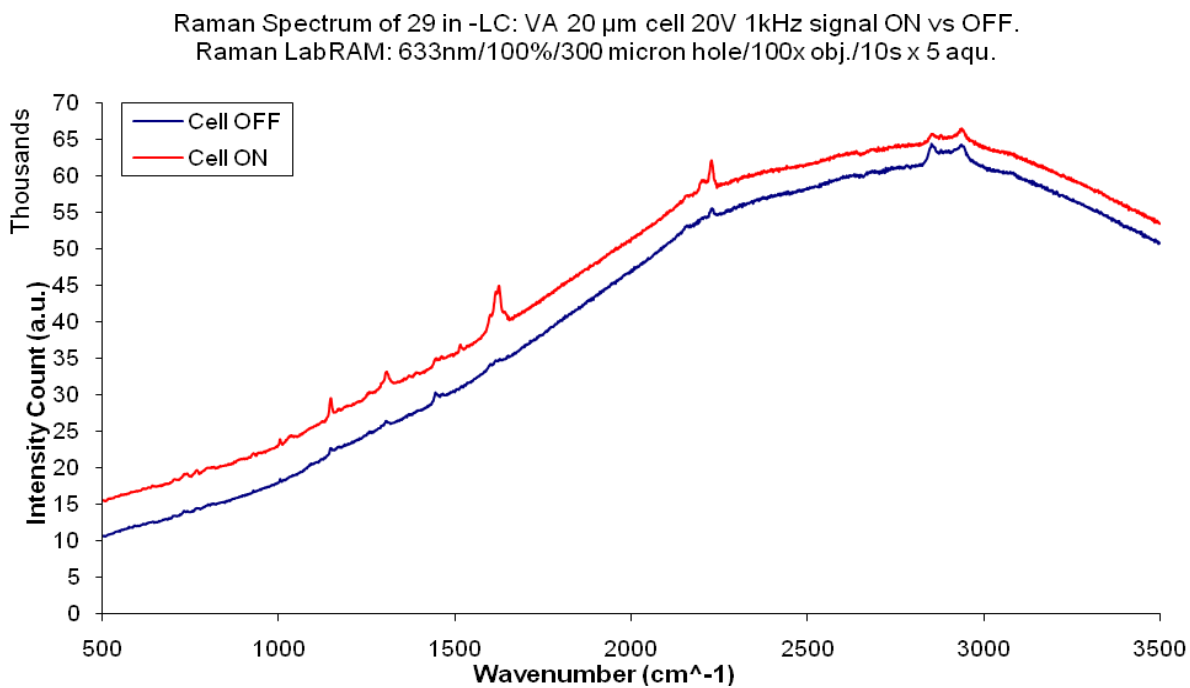


Figure 13c – Raman data of dopant **29** orientated when the cell is switched on.

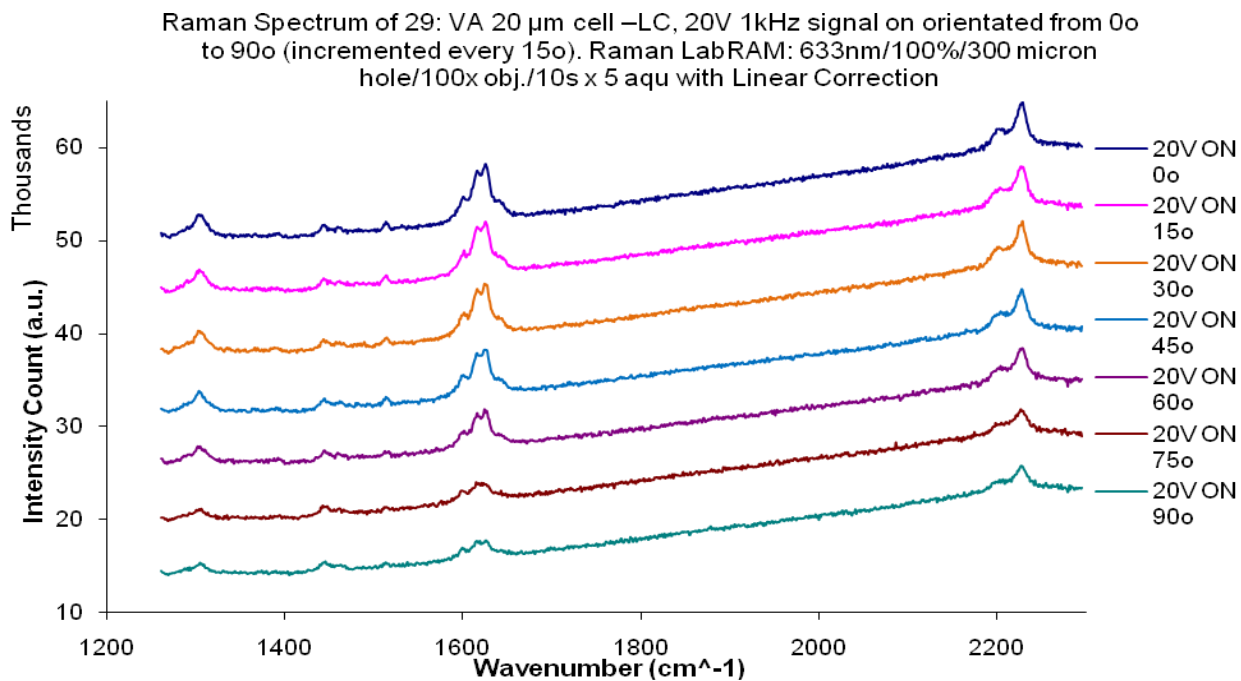


Figure 13d – Raman data of dopant **29** orientated when the cell is switched off.

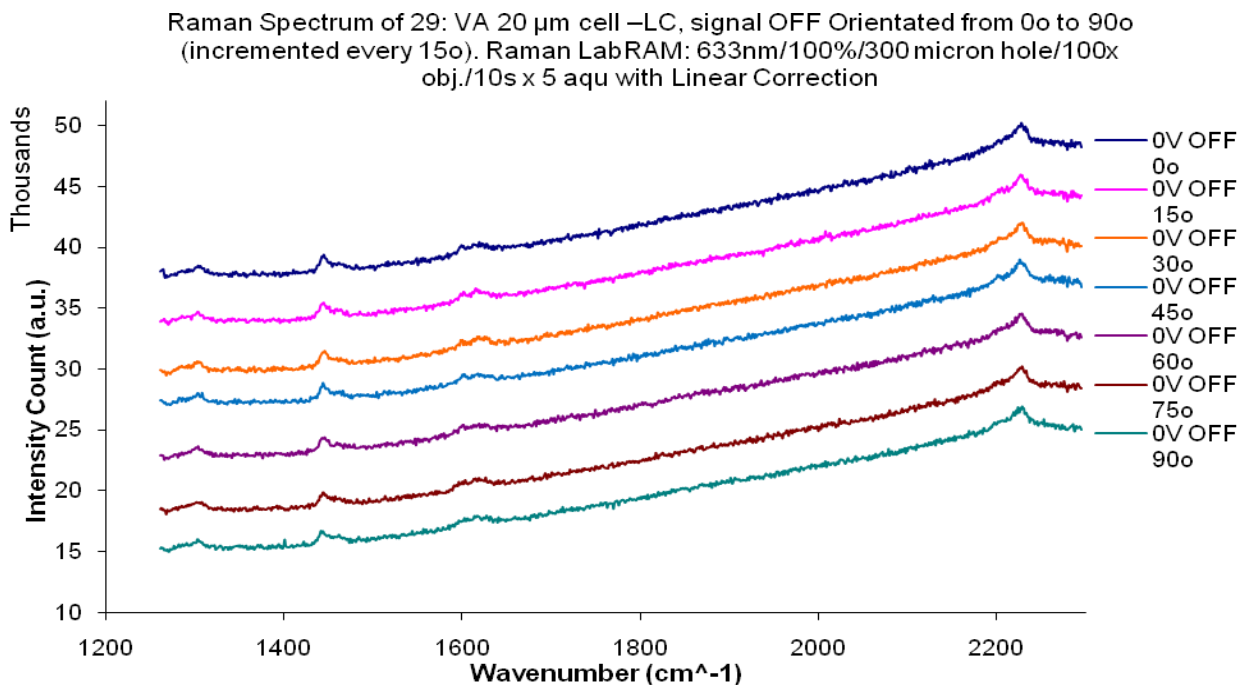


Figure 14 – Optical transmittance profile of prepared –LC cell.

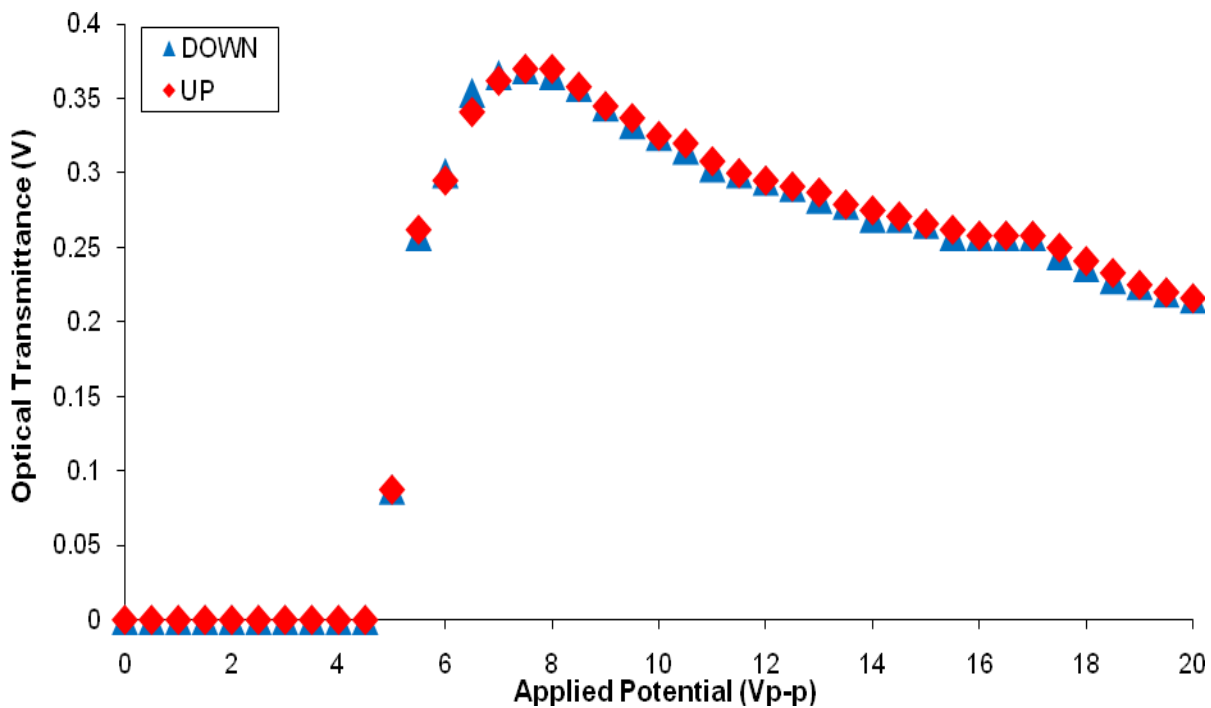


Figure 15a – -LC doped with 14: 8-15V p-p optical transmittance profiles

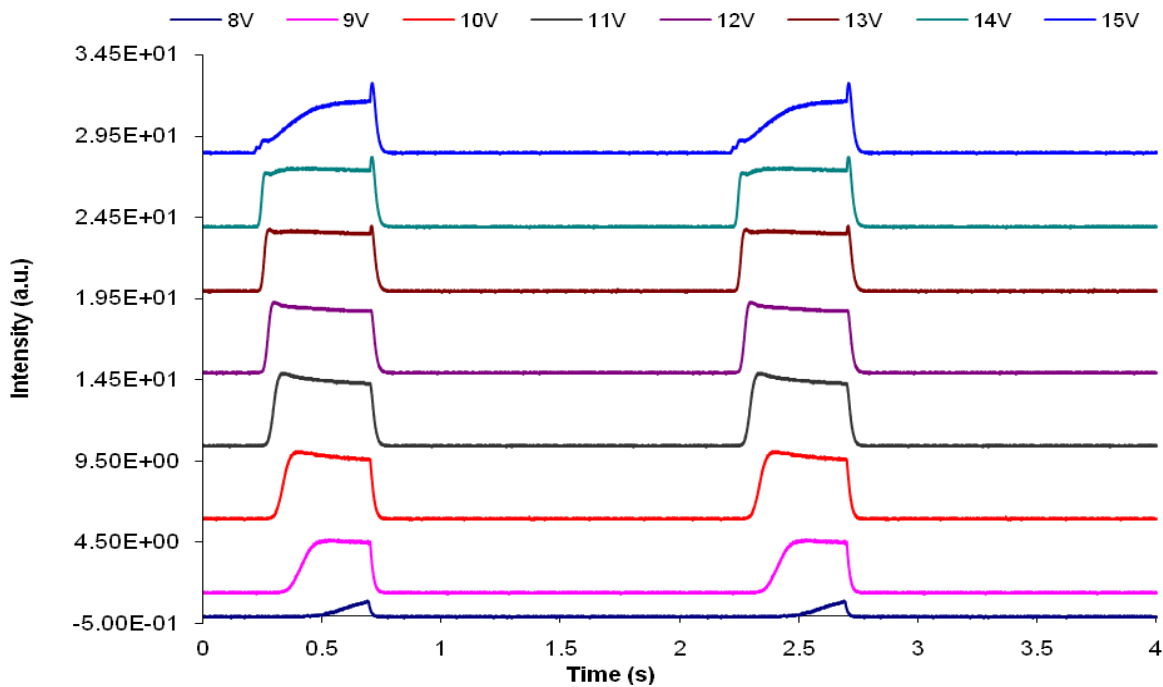


Figure 15b – Doped –LC with **14**: transmittance profile of varying periods at 12 V p-p

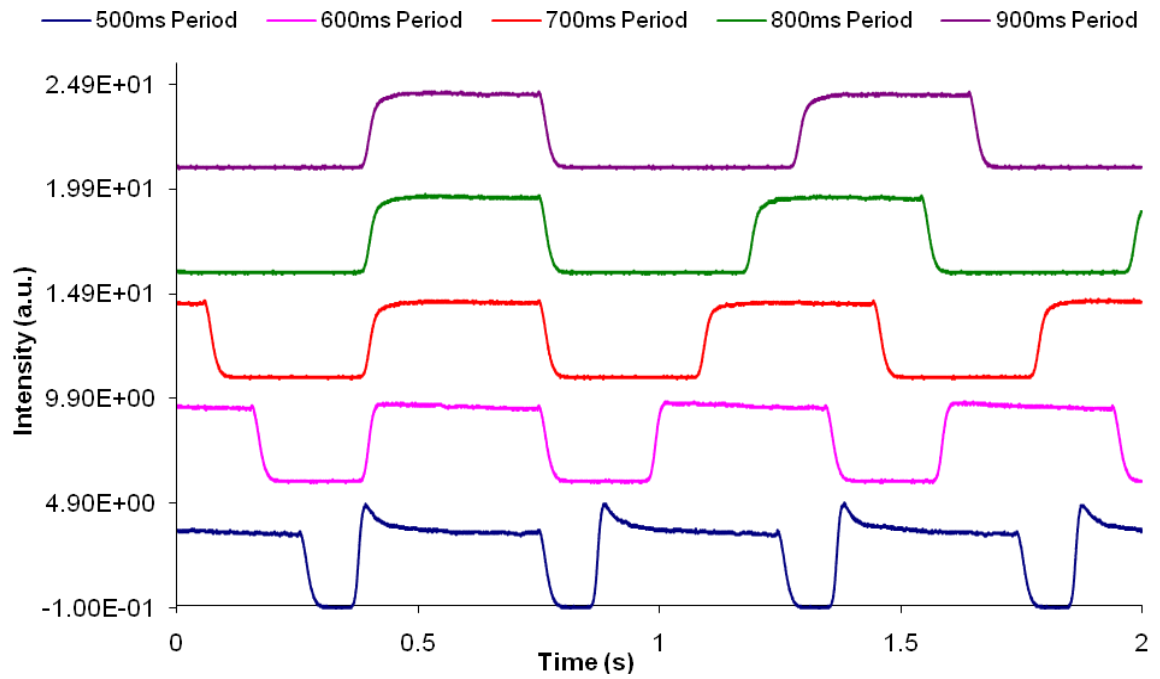


Figure 16 – -LC 7-14 V p-p Optical Intensity Profiles

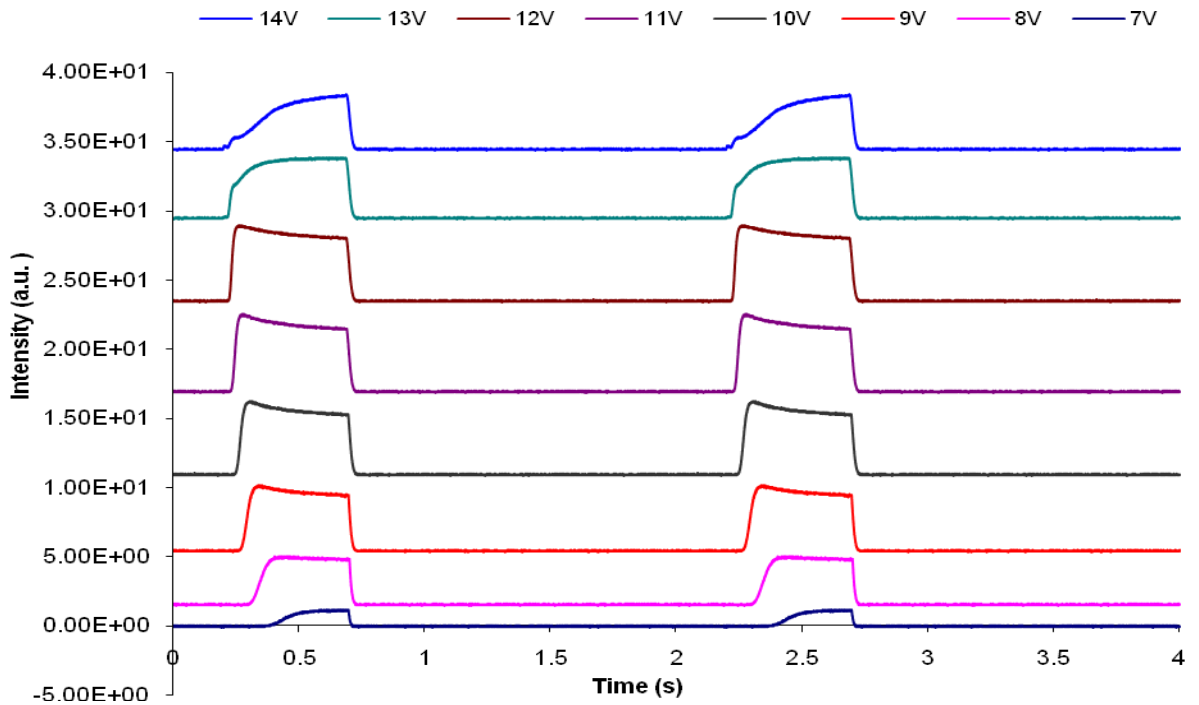


Figure 17a – Dopant 14 (C≡C) peak of doped LC cell (TR Raman integral data of the switch)

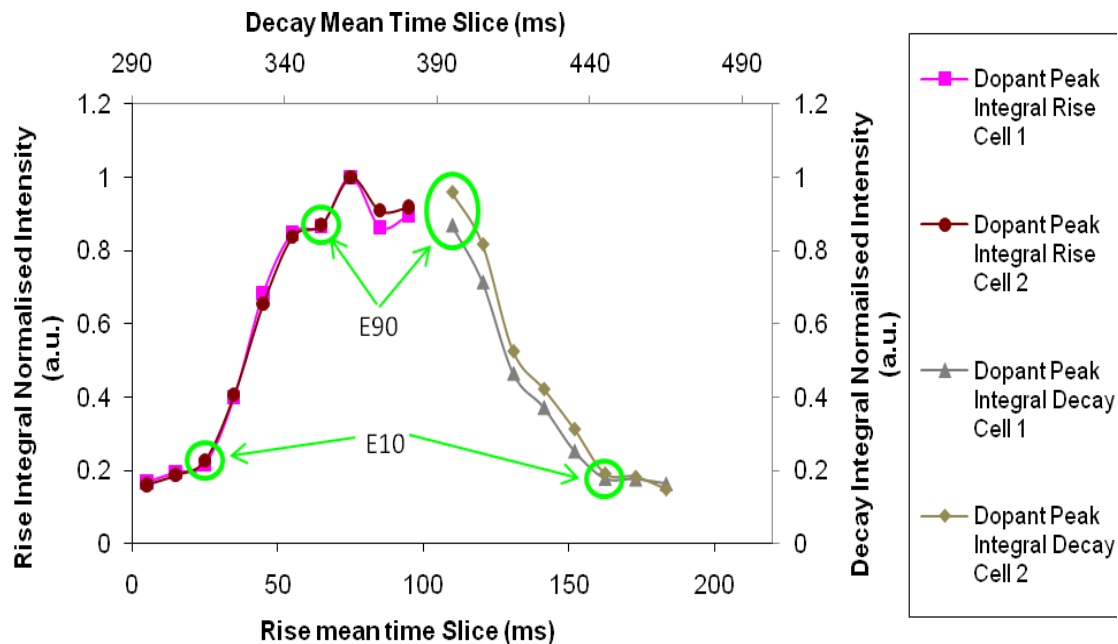


Figure 17b – LC peak of doped cell (TR Raman integral data of the switch)

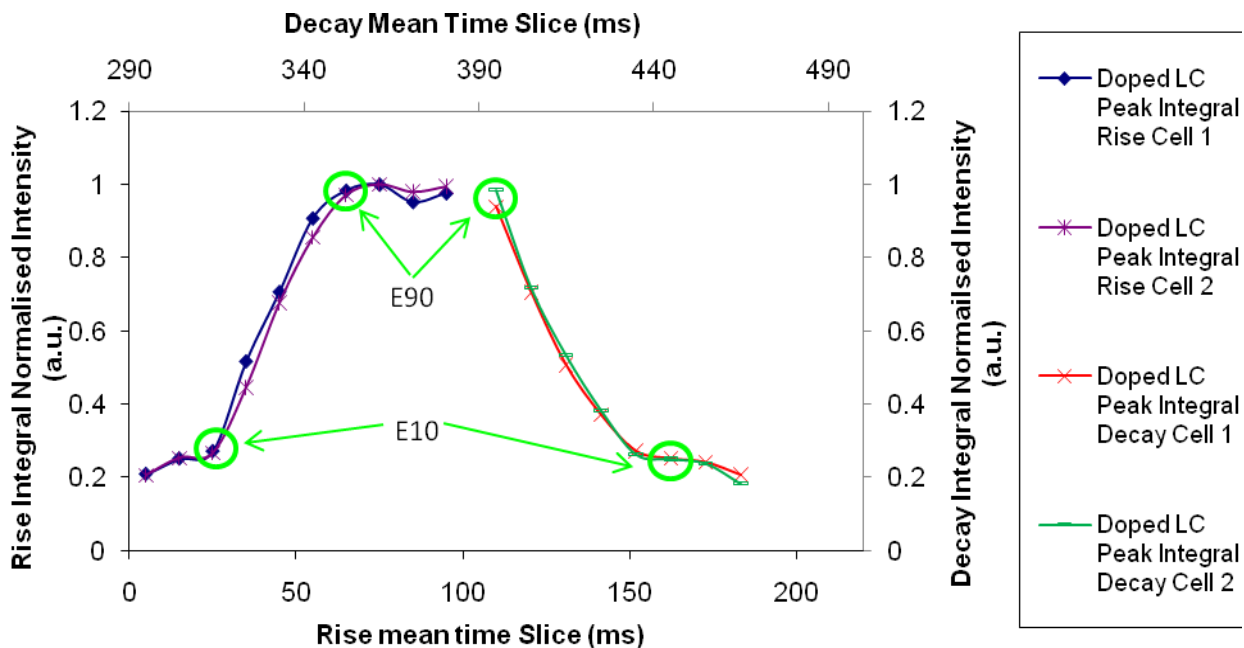


Figure 17c – LC peak of undoped –LC cell (TR Raman integral data of the switch)

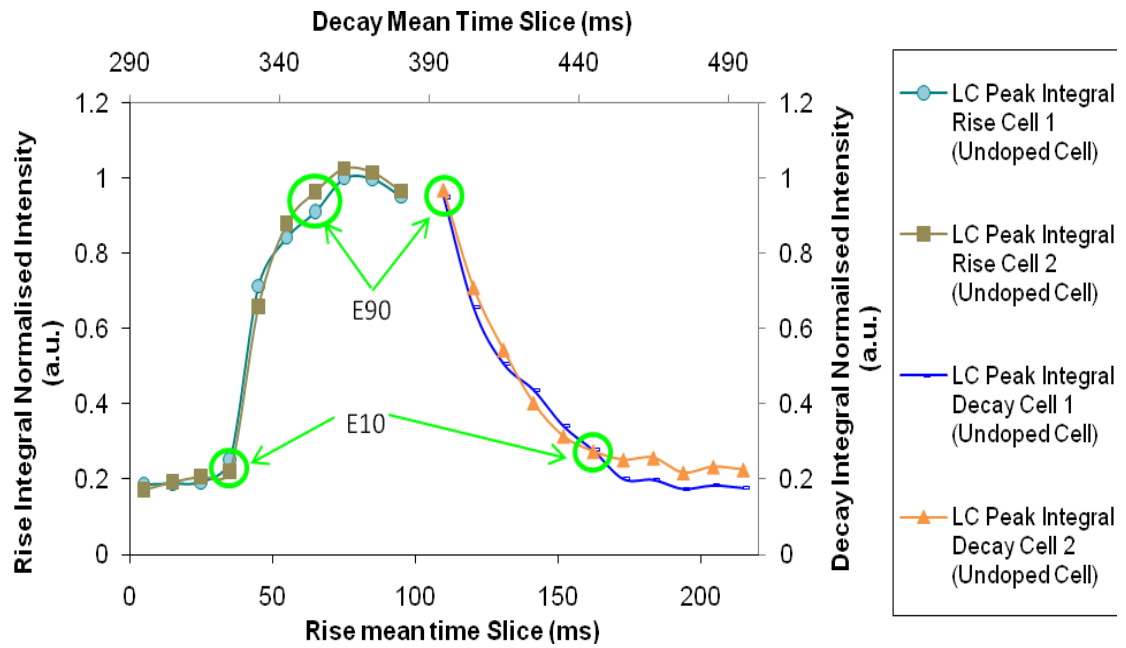


Figure 18a – Rise EO data for undoped -LC cell blown up

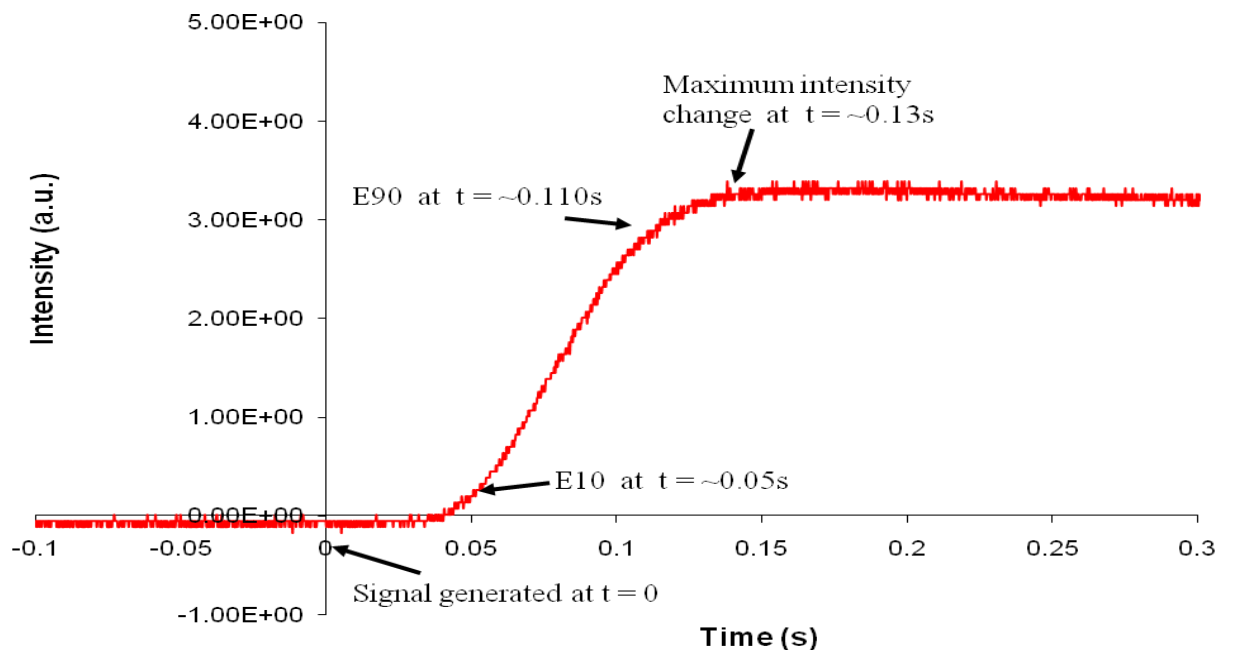


Figure 18b – Decay EO data for undoped -LC cell blown up

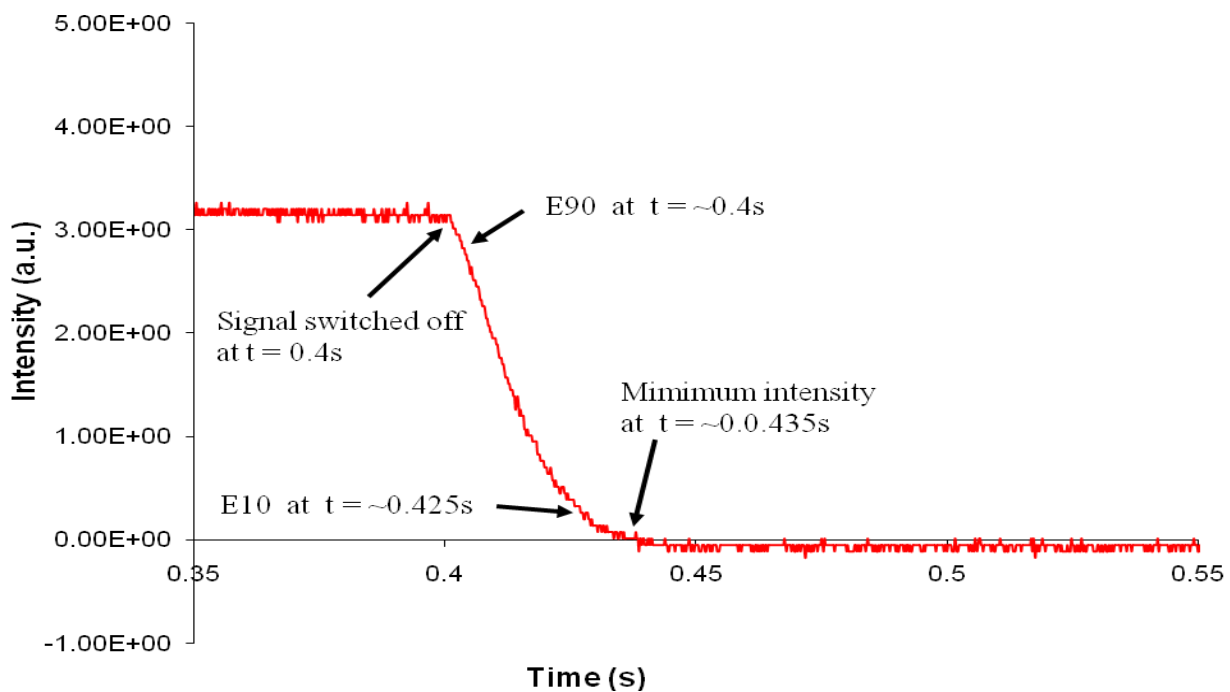


Figure 19a – Raman data of undoped +LC BL0037 when the cell is switched on and off

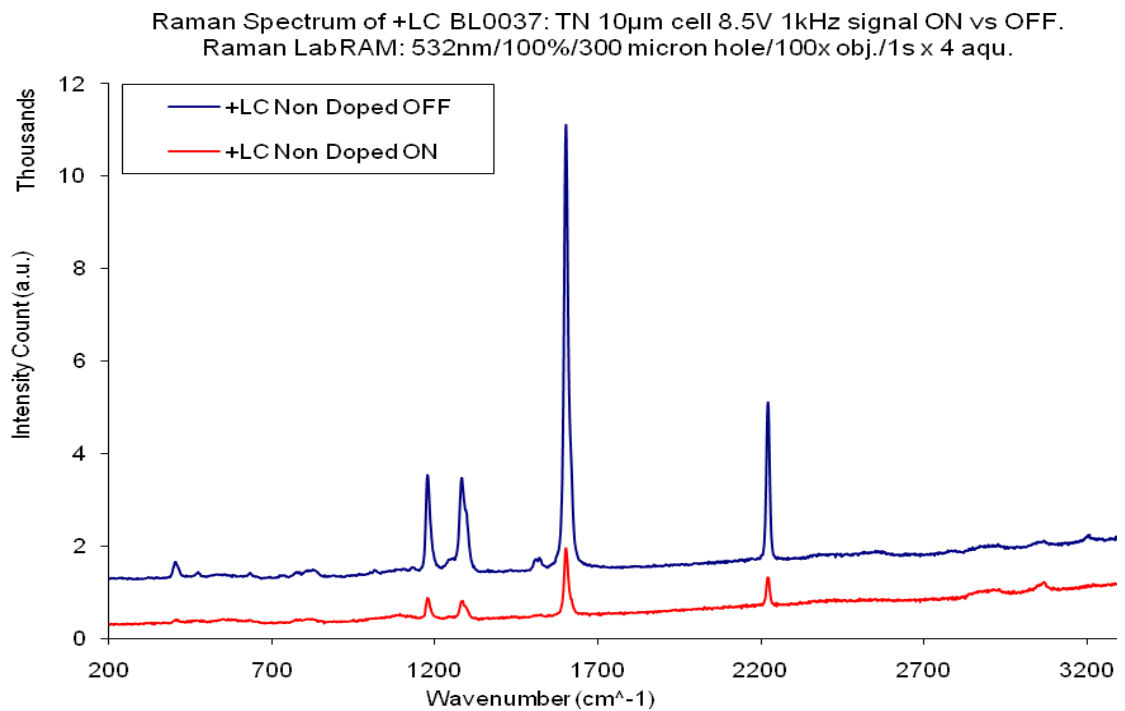


Figure 19b – Raman data of undoped +LC BL0037 orientated when the cell is switched on

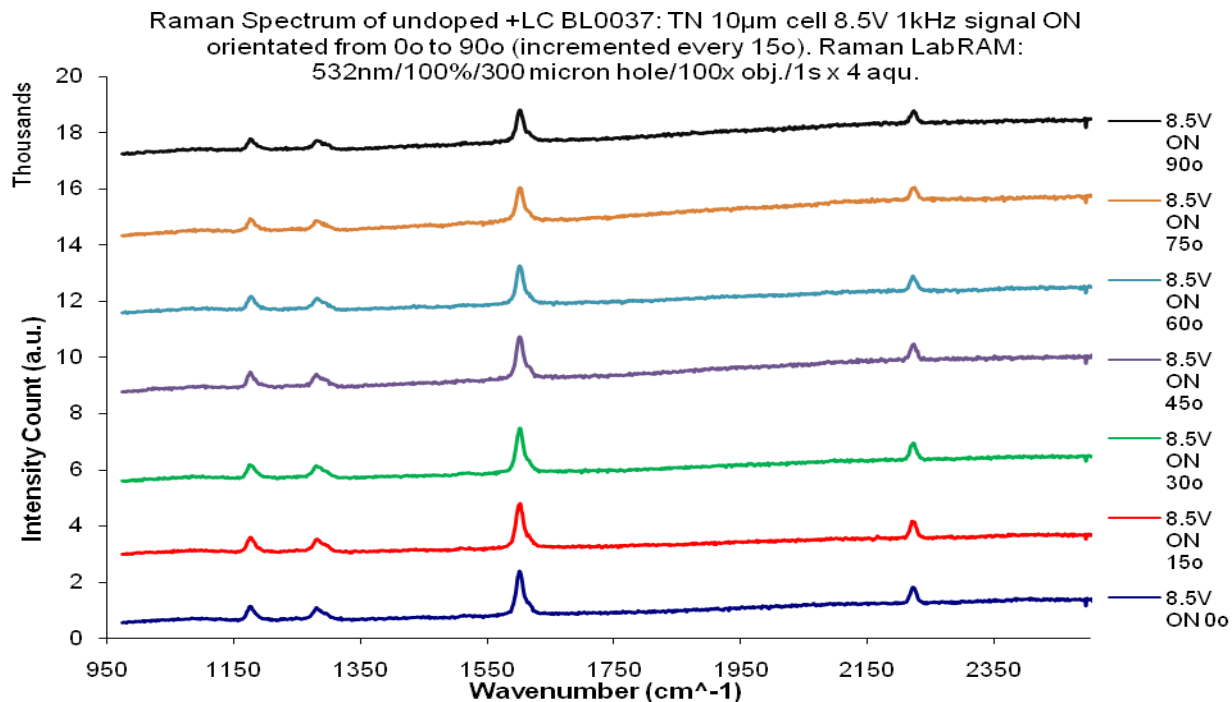


Figure 19c – Raman data of undoped +LC BL0037 orientated when the cell is switched off

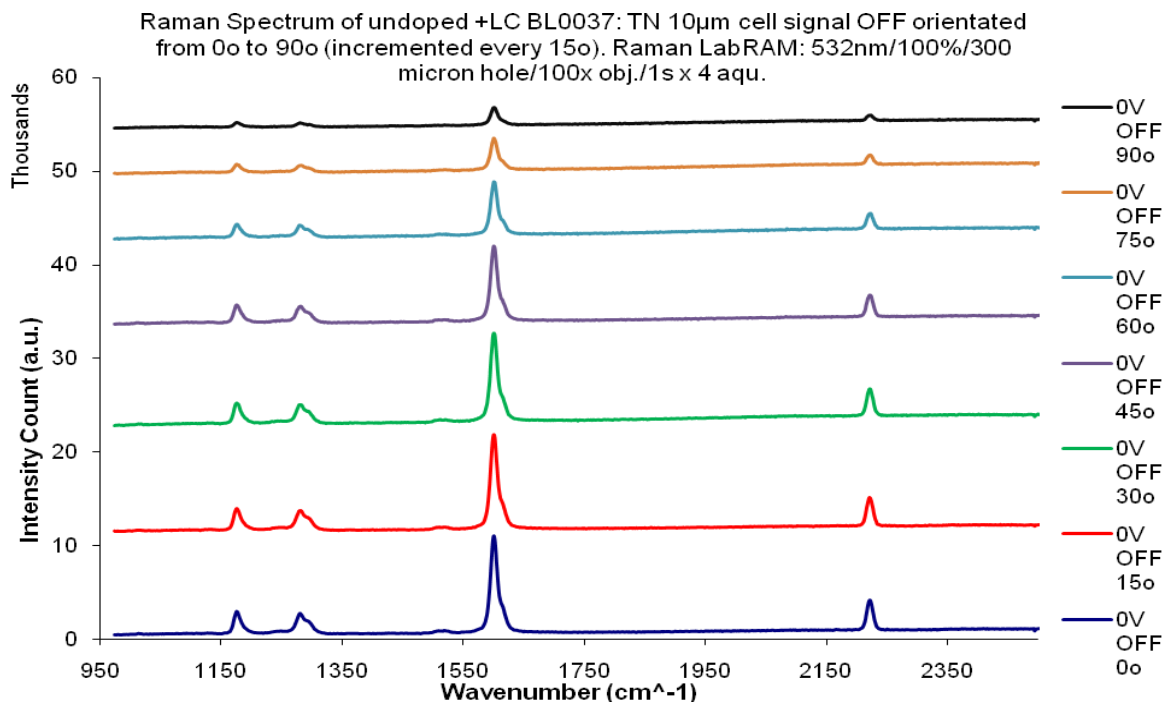


Figure 20 – Hysteresis data of the second +LC BL0037 cell

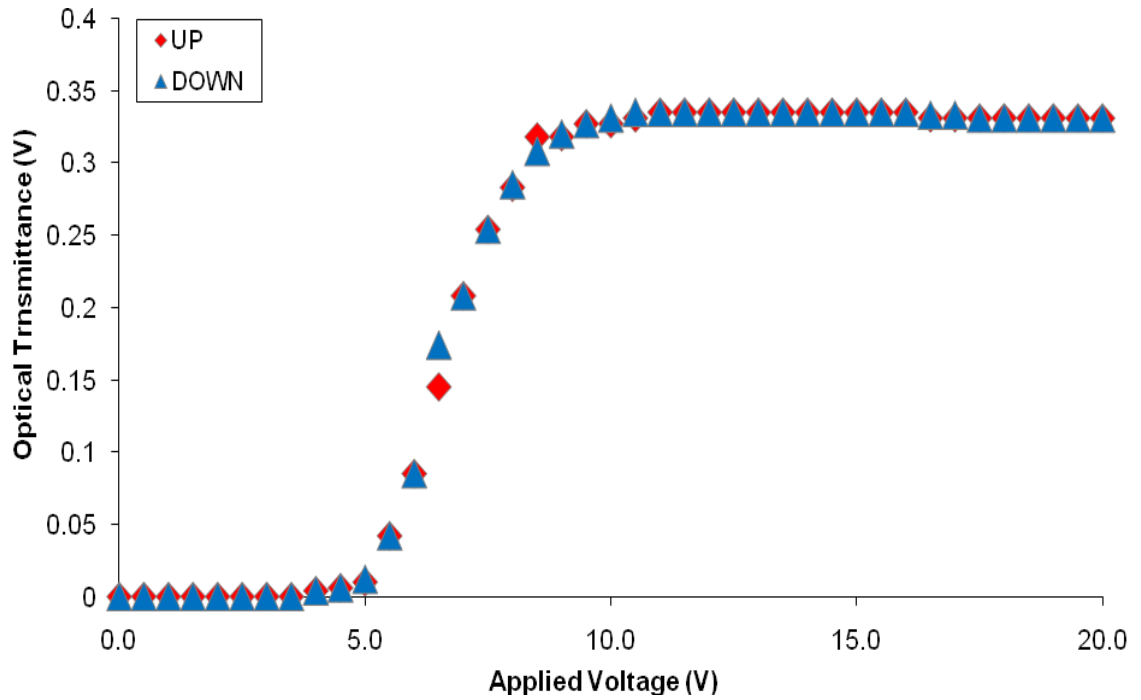


Figure 21a – Optical transmittance profile of the undoped +LC at 12V

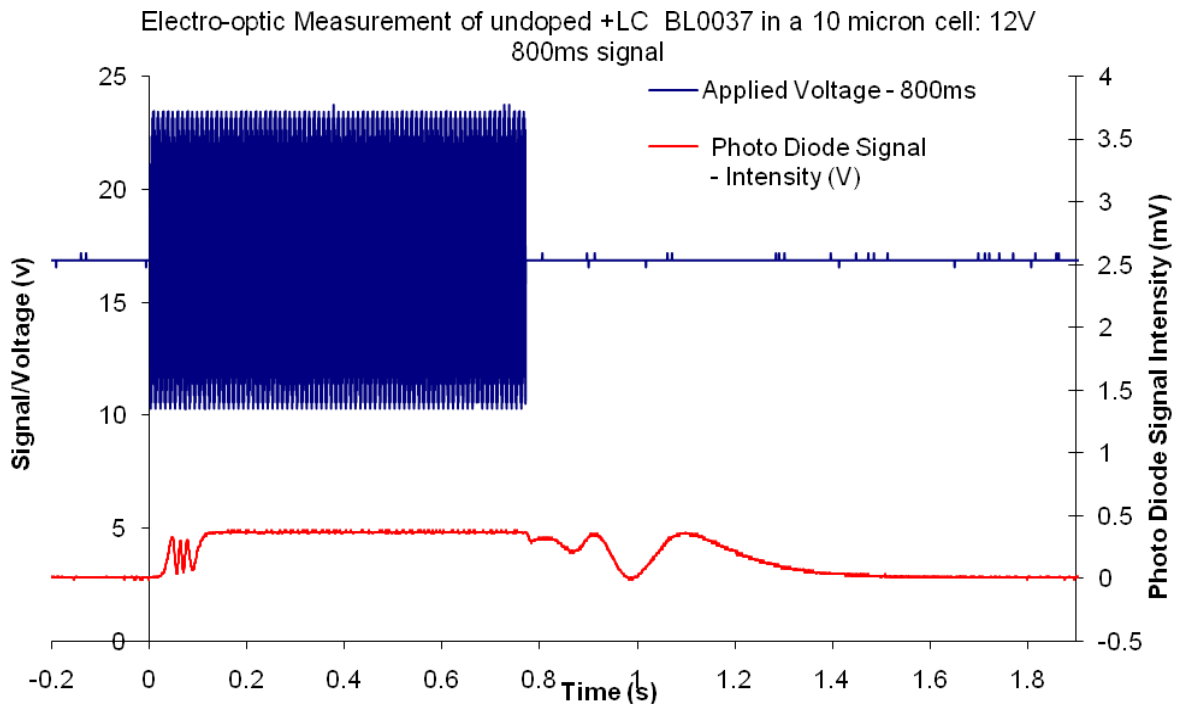


Figure 21b – Optical transmittance profile of the undoped +LC at 16V

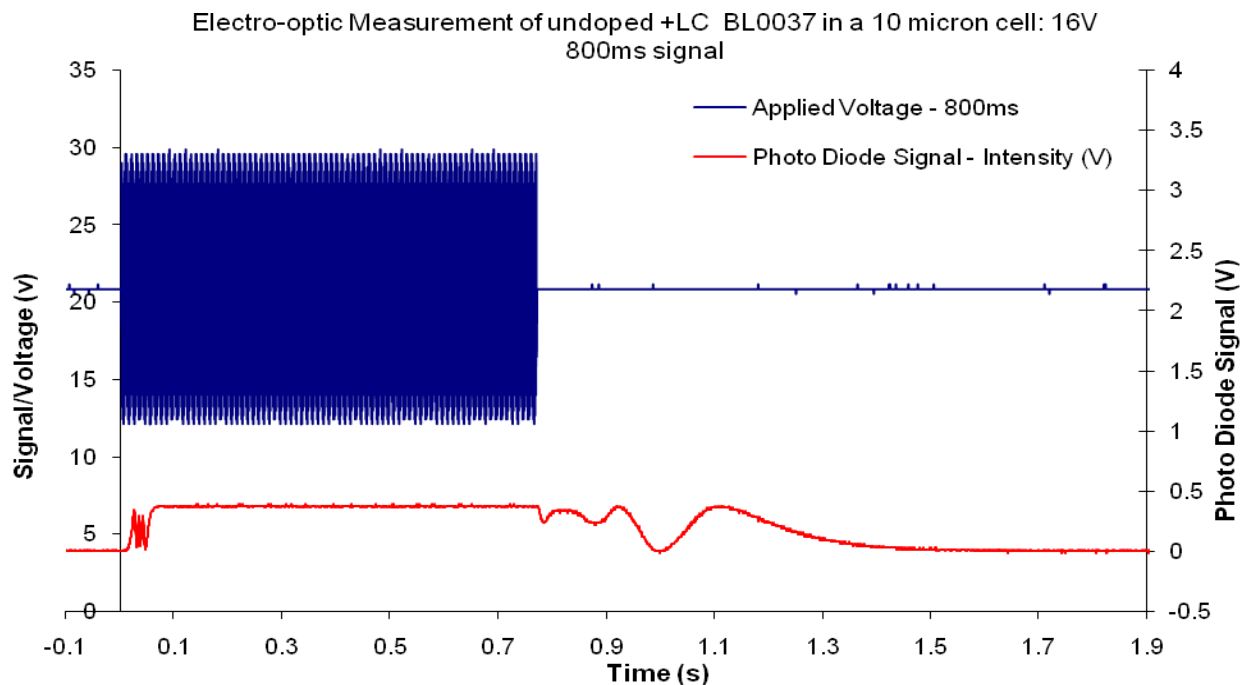
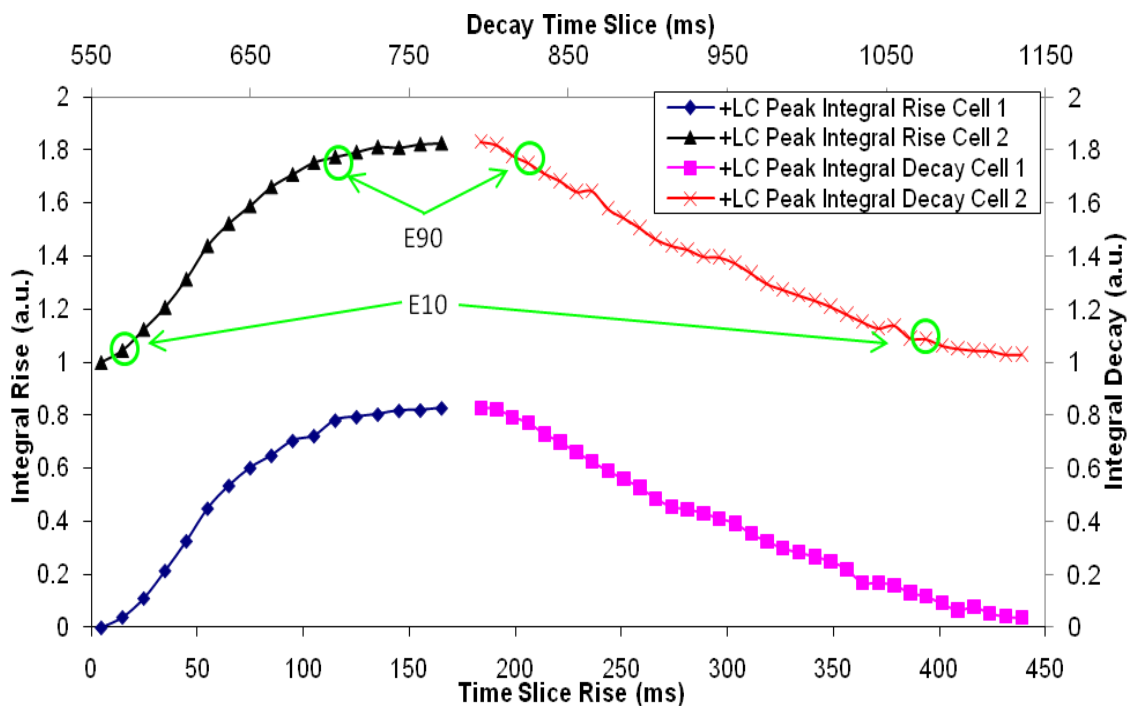


Figure 22 + LC peak of undoped cell TR Raman normalised integral data of the switch



Appendix C

Crystallographic Data & Tables for Chapter 5

APPENDIX C

1. Crystallography data for **15**

Crystal data for **15**: C₁₅H₁₄N₂O_{0.74}, M = 238.28, triclinic, space group P-1 (No. 2), a = 5.7450(5), b = 14.3643(11), c = 15.6327(13) Å, V = 1229.92(18) Å³, Z = 4, D_c = 1.287 Mg m⁻³, F₀₀₀ = 504, Mo Kα radiation, λ = 0.71073 Å, T = 120 K, 2θ_{max} = 55.0°, 11894 reflections collected, 5618 unique (R_{int} = 0.0309). Final GooF = 0.896, R₁ = 0.0420, wR₂ = 0.1020, R indices based on 3830 reflections with I > 2.00σ (I) (refinement on F²), 327 parameters, 0 restraints. Lp and absorption corrections applied, μ = 0.082 mm⁻¹.

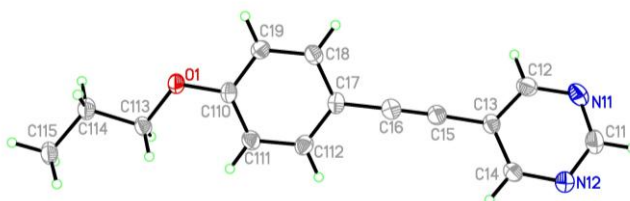


Figure 1. Crystallographic ORTEP diagram of compound **15**.

Table 1. Crystal data and structure refinement for **15**.

Identification code	06srv098
Empirical formula	C ₁₅ H ₁₄ N ₂ O
Formula weight	238.28
Temperature	120(2) K
Wavelength	0.71073 Å
Crystal system	Triclinic
Space group	P-1

Unit cell dimensions	$a = 5.7450(5) \text{ \AA}$	$\alpha = 74.135(2)^\circ$.
	$b = 14.3643(11) \text{ \AA}$	$\beta = 82.466(2)^\circ$.
	$c = 15.6327(13) \text{ \AA}$	$\gamma = 89.121(2)^\circ$.
Volume	1229.92(18) \AA^3	
Z	4	
Density (calculated)	1.287 Mg/m^3	
Absorption coefficient	0.082 mm^{-1}	
F(000)	504	
Crystal size	0.80 x 0.48 x 0.04 mm^3	
Theta range for data collection	1.71 to 27.50 $^\circ$.	
Index ranges	$-7 \leq h \leq 7$, $-18 \leq k \leq 18$, $-20 \leq l \leq 20$	
Reflections collected	11894	
Independent reflections	5618 [R(int) = 0.0309]	
Completeness to theta = 27.50 $^\circ$	99.1 %	
Absorption correction	Integration	
Max. and min. transmission	0.9967 and 0.9517	
Refinement method	Full-matrix least-squares on F^2	
Data / restraints / parameters	5618 / 0 / 327	
Goodness-of-fit on F^2	0.896	
Final R indices [I > 2sigma(I)]	R1 = 0.0420, wR2 = 0.1020	
R indices (all data)	R1 = 0.0642, wR2 = 0.1095	
Extinction coefficient	0	
Largest diff. peak and hole	0.260 and -0.198 e.\AA^{-3}	

Table 2. Atomic coordinates ($\times 10^4$) and equivalent isotropic displacement parameters ($\text{\AA}^2 \times 10^3$) for **15**. $U(\text{eq})$ is defined as one third of the trace of the orthogonalized U_{ij} tensor.

	x	y	z	$U(\text{eq})$
O(1)	5246(2)	2568(1)	4016(1)	26(1)
N(11)	-4315(2)	8445(1)	919(1)	34(1)
N(12)	-517(2)	8871(1)	91(1)	30(1)
C(11)	-2748(2)	9040(1)	328(1)	33(1)
C(12)	-3506(2)	7588(1)	1333(1)	30(1)
C(13)	-1180(2)	7330(1)	1168(1)	23(1)
C(14)	242(2)	8017(1)	519(1)	25(1)
C(15)	-257(2)	6435(1)	1635(1)	26(1)
C(16)	648(2)	5725(1)	2038(1)	26(1)
C(17)	1814(2)	4898(1)	2529(1)	25(1)
C(18)	977(2)	4424(1)	3424(1)	26(1)
C(19)	2164(2)	3658(1)	3901(1)	26(1)
C(110)	4200(2)	3336(1)	3491(1)	23(1)
C(111)	5041(2)	3790(1)	2601(1)	26(1)
C(112)	3859(2)	4571(1)	2130(1)	27(1)
C(113)	7280(2)	2183(1)	3602(1)	24(1)
C(114)	8237(2)	1401(1)	4318(1)	29(1)
C(115)	10499(2)	1001(1)	3942(1)	31(1)
O(2)	10329(2)	7663(1)	3894(1)	24(1)

N(21)	-580(2)	13022(1)	1261(1)	31(1)
N(22)	2653(2)	13914(1)	283(1)	27(1)
C(21)	426(2)	13799(1)	653(1)	30(1)
C(22)	830(2)	12290(1)	1526(1)	27(1)
C(23)	3212(2)	12319(1)	1215(1)	22(1)
C(24)	4031(2)	13167(1)	575(1)	25(1)
C(25)	4639(2)	11516(1)	1567(1)	24(1)
C(26)	5658(2)	10817(1)	1936(1)	24(1)
C(27)	6893(2)	10004(1)	2418(1)	22(1)
C(28)	6033(2)	9508(1)	3304(1)	24(1)
C(29)	7226(2)	8739(1)	3776(1)	24(1)
C(210)	9304(2)	8440(1)	3372(1)	21(1)
C(211)	10194(2)	8924(1)	2493(1)	22(1)
C(212)	8990(2)	9704(1)	2026(1)	23(1)
C(213)	12372(2)	7272(1)	3494(1)	23(1)
C(214)	13232(2)	6463(1)	4213(1)	27(1)
C(215)	15483(2)	6041(1)	3859(1)	30(1)

Table 3. Bond lengths [\AA] and angles [$^\circ$] for **15**.

O(1)-C(110)	1.3654(14)	N(12)-C(14)	1.3240(15)
O(1)-C(113)	1.4381(14)	N(12)-C(11)	1.3244(17)
N(11)-C(11)	1.3291(18)	C(11)-H(11)	0.9500
N(11)-C(12)	1.3326(16)	C(12)-C(13)	1.3919(17)

C(12)-H(12)	0.9500	O(2)-C(210)	1.3659(13)
C(13)-C(14)	1.3900(17)	O(2)-C(213)	1.4370(14)
C(13)-C(15)	1.4259(17)	N(21)-C(22)	1.3252(15)
C(14)-H(14)	0.9500	N(21)-C(21)	1.3341(16)
C(15)-C(16)	1.1941(17)	N(22)-C(21)	1.3265(16)
C(16)-C(17)	1.4352(17)	N(22)-C(24)	1.3372(15)
C(17)-C(112)	1.3932(18)	C(21)-H(21)	0.9500
C(17)-C(18)	1.4026(17)	C(22)-C(23)	1.3883(17)
C(18)-C(19)	1.3758(17)	C(22)-H(22)	0.9500
C(18)-H(18)	0.9500	C(23)-C(24)	1.3914(17)
C(19)-C(110)	1.3929(17)	C(23)-C(25)	1.4311(16)
C(19)-H(19)	0.9500	C(24)-H(24)	0.9500
C(110)-C(111)	1.3895(17)	C(25)-C(26)	1.1982(16)
C(111)-C(112)	1.3855(16)	C(26)-C(27)	1.4380(16)
C(111)-H(111)	0.9500	C(27)-C(212)	1.3958(17)
C(112)-H(112)	0.9500	C(27)-C(28)	1.4011(17)
C(113)-C(114)	1.5065(16)	C(28)-C(29)	1.3772(16)
C(113)-H(13A)	0.9900	C(28)-H(28)	0.9500
C(113)-H(13B)	0.9900	C(29)-C(210)	1.3940(17)
C(114)-C(115)	1.5254(17)	C(29)-H(29)	0.9500
C(114)-H(14A)	0.9900	C(210)-C(211)	1.3914(16)
C(114)-H(14B)	0.9900	C(211)-C(212)	1.3885(16)
C(115)-H(15A)	0.9800	C(211)-H(211)	0.9500
C(115)-H(15B)	0.9800	C(212)-H(212)	0.9500
C(115)-H(15C)	0.9800	C(213)-C(214)	1.5081(16)

C(213)-H(23A)	0.9900	C(112)-C(17)-C(18)	118.57(11)
C(213)-H(23B)	0.9900	C(112)-C(17)-C(16)	120.26(11)
C(214)-C(215)	1.5226(17)	C(18)-C(17)-C(16)	121.14(12)
C(214)-H(24A)	0.9900	C(19)-C(18)-C(17)	120.67(12)
C(214)-H(24B)	0.9900	C(19)-C(18)-H(18)	119.7
C(215)-H(25A)	0.9800	C(17)-C(18)-H(18)	119.7
C(215)-H(25B)	0.9800	C(18)-C(19)-C(110)	120.08(12)
C(215)-H(25C)	0.9800	C(18)-C(19)-H(19)	120.0
C(110)-O(1)-C(113)	117.37(9)	C(110)-C(19)-H(19)	120.0
C(11)-N(11)-C(12)	115.40(11)	O(1)-C(110)-C(111)	124.13(11)
C(14)-N(12)-C(11)	115.47(11)	O(1)-C(110)-C(19)	115.80(11)
N(12)-C(11)-N(11)	127.77(12)	C(111)-C(110)-C(19)	120.07(11)
N(12)-C(11)-H(11)	116.1	C(112)-C(111)-C(110)	119.55(12)
N(11)-C(11)-H(11)	116.1	C(112)-C(111)-H(111)	120.2
N(11)-C(12)-C(13)	122.71(12)	C(110)-C(111)-H(111)	120.2
N(11)-C(12)-H(12)	118.6	C(111)-C(112)-C(17)	121.04(12)
C(13)-C(12)-H(12)	118.6	C(111)-C(112)-H(112)	119.5
C(14)-C(13)-C(12)	115.41(11)	C(17)-C(112)-H(112)	119.5
C(14)-C(13)-C(15)	121.09(11)	O(1)-C(113)-C(114)	108.00(10)
C(12)-C(13)-C(15)	123.49(12)	O(1)-C(113)-H(13A)	110.1
N(12)-C(14)-C(13)	123.20(12)	C(114)-C(113)-H(13A)	110.1
N(12)-C(14)-H(14)	118.4	O(1)-C(113)-H(13B)	110.1
C(13)-C(14)-H(14)	118.4	C(114)-C(113)-H(13B)	110.1
C(16)-C(15)-C(13)	175.14(14)	H(13A)-C(113)-H(13B)	108.4
C(15)-C(16)-C(17)	177.47(14)	C(113)-C(114)-C(115)	111.13(11)

C(113)-C(114)-H(14A)	109.4	C(23)-C(24)-H(24)	118.5
C(115)-C(114)-H(14A)	109.4	C(26)-C(25)-C(23)	173.23(14)
C(113)-C(114)-H(14B)	109.4	C(25)-C(26)-C(27)	176.88(14)
C(115)-C(114)-H(14B)	109.4	C(212)-C(27)-C(28)	118.47(10)
H(14A)-C(114)-H(14B)	108.0	C(212)-C(27)-C(26)	121.17(11)
C(114)-C(115)-H(15A)	109.5	C(28)-C(27)-C(26)	120.35(11)
C(114)-C(115)-H(15B)	109.5	C(29)-C(28)-C(27)	120.71(11)
H(15A)-C(115)-H(15B)	109.5	C(29)-C(28)-H(28)	119.6
C(114)-C(115)-H(15C)	109.5	C(27)-C(28)-H(28)	119.6
H(15A)-C(115)-H(15C)	109.5	C(28)-C(29)-C(210)	120.20(11)
H(15B)-C(115)-H(15C)	109.5	C(28)-C(29)-H(29)	119.9
C(210)-O(2)-C(213)	118.10(9)	C(210)-C(29)-H(29)	119.9
C(22)-N(21)-C(21)	115.63(11)	O(2)-C(210)-C(211)	124.50(11)
C(21)-N(22)-C(24)	115.35(11)	O(2)-C(210)-C(29)	115.45(10)
N(22)-C(21)-N(21)	127.40(12)	C(211)-C(210)-C(29)	120.05(11)
N(22)-C(21)-H(21)	116.3	C(212)-C(211)-C(210)	119.35(11)
N(21)-C(21)-H(21)	116.3	C(212)-C(211)-H(211)	120.3
N(21)-C(22)-C(23)	123.27(12)	C(210)-C(211)-H(211)	120.3
N(21)-C(22)-H(22)	118.4	C(211)-C(212)-C(27)	121.21(11)
C(23)-C(22)-H(22)	118.4	C(211)-C(212)-H(212)	119.4
C(22)-C(23)-C(24)	115.26(11)	C(27)-C(212)-H(212)	119.4
C(22)-C(23)-C(25)	119.88(11)	O(2)-C(213)-C(214)	107.80(10)
C(24)-C(23)-C(25)	124.86(11)	O(2)-C(213)-H(23A)	110.1
N(22)-C(24)-C(23)	123.06(12)	C(214)-C(213)-H(23A)	110.1
N(22)-C(24)-H(24)	118.5	O(2)-C(213)-H(23B)	110.1

C(214)-C(213)-H(23B)	110.1	H(24A)-C(214)-H(24B)	108.0
H(23A)-C(213)-H(23B)	108.5	C(214)-C(215)-H(25A)	109.5
C(213)-C(214)-C(215)	111.37(11)	C(214)-C(215)-H(25B)	109.5
C(213)-C(214)-H(24A)	109.4	H(25A)-C(215)-H(25B)	109.5
C(215)-C(214)-H(24A)	109.4	C(214)-C(215)-H(25C)	109.5
C(213)-C(214)-H(24B)	109.4	H(25A)-C(215)-H(25C)	109.5
C(215)-C(214)-H(24B)	109.4	H(25B)-C(215)-H(25C)	109.5

Symmetry transformations used to generate equivalent atoms

Table 4. Anisotropic displacement parameters ($\text{\AA}^2 \times 10^3$) for **15**. The anisotropic displacement factor exponent takes the form: $-2\pi^2 [h^2 a^{*2} U^{11} + \dots + 2 h k a^* b^* U^{12}]$

	U ¹¹	U ²²	U ³³	U ²³	U ¹³	U ¹²
O(1)	29(1)	25(1)	24(1)	-4(1)	-4(1)	9(1)
N(11)	23(1)	37(1)	42(1)	-13(1)	-5(1)	8(1)
N(12)	30(1)	28(1)	30(1)	-5(1)	-3(1)	5(1)
C(11)	32(1)	28(1)	39(1)	-7(1)	-10(1)	8(1)
C(12)	25(1)	34(1)	29(1)	-8(1)	-1(1)	2(1)
C(13)	25(1)	24(1)	22(1)	-8(1)	-6(1)	4(1)
C(14)	23(1)	29(1)	26(1)	-10(1)	-3(1)	4(1)
C(15)	27(1)	28(1)	25(1)	-8(1)	-5(1)	3(1)
C(16)	27(1)	27(1)	27(1)	-10(1)	-6(1)	2(1)
C(17)	28(1)	21(1)	27(1)	-7(1)	-9(1)	3(1)

C(18)	23(1)	25(1)	31(1)	-9(1)	-3(1)	4(1)
C(19)	28(1)	24(1)	24(1)	-5(1)	-2(1)	1(1)
C(110)	25(1)	19(1)	27(1)	-7(1)	-8(1)	3(1)
C(111)	27(1)	27(1)	25(1)	-9(1)	-3(1)	6(1)
C(112)	33(1)	25(1)	22(1)	-6(1)	-5(1)	3(1)
C(113)	24(1)	23(1)	26(1)	-8(1)	-4(1)	6(1)
C(114)	32(1)	27(1)	28(1)	-7(1)	-7(1)	8(1)
C(115)	28(1)	26(1)	35(1)	-4(1)	-9(1)	7(1)
O(2)	25(1)	23(1)	23(1)	-3(1)	-3(1)	9(1)
N(21)	25(1)	25(1)	38(1)	-1(1)	0(1)	5(1)
N(22)	25(1)	25(1)	28(1)	-3(1)	-5(1)	1(1)
C(21)	26(1)	24(1)	35(1)	-3(1)	-5(1)	6(1)
C(22)	26(1)	22(1)	28(1)	-2(1)	-2(1)	2(1)
C(23)	23(1)	23(1)	22(1)	-8(1)	-7(1)	4(1)
C(24)	21(1)	26(1)	26(1)	-6(1)	-4(1)	2(1)
C(25)	23(1)	25(1)	24(1)	-7(1)	-5(1)	2(1)
C(26)	23(1)	24(1)	26(1)	-7(1)	-4(1)	2(1)
C(27)	24(1)	19(1)	25(1)	-6(1)	-8(1)	2(1)
C(28)	19(1)	23(1)	28(1)	-8(1)	-2(1)	3(1)
C(29)	25(1)	22(1)	22(1)	-4(1)	-1(1)	0(1)
C(210)	23(1)	18(1)	23(1)	-6(1)	-7(1)	1(1)
C(211)	21(1)	24(1)	23(1)	-8(1)	-2(1)	4(1)
C(212)	27(1)	22(1)	19(1)	-3(1)	-3(1)	1(1)
C(213)	22(1)	22(1)	25(1)	-9(1)	-4(1)	5(1)
C(214)	29(1)	25(1)	27(1)	-6(1)	-6(1)	7(1)

C(215) 28(1) 27(1) 35(1) -7(1) -7(1) 8(1)

Table 5. Hydrogen coordinates ($\times 10^4$) and isotropic displacement parameters ($\text{\AA}^2 \times 10^3$) for **15**.

	x	y	z	U(eq)
H(11)	-3293	9660	42	39
H(12)	-4561	7135	1758	35
H(14)	1837	7867	375	31
H(18)	-423	4633	3705	31
H(19)	1595	3348	4510	31
H(111)	6417	3566	2318	31
H(112)	4453	4889	1526	32
H(13A)	8483	2702	3328	29
H(13B)	6845	1911	3126	29
H(14A)	7052	870	4565	34
H(14B)	8549	1669	4813	34
H(15A)	11207	566	4435	46
H(15B)	11600	1537	3628	46
H(15C)	10145	643	3522	46
H(21)	-566	14331	464	35
H(22)	178	11717	1950	32
H(24)	5645	13218	333	30

H(28)	4611	9703	3583	28
H(29)	6631	8412	4378	28
H(211)	11610	8723	2216	27
H(212)	9605	10040	1428	28
H(23A)	13611	7781	3246	27
H(23B)	11971	7023	2999	27
H(24A)	12004	5946	4437	32
H(24B)	13521	6711	4722	32
H(25A)	16052	5547	4350	45
H(25B)	16678	6557	3611	45
H(25C)	15169	5747	3388	45

2. Crystallography data for **18**

Crystal data for **18**: C₁₉ H₁₈ Si, M = 274.42, triclinic, space group P-1 (No. 2), a = 10.1493(7), b = 11.8886(9), c = 14.1313(10) Å, V = 1554.44(19) Å³, Z = 4, D_c = 1.173 Mg m⁻³, F₀₀₀ = 584, Mo Kα radiation, λ = 0.71073 Å, T = 120 K, 2θ_{max} = 52.74°, 15220 reflections collected, 6328 unique (R_{int} = 0.0559). Final *Goof* = 1.019, R₁ = 0.0576, wR₂ = 0.1262, R indices based on 4172 reflections with I > 2.00σ (I) (refinement on F²), 367 parameters, 0 restraints. Lp and absorption corrections applied, μ = 0.139 mm⁻¹.

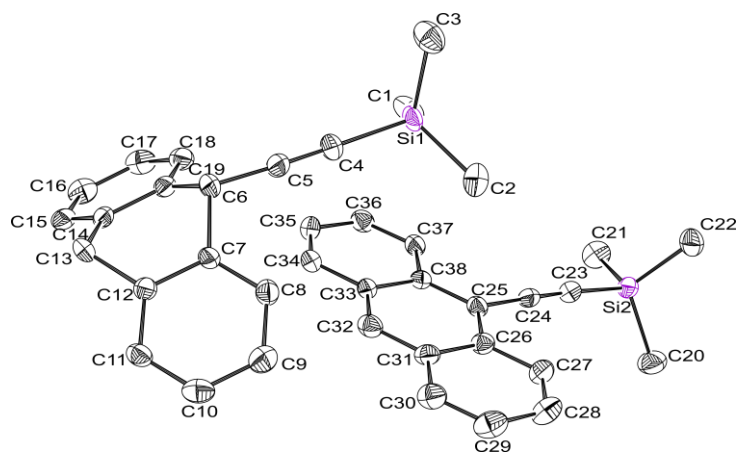


Figure 2. Crystallographic ORTEP diagram of compound **18**.

Table 6. Crystal data and structure refinement for **18**.

Identification code	09srv145	
Empirical formula	C ₁₉ H ₁₈ Si	
Formula weight	274.42	
Temperature	120(2) K	
Wavelength	0.71073 Å	
Crystal system	Triclinic	
Space group	P -1	
Unit cell dimensions	a = 10.1493(7) Å	α = 94.4930(10)°.
	b = 11.8886(9) Å	β = 93.7850(10)°.
	c = 14.1313(10) Å	γ = 113.1330(10)°.
Volume	1554.44(19) Å ³	
Z	4	
Density (calculated)	1.173 Mg/m ³	
Absorption coefficient	0.139 mm ⁻¹	
F(000)	584	

Crystal size	0.30 x 0.24 x 0.21 mm ³
Theta range for data collection	1.45 to 26.37°.
Index ranges	-12<=h<=12, -14<=k<=14, -17<=l<=17
Reflections collected	15220
Independent reflections	6328 [R(int) = 0.0559]
Completeness to theta = 25.00°	99.8 %
Absorption correction	Semi-empirical from equivalents
Max. and min. transmission	0.971 and 0.865
Refinement method	Full-matrix least-squares on F ²
Data / restraints / parameters	6328 / 0 / 367
Goodness-of-fit on F ²	1.019
Final R indices [I>2sigma(I)]	R1 = 0.0576, wR2 = 0.1262
R indices (all data)	R1 = 0.1008, wR2 = 0.1426
Largest diff. peak and hole	0.473 and -0.277 e.Å ⁻³

Table 7. Atomic coordinates (x 10⁴) and equivalent isotropic displacement parameters (Å²x 10³) for **18**. U(eq) is defined as one third of the trace of the orthogonalized U^{ij} tensor.

	x	y	z	U(eq)
Si(1)	2157(1)	4409(1)	4093(1)	25(1)
Si(2)	-2472(1)	-91(1)	-690(1)	26(1)
C(1)	2969(4)	3879(3)	3111(2)	39(1)
C(2)	184(3)	3843(3)	3799(3)	49(1)

C(3)	2596(4)	3910(3)	5242(2)	41(1)
C(4)	2947(3)	6098(2)	4240(2)	30(1)
C(5)	3471(3)	7192(2)	4340(2)	27(1)
C(6)	4146(3)	8550(2)	4508(2)	25(1)
C(7)	3043(3)	9110(2)	4287(2)	23(1)
C(8)	1575(3)	8440(2)	4179(2)	25(1)
C(9)	636(3)	9021(3)	4023(2)	31(1)
C(10)	1187(3)	10278(3)	3978(2)	32(1)
C(11)	2664(3)	10952(2)	4083(2)	26(1)
C(12)	3598(3)	10372(2)	4233(2)	22(1)
C(13)	5201(3)	11078(2)	4362(2)	25(1)
C(14)	5879(3)	10343(2)	3798(2)	23(1)
C(15)	6958(3)	10875(3)	3226(2)	28(1)
C(16)	7544(3)	10170(3)	2715(2)	33(1)
C(17)	7013(3)	8912(3)	2782(2)	34(1)
C(18)	5934(3)	8369(3)	3347(2)	28(1)
C(19)	5345(3)	9072(2)	3858(2)	24(1)
C(20)	-3953(4)	-133(3)	-1556(2)	47(1)
C(21)	-1032(3)	-276(3)	-1341(2)	41(1)
C(22)	-3160(3)	-1325(3)	106(2)	37(1)
C(23)	-1726(3)	1422(2)	32(2)	27(1)
C(24)	-1233(3)	2449(2)	448(2)	23(1)
C(25)	-639(3)	3688(2)	909(2)	22(1)
C(26)	-1544(3)	4181(2)	1338(2)	24(1)
C(27)	-3040(3)	3484(3)	1359(2)	29(1)

C(28)	-3886(3)	3995(3)	1768(2)	36(1)
C(29)	-3296(3)	5236(3)	2169(2)	36(1)
C(30)	-1871(3)	5933(3)	2176(2)	32(1)
C(31)	-943(3)	5435(2)	1768(2)	26(1)
C(32)	532(3)	6130(2)	1780(2)	28(1)
C(33)	1445(3)	5646(2)	1373(2)	22(1)
C(34)	2947(3)	6359(2)	1387(2)	29(1)
C(35)	3811(3)	5880(3)	981(2)	30(1)
C(36)	3228(3)	4658(2)	524(2)	29(1)
C(37)	1797(3)	3948(2)	497(2)	24(1)
C(38)	855(3)	4404(2)	921(2)	22(1)

Table 8. Bond lengths [\AA] and angles [$^\circ$] for **18**.

Si(1)-C(4)	1.835(3)	C(1)-H(1C)	0.9800
Si(1)-C(2)	1.850(3)	C(2)-H(2A)	0.9800
Si(1)-C(1)	1.850(3)	C(2)-H(2B)	0.9800
Si(1)-C(3)	1.857(3)	C(2)-H(2C)	0.9800
Si(2)-C(23)	1.841(3)	C(3)-H(3A)	0.9800
Si(2)-C(21)	1.851(3)	C(3)-H(3B)	0.9800
Si(2)-C(20)	1.857(3)	C(3)-H(3C)	0.9800
Si(2)-C(22)	1.861(3)	C(4)-C(5)	1.188(4)
C(1)-H(1A)	0.9800	C(5)-C(6)	1.477(4)
C(1)-H(1B)	0.9800	C(6)-C(19)	1.534(4)

C(6)-C(7)	1.538(4)	C(18)-H(18)	0.9500
C(6)-C(13)#1	1.644(4)	C(20)-H(20A)	0.9800
C(7)-C(8)	1.378(4)	C(20)-H(20B)	0.9800
C(7)-C(12)	1.390(3)	C(20)-H(20C)	0.9800
C(8)-C(9)	1.395(4)	C(21)-H(21A)	0.9800
C(8)-H(8)	0.9500	C(21)-H(21B)	0.9800
C(9)-C(10)	1.383(4)	C(21)-H(21C)	0.9800
C(9)-H(9)	0.9500	C(22)-H(22A)	0.9800
C(10)-C(11)	1.385(4)	C(22)-H(22B)	0.9800
C(10)-H(10)	0.9500	C(22)-H(22C)	0.9800
C(11)-C(12)	1.390(4)	C(23)-C(24)	1.206(4)
C(11)-H(11)	0.9500	C(24)-C(25)	1.435(3)
C(12)-C(13)	1.499(4)	C(25)-C(26)	1.413(4)
C(13)-C(14)	1.519(4)	C(25)-C(38)	1.415(4)
C(13)-C(6)#1	1.644(4)	C(26)-C(27)	1.420(4)
C(13)-H(13)	1.0000	C(26)-C(31)	1.435(4)
C(14)-C(15)	1.381(4)	C(27)-C(28)	1.364(4)
C(14)-C(19)	1.402(3)	C(27)-H(27)	0.9500
C(15)-C(16)	1.389(4)	C(28)-C(29)	1.410(4)
C(15)-H(15)	0.9500	C(28)-H(28)	0.9500
C(16)-C(17)	1.389(4)	C(29)-C(30)	1.354(4)
C(16)-H(16)	0.9500	C(29)-H(29)	0.9500
C(17)-C(18)	1.377(4)	C(30)-C(31)	1.424(4)
C(17)-H(17)	0.9500	C(30)-H(30)	0.9500
C(18)-C(19)	1.390(4)	C(31)-C(32)	1.395(4)

C(32)-C(33)	1.399(4)	Si(1)-C(1)-H(1B)	109.5
C(32)-H(32)	0.9500	H(1A)-C(1)-H(1B)	109.5
C(33)-C(34)	1.422(4)	Si(1)-C(1)-H(1C)	109.5
C(33)-C(38)	1.433(3)	H(1A)-C(1)-H(1C)	109.5
C(34)-C(35)	1.353(4)	H(1B)-C(1)-H(1C)	109.5
C(34)-H(34)	0.9500	Si(1)-C(2)-H(2A)	109.5
C(35)-C(36)	1.415(4)	Si(1)-C(2)-H(2B)	109.5
C(35)-H(35)	0.9500	H(2A)-C(2)-H(2B)	109.5
C(36)-C(37)	1.359(4)	Si(1)-C(2)-H(2C)	109.5
C(36)-H(36)	0.9500	H(2A)-C(2)-H(2C)	109.5
C(37)-C(38)	1.415(4)	H(2B)-C(2)-H(2C)	109.5
C(37)-H(37)	0.9500	Si(1)-C(3)-H(3A)	109.5
C(4)-Si(1)-C(2)	109.33(14)	Si(1)-C(3)-H(3B)	109.5
C(4)-Si(1)-C(1)	108.09(14)	H(3A)-C(3)-H(3B)	109.5
C(2)-Si(1)-C(1)	110.23(16)	Si(1)-C(3)-H(3C)	109.5
C(4)-Si(1)-C(3)	107.04(13)	H(3A)-C(3)-H(3C)	109.5
C(2)-Si(1)-C(3)	110.86(16)	H(3B)-C(3)-H(3C)	109.5
C(1)-Si(1)-C(3)	111.18(14)	C(5)-C(4)-Si(1)	179.3(3)
C(23)-Si(2)-C(21)	108.83(13)	C(4)-C(5)-C(6)	177.5(3)
C(23)-Si(2)-C(20)	108.09(13)	C(5)-C(6)-C(19)	110.9(2)
C(21)-Si(2)-C(20)	109.72(15)	C(5)-C(6)-C(7)	111.2(2)
C(23)-Si(2)-C(22)	109.44(13)	C(19)-C(6)-C(7)	106.9(2)
C(21)-Si(2)-C(22)	110.15(14)	C(5)-C(6)-C(13)#1	107.1(2)
C(20)-Si(2)-C(22)	110.56(15)	C(19)-C(6)-C(13)#1	110.8(2)
Si(1)-C(1)-H(1A)	109.5	C(7)-C(6)-C(13)#1	110.0(2)

C(8)-C(7)-C(12)	120.0(2)	C(15)-C(14)-C(13)	122.5(2)
C(8)-C(7)-C(6)	123.6(2)	C(19)-C(14)-C(13)	117.5(2)
C(12)-C(7)-C(6)	116.4(2)	C(14)-C(15)-C(16)	120.8(3)
C(7)-C(8)-C(9)	120.4(2)	C(14)-C(15)-H(15)	119.6
C(7)-C(8)-H(8)	119.8	C(16)-C(15)-H(15)	119.6
C(9)-C(8)-H(8)	119.8	C(17)-C(16)-C(15)	118.8(3)
C(10)-C(9)-C(8)	119.7(3)	C(17)-C(16)-H(16)	120.6
C(10)-C(9)-H(9)	120.2	C(15)-C(16)-H(16)	120.6
C(8)-C(9)-H(9)	120.2	C(18)-C(17)-C(16)	121.0(3)
C(9)-C(10)-C(11)	120.0(3)	C(18)-C(17)-H(17)	119.5
C(9)-C(10)-H(10)	120.0	C(16)-C(17)-H(17)	119.5
C(11)-C(10)-H(10)	120.0	C(17)-C(18)-C(19)	120.4(3)
C(10)-C(11)-C(12)	120.3(2)	C(17)-C(18)-H(18)	119.8
C(10)-C(11)-H(11)	119.8	C(19)-C(18)-H(18)	119.8
C(12)-C(11)-H(11)	119.8	C(18)-C(19)-C(14)	119.0(2)
C(11)-C(12)-C(7)	119.7(2)	C(18)-C(19)-C(6)	124.0(2)
C(11)-C(12)-C(13)	121.6(2)	C(14)-C(19)-C(6)	116.9(2)
C(7)-C(12)-C(13)	118.7(2)	Si(2)-C(20)-H(20A)	109.5
C(12)-C(13)-C(14)	108.2(2)	Si(2)-C(20)-H(20B)	109.5
C(12)-C(13)-C(6)#1	112.6(2)	H(20A)-C(20)-H(20B)	109.5
C(14)-C(13)-C(6)#1	113.5(2)	Si(2)-C(20)-H(20C)	109.5
C(12)-C(13)-H(13)	107.4	H(20A)-C(20)-H(20C)	109.5
C(14)-C(13)-H(13)	107.4	H(20B)-C(20)-H(20C)	109.5
C(6)#1-C(13)-H(13)	107.4	Si(2)-C(21)-H(21A)	109.5
C(15)-C(14)-C(19)	120.0(2)	Si(2)-C(21)-H(21B)	109.5

H(21A)-C(21)-H(21B)	109.5	C(30)-C(29)-H(29)	119.8
Si(2)-C(21)-H(21C)	109.5	C(28)-C(29)-H(29)	119.8
H(21A)-C(21)-H(21C)	109.5	C(29)-C(30)-C(31)	120.9(3)
H(21B)-C(21)-H(21C)	109.5	C(29)-C(30)-H(30)	119.6
Si(2)-C(22)-H(22A)	109.5	C(31)-C(30)-H(30)	119.6
Si(2)-C(22)-H(22B)	109.5	C(32)-C(31)-C(30)	121.8(3)
H(22A)-C(22)-H(22B)	109.5	C(32)-C(31)-C(26)	119.2(2)
Si(2)-C(22)-H(22C)	109.5	C(30)-C(31)-C(26)	118.9(2)
H(22A)-C(22)-H(22C)	109.5	C(31)-C(32)-C(33)	122.0(2)
H(22B)-C(22)-H(22C)	109.5	C(31)-C(32)-H(32)	119.0
C(24)-C(23)-Si(2)	175.5(2)	C(33)-C(32)-H(32)	119.0
C(23)-C(24)-C(25)	177.9(3)	C(32)-C(33)-C(34)	121.7(2)
C(26)-C(25)-C(38)	120.8(2)	C(32)-C(33)-C(38)	119.4(2)
C(26)-C(25)-C(24)	120.0(2)	C(34)-C(33)-C(38)	118.9(2)
C(38)-C(25)-C(24)	119.2(2)	C(35)-C(34)-C(33)	120.9(3)
C(25)-C(26)-C(27)	122.5(2)	C(35)-C(34)-H(34)	119.6
C(25)-C(26)-C(31)	119.4(2)	C(33)-C(34)-H(34)	119.6
C(27)-C(26)-C(31)	118.1(2)	C(34)-C(35)-C(36)	120.4(3)
C(28)-C(27)-C(26)	121.0(3)	C(34)-C(35)-H(35)	119.8
C(28)-C(27)-H(27)	119.5	C(36)-C(35)-H(35)	119.8
C(26)-C(27)-H(27)	119.5	C(37)-C(36)-C(35)	120.5(3)
C(27)-C(28)-C(29)	120.7(3)	C(37)-C(36)-H(36)	119.8
C(27)-C(28)-H(28)	119.7	C(35)-C(36)-H(36)	119.8
C(29)-C(28)-H(28)	119.7	C(36)-C(37)-C(38)	121.2(2)
C(30)-C(29)-C(28)	120.5(3)	C(36)-C(37)-H(37)	119.4

C(38)-C(37)-H(37)	119.4	C(37)-C(38)-C(33)	118.2(2)
C(37)-C(38)-C(25)	122.6(2)	C(25)-C(38)-C(33)	119.2(2)

Symmetry transformations used to generate equivalent atoms: #1 -x+1,-y+2,-z+1

Table 9. Anisotropic displacement parameters ($\text{\AA}^2 \times 10^3$) for **18**. The anisotropic displacement factor exponent takes the form: $-2\pi^2 [h^2 a^* 2U^{11} + \dots + 2 h k a^* b^* U^{12}]$

	U ¹¹	U ²²	U ³³	U ²³	U ¹³	U ¹²
Si(1)	31(1)	13(1)	29(1)	1(1)	0(1)	6(1)
Si(2)	25(1)	21(1)	28(1)	-1(1)	-4(1)	7(1)
C(1)	61(2)	31(2)	32(2)	7(1)	6(2)	24(2)
C(2)	36(2)	33(2)	65(2)	7(2)	-4(2)	2(2)
C(3)	57(2)	31(2)	36(2)	3(1)	6(2)	19(2)
C(4)	33(2)	18(1)	37(2)	1(1)	-2(1)	9(1)
C(5)	23(2)	22(2)	35(2)	1(1)	-2(1)	10(1)
C(6)	26(2)	16(1)	33(2)	1(1)	0(1)	8(1)
C(7)	25(2)	17(1)	25(1)	1(1)	-3(1)	9(1)
C(8)	27(2)	22(1)	24(1)	2(1)	1(1)	7(1)
C(9)	26(2)	36(2)	32(2)	4(1)	2(1)	12(1)
C(10)	33(2)	38(2)	33(2)	4(1)	2(1)	23(2)
C(11)	34(2)	21(1)	25(1)	0(1)	-2(1)	15(1)
C(12)	24(2)	20(1)	20(1)	0(1)	-1(1)	9(1)
C(13)	28(2)	16(1)	31(2)	5(1)	2(1)	9(1)

C(14)	17(1)	20(1)	29(1)	-1(1)	-3(1)	7(1)
C(15)	29(2)	27(2)	26(1)	-1(1)	-9(1)	11(1)
C(16)	31(2)	43(2)	27(2)	4(1)	4(1)	17(2)
C(17)	39(2)	40(2)	28(2)	-5(1)	-1(1)	24(2)
C(18)	34(2)	25(1)	25(1)	-3(1)	-6(1)	14(1)
C(19)	23(2)	20(1)	28(1)	-2(1)	-6(1)	10(1)
C(20)	43(2)	38(2)	55(2)	-2(2)	-18(2)	17(2)
C(21)	43(2)	45(2)	33(2)	-2(1)	3(1)	18(2)
C(22)	39(2)	24(2)	42(2)	-1(1)	-1(1)	8(1)
C(23)	24(2)	28(2)	28(2)	4(1)	1(1)	10(1)
C(24)	21(1)	25(1)	26(1)	3(1)	0(1)	12(1)
C(25)	26(2)	18(1)	22(1)	1(1)	0(1)	9(1)
C(26)	26(2)	25(1)	22(1)	1(1)	-1(1)	11(1)
C(27)	24(2)	30(2)	31(2)	1(1)	0(1)	11(1)
C(28)	25(2)	46(2)	35(2)	-2(1)	0(1)	15(2)
C(29)	36(2)	46(2)	34(2)	-5(1)	3(1)	26(2)
C(30)	37(2)	29(2)	31(2)	-6(1)	-3(1)	18(1)
C(31)	29(2)	26(1)	25(1)	0(1)	-5(1)	15(1)
C(32)	34(2)	22(1)	27(1)	-1(1)	-2(1)	14(1)
C(33)	23(2)	17(1)	25(1)	2(1)	-2(1)	7(1)
C(34)	28(2)	20(1)	37(2)	6(1)	-2(1)	7(1)
C(35)	22(2)	26(2)	37(2)	8(1)	2(1)	4(1)
C(36)	28(2)	29(2)	35(2)	9(1)	9(1)	15(1)
C(37)	25(2)	20(1)	29(1)	4(1)	3(1)	10(1)
C(38)	23(2)	22(1)	20(1)	5(1)	-1(1)	9(1)

Table 10. Hydrogen coordinates ($\times 10^4$) and isotropic displacement parameters ($\text{\AA}^2 \times 10^3$) for **18**.

	x	y	z	U(eq)
H(1A)	2950	4329	2562	59
H(1B)	2420	2995	2925	59
H(1C)	3969	4031	3326	59
H(2A)	-224	4183	4300	73
H(2B)	-246	2942	3755	73
H(2C)	-23	4106	3187	73
H(3A)	3642	4176	5364	61
H(3B)	2129	3011	5208	61
H(3C)	2249	4281	5761	61
H(8)	1198	7577	4211	30
H(9)	-376	8556	3948	37
H(10)	553	10679	3876	38
H(11)	3040	11816	4052	31
H(13)	5415	11862	4070	30
H(15)	7304	11734	3180	34
H(16)	8293	10540	2328	40
H(17)	7401	8420	2433	41
H(18)	5591	7509	3389	34
H(20A)	-4686	13	-1210	70
H(20B)	-4387	-941	-1935	70

H(20C)	-3567	507	-1981	70
H(21A)	-608	425	-1706	61
H(21B)	-1441	-1039	-1778	61
H(21C)	-284	-312	-883	61
H(22A)	-2358	-1314	538	55
H(22B)	-3613	-2127	-282	55
H(22C)	-3872	-1185	480	55
H(27)	-3459	2650	1084	34
H(28)	-4883	3509	1783	43
H(29)	-3903	5586	2437	43
H(30)	-1486	6765	2456	38
H(32)	928	6956	2074	33
H(34)	3350	7184	1685	35
H(35)	4814	6365	1002	36
H(36)	3841	4332	235	35
H(37)	1423	3130	187	29

3. Crystallography data for 19

Crystal data for **19**: C₂₅ H₂₂ Si, M = 350.52, monoclinic, space group P2(1)/c (No. 14), a = 15.9236(9) b = 7.9583(4), c = 16.5790(9) Å, V = 1993.76(19) Å³, Z = 4, D_c = 1.168 Mg m⁻³, F₀₀₀ = 744, Mo Kα radiation, λ = 0.71073 Å, T = 120 K, 2θ_{max} = 54.98°, 16259 reflections collected, 4583 unique (R_{int} = 0.0962). Final *Goof* = 1.081, R1 = 0.0531, wR2 = 0.1025, R indices based on 3494 reflections with I > 2.00σ (I) (refinement on F²), 323 parameters, 0 restraints. Lp and absorption corrections applied,

$\mu = 0.123 \text{ mm}^{-1}$.

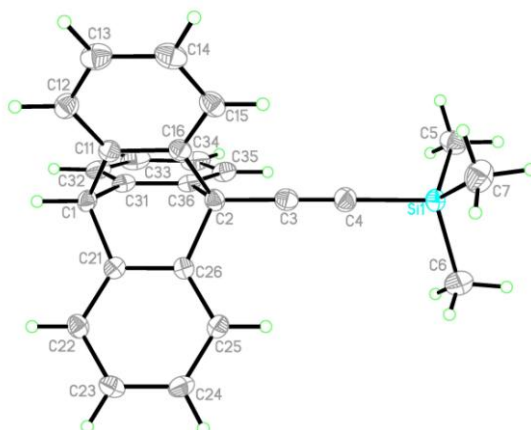


Figure 3. Crystallographic ORTEP diagram of compound **19**

Table 11. Crystal data and structure refinement for **19**.

Identification code	06srv082
Empirical formula	C ₂₅ H ₂₂ Si
Formula weight	350.52
Temperature	120(2) K
Wavelength	0.71073 Å
Crystal system	Monoclinic
Space group	P2(1)/c
Unit cell dimensions	$a = 15.9236(9) \text{ Å}$ $\alpha = 90^\circ$. $b = 7.9583(4) \text{ Å}$ $\beta = 108.3830(10)^\circ$. $c = 16.5790(9) \text{ Å}$ $\gamma = 90^\circ$.
Volume	1993.76(19) Å ³
Z	4
Density (calculated)	1.168 Mg/m ³
Absorption coefficient	0.123 mm ⁻¹

F(000)	744
Crystal size	0.28 x 0.16 x 0.12 mm ³
Theta range for data collection	2.51 to 27.49°.
Index ranges	-20<=h<=20, -10<=k<=10, -21<=l<=21
Reflections collected	16259
Independent reflections	4583 [R(int) = 0.0962]
Completeness to theta = 27.49°	99.9 %
Absorption correction	Integration
Max. and min. transmission	0.9882 and 0.9636
Refinement method	Full-matrix least-squares on F ²
Data / restraints / parameters	4583 / 0 / 323
Goodness-of-fit on F ²	1.081
Final R indices [I>2sigma(I)]	R1 = 0.0531, wR2 = 0.1025
R indices (all data)	R1 = 0.0769, wR2 = 0.1109
Extinction coefficient	0
Largest diff. peak and hole	0.423 and -0.391 e.Å ⁻³

Table 12 Atomic coordinates (x 10⁴) and equivalent isotropic displacement parameters (Å²x 10³) for **19**. U(eq) is defined as one third of the trace of the orthogonalized U^{ij} tensor.

	x	y	z	U(eq)
Si(1)	3566(1)	9392(1)	2038(1)	21(1)
C(1)	1587(1)	3295(2)	-1129(1)	19(1)

C(2)	2329(1)	5522(2)	30(1)	19(1)
C(3)	2750(1)	6775(2)	679(1)	23(1)
C(4)	3091(1)	7808(2)	1208(1)	25(1)
C(5)	3517(2)	8510(3)	3054(1)	29(1)
C(6)	2894(2)	11332(3)	1747(2)	39(1)
C(7)	4726(2)	9815(3)	2081(2)	35(1)
C(11)	2583(1)	3068(2)	-758(1)	19(1)
C(12)	3085(1)	1836(2)	-980(1)	23(1)
C(13)	3996(1)	1793(3)	-572(1)	29(1)
C(14)	4393(1)	2973(3)	39(1)	29(1)
C(15)	3891(1)	4212(3)	266(1)	24(1)
C(16)	2986(1)	4248(2)	-136(1)	19(1)
C(21)	1450(1)	5091(2)	-1462(1)	18(1)
C(22)	988(1)	5576(2)	-2284(1)	21(1)
C(23)	906(1)	7291(3)	-2481(1)	23(1)
C(24)	1282(1)	8469(2)	-1864(1)	24(1)
C(25)	1756(1)	7985(2)	-1036(1)	21(1)
C(26)	1838(1)	6295(2)	-845(1)	18(1)
C(31)	1234(1)	3255(2)	-378(1)	20(1)
C(32)	586(1)	2194(2)	-274(1)	25(1)
C(33)	302(1)	2382(3)	432(1)	30(1)
C(34)	676(1)	3594(3)	1038(1)	30(1)
C(35)	1346(1)	4632(2)	950(1)	24(1)
C(36)	1619(1)	4455(2)	245(1)	20(1)

Table 13. Bond lengths [\AA] and angles [$^\circ$] for **19**.

Si(1)-C(4)	1.843(2)	C(11)-C(16)	1.393(2)
Si(1)-C(5)	1.850(2)	C(12)-C(13)	1.395(3)
Si(1)-C(6)	1.854(2)	C(12)-H(12)	0.99(2)
Si(1)-C(7)	1.857(2)	C(13)-C(14)	1.379(3)
C(1)-C(11)	1.520(3)	C(13)-H(13)	0.96(2)
C(1)-C(31)	1.520(3)	C(14)-C(15)	1.393(3)
C(1)-C(21)	1.523(2)	C(14)-H(14)	0.98(2)
C(1)-H(1)	1.021(19)	C(15)-C(16)	1.384(3)
C(2)-C(3)	1.464(3)	C(15)-H(15)	0.96(2)
C(2)-C(16)	1.542(3)	C(21)-C(22)	1.384(3)
C(2)-C(26)	1.542(2)	C(21)-C(26)	1.396(2)
C(2)-C(36)	1.543(3)	C(22)-C(23)	1.400(3)
C(3)-C(4)	1.200(3)	C(22)-H(22)	0.92(2)
C(5)-H(5A)	0.95(3)	C(23)-C(24)	1.376(3)
C(5)-H(5B)	0.98(2)	C(23)-H(23)	0.92(2)
C(5)-H(5C)	0.99(3)	C(24)-C(25)	1.397(3)
C(6)-H(6A)	0.93(3)	C(24)-H(24)	0.94(2)
C(6)-H(6B)	1.00(3)	C(25)-C(26)	1.378(3)
C(6)-H(6C)	0.99(3)	C(25)-H(25)	0.96(2)
C(7)-H(7A)	0.95(3)	C(31)-C(32)	1.385(3)
C(7)-H(7B)	0.98(3)	C(31)-C(36)	1.398(3)
C(7)-H(7C)	1.01(3)	C(32)-C(33)	1.390(3)
C(11)-C(12)	1.386(3)	C(32)-H(32)	0.99(2)

C(33)-C(34)	1.384(3)	C(3)-C(4)-Si(1)	177.18(19)
C(33)-H(33)	0.96(2)	Si(1)-C(5)-H(5A)	110.3(15)
C(34)-C(35)	1.393(3)	Si(1)-C(5)-H(5B)	111.0(14)
C(34)-H(34)	0.99(2)	H(5A)-C(5)-H(5B)	108.9(19)
C(35)-C(36)	1.378(3)	Si(1)-C(5)-H(5C)	112.3(15)
C(35)-H(35)	0.96(2)	H(5A)-C(5)-H(5C)	106(2)
C(4)-Si(1)-C(5)	107.19(10)	H(5B)-C(5)-H(5C)	108(2)
C(4)-Si(1)-C(6)	107.92(11)	Si(1)-C(6)-H(6A)	109.7(17)
C(5)-Si(1)-C(6)	111.49(12)	Si(1)-C(6)-H(6B)	112.3(17)
C(4)-Si(1)-C(7)	108.79(11)	H(6A)-C(6)-H(6B)	106(2)
C(5)-Si(1)-C(7)	111.18(12)	Si(1)-C(6)-H(6C)	111.0(16)
C(6)-Si(1)-C(7)	110.14(12)	H(6A)-C(6)-H(6C)	108(2)
C(11)-C(1)-C(31)	105.94(15)	H(6B)-C(6)-H(6C)	109(2)
C(11)-C(1)-C(21)	105.71(14)	Si(1)-C(7)-H(7A)	111.2(15)
C(31)-C(1)-C(21)	105.53(14)	Si(1)-C(7)-H(7B)	112.7(15)
C(11)-C(1)-H(1)	112.4(10)	H(7A)-C(7)-H(7B)	111(2)
C(31)-C(1)-H(1)	114.0(11)	Si(1)-C(7)-H(7C)	109.5(16)
C(21)-C(1)-H(1)	112.6(10)	H(7A)-C(7)-H(7C)	107(2)
C(3)-C(2)-C(16)	113.60(15)	H(7B)-C(7)-H(7C)	105(2)
C(3)-C(2)-C(26)	113.46(15)	C(12)-C(11)-C(16)	120.29(17)
C(16)-C(2)-C(26)	105.43(14)	C(12)-C(11)-C(1)	126.31(17)
C(3)-C(2)-C(36)	113.86(15)	C(16)-C(11)-C(1)	113.40(16)
C(16)-C(2)-C(36)	105.44(14)	C(11)-C(12)-C(13)	119.18(19)
C(26)-C(2)-C(36)	104.13(14)	C(11)-C(12)-H(12)	119.8(12)
C(4)-C(3)-C(2)	179.6(2)	C(13)-C(12)-H(12)	121.0(12)

C(14)-C(13)-C(12)	120.3(2)	C(26)-C(25)-C(24)	118.56(18)
C(14)-C(13)-H(13)	120.7(13)	C(26)-C(25)-H(25)	120.5(12)
C(12)-C(13)-H(13)	119.0(13)	C(24)-C(25)-H(25)	121.0(12)
C(13)-C(14)-C(15)	120.76(19)	C(25)-C(26)-C(21)	120.87(17)
C(13)-C(14)-H(14)	119.5(14)	C(25)-C(26)-C(2)	126.04(16)
C(15)-C(14)-H(14)	119.7(14)	C(21)-C(26)-C(2)	113.08(15)
C(16)-C(15)-C(14)	118.91(19)	C(32)-C(31)-C(36)	119.66(18)
C(16)-C(15)-H(15)	118.8(13)	C(32)-C(31)-C(1)	126.67(17)
C(14)-C(15)-H(15)	122.2(13)	C(36)-C(31)-C(1)	113.66(15)
C(15)-C(16)-C(11)	120.55(17)	C(31)-C(32)-C(33)	119.5(2)
C(15)-C(16)-C(2)	126.09(17)	C(31)-C(32)-H(32)	121.3(12)
C(11)-C(16)-C(2)	113.35(16)	C(33)-C(32)-H(32)	119.2(12)
C(22)-C(21)-C(26)	120.36(17)	C(34)-C(33)-C(32)	120.49(19)
C(22)-C(21)-C(1)	126.14(16)	C(34)-C(33)-H(33)	120.4(13)
C(26)-C(21)-C(1)	113.50(16)	C(32)-C(33)-H(33)	119.1(13)
C(21)-C(22)-C(23)	118.85(18)	C(33)-C(34)-C(35)	120.3(2)
C(21)-C(22)-H(22)	121.0(13)	C(33)-C(34)-H(34)	120.9(13)
C(23)-C(22)-H(22)	120.2(13)	C(35)-C(34)-H(34)	118.7(13)
C(24)-C(23)-C(22)	120.32(18)	C(36)-C(35)-C(34)	119.05(19)
C(24)-C(23)-H(23)	120.9(14)	C(36)-C(35)-H(35)	119.6(12)
C(22)-C(23)-H(23)	118.8(14)	C(34)-C(35)-H(35)	121.3(12)
C(23)-C(24)-C(25)	121.02(18)	C(35)-C(36)-C(31)	120.95(17)
C(23)-C(24)-H(24)	118.1(13)	C(35)-C(36)-C(2)	126.15(17)
C(25)-C(24)-H(24)	120.9(13)	C(31)-C(36)-C(2)	112.88(16)

Symmetry transformations used to generate equivalent atoms:

Table 14. Anisotropic displacement parameters ($\text{\AA}^2 \times 10^3$) for **19**. The anisotropic displacement factor exponent takes the form: $-2\pi^2 [h^2 a^{*2} U^{11} + \dots + 2 h k a^* b^* U^{12}]$

	U ¹¹	U ²²	U ³³	U ²³	U ¹³	U ¹²
Si(1)	23(1)	20(1)	18(1)	-3(1)	5(1)	0(1)
C(1)	18(1)	16(1)	22(1)	-2(1)	5(1)	-3(1)
C(2)	21(1)	20(1)	17(1)	-1(1)	6(1)	-2(1)
C(3)	26(1)	22(1)	20(1)	3(1)	8(1)	0(1)
C(4)	32(1)	23(1)	21(1)	0(1)	8(1)	-2(1)
C(5)	31(1)	35(1)	20(1)	1(1)	9(1)	6(1)
C(6)	43(2)	28(1)	40(1)	2(1)	6(1)	8(1)
C(7)	30(1)	32(1)	46(1)	-3(1)	16(1)	-5(1)
C(11)	22(1)	19(1)	17(1)	1(1)	8(1)	-1(1)
C(12)	25(1)	22(1)	24(1)	-1(1)	10(1)	1(1)
C(13)	27(1)	30(1)	32(1)	4(1)	14(1)	7(1)
C(14)	20(1)	35(1)	30(1)	8(1)	7(1)	2(1)
C(15)	23(1)	28(1)	20(1)	4(1)	5(1)	-4(1)
C(16)	21(1)	20(1)	17(1)	3(1)	7(1)	-1(1)
C(21)	15(1)	18(1)	21(1)	0(1)	8(1)	-2(1)
C(22)	18(1)	23(1)	20(1)	-1(1)	5(1)	-4(1)
C(23)	20(1)	27(1)	21(1)	5(1)	4(1)	0(1)
C(24)	24(1)	18(1)	30(1)	4(1)	8(1)	1(1)

C(25)	23(1)	18(1)	23(1)	-1(1)	9(1)	-2(1)
C(26)	17(1)	20(1)	17(1)	-1(1)	7(1)	-1(1)
C(31)	17(1)	17(1)	25(1)	5(1)	7(1)	2(1)
C(32)	21(1)	20(1)	33(1)	8(1)	7(1)	1(1)
C(33)	24(1)	27(1)	41(1)	14(1)	16(1)	2(1)
C(34)	32(1)	31(1)	34(1)	13(1)	20(1)	12(1)
C(35)	28(1)	23(1)	25(1)	4(1)	12(1)	6(1)
C(36)	21(1)	17(1)	22(1)	5(1)	8(1)	4(1)

Table 15. Hydrogen coordinates ($\times 10^4$) and isotropic displacement parameters ($\text{\AA}^2 \times 10^3$) for **19**.

	x	y	z	U(eq)
H(1)	1304(12)	2430(20)	-1589(12)	14(5)
H(5A)	3857(16)	7500(30)	3188(15)	38(7)
H(5B)	3743(15)	9310(30)	3518(16)	41(7)
H(5C)	2909(18)	8210(30)	3030(16)	51(8)
H(6A)	2929(18)	11750(30)	1232(19)	55(8)
H(6B)	3119(19)	12250(40)	2169(19)	65(9)
H(6C)	2265(19)	11110(30)	1684(17)	55(8)
H(7A)	4748(16)	10410(30)	1590(16)	43(7)
H(7B)	5088(17)	8790(30)	2164(16)	47(7)
H(7C)	5024(18)	10550(40)	2591(19)	61(8)

H(12)	2793(13)	990(30)	-1418(13)	24(5)
H(13)	4343(15)	950(30)	-732(14)	33(6)
H(14)	5025(16)	2890(30)	342(15)	35(6)
H(15)	4151(15)	5040(30)	698(15)	35(6)
H(22)	733(13)	4790(30)	-2697(14)	23(5)
H(23)	595(14)	7610(30)	-3023(14)	28(6)
H(24)	1225(13)	9610(30)	-2022(13)	25(6)
H(25)	2020(13)	8800(30)	-609(13)	25(5)
H(32)	312(13)	1320(30)	-699(13)	24(5)
H(33)	-166(14)	1680(30)	488(13)	27(6)
H(34)	485(14)	3720(30)	1546(14)	27(6)
H(35)	1620(13)	5460(30)	1372(13)	21(5)

4. Crystallography data for **21**

Crystal data for **21**: C₃₁ H₂₄ O, M = 412.50, triclinic, space group P-1 (No. 2), a = 9.0176(7), b = 9.1859(7), c = 13.7607(10) Å, V = 1107.93(14) Å³, Z = 2, D_c = 1.237 Mg m⁻³, F₀₀₀ = 436, Mo Kα radiation, λ = 0.71073 Å, T = 120 K, 2θ_{max} = 50.04°, 7999 reflections collected, 3912 unique (R_{int} = 0.0326). Final *Goof* = 1.043, R₁ = 0.0626, wR₂ = 0.1599, R indices based on 2490 reflections with I > 2.00σ (I) (refinement on F²), 290 parameters, 0 restraints. Lp and absorption corrections applied, μ = 0.073 mm⁻¹.

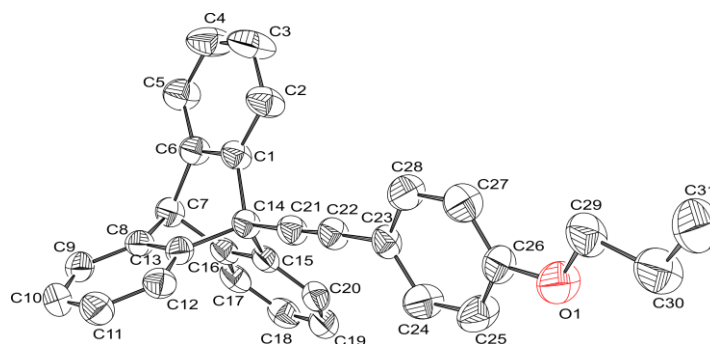


Figure 4. Crystallographic ORTEP diagram of compound **21**

Table 16. Crystal data and structure refinement for **21**.

Identification code	09srv142	
Empirical formula	C ₃₁ H ₂₄ O	
Formula weight	412.50	
Temperature	120(2) K	
Wavelength	0.71073 Å	
Crystal system	Triclinic	
Space group	P -1	
Unit cell dimensions	a = 9.0176(7) Å	α = 00.5550(10)°.
	b = 9.1859(7) Å	β = 0.4580(10)°.
	c = 13.7607(10) Å	γ = 98.374(2)°.
Volume	1107.93(14) Å ³	
Z	2	
Density (calculated)	1.237 Mg/m ³	
Absorption coefficient	0.073 mm ⁻¹	
F(000)	436	
Crystal size	0.38 x 0.30 x 0.28 mm ³	
Theta range for data collection	1.51 to 25.02°.	

Index ranges	-10<=h<=10, -8<=k<=10, -16<=l<=16
Reflections collected	7999
Independent reflections	3912 [R(int) = 0.0326]
Completeness to theta = 25.00°	99.9 %
Absorption correction	Semi-empirical from equivalents
Max. and min. transmission	0.980 and 0.924
Refinement method	Full-matrix least-squares on F ²
Data / restraints / parameters	3912 / 0 / 290
Goodness-of-fit on F ²	1.043
Final R indices [I>2sigma(I)]	R1 = 0.0626, wR2 = 0.1599
R indices (all data)	R1 = 0.1028, wR2 = 0.1814
Largest diff. peak and hole	0.516 and -0.265 e.Å ⁻³

Table 17. Atomic coordinates (x 10⁴) and equivalent isotropic displacement parameters (Å²x 10³) for **21**. U(eq) is defined as one third of the trace of the orthogonalized U^{ij} tensor.

	x	y	z	U(eq)
O(1)	7687(3)	-4607(3)	-36(2)	73(1)
C(1)	1328(3)	1612(3)	2542(2)	41(1)
C(2)	778(3)	830(4)	1630(2)	56(1)
C(3)	-637(4)	1002(5)	1304(2)	76(1)
C(4)	-1465(4)	1943(5)	1871(2)	75(1)
C(5)	-916(3)	2738(4)	2792(2)	58(1)

C(6)	475(3)	2560(3)	3128(2)	43(1)
C(7)	1242(3)	3294(3)	4124(2)	43(1)
C(8)	2757(3)	4111(3)	3899(2)	38(1)
C(9)	3320(3)	5594(3)	4249(2)	48(1)
C(10)	4766(4)	6146(3)	4027(2)	55(1)
C(11)	5625(3)	5221(3)	3453(2)	54(1)
C(12)	5060(3)	3736(3)	3091(2)	45(1)
C(13)	3625(3)	3184(3)	3315(2)	38(1)
C(14)	2858(3)	1546(3)	3029(2)	38(1)
C(15)	2486(3)	1091(3)	4036(2)	39(1)
C(16)	1613(3)	2027(3)	4606(2)	39(1)
C(17)	1194(3)	1767(3)	5536(2)	47(1)
C(18)	1672(3)	603(4)	5895(2)	53(1)
C(19)	2568(3)	-292(3)	5342(2)	53(1)
C(20)	2983(3)	-62(3)	4404(2)	46(1)
C(21)	3748(3)	551(3)	2406(2)	42(1)
C(22)	4411(3)	-310(3)	1892(2)	42(1)
C(23)	5231(3)	-1392(3)	1338(2)	41(1)
C(24)	6175(3)	-2085(4)	1850(2)	58(1)
C(25)	6966(4)	-3138(4)	1365(2)	66(1)
C(26)	6852(3)	-3536(3)	353(2)	50(1)
C(27)	5937(4)	-2878(4)	-174(2)	57(1)
C(28)	5119(4)	-1807(4)	323(2)	57(1)
C(29)	7718(4)	-5061(4)	-1080(2)	65(1)
C(30)	8712(4)	-6296(5)	-1258(3)	81(1)

C(31) 8892(5) -6823(5) -2330(3) 87(1)

Table 18. Bond lengths [Å] and angles [°] for **21**.

O(1)-C(26)	1.360(3)	C(9)-H(9)	0.9500
O(1)-C(29)	1.422(4)	C(10)-C(11)	1.379(4)
C(1)-C(2)	1.376(4)	C(10)-H(10)	0.9500
C(1)-C(6)	1.395(4)	C(11)-C(12)	1.384(4)
C(1)-C(14)	1.543(3)	C(11)-H(11)	0.9500
C(2)-C(3)	1.389(4)	C(12)-C(13)	1.379(4)
C(2)-H(2)	0.9500	C(12)-H(12)	0.9500
C(3)-C(4)	1.365(4)	C(13)-C(14)	1.541(4)
C(3)-H(3)	0.9500	C(14)-C(21)	1.467(4)
C(4)-C(5)	1.389(4)	C(14)-C(15)	1.546(4)
C(4)-H(4)	0.9500	C(15)-C(20)	1.382(4)
C(5)-C(6)	1.376(4)	C(15)-C(16)	1.390(3)
C(5)-H(5)	0.9500	C(16)-C(17)	1.390(4)
C(6)-C(7)	1.524(4)	C(17)-C(18)	1.378(4)
C(7)-C(16)	1.515(4)	C(17)-H(17)	0.9500
C(7)-C(8)	1.523(4)	C(18)-C(19)	1.372(4)
C(7)-H(7)	1.0000	C(18)-H(18)	0.9500
C(8)-C(9)	1.379(4)	C(19)-C(20)	1.391(4)
C(8)-C(13)	1.391(3)	C(19)-H(19)	0.9500
C(9)-C(10)	1.386(4)	C(20)-H(20)	0.9500

C(21)-C(22)	1.192(3)	C(1)-C(2)-C(3)	118.9(3)
C(22)-C(23)	1.435(4)	C(1)-C(2)-H(2)	120.6
C(23)-C(28)	1.379(4)	C(3)-C(2)-H(2)	120.6
C(23)-C(24)	1.392(4)	C(4)-C(3)-C(2)	120.8(3)
C(24)-C(25)	1.365(4)	C(4)-C(3)-H(3)	119.6
C(24)-H(24)	0.9500	C(2)-C(3)-H(3)	119.6
C(25)-C(26)	1.373(4)	C(3)-C(4)-C(5)	120.6(3)
C(25)-H(25)	0.9500	C(3)-C(4)-H(4)	119.7
C(26)-C(27)	1.367(4)	C(5)-C(4)-H(4)	119.7
C(27)-C(28)	1.397(4)	C(6)-C(5)-C(4)	119.1(3)
C(27)-H(27)	0.9500	C(6)-C(5)-H(5)	120.5
C(28)-H(28)	0.9500	C(4)-C(5)-H(5)	120.5
C(29)-C(30)	1.532(5)	C(5)-C(6)-C(1)	120.2(2)
C(29)-H(29A)	0.9900	C(5)-C(6)-C(7)	126.7(2)
C(29)-H(29B)	0.9900	C(1)-C(6)-C(7)	113.1(2)
C(30)-C(31)	1.484(5)	C(16)-C(7)-C(8)	104.9(2)
C(30)-H(30A)	0.9900	C(16)-C(7)-C(6)	106.1(2)
C(30)-H(30B)	0.9900	C(8)-C(7)-C(6)	106.3(2)
C(31)-H(31A)	0.9800	C(16)-C(7)-H(7)	113.0
C(31)-H(31B)	0.9800	C(8)-C(7)-H(7)	113.0
C(31)-H(31C)	0.9800	C(6)-C(7)-H(7)	113.0
C(26)-O(1)-C(29)	119.7(2)	C(9)-C(8)-C(13)	120.2(3)
C(2)-C(1)-C(6)	120.4(2)	C(9)-C(8)-C(7)	126.5(2)
C(2)-C(1)-C(14)	126.1(2)	C(13)-C(8)-C(7)	113.2(2)
C(6)-C(1)-C(14)	113.5(2)	C(8)-C(9)-C(10)	119.4(3)

C(8)-C(9)-H(9)	120.3	C(17)-C(16)-C(7)	126.3(2)
C(10)-C(9)-H(9)	120.3	C(18)-C(17)-C(16)	119.8(3)
C(11)-C(10)-C(9)	120.2(3)	C(18)-C(17)-H(17)	120.1
C(11)-C(10)-H(10)	119.9	C(16)-C(17)-H(17)	120.1
C(9)-C(10)-H(10)	119.9	C(19)-C(18)-C(17)	120.3(3)
C(10)-C(11)-C(12)	120.7(3)	C(19)-C(18)-H(18)	119.9
C(10)-C(11)-H(11)	119.6	C(17)-C(18)-H(18)	119.9
C(12)-C(11)-H(11)	119.6	C(18)-C(19)-C(20)	120.8(3)
C(13)-C(12)-C(11)	119.1(3)	C(18)-C(19)-H(19)	119.6
C(13)-C(12)-H(12)	120.4	C(20)-C(19)-H(19)	119.6
C(11)-C(12)-H(12)	120.4	C(15)-C(20)-C(19)	119.0(3)
C(12)-C(13)-C(8)	120.4(2)	C(15)-C(20)-H(20)	120.5
C(12)-C(13)-C(14)	126.0(2)	C(19)-C(20)-H(20)	120.5
C(8)-C(13)-C(14)	113.6(2)	C(22)-C(21)-C(14)	176.8(3)
C(21)-C(14)-C(13)	114.5(2)	C(21)-C(22)-C(23)	175.6(3)
C(21)-C(14)-C(1)	113.1(2)	C(28)-C(23)-C(24)	117.7(2)
C(13)-C(14)-C(1)	105.7(2)	C(28)-C(23)-C(22)	123.6(3)
C(21)-C(14)-C(15)	113.9(2)	C(24)-C(23)-C(22)	118.7(2)
C(13)-C(14)-C(15)	103.52(18)	C(25)-C(24)-C(23)	121.4(3)
C(1)-C(14)-C(15)	105.2(2)	C(25)-C(24)-H(24)	119.3
C(20)-C(15)-C(16)	120.4(2)	C(23)-C(24)-H(24)	119.3
C(20)-C(15)-C(14)	126.6(2)	C(24)-C(25)-C(26)	120.4(3)
C(16)-C(15)-C(14)	113.0(2)	C(24)-C(25)-H(25)	119.8
C(15)-C(16)-C(17)	119.7(3)	C(26)-C(25)-H(25)	119.8
C(15)-C(16)-C(7)	113.9(2)	O(1)-C(26)-C(27)	125.6(3)

O(1)-C(26)-C(25)	114.5(3)	H(29A)-C(29)-H(29B)	108.7
C(27)-C(26)-C(25)	119.9(3)	C(31)-C(30)-C(29)	111.3(3)
C(26)-C(27)-C(28)	119.7(3)	C(31)-C(30)-H(30A)	109.4
C(26)-C(27)-H(27)	120.2	C(29)-C(30)-H(30A)	109.4
C(28)-C(27)-H(27)	120.2	C(31)-C(30)-H(30B)	109.4
C(23)-C(28)-C(27)	121.0(3)	C(29)-C(30)-H(30B)	109.4
C(23)-C(28)-H(28)	119.5	H(30A)-C(30)-H(30B)	108.0
C(27)-C(28)-H(28)	119.5	C(30)-C(31)-H(31A)	109.5
O(1)-C(29)-C(30)	106.0(3)	C(30)-C(31)-H(31B)	109.5
O(1)-C(29)-H(29A)	110.5	H(31A)-C(31)-H(31B)	109.5
C(30)-C(29)-H(29A)	110.5	C(30)-C(31)-H(31C)	109.5
O(1)-C(29)-H(29B)	110.5	H(31A)-C(31)-H(31C)	109.5
C(30)-C(29)-H(29B)	110.5	H(31B)-C(31)-H(31C)	109.5

Symmetry transformations used to generate equivalent atoms:

Table 19. Anisotropic displacement parameters ($\text{\AA}^2 \times 10^3$) for **21**. The anisotropic displacement factor exponent takes the form: $-2\pi^2 [h^2 a^{*2} U^{11} + \dots + 2 h k a^* b^* U^{12}]$

	U ¹¹	U ²²	U ³³	U ²³	U ¹³	U ¹²
O(1)	75(2)	87(2)	57(1)	-11(1)	4(1)	44(1)
C(1)	37(1)	45(2)	38(1)	-3(1)	2(1)	8(1)
C(2)	47(2)	73(2)	41(2)	-11(2)	-1(1)	15(2)
C(3)	52(2)	116(3)	48(2)	-16(2)	-13(2)	19(2)

C(4)	46(2)	117(3)	58(2)	-6(2)	-11(2)	29(2)
C(5)	44(2)	74(2)	55(2)	-2(2)	2(1)	23(2)
C(6)	38(2)	49(2)	41(2)	1(1)	2(1)	12(1)
C(7)	39(2)	44(2)	43(2)	-6(1)	4(1)	17(1)
C(8)	38(1)	41(2)	35(1)	2(1)	-3(1)	11(1)
C(9)	54(2)	40(2)	49(2)	0(1)	-6(1)	16(1)
C(10)	61(2)	38(2)	64(2)	6(2)	-12(2)	1(2)
C(11)	44(2)	54(2)	62(2)	13(2)	-2(1)	-1(2)
C(12)	39(2)	51(2)	43(2)	7(1)	1(1)	7(1)
C(13)	39(2)	38(2)	36(1)	4(1)	1(1)	11(1)
C(14)	35(1)	39(2)	37(1)	-4(1)	4(1)	11(1)
C(15)	35(1)	37(2)	38(1)	-4(1)	-3(1)	4(1)
C(16)	35(1)	42(2)	37(1)	-4(1)	1(1)	4(1)
C(17)	41(2)	51(2)	40(2)	-8(1)	3(1)	0(1)
C(18)	58(2)	57(2)	38(2)	6(2)	-2(1)	-6(2)
C(19)	62(2)	46(2)	50(2)	7(1)	-8(2)	2(2)
C(20)	48(2)	38(2)	48(2)	-1(1)	-3(1)	7(1)
C(21)	38(2)	43(2)	41(2)	-1(1)	0(1)	8(1)
C(22)	38(2)	43(2)	41(1)	-1(1)	5(1)	9(1)
C(23)	37(1)	39(2)	43(2)	-3(1)	7(1)	9(1)
C(24)	59(2)	77(2)	39(2)	-2(2)	4(1)	29(2)
C(25)	70(2)	84(2)	49(2)	2(2)	2(2)	43(2)
C(26)	45(2)	51(2)	55(2)	-3(1)	9(1)	22(1)
C(27)	71(2)	69(2)	32(2)	-4(1)	8(1)	26(2)
C(28)	69(2)	64(2)	40(2)	0(1)	0(1)	30(2)

C(29)	65(2)	68(2)	56(2)	-12(2)	8(2)	20(2)
C(30)	63(2)	97(3)	73(2)	-19(2)	5(2)	28(2)
C(31)	100(3)	87(3)	71(2)	-8(2)	12(2)	35(2)

Table 20. Hydrogen coordinates ($\times 10^4$) and isotropic displacement parameters ($\text{\AA}^2 \times 10^3$) for **21**.

	x	y	z	U(eq)
H(2)	1356	183	1231	67
H(3)	-1033	458	679	91
H(4)	-2426	2055	1633	90
H(5)	-1493	3395	3183	69
H(7)	624	3963	4546	51
H(9)	2723	6232	4639	57
H(10)	5166	7165	4271	66
H(11)	6615	5609	3305	64
H(12)	5654	3104	2692	54
H(17)	580	2390	5923	56
H(18)	1381	419	6529	64
H(19)	2909	-1078	5603	64
H(20)	3598	-688	4022	55
H(24)	6270	-1819	2550	70

H(25)	7600	-3599	1730	79
H(27)	5857	-3148	-875	69
H(28)	4477	-1359	-45	68
H(29A)	8143	-4208	-1390	78
H(29B)	6694	-5448	-1364	78
H(30A)	9710	-5909	-931	97
H(30B)	8257	-7150	-958	97
H(31A)	7902	-7137	-2662	130
H(31B)	9453	-7672	-2422	130
H(31C)	9440	-6007	-2613	130

5. Crystallography data for compound **39**.

Crystal data for **39**: C₁₁ H₁₀ F₆ O, M = 272.19, monoclinic, space group C 2/c (No. 15), a = 23.6068(4), b = 23.5051(4), c = 18.5135(4) Å, V = 9339.1(3) Å³, Z = 32, D_c = 1.549 Mg m⁻³, F₀₀₀ = 4416, Mo Kα radiation, λ = 0.71073 Å, T = 120 K, 2θ_{max} = 52.74°, 40576 reflections collected, 9546 unique (R_{int} = 0.0559). Final *Goof* = 1.039, R₁ = 0.0552, wR₂ = 0.1349, R indices based on 7653 reflections with I > 2.00σ (I) (refinement on F²), 751 parameters, 639 restraints. Lp and absorption corrections applied, μ = 0.162 mm⁻¹.

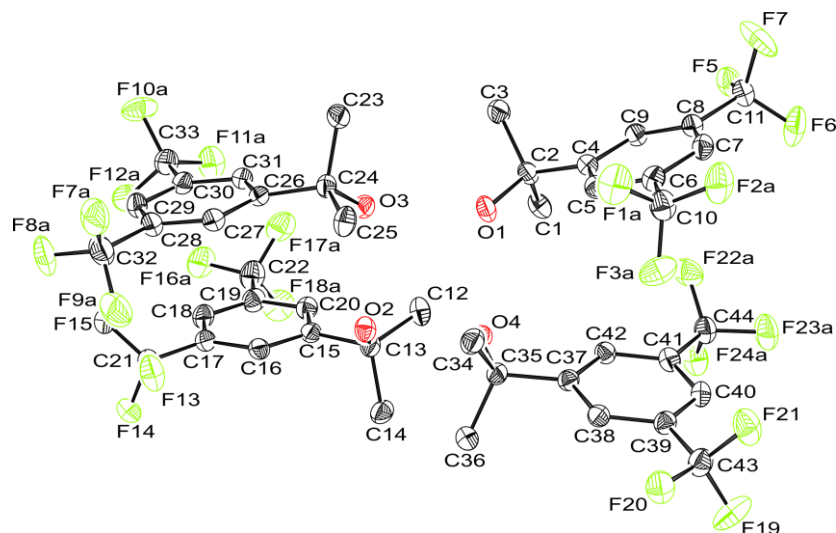


Figure 5. Crystallographic ORTEP diagram of compound **39**

Table 21. Crystal data and structure refinement for **39**.

Identification code	09srv148	
Empirical formula	C ₁₁ H ₁₀ F ₆ O	
Formula weight	272.19	
Temperature	120(2) K	
Wavelength	0.71073 Å	
Crystal system	Monoclinic	
Space group	C 2/c	
Unit cell dimensions	a = 23.6068(4) Å	α = 90°.
	b = 23.5051(4) Å	β = 114.6170(10)°.
	c = 18.5135(4) Å	γ = 90°.
Volume	9339.1(3) Å ³	
Z	32	
Density (calculated)	1.549 Mg/m ³	
Absorption coefficient	0.162 mm ⁻¹	

F(000)	4416
Crystal size	0.40 x 0.40 x 0.40 mm ³
Theta range for data collection	1.28 to 26.37°.
Index ranges	-29<=h<=29, -27<=k<=29, -23<=l<=23
Reflections collected	40576
Independent reflections	9546 [R(int) = 0.0271]
Completeness to theta = 25.00°	99.9 %
Absorption correction	Semi-empirical from equivalents
Max. and min. transmission	0.937 and 0.865
Refinement method	Full-matrix least-squares on F ²
Data / restraints / parameters	9546 / 639 / 751
Goodness-of-fit on F ²	1.039
Final R indices [I>2sigma(I)]	R1 = 0.0552, wR2 = 0.1349
R indices (all data)	R1 = 0.0695, wR2 = 0.1482
Largest diff. peak and hole	0.760 and -0.851 e.Å ⁻³

Table 22. Atomic coordinates (x 10⁴) and equivalent isotropic displacement parameters (Å²x 10³) for **39**. U(eq) is defined as one third of the trace of the orthogonalized U^{ij} tensor.

	x	y	z	U(eq)
F(1A)	3859(3)	2806(3)	6669(4)	49(1)
F(1B)	4099(2)	2704(2)	6876(2)	49(1)
F(1C)	3576(2)	2830(3)	6048(6)	49(1)

F(2A)	4620(2)	2426(2)	6541(4)	48(1)
F(2B)	4496(2)	2404(2)	6081(4)	48(1)
F(2C)	4459(3)	2549(2)	6908(3)	48(1)
F(3A)	3769(2)	2700(2)	5487(2)	45(1)
F(3B)	3595(2)	2806(2)	5658(3)	45(1)
F(3C)	4249(4)	2521(2)	5651(4)	45(1)
F(5)	6192(1)	4593(1)	6627(1)	38(1)
F(6)	6211(1)	3744(1)	6241(1)	53(1)
F(7)	6371(1)	3907(1)	7448(1)	66(1)
F(7A)	45(2)	5311(2)	6674(2)	52(1)
F(7B)	23(5)	5119(2)	6344(7)	52(1)
F(7C)	-23(3)	5579(3)	6777(2)	52(1)
F(8A)	-470(2)	6042(2)	5974(3)	56(1)
F(8B)	-232(5)	5972(5)	6504(7)	56(1)
F(8C)	-523(2)	5980(3)	5615(4)	56(1)
F(9A)	-306(2)	5294(2)	5428(2)	56(1)
F(9B)	-485(4)	5654(6)	5310(3)	56(1)
F(9C)	-186(3)	5145(2)	5672(4)	56(1)
F(10A)	1440(20)	7532(19)	6891(15)	48(3)
F(10B)	1380(40)	7480(30)	6900(20)	48(3)
F(11A)	1758(2)	7462(5)	5930(3)	45(1)
F(11B)	1874(3)	7451(8)	6185(6)	45(1)
F(12A)	803(10)	7574(18)	5680(20)	42(3)
F(12B)	858(16)	7600(30)	5620(30)	42(3)
F(13)	-272(1)	6062(1)	3996(1)	45(1)

F(14)	-609(1)	6743(1)	3148(1)	41(1)
F(15)	-242(1)	6926(1)	4394(1)	40(1)
F(16A)	1213(3)	8300(2)	4094(3)	48(1)
F(16B)	1335(5)	8242(4)	4341(5)	48(1)
F(16C)	1076(3)	8284(3)	3690(7)	48(1)
F(16D)	1106(7)	8167(6)	3287(8)	48(1)
F(17A)	2122(1)	7935(3)	4501(2)	49(1)
F(17B)	2163(2)	7904(5)	4311(6)	49(1)
F(17C)	1991(4)	8020(4)	4634(3)	49(1)
F(17D)	1594(10)	8169(7)	4583(7)	49(1)
F(18A)	1624(3)	8037(2)	3270(2)	50(1)
F(18B)	1362(5)	8105(4)	3183(3)	50(1)
F(18C)	1794(6)	7942(5)	3394(6)	50(1)
F(18D)	2087(5)	7896(7)	3864(14)	50(1)
F(19)	2909(1)	1881(1)	2620(1)	54(1)
F(20)	2400(1)	1801(1)	3344(1)	39(1)
F(21)	3386(1)	1669(1)	3850(1)	44(1)
F(22A)	4546(2)	4024(2)	4496(2)	44(1)
F(22B)	4719(2)	3695(3)	4587(2)	44(1)
F(22C)	4786(2)	3395(2)	4297(4)	44(1)
F(23A)	4706(2)	3340(2)	3802(4)	46(1)
F(23B)	4524(2)	3428(2)	3392(3)	46(1)
F(23C)	4316(3)	3777(3)	3145(2)	46(1)
F(24A)	4175(2)	4064(2)	3236(2)	42(1)
F(24B)	4196(2)	4233(1)	3548(4)	42(1)

F(24C)	4389(3)	4215(2)	4192(4)	42(1)
O(1)	3287(1)	4783(1)	5693(1)	29(1)
O(2)	1685(1)	5332(1)	4197(1)	27(1)
O(3)	2416(1)	5535(1)	5760(1)	27(1)
O(4)	2427(1)	4428(1)	4197(1)	28(1)
C(1)	3971(1)	5293(1)	5245(1)	31(1)
C(2)	3922(1)	4957(1)	5923(1)	24(1)
C(3)	4110(1)	5323(1)	6668(2)	33(1)
C(4)	4327(1)	4425(1)	6108(1)	23(1)
C(5)	4083(1)	3886(1)	6090(1)	25(1)
C(6)	4467(1)	3408(1)	6263(1)	26(1)
C(7)	5099(1)	3460(1)	6464(1)	27(1)
C(8)	5343(1)	4000(1)	6485(1)	25(1)
C(9)	4963(1)	4478(1)	6306(1)	24(1)
C(10)	4185(1)	2833(1)	6222(1)	34(1)
C(11)	6027(1)	4060(1)	6702(2)	30(1)
C(12)	2423(1)	5881(1)	3885(2)	32(1)
C(13)	1739(1)	5768(1)	3678(1)	24(1)
C(14)	1405(1)	5549(1)	2827(1)	33(1)
C(15)	1393(1)	6288(1)	3784(1)	24(1)
C(16)	816(1)	6211(1)	3812(1)	25(1)
C(17)	475(1)	6675(1)	3865(1)	27(1)
C(18)	699(1)	7227(1)	3897(1)	30(1)
C(19)	1275(1)	7303(1)	3882(1)	31(1)
C(20)	1621(1)	6837(1)	3821(1)	27(1)

C(21)	-157(1)	6598(1)	3855(1)	32(1)
C(22)	1534(1)	7888(1)	3919(1)	42(1)
C(23)	2649(1)	5383(1)	7125(1)	32(1)
C(24)	2147(1)	5326(1)	6279(1)	23(1)
C(25)	1956(1)	4709(1)	6082(2)	32(1)
C(26)	1602(1)	5717(1)	6181(1)	23(1)
C(27)	1036(1)	5511(1)	6133(1)	26(1)
C(28)	565(1)	5888(1)	6092(1)	30(1)
C(29)	653(1)	6469(1)	6101(1)	30(1)
C(30)	1218(1)	6674(1)	6138(1)	28(1)
C(31)	1688(1)	6304(1)	6175(1)	25(1)
C(32)	-37(1)	5648(1)	6051(1)	40(1)
C(33)	1321(1)	7302(1)	6177(1)	35(1)
C(34)	2104(1)	3602(1)	4709(1)	29(1)
C(35)	2213(1)	3853(1)	4015(1)	23(1)
C(36)	1608(1)	3870(1)	3260(1)	30(1)
C(37)	2703(1)	3509(1)	3870(1)	22(1)
C(38)	2600(1)	2932(1)	3679(1)	23(1)
C(39)	3037(1)	2612(1)	3540(1)	24(1)
C(40)	3588(1)	2857(1)	3586(1)	26(1)
C(41)	3691(1)	3427(1)	3779(1)	25(1)
C(42)	3255(1)	3752(1)	3918(1)	23(1)
C(43)	2928(1)	1994(1)	3338(2)	31(1)
C(44)	4282(1)	3701(1)	3840(1)	30(1)

Table 23. Bond lengths [\AA] and angles [$^\circ$] for **39**.

F(1A)-C(10)	1.347(3)	F(11A)-C(33)	1.345(3)
F(1B)-C(10)	1.344(3)	F(11B)-C(33)	1.344(3)
F(1C)-C(10)	1.337(3)	F(12A)-C(33)	1.344(3)
F(2A)-C(10)	1.346(3)	F(12B)-C(33)	1.344(3)
F(2B)-C(10)	1.335(2)	F(13)-C(21)	1.338(3)
F(2C)-C(10)	1.339(3)	F(14)-C(21)	1.343(3)
F(3A)-C(10)	1.341(3)	F(15)-C(21)	1.340(3)
F(3B)-C(10)	1.350(3)	F(16A)-C(22)	1.350(2)
F(3C)-C(10)	1.345(3)	F(16B)-C(22)	1.353(3)
F(5)-C(11)	1.337(3)	F(16C)-C(22)	1.354(3)
F(6)-C(11)	1.333(3)	F(16D)-C(22)	1.355(3)
F(7)-C(11)	1.327(3)	F(17A)-C(22)	1.361(3)
F(7A)-C(32)	1.345(2)	F(17B)-C(22)	1.354(3)
F(7B)-C(32)	1.341(3)	F(17C)-C(22)	1.350(3)
F(7C)-C(32)	1.339(3)	F(17D)-C(22)	1.351(3)
F(8A)-C(32)	1.342(2)	F(18A)-C(22)	1.350(2)
F(8B)-C(32)	1.347(3)	F(18B)-C(22)	1.350(3)
F(8C)-C(32)	1.342(3)	F(18C)-C(22)	1.354(3)
F(9A)-C(32)	1.348(3)	F(18D)-C(22)	1.351(3)
F(9B)-C(32)	1.340(3)	F(19)-C(43)	1.338(3)
F(9C)-C(32)	1.345(3)	F(20)-C(43)	1.332(3)
F(10A)-C(33)	1.343(3)	F(21)-C(43)	1.340(3)
F(10B)-C(33)	1.343(3)	F(22A)-C(44)	1.344(2)

F(22B)-C(44)	1.337(3)	C(4)-C(5)	1.387(3)
F(22C)-C(44)	1.345(3)	C(4)-C(9)	1.395(3)
F(23A)-C(44)	1.337(2)	C(5)-C(6)	1.393(3)
F(23B)-C(44)	1.349(3)	C(5)-H(5)	0.9500
F(23C)-C(44)	1.336(3)	C(6)-C(7)	1.384(3)
F(24A)-C(44)	1.345(2)	C(6)-C(10)	1.496(3)
F(24B)-C(44)	1.343(3)	C(7)-C(8)	1.389(3)
F(24C)-C(44)	1.345(3)	C(7)-H(7)	0.9500
O(1)-C(2)	1.436(3)	C(8)-C(9)	1.389(3)
O(1)-H(1)	0.8400	C(8)-C(11)	1.499(3)
O(2)-C(13)	1.446(3)	C(9)-H(9)	0.9500
O(2)-H(2)	0.8400	C(12)-C(13)	1.521(3)
O(3)-C(24)	1.441(3)	C(12)-H(12A)	0.9800
O(3)-H(3)	0.8400	C(12)-H(12B)	0.9800
O(4)-C(35)	1.435(3)	C(12)-H(12C)	0.9800
O(4)-H(4)	0.8400	C(13)-C(15)	1.527(3)
C(1)-C(2)	1.527(3)	C(13)-C(14)	1.527(3)
C(1)-H(1A)	0.9800	C(14)-H(14A)	0.9800
C(1)-H(1B)	0.9800	C(14)-H(14B)	0.9800
C(1)-H(1C)	0.9800	C(14)-H(14C)	0.9800
C(2)-C(4)	1.524(3)	C(15)-C(20)	1.389(3)
C(2)-C(3)	1.526(3)	C(15)-C(16)	1.395(3)
C(3)-H(3A)	0.9800	C(16)-C(17)	1.386(3)
C(3)-H(3B)	0.9800	C(16)-H(16)	0.9500
C(3)-H(3C)	0.9800	C(17)-C(18)	1.392(3)

C(17)-C(21)	1.495(3)	C(31)-H(31)	0.9500
C(18)-C(19)	1.383(3)	C(34)-C(35)	1.528(3)
C(18)-H(18)	0.9500	C(34)-H(34A)	0.9800
C(19)-C(20)	1.399(3)	C(34)-H(34B)	0.9800
C(19)-C(22)	1.495(4)	C(34)-H(34C)	0.9800
C(20)-H(20)	0.9500	C(35)-C(37)	1.524(3)
C(23)-C(24)	1.526(3)	C(35)-C(36)	1.528(3)
C(23)-H(23A)	0.9800	C(36)-H(36A)	0.9800
C(23)-H(23B)	0.9800	C(36)-H(36B)	0.9800
C(23)-H(23C)	0.9800	C(36)-H(36C)	0.9800
C(24)-C(25)	1.519(3)	C(37)-C(42)	1.390(3)
C(24)-C(26)	1.528(3)	C(37)-C(38)	1.398(3)
C(25)-H(25A)	0.9800	C(38)-C(39)	1.385(3)
C(25)-H(25B)	0.9800	C(38)-H(38)	0.9500
C(25)-H(25C)	0.9800	C(39)-C(40)	1.392(3)
C(26)-C(27)	1.389(3)	C(39)-C(43)	1.496(3)
C(26)-C(31)	1.396(3)	C(40)-C(41)	1.382(3)
C(27)-C(28)	1.398(3)	C(40)-H(40)	0.9500
C(27)-H(27)	0.9500	C(41)-C(42)	1.391(3)
C(28)-C(29)	1.380(4)	C(41)-C(44)	1.496(3)
C(28)-C(32)	1.501(3)	C(42)-H(42)	0.9500
C(29)-C(30)	1.393(3)	C(2)-O(1)-H(1)	109.5
C(29)-H(29)	0.9500	C(13)-O(2)-H(2)	109.5
C(30)-C(31)	1.387(3)	C(24)-O(3)-H(3)	109.5
C(30)-C(33)	1.494(3)	C(35)-O(4)-H(4)	109.5

C(2)-C(1)-H(1A)	109.5	C(7)-C(6)-C(10)	119.98(19)
C(2)-C(1)-H(1B)	109.5	C(5)-C(6)-C(10)	118.98(19)
H(1A)-C(1)-H(1B)	109.5	C(6)-C(7)-C(8)	118.5(2)
C(2)-C(1)-H(1C)	109.5	C(6)-C(7)-H(7)	120.8
H(1A)-C(1)-H(1C)	109.5	C(8)-C(7)-H(7)	120.8
H(1B)-C(1)-H(1C)	109.5	C(7)-C(8)-C(9)	120.8(2)
O(1)-C(2)-C(4)	108.16(17)	C(7)-C(8)-C(11)	118.8(2)
O(1)-C(2)-C(3)	107.67(18)	C(9)-C(8)-C(11)	120.4(2)
C(4)-C(2)-C(3)	109.87(18)	C(8)-C(9)-C(4)	120.6(2)
O(1)-C(2)-C(1)	109.29(18)	C(8)-C(9)-H(9)	119.7
C(4)-C(2)-C(1)	110.70(18)	C(4)-C(9)-H(9)	119.7
C(3)-C(2)-C(1)	111.05(19)	F(1C)-C(10)-F(2C)	105.8(5)
C(2)-C(3)-H(3A)	109.5	F(2B)-C(10)-F(1B)	108.0(4)
C(2)-C(3)-H(3B)	109.5	F(1C)-C(10)-F(3C)	105.7(5)
H(3A)-C(3)-H(3B)	109.5	F(2C)-C(10)-F(3C)	107.7(5)
C(2)-C(3)-H(3C)	109.5	F(3A)-C(10)-F(2A)	112.4(4)
H(3A)-C(3)-H(3C)	109.5	F(3A)-C(10)-F(1A)	104.4(4)
H(3B)-C(3)-H(3C)	109.5	F(2A)-C(10)-F(1A)	102.9(4)
C(5)-C(4)-C(9)	118.5(2)	F(2B)-C(10)-F(3B)	106.8(4)
C(5)-C(4)-C(2)	122.06(19)	F(1B)-C(10)-F(3B)	101.1(4)
C(9)-C(4)-C(2)	119.44(19)	F(2B)-C(10)-C(6)	115.1(3)
C(4)-C(5)-C(6)	120.5(2)	F(1C)-C(10)-C(6)	115.3(3)
C(4)-C(5)-H(5)	119.7	F(2C)-C(10)-C(6)	111.9(3)
C(6)-C(5)-H(5)	119.7	F(3A)-C(10)-C(6)	112.6(3)
C(7)-C(6)-C(5)	121.0(2)	F(1B)-C(10)-C(6)	112.8(3)

F(3C)-C(10)-C(6)	109.9(3)	C(13)-C(14)-H(14C)	109.5
F(2A)-C(10)-C(6)	112.3(3)	H(14A)-C(14)-H(14C)	109.5
F(1A)-C(10)-C(6)	111.5(3)	H(14B)-C(14)-H(14C)	109.5
F(3B)-C(10)-C(6)	112.0(3)	C(20)-C(15)-C(16)	118.9(2)
F(7)-C(11)-F(6)	107.1(2)	C(20)-C(15)-C(13)	122.2(2)
F(7)-C(11)-F(5)	106.5(2)	C(16)-C(15)-C(13)	118.8(2)
F(6)-C(11)-F(5)	105.69(19)	C(17)-C(16)-C(15)	120.4(2)
F(7)-C(11)-C(8)	112.1(2)	C(17)-C(16)-H(16)	119.8
F(6)-C(11)-C(8)	112.2(2)	C(15)-C(16)-H(16)	119.8
F(5)-C(11)-C(8)	112.78(19)	C(16)-C(17)-C(18)	120.9(2)
C(13)-C(12)-H(12A)	109.5	C(16)-C(17)-C(21)	120.7(2)
C(13)-C(12)-H(12B)	109.5	C(18)-C(17)-C(21)	118.3(2)
H(12A)-C(12)-H(12B)	109.5	C(19)-C(18)-C(17)	118.7(2)
C(13)-C(12)-H(12C)	109.5	C(19)-C(18)-H(18)	120.7
H(12A)-C(12)-H(12C)	109.5	C(17)-C(18)-H(18)	120.7
H(12B)-C(12)-H(12C)	109.5	C(18)-C(19)-C(20)	120.9(2)
O(2)-C(13)-C(12)	109.52(17)	C(18)-C(19)-C(22)	120.3(2)
O(2)-C(13)-C(15)	106.43(17)	C(20)-C(19)-C(22)	118.8(2)
C(12)-C(13)-C(15)	113.33(19)	C(15)-C(20)-C(19)	120.2(2)
O(2)-C(13)-C(14)	107.26(18)	C(15)-C(20)-H(20)	119.9
C(12)-C(13)-C(14)	110.88(19)	C(19)-C(20)-H(20)	119.9
C(15)-C(13)-C(14)	109.14(18)	F(13)-C(21)-F(15)	106.9(2)
C(13)-C(14)-H(14A)	109.5	F(13)-C(21)-F(14)	106.6(2)
C(13)-C(14)-H(14B)	109.5	F(15)-C(21)-F(14)	105.94(18)
H(14A)-C(14)-H(14B)	109.5	F(13)-C(21)-C(17)	113.22(19)

F(15)-C(21)-C(17)	112.3(2)	C(23)-C(24)-C(26)	109.01(18)
F(14)-C(21)-C(17)	111.4(2)	C(24)-C(25)-H(25A)	109.5
F(18A)-C(22)-F(16A)	109.8(4)	C(24)-C(25)-H(25B)	109.5
F(17D)-C(22)-F(18D)	108.9(12)	H(25A)-C(25)-H(25B)	109.5
F(18B)-C(22)-F(16B)	108.7(6)	C(24)-C(25)-H(25C)	109.5
F(17C)-C(22)-F(18C)	105.5(7)	H(25A)-C(25)-H(25C)	109.5
F(17C)-C(22)-F(16C)	110.9(7)	H(25B)-C(25)-H(25C)	109.5
F(18C)-C(22)-F(16C)	104.5(7)	C(27)-C(26)-C(31)	118.8(2)
F(18B)-C(22)-F(17B)	109.4(7)	C(27)-C(26)-C(24)	122.5(2)
F(16B)-C(22)-F(17B)	103.9(6)	C(31)-C(26)-C(24)	118.55(19)
F(17D)-C(22)-F(16D)	107.8(12)	C(26)-C(27)-C(28)	120.3(2)
F(18D)-C(22)-F(16D)	109.0(12)	C(26)-C(27)-H(27)	119.8
F(18A)-C(22)-F(17A)	101.4(4)	C(28)-C(27)-H(27)	119.8
F(16A)-C(22)-F(17A)	103.9(4)	C(29)-C(28)-C(27)	120.9(2)
C(24)-C(23)-H(23A)	109.5	C(29)-C(28)-C(32)	120.4(2)
C(24)-C(23)-H(23B)	109.5	C(27)-C(28)-C(32)	118.7(2)
H(23A)-C(23)-H(23B)	109.5	C(28)-C(29)-C(30)	118.7(2)
C(24)-C(23)-H(23C)	109.5	C(28)-C(29)-H(29)	120.7
H(23A)-C(23)-H(23C)	109.5	C(30)-C(29)-H(29)	120.7
H(23B)-C(23)-H(23C)	109.5	C(31)-C(30)-C(29)	121.0(2)
O(3)-C(24)-C(25)	109.50(17)	C(31)-C(30)-C(33)	120.4(2)
O(3)-C(24)-C(23)	106.52(18)	C(29)-C(30)-C(33)	118.6(2)
C(25)-C(24)-C(23)	110.85(19)	C(30)-C(31)-C(26)	120.3(2)
O(3)-C(24)-C(26)	107.40(17)	C(30)-C(31)-H(31)	119.9
C(25)-C(24)-C(26)	113.28(19)	C(26)-C(31)-H(31)	119.9

F(9B)-C(32)-F(7B)	109.3(8)	F(10B)-C(33)-C(30)	108(3)
F(7C)-C(32)-F(8C)	109.4(4)	F(12B)-C(33)-C(30)	114(3)
F(8A)-C(32)-F(7A)	109.3(3)	F(12A)-C(33)-C(30)	111(2)
F(7C)-C(32)-F(9C)	108.0(5)	F(11B)-C(33)-C(30)	113.3(8)
F(8C)-C(32)-F(9C)	103.0(5)	F(11A)-C(33)-C(30)	113.1(5)
F(9B)-C(32)-F(8B)	107.7(8)	C(35)-C(34)-H(34A)	109.5
F(7B)-C(32)-F(8B)	106.1(8)	C(35)-C(34)-H(34B)	109.5
F(8A)-C(32)-F(9A)	105.6(3)	H(34A)-C(34)-H(34B)	109.5
F(7A)-C(32)-F(9A)	102.6(3)	C(35)-C(34)-H(34C)	109.5
F(7C)-C(32)-C(28)	111.5(3)	H(34A)-C(34)-H(34C)	109.5
F(9B)-C(32)-C(28)	112.0(5)	H(34B)-C(34)-H(34C)	109.5
F(7B)-C(32)-C(28)	112.9(5)	O(4)-C(35)-C(37)	108.72(17)
F(8A)-C(32)-C(28)	114.1(3)	O(4)-C(35)-C(34)	109.46(17)
F(8C)-C(32)-C(28)	111.4(4)	C(37)-C(35)-C(34)	110.51(18)
F(7A)-C(32)-C(28)	112.5(2)	O(4)-C(35)-C(36)	107.04(18)
F(9C)-C(32)-C(28)	113.1(4)	C(37)-C(35)-C(36)	109.99(17)
F(8B)-C(32)-C(28)	108.6(5)	C(34)-C(35)-C(36)	111.03(19)
F(9A)-C(32)-C(28)	112.0(3)	C(35)-C(36)-H(36A)	109.5
F(10B)-C(33)-F(12B)	108(5)	C(35)-C(36)-H(36B)	109.5
F(10A)-C(33)-F(12A)	104(3)	H(36A)-C(36)-H(36B)	109.5
F(10B)-C(33)-F(11B)	102(3)	C(35)-C(36)-H(36C)	109.5
F(12B)-C(33)-F(11B)	110(2)	H(36A)-C(36)-H(36C)	109.5
F(10A)-C(33)-F(11A)	110.1(17)	H(36B)-C(36)-H(36C)	109.5
F(12A)-C(33)-F(11A)	104.2(13)	C(42)-C(37)-C(38)	118.35(19)
F(10A)-C(33)-C(30)	114.2(19)	C(42)-C(37)-C(35)	122.11(19)

C(38)-C(37)-C(35)	119.54(19)	F(19)-C(43)-C(39)	111.8(2)
C(39)-C(38)-C(37)	120.5(2)	F(21)-C(43)-C(39)	111.9(2)
C(39)-C(38)-H(38)	119.7	F(22B)-C(44)-F(24B)	110.4(4)
C(37)-C(38)-H(38)	119.7	F(23A)-C(44)-F(22A)	109.3(3)
C(38)-C(39)-C(40)	121.0(2)	F(23C)-C(44)-F(24C)	105.8(4)
C(38)-C(39)-C(43)	120.6(2)	F(23C)-C(44)-F(22C)	106.6(4)
C(40)-C(39)-C(43)	118.4(2)	F(24C)-C(44)-F(22C)	103.7(4)
C(41)-C(40)-C(39)	118.5(2)	F(23A)-C(44)-F(24A)	104.1(3)
C(41)-C(40)-H(40)	120.8	F(22A)-C(44)-F(24A)	104.4(3)
C(39)-C(40)-H(40)	120.8	F(22B)-C(44)-F(23B)	106.8(4)
C(40)-C(41)-C(42)	121.0(2)	F(24B)-C(44)-F(23B)	103.1(4)
C(40)-C(41)-C(44)	119.67(19)	F(23C)-C(44)-C(41)	114.3(3)
C(42)-C(41)-C(44)	119.30(19)	F(23A)-C(44)-C(41)	114.7(2)
C(37)-C(42)-C(41)	120.7(2)	F(22B)-C(44)-C(41)	111.6(3)
C(37)-C(42)-H(42)	119.7	F(24B)-C(44)-C(41)	112.9(3)
C(41)-C(42)-H(42)	119.7	F(22A)-C(44)-C(41)	112.3(2)
F(20)-C(43)-F(19)	107.2(2)	F(24C)-C(44)-C(41)	113.8(3)
F(20)-C(43)-F(21)	106.37(19)	F(22C)-C(44)-C(41)	111.7(3)
F(19)-C(43)-F(21)	105.87(19)	F(24A)-C(44)-C(41)	111.3(2)
F(20)-C(43)-C(39)	113.17(19)	F(23B)-C(44)-C(41)	111.6(3)

Symmetry transformations used to generate equivalent atoms:

Table 24. Anisotropic displacement parameters ($\text{\AA}^2 \times 10^3$) for **39**. The anisotropic displacement factor exponent takes the form: $-2\pi^2 [h^2 a^{*2} U^{11} + \dots + 2 h k a^* b^* U^{12}]$

	U ¹¹	U ²²	U ³³	U ²³	U ¹³	U ¹²
F(1A)	54(2)	36(1)	69(2)	2(1)	38(1)	-9(1)
F(1B)	54(2)	36(1)	69(2)	2(1)	38(1)	-9(1)
F(1C)	54(2)	36(1)	69(2)	2(1)	38(1)	-9(1)
F(2A)	51(1)	22(1)	79(2)	-3(2)	34(2)	2(1)
F(2B)	51(1)	22(1)	79(2)	-3(2)	34(2)	2(1)
F(2C)	51(1)	22(1)	79(2)	-3(2)	34(2)	2(1)
F(3A)	63(2)	28(1)	43(1)	-11(1)	23(1)	-15(1)
F(3B)	63(2)	28(1)	43(1)	-11(1)	23(1)	-15(1)
F(3C)	63(2)	28(1)	43(1)	-11(1)	23(1)	-15(1)
F(5)	24(1)	33(1)	53(1)	-6(1)	14(1)	-4(1)
F(6)	41(1)	41(1)	94(1)	-22(1)	45(1)	-6(1)
F(7)	23(1)	111(2)	53(1)	38(1)	5(1)	11(1)
F(7A)	40(1)	71(2)	58(2)	6(2)	32(1)	-3(2)
F(7B)	40(1)	71(2)	58(2)	6(2)	32(1)	-3(2)
F(7C)	40(1)	71(2)	58(2)	6(2)	32(1)	-3(2)
F(8A)	28(1)	65(1)	83(2)	-2(2)	29(2)	9(1)
F(8B)	28(1)	65(1)	83(2)	-2(2)	29(2)	9(1)
F(8C)	28(1)	65(1)	83(2)	-2(2)	29(2)	9(1)
F(9A)	32(2)	65(2)	69(2)	-8(2)	19(1)	-11(1)

F(9B)	32(2)	65(2)	69(2)	-8(2)	19(1)	-11(1)
F(9C)	32(2)	65(2)	69(2)	-8(2)	19(1)	-11(1)
F(10A)	69(9)	30(7)	34(1)	-10(2)	9(2)	1(4)
F(10B)	69(9)	30(7)	34(1)	-10(2)	9(2)	1(4)
F(11A)	45(2)	29(1)	66(4)	0(4)	27(3)	0(2)
F(11B)	45(2)	29(1)	66(4)	0(4)	27(3)	0(2)
F(12A)	52(4)	29(3)	38(5)	2(2)	11(3)	11(4)
F(12B)	52(4)	29(3)	38(5)	2(2)	11(3)	11(4)
F(13)	33(1)	36(1)	73(1)	3(1)	27(1)	2(1)
F(14)	25(1)	54(1)	35(1)	-5(1)	4(1)	7(1)
F(15)	29(1)	52(1)	38(1)	-11(1)	14(1)	6(1)
F(16A)	60(1)	24(1)	62(2)	-5(1)	28(1)	2(1)
F(16B)	60(1)	24(1)	62(2)	-5(1)	28(1)	2(1)
F(16C)	60(1)	24(1)	62(2)	-5(1)	28(1)	2(1)
F(16D)	60(1)	24(1)	62(2)	-5(1)	28(1)	2(1)
F(17A)	58(1)	34(1)	58(2)	-13(1)	29(1)	-10(1)
F(17B)	58(1)	34(1)	58(2)	-13(1)	29(1)	-10(1)
F(17C)	58(1)	34(1)	58(2)	-13(1)	29(1)	-10(1)
F(17D)	58(1)	34(1)	58(2)	-13(1)	29(1)	-10(1)
F(18A)	64(2)	34(1)	56(1)	9(1)	29(1)	-6(1)
F(18B)	64(2)	34(1)	56(1)	9(1)	29(1)	-6(1)
F(18C)	64(2)	34(1)	56(1)	9(1)	29(1)	-6(1)
F(18D)	64(2)	34(1)	56(1)	9(1)	29(1)	-6(1)
F(19)	92(1)	35(1)	48(1)	-17(1)	41(1)	-9(1)
F(20)	34(1)	25(1)	59(1)	-8(1)	20(1)	-7(1)

F(21)	37(1)	24(1)	67(1)	4(1)	18(1)	6(1)
F(22A)	27(1)	55(2)	46(1)	-2(1)	12(1)	-12(1)
F(22B)	27(1)	55(2)	46(1)	-2(1)	12(1)	-12(1)
F(22C)	27(1)	55(2)	46(1)	-2(1)	12(1)	-12(1)
F(23A)	30(1)	47(1)	71(2)	0(2)	30(1)	2(1)
F(23B)	30(1)	47(1)	71(2)	0(2)	30(1)	2(1)
F(23C)	30(1)	47(1)	71(2)	0(2)	30(1)	2(1)
F(24A)	34(1)	32(1)	67(2)	5(1)	29(1)	-3(1)
F(24B)	34(1)	32(1)	67(2)	5(1)	29(1)	-3(1)
F(24C)	34(1)	32(1)	67(2)	5(1)	29(1)	-3(1)
O(1)	19(1)	31(1)	37(1)	0(1)	11(1)	4(1)
O(2)	28(1)	24(1)	29(1)	6(1)	14(1)	7(1)
O(3)	28(1)	31(1)	24(1)	1(1)	13(1)	2(1)
O(4)	31(1)	21(1)	31(1)	-4(1)	12(1)	1(1)
C(1)	24(1)	29(1)	35(1)	7(1)	8(1)	4(1)
C(2)	19(1)	23(1)	29(1)	-1(1)	7(1)	1(1)
C(3)	28(1)	28(1)	36(1)	-7(1)	7(1)	5(1)
C(4)	22(1)	25(1)	22(1)	-1(1)	8(1)	2(1)
C(5)	22(1)	26(1)	27(1)	-2(1)	10(1)	0(1)
C(6)	29(1)	24(1)	29(1)	-1(1)	14(1)	0(1)
C(7)	28(1)	24(1)	30(1)	2(1)	14(1)	6(1)
C(8)	22(1)	29(1)	24(1)	0(1)	10(1)	2(1)
C(9)	23(1)	23(1)	26(1)	0(1)	10(1)	0(1)
C(10)	33(1)	25(1)	44(1)	1(1)	16(1)	1(1)
C(11)	24(1)	31(1)	36(1)	2(1)	12(1)	4(1)

C(12)	29(1)	30(1)	41(1)	8(1)	18(1)	7(1)
C(13)	27(1)	24(1)	24(1)	4(1)	12(1)	6(1)
C(14)	40(1)	33(1)	24(1)	1(1)	12(1)	12(1)
C(15)	25(1)	26(1)	20(1)	2(1)	7(1)	5(1)
C(16)	24(1)	24(1)	24(1)	-1(1)	7(1)	4(1)
C(17)	25(1)	29(1)	25(1)	-2(1)	8(1)	6(1)
C(18)	33(1)	24(1)	33(1)	-1(1)	13(1)	8(1)
C(19)	36(1)	26(1)	33(1)	0(1)	14(1)	3(1)
C(20)	29(1)	27(1)	28(1)	1(1)	13(1)	2(1)
C(21)	26(1)	33(1)	33(1)	-5(1)	10(1)	6(1)
C(22)	47(2)	29(1)	54(2)	0(1)	26(1)	2(1)
C(23)	28(1)	42(1)	24(1)	4(1)	10(1)	10(1)
C(24)	24(1)	23(1)	25(1)	2(1)	12(1)	4(1)
C(25)	36(1)	24(1)	42(1)	1(1)	23(1)	4(1)
C(26)	23(1)	27(1)	19(1)	-2(1)	8(1)	3(1)
C(27)	24(1)	28(1)	24(1)	-1(1)	10(1)	1(1)
C(28)	23(1)	40(1)	28(1)	-1(1)	10(1)	3(1)
C(29)	26(1)	35(1)	30(1)	1(1)	12(1)	9(1)
C(30)	29(1)	28(1)	25(1)	-2(1)	11(1)	5(1)
C(31)	23(1)	27(1)	23(1)	-2(1)	9(1)	2(1)
C(32)	26(1)	50(2)	45(2)	2(1)	15(1)	2(1)
C(33)	37(1)	29(1)	37(1)	-3(1)	14(1)	7(1)
C(34)	30(1)	32(1)	30(1)	-4(1)	16(1)	-1(1)
C(35)	22(1)	21(1)	26(1)	-4(1)	10(1)	0(1)
C(36)	24(1)	33(1)	31(1)	-4(1)	9(1)	2(1)

C(37)	23(1)	22(1)	21(1)	0(1)	9(1)	1(1)
C(38)	21(1)	23(1)	24(1)	-1(1)	9(1)	-1(1)
C(39)	27(1)	21(1)	23(1)	1(1)	10(1)	3(1)
C(40)	24(1)	25(1)	30(1)	1(1)	14(1)	5(1)
C(41)	23(1)	26(1)	27(1)	3(1)	11(1)	2(1)
C(42)	22(1)	20(1)	25(1)	0(1)	9(1)	1(1)
C(43)	32(1)	26(1)	37(1)	-3(1)	17(1)	0(1)
C(44)	26(1)	30(1)	38(1)	0(1)	17(1)	1(1)

Table 25. Hydrogen coordinates ($\times 10^4$) and isotropic displacement parameters ($\text{\AA}^2 \times 10^3$) for **39**.

	x	y	z	U(eq)
H(1)	3080	5058	5747	35
H(2)	1874	5038	4161	32
H(3)	2154	5506	5286	32
H(4)	2707	4445	4662	34
H(1A)	3823	5057	4765	46
H(1B)	4406	5399	5392	46
H(1C)	3715	5637	5142	46
H(3A)	3829	5650	6556	49
H(3B)	4539	5458	6829	40
H(3C)	4085	5096	7098	60

H(5)	3651	3841	5959	30
H(7)	5359	3133	6583	32
H(9)	5137	4844	6318	29
H(12A)	2624	6037	4424	48
H(12B)	2459	6154	3506	48
H(12C)	2628	5524	3858	48
H(14A)	1615	5207	2761	49
H(14B)	1413	5843	2456	49
H(14C)	971	5458	2717	49
H(16)	657	5837	3795	30
H(18)	462	7544	3928	36
H(20)	2014	6896	3805	33
H(23A)	3005	5141	7189	48
H(23B)	2479	5265	7503	48
H(23C)	2786	5780	7226	48
H(25A)	1626	4683	5542	48
H(25B)	1802	4558	6461	48
H(25C)	2317	4485	6116	48
H(27)	968	5113	6128	31
H(29)	335	6723	6083	36
H(31)	2069	6452	6198	30
H(34A)	1783	3824	4788	44
H(34B)	2493	3616	5192	44
H(34C)	1966	3206	4590	44
H(36A)	1689	4031	2825	45

H(36B)	1301	4106	3350	45
H(36C)	1443	3483	3120	45
H(38)	2226	2757	3644	27
H(40)	3886	2637	3488	31
H(42)	3334	4144	4048	27

Table 26. Hydrogen bonds for **39** [\AA and $^\circ$].

D-H...A	d(D-H)	d(H...A)	d(D...A)	$\angle(\text{DHA})$
O(1)-H(1)...O(3)	0.84	1.94	2.752(2)	163.9
O(2)-H(2)...O(4)	0.84	1.92	2.753(2)	170.7
O(3)-H(3)...O(2)	0.84	1.90	2.725(2)	168.0
O(4)-H(4)...O(1)	0.84	1.99	2.794(2)	158.9

Symmetry transformations used to generate equivalent atoms: